ISBN: 978-3-95450-261-5 ISSN: 2673-7000 doi: 10.18429/JACoW-NAPAC2025-MOXP02

APS UPGRADE: COMMISSIONING THE WORLD'S FIRST LIGHT SOURCE BASED ON SWAP-OUT INJECTION*

V. Sajaev†, M. Borland, J. Calvey, J. Dooling, L. Emery, K. Harkay, N. Kuklev, O. Mohsen, Y. Sun, N. Arnold, T. Berenc, A. Brill, H. Bui, J. Carwardine, W. Cheng, T. Fors, M. Kelly, R. Lindberg, G. Shen, M. Smith, F. Rafael, H. Shang, R. Soliday, U. Wienands, B. Yang
Argonne National Laboratory, Lemont, IL, USA

Abstract

The Advanced Photon Source (APS) has recently completed a major upgrade, replacing its 25-year-old storage ring with a cutting-edge hybrid seven-bend achromat lattice enhanced by six additional reverse bends. The new design achieves a natural emittance of 42 pm-rad, enabling the production of X-rays up to 500 times brighter than those generated by the original APS. A key innovation of the upgrade is the implementation of a swap-out injection scheme, which replaces entire depleted bunches instead of performing traditional top-up injection. This approach enables on-axis injection to accommodate for the reduced dynamic aperture resulting from strong focusing. This paper outlines the commissioning process, shares initial operating experience with swap-out injection, and presents performance data for new systems such as the bunch-lengthening cavity.

INTRODUCTION

The Advanced Photon Source (APS) recently completed a major upgrade [1], replacing its original double-bend achromat-based [2] storage ring [3] with a hybrid seven-bend achromat lattice, similar to the one implemented earlier at ESRF-EBS [4]. To further reduce the natural emittance, the APS Upgrade (APS-U) lattice incorporates six reverse bends in addition to the seven main bending magnets [5, 6]. The new design also utilizes swap-out injection [7, 8], which enables operation with a smaller dynamic aperture – a key factor in achieving ultra-low emittance.

As part of the upgrade, the electron beam energy was reduced from 7 GeV to 6 GeV, necessitating modifications of all insertion devices. The project also included the construction of seven entirely new beamlines, as well as significant modifications to most of the remaining beamlines to accommodate for the new source characteristics. Although the injector complex – comprising a 450-MeV linear accelerator [9], the Particle Accumulator Ring (PAR) [10], and the booster [11] – was not part of the official APS-U scope, it underwent targeted refurbishment in parallel to enhance reliability and operational performance.

APS operations were halted on April 24, 2023, to begin the storage ring replacement and injector maintenance. The linac was restarted in September 2023, followed by the PAR in October, and the booster in Febuary 2024 [12, 13]. Assembly of the upgraded storage ring was completed on February 15, and, after extensive tests without beam, the commissioning approval was granted on April 10, 2024. In this paper, we present an overview of the commissioning process and summarize the performance of the new storage ring.

APS-U COMMISSIONING

BTS Commissioning

Commissioning officially started when the beam was extracted from the Booster into the Booster-to-Storage Ring (BTS) transfer line. The Booster-to-Storage Ring (BTS) transfer line is divided into two sections by the wall separating the booster and storage ring tunnels. The booster-side section of the BTS remained unchanged, while the storage ring (SR) section was completely redesigned to accommodate the new SR geometry. A key feature of the redesigned BTS is the emittance exchange section, which consists of six skew quadrupoles configured to exchange the horizontal and vertical emittances of the beam extracted from the booster [14]. This exchange is necessary to match the injected beam to the narrow 2.8 mm horizontal gap between the outboard wall of the septum magnet and the inboard blade of the first injection kicker.

The original BTS section features a relatively large-aperture vacuum chamber and three one-plane stripline BPMs. In contrast, the new SR-side BTS section has a reduced aperture and is equipped with 11 two-plane button BPMs, providing improved diagnostics suited to the tighter aperture.

When the first beam was extracted from the booster, it successfully traversed the booster-side section of the BTS but was lost between the last BPM in the large-aperture booster section and the first BPM in the redesigned, smaller-aperture storage ring (SR) section. Trajectory correction program failed to advance the beam beyond that point using corrector magnets only. Subsequently, a transmission optimization routine that varied both corrector magnets and quadrupole strengths was able to push the beam farther along the BTS – nearly to its end – but still with significant losses, and no beam could be injected into the storage ring.

Further investigation revealed that the quadrupole changes made by the optimization routine, which improved beam transport past the initial loss point, were consistent with a scenario in which all five quadrupoles in the legacy (booster-side) section of the BTS were powered with reversed polarity. This hypothesis was confirmed by trajectory response measurements. The reversed polarity had a plausible explanation: the original APS was designed to operate with positrons,

* Work supported by the U.S. Department of Energy, Office of Science, Office of Basic Energy Sciences, under Contract No. DE-AC02-06CH11357.

† sajaev@anl.gov

Content from this work may be used under the terms of the CC BY 4.0 licence (© 2022). Any distribution of this work must maintain attribution to the author(s), title of the work, publisher, and DOI.

ISBN: 978-3-95450-261-5 ISSN: 2673-7000 doi: 10.18429/JACoW-NAPAC2025-MOYD01

THE FUTURE CIRCULAR COLLIDER IN EUROPE*

M. Benedikt, F. Zimmermann†, CERN, Geneva, Switzerland

Abstract

The proposed Future Circular Collider (FCC) integrated programme consists of two stages: An electron–positron collider serving as a highest-luminosity Higgs-boson, electroweak and top-quark factory, followed by a proton–proton collider with a collision energy around 100 TeV. In 2021, the CERN Council initiated the FCC Feasibility Study. This study covered, inter alia, physics objectives and potential, geology, civil engineering, technical infrastructure, territorial implementation, environmental aspects, R&D needs for the accelerators and detectors, socio-economic benefits, and cost. The Feasibility Study was completed on 31 March 2025. The subsequent European Strategy Symposium has singled out the FCC as the by-far preferred future collider option for CERN. We present a few study highlights, the status, and the next steps.

INTRODUCTION

A circular Higgs factory was first proposed in 2011, after initial hints at a possible discovery from the LHC experiments [2]. This concept was then driven forward in 2012–2013, mostly as a community initiative. In response to the 2013 Update of the European Strategy for Particle Physics (ESPP) [3], in 2014 the global Future Circular Collider (FCC) study was set up. This study, which was partly supported by the EU co-funded EuroCirCol project [4], resulted in four volumes of Conceptual Design Report (CDR), notably volume 2 on the FCC-ee lepton collider [5]. Following the 2020 ESPP Update (ESPPU) [6], the CERN Council launched the FCC Feasibility Study (FS). Like the concept study, the FS was organised as an international collaboration comprising more than 150 participating institutes from around the world. Parts of the FS work were carried out within the EU co-funded FCC Innovation Study [7]. The resulting Feasibility Study Report (FSR) was submitted as complementary input to the 2025/26 ESPP Update [8–10]. It presents a baseline technical design and discusses, as requested, numerous other key feasibility aspects, including tunnel construction, cost, sustainability and environmental conditions.

THE FCC INTEGRATED PROGRAMME

The FCC 'integrated programme' consists of an initial electron-positron collider FCC-ee, which is followed by a proton-proton collider, FCC-hh. This sequence is well matched to the current scientific landscape after 15 years of LHC operation. The proposed staging takes into account: (1) the physics priorities as developed and stated by ESPPU 2013 and 2020; and (2) the relative technology readiness and costs of FCC-ee and FCC-hh. The FCC integrated programme is also aligned with the 2023 US Particle Physics Project Prioritization Panel (P5) recommendations [11].

Both FCC-ee and FCC-hh are installed in the same 91 km circumference tunnel close to CERN. The FCC-hh reuses all the FCC-ee civil engineering and much of the technical infrastructure, thereby maximising the return on investment. The FCC layout features 8 arcs of equal length, 4 technical straights and 4 experimental straights, as is illustrated in Fig. 1. Taking advantage of the four-fold superperiodicity for maximum performance, FCC-ee and FCC-hh each accommodate four detectors. Parameters and luminosity scenarios for the FCC-hh are presented in Ref. [12].

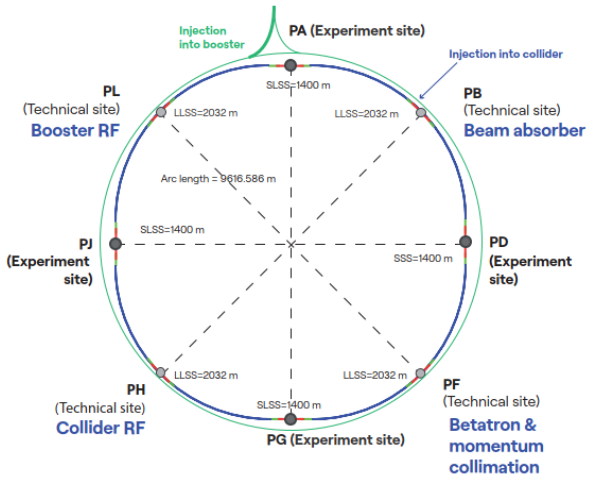


Figure 1: The layout of the FCC-ee, illustrating the four collision points and the four technical insertions [9].

FCC-ee DESIGN AND OPERATION PLAN

For maximum performance, the FCC-ee is conceived as a double-ring collider with separate beam pipes for electrons and positrons, which does not only allow for storing a large number of bunches but also for tapering of magnet strengths to match the local energy of each beam, even with an 'energy sawtooth' due to synchrotron radiation. The luminosity is maximised by regular top-up injection from a full-energy booster synchrotron, which shares the collider tunnel.

The FCC-ee operates at four baseline centre-of-mass energies, corresponding to the Z pole, the WW pair production, the ZH production peak, and the $t\bar{t}$ production threshold, always delivering the highest possible luminosities to four experiments. The main parameters for each FCC-ee mode of operation are listed in Table 1. Both natural bunch lengths due to synchrotron radiation (SR) and collision values including beamstrahlung (BS) are shown in the table. The FCC-ee collider rings feature a combination of 400 MHz

* This title is a modified update of Ref. [1]

† frank.zimmermann@cern.ch

Content from this work may be used under the terms of the CC BY 4.0 licence (© 2022). Any distribution of this work must maintain attribution to the author(s), title of the work, publisher, and DOI.

ISBN: 978-3-95450-261-5 ISSN: 2673-7000 doi: 10.18429/JACoW-NAPAC2025-MOYD02

RECENT EXPERIENCE WITH HIGH-LUMINOSITY OPERATION OF SuperKEKB

Y. Ohnishi*, High Energy Accelerator Research Organization (KEK), Tsukuba, Japan
on behalf of the SuperKEKB team

Content from this work may be used under the terms of the CC BY 4.0 licence (© 2022). Any distribution of this work must maintain attribution to the author(s), title of the work, publisher, and DOI.

Abstract

SuperKEKB is a positron-electron collider employing the nano-beam scheme which enable an extremely low beta function at the interaction point (IP) compared to the bunch length. The vertical beta function at the IP is less than 1 mm, the smallest among all existing and previous colliders. We discuss recent results on beam-beam interactions and the performance of the crab-waist scheme, which enhances luminosity. Sudden beam loss, which cannot be explained by conventional beam dynamics, and the nonlinear collimator – a key device for reducing both beam background and impedance – are also highlighted as crucial issues. This paper presents recent machine operation results and performance achievements of SuperKEKB, which provide insight into the design of future high-energy and high-luminosity colliders.

INTRODUCTION

The luminosity for e^+e^- colliders is expressed by

$$L = \frac{N_+ N_- n_b f_0}{2\pi\sqrt{\sigma_{x+}^{*2} + \sigma_{x-}^{*2}}\sqrt{\sigma_{y+}^{*2} + \sigma_{y-}^{*2}}} R_L, \tag{1}$$

where $N_\pm$ is the bunch population for positrons or electrons, n_b is the number of bunches, f_0 is the revolution frequency, $\sigma_{x,y}^*$ is the transverse beam size at the interaction point (IP), and R_L is the luminosity reduction factor due to the geometrical loss such as an hourglass and a crossing angle effects.

For flat beams, achieving a vertical beam size σ_y^* in the range of 30-50 nm is typically a design goal for high-luminosity colliders [1]. This implies that both the vertical beta function at the IP, β_y^*, and the vertical emittance, ε_y, must be below 1 mm and 10 pm, respectively. The hourglass requirement to reduce the luminosity reduction is

$$\beta_y^* > \frac{\sigma_z}{\sqrt{1+\Phi^2}}, \tag{2}$$

where Φ is the Piwinski angle defined by

$$\Phi = \frac{\sigma_z}{\sigma_x^*}\tan\frac{\theta_c}{2}, \tag{3}$$

σ_z is the bunch length, and θ_c is the crossing angle. However, it is difficult to shorten σ_z to less than 1 mm. To overcome the hourglass effect, a large Piwinski angle is required, which implies a large crossing angle and a low emittance. This approach is known as the nano-beam scheme. In the case of SuperKEKB, Φ is approximately 12 with the current machine parameters, and σ_z is typically about 6 mm. Accordingly, β_y^* can, in principle, be squeezed down to 0.5 mm.

In the nano-beam scheme, the luminosity reduction becomes

$$R_L = \left(1 + \frac{\sigma_{z+}^2 + \sigma_{z-}^2}{\sigma_{x+}^{*2} + \sigma_{x-}^{*2}}\tan^2\frac{\theta_c}{2}\right)^{-1/2} R_H, \tag{4}$$

where R_H is the another luminosity reduction factor, which can be approximated to be 1. The luminosity formula is modified by using Eq.(4):

$$L = \frac{N_+ N_- n_b f_0}{\pi\theta_c\sqrt{\sigma_{z+}^2 + \sigma_{z-}^2}\sqrt{\sigma_{y+}^{*2} + \sigma_{y-}^{*2}}}. \tag{5}$$

The horizontal beam size at the IP, σ_x^* does not affect the luminosity explicitly.

On the other hand, the vertical beam-beam parameter is written by

$$\xi_{y\pm} = \frac{r_e}{\pi\gamma_\pm}\frac{\beta_{y\pm}^* N_\mp}{\theta_c\sigma_{z\pm}\sigma_{y\mp}^*} \propto N_\mp\sqrt{\frac{\beta_y^*}{\varepsilon_{y\mp}}}, \tag{6}$$

where $\gamma_\pm$ is the Lorentz factor. If β_y^* is the same value between two rings, ξ_y is proportional to square root of the ratio of β_y^* to ε_y. If the ratio can be constant, the luminosity increases as squeezing β_y^* and decreasing ε_y with keeping constant ξ_y.

Two advanced technologies have been adopted in the recent colliders: the nano-beam scheme, as described in the previous section, and the crab-waist scheme [2]. To implement the crab-waist scheme, a Hamiltonian of the form $H_{cw} = (1/2\tan\theta_c)x^* p_y^{*2}$ is introduced at the IP. The sextupoles located on both sides of the IP are employed to shift the vertical waist along the beam axis in response to the horizontal beam position. The phase advance between each crab-waist sextupole and the IP is adjusted to be $n\pi$ in the horizontal plane and $(m+1/2)\pi$ in the vertical place.

At SuperKEKB, the sextupoles used for the local chromaticity correction can also function as the crab-waist sextupoles [3]. The lattice design of the interaction region (IR) in the LER is shown in Fig. 1. The lattice design in the HER is similar to that of the LER. Two sextupoles are connected by $-I'$ transformation and the vertical phase advance between the first sextupole and the IP is almost $3\pi/2$ and π in the horizontal plane. Their magnetic field strength, k values are

$$K_2^{(1,2)} = K_2 \mp K_{2,cw}/2, \tag{7}$$

where

$$K_{2,cw} = \frac{R_{cw}}{\tan\theta_c}\frac{1}{\beta_y^s\beta_y^*}\sqrt{\frac{\beta_x^*}{\beta_x^s}}, \tag{8}$$

* yukiyoshi.onishi@kek.jp

ISBN: 978-3-95450-261-5 ISSN: 2673-7000 doi: 10.18429/JACoW-NAPAC2025-MOYN01

OPERATION OF THE APS-U INJECTORS WITH HIGH SINGLE BUNCH CHARGE*

J. Calvey†, T. Berenc, J. Dooling, K. Harkay, O. Mohsen, A. Nassiri, A. Puttkammer, F. Rafael, H. Shang, T. Smith, Y. Sun, G. Waldschmidt, U. Wienands, K. P. Wootton
Argonne National Laboratory, Lemont, IL, USA

Abstract

The APS-Upgrade uses swap-out injection, which means the injectors must supply a full charge bunch (up to 16 nC) to replace a depleted one in the storage ring. The APS injector chain consists of a linac, particle accumulator ring (PAR), and booster synchrotron. These machines were kept in place for the APS-U, with several improvements to support high charge operation. Major upgrades include a new timing system, improved diagnostics, and a new amplifier for bunch compression in the PAR. So far, the injectors have supported up to 140 mA storage ring current in the high charge (48 bunch) mode. This paper will summarize the work needed to achieve high injector charge, and report on operational experience so far.

INTRODUCTION

The APS-Upgrade (APS-U) is a 4th generation electron storage ring (SR) light source, which began operating in April 2024 [1]. It makes use of a seven-bend hybrid multi-bend achromat lattice with reverse bends to achieve a natural emittance of 42 pm at 6 GeV. The dynamic aperture of this lattice is too small to simultaneously accommodate both the stored and injected beam, which precludes top-up injection. As a result, a depleted bunch in the storage ring must be fully replaced by a high charge bunch from the injector, a process known as "swap-out" injection.

The APS-U has two modes of operation: a "brightness" mode with many (presently 216) low charge bunches, and a "timing" mode with 48 high charge bunches. Both modes have a desired storage ring current of 200 mA. In brightness mode, the highest injector charge required is about 5 nC, which is not difficult for the APS-U injectors. In timing mode, up to 17 nC injected charge is required, which is very challenging.

For the APS-Upgrade, it was decided to leave the old APS injector chain in place, and make individual improvements when needed. The injector chain consists of three machines, shown in Fig. 1), which operate at a 1-Hz rep rate:

- A linear accelerator (linac), which generates bunches of ~1 nC charge, and accelerates them to ~425 MeV.
- A particle accumulator ring (PAR), which captures and accumulates linac bunches in a single rf bucket, up to the desired charge. A 12th harmonic cavity (RF12) turns on 750 ms into the PAR cycle, which compresses the bunch before injection into the booster.

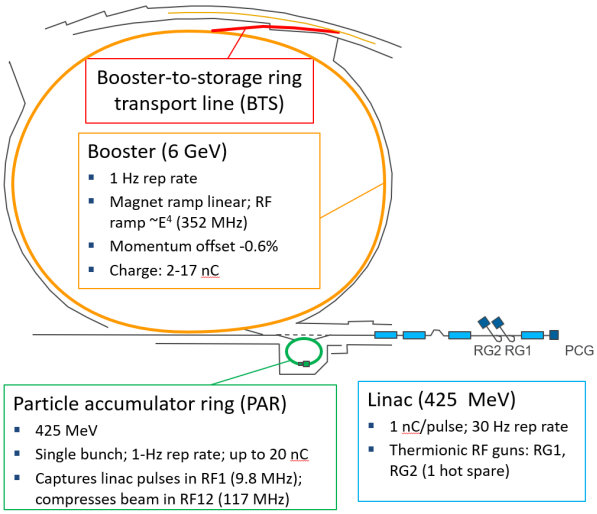


Figure 1: APS-U injector complex.

- A booster synchrotron, which accelerates the bunch up to 6 GeV before extraction to the storage ring. To reduce the extracted beam size, the booster is operated with a momentum offset of -0.6%.

There were many challenges in adapting these three machines for APS-U high charge operation.

LINAC CHALLENGES

For APS-U high charge mode, the linac must produce up to 20 bunches of at least 1 nC charge at a 30 Hz rate at 425 MeV or higher. The linac was nominally capable of meeting this requirement, but not with the consistency and reliability demanded by the APS-U. To close this gap, a linac refurbishment plan was implemented. Key items of this project include:

RF Upgrades

New 50 MW RF stations composed of a klystron and solid state modulator were procured, to provide higher linac energy and improved reliability. The first new RF station was procured and installed in an RF Test Stand for testing. Two additional new RF stations (Fig. 2) have been procured, installed and commissioned to support APS operations [2].

Along with the 50 MW RF stations, the RF control and diagnostic system was upgraded to a new digital LLRF system. A new Micro TCA.0 based digital low level RF (LLRF) system provides lower RF power and phase jitter levels.

* Work supported by the U.S. D.O.E., Office of Science, Office of Basic Energy Sciences, under contract number DE-AC02- 06CH11357.

† jcalvey@anl.gov

Content from this work may be used under the terms of the CC BY 4.0 licence (© 2022). Any distribution of this work must maintain attribution to the author(s), title of the work, publisher, and DOI.

ISBN: 978-3-95450-261-5 ISSN: 2673-7000 doi: 10.18429/JACoW-NAPAC2025-MOYN03

COMMISSIONING OF THE HEPS*

Y. Jiao†, W. Bao, J.S. Cao, S.Y. Chen, X.H. Cui, Y.H. Dong, Z. Duan, Y.Y. Guo, P. He, X.Y. Huang, Y.S. Huang, D.H. Ji, H.F. Ji, W. Kang, D.B. Li, J. Li, J.Y. Li, N. Li, X.Y. Li, Z.Q. Li, S.Y. Lin, Y.Z. Liu, X.H. Lu[1], Y.H. Lu, C. Meng, W.M. Pan, Y.M. Peng, L.Y. Qin, H.M. Qu, M.Y. Su, S.K. Tian, J.Q. Wang, N. Wang, Z.H. Wang, Y.Y. Wei, Y.F. Wu, G. Xu, H.S. Xu, F. Yan, Y.C. Yang, C.H. Yu, F.C. Zeng, J. Zhang, F.C. Zhao, Y.L. Zhao, Z.H. Zhao, H.J. Zheng
Institute of High Energy Physics, Beijing, China
[1]also at Spallation Neutron Source Science Center, Dongguan, China

Content from this work may be used under the terms of the CC BY 4.0 licence (© 2022). Any distribution of this work must maintain attribution to the author(s), title of the work, publisher, and DOI.

Abstract

The High Energy Photon Source (HEPS) is the first 4th generation light source being built in China, with a beam energy of 6 GeV, a circumference of 1360 m and a natural emittance of a few tens of picometers. As a green-field light source, the HEPS construction started in 2019 and is scheduled to be completed in 2025. Now civil construction, component fabrication and tunnel installation, and beam commissioning of the HEPS has been basically finished. In this report, the accelerator and especially the storage ring commissioning results, and main physics issues faced and corresponding measures during the beam commissioning will be presented.

INTRODUCTION

The High Energy Photon Source (HEPS) is the first fourth-generation synchrotron radiation facility project in China, and also China's the first synchrotron radiation light source project in high-energy region [1, 2].

Table 1: HEPS Main Performance Parameters

Parameter	Value	Unit
Beam energy	6	GeV
Beam current	200	mA
Circumference	1360.4	M
Natural emittance	34.8	pm·rad
Momentum compaction	1.83	10^{-5}
Energy loss per turn (w/o ID)	2.64	MeV

The HEPS storage ring is designed with electron energy of 6 GeV and natural emittance of 35 pm·rad. It is capable to accommodate not fewer than 90 high-performance beamlines (with 15 beamlines for Phase I). HEPS can provide X-rays with energies up to 300 keV, delivering synchrotron radiation with brightness of up to 1×10^{22} phs/(s·mm²·mrad²·0.1%BW) level at typical hard X-ray wavelength. It will feature spatial resolution on the order of 10 nanometers, energy resolution on the order of 1 meV, and temporal resolution on the order of 100 picoseconds. Main performance parameters of the HEPS are listed in Table 1.

After more than ten years' R&D, including the HEPS test facility project (2016-2018), the HEPS project started construction in mid-2019 [3] and has achieved multiple significant milestones [4]. In July 2022, the main civil construction was essentially completed; in 2023, beam commissioning of the Linac and booster was completed; in 2024, storage ring main equipment fabrication and tunnel installation were finished (with the exception of some devices whose fabrication and installation were delayed) and initial beam commissioning were completed; in March 2025 joint commissioning of the accelerator and beamlines was launched, and in May 2025 a few pilot experiments were performed. Right now, the last round of equipment installation is under way.

From the perspective of beam physics, following the completion of the preliminary design report in 2018 [5, 6], modification of the accelerator's overall design was performed and finished by the end of 2019 to address emerging challenges in the hardware and engineering design [7-11]. Before the end of 2021, design and studies on relevant physics issues were basically completed based on the final design [12,13]. From 2022 to the present, pre-commissioning preparations and beam commissioning were conducted. Pre-commissioning preparations include planning for the beam commissioning, commissioning process simulation, commissioning software development, and joint-debugging before the commissioning. It is worth mentioning that we developed a new modular framework for high-level application development, named *Pyapas*, based on which we developed the required high-level applications and adopted them in the HEPS commissioning [14-16]. Regarding the beam commissioning, in 2023 we completed the injector commissioning with beam parameters satisfying the design specifications. Details can be found in Refs. [17-19]. In 2024, storage ring commissioning was initiated and much advancement has been achieved. In the following specific progress on storage ring commissioning will be introduced in a detail.

STORAGE RING COMMISSIONING

As mentioned above, a few hardware systems were not fully ready at day one of the commissioning, e.g., stripline kickers and power supplies, some insertion devices (IDs) and ID vacuum chambers, 166 MHz RF cavities,

* Work supported by High Energy Photon Source (HEPS), a major national science and technology infrastructure and NSFC (12275284, 11922512).
† jiaoyi@ihep.ac.cn.

ISBN: 978-3-95450-261-5 ISSN: 2673-7000 doi: 10.18429/JACoW-NAPAC2025-MOZN01

EXPLORATION OF ULTRA-HIGH DOSE RATE RADIOBIOLOGY WITH LASER-DRIVEN PROTONS AT BELLA

L. Obst-Huebl*, J. L. Inman, J. T. De Chant[1], K. Nakamura, A. J. Gonsalves, A. McIlvenny, J. Bin, B. Simmons, C. G. R. Geddes, C. B. Schroeder, C. Y. Ralston, J. van Tilborg, J.-H. Mao, S. Hakimi, S. Kidd, S. Subramanian, A. Snijders, E. Esarey
Lawrence Berkeley National Laboratory, Berkeley, CA, USA
B. Stassel, University of Michigan, Ann Arbor, MI, USA
C. A. J. Palmer, Queen's University Belfast, Belfast BT7 1NN, UK
L. Geulig, Ludwig-Maximilians-Universitaet Munich, Geschwister-Scholl-Platz 1, Munich, Germany
[1]also at Michigan State University, East Lansing, MI, USA

Content from this work may be used under the terms of the CC BY 4.0 licence (© 2022). Any distribution of this work must maintain attribution to the author(s), title of the work, publisher, and DOI.

INTRODUCTION

Laser-driven proton sources are of interest for various applications due to their ability to produce short proton bunches with high charge and low emittance. These sources can be used in biological studies investigating improvements to radiation cancer therapy. Recently, the differential sparing effect on normal tissues versus tumors using the delivery of high radiation doses, typically above 10 Gy, at extremely high dose rates, called FLASH effect, has received increasing attention [1, 2]. However, the molecular and cellular mechanisms underlying the sparing effect are not yet fully understood. To explore these mechanisms, we have fielded capabilities at the BELLA petawatt (PW) laser of Lawrence Berkeley National Laboratory (LBNL) to deliver laser-driven proton bunches at ultra-high instantaneous dose rate up to 10^8 Gy/s. This allowed us to investigate in vitro and in vivo the damage to normal tissue after exposure with laser-driven protons and prescribed doses of up to several 10 Gy [3, 4]. Reference measurements using 320 kV x-rays using an x-ray tube (X-RAD320) at clinical dose rates and soft x-rays with tunable dose rates at the Advanced Light Source of LBNL were established. Recent improvements to the laser-driven proton source, delivery beamline, and diagnostic suite have also enabled first peptide sample irradiations to explore the sparing effect on the molecular level. This paper gives an overview of capabilities available at LBNL for radiobiological research with ultra-high instantaneous dose rate laser-driven proton beams.

The general proton beamline setup at the BELLA PW is displayed in Figure 1 and consists of a target normal sheath acceleration (TNSA) proton source, magnetic proton transport optics, scatter foils for beam smoothing, apertures, a dipole, an exit window, and a biosample station with dosimetry diagnostics located in air. The dipole magnet is used to deflect protons downward onto the samples that are placed below the plane of the laser, to avoid exposure to electrons, x-rays and gamma-rays possibly also emitted by the proton source. More details on available proton sources, transport optics, beam diagnostics and sample stations are given in the following sections. The proton beam propagation through the beamline is modeled using a homemade MATLAB simulation code that combines the features of a traditional map code, through the integration of COSY INFINITY [5], with a Monte Carlo (MC) based radiation transport code [6].

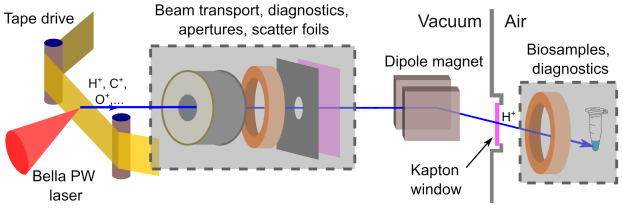


Figure 1: Laser-driven proton beamline for radiobiological studies at the BELLA PW laser of LBNL. Details of the general setup and options for beamline components in the grey placeholder boxes are given in the main text.

Proton bunches accelerated via TNSA are ultra-short on the order of picoseconds at the source and then spread in time leading to nanosecond to few 10 ns bunch lengths when reaching the sample location. Time of flight analysis using the distance from TNSA source to sample combined with proton bunch propagation simulations and dose measurements result in a peak dose rate on the order of 10^7 to 10^8 Gy/s for irradiations with BELLA protons, depending on the configuration.

PROTON SOURCES

Proton bunches are accelerated via target normal sheath acceleration (TNSA) from a 13 µm thick kapton tape drive using the BELLA PW laser [7] at LBNL with up to 40 J laser pulse energy and down to 35 fs laser pulse length. The laser system and tape drive target allow for shot repetition rates up to 1 Hz, although irradiations were thus far conducted at shot rates of approximately one shot every 5 to 20 seconds. Two laser focusing geometries ("interaction points") are available that lead to different proton beam parameters, while both produce typical TNSA proton spectra with characteristic exponential shapes and cut-off energies. In the first (interaction point 1, iP1), the laser is focused using a 13.5 m focal length off-axis parabolic (OAP) mirror to a spot size

* lobsthuebl@lbl.gov

ISBN: 978-3-95450-261-5 ISSN: 2673-7000 doi: 10.18429/JACoW-NAPAC2025-MOP001

ACCELERATOR DRIFT COMPENSATION VIA A MODIFIED MG-GPO ALGORITHM*

R. W. Y. Yeung[1], X. Huang,† Z. Zhang, SLAC, Menlo Park, CA, USA
Y. Hao, FRIB, East Lansing, MI, USA
[1]also at FRIB

Content from this work may be used under the terms of the CC BY 4.0 licence (© 2022). Any distribution of this work must maintain attribution to the author(s), title of the work, publisher, and DOI.

Abstract

Performance drift over long periods of operation due to changes in machines settings or the environment has been a longstanding problem for particle accelerators. Algorithms which are capable of tuning machine settings while keeping the performance within a desired threshold can be used to compensate for such drifts. We have developed a modified version of the Multi-Generation Gaussian Process Optimizer (MG-GPO) which is capable of tuning accelerator settings during user operation. The modified algorithm uses Gaussian Process regression to predict the performance of potential trial settings and removes ones with a high probability of giving too poor of a performance before selection for evaluation on the machine. The modified MG-GPO has been tested on analytic functions and applied to the SPEAR3 kicker-bump matching problem in both simulations and experiments as a proof of concept.

INTRODUCTION

Accelerator operation and commissioning benefit from online optimization algorithms that can be used to compensate for the differences between the accelerator design and the physical machine. Popular choices of optimization algorithms include the Nelder-Mead simplex method [1], the robust conjugate direction search [2], particle swarm optimization [3], and Bayesian optimization [4], which can efficiently provide optimal accelerator settings.

However, during the optimization process, these algorithms may sample accelerator settings which produce an unacceptably poor performance. This drawback is pertinent because initially-optimal settings in a particle accelerator often deteriorate in performance due to various changes in the environment, and the tendency of such algorithms to introduce poor performance in the process of finding the optimum will preclude their use during the accelerator's normal operation. The typical solution is to insert dedicated tuning periods in the schedule to re-optimize the accelerator after its performance deteriorates too much, leading to undesired interruptions to the user program. Therefore, developing online optimization algorithms that can be used to tune for optimal accelerator performance while keeping the performance within an acceptable threshold during the tuning process would be an impactful direction of research.

In this study, we have modified the Multi-Generation Gaussian Process Optimizer (MG-GPO) algorithm [5] to compensate for accelerator performance drift. The algorithm has been applied to the kicker-bump matching (KBM) problem in both simulation and experiment. In a simulated 4-dimensional KBM problem as well as an experimental 2-dimensional KBM problem, the algorithm shows promise in optimizing and maintaining the performance of the accelerator.

THE ALGORITHM

The algorithm developed in this study is based on modifications to the MG-GPO algorithm, a population-based evolutionary algorithm that incorporates Gaussian Process (GP) regression in seed selections [5]. The main modifications applied to the MG-GPO algorithm concern the modification of the GP regression algorithm to predict a time-varying input, the addition of a safety threshold, and the replacement of the candidate point generation mechanism. While MG-GPO is capable of optimizing multiple objectives simultaneously, our modified version currently addresss one objective at a time. Each candidate point represents the settings of the algorithm in the parameter space.

Candidate Point Generation

The original MG-GPO's candidate point generation schema presents several difficulties for maintaining optimized settings for a time-dependent objective function.

First, the seed points are taken from the best outputs saved from all previous generations. The positions of the points are saved according to their objective values at the time of their evaluation. With a drifting objective function, the objective value at the time of evaluation will differ from the objective value later. To address this, the seed points were changed to depend on the outputs of only the previous generation instead of on all the generations that have elapsed.

Assuming that the objective function is L-Lipschitz continuous, i.e.

$$|f(\vec{x}) - f(\vec{x}_0)| \leq L|\vec{x} - \vec{x}_0| \tag{1}$$

for objective function $f, \vec{x}, \vec{x}_0 \in \mathbf{D}$, where $\mathbf{D}$ is the domain of f, the minimum of each evaluation would be close to that of the previous generation. Given the continuity of the minimum over time, the minimum of a generation would necessarily be in the vicinity of the minimum of the previous. As such, a search near the previous minimum is sufficient to capture the new minimum, and the reliance on both MOGA and MOPSO as in the original MG-GPO is unnecessary for our purposes. Our acquisition function is modified accordingly

* Work supported by DOE Contract No. DE-AC02-76SF00515
† xiahuang@slac.stanford.edu

ISBN: 978-3-95450-261-5 ISSN: 2673-7000 doi: 10.18429/JACoW-NAPAC2025-MOP002

ADVANCING ACCELERATOR VIRTUAL BEAM DIAGNOSTICS THROUGH LATENT EVOLUTION MODELING: AN INTEGRATED SOLUTION TO FORWARD, INVERSE, TUNING, AND UQ PROBLEMS *

M. Rautela †, A. Scheinker, Los Alamos National Laboratory, Los Alamos, NM, USA

Abstract

Virtual beam diagnostics relies on computationally intensive beam dynamics simulations where high-dimensional charged particle beams evolve through the accelerator. We propose Latent Evolution Model (LEM), a hybrid machine learning framework with an autoencoder that projects high-dimensional phase spaces into lower-dimensional representations, coupled with transformers to learn temporal dynamics in the latent space. This approach provides a common foundational framework addressing multiple interconnected challenges in beam diagnostics. For *forward modeling*, a Conditional Variational Autoencoder (CVAE) encodes 15 unique projections of the 6D phase space into a latent representation, while a transformer predicts downstream latent states from upstream inputs. For *inverse problems*, we address two distinct challenges: (a) predicting upstream phase spaces from downstream observations by utilizing the same CVAE architecture with transformers trained on reversed temporal sequences along with aleatoric uncertainty quantification, and (b) estimating RF settings from the latent space of the trained LEM using a dedicated dense neural network that maps latent representations to RF parameters. For *tuning problems*, we leverage the trained LEM and RF estimator within a Bayesian optimization framework to determine optimal RF settings that minimize beam loss. This paper summarizes our recent efforts and demonstrates how this unified approach effectively addresses these traditionally separate challenges.

INTRODUCTION

Particle accelerators are high-dimensional spatiotemporal dynamical systems governed by hundreds to thousands of radio-frequency (RF) cavity and magnet parameters. The behavior of charged particle beams, in the form of a 6D phase space (x, y, z, p_x, p_y, p_z), evolves as the beam propagates through the accelerator components. Accurate prediction and control of the beam's phase space distribution are critical for minimizing beam loss and optimizing performance. During operation, time-consuming manual tuning is often required to achieve optimal performance. With limited experimental observations of the beam, the role of virtual diagnostics becomes crucial. In recent years, machine learning models have emerged as a promising tool for non-invasive virtual beam diagnostics in particle accelerators [1,2]. From a physics perspective, charged particle beam dynamics constitute a spatiotemporal phenomenon. The accelerator is a complex spatiotemporal dynamical system governed by numerous parameters. The problem of machine learning–based virtual beam diagnostics can be decomposed into multiple subproblems to systematically manage the complexity. Much of the recent progress in this direction employs standalone machine learning models to solve forward, inverse, and optimization problems.

Various ML-based models for accelerator diagnostics include integrated model-independent feedback with neural networks for automated shaping of the longitudinal phase space (LPS) of electron beams [3], predicting LPS distributions [4,5], phase advance scan evaluations [6], and arrival time or beam energy [7]. Physics-informed architectures, such as polynomial neural networks with symplectic regularization [8], deep Lie map networks for magnetic field error identification [9], and convolutional autoencoders for relating high-dimensional phase space data to beam loss [10], have further enhanced predictive accuracy. Fault analysis methods include explainable SHAP-based breakdown prediction in high-gradient cavities [11], classification of superconducting RF cavity faults [12], and conditional generative models for predicting errant pulses [13]. Backcasting efforts map downstream diagnostics to upstream phase space using adaptive ML [14], invertible neural networks for bidirectional prediction [15], tomography-based reconstruction [16], and differentiable particle tracking [17].

Bayesian optimization (BO) and its variants [18–22], deep reinforcement learning [23–25], enhanced genetic algorithms (GAs) and multi-objective GAs (MOGAs) [26–29] are deployed for optimization, tuning and control of accelerators. Other methods like model-independent feedback [30], safe extremum-seeking [31] are also utilized for tuning of accelerators.

In this paper, we present the utility of latent evolution models (LEMs) as a unified framework that addresses three key problems in accelerator beam diagnostics: (1) forward modeling, i.e. predicting the beam's downstream phase space given upstream measurements [32,33]; (2a) inverse phase space reconstruction, i.e. inferring upstream beam distributions from downstream diagnostics along with aleatoric uncertainty quantification [34,35]; (2b) inverse system parameter estimation, i.e. determining the accelerator settings (such as radio-frequency cavity phases and amplitudes) given beam distribution [36]; and (3) accelerator tuning/optimization, i.e. finding the optimal machine parameter settings to achieve desired beam performance (e.g. minimizing beam loss) [37]. Contrary to existing ML frameworks, the modular architectural design of LEMs solve multiple

* Work supported by the LANL LDRD Program Directed Research (DR) project 20220074DR

† mrautela@lanl.gov

Content from this work may be used under the terms of the CC BY 4.0 licence (© 2022). Any distribution of this work must maintain attribution to the author(s), title of the work, publisher, and DOI.

ISBN: 978-3-95450-261-5 ISSN: 2673-7000 doi: 10.18429/JACoW-NAPAC2025-MOP003

AI-READY CONTROL INFRASTRUCTURE FOR CYCLOTRON SYSTEMS USING GPU-ACCELERATED PYTHON GUIS AND LABVIEW OVER ZEROMQ

C. Lopez*, G. Soto, M. Backfish, I. Lopez, R. Sahebzada, M. Novotny, H. Berns, E. Prebys†
Crocker Nuclear Laboratory, University of California, Davis, CA, USA

Content from this work may be used under the terms of the CC BY 4.0 licence (© 2022). Any distribution of this work must maintain attribution to the author(s), title of the work, publisher, and DOI.

Abstract

We present a modular, high-performance control and monitoring framework for the 76-inch isochronous cyclotron at the Crocker Nuclear Laboratory. The system integrates GPU-accelerated Python graphical interfaces with deterministic LabVIEW control running on CompactRIO hardware, connected through asynchronous ZeroMQ messaging. Real-time data acquisition, actuator control, and feedback are complemented by an independent SQLite-based logging process, achieving sustained 100 Hz multi-channel writes without impacting GUI responsiveness. The architecture leverages Python multiprocessing to decouple rendering, communication, and logging tasks, ensuring sub-millisecond end-to-end latency under load. While AI-based optimization is not yet deployed, the hardware, software, and data infrastructure are explicitly designed to enable future machine learning inference and autonomous control without structural changes. This work establishes an AI-ready foundation for digital transformation and data-driven optimization of cyclotron operations.

INTRODUCTION

Modern particle accelerators demand increasingly sophisticated control systems capable of high-speed feedback, reliable data acquisition, and scalable interfaces for long-term adaptability. The Crocker Nuclear Laboratory at the University of California, Davis, operates a 76-inch isochronous cyclotron that has historically relied on fully analog control systems. These systems, while robust, present limitations in flexibility, observability, and compatibility with modern optimization and AI-assisted control methodologies [1,2].

To address these challenges, we have developed and deployed a novel, hybrid control infrastructure that integrates real-time deterministic control via LabVIEW [3] and CompactRIO hardware with GPU-accelerated Python graphical interfaces [4]. The new architecture allows high-resolution control and monitoring of beamline components, while maintaining compatibility with the existing analog hardware via galvanic isolation and custom DAQ integration. Real-time communication between system layers is enabled through ZeroMQ, allowing decoupled asynchronous messaging between LabVIEW and Python processes.

The architecture emphasizes modularity, responsiveness, and extensibility, enabling concurrent real-time GUI interaction, deterministic hardware control, and data logging. While this work does not present machine learning inference directly, it establishes the foundational infrastructure necessary to support such AI-driven decision-making systems [5].

* cslopez@ucdavis.edu
† eprebys@ucdavis.edu

SYSTEM ARCHITECTURE

The system architecture follows a modular four-layer design, encompassing the Field, Control, Supervisory, and Application layers. Each layer is physically and functionally decoupled, allowing for reliable operation, simplified troubleshooting, and future scalability. Figure 1 illustrates the complete signal flow and data processing across the architecture.

Field Layer

This layer serves as the direct interface to the cyclotron's analog infrastructure, including power supplies, electromagnets, sensors, and beam diagnostic instruments. Both analog and digital I/O channels are connected through National Instruments (NI) C Series modules (NI-9264, NI-9228, NI-9205, NI-9403) [6], with all signals routed through custom-built galvanic isolation [7] boards. This approach enables non-intrusive signal acquisition from legacy analog meters, preserving their role as reference indicators in the existing control system while allowing the new digital system to access the same information in real time.

A custom ammeter supports current measurements from the picoamp to microamp range, producing both an analog voltage output and digital range encoding. This feedback is passed to the Control Layer to support precise, real-time beam current monitoring.

Control Layer

This layer runs real-time deterministic logic on a CompactRIO platform with LabVIEW RTOS, managing signal generation, ramping, on/off toggling, and continuous acquisition at fixed intervals (1–10 ms). Interfacing directly with the Field Layer via NI C Series modules, it ensures precise timing and stable beamline control. All state variables are passed to the Supervisory Layer for integration with higher-level operations and potential AI-driven optimization.

Supervisory Layer

Operating on a Windows-based workstation running LabVIEW, the Supervisory Layer functions as the bridge between deterministic hardware control and the Application Layer's GPU-accelerated user interfaces. It uses a Ze-

ISBN: 978-3-95450-261-5 ISSN: 2673-7000 doi: 10.18429/JACoW-NAPAC2025-MOP004

ANALOG SIGNAL MULTIPLEXING SYSTEM FOR THE IOTA PROTON INJECTOR

Daniel R. MacLean[1,†], Dean R. Edstrom[1]
[1]Fermi National Accelerator Laboratory, Batavia, IL, United States

Abstract

The Fermilab Accelerator Science and Technology (FAST) Facility at FNAL is a dedicated research and development center focused on advancing particle accelerator technologies for future applications worldwide. Currently, a key objective of FAST Operations is to commission the 2.5 MeV IOTA Proton Injector (IPI) and enable proton injection into the Integrable Optics Test Accelerator (IOTA) storage ring. The low and medium-energy sections of the IPI include four frame-style dipole trims and two multi-function correctors with independently controlled coils, requiring readout of 32 analog channels for current and voltage monitoring in total. To reduce cost and optimize rack space within the PLC-based control system, a 32-to-4 analog signal multiplexing system was designed and implemented. This system enables real-time readback of excitation parameters from all magnetic correctors. This paper presents the design, construction, implementation, and performance of the multiplexing system.

IPI OVERVIEW

The IOTA Proton Injector is located at the Fermi Accelerator Science and Technology Facility, a dedicated research and development facility focusing on the advancement of particle accelerator technology. The approximately ~12-Meter long IPI beamline will deliver 2.5 MeV protons to the IOTA storage ring for injection onto orbit, in order to carry out studies on nonlinear beam dynamics as well as to supplement ongoing research on electron beam cooling.

IPI is divided into four primary segments. The 50 kV Proton Source Stand produces beam within a Duoplasmatron Ion Source, which is then extracted into the Low-Energy Beam Transport (LEBT) section. Next, the proton beam is accelerated to the design energy of 2.5 MeV by a Radio-Frequency Quadrupole (RFQ) and is transported into a Medium-Energy Beam Transport (MEBT) section. The MEBT finally delivers the proton beam to IOTA where it is injected onto orbit for studies [1, 2].

MAGNETIC ELEMENTS

Along the IPI beamline there are twelve focusing quadrupole magnets, two large bend dipoles, as well as several magnetic corrector elements comprised of four window-style horizontal-vertical (H-V) trim dipoles and two multi-function corrector (MFC) magnets with four independently powered coils each. The two bend dipoles define a 15° dog-leg section for the purpose of improved matching into the IOTA ring. The H-V trims function as effectively two independent steering dipoles within a single package (two pairs of independently powered coils). MFCs can be configured to act as either a horizontal or vertical trim, as well as a skew-quadrupole element. Corrector elements, for the purposes of this system, refers to the trim dipoles and multi-function correctors. Table 1 summarizes all powered electromagnets used in IPI, and Figure 1 shows the corrector elements powered specifically by the system discussed here [2].

Table 1: IPI Beamline Magnetic Elements: Boldfaced Elements are Readout by the System Discussed Here

Element Type	Magnet Count	# Powered Channels/Magnet
Quadrupoles	12	1
Bend Dipoles	2	1
Trim Dipoles	**4**	**2**
MFCs	**2**	**4**

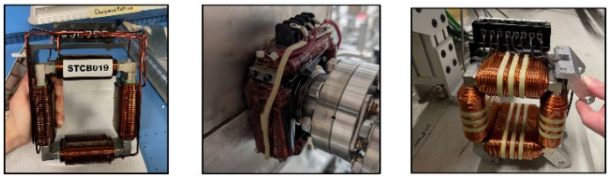


Figure 1: IPI magnet corrector elements, left to right: Dipole trim (Style #1), dipole trim (Style #2), multi-function corrector.

POWER & READBACKS

Power is provided to the IPI magnetic corrector elements by a bipolar ±2 Amp current regulator chassis, which is in turn powered by two 33 Volt, 33 Amp DC bulk power supplies connected in-series and referenced to the system common at the center, providing two bipolar voltage rails about Ground of ±15 Vdc. 16 channels – i.e. individual magnet coils - are powered by this system in-total, each with corresponding current and voltage sense readbacks. Analog V/I Readbacks are output by the 2-Amp regulator chassis and routed back to the PLC-based magnet control system. These readbacks are DC levels scaled to the full range of voltage & current output of the regulator. The bipolar readback levels range from -10 to +10 Vdc and are derived from sense-resistors at the output terminals of each channel within the regulator chassis; the nominal scaling of the current readbacks for each individual channel is therefore 0.2 Amps/Volt.

*FERMILAB-CONF-25-0457-AD
† dmaclean@fnal.gov

Content from this work may be used under the terms of the CC BY 4.0 licence (© 2022). Any distribution of this work must maintain attribution to the author(s), title of the work, publisher, and DOI.

ISBN: 978-3-95450-261-5 ISSN: 2673-7000 doi: 10.18429/JACoW-NAPAC2025-MOP005

A NEW PYTHON MIDDLE LAYER FRAMEWORK: Particle Accelerator MIddle LAyer (PAMILA)*

Yoshiteru Hidaka†, Daniel Allan, Max Rakitin, Brookhaven National Laboratory, Upton, NY, USA

Content from this work may be used under the terms of the CC BY 4.0 licence (© 2022). Any distribution of this work must maintain attribution to the author(s), title of the work, publisher, and DOI.

Abstract

MATLAB Middle Layer (MML) for accelerator control has been used by many facilities worldwide over the years. With the rise of Python's popularity, particularly for leveraging its advanced artificial intelligence and machine learning libraries, an international collaboration is underway to develop a similar software framework in Python. As part of this effort, we propose a new Python middle layer package, which is built on top of the pint unit-conversion package, and capable of handling any type of device-dependent unit conversion (including multiple-input multiple-output) for magnets and other equipment. This package is also compatible with a suite of modern experimental orchestration and data management tools widely used by beamlines at many light sources (i.e., bluesky, ophyd, and tiled), and provides a more modular approach for implementing high-level applications, facilitating reuse, while exposing comprehensive, yet manageable, options to end users.

INTRODUCTION

MATLAB Middle Layer (MML) [1] has been developed over many years and is still in wide use at synchrotron light sources for its user-friendly interface, GUI tools, and simulation capabilities that can significantly reduce beam time required for application testing. It promotes collaboration by enabling cross-facility reuse of common tools. However, MML has fragmented into different versions, and modernizing it would require rewriting its core in MATLAB, a proprietary language increasingly unfamiliar to newer generations of scientists.

In contrast, Python is an open-source programming language, widely adopted and supported by a rich ecosystem of scientific libraries. Replacing MML with a Python-based alternative broadens accessibility, simplifies integration with other modern tools (especially for AI and ML), and better supports the future of accelerator development. At NSLS-II, aphla [2] was developed for this purpose, and has been used since commissioning. However, it has never achieved the original goal of becoming a Python equivalent of MML.

With this background, an international collaboration among accelerator physicists has recently begun developing the Python Accelerator Middle Layer (pyAML) [3]. During its initial exploratory phase [4], a concept code called Particle Accelerator for MIddle LAyer (PAMILA) [5] was created to test new ideas, some of which might eventually be incorporated into pyAML. This paper describes the key features of PAMILA.

* Work supported by U.S. DOE under Contract No. DE-SC0012704. The research described herein is Fundamental Research as defined in EAR (15 CFR §734.8), or Part 810 (10 CFR §810.3), as applicable, and as described in the USD (AT&L) memoranda on Fundamental Research, dated May 24, 2010, and on Contracted Fundamental Research, dated June 26, 2008.

† yhidaka@bnl.gov

CORE FEATURES

PAMILA introduces three key features. First, it supports not only typical single-input single-output (SISO) unit conversions but also more complex multi-input multi-output (MIMO) conversions. Second, it is compatible with the bluesky ecosystem (e.g., bluesky, ophyd, and tiled). Lastly, high-level applications (HLAs) are implemented as *flows* composed of *stages*, rather than conventional function-based HLAs as in MML, thereby maximizing its modular nature and hence reusability.

UNIT CONVERSIONS

PAMILA distinguishes between two types of unit conversion. The first is *universal unit conversion*, the type that scientists commonly associate with the term "unit conversion," where conversions are always intra-dimensional, that is, the unit dimensions remain unchanged. Examples include converting milliamperes to amperes, millimeters to nanometers, or gigahertz to hertz. These are handled automatically by the unit-handling Python package pint [6].

The second type is what we refer to as *representation conversion*. Unlike universal conversion, this is always device dependent and often inter-dimensional (i.e., the unit dimensions do change), though this is not a strict requirement. For instance, a power supply current in [A] may be converted to the kick angle of an orbit corrector electromagnet in [mrad], or an integrated quadrupole strength in [m^{-1}] may be mapped to the corresponding power supply current [A] driving the quadrupole magnet. The term *representation* is used because both the input and output values of a conversion describe the magnitude of the same physical quantity (e.g., magnet strength), but in different forms or *representations*.

In MML, this distinction is not clearly made. However, in cases involving MIMO conversions, it becomes evident that 'unit' conversion and 'representation' conversion are fundamentally different processes. Consider a combined-function magnet powered by two separate power supplies generating dipole and quadrupole field components. The currents I_1 and I_2 influence the dipole strength b_1 and quadrupole strength b_2. Even though both currents have the same unit (amperes), they must be treated as separate representations to convert to and from b_1 and b_2.

Figure 1 illustrates the data flows for get/put operations in a SISO case. For get, a value is first retrieved from a process variable (PV) at the low level and wrapped in a pint

ISBN: 978-3-95450-261-5 ISSN: 2673-7000 doi: 10.18429/JACoW-NAPAC2025-MOP006

A SELF-SUPERVISED TRANSFORMER FOR RF CAVITY SIGNAL DENOISING*

V. Rajesh[1,†], J.P. Edelen, C.C. Hall, RadiaSoft LLC, Boulder, CO, USA
A.L. Edelen, F. H. O'Shea, SLAC National Accelerator Laboratory, Menlo Park, CA, USA
[1]also at Liberty High School, Frisco, USA

Content from this work may be used under the terms of the CC BY 4.0 licence (© 2022). Any distribution of this work must maintain attribution to the author(s), title of the work, publisher, and DOI.

Abstract

A frequent occurrence within industrial particle accelerator systems is electromagnetic noise accumulating within RF Cavity Sensor readings, attributed to their electromagnetically dirtier operating environments and production, with less of an emphasis on their performance optimization. This phenomenon prevents signals from accurately relaying information to beam operators and specialists and prevents data from successfully participating in feedback loops, making machine control much more difficult. Previous work has shown machine learning-based techniques as promising solutions for denoising that maintains signal quality and features. In this paper, we design, implement, and benchmark a self-supervised transformer-based machine learning algorithm that denoises In-Phase and Quadrature (I/Q) RF Cavity Signals without the need to reference a clean ground truth.

INTRODUCTION

Particle accelerators have seen wider use in areas other than scientific research. Industrial particle accelerators, specifically, have been used in a wide range of applications, such as polymer crosslinking, food irradiation, cancer treatment, and semiconductor manufacturing [1]. Due to their mass-produced nature, relaxed requirement for stability and beam quality, and high uptime requirements, particle accelerators with industrial applications undergo far less performance tuning than their research counterparts. This fact, coupled with recent advances in accelerator technology that have given way for more commercial applications with stricter tolerances to control, means that more attention must be paid to industrial deployment to improve system performance, specifically, the noise accumulated in sensor readings within these systems.

A problem that arises within industrial particle accelerators is that their operating conditions are far more electromagnetically "dirty," leading to their sensor readings accruing a lot of noise, which creates a set of data that does not clearly reflect the actual conditions that are occurring within the particle accelerator. The high amounts of noise in the readings from recording points, such as the inside of the RF cavity, greatly reduce the ability for machine operators to accurately control the accelerator. Our work is focused on the application of machine learning technology to improve signal processing for RF systems to achieve a higher degree of stability.

Previous research has shown machine learning algorithms to be viable solutions for a robust denoising process for RF signals. Our previous work has demonstrated the success of various autoencoder-based approaches, ones that use the latent space bottleneck to prevent the machine learning model from learning signal noise [2]. A limitation of this method was identified when the best performing Variational Recurrent Autoencoder (VRAE) of the previous study was applied to the IQ training data generated for this investigation. Numerous models were trained under different paradigms with limited success. Moreover, in all cases the models struggled to generalize, producing inconsistent results as the noise power spectrum was varied.

While researching alternative methods that were better suited to handle the feature space of the new training data, approaches that utilized transformers demonstrated promising results. A transformer is a type of machine learning algorithm that uses a mechanism called "attention" to assist the model in differentiating each part of a set of input data and how they relate to each other [3]. Although used mainly in supervised learning cases, transformer-based methods have been used to successfully denoise EEG and ECoG signals, gravitational wave data, and mechanical vibration signals [4–6].

Our work focuses on the design of a novel, transformer-based machine learning process to effectively denoise In-Phase and Quadrature (IQ) signals that are commonly seen in RF Cavity readings. This is done in a completely unsupervised fashion, meaning that the machine learning model never receives a reference of a clean, ground-truth signal in its training process. We see almost a 400 % improvement in MSE when comparing noisy signals and transformer reconstructions to the clean ground truth(s) available for training, and the transformer model achieving substantial denoising performance in signals frequencies past 0.15 MHz.

METHODS

Our approach is to utilize a transformer-based model to denoise signals but adapt the training mechanism of the model to handle the denoising in a self-supervised fashion. As in a realistic accelerator deployment environment there is no way to obtain a clean benchmark of the noisy signal that is sent for denoising, we must train the machine learning model to operate with no reference to a clean signal, and only use the ground-truth signal to benchmark and evaluate the robustness of the model we have trained.

* This material is based upon work supported by the U.S. Department of Energy, Office of Science, Office of Accelerator R&D and Production Award Number DE-SC0023641.

† viksharrajesh@gmail.com

ISBN: 978-3-95450-261-5 ISSN: 2673-7000 doi: 10.18429/JACoW-NAPAC2025-MOP007

ANOMALY DETECTION OF SLOW-MOVING VARIABLES AT LANSCE FOR IMPROVED BEAM QUALITY*

E.-C. Huang†, N. Yampolsky
Los Alamos National Laboratory, Los Alamos, NM, USA

Abstract

Modern accelerator facilities operate with a large amount of variables, many of which can influence beam quality. While most of these variables are constrained within predefined boundary conditions, slow fluctuations over extended periods—from tens of minutes to a full day—can still significantly degrade beam performance. Due to their gradual nature and the difficulty in distinguishing meaningful trends from background noise, such variables often go unnoticed and remain unoptimized by operators for days.

This study investigates the use of machine learning algorithms to identify and analyze these slow-moving variables. By applying advanced time-series analysis and feature importance ranking, the proposed approach reveals hidden correlations between slow variable drifts and one key beam quality metric: the ring loss at the Los Alamos Neutron Science Center. The results demonstrate the potential of machine learning to detect subtle anomalies and offer actionable insights to mitigate persistent beam quality issues that can disrupt operations for weeks at a time.

INTRODUCTION

Modern accelerator facilities like the Los Alamos Neutron Science Center (LANSCE) rely on hundreds of thousands of interdependent variables to maintain beam stability and performance. While many of these variables are normally bounded by alarms based on standard tolerances, a significant class of slow-moving variables — those that drift subtly over timescales ranging from tens of minutes to one day — often escape the alarm detection. These slow drifts can introduce long-term degradation in beam quality, particularly impacting target metrics such as the ring loss, which is critical to operational efficiency. Unlike transient faults, which are typically caught by the alarm system, these trends are masked by noise, rarely cross thresholds, and may involve high-dimensional correlations.

In addition to degrading performance, slow drifts can also mislead operator judgment. Because these changes unfold gradually, their effects can overlap with operator interventions. For instance, a recent tuning action may seem to improve or worsen beam quality, when in fact a slow-moving variable was the true cause. This makes it harder for operators to evaluate the impact of their changes and can delay effective optimization.

The situation worsens for LANSCE as we are migrating from the obsolete DataWatcher [1] system developed in-house decades ago to the modern Control System Studio/Phoebus [2]. Furthermore, old equipment often lacks the extensive diagnostics ready for an alarm system.

To address this, we developed a lightweight analysis framework that targets two distinct types of slow anomalies. First, we use dynamic correlation analysis to detect undesired oscillations. Separately, we apply L1-based feature selection to rank variables based on their relevance to the drift of key performance indicators, such as the ring loss.

We integrate this analysis into a real-time GUI interface called *BlameIt*, enabling seamless queries of LANSCE archivers, interactive diagnostics, and targeted analysis. Our results show that this approach is well-suited to detecting operationally relevant anomalies that traditional alarms or residual-based models tend to miss.

DATA DESCRIPTION AND METHODS

LANSCE is currently at its 3rd generation of data archiver using the EPICS Archiver Appliance (EAA) [3] since 2024, while InfluxDB [4] was used briefly between 2019 to 2024, and DSRP, a home-grown system, was used since the 90s. A data warehouse was developed to unify the archived data access for all three periods. Asynchronous data acquisition and improved regular expression search has been added to the local fork of arvpyf [5]. Currently, LANSCE operates with more than 200k PVs while >130k channels are archived with various intervals, mostly between 1s to 1 minute. However, for analysis simplicity and intuitive understanding for operators, we limit our analysis to PVs with the LANSCE standard PV names, which contain strictly 10 capital alphanumeric characters marked by the PV's respective beamline, device type, device number, and the channel ID. PVs with non-standard names are generally derived or intermediate PVs that are often strongly collinear with at least one standard PV.

Furthermore, since we are focusing on slow-moving effects, the analysis by default excludes most binary PVs. Binary PVs generally causes sudden jumps that could easily trigger an alarm or fast protect. To reduce PVs with high collinearity with the target PV, say the ring loss, the analysis by default also excludes most beam diagnostics PVs, like beam currents and individual loss monitors. These variables co-moves with the target PV but are not the contributor. After these selection process, the analysis is left with around 5k variables.

Given the high dimensionality of the system and the presence of strong collinearity among many of them, our anomaly detection strategy focuses on two complementary goals: (1) the detection undesired oscillatory behavior and (2) the identification of gradual drifts. Furthermore, since the goal is to deploy it as a near-online tool for the

* Work supported by LANL's LDRD program under 20240474MFR
† en-chuan@lanl.gov

Content from this work may be used under the terms of the CC BY 4.0 licence (© 2022). Any distribution of this work must maintain attribution to the author(s), title of the work, publisher, and DOI.

ISBN: 978-3-95450-261-5 ISSN: 2673-7000 doi: 10.18429/JACoW-NAPAC2025-MOP008

APPLICATION OF BAYESIAN OPTIMIZATION TO BtA INJECTION AT BNL*

E. Hamwi†,[1], P. Adams[2], K. A. Brown[2], A. Burkhart[2],
G. H. Hoffstaetter de Torquat[1,2], W. Lin[2], V. Schoefer[2], R. Terheide[2]
[1]CLASSE, Cornell University, Ithaca, NY, USA
[2]Collider-Accelerator Department, Brookhaven National Laboratory, Upton, NY, USA

Abstract

Drifting optimal settings and changing working conditions force accelerator operators to keep re-tuning control systems. At BNL, the RHIC injector complex accelerates many different ion species by varying a multitude of control knobs. In this report, we investigate the use of Bayesian optimization (BO) of the Booster-to-AGS (BtA) transfer line to maximize the beam brightness in the AGS. The most suitable magnets were chosen by an investigation of the betatron phase advance to facilitate an efficient BO process, using up to 4 steering magnets and up to 3 quadrupoles. To quantify the beam intensity, we used an integrated current transformer, while the beam emittance was estimated via an Ionization Profile Monitor (IPM). It was demonstrated that the chosen magnets effectively recovered a high intensity beam from a poorly tuned configuration, using an Xopt implementation of BO, without increasing the beam profile. A new electron-collecting IPM is being configured with better systematics and lower noise compared to the current ion-collecting IPM, which can further improve this process.

INTRODUCTION

The Booster to AGS (BtA) transfer line transports beam bunches from the Booster to the AGS and also matches the beam Twiss parameters and dispersion functions to the circulating beam in the AGS at the injection point [1]. The beam is extracted at the F6 extraction septum in the Booster, and injected at the L20 injection septum in the AGS, as shown in Fig. 1.

The BtA line consists of 15 quadrupoles, 5 bends, 2 horizontal correctors, 4 vertical corrector, a stripping foil for operations with heavy ions, and four sets of multi-wire profile monitors [2]. In order to make sure the beam is injected properly at the AGS injection point, beam matching is performed so that the beam parameters at the end of the BtA line matches the circulating beam parameters in the AGS. The transfer line optics do not generate multiples of $\pi/2$ phase advance between correctors or quadrupoles, which makes it nontrivial to uncouple the effects of different correctors and quads on beam alignment and shape, respectively.

* Work supported by Brookhaven Science Associates, LLC under Contract No. DE-SC0012704 with the U.S. Department of Energy and by DOE-NP No. DE SC-0024287.

† eh652@cornell.edu

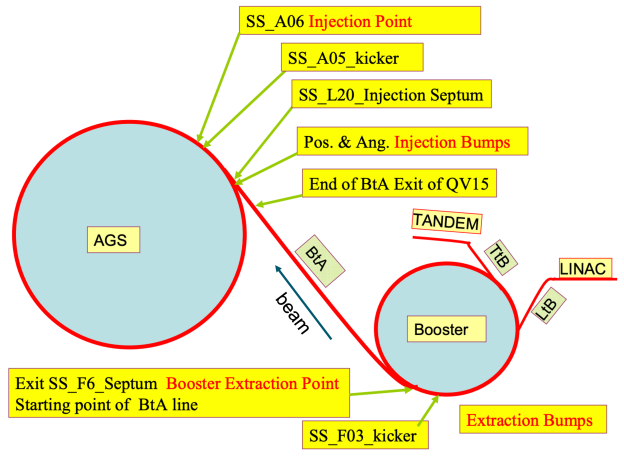


Figure 1: Schematic diagram of the BtA line, and its connections with the Booster and the AGS.

BAYESIAN OPTIMIZATION

Bayesian Optimization (BO) is a powerful and sample-efficient strategy for optimizing objective functions that are expensive to evaluate, noisy, or lack an analytical form. By constructing a probabilistic surrogate model, typically a Gaussian Process (GP), BO balances exploration and exploitation to identify optimal regions of the search space with minimal evaluations. This makes it particularly well-suited for tuning parameters in experimental and simulation-based accelerator physics problems [3].

The Xopt package is an open-source, extensible framework developed to streamline the application of BO in scientific workflows [4]. It supports multiple surrogate models and acquisition strategies, and is designed to interface easily with experimental control systems. Badger, a graphical user interface built on top of Xopt, provides an intuitive platform for configuring optimization problems and monitoring optimization progress in real time. Together, Xopt and Badger enable practical deployment of BO in accelerator operations, facilitating automated tuning and performance improvement across complex, multi-parameter systems.

In our optimizations, we focused on small dimensional parameter spaces $D < 8$ for which BO is a great candidate tool. Due to uncertainties in magnet alignment and the presence of nonlinear magnetic fields, we opted to use a GP surrogate model with radial basis function (RBF) kernel to represent the underlying physical system since the RBF kernel is intrinsically capable of handling nonlinearity. The only caveat of using a GP model is that it is not infinitely trainable, with

Content from this work may be used under the terms of the CC BY 4.0 licence (© 2022). Any distribution of this work must maintain attribution to the author(s), title of the work, publisher, and DOI.

ISBN: 978-3-95450-261-5 ISSN: 2673-7000 doi: 10.18429/JACoW-NAPAC2025-MOP009

A REACTIVE FERROELECTRIC TUNER FOR MICROPHONICS COMPENSATION*

S. V. Kuzikov†
Thomas Jefferson National Accelerator Facility, Newport News, VA, USA

Abstract

Jefferson Lab (JLab) is actively pursuing an extensive research program focused on developing advanced Nb_3Sn superconducting technology for particle acceleration. Due to the brittle nature of Nb_3Sn coatings, a Ferroelectric Tuner (FRT) currently represents the most viable approach for microphonics compensation in these next-generation cavities. We suggest a novel, fast-responding FRT integrated directly into the main coupler, eliminating the need for an additional RF port. Leveraging a unique RF design based on a magic-T configuration, this advanced FRT will enable microphonics compensation in the ±30 Hz range without undesirable changes to the external quality factor.

INTRODUCTION

One of the major challenges faced by the SRF accelerators is microphonics [1-3]. Microphonics refers to frequency detuning of SRF cavities caused by external vibrations. As the cavities detune, additional RF power is required to maintain the desired accelerating gradient. For example, CEBAF cavities are currently unable to utilize the full RF power available from their klystrons [4]. This limitation significantly increases both the capital and operational costs of the accelerator.

An FRT can be considered a fast phase shifter coupled to the SRF cavity, capable of altering the total reactive power delivered from the RF source to the cavity [5-8]. This phase shift results from changes in the dielectric permittivity of an inserted ferroelectric sample. The permittivity can be rapidly adjusted—typically within nanoseconds—by applying a bias voltage. Dielectric permittivity values typically range from 100 to 200 for bias electric fields between 0 and 10 kV/cm, with loss tangents as low as 10^{-3} [9].

Preliminary analysis and experimental results from CERN with an FRT connected to an SRF cavity [6, 7], along with room-temperature tests conducted by Euclid Techlabs [8], indicate that FRTs can support stable operation of SRF cavities such as the 1500 MHz C100 (CEBAF) and novel Nb_3Sn cavities. These studies suggest that up to 50% of the RF power—currently used to counteract detuning—could instead be redirected to beam acceleration.

FRT CONCEPT

Our concept is based on an analytical solution that defines the required amplitude and phase characteristics of the reflected signal from the FRT in order to (1) shift the cavity's resonant frequency appropriately, and (2) maintain a constant external quality factor (Q_{ext}). To explore this, we consider a universal model (Fig. 1) that includes the main coupler and a "black box" representing the tuner used for microphonics compensation. Analyzing this simplified system requires determination: (1) how the phase of the reflection from the black box must be controlled to detune the SRF cavity frequency over the desired range, and (2) how the amplitude of the reflection must be adjusted in conjunction with the phase shift to ensure that the total reflected signal remains constant on amplitude—thus preserving the cavity's external Q-factor.

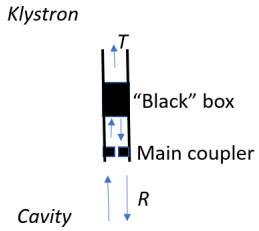


Figure 1: "Black" box FRT model.

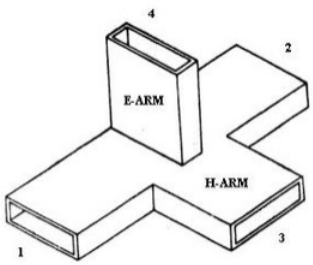


Figure 2: Magic T.

We begin this analysis with the simplest case, assuming negligible losses in the black box. Losses will be included in final simulations to show how good a lossless approach is. Without losses, the complex reflection coefficient of the resonant system (main coupler + black box) is given by the following equation:

$$R = r_0 - \frac{(1-r_0^2)\cdot r\cdot e^{i\varphi}}{1-r_0\cdot r\cdot e^{i\varphi}}. \quad (1)$$

Where r_0 – is amplitude of reflection from the main coupler (it can be considered as the real number), r – is an amplitude of the reflection from the black box (real number), φ - is a phase of black box reflection so that the complex "black" box reflection equals $r\cdot e^{i\varphi}$. The frequency shift due to the black box insertion is naturally proportional to the argument of R. Now we need to require that the amplitude of the reflection R from the equation (1) must be constant and equal to the reflection from the unperturbed SRF cavity for any value of the "black" box phase φ. This

*This material was supported by the U.S. Department of Energy, Office of Science, Office of Nuclear Physics (contract DE-AC05-06OR23177).
† kuzikov@jlab.org

Content from this work may be used under the terms of the CC BY 4.0 licence (© 2022). Any distribution of this work must maintain attribution to the author(s), title of the work, publisher, and DOI.

ISBN: 978-3-95450-261-5 ISSN: 2673-7000 doi: 10.18429/JACoW-NAPAC2025-MOP010

AtomicAndPhysicalConstants.jl: A FAST JULIA PACKAGE TO ACCESS PARTICLE PROPERTIES AND FUNDAMENTAL CONSTANTS*

L. Li†, D. Sagan, CLASSE, Cornell University, Ithaca, NY, USA
D. Abell, University of Maryland, College Park, College Park, MD, USA
A. Coxe, Virginia Commonwealth University, Richmond, VA, USA

Abstract

To support constants lookup for the SciBmad project, we introduced `AtomicAndPhysicalConstants.jl`, a Julia package that provides physical constants, subatomic particle properties, and atomic isotope data. It aggregates datasets from NIST (CODATA) and the Particle Data Group, offering a unified interface. The package supports configurable unit systems and data types, and integrates with the Julia package `Unitful.jl`. The package emphasizes speed and ease of use, making it well-suited for high-performance simulations and physics-driven modeling.

INTRODUCTION

In accelerator and beam physics, the Bmad [1] ecosystem – developed at Cornell University's Laboratory for Elementary Particle Physics – has long served as a key framework for simulating charged-particle dynamics.

Currently, a new Julia-based simulation environment called SciBmad [2] is being developed to take advantage of Julia's strengths in performance, robust support for parallelism, and native multiple dispatch.

As part of the SciBmad ecosystem, the Julia package `AtomicAndPhysicalConstants.jl` was developed to fill the need for providing fast and stable access to physical constants. It provides 16 common constants, 14 subatomic particle, all NIST isotopes data, and supports 3 sets of unit systems and 3 data types to fit various needs.

Key Features

- **Configurable units and types** – Specify unit systems (`MKS`, `CGS`, or `ACCELERATOR`) and numeric representations (`Float64`, `Unitful` [3], or `DynamicQuantities` [4]) through a single macro call.
- **Data integration** – Pulls constants from CODATA (Committee on Data of the International Science Council) [5], NIST (National Institute of Standards and Technology) [6], and PDG (Particle Data Group) [7], with support for historical datasets.

Comparison with Existing Packages

Several Julia packages also provide access to physical constants. One of the most widely used package is `PhysicalConstants.jl` [8], which provides reliable static constants with uncertainty support. `AtomicAndPhysicalConstants.jl` offers a direct interface for constants access and an option to customize units and variable types. Another key differentiator is the `Species` type, which encapsulates particle attributes, such as mass and charge, for simpler access.

CUSTOMIZING UNITS AND TYPES

A key feature of `AtomicAndPhysicalConstants.jl` is the macro `@APCdef`, which enables users to configure global behaviors for the package, including the choice of unit system, variable type, and variable scoping. This allows users to work with constants within a consistent framework of units and variable types under a wide range of physical modeling needs, such as SciBmad and `DifferentialEquations.jl` [9].

However, custom unit and variable type usually lead to type instability and slow run-time performance. A typical approach is using functions to get constants and species properties and convert them to proper units and type at run time. This conversion not only introduces extra computation, but also makes the function type-unstable. If the return type is not decided at compile time, the compiler could not optimize the program, causing more memory and time usage.

We solve this by using a macro to generate code in the name space. Once the units and types are decided, constants and getter functions with a fixed unit and type will be written. Although this approach slows program at the macro call, it avoids converting units and specifies a certain type, making the program fast at run time.

`@APCdef` Usage

The `@APCdef` macro serves as the primary configuration interface and must be invoked once during package initialization (A second invocation raises an error). It assigns units and data types for all constants, including fundamental physical constants as well as `Species` mass and charge values (see Section 3). Upon invocation, the macro generates these constants and attaches appropriate getter functions—*e.g.* `massof()` and `chargeof()`—which return species properties.

The macro supports multiple unit systems through the `unitsystem` keyword, allowing users to choose from predefined conventions: `ACCELERATOR` (a unit system that contains commonly used units in accelerator physics), `MKS` (SI standard units), and `CGS` (centimeter-gram-seconds). Each system sets base units for mass, length, time, energy, and

* Work supported by Brookhaven Science Associates, LLC under Contract Nos. DE-SC0012704 and DE-SC0018008 with the U.S. Department of Energy.
† ll963@cornell.edu

Content from this work may be used under the terms of the CC BY 4.0 licence (© 2022). Any distribution of this work must maintain attribution to the author(s), title of the work, publisher, and DOI.

ISBN: 978-3-95450-261-5 ISSN: 2673-7000 doi: 10.18429/JACoW-NAPAC2025-MOP011

AUTOMATED RF PHASE ADJUSTMENT FOR BEAM STABILIZATION IN THE FERMILAB LINAC*

R. R. Chichili†[1], J. A. Sulskis[1,2], R. Sharankova[3], B.Vamanan[1], S. Ravi[1]
[1]University of Illinois at Chicago, Chicago, IL, USA
[2]also at Georgia Tech Research Institute, Atlanta, GA, USA
[3]Fermi National Accelerator Laboratory, Batavia, IL, USA

Content from this work may be used under the terms of the CC BY 4.0 licence (© 2022). Any distribution of this work must maintain attribution to the author(s), title of the work, publisher, and DOI.

Abstract

The Fermilab Linac experiences longitudinal beam phase drift, leading to increased particle loss, conventionally corrected through labor-intensive manual RF adjustments. This project explores machine learning-based automation for drift correction, employing a prototype-based classification approach. Our model utilizes a 34-dimensional feature set (RF settings and BPM readings) and leverages a 7x27 response matrix for system modeling. To overcome limited real-world data, we generate synthetic data, enhancing model training and generalizability. Custom loss functions, including a surrogate energy-consistent loss and a temporal smoothness constraint, ensure physically plausible drift predictions. The goal is a robust system for autonomous phase adjustments, ensuring stable beam acceleration and reduced manual intervention.

INTRODUCTION

The Fermilab Linac delivers 400 MeV H^- beam. An ion source, a LEBT, a Radio Frequency Quadrupole (RFQ), and a MEBT including a Buncher cavity inject 750 keV beam into the Linac. It consists of 5 drift tube cavities, two side-coupled bunchers, and 7 side-coupled cavities. Environmental changes and instabilities from the ion source and RFQ result in longitudinal beam phase drift, which causes increased particle loss due to emittance blow-up, and is traditionally corrected manually by small adjustments to cavity phase settings [1]. This labor-intensive manual process is a hindrance to maintaining stable beam acceleration.

To solve this, we're exploring a machine learning-based approach. Our model is a prototype-based classifier [2] that learns to map BPM beam phase readings to optimal RF cavity settings. It uses a 34-dimensional feature set (comprising 7 RF cavity phase settings for the RFQ, Buncher and drift tube cavities and 27 Beam Position Monitor (BPM) readings of beam phase). A key part of our strategy is generating synthetic data from this matrix to overcome the scarcity of real-world data and improve the model's ability to generalize.

The model uses custom loss functions that are grounded in physics. A surrogate energy-consistent loss penalizes corrections that lead to implausible energy changes, and a temporal smoothness constraint prevents abrupt adjustments. These functions ensure that the predictions are physically sound. Our overall goal is to build a robust, autonomous system that provides precise phase adjustments, leading to stable beam operation and minimal manual intervention.

SYSTEM DESIGN

Our system is built around a machine learning-based approach for automated RF phase adjustment in the Fermilab Linac. At its core is a prototype-based classification model [2] designed to identify optimal correction strategies.

Data Representation and Feature Engineering

The model's input is a 34-dimensional feature set comprising 7 RF cavity settings and 27 BPM phase readings. BPMs measure beam phase relative to the cavity RF reference signal. To model the linear relationship between these parameters, we construct a 7×27 response matrix [3]. This matrix is derived from experimental data using Fast Fourier Transform (FFT) filtering and normalization, providing the fundamental physical relationship $\Delta\mathbf{BPM} = \mathbf{R}^\top \cdot \Delta\mathbf{RF}$ and serving as a basis for synthetic data generation.

Synthetic Data Generation

Due to the limited availability of real-world experimental data, we generate synthetic data by leveraging the constructed response matrix. This process simulates diverse operational drift scenarios around nominal setpoints, creating a robust training dataset that enhances the model's ability to generalize across various conditions.

Model Architecture and Classification

We employ a feedforward neural network that maps 27-dimensional BPM input vectors to 7-dimensional output vectors representing nominal RF cavity settings. Nominal conditions were defined as cavity phase settings which resulted in good Linac operation conditions and minimal beam loss. This is a prototype-based classification framework [4] where known nominal configurations are treated as distinct class prototypes. During training, a cross-entropy loss [4] function is used, based on the proximity of the model's output to these prototypes, allowing for a scalable and efficient correction strategy.

* This work has been authored in part by FermiForward Discovery Group, LLC under Contract No. 89243024CSC000002 with the U.S. Department of Energy, Office of Science, Office of High Energy Physics and work supported by Discovery Partners Institute https://dpi.uillinois.edu/

† rchic@uic.edu Code: `https://github.com/jaysulk/uic_fnal_linac_phase_comp`

ISBN: 978-3-95450-261-5 ISSN: 2673-7000 doi: 10.18429/JACoW-NAPAC2025-MOP012

AUTOMATION OF SAMPLE ALIGNMENT FOR NEUTRON BEAMLINES

A. Chen, J. P. Edelen*, RadiaSoft LLC, Boulder, CO, USA
C. Hoffmann, S. Calder, Oak Ridge National Laboratory, Oak Ridge, TN, USA

Content from this work may be used under the terms of the CC BY 4.0 licence (© 2022). Any distribution of this work must maintain attribution to the author(s), title of the work, publisher, and DOI.

Abstract

Neutron scattering experiments are crucial for the exploration of molecular structure in compounds. The HB-2A neutron powder diffractometer at the High Flux Isotope Reactor at Oak Ridge National Laboratory conducts magnetic studies of samples by illuminating them with different energy neutron beams and recording the scattered neutrons. Proper and consistent alignment of the sample is necessary to ensure that high quality data is collected throughout an experiment. This process is currently performed manually by beamline scientists. RadiaSoft, in collaboration with the beamline scientists and engineers at ORNL, has developed a reinforcement learning-based agent capable of aligning and isolating samples. We use a Q learning structure to train the agent. The agent identifies the method to move the sample to the center of the beam and the proper amount to close the neutron camera slits. We then move the sample and close the slits using a custom Python-based EPICS IOC interfaced with the sample and slit motors. In this paper, we provide an overview of our reinforcement learning tools and show our results aligning samples like those at ORNL.

INTRODUCTION

Automation of alignment processes for accelerators allows for increased experimentation efficiency. RadiaSoft and ORNL have been in a multi-year collaboration to develop machine learning tools for noise reduction [1], sample identification, and alignment [2]. Much of this work has focused on the TOPAZ single crystal diffractometer, but recent studies have shown success for sample alignment using the neutron camera at the HB-2A neutron powder diffractometer.

The HB-2A beamline is primarily used for magnetic structure determination [3] and services many experiments at ultra-low temperatures. It permits the application of high external fields and pressure. Its low-noise environment, paired with the constant wavelength and simple profile of its neutron beam, allows for interchangeable sample environments with minimal calibration. The beamline also permits a variety of sample changing options, allowing multiple samples to be loaded per session. A picture of the diffractometer end station is in Fig. 1.

Sample alignment at HB-2A has previously been carried out manually by beamline scientists. Automation of sample alignment would increase the efficiency of beam operations, but poses two primary challenges: the sample is not visible when not illuminated by the beam, and the presence of multiple samples necessitates slit closure to illuminate only one sample at a time. Additionally, when multiple samples are present within the beam, the beam slits must close so that only one sample is illuminated. Finding a way to overcome these challenges would streamline beam operations by reducing beam time necessary for sample alignment.

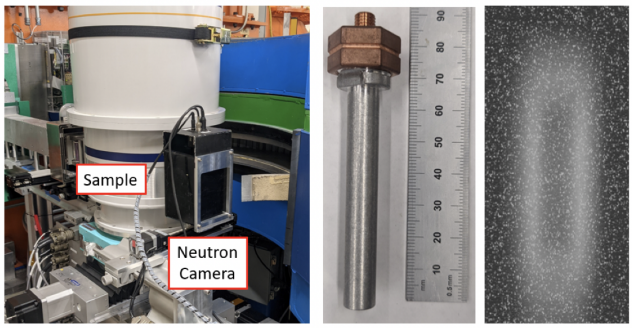


Figure 1: The HB-2A powder neutron diffraction instrument. (Left) The sample and detector area. (Middle) A standard sample holder (scale in millimeters). (Right) An example of a neutron image, with the powder sample appearing as a shadow-like image in the white beam.

ENVIRONMENT SETUP

Our reinforcement model was trained in a custom Gymnasium environment that creates a simulated version of the HB-2A neutron camera. We simulate motor movement by moving the sample one pixel at a time in any lateral direction. An example of the simulated beamline is in Fig. 2. The reward function for the sample is defined as $-r^2$ for samples within the beam and $-r^4$ for samples outside of the beam, where r is the distance between the sample center of mass and the center of the image. When the sample is outside the beam, it is not illuminated and is therefore unable to be detected. For multiple sample images, we select one sample at a time to center and close the slits around.

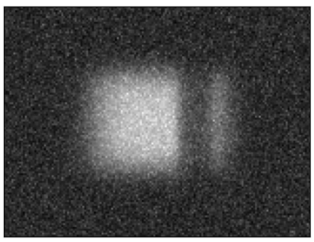


Figure 2: Neutron camera image at environment initialization.

When no sample is detected, we assign a random outside-of-beam position to the sample center. The image is re-scanned every 10 steps to determine whether the sample is re-positioned within the beam. Once the sample center is located at the center of the beam (Fig. 3), the camera slits are closed so that only the sample is visible (Fig. 4).

* jedelen@radiasoft.net

ISBN: 978-3-95450-261-5 ISSN: 2673-7000 doi: 10.18429/JACoW-NAPAC2025-MOP013

AUTOMATION OF SAMPLE IDENTIFICATION FOR NEUTRON BEAMLINES

A. Chen, J. Einstein-Curtis, M. Henderson, J. P. Edelen*, RadiaSoft LLC, Boulder, CO, USA
B. Krishna, C. Hoffmann, G. Taufer, S. Calder
Oak Ridge National Laboratory, Oak Ridge, TN, USA

Content from this work may be used under the terms of the CC BY 4.0 licence (© 2022). Any distribution of this work must maintain attribution to the author(s), title of the work, publisher, and DOI.

Abstract

Neutron scattering experiments are a critical tool for the investigation of molecular structure in compounds. The HB-2A neutron powder diffractometer at the High Flux Isotope Reactor at ORNL conducts magnetic studies of samples by illuminating them with different energy neutron beams and recording the scattered neutrons. Proper identification and alignment of the sample during an experiment is key to ensuring high quality data is collected. At present, this process is performed manually by beamline scientists. RadiaSoft, in collaboration with the beamline scientists and engineers at ORNL, has developed a machine learning-based software automating sample identification. We utilize a fully connected convolutional neural network configured in a U-Net architecture to identify the sample and its center of mass. We then move the sample using a custom Python-based EPICS IOC interfaced with the motors. In this paper, we provide an overview of our machine learning tools and show our results identifying samples at ORNL.

INTRODUCTION

Automation of alignment processes for accelerators and accelerator users is broad area of research. For example, recent work from NSLS-II has focused on the application of different Bayesian optimization approaches for alignment for x-ray beamlines [1, 2]. Additionally, RadiaSoft has been engaged in a multi-year collaboration to utilize machine learning for sample identification, noise reduction [3], and alignment [4]. While work on alignment automation and testing has largely focused on the TOPAZ single crystal diffractometer, recent studies have shown success for sample alignment using the neutron camera at HB-2A.

The HB-2A beamline is primarily used for magnetic structure determination [5] and permits the application of high external fields and pressure, and services many ultra-low temperature experiments. Figure 1 shows a picture of the diffractometer end station. The constant wavelength and simple profile of its neutron beam, along with its relatively low noise environment, allows for interchangeable sample environments on HB-2A with minimal calibration. The beamline also features a variety of sample changing options that allow multiple samples to be loaded per session to increase throughput.

There are several challenges associated with sample alignment at HB-2A. The two primary challenges are that the sample is not visible when it is not illuminated by the beam.

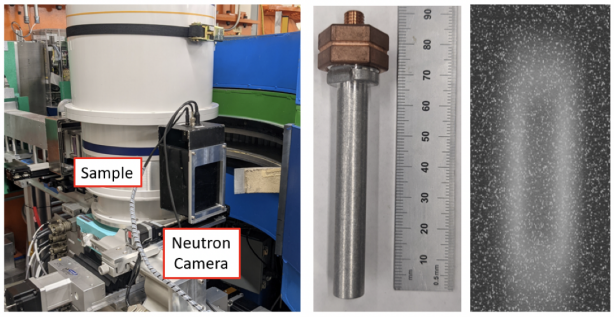


Figure 1: The HB-2A powder neutron diffraction instrument. Left: the sample and detector area. Center: a standard sample holder (in millimeters). Right: an example of a neutron image, with the powder sample appearing as a shadow-like image in the white beam.

Additionally, the presence of multiple samples necessitates precise positioning of the sample combined with slit closure to prevent from illuminating more than one sample at a time. Moreover, the use of neutron cameras for positioning relies on the ability to accurately identify the sample even when the signal to noise ratio is low. Each of these issues present challenges for control. While human operators are adept at sample identification, automation of this process is necessary to streamline the operation of the beamline.

In previous work we have utilized operator based image contouring to establish a ground truth for training ML based sample identification models. While effective, this requires beam-time to develop a training dataset and an operator to label images which is error prone and time consuming. As an alternative we have developed a generalized model of the HB-2A system that allows us to consider an object that is illuminated by the neutron beam and then generate a simulated neutron camera image. In this paper we will review our simulation tools, provide an analysis of model training using the new dataset, and then model testing on experimental data and compare the predicted sample center with the operator identified sample center.

SIMULATION TOOLS

We built a simulator that creates a beam using a super-gaussian distribution that allows us to shape the profile to be more akin to a uniform beam with smooth edges. The sample then absorbs some of the beam casting a shadow, a parameter that can be modulated depending on the type of sample in question. Slits were also integrated into the simulation to enable full replication of the experimental setup at HB-2A.

* jedelen@radiasoft.net

ISBN: 978-3-95450-261-5 ISSN: 2673-7000 doi: 10.18429/JACoW-NAPAC2025-MOP015

BEAM SCATTERING THROUGH FOIL*

B. Dhital†, P. Adams, K.A. Brown, T. Olsen, N. Tsoupas, W. Lin
Brookhaven National Laboratory, NY, USA
D. Sagan, Cornell University, NY, USA

Abstract

This paper describes the foil structure used at the beam extraction point in the NASA Space Radiation Laboratory (NSRL) beamline. The stripping foil removes electrons from incoming ions, rendering them partially or fully stripped. Foils of various materials and thicknesses are employed, enabling ion species at different energies to pass through. As charged particles traverse a foil, the outgoing particles exhibit a Gaussian-like angular distribution. This distribution is subsequently transformed into a uniform profile by a set of octupole magnets, essential for various beam experiments at the NSRL target. We utilize the Bmad and SRIM computer codes to calculate the energy loss through the foils for different ion species, energies, and charge states. After preparing ion beam species in the Booster, we determine the energy loss by measuring the horizontal beam profile at the multi-wire MW063 location in the NSRL beamline. Finally, we present a summary of energy loss calculations obtained through Bmad, SRIM, and experimental data.

INTRODUCTION

When charged particles pass through a thin, material medium, they receive a random directional "kick", altering their angle of motion. This interaction collectively shapes the resulting phase space into a more Gaussian-like angular distribution [1]. In addition to this angular modification, particles also lose energy and may undergo charge-changing interactions as they pass through the material. These effects are crucial for shaping the ion species beam used at the NASA Space Radiation Laboratory (NSRL). These experiments require a large uniform beam area which is achieved through two octupole magnets in opposing polarity [2, 3] which would not be possible with the distorted, one-third integer resonant slow extracted phase space produced by such an extraction scheme [4–6].

The multiple scattering process through a foil is dominated by a screened Coulomb interaction between the projectiles (protons and ions) and target atom. A foil element in general, represents a planar sheet of material which strips electrons from an incoming particle towards it. In conjunction, there will be scattering of the particle trajectory as well as an associated energy loss [7]. In this paper, we measure the multiple scattering of primary beam ions incident upon the copper foils at NSRL beamline and compare the measurement with the results calculated from Bmad [7] and the SRIM code [8, 9].

* Work supported by Brookhaven Science Associates, LLC, under Contract No. DE-AC02-98CH10886 with the U.S. Department of Energy and by NASA (Contract No. T570X), and by NSF under Award PHY-1549132.

† bdhital@bnl.gov

ACCELERATOR & BEAMLINE OVERVIEW

The Booster is a 201.78 m circumference separated-function synchrotron that accelerates protons and heavy ions from EBIS, Tandem, and LINAC injectors using one-third integer resonant slow extraction [3, 5], with ions heavier than protons accelerated in intermediate charge states [10] (Fig. 1). Ions are extracted from the Booster using the one-third integer resonant slow extraction method [5].

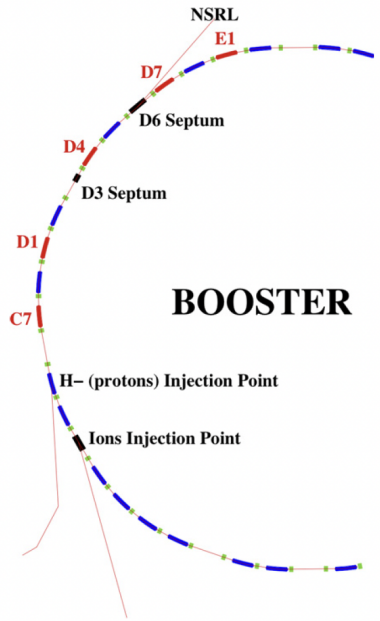


Figure 1: Layout of the portion of the Booster ring showing five extraction bumps (C7, D1, D4, D7, and E1) and two extraction septa magnets (D3 and D6) to enhance slow resonant extraction of beam to the NSRL beamline.

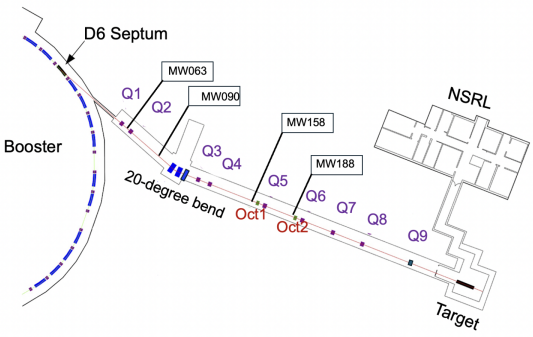


Figure 2: Layout of the NSRL beam line starting at D6 septum magnet where slow extracted beam from the Booster passes through the foil element.

Content from this work may be used under the terms of the CC BY 4.0 licence (© 2022). Any distribution of this work must maintain attribution to the author(s), title of the work, publisher, and DOI.

ISBN: 978-3-95450-261-5 ISSN: 2673-7000 doi: 10.18429/JACoW-NAPAC2025-MOP016

BENCHMARKING THE USE OF BPM QUADRUPOLE MOMENTS TO MEASURE EMITTANCE*

M.A. Balcewicz†, C.Y. Tan, Fermi National Accelerator Laboratory, Batavia, IL, USA

Abstract

For the PIP-II program, transverse emittance in the Fermilab Booster must remain well controlled at higher bunch intensities. 4-plate beam position monitors (BPMs) have a small but measurable quadrupole moment, making it possible to infer transverse emittance. By compositing many BPMs together, it becomes possible to improve the quality of the quadrupole signal. The Fermilab Booster BPM system has been used to measure these quadrupole moments in the past year and derive emittances from them. Recent benchmarks show that the derived BPM emittances show similar emittance evolution and value to IPM and Multiwire data. This approach can both supplement and complement existing non-intercepting emittance monitors in accelerators.

INTRODUCTION

The Fermilab Booster is a rapid cycling synchrotron that accelerates particles to 8 GeV kinetic energy and injects into the Main Injector and Recycler. For the PIP-II program bunch intensities are expected to increase to 6.7×10^{12} particles per pulse (ppp), space charge driven emittance growth at this intensity is significant. The normalized emittance acceptance of the MI-8 line is designed to be approximately 25 π·mm·mrad [1], with an additional 2″ by 2″ collimator to remove halo [2] added later.

Intercepting multiwire (MW) systems exist in the Linac transfer line injecting into Booster, MI-8 line, and Booster beam dump. The MWs in the MI-8 line are of particular note as they show good agreement with one another [3] and provide absolute measures of emittance. Within the Booster cycle, non-intercepting Ionization Profile Monitors (IPMs) are used.

Without any fitting or calibration on the IPM system, the measured emittance is significantly larger than measured in the transfer line [4, 5]. The reason for the larger emittance has been suggested to be from a combination of space charge forces widening the distribution collected on the Micro-Channel Plate (MCP) [6] along with decreased MCP sensitivity at the closed orbit center of the bunch where more ions impact [6]. Furthermore, only the vertical channel of the IPM system is deemed reliable because the horizontal beta function at the IPM is 3× smaller than the vertical, thus reducing its sensitivity.

Although work has been done to correct these effects for the IPM system [7], it has nonetheless served to be an inspiration to find other methods to continuously measure emittances within the Booster ramp in both planes. A method for inferring the emittance using BPM quadrupole moments has been derived and implemented within the Booster. This method shows promise and is not sensitive to MCP gain effects or ion drift effects. This method is then compared to and cross calibrated against other instruments. Although this method has successfully measured horizontal emittances, this proceeding will focus on the vertical plane to minimize dispersive effects.

BPM EMITTANCE MEASUREMENT

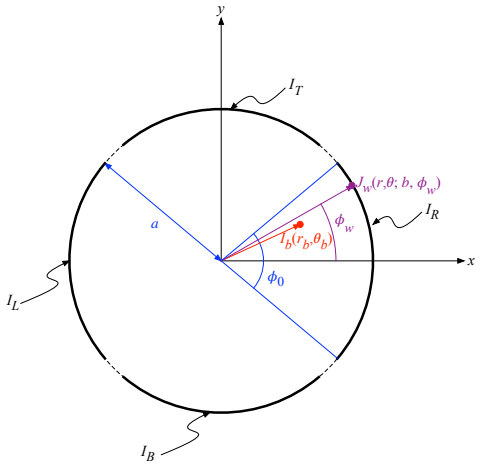


Figure 1: Transverse cross section of 4-plate BPM. Plates have a radius a and subtend an angle ϕ_0. A test current I_b creates surface current J_w on the plates, which can be integrated to find the total current from the test current.

For a detailed derivation for using BPMs to measure emittance please see [8, 9]. A sketch of the method will be given here for context.

Let us imagine a four plate BPM pickup with a current distribution inside it as shown in Fig. 1. The current distribution drives image currents along the BPM, the sums and ratios of which correspond primarily to the dipole moments d_x and d_y and total current. Plates of non-ideal geometries also measure a small quadrupole mode q. Assuming a given distribution, this quadrupole mode at an individual BPM can be directly related to emittance, optical functions, and momentum spread with the equation:

$$\Delta_q \equiv q - (d_x^2 - d_y^2)\phi_0 \cot\frac{\phi_0}{2} = \frac{2}{a^2}\frac{\sin\phi_0}{\phi_0}\left[\frac{\beta_x\epsilon_x}{\pi} - \frac{\beta_y\epsilon_y}{\pi} + (D_x\sigma_p)^2\right] \quad (1)$$

Inferring emittance in this way has been attempted in the past [10–12], but suffers from poor signal compared to the

* This manuscript has been authored by FermiForward Discovery Group, LLC under Contract No. 89243024CSC000002 with the U.S. Department of Energy, Office of Science, Office of High Energy Physics.

† balcewic@fnal.gov

Content from this work may be used under the terms of the CC BY 4.0 licence (© 2022). Any distribution of this work must maintain attribution to the author(s), title of the work, publisher, and DOI.

ISBN: 978-3-95450-261-5 ISSN: 2673-7000 doi: 10.18429/JACoW-NAPAC2025-MOP018

MODERNIZING WIRE SCAN DIAGNOSTICS FOR REPRODUCIBLE, REAL-TIME BEAM MEASUREMENTS THROUGH A MODULAR PYTHON MIDDLE LAYER INTEGRATED WITH EPICS*

T. Kabana†, S. Chowdhury, B. Jacobson, N. Neveu , E. Yang, C. Zimmer
SLAC National Accelerator Laboratory, Stanford, CA, USA

Abstract

As part of a broader effort to modernize beam diagnostics at SLAC, we are developing a new middle-layer application to support wire scan measurements using Python. This tool is designed to replace aging MATLAB GUIs with a streamlined framework that interfaces directly with EPICS and Beam Synchronous Acquisition systems. The middle layer manages the complete wire scan workflow while emphasizing modularity, reproducibility, and integration with existing controls infrastructure. This paper will cover the system architecture, practical implementation details, and lessons learned in deploying a diagnostic tool suited to the high-throughput, real-time needs of accelerator operations.

INTRODUCTION

Wire scan diagnostics are a common tool in accelerator operations, providing precise measurements of transverse beam profiles [1]. Historically, these systems have relied on rigid, all-in-one software that is difficult to maintain, extend, or reuse. The existing MATLAB GUI spans several thousand lines of code and contains configuration data, scanning logic, analysis routines and display controls in a single file. As machine complexity and measurement demands grow, more flexible, modular tools are needed to enable rapid development, robust testing, and integration with diverse hardware

To address these needs, we developed a modern Python based wire scan framework with an object-oriented middle layer that encapsulates EPICS process variables (PVs) and controls logic into reusable device abstractions [2]. Motion control, data acquisition, and analysis are implemented as independent components, improving testability, simplifying debugging, and accelerating hardware integration. Configuration is defined in structured YAML files validated with Pydantic [3], allowing measurement setups to be defined without modifying core logic.

This paper describes the system architecture, implementation, and operational features, including its GUI interface, dynamic configuration, and structured data output. Designed for real-time beam measurements, the tool is in use for development and testing at SLAC, with plans for broader deployment across beamline diagnostics.

SYSTEM ARCHITECTURE

The core of the wire scan modernization effort is an object-oriented middle layer written in Python. This architecture abstracts hardware controls into modular device classes, each encapsulating EPICS PVs, device metadata, and control logic. The design is built around a set of abstract base classes that enforce a consistent interface across hardware types, enabling flexible behavior and extensive code reuse.

Each physical device, such as a wire scanner, BPM, or beam loss detector, is represented by a Python class instance. Device classes define PVs as class attributes using standardized descriptors, making PV access and manipulation intrinsic to the object. For example, reading a wire position or writing a motion command is expressed naturally as *wire_device.position* or *wire_device.start_scan()*, abstracting away lower-level PV handling and promoting readable, maintainable code.

In parallel, device metadata and PV definitions are also declared in external YAML files, a human-readable, structured data format. These files define the beampath layout, region groupings, and all associated devices and PVs in a hierarchical, easy-to-maintain structure. Upon initialization, the system dynamically loads this configuration and binds the defined PVs to the appropriate device classes. This dual-layered approach of external YAML for structure and internal Python for logic enables rapid deployment of new measurement setups without modifying application code.

The result is a flexible, declarative system in which devices are defined through a combination of structured metadata and object-oriented logic. This design allows developers to test, extend, or swap out devices with minimal effort, streamlining both prototyping and production use. It also supports unit testing through mock device classes that inherit from the same base interfaces.

CONFIGURATION AND METADATA MANAGEMENT

External YAML configuration files support flexible deployment and eliminate the need for code changes. Well-suited for complex beamline configurations, YAML's hierarchical nature defines each device's PVs, name, location, and initialization data. At runtime, this metadata is loaded and bound to the corresponding device classes, making PVs intrinsic to each object and eliminating hard-coded logic.

All configurations are validated using Pydantic, which enforces strict schema compliance, catching errors at startup with clear messages indicating the exact field, expected type, and problematic value. It also provides strong typing and structured serialization allowing measurement results to be exported to YAML, JSON, or HDF5 formats.

* Work supported by U.S. Department of Energy, Contract DEAC02-76SF00515
† kabanaty@slac.stanford.edu

Content from this work may be used under the terms of the CC BY 4.0 licence (© 2022). Any distribution of this work must maintain attribution to the author(s), title of the work, publisher, and DOI.

ISBN: 978-3-95450-261-5 ISSN: 2673-7000 doi: 10.18429/JACoW-NAPAC2025-MOP019

BUNCH DURATION MEASUREMENTS IN THE APS-U BOOSTER*

J. C. Dooling†, J. R. Calvey, O. Mohsen, Argonne National Laboratory, Lemont, IL, USA

Content from this work may be used under the terms of the CC BY 4.0 licence (© 2022). Any distribution of this work must maintain attribution to the author(s), title of the work, publisher, and DOI.

Abstract

We present the results of time-based, bunch length measurements in the Advanced Photon Source Upgrade booster synchrotron using the bunch duration monitor (BDM) optical diagnostic. The BDM diagnostic is based on the detection of visible-wavelength synchrotron radiation. The detector is a metal-semiconductor-metal device followed by 42 dB of wide-band amplifier gain. Bunch duration is determined by de-convolving the raw output signal with the circuit's impulse response function. The BDM allows measurement of bunch duration over virtually the entire booster ramp. Defocusing in the optical path was necessary to overcome thermal steering from the in-tunnel mirror. Also, the effects of detector saturation must be considered to ensure a linear response. Presently, the booster increases bunch energy from 425 MeV to 6 GeV. Booster charge varies from 5 nC to 15 nC depending on storage ring operating modes. BDM data reveal that the bunch undergoes large longitudinal oscillations shortly after injection into the booster. The longitudinal oscillations are compared with elegant simulations. These oscillations are a source of injection loss especially at higher charge.

INTRODUCTION

The Advanced Photon Source Upgrade (APS-U) booster synchrotron provides the major boost in energy from the linac at 400-450 MeV to storage ring (SR) at 6 GeV. Bunch duration is an important parameter for efficient booster operation, especially at injection [1].

EXPERIMENTAL ARRANGEMENT

The booster BDM is located within the Synchrotron Light Monitor 2 (SLM2) enclosure in the A015 optics lab directly above the booster tunnel. The BDM front-end electronics is similar to that described earlier for the APS particle accumulator ring [2]. An in-tunnel mirror reflects synchrotron radiation up out of the booster tunnel to an optics station above the shield wall.

Saturation Effects

Broadening of the pulse duration measurement is observed when the signal is strong, leading to incorrect BDM results [3]. Saturation effects can be mitigated if de-convolved pulse amplitudes are kept below 8 V. We accomplished this requirement by defocusing the image on the detector as discussed in the next subsection.

Defocusing Optics

The active region size of the MSM detector is 0.2 mm by 0.2 mm. When the detector was placed near the focus of the final focusing lens, in addition to saturation, motion of the image spot due to thermal distortion of the in-tunnel mirror made measurements challenging. Initially, an ND1.0 neutral density filter was placed between the lens and the detector. In order to minimize the thermal effects, the filter was removed and the detector was placed closer to the lens. The spot on the detector was then defocused and larger; this significantly improved availability of the diagnostic by reducing the need for realignment. The modification is shown schematically in Fig. 1.

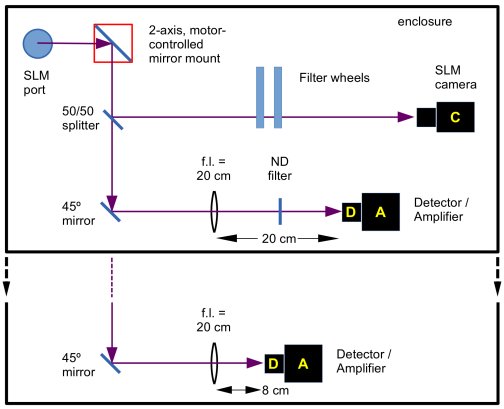


Figure 1: Optical layout of the booster SLM2 enclosure with the defocus modification of the BDM (D/A) line indicated.

MEASUREMENTS

The BDM diagnostic with modified optics was employed to measure bunch duration throughout the booster energy ramp at different charge levels. With the modified optics, the diagnostic can routinely gather data during operations. Signal optimization using a 2-axis picomotor-controlled mirror mount is done only occasionally now; for example, when changing from low- to high-charge operations or significantly changing the repetition rate.

Due to the inverse-square dependence of synchrotron radiation power on bending radius, ρ [4], the synchrotron radiation power from the booster at injection is much less than that from the particle accumulator ring (PAR), $\rho_{\mathrm{PAR}} = 1.02\,\mathrm{m}$ versus $\rho_{\mathrm{Boo}} = 33.3\,\mathrm{m}$; thus the booster BDM signal at injection tends to be weaker than that from the PAR BDM at PAR extraction.

The PAR collects charge from the s-band linac as a series of 30-Hz pulses into a single bunch ($h = 1$, fundamental RF frequency, $f_0 = 9.78\,\mathrm{MHz}$), then compresses the bunch with a 12^{th}-harmonic cavity for injection to the booster at a maximum rate of 1 Hz. In all cases presented here, linac energy and hence PAR and booster injection energy, were 425 MeV. Depending on stored charge, the rms bunch duration at extraction from the PAR ranges from 300-600 ps;

* Work supported by the U.S. D.O.E.,Office of Science, Office of Basic Energy Sciences, under contract number DE-AC02- 06CH11357.

† dooling@anl.gov

ISBN: 978-3-95450-261-5 ISSN: 2673-7000 doi: 10.18429/JACoW-NAPAC2025-MOP020

TOWARDS REAL-TIME CALIBRATION OF CBPMS USING SYNCHRONOUS RF INJECTION

M. S. McCallum*, G. Boorman, S. Gibson, A. Lyapin
John Adams Institute, Royal Holloway, University of London, Egham, United Kingdom
K.O. Kruchinin†, A. Aryshev, K. Popov,
High Energy Accelerator Research Organization (KEK), Tsukuba, Ibaraki, Japan

Content from this work may be used under the terms of the CC BY 4.0 licence (© 2022). Any distribution of this work must maintain attribution to the author(s), title of the work, publisher, and DOI.

Abstract

Cavity beam position monitors (CBPMs) are very high-precision devices that, in recent years, have progressed from experimental equipment to standard linac diagnostics in many prominent facilities, most notably free-electron lasers. However, the high sensitivity of these devices comes at the cost of a limited measurement range, even with high dynamic-range electronics. Furthermore, CBPMs need to be calibrated in situ, ideally by introducing a known beam offset, which is often impractical in large installations. This paper reports on a method to match CBPM beam signals by injecting tightly controlled synchronised bursts of radio frequency (RF) oscillations into the sensor cavity and reading back their superposition. The method allows compensation for static beam offsets (with beam) and calibrates CBPMs electronically (no beam required), thus removing some of the operational hurdles. We discuss the first demonstration of this method at the Accelerator Test Facility 2 (ATF2).

INTRODUCTION AND CALIBRATION CONTEXT

Cavity Beam Position Monitors (CBPMs) are high-precision diagnostic devices capable of measuring beam positions with resolutions on the order of tens of nanometres [1–3]. They have become standard in modern facilities such as free-electron lasers and test accelerators like ATF2 [4]. However, their high sensitivity requires frequent recalibration—typically via beam steering or injection of a reference signal—which can be impractical in installations with limited flexibility [5].

CBPMs operate by coupling to the dipole mode excited as an electron bunch passes through a cylindrical cavity. The resulting signal amplitude is proportional to the beam offset and decays exponentially in time:

$$V(t,x) = k\,x\,e^{-\frac{t}{\tau}}\cos(\omega_0 t + \phi) \quad (1)$$

where x is the transverse offset, k is a proportionality constant, ω_0 is the mode frequency, τ is the decay constant, and ϕ is the phase offset.

Recalibration is sometimes triggered by temperature drift or local oscillator instability. At ATF2, for example, a calibration tone is injected after the CBPM to serve as a stable reference, with amplitude and phase drift measured below 0.1% and 0.05° h^{-1}, respectively [4, 6]. Nevertheless, calibration remains an operational burden.

This paper presents a complementary method for CBPM calibration based on injecting radio frequency (RF) pulses directly into the cavity. By synchronising and phasing these signals relative to the beam-induced signal, we show that it is possible to cancel the beam signal or reproduce it without beam [7]. The first demonstration of this approach was carried out at ATF2 in Japan [8]. This has the potential to enable partial calibration without beam and may support real-time in situ signal processing.

EXPERIMENTAL METHOD

The experiment was carried out at the Accelerator Test Facility 2 (ATF2) at KEK, Japan, using one of the operational cavity BPMs from the ATF2 system [4]. A schematic and detailed description of the earlier configuration are provided in our IBIC 2024 paper [8].

For the June 2024 measurements, we upgraded the injection system with a custom-built RF generator delivering a continuous-wave signal approximately 20 MHz above the cavity's resonant frequency. This frequency offset ensures that, after mixing, only the down-converted component overlaps the cavity's dipole mode, while the up-converted sideband lies outside its 10 MHz bandwidth. Consequently, the cavity itself acts as a narrowband filter, suppressing non-resonant components and yielding a cleaner time-domain signal.

In the previous configuration, we had used a Highland Technology T240 fast pulse generator to produce the RF burst. In the new setup, the CW carrier is gated by a fast RF switch driven by a precision delay generator, eliminating unwanted spectral artefacts around the resonant frequency. A 26 MHz burst from an arbitrary waveform generator is mixed with the carrier and triggered by the facility-wide 3.125 Hz distributed trigger, ensuring synchronisation in both time and phase.

The combined RF pulse is injected into the BPM's input port, and the output is fed through the standard down-conversion chain for digitisation.

A beam shift campaign was carried out in June 2024 over offsets ranging from 270 µm to 450 µm. At each position, the injected RF burst was adjusted to cancel the beam-induced signal, and waveforms were acquired via EPICS for offline analysis. From these data, we extracted the amplitudes of both the beam and injected pulses to quantify the matching fidelity at each offset. In principle, integrating these meas-

* Contact Email: mark.mccallum@rhul.ac.uk
† Present address: SLAC National Accelerator Laboratory, Menlo Park, California, USA. Email: konkruz@slac.stanford.edu

ISBN: 978-3-95450-261-5 ISSN: 2673-7000 doi: 10.18429/JACoW-NAPAC2025-MOP021

COMPACT 3D ELECTRO-OPTIC SAMPLING BEAM POSITION MONITOR*

T. Hodgetts†,[1], L. Amoudry[1], G. Andonian[1], C. Hansel[2], A. Knetsch[3], M. Litos[2], D. Matteo[1], E. Ros[2]
[1]RadiaBeam, Santa Monica, CA, USA
[2]University of Colorado Boulder, Boulder, CO, USA
[3]SLAC National Accelerator Laboratory, Menlo Park, CA, USA

Abstract

RadiaBeam and University of Colorado Boulder have developed a 3D beam position monitor based on the well-established electro-optic sampling (EOS) technique, enabling non-interceptive, ultrafast position monitoring of high-intensity femtosecond beams. Based on the initial prototype of the 2D EOS-BPM, using 1 pair of crystals, installed at SLAC FACET-II, this 3D design has undergone several iterations. A fully functional prototype was manufactured and bench tested using Off-Axis Parabolic (OAP) mirrors to focus the laser on 2 sets of 2 crystals. However, due to the difficulty of working with OAPs and the offset of the crystal pairs, a new EOS-BPM was developed using an axicon lens to shape the laser into an annulus at the crystal plane. This dramatically simplifies the setup, reduces its footprint, and provides full 3D information from a single laser beam. Once installed, the EOS-BPM can yield the full 3D centroid positioning of two bunches in a wakefield accelerator, or the tilt of a beam used to power a light source. Under ideal conditions, simulation-based estimates show temporal and transverse resolution for the beam centroids of a two-bunch wakefield accelerator beam of order 50 fs and 1 μm, respectively.

INTRODUCTION

The EOS-BPM technique [1,2] offers a non-invasive method of measuring beam position without sacrificing beam quality (Fig. 1). We previously developed a 3D EOS-BPM prototype (Fig. 2) using 4x independently synchronized lasers and 2x pairs of crystals offset from each other. Due to the difficulty of aligning OAP mirrors, each mirror needed to be mounted on a stage with five degrees of freedom (DOF). In addition, all stages were motorized to allow for alignment in-vacuum. Each crystal assembly was also motorized in two directions to allow the user to change the position of the laser on the crystal should the crystal exhibit localized damage. Here we report on mechanical upgrades to the 3D EOS-BPM design based on axicon focusing of the probe laser, resulting in a more compact and less complex device.

Since the laser arrives at an angle, as seen in Fig. 1, the temporal dimension of the electron beam is mapped to the laser beam's spatial dimension (spatial encoding). A camera detects the polarization changes, providing relative temporal spacing of a two-bunch electron beam and transverse spatial offset. See Ref. [2] for more details.

* Work supported by DOE Grant Number DE-SC001796.
† tara@radiabeam.com

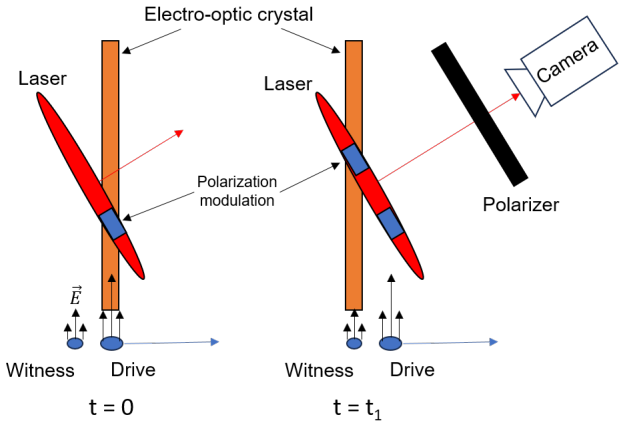


Figure 1: EOS-BPM operating principle. An ultrafast laser pulse has its polarization modulated via the electro-optic effect, with strong THz fields originating from the electron beam.

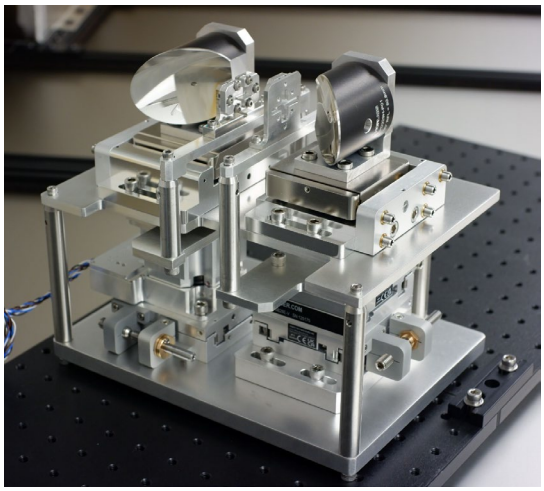


Figure 2: Phase I EOS prototype.

DESIGN IMPROVEMENTS

In the upgraded design, the focusing element is an axicon lens, replacing off-axis parabolic mirrors (OAPs) in the previous iteration. This change provides multiple technical and practical benefits over the OAPs. The axicon shapes an incident gaussian or flat-top laser beam into an annulus in the far field, with divergence angle defined by the axicon geometry. This automatically enables the spatial encoding at the nonlinear crystal plane required for high time-resolution of the EOS-BPM. The extended "donut"

Content from this work may be used under the terms of the CC BY 4.0 licence (© 2022). Any distribution of this work must maintain attribution to the author(s), title of the work, publisher, and DOI.

ISBN: 978-3-95450-261-5 ISSN: 2673-7000 doi: 10.18429/JACoW-NAPAC2025-MOP025

DESIGN, CHARACTERIZATION, AND VALIDATION OF A PULSED RF BURST SOURCE FOR IN-SITU CAVITY BEAM POSITION MONITOR CALIBRATION

K.O. Kruchinin*
High Energy Accelerator Research Organization (KEK), Ibaraki, Tsukuba, Japan
G. Boorman, A. Lyapin, M.S. McCallum
John Adams Institute at Royal Holloway, University of London, Egham, United Kingdom

Content from this work may be used under the terms of the CC BY 4.0 licence (© 2022). Any distribution of this work must maintain attribution to the author(s), title of the work, publisher, and DOI.

Abstract

Beam Position Monitors (BPMs) are critical instruments in accelerator facilities, providing precise beam orbit measurements with tens of nanometers resolutions, essential for the operation of current linac-based Free Electron Lasers (FELs) and future linear colliders. In this report, we introduce the development and successful testing of a pulsed RF burst source specifically designed for BPM calibration. The source was initially characterized and installed at the ATF2 facility in KEK, Japan. The system injects tailored Radio Frequency (RF) pulses into the BPM cavity via one of the two output ports. With the capability to adjust frequency and pulse width, to emulate beam pulses, the system demonstrated nearly complete cancellation of beam-generated signals when the injected RF pulse overlapped with the beam pulse. This source has the potential for in-situ BPM calibration, mitigation of static signal contributions caused by cavity misalignments and capacity for wakefield compensation. Dedicated hardware development for further refinement of the source is underway at Royal Holloway, University of London, UK, using two *Texas Instruments LMX2820* high-frequency synthesizers triggered by a shared external source to achieve precise phase synchronization between distinct frequencies at defined delays. Preliminary measurements indicate a phase jitter of about 1.2 degrees, currently limited by the trigger signal's slow rising edge (tens of ns), while system requirements demand sub-nanosecond (hundreds of ps) precision for robust, high-frequency phase locking.

INTRODUCTION

Cavity BPMs of various designs are widely deployed across accelerator facilities worldwide [1–5], serving as the cornerstone for high-resolution beam orbit measurements. These devices are essential, offering the only means of achieving tens of nanometer scale resolution — a capability demonstrated most notably at the Accelerator Test Facility (ATF) [6] at KEK, Japan. As part of the final focus system prototype for the proposed International Linear Collider (ILC), the ATF has set benchmark performance standards for cavity BPM technology [7–9].

Despite their critical role, several challenges persist in the design and operation of cavity BPM systems. Cavities are typically mounted in close proximity to optical elements such as quadrupole magnets, often with axial offsets on the order of hundreds of micrometers. These misalignments significantly constrain the useful dynamic range of the BPM system. In addition, regular calibration is often required to mitigate drift effects caused by environmental temperature fluctuations and instabilities in front-end electronics, such as phase shifts [10]. Current calibration procedures [11] — whether through physical displacement of the cavity or beam-based methods like dogleg bumps — are time-consuming and resource-intensive, especially at large facilities managing dozens or even hundreds of BPM units. Furthermore, cavity BPMs are known to introduce wakefields [12] that contribute to emittance degradation, posing a substantial obstacle in maintaining beam quality at the nanometer scale — an essential requirement for next-generation linear colliders.

To address these limitations, we propose a novel technique involving the injection of short, pulsed radio frequency (RF) bursts directly into the cavity via one of its output ports [13]. These pulses are shaped to emulate the electromagnetic signature of an actual beam passage. When synchronized with the beam signal, the injected RF pulse can partially cancel the cavity response, enabling effective calibration without beam presence. This approach not only facilitates fast and fully automated calibration but also provides a method for compensating static signal offsets arising from mechanical misalignments. Additionally, in a dynamic compensation mode, preliminary results suggest that this technique can mitigate wakefields by up to 50%, through pre-filling the cavity with inverse-polarity fields at the moment of beam excitation.

Results of the injected beam overlapping with the BPM signal generated by the ATF beam and calibration procedure have been presented previously in [14, 15]. In this paper, we present the design, characterization, and validation of an RF burst source tailored for such applications. We detail its key performance metrics, tunability, and limitations, and outline a development roadmap toward fully integrated, in-situ calibration solutions for cavity BPM systems.

RF SOURCE DESIGN

The first prototype of the pulse injection source was developed at ATF using discrete components and sources. The schematic diagram of the final version is shown in Fig. 1. A custom-made local oscillator (LO) operating at 6452 MHz was used as the input signal. This same LO was also fed into the BPM front-end for down-conversion.

* konkruz@slac.stanford.edu (present address: SLAC National Accelerator Laboratory, Menlo Park, CA, USA)

ISBN: 978-3-95450-261-5 ISSN: 2673-7000 doi: 10.18429/JACoW-NAPAC2025-MOP026

DESIGN OF PHASE DIVERSITY ELECTRO-OPTIC SAMPLING OF THz COHERENT TRANSITION RADIATION

S. J. Kelham*, G. Ha, Northern Illinois University, Dekalb, IL, United States
P. Piot, Argonne National Laboratory, Lemont, IL, United States

Content from this work may be used under the terms of the CC BY 4.0 licence (© 2022). Any distribution of this work must maintain attribution to the author(s), title of the work, publisher, and DOI.

Abstract

We report progress on the design of a Phase Diversity Electro-Optic Sampling (DEOS)-based longitudinal profile measurement system. The current design uses THz coherent transition radiation (CTR) to convey the bunch longitudinal information. A 1550 nm fiber laser available at the Argonne Wakefield Accelerator facility will be used as the probe for electro-optic sampling. Specifically, we discuss pulse synchronization and probe beam transport, the design and optimization of the probe beam stretcher, and the design of the probe beam detection system.

INTRODUCTION

Electro-optic sampling (EOS) has emerged as one of the most promising non-invasive diagnostics for characterizing relativistic electron bunches [1–3]. Recent advancement in spectral encoding techniques—particularly the development of Phase-Diversity Electro-Optic Sampling (DEOS) [4]—has enabled single-shot measurements with temporal resolutions at or even below the conventional limit set by probe duration and bandwidth [5]. These advances may enable accurate, high-resolution, non-invasive measurements of bunch profile in the sub-picosecond regime. Such capability could be particularly important for advanced accelerator concepts (AAC) that require various shaped bunches [6, 7].

Such shaped electron bunches for AAC typically have rms bunch lengths of 0.1-10 ps [8, 9], which falls within the range where traditional EOS methods may face resolution limitations. In addition to sub-picosecond bunch lengths, measurement of shaped, non-symmetric electron bunches [10,11], which can be produced by several different ways [12–14], could be a new challenge. These shaped profiles usually include sharp edges, fine structures, or steep gradients.

Efforts are underway to address this challenge in measuring shaped bunch profiles. We are preparing experiments to explore the measurement of shaped bunches using DEOS method. Producing various shaped bunches are rather straightforward at Argonne Wakefield Accelerator (AWA) facility [15]. Thus, as the first step, we are building DEOS system and plan to validate it using CTR from an existing OTR screen on the beamline.

It is worth note that we have designed a similar measurement system with 785 nm photocathode laser as a probe beam source [16]. Here the photocathode laser's bandwidth is limited due to amplification process for intense photoemission. A 3 nm bandwidth of the photocathode laser significantly limits the resolution of the spectral encoding measurement. Also, the system included a free-space motorized delay stage for synchronization between the IR probe beam and the THz CTR. It introduced challenges on alignment and coarse and fine timing synchronization.

In this paper, we present a recent design with a different probe beam source and controls, which can significantly improve the resolution and ease the synchronization. Recently, Menlo Systems 1550 nm fiber laser and RF delay circuit have been successfully implemented at the AWA facility. The delay control of the fiber laser pulse train with respect to the master clock was demonstrated, making the fiber laser as preferred probe beam for the DEOS experiment. To accommodate the new probe laser, the transport, stretcher, and detection line must be redesigned. Figure 1 shows the layout of the current design. We will discuss the design procedure for this new system.

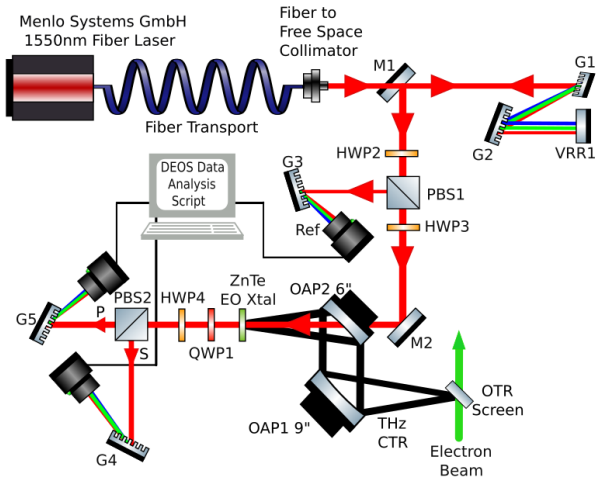


Figure 1: Optics diagram of proposed CTR THz bunch profile monitor. Probe beam is transported by polarization maintaining fibers and dispersion compensating fibers. THz CTR is generated by beam interaction with an OTR screen and focused to a ZnTe crystal using off-axis parabolic mirrors. Unmodulated reference and modulated S and P polarizations will be recorded for DEOS reconstruction.

PROBE BEAM STRETCHER DESIGN FOR 1550 nm FIBER LASER

In a spectral encoding measurement, the probe beam is given a linear frequency chirp to create a time-to-wavelength mapping. The analysis of the probe beam's modulated spectra can return the electron bunch temporal profile. There are various methods for giving the probe beam a frequency chirp, but we have opted for a system of two gratings to act as

* z1904611@students.niu.edu

ISBN: 978-3-95450-261-5 ISSN: 2673-7000 doi: 10.18429/JACoW-NAPAC2025-MOP028

FACILITY-SCALE DIFFERENTIABLE VIRTUAL ACCELERATOR AT FERMILAB*

N. Kuklev†, M. Wallbank, N. Banerjee, J. Jarvis, A. Romanov
Fermi National Accelerator Laboratory, Batavia, IL, USA

Content from this work may be used under the terms of the CC BY 4.0 licence (© 2022). Any distribution of this work must maintain attribution to the author(s), title of the work, publisher, and DOI.

Abstract

As the design complexity of modern accelerators grows, there is more interest in using advanced simulations and algorithms that have fast execution time or yield additional insights. One notable example are the gradients of physical observables with respect to design parameters, which are broadly useful in optimization and uncertainty analysis. The IOTA/FAST facility has been working on implementing and experimentally validating an end-to-end virtual accelerator test stand that is both fast and gradient-aware, allowing for rapid prototyping of new software and experiments with minimal beam time costs. We describe the selection and benchmarking of both physics and ML codes for linac and ring simulation, including obtaining parameter gradients with autodiff. We will also show the development of generic interfaces between surrogate and physics-based sections, and how the control interface is exposed as either a deterministic discrete event simulator or a fully asynchronous EPICS/ACNET soft IOC. We will also discuss challenges in model calibration and uncertainty quantification, as well as future plans to extend modelling to other Fermilab accelerators like PIP-II and Booster.

INTRODUCTION

Particle accelerator projects face increasing performance demands, resulting in tighter tolerances on lattice accuracy and stability. Achieving these tolerances requires both more advanced diagnostics and more commissioning time, which contributes to rising costs and lower beam availability.

A common approach to reduce commissioning risks is to implement realistic versions of key accelerator systems as simulations and use them to validate commissioning procedures. A recent successful example of this approach is the Advanced Photon Source Upgrade Project (APS-U), which had a commissioning plan that included advanced ELEGANT simulations, detailed task scheduling, and many validation studies, including within a dedicated EPICS control network [1–3].

So far most commissioning simulation projects have focused on the specific needs and quirks of their respective machines, avoiding complexity through implementing only the physics models and control system behaviors relevant to a particular project. This approach is not scalable, especially for a research facility like FAST/IOTA, since our machines are in constant flux and undergoing upgrades as the various experiments and elements are installed. Moreover, Fermilab main complex is currently undergoing several major upgrades, PIP-II (Proton Improvement Plan II) and ACORN (Accelerator Controls Operations Research Network). These will result in a mix of ACNET and EPICS controls systems, with brand new beamlines and devices having to interface with those over 40 years old.

Given the above complexity, significant validation and practice will be needed to ensure smooth PIP-II commissioning and operation. We require a tool capable of testing classic methods (such as optics measurements via LOCO [4, 5], orbit feedback, multi-wire measurements, and many others), but also amenable to training and validating a new generation of machine learning (ML) tools. Notable examples of the latter include Bayesian optimization (BO) [6–9], reinforcement learning (RL) [10], and phase space reconstruction [11]. ML methods are especially promising to address issues that have previously relied on operational experience or incomplete, qualitative simulations. This paper presents our recent progress in development of a virtual accelerator (digital twin) toolkit as a potential unified facility-scale solution for Fermilab and potentially other accelerators. We will first describe the key requirements and resulting architectural details. Then, we will show use cases and our first upcoming project, the IOTA proton injector commissioning.

VIRTUAL ACCELERATOR

Throughout this paper, we will use the term '(surrogate) model' to describe the specific (approximate) implementation of an accelerator or system. For example, an ImpactX simulation and a neural network (respectively) that can track beam with space charge. We will use the term 'virtual accelerator' to describe a framework that exposes and coordinates both standard and surrogate models to form a complete simulated control and physics environment. In the industry, the term 'digital twin' is also popular. One can think of virtual accelerators as backend engines for a virtual test stand, whereby various programs and users can interact with the models in a configurable environment with an appropriate mix of control systems, simulation fidelities, and computational requirements.

Our plan for virtual accelerator development has three main goals aligned with both the Fermilab project priorities and the more global challenges described in the recent DOE GARD accelerator and beam physics roadmap [12, 13]:

- To provide a robust virtual test stand for testing tools and procedures, including commissioning and operational applications as well as research codes.

* This manuscript has been authored by FermiForward Discovery Group, LLC under Contract No. 89243024CSC000002 with the U.S. Department of Energy, Office of Science, Office of High Energy Physics.

† nkuklev@fnal.gov

ISBN: 978-3-95450-261-5 ISSN: 2673-7000 doi: 10.18429/JACoW-NAPAC2025-MOP029

DEVELOPMENT AND APPLICATIONS OF DIFFERENTIABLE COHERENT OPTICAL TRANSITION RADIATION SIMULATIONS

R. Roussel*, SLAC National Accelerator Laboratory, Menlo Park, CA, USA
R. Aguilar, M. LaBerge, F. L. Wu, A. Irman, J. Kelling, U. Schramm,
Helmholtz-Zentrum Dresden-Rossendorf, Dresden, Germany
M. Downer, Z. Ouyang, The University of Texas at Austin, Austin, TX, USA

Content from this work may be used under the terms of the CC BY 4.0 licence (© 2022). Any distribution of this work must maintain attribution to the author(s), title of the work, publisher, and DOI.

Abstract

Optical transition radiation (OTR) beam profile monitors are widely used to measure the transverse profiles of low-charge electron bunches at advanced linear accelerator facilities such as LCLS-II and FACET-II. However, in scenarios involving strong longitudinal compression or microbunching-induced current spikes, the incoherent OTR signal—proportional to the transverse beam density—is often dominated by coherent OTR (COTR). The resulting COTR patterns exhibit complex dependencies on the full spatiotemporal structure of the beam, rendering conventional profile interpretation ineffective. In this work, we present a novel, backwards-differentiable simulation framework for COTR emission, enabling gradient-based inference of beam characteristics directly from COTR images. We further integrate this framework with the generative phase space reconstruction (GPSR) method to recover high-fidelity 4D transverse phase space distributions of strongly compressed beams. Simulation results demonstrate the ability of this approach to accurately reconstruct detailed beam structure from COTR-based diagnostics, offering a new path toward high-resolution characterization of ultrashort electron bunches.

INTRODUCTION

Optical transition radiation (OTR) beam diagnostics are a common method to diagnose the transverse profile of the beam distribution in both conventional accelerators such as LCLS or FACET-II and novel accelerators such as laser wakefield accelerators (LWFA). Generally, particle beams that intercept metallic foils emit OTR radiation, which can then be imaged using cameras. In cases where the longitudinal bunch length is longer than the imaging wavelength, the radiation is incoherent (IOTR) and thus the intensity of the transverse radiation pattern is proportional to the transverse beam profile. However, in cases where the beam is shorter than the imaging wavelength, either due to longitudinal compression in magnetic chicanes, longitudinal micro-bunching, or short pulse durations generated by LWFA sources, the emitted radiation is coherent (COTR), leading to a more complex relationship between the transverse particle distribution and transverse radiation pattern. As a result, OTR screens located in areas where short pulse durations are present tend to be corrupted by COTR, making it challenging to diagnose the transverse beam distribution.

* rroussel@slac.stanford.edu

To address this problem, we have implemented so-called backwards differentiable simulations of incoherent and coherent OTR that can be used to effectively infer transverse beam properties from beam profile measurements that contain COTR. Backwards differentiable simulations are a simulation methodology that tracks the derivatives of each individual computation to enable inexpensive computations of output gradients with respect to large numbers of input parameters. These gradients can then be used to infer beamline [1] or beam distribution properties [2] through the use of gradient-based optimization algorithms, which scale effectively to large numbers of free parameters.

In this work, we describe the implementation of differentiable COTR calculations. We then demonstrate on a synthetic test case how differentiable beam dynamics simulations containing COTR phenomena can be used to reconstruct transverse 4-dimensional phase space distribution structure of short beam distributions. This opens the door to resolving beam distribution structure in locations where diagnostics were previously unavailable, namely after longitudinal bunch compression at free electron lasers or at LWFA facilities.

DIFFERENTIABLE COTR SIMULATIONS

The goal of our simulation is to calculate the intensity distribution of both incoherent and coherent OTR signals at M wavelengths on a 2D, transverse mesh grid of $H \times W$ pixels on our diagnostic screen given a distribution of N macro-particle coordinates $X = \{\mathbf{x}_1, \mathbf{x}_2, \dots\}$ in 6D phase space. To enable backwards-differentiability we implement each stage of the OTR calculation in the Python library PyTorch [3]. We also implement the simulation in a manner such that it is vectorized, meaning that it can execute multiple, batched calculations of OTR signals for multiple incoming beam distributions at once. This leverages parallel computing capabilities of CPUs and more importantly GPUs, which PyTorch natively supports. For notation simplicity, we neglect the batch dimensions here.

We compute the incoherent and coherent portions of the OTR separately. First, we estimate the density of the beam distribution in position space $\rho(x, y, z)$ from macro-particle coordinates using the kernel density estimation technique, which is vectorized and maintains differentiability with respect to the particle coordinates. We then obtain the IOTR by integrating the beam density over the longitudinal axis, resulting in a 2D profile, $g(x, y)$. Finally, we convolve it over x and y with the OTR point spread function (PSF) [4], which

ISBN: 978-3-95450-261-5 ISSN: 2673-7000 doi: 10.18429/JACoW-NAPAC2025-MOP030

DESIGN AND DEVELOPMENT OF AN UPGRADED FAST ORBIT FEEDBACK SYSTEM FOR NSLS-IIU

S. Kongtawong*,[1,2], K. Ha[1], Y. Hidaka[1], G. Wang[1], Y. Tian[1], T. Shaftan[1]
[1]National Synchrotron Light Source II, Upton, NY, USA
[2]Synchrotron Light Research Institute, Nakhon Ratchasima, Thailand

Abstract

As light source facilities evolve, upgrading fast orbit feedback systems is essential for improving beam stability. NSLS-II is planning an upgrade to NSLS-IIU, which introduces stricter stability requirements for advanced experiments. To address this, we developed a next-generation fast orbit feedback prototype system to enhance noise suppression and extend control bandwidth beyond 1 kHz. A system-wide evaluation was conducted, covering beam position monitors, cell controllers, power supply controllers, power supplies, and vacuum chamber effects. Latency and bandwidth bottlenecks were identified in the cell and power supply controllers. A new cell controller was designed to increase the sampling rate from 10 kHz to 31.5 kHz and reduce system latency to under 70 µs. The transfer function and gain measurements of a single-input-single-output system show a 10-dB improvement in noise suppression and an extension of bandwidth into the kHz range. We present the development and performance results of the upgraded system, offering a path toward higher beam stability at NSLS-IIU.

INTRODUCTION

Recent upgrades and new synchrotron light source facilities around the world are pushing toward significantly lower emittance. NSLS-II is planning an upgrade to NSLS-IIU, which will reduce the horizontal emittance to as low as 23 pm·rad at 3 GeV or 42 pm·rad at 4 GeV [1,2]. With the resulting beam size reduction, maintaining high electron beam orbit stability becomes increasingly critical for operational performance.

In addition to minimizing sources of mechanical and environmental vibrations, NSLS-II aims to enhance the performance of its fast orbit feedback (FOFB) system by increasing both suppression gain and feedback bandwidth. The current FOFB system operates with a unity-gain bandwidth of approximately 300–350 Hz [3]. The upgrade targets extending this bandwidth into the kilohertz range, in line with trends at other advanced facilities [4–6].

This paper presents the design and development of new digital processing components, along with experimental results. We demonstrate that, even with the existing power supplies and vacuum chambers, a unity-gain bandwidth exceeding 1 kHz can be achieved.

* skongtawong@bnl.gov

SYSTEM CHARACTERIZATION AND DESIGN SPECIFICATIONS

We began by re-evaluating the latency and transfer function of the existing FOFB system to validate a dynamic model developed for NSLS-II. The FOFB system architecture, shown in Fig. 1, consists of several components, with performance primarily limited by the digital processing latency of the cell controller (CC) and the bandwidth of the corrector power supplies. The system currently supports 240 beam position monitors (BPMs) and controls up to 90 power supplies per plane.

At the core of the system, the CC receives BPM data and computes corrections using a 480×180 response matrix [7]. However, due to resource constraints in the Xilinx Virtex-6 FPGA in the CC, matrix operations are implemented sequentially rather than fully in parallel, introducing a processing delay of approximately 110 µs, making this stage the dominant latency source in the system.

In addition to processing latency, the power supply (PS) bandwidth further constrains the system. The current correctors have bandwidths of approximately 4 kHz in the horizontal plane and 1.5 kHz in the vertical plane. In 2019, upgraded power supplies with bandwidths of 6.3 kHz (horizontal) and 3.3 kHz (vertical) were developed and installed in Cells 23–28, covering one-fifth of the storage ring for testing.

To model the system behavior, we use the following transfer function:

$$G(s) = \frac{\text{Const.}}{(s + p_{\text{ps}})(s + p_{\text{chamber}})} \times \left(\frac{1 - e^{-sT_{\text{avg}}}}{s}\right)\left(\frac{1 - e^{-sT_{\text{zoh}}}}{s}\right)\exp(-sT_{\text{latency}})H_{\text{PID}} \quad (1)$$

where

- p_{ps} is the power supply pole ($2\pi \times$ bandwidth),
- p_{chamber} is the vacuum chamber pole (bandwidth 13 kHz),
- T_{avg} is the FA (Fast Acquisition) averaging time (at 10 kHz),
- T_{zoh} is the zero-order hold delay from the DAC (at 10 kHz),
- T_{latency} is the total system latency,
- H_{PID} is the digital PID controller.

To verify the model parameters, we conducted bench measurements of delay and filtering at each stage, followed by

Content from this work may be used under the terms of the CC BY 4.0 licence (© 2022). Any distribution of this work must maintain attribution to the author(s), title of the work, publisher, and DOI.

ISBN: 978-3-95450-261-5 ISSN: 2673-7000 doi: 10.18429/JACoW-NAPAC2025-MOP032

DIGITAL CAMERA PERFORMANCE IN A HIGH-RADIATION ACCELERATOR TEST BEAM FACILITY*

S. Perez†, S. Gessner, C. Hast, I. Rajkovic
SLAC National Accelerator Laboratory, Menlo Park, CA, USA

Abstract

Digital cameras are critical diagnostics at test beam facilities. At FACET-II, there are over 100 digital cameras in operation. Scattered electrons from the 10 GeV beam cause high levels of ionizing radiation, which makes profile monitors susceptible to two types of failures: single-event upsets (SEU) and permanent death. We developed software infrastructure to detect camera failures and track SEUs over time. Additionally, we installed digital radiation monitors (RADFETs) at the locations of 10 cameras to measure local dosage. We find strong correlations between the SEU rate and local dose. This information is used to optimize camera placement and predict failure rates in the experiment.

INTRODUCTION

FACET-II [1] positions SLAC as a world leader in developing cutting-edge plasma wakefield acceleration (PWFA) [2] technology for future accelerators by providing 10 GeV electron beams optimized for PWFA experiments. However, producing extremely high-energy beams poses some challenges. Scattered electrons from the beam cause high levels of ionizing radiation, which creates concerns for the electronic equipment in the accelerator. Digital cameras at FACET-II are susceptible to failures in the form of single-event upsets (SEU) and permanent death. In the case of an SEU, the camera is disconnected from the camera server, but it can be recovered by power cycling the device. High radiation doses can also lead to permanent death, which is more costly and disruptive to experimental programs.

A study was conducted to understand radiation effects and investigate ways to mitigate damage to digital cameras. Digital radiation monitors have been installed at the locations of 10 cameras. They provide useful information about local radiation dosage during experiments. Additionally, a new software tool known as Camera Watchdog was deployed to monitor and automatically power cycle cameras in the case of an SEU. The Camera Watchdog also updates the total number of reboots executed for each camera, which is used as a proxy for the SEU rate. In this paper, we show that a combination of camera monitoring software and digital radiation monitors can provide valuable information about the longevity of digital cameras, which allows us to optimize camera placement and predict camera failures.

* Work supported by the U.S. Department of Energy under DOE Contract No. DE-AC02-76SF00515.

† shperez@slac.stanford.edu

RADIATION IN THE FACET-II ACCELERATOR

Past data have shown that radiation is highest near the beam dump. Additionally, there are hot spots, or locations where radiation is most concentrated. Hot spots have been identified through radiation dose measurements and trial and error. Where possible, cameras were moved away from hot spots to prevent further damage. Previously recorded data from radiation monitors have also shown that radiation levels are higher during PWFA experiments as a result of plasma interactions. Another source of radiation is beam tuning, which can lead to large beam losses. Reducing the time electronics are exposed to the radiation environment is an effective way to protect cameras from radiation; however, it is not possible to install cameras for just one experiment. It is also not possible to replace a camera in the middle of an experiment, so it is very important to keep track of radiation damage to equipment.

Table 1: Digital Cameras with RADFETs at FACET-II

Camera Name	Region	Model and Sensor
FrontView	IP Area	Allied Vision Mako CCD
IPOTR1	IP Area	Allied Vision Mako CCD
IPOTR2	IP Area	Allied Vision Mako CCD
DSOTR	IP Area	Allied Vision Manta CCD
DTOTR2	Dump	Allied Vision Mako CCD
CHER	Dump	Hamamatsu Orca CMOS
LBG LFOV	Dump	Hamamatsu Orca CMOS
GAMMA1	Dump	Allied Vision Mako CCD
LFOV	Dump	Allied Vision Mako CCD
GAMMA2	Dump	Hamamatsu Orca CMOS

HARDWARE

Digital cameras are critical diagnostics because they measure non-scalar parameters, such as beam energy spectrum and spot size. There are more than 100 cameras in operation at FACET-II, and about half of these are in the experimental area where radiation levels are highest. Most profile monitors at FACET-II are Allied Vision Mako or Manta CCD cameras. There are also a few Hamamatsu Orca CMOS cameras near the beam dump.

We placed radiation-sensing field-effect transistors (RADFETs) at the locations of 10 cameras in the experimental area, as depicted in Fig. 1. Table 1 shows the name, region in the linac, and model and sensor type for each camera included in the study.

Content from this work may be used under the terms of the CC BY 4.0 licence (© 2022). Any distribution of this work must maintain attribution to the author(s), title of the work, publisher, and DOI.

ISBN: 978-3-95450-261-5 ISSN: 2673-7000 doi: 10.18429/JACoW-NAPAC2025-MOP034

EFFICIENT 6-DIMENSIONAL PHASE SPACE MEASUREMENTS AND APPLICATIONS TO AUTONOMOUS MONITORING AT LCLS-II

R. Roussel*, C. Garnier, D. Kennedy, W. Colocho, A. Le, G. Bhardwaj,
A. Edelen, SLAC National Accelerator Laboratory, Menlo Park, CA, USA
J. P. Gonzalez-Aguilera, University of Chicago, Chicago, IL, USA

Content from this work may be used under the terms of the CC BY 4.0 licence (© 2022). Any distribution of this work must maintain attribution to the author(s), title of the work, publisher, and DOI.

Abstract

Increasing the performance and capabilities of free electron lasers, such as LCLS-II, hinges on our ability to precisely control and measure the 6-dimensional phase space distribution of the beam. However, conventional tomographic techniques necessitate a substantial number of measurements and computational resources to characterize a single beam distribution, using many hours of valuable beam time. Novel diagnostic techniques are needed to significantly reduce the number of measurements required to reconstruct detailed, 6-dimensional beam features to enable feedback for precision beam shaping for accelerators and characterize unknown physical phenomena. In this work, we present a novel approach to analyzing experimental measurements using differentiable beam dynamics simulations and generative representations of 6-dimensional phase space distributions. We discuss developments in combining this work with advanced accelerator control algorithms and parasitic beam measurements to autonomously monitor the 6-dimensional phase space distribution of the beam at LCLS-II during accelerator operations.

INTRODUCTION

Developing a precise understanding of particles distribution in 6-dimensional position-momentum space in real accelerators is key to maximizing the performance of current accelerator facilities and enabling future accelerators. Current accelerator applications, such as Free Electron Lasers (FELs) require precise control over beam properties in order to maximize FEL pulse intensity, while future accelerators, such as wakefield-based accelerator schemes also benefit from detailed control over the distribution of particles in 6-dimensional phase space [1].

However, currently used techniques for precisely measuring or predicting high-dimensional (> 4 dimensions) beam distributions from experimental data have not been able to adequately address this diagnostic challenge in practical settings. Direct or tomographic measurements of 5- or 6-dimensional phase space distributions have been demonstrated in only a handful of specific situations with specialized diagnostic elements, requiring a substantial number of individual measurements over a large amount of dedicated beam time (> 18 hrs) [2, 3]. On the other hand, using 2-dimensional projections of the beam distribution, such as beam profile monitors, provides substantially more information about the beam distribution than lower dimensional measurements, enabling significantly fewer measurements to reconstruct the beam distribution. Unfortunately, the computational costs of scaling conventional algebraic reconstruction techniques (ART [4], SART [5], MENT [6, 7]) to reconstructing 6-dimensional distributions from 2-dimensional images precludes the use of these algorithms in a practical setting [8].

To address these challenges, we introduced the Generative Phase Space Reconstruction (GPSR) technique [9, 10] to efficiently reconstruct high dimensional beam distribution features from experimental data such that the reconstruction analysis can be performed in an online setting. As a result, we have conducted multiple 6-dimensional phase space measurements at several accelerator facilities, including the Argonne Wakefield Accelerator (AWA) [11] and the Pohang XFEL facility [12]. In this work we describe the GPSR technique as it applies to the parasitic DIAG0 diagnostic line at LCLS-II and describe efforts to enable autonomous monitoring of the 6-dimensional phase space distribution of the beam during normal user operations and machine development time.

GENERATIVE PHASE SPACE RECONSTRUCTION USING THE DIAG0 BEAMLINE

Generative phase space reconstruction is an analysis method that aims to predict the 6-dimensional phase space distribution from tomography-style measurements of the beam distribution. Similar to standard tomography techniques, we rotate the phase space distribution of the beam along multiple axes by using quadrupoles, transverse deflecting cavities, and dipoles while imaging the two dimensional distribution of the beam via a set of diagnostic screens. Instead of reconstructing the beam distribution at a grid of points in phase space by solving a system of linear equations via an iterative solver (e.g. ART/SART), we utilize a machine learning based parameterization of the beam distribution and a differentiable physics simulation to solve for the beam distribution.

GPSR parametrizes a beam distribution in 6-dimensional phase space using a transformer neural network, which transforms particle coordinates drawn from a Multivariate Normal distribution into realistic macro-particle coordinates in position-momentum space. As a result, the structure of the generated macro-particle distribution is governed by the parameters of the neural network, which can efficiently represent arbitrary, high-dimensional features in phase space. To effectively solve for the exact distribution

* rroussel@slac.stanford.edu

ISBN: 978-3-95450-261-5 ISSN: 2673-7000 doi: 10.18429/JACoW-NAPAC2025-MOP035

EXPERIMENTAL LONGITUDINAL EMITTANCE MANIPULATION USING LASER-BASED PHOTOIONIZATION IN THE FERMILAB LINAC*

P. Landon†,1, E. Kearns, Boston University, Boston, MA, USA,
J. Ruan, D. Johnson, T. Johnson, T. Thompson, Fermilab, Batavia, IL, USA
[1]also at Fermilab, Batavia, IL, USA

Content from this work may be used under the terms of the CC BY 4.0 licence (© 2022). Any distribution of this work must maintain attribution to the author(s), title of the work, publisher, and DOI.

Abstract

A series of simulations and beam studies were conducted at Fermilab's linear accelerator to evaluate the effectiveness of longitudinal emittance control via laser-induced photoionization. While similar laser techniques have been employed at Fermilab to enhance injection and extraction efficiency into the Booster, the work presented here focuses on extending these methods to bunch-by-bunch manipulation. This approach utilizes fine-scale correction of the H- bunches' longitudinal spatial distribution. In theory, loosely confined particles in longitudinal phase space contribute to emittance growth during acceleration. By selectively removing these outlying particles through laser scraping ($H^-+\gamma \rightarrow H+e^-$), this growth can be reduced. This report presents experimental results from both symmetric and asymmetric longitudinal scraping of H^- bunches in the Fermilab linac, which were subsequently injected into Booster, and evaluates the broader applicability of this method for future high-intensity accelerator operations.

MOTIVATION

The motivation of this paper is to expand upon the results shared in previous literature [1]. Prior simulation results confirmed a 10% reduction in the longitudinal RMS emittance by photoionzing 2% of the beam halo out of the RFQ. These findings motivated an experimental investigation of energy dispersion reduction within the Fermilab Linac and Booster accelerator systems. The results shared here again utilize Fermilab's chopping system called the Laser Notcher [2]. Experimental verification of simulated models as well as novel timing techniques were investigated to explore the efficacy of energy dispersion reduction in the Fermilab Booster via laser scraping.

PHOTO-DETACHMENT FOR H^- USING THE LASER NOTCHER

The Laser Notcher photo-detaches the loosely bound electron in H^- to neutralize the ion's ability to accelerate [3]. The electron's photoionization cross-section is $4.2 \times 10^{-17}\, cm^2$ which is centered at a photon energy of 1.51 eV ($\lambda = 821\, nm$) in its center-of-mass frame [4]. The optimal cross section sits at a wavelength of 821 nm, but the Laser Notcher prioritizes laser amplification and uses a 1064 nm (1.165 eV) laser with a cross section of $3.66 \times 10^{-17}\, cm^2$. When characterizing the Laser Notcher's photo-detachment efficiency, it was assumed to have a high probability of interaction between photons and electrons with no depletion of photons relative to the electron detachment [4]. This allows the fractional neutralization of H^- to be given by Eq. (1) [5]

$$F_{neut} = \frac{N}{N_0} = (1 - e^{-f_{CM}\sigma(E_\gamma)\tau}) \tag{1}$$

where f_{cm} is the photon flux at the interaction point in the rest frame of the H^- [$\frac{Photons}{cm^2 \cdot s}$], $\sigma(E_\gamma)$ is the cross-section for a given photon energy E_γ, and τ is the interaction time of the photons and ions.

The center of mass flux may be represented in lab frame as

$$f_{cm} = \frac{E_{laser}}{A_{laser}\tau_{laser}} \frac{\lambda_{Lab}}{hc} \gamma(1 - \beta\cos(\theta)) \tag{2}$$

where $E_{laser}/A_{laser}\tau_{laser}$ is the average intensity of a gaussian laser pulse, λ_{Lab}/hc is the normalization factor for the lab frame photon energy, and $\gamma(1 - \beta\cos(\theta))$ is the relativistic Doppler shift factor.

EXPERIMENTAL VERIFICATION OF LASER SCRAPING SIMULATIONS

To verify the validity of previous laser scraping simulations, experiments were conducted to recreate the fractional neutralization found in Equation 1. This was done by attenuating the laser using an Electro-Optic Modulator (EOM). Starting from the maximum neutralization rate, with an efficiency of approximately 90%, the amplitude was attenuated to 30–90% of that initial value. The resulting data were then fit using the same modeling program described in [1].

Figure 1 shows experimental data fitted using the simulated model. The x-axis is presented in arbitrary units, as the available instrumentation could not accurately determine the pulse energy. Additional studies will be conducted to quantify the Laser Notcher energy attenuation levels. Although the exact laser pulse energy values are unavailable, a simulated fit was produced using the same modeling program described in [1].

EXPERIMENTAL LONGITUDINAL SCRAPING RESULTS

As previously stated in [1], the temporal resolution of the laser was limited by the Arbitrary Wave Generator (AWG) to 0.5 ns. As a result, the current Laser Notcher system achieves timing precision only on the order of one-quarter of

* This work was supported by the U.S. Department of Energy under contract No. DE-SC0015628.

† landonp@bu.edu

ISBN: 978-3-95450-261-5 ISSN: 2673-7000 doi: 10.18429/JACoW-NAPAC2025-MOP037

CALCULATING BEAM EXTINCTION IN A PULSED PROTON BEAM USING FPGA-BASED PEAK DETECTION *

R. Hensley†, E. Prebys, University of California Davis, Davis, CA, USA
A. Gaponenko, Fermi National Accelerator Laboratory, Batavia, IL, USA

Abstract

The Mu2e experiment at Fermilab imposes stringent requirements on the elimination of out-of-time beam in its pulsed proton beam, a requirement known as "extinction". Utilizing a new μTCA-based FPGA data acquisition system, we recorded live particle data from scattered particles incident on an array of quartz Cherenkov radiators and photomultiplier tubes to measure the extinction in the inter-pulse gaps in the pulsed proton beam. Minuscule errors in the derived signal period can make a measurement of the extinction impossible, so after taking a Fourier transform, further optimizations on the period were done based on the assumption that the signal period is stable over the full time of the beam spill while it is being resonantly extracted. After these optimizations, the beam extinction was shown to be on the level of 10^{-3}.

INTRODUCTION

The Mu2e Experiment

The Mu2e experiment requires a pulsed proton beam with a well-defined timing structure and minimal protons present between beam pulses as shown in Fig. 1. The experiment is designed to search for the evidence of lepton flavor violation through the neutrino-less decay of a muon to an electron. Detecting ten signal events in a year would be enough [1].

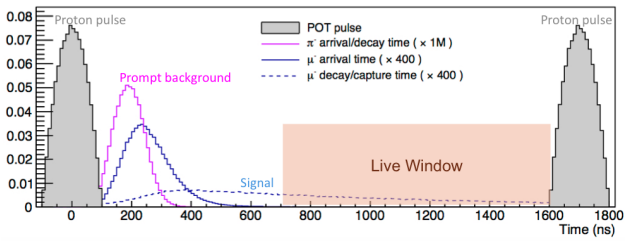


Figure 1: Mu2e uses a proton beam of pulses separated by 1695 nsec with a level of extinction of 10^{-10} between pulses.

Proton pulses are transferred to the experimental hall every 1695 nsec. To ensure clean signal identification, an approximately 995 nsec live signal timing region has been defined between the incoming proton pulses where the desired electron signal can be expected following a 700 ns veto window where background is expected to be the highest. A 5σ discovery requires ≈ 7.5 events against the estimated background of 0.41 over three years.

* Work supported by US Department of Energy Grant DE-SC0009999
† rshensley@ucdavis.edu

Proton Beam Extinction

Mu2e requires the minimization of out-of-time particles between pulses in the proton beam [1]. The beam extinction is defined as the ratio of the number of particles in the inter-pulse time to the nominal pulse intensity (39×10^6 protons per pulse) [2]. The experiment requires the extinction to be less than 10^{-10} [3].

Extinction in the experiment will be achieved in two steps. First, the natural formation of the bunches in the Recycler Ring and Delivery Ring is expected to provide extinction on the order of 10^{-5}. The remaining extinction will be provided by a system of resonant, fast-switching dipole magnets, collectively called the "AC Dipole", and collimators, configured in such a way that only in-time beam is transmitted to the target and out-of-time beam will be stopped by the collimators. The AC Dipole system will provide an additional extinction factor of approximately 10^{-7}, thus exceeding the required 10^{-10} level [2] by two orders of magnitude.

UPSTREAM EXTINCTION MONITOR

Detector Setup

To obtain an early estimation of beam extinction and to evaluate extinction system performance, an "upstream extinction monitor" system has been installed in the M4 beamline at Fermilab. The detector consists of three quartz Cherenkov radiators and Hamamatsu R7056 photomultiplier tubes (PMTs) arranged in a line, as shown in Fig. 2. They are placed 1 m downstream from a vacuum window and at an angle to intercept scattered particles. The data from scattered beam particles will then be integrated over many beam transfers to obtain an estimate of the extinction.

Insufficient extinction is an accelerator issue that is difficult to amend after the start of data-taking in the experiment, so it is crucial to discover any inadequacies in extinction in

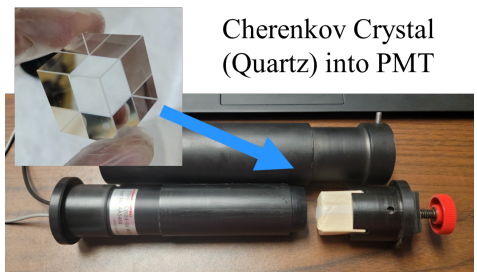


Figure 2: A quartz crystal (25 mm cube) used in the upstream extinction monitor Cherenkov detectors. The quartz crystals are instrumented with PMTs, which have their signals digitized by the FPGA-based data acquisition system.

Content from this work may be used under the terms of the CC BY 4.0 licence (© 2022). Any distribution of this work must maintain attribution to the author(s), title of the work, publisher, and DOI.

ISBN: 978-3-95450-261-5 ISSN: 2673-7000 doi: 10.18429/JACoW-NAPAC2025-MOP039

FAST ADAPTIVE NEURAL CONTROL OF RESONANT EXTRACTION AT FERMILAB

A. Whitbeck*, J. Berlioz, K. Danison-Fieldhouse, K. Hazelwood, M. Khan,
J. Mitrevski, A. Narayanan, J. St. John, N. Tran, Fermilab, Batavia, IL, USA
J. Ji, M. Walter, Toyota Technical Institute of Chicago, Chicago, IL, USA

Abstract

We present progress on the development of a machine learning (ML) regulation system for third-order resonant extraction of the beam delivered to the Mu2e experiment at Fermilab. We consider classical and ML-based controllers optimized on semi-analytic simulations and provide performance comparisons for several models. Additionally, we discuss the efficiency of each model in training, which has implications for future work on adaptive control. We also discuss progress on developing optimized implementations of ML models for edge-based inference.

INTRODUCTION

The Fermilab Muon Delivery Ring provides proton beam over many turns to the muon production target for the Mu2e experiment using a third-order resonant extraction. The tune of the machine is controlled using a series of fast-ramping quadrupole magnets. While the nominal quadrupole ramp waveform is sourced from a spill-by-spill optimization loop, the fast disturbances in the system are regulated by a dedicated hardware-based controller. The controller reads the digitized signal from the wall current monitor in the M4 extraction beamline to track the extracted beam current and provides updates to the quad controller at 10 kHz. Controllers will be run in a field-programmable gate array (FPGA) to meet the latency requirements of the system. Here, we extend previous work [1] and explore possible controller implementations, evaluate their performance, and compare optimization strategies. The requirements of the system and further details of the Mu2e Spill Regulation System (SRS) are described in Ibrahim *et al.* [2, 3].

DATA AND METHODOLOGIES

Our study builds on an analytically derived model that efficiently approximates spill dynamics [1, 3]. Spill quality is quantified by the *spill-duty factor* (SDF), SDF $= (1 + \sigma^2_{\text{spill}})^{-1}$, where σ_{spill} is the standard deviation of the normalised spill intensity $\{s_t\}_{t=1}^{T}$. The goal of the regulator is to maximize this objective.

Each episode represents a single spill of fixed horizon $T = 430$ control cycles. At step t, the agent observes the one-dimensional state s_t and outputs an action $a_t \in \mathbb{R}$, which is added to the pre-programmed quadrupole-current ramp. State transitions are generated by the analytical spill model. Figure 1 illustrates the spill dynamics, comparing raw and corrected spill intensities along with the corresponding control signals.

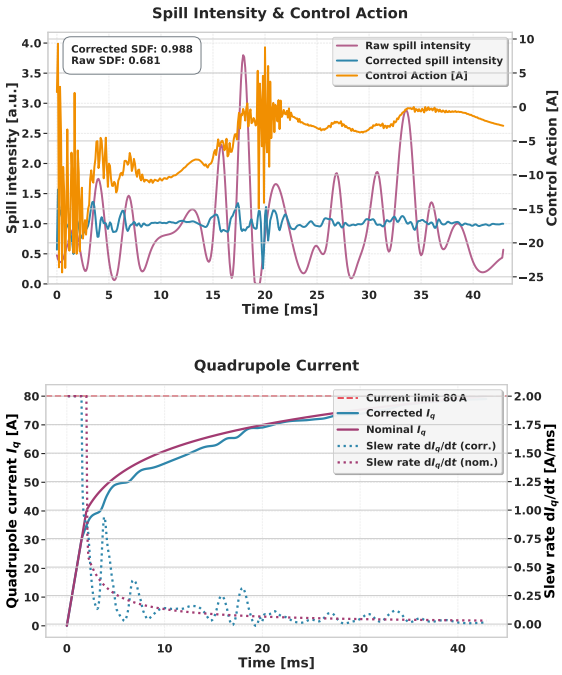


Figure 1: (Upper) Time history of the raw spill intensity versus the corrected spill intensity after feedback during a single 43 ms extraction. The overlaid control signal (right axis) is the current increment commanded to the quadrupole magnet every 0.1 ms. (Bottom) The quadrupole current and its rate of change. The magenta line tracks the nominal ramp I_q, the blue line represents the corrected I_q respecting the hardware limit of 80 A (red dashed), and the dotted lines give the corresponding slew rate $\mathrm{d}I_q/\mathrm{d}t$ per 0.1 ms step.

We have re-implemented the existing differentiable PyTorch simulator to support fully-batched operations [1, 4], enabling the concurrent simulation of thousands of spills on modern GPUs and significantly reducing training time. In addition, we provide an Farama Gymnasium-compatible wrapper [5] that standardises the interface between the agent and the simulator, thereby streamlining the development and comparative evaluation of control algorithms, especially those based on reinforcement learning.

In this work, we investigate two primary classes of controllers: the classical proportional-integral-derivative (PID) model and models based on neural networks (NN). Each

* awhitbe1@fnal.gov

Content from this work may be used under the terms of the CC BY 4.0 licence (© 2022). Any distribution of this work must maintain attribution to the author(s), title of the work, publisher, and DOI.

ISBN: 978-3-95450-261-5 ISSN: 2673-7000 doi: 10.18429/JACoW-NAPAC2025-MOP040

FAST BEAM PROBE DEVELOPMENT FOR LONGITUDINAL BUNCH MEASUREMENTS AT UC DAVIS CROCKER NUCLEAR LABORATORY CYCLOTRON*

L. Knudson†, E. Prebys, M. Backfish,
Crocker Nuclear Laboratory, University of California Davis, Davis, CA, USA

Abstract

The UC Davis Crocker Nuclear Laboratory (CNL) operates a 76-inch Isochronous Cyclotron dating to the 1960s. Recent experiments have revealed unexplained beam behavior, which cannot be directly measured with the current diagnostics. Direct measurements of the beam in the Cyclotron are challenging due to the harsh environment, including high radiation, strong magnetic fields, RF interference, and spatial constraints. To address this, we are developing a novel beam probe capable of resolving longitudinal bunch structure across 16 positions simultaneously. The fast beam probe consists of a segmented fast plastic scintillator array coupled via fiber optics to external Silicon Photomultipliers (SiPMs), mounted on a radially translating probe. We report on the probe's performance from in-air tests at the general-purpose beamline. The results demonstrate sub-nanosecond resolution, consistent sensitivity across channels, and clear signatures of beam dynamics, establishing the system's viability for measurements inside the CNL Cyclotron.

MOTIVATION

The CNL Cyclotron is a historic machine that has been operating since the 1960s with a wide variety of applications, including cancer treatment, radiation effects testing, air quality research, and more [1]. In recent years, interest in the isotope astatine-211 has increased, prompting CNL to commission a production process, which is described elsewhere [2]. It was determined that the optimal production area was a target, internal to the Cyclotron, using a 28 MeV alpha beam tune. A stack of Type HD-V2 Gafchromic film was placed on the end of the beam probe to destructively measure the transverse beam profile at the 25.25-inch position. The stack of film was exposed for approximately one minute by an alpha beam, resulting in a 12.7 mm radial and axial profile. The size of the measured profile was unexpected to CNL personnel and indicates significant oscillations in the Cyclotron that are not understood.

FAST BEAM PROBE CONSTRUCTION

The fast beam probe was designed around the harsh environment of the CNL Cyclotron, namely strong magnetic fields, radiation, RF interference, and spatial constraints, while being able to measure longitudinal bunches at various radial positions. The detector consists of a 4×4 array of fast plastic scintillators (Eljen EJ-232Q 0.5% benzophenone) coupled to UV-VIS fused silica fibers, seen in Fig. 1, which transmit light to an Onsemi 16-channel SiPM array (Array-J) outside the Cyclotron [3–5]. Each 3 mm × 3 mm × 10 mm scintillator is optically coupled to four 2.93 m fibers, which are in turn matched one-to-one to SiPM channels. The SiPM array is actively cooled and read out using a 16+1 channel, 12-bit, 5 GS/s CAEN digitizer [6]. Full construction details and optimization considerations can be found in [7].



Figure 1: The top image shows the fast beam probe positioned in the general purpose beamline for the in-air test. The bottom image shows a rendering of the target portion of the detector, showcasing the scintillator array and fiber optics with the supporting geometry.

IN-AIR MEASUREMENT

An in-air test of the fast beam probe was performed at the CNL general purpose beamline seen in Fig. 1. The scintillator array was positioned in the beam path 10 cm away from the Kapton vacuum window, with the 3 mm × 3 mm scintillator face oriented perpendicular to the beam path. The CNL Cyclotron provided a focused beam of 67.5 MeV protons with an RF structure of 22.5 MHz. The beam current was tuned such that at most 1 particle per detector channel per bunch was present. All 16 SiPM channelsand the Cyclotron

* Work supported by University of California Office of the President grant LF-20-653232 and US Department of Energy Grant DE-NA0003996
† lsknudson@ucdavis.edu

Content from this work may be used under the terms of the CC BY 4.0 licence (© 2022). Any distribution of this work must maintain attribution to the author(s), title of the work, publisher, and DOI.

ISBN: 978-3-95450-261-5 ISSN: 2673-7000 doi: 10.18429/JACoW-NAPAC2025-MOP042

FPGA-BASED SPILL REGULATION SYSTEM FOR THE MUON DELIVERY RING AT FERMILAB

J. R. Berlioz*, D. Bracey, B. Fellenz, M. A. Ibrahim, V. Nagaslaev,
A. Narayanan, P. Prieto, K. Danison-Fieldhouse, W. Sullivan
Fermi National Accelerator Laboratory†, Batavia, IL, USA

Abstract

The Muon to Electron Experiment (Mu2e) requires a uniform beam profile from the Muon Delivery Ring to meet their experimental needs. A specialized Spill Regulation System (SRS) has been developed to help achieve consistent spill uniformity. The system is based on a custom-designed carrier board featuring an Arria 10 SoC, capable of executing real-time feedback control. The FPGA processes beam pulses of approximately 200 ns every 1.695 µs, allowing for continuous monitoring of the extracted spill intensity through fast bunch integration. The system directly controls three quadrupole magnets, which work in conjunction with sextupole magnets to achieve third-order resonant extraction. Furthermore, the board interfaces with Fermilab's Accelerator Control Network (ACNET), enabling operators to modify spill regulation settings in real-time via the control network while providing diagnostic waveforms. These waveforms help operators monitor the process and fine-tune the feedback mechanisms. This paper presents an overview of the board's architecture and its initial progress toward regulating beam extraction. This initial version of the regulation system aims to evaluate baseline performance to inform future system improvements.

Content from this work may be used under the terms of the CC BY 4.0 licence (© 2022). Any distribution of this work must maintain attribution to the author(s), title of the work, publisher, and DOI.

INTRODUCTION

Achieving uniform spill intensity during slow resonant extraction is critical for fixed-target experiments like Mu2e, as detector performance and data quality depend strongly on spill uniformity. Factors such as magnet current fluctuations, power supply ripple, and dynamic beam instabilities can degrade spill quality. Thus, effective regulation must quickly counteract these disturbances.

Previous preliminary studies on this challenge explored applying two different regulation schemes [1–3]. One uses RF Knockout (RFKO) striplines, while another uses the fast-ramping tune quadrupoles. In this work we focus on the latter, leaving RFKO-based regulation for future study. The layout for the fast-ramping quadrupole current regulation scheme is illustrated in Fig. 1 and was operationally tested with only extracted beam integration using the first version of the SRS board during a three-month run starting in May 2025.

Three quadrupole magnets regulate the beam tune, facilitating third-order resonant extraction. Increasing quadrupole current progressively moves the beam into the extraction region. A gap monitor provides the measurement of the circulating beam, while a wall current monitor (WCM) in the extraction line measures the extracted beam. An example of the extracted spill structure is shown in Fig. 2, which displays a 20 ms segment recorded without feedback loop. Because both monitors are AC-coupled systems, the signal shows a shifting baseline. The lower trace highlights the microbunch structure, which occurs every 1.695 µs with a pulse width of approximately 200 ns. These beam measurement serve as the primary inputs to the regulation system. The extracted spill intensity from the WCM, in particular, is processed by the SRS board to generate corrective actions on the quadrupole magnets.

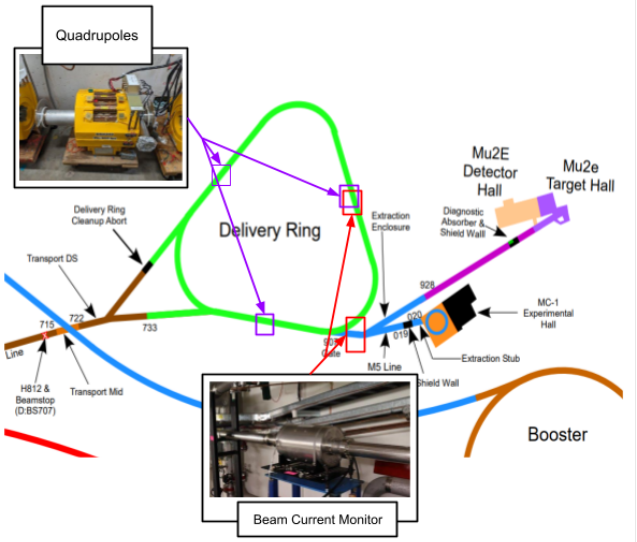


Figure 1: Layout of the three tune quadrupoles in the Delivery Ring. Beam current monitors provide measurements of both the circulating and extracted beam for the feedback loops.

HARDWARE SETUP

The Mu2e SRS board used is shown in Fig. 3. It features sixteen 14-bit ADC channels at 125 MSPS, sixteen precision outputs from four DACs, and four high-speed outputs from two dual DACs. The main board is a ReflexCES Arria 10 SoM Turbo, which integrates an Intel Arria 10 GX FPGA with embedded dual-core ARM Cortex-A9 processors. This system-on-module provides high-performance

* jberlioz@fnal.gov

† This manuscript has been authored by FermiForward Discovery Group, LLC under Contract No. 89243024CSC000002 with the U.S. Department of Energy, Office of Science, Office of High Energy Physics.

ISBN: 978-3-95450-261-5 ISSN: 2673-7000 doi: 10.18429/JACoW-NAPAC2025-MOP043

FPGA IMPLEMENTATION OF A DIGITAL SIGNAL COMPONENT SEPARATOR AND A DISTURBANCE COMPENSATOR FOR THE LANSCE 805 MHz SOLID-STATE HIGH POWER RF AMPLIFIER*

S. Kwon†, J. T. M. Lyles, M. Brown, M. Sanchez Barrueta, J. T. Bradley III, W. Hall, S. J. Russell, J. A. Valladares, P. J. Van Rooy, P. Torrez, Los Alamos National Laboratory, Los Alamos, NM, USA

Abstract

Because of aging, and product discontinuity, LANSCE is investigating the replacement of high power RF amplifiers. A promising candidate is the GaN solid-state power amplifier (SSPA). For a high drain voltage, the drain power dissipation of SSPA is increased as the operating efficiency becomes low. The outphasing technique provides high efficiency operation of the SSPA. The signal component separator (SCS) of the outphasing amplifier converts one Amplitude Modulation-Phase Modulation (AM-PM) signal to two PM only signals. In this paper, the digital implementations of the two-way digital SCS and the four-way digital SCS are addressed. In addition, feedback linearizers are designed and implemented to suppress the input disturbances that exist on the signal forward paths of the outphasing amplifiers.

INTRODUCTION

The high power RF amplifiers, klystrons, of LANSCE 805 MHz CCLs have been operating for more than 5 decades. Because of aging, and product discontinuity, LANSCE is investigating the replacement of high power RF amplifiers. One of the highly promising amplifiers are the GaN amplifiers [1]. Currently, an available GaN amplifier can produce 5 kW pulsed RF power. Hence, in order to produce the equivalent or better performance than a LANSCE klystron of which peak power is 1.25 MW, a multitude of Solid-State Power Amplifiers (SSPA) are to be combined together. For a high drain voltage, the drain power dissipation is increased as the operating efficiency becomes low [1]. In order to operate the SSPA at high efficiency, the amplifier is operated as close as possible to the 1 dB compression zone. The outphasing technique can provide this requirement of the SSPA operation. In the outphasing amplifier, the Amplitude Modulation-Phase Modulation (AM-PM) input signal is converted to con-stant envelope PM signals, so that each amplifier of the forward signal path linearly amplifies constant envelope PM input signals [2, 3]. The combiner sums the amplified PM signals, yielding the signal of linear amplification of the outphasing amplifier input signal.

The core part of the outphasing amplifier is the signal component separator (SCS) that converts the AM-PM input signal to constant envelope PM signals. Most SCS techniques are implemented on the analog circuits [2]. In this paper, a digital signal component separator (DSCS) in Inphase/Quadrature (I/Q) coordinated is addressed. The DSCS is implemented on an Intel Stratix III commercial board which supports four 150 MSPS ADCs and four 250 MSPS DACs.

In addition to the DSCS, a compensator for the slowly varying amplitude and phase disturbances that may exist on the RF forward paths are investigated. The sources of these disturbances may be the parameter drifts of the amplifiers themselves, droops and ripples of DC power source, or temperature variation caused by the imperfect cooling system. In this outphasing amplifier design, a digital feedback linearizer is implemented to compensate for these disturbances. The disturbance suppression performance of the feedback linearizer is verified on a low power testbench and the results are reported.

OUTPHASING AMPLIFIER AND SIGNAL COMPONENT SEPARATOR

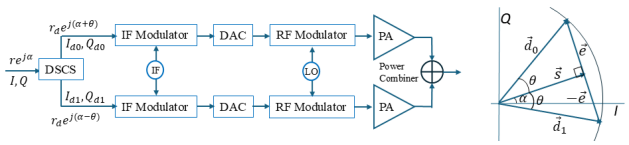


Figure 1: Two-way DSCS outphasing amplifier schematic and vector diagram.

The phase modulated components are generated using vector decomposition of the baseband signal in I/Q coordinate.

Consider the phasor diagram shown in Fig. 1. The input vector $\vec{s}$ can be expressed as the complex form in I/Q coordinate as:

$$\vec{s} = re^{j\alpha} = I + jQ \tag{1}$$

$$|\vec{s}| = r \leq 1, \alpha = \text{atan}\left(\frac{Q}{I}\right)$$

When the vector $\vec{s}$ is projected to the unit circle, the projecting vector is defined by:

$$\vec{e} = e_I + je_Q \tag{2}$$

$$e_I = -\sin(\alpha)\sqrt{1-r^2}$$

$$e_Q = +\cos(\alpha)\sqrt{1-r^2}$$

and the two signals of two-way SCS are given by:

$$\vec{d}_0 = r_d e^{j(\alpha+\theta)} = I_{d0} + jQ_{d0} \tag{3}$$

$$\vec{d}_1 = r_d e^{j(\alpha-\theta)} = I_{d1} + jQ_{d1} \tag{4}$$

* Work supported by LANL LDRD DI.

† skwon@lanl.gov

Content from this work may be used under the terms of the CC BY 4.0 licence (© 2022). Any distribution of this work must maintain attribution to the author(s), title of the work, publisher, and DOI.

ISBN: 978-3-95450-261-5 ISSN: 2673-7000 doi: 10.18429/JACoW-NAPAC2025-MOP044

GTPSA.jl : A SciBmad INTERFACE TO THE GENERALISED TRUNCATED POWER SERIES ALGEBRA LIBRARY*

M. G. Signorelli†, G. H. Hoffstaetter[1], D. Sagan, CLASSE, Cornell University, Ithaca, NY, USA
L. Deniau, CERN, Geneva, Switzerland
O. Beznosov, LANL, Los Alamos, NM, USA
[1]also at Brookhaven National Laboratory, Upton, NY, USA

Abstract

A full-featured interface package to the Generalised Truncated Power Series Algebra (GTPSA) library in MAD-NG has been implemented in the Julia programming language. GTPSA performs fast Taylor-mode automatic differentiation (AD) of functions to arbitrary orders in the specified variables and parameters. In particular, GTPSA excels at computing derivatives to high orders (>1) and high numbers of variables/parameters, making it an extremely powerful tool for use in optimization and in computing parametric Taylor maps. This Julia interface offers another simple way of using the GTPSA library, and will be used extensively in the SciBmad accelerator physics software ecosystem. The interface can also be easily called from Python, via the `juliacall` package. In this paper, we showcase features implemented in the interface package including performance enhancements, and present an example of integrating a GTPSA map using polymorphic integrators already implemented in Julia.

INTRODUCTION

To understand and analyze the beam dynamics in a particle accelerator, we express the motion through the accelerator as a Taylor series expanded around the "reference trajectory" - the closed orbit in a periodic ring, or the "ideal" particle in an open beamline - and optionally the parameters of the accelerator (quadrupole strengths, lengths, etc). This Taylor map is referred to as a (parametric) differential-algebraic (DA) map. Once a DA map is computed, canonical perturbation theory can then be applied to extract *all* information on the dynamics, up to the truncation order of the series; this includes the Twiss parameters, amplitude-dependent tunes, chromatic beta beat, so-called second order dispersion, resonance driving terms (RDTs), etc., and how all of these quantities depend on the parameters.

A code that can compute high order Taylor maps is a necessary tool in the design of particle accelerators. However, accurately computing all the higher order cross-derivatives is very nontrivial; finite differencing methods for example can be highly sensitive to the chosen step size for each individual variable, can suffer round-off errors that grow with the order of the partial derivative, and can include higher-order errors in the low-order derivatives, proportional to the step size. Furthermore, as the number of variables and truncation order increases, the number of partial derivatives to compute and store grows exponentially.

Automatic differentiation (AD) is a method which computes derivatives without any approximation - being exact to numerical precision - by relying on the fact that the chain rule can be repeatedly applied to a sequence of elementary arithmetic operations and math functions [1]. A "differentiable" code is one whose derivatives can be computed using AD. Truncated Power Series Algebra (TPSA) is a method of AD that is highly-optimized for computing high order derivatives, including potentially many variables and parameters; this makes TPSA ideal for accelerator physics.

Therefore, as has been recognized since the early 1990s [2–4], accelerator physics simulation codes must be differentiable via a TPSA package to properly compute and analyze DA maps. The Generalised Truncated Power Series Algebra (GTPSA) library, written in C, has been shown to outperform many well-known TPSA libraries [5]. GTPSA also uniquely allows the user to specify custom truncation orders for individual variables and parameters, enabling better flexibility without a performance cost. To harness the power of GTPSA for use both in the new SciBmad accelerator physics code and in the broader optimization and AD community, we have implemented a full featured interface package in the Julia programming language. GTPSA bindings have also been implemented in two open-source, widely-used Julia packages: `DifferentiationInterface.jl` [6, 7] which enables GTPSA to be used generically alongside any other Julia AD package, and `DiffEqBase.jl` which enables integration of GTPSA maps using any of the differentiable integrators already available in `DifferentialEquations.jl` [8]. And, with the Python package `juliacall` [9], `GTPSA.jl` can be easily called from Python. In this paper, we present all such features implemented in `GTPSA.jl`.

TRUNCATED POWER SERIES ALGEBRA

The most natural AD implementation utilizes *forward-accumulation*, which works by defining a new number type called a *dual*. The dual number stores two numbers: one which acts like a regular number, and one which is the exact partial derivative of any previously evaluated function. All elementary arithmetic operators and functions are properly overloaded for the dual to apply the chain rule and compute this derivative exactly. In this case, the chain rule is traversed from the input to the output, hence the name "forward".

In a fully polymorphic code, higher order derivatives can be computed by nesting dual numbers. However, this can

* Work supported by Brookhaven Science Associates, LLC under Contract No. DE-SC0012704 with the U.S. Department of Energy.
† mgs255@cornell.edu

Content from this work may be used under the terms of the CC BY 4.0 licence (© 2022). Any distribution of this work must maintain attribution to the author(s), title of the work, publisher, and DOI.

ISBN: 978-3-95450-261-5 ISSN: 2673-7000 doi: 10.18429/JACoW-NAPAC2025-MOP045

HED-Melt: A COUPLED FRAMEWORK FOR MODELING HIGH-ENERGY-DENSITY CONDITIONS IN ACCELERATORS *

A. J. Dick†, J. Dooling, M. Borland, A. Grannan, Y. Lee, R. R. Lindberg, G. Navrotski
Argonne National Laboratory, Lemont, IL, USA
D. Lee, S. Riedel, University of California Santa Cruz, Santa Cruz, CA, USA
N. Cook, RadiaSoft, Boulder, CO, USA

Abstract

The high-brightness beams used by modern light sources and accelerators present a new challenge for machine protection. These beams, through impacts on beam-intercepting components, may generate high-energy-density (HED) conditions capable of causing significant damage. One significant issue in studying these dynamics is the lack of simulation tools that capture all of the relevant physics. Particle tracking and particle-matter interaction codes are widely used in accelerator design but there is not significant interfacing between the two and few codes are available to simulate the melting and vaporization seen in some beam strikes. `HED-Melt` (**H**igh **E**nergy **D**ensity **M**odeling of **El**ectron Beam Impacts **T**oolkit) is a framework for coupling three physics codes, `elegant`, `FLUKA`, and `FLASH` to model HED conditions in various accelerator components. The toolkit automatically interfaces between the three codes to run a full-physics simulation of HED conditions for a user-defined machine lattice.

INTRODUCTION

The HED-Melt framework automatically interfaces between and executes three physics codes, `elegant` [1, 2], `FLUKA` [3], and `FLASH` [4] for full beam impact simulations in accelerators. Figure 1 shows the workflow of the coupled codes.

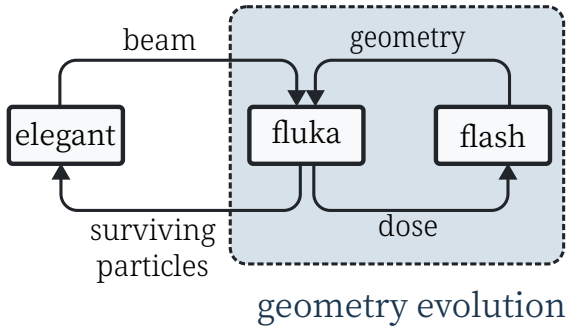


Figure 1: Diagram of HED-Melt workflow showing the information that is passed between codes. The geometry evolution loop occurs multiple times each revolution.

Each of the three codes is responsible for a distinct physics regime. A typical simulation will begin by tracking the beam in `elegant`, initiating an rf fault, until the beam begins to interact with the collimator. At this point, the particle distribution is passed in batches to `FLUKA` where it is used to simulate the energy deposited in, e.g., a collimator. `FLUKA` returns the surviving particles to `elegant` and produces a 3D dosemap that is used by `FLASH`, which simulates the energy deposition and thermodynamic evolution of the impacted material. When a cell is vaporized in `FLASH`, HED-Melt updates the geometry definition used by `FLUKA`. This turn-by-turn treatment gives more accurate modeling of material damage [5]. As the material erodes, the transmission of particles increases, resulting in a protracted beam loss. A static treatment of material geometry can significantly underestimate damage. The modular design allows for significant flexibility in the simulation configuration. Other facilities may use HED-Melt in their design processes to fully model beam impacts or to simply get an estimate of energy absorbed by beamline components.

SETUP AND EXECUTION

In order to keep the framework as accessible as possible, HED-Melt has minimal dependencies, beyond those required by each of the codes, and runs in standard High-Performance-Computing batch job environments. We have also developed tools for setting up generalized beam-dump simulations. The simulation parameters are defined by the user in a YAML "setup" file that is used by a python script to create the directory structure and program files. The user must supply certain parameters in the setup file, which define the loop structure. Additional parameters may be added to template files, which can be filled in at setup to make it easier to modify whole simulations.

The setup file has two main object types, the "simulation" block and three "code" blocks for `elegant`, `FLUKA`, and `FLASH`. The simulation block has the form

```
simulation:
    rootname: example
    domain:
        x: {min: -0.1, max: 0.1, n: 128}
        y: {min: -0.1, max: 0.1, n: 128}
        z: {min: 0.0, max: 1.0, n: 32}
    geometry:
        type: "slab"
        material: "Al"
        center: {x: 0, y: 0, z: 0.5}
        size: {x: 0.02, y: 0.02, z: 0.1}
    params:
```

* Work supported by the U.S. D.O.E.,Office of Science, Office of Basic Energy Sciences, under contract number DE-AC02- 06CH11357.

† ajdick@anl.gov

Content from this work may be used under the terms of the CC BY 4.0 licence (© 2022). Any distribution of this work must maintain attribution to the author(s), title of the work, publisher, and DOI.

ISBN: 978-3-95450-261-5 ISSN: 2673-7000 doi: 10.18429/JACoW-NAPAC2025-MOP048

IMPLEMENTATION OF A 1550-nm LASER SYSTEM FOR BEAM CHARACTERIZATION AT THE ARGONNE WAKEFIELD ACCELERATOR*

A. Ody[1†], W. Liu[1], P. Piot[1], J. G. Power[1], I. Wilke[2], D. S. Doran[1], S. Kelham[3], J. Ruan[4], V. Scarpine[4], R.M. Thurman-Keup[4], C. Whiteford[1], E. E. Wisniewski[1] S. Toroghi[5], P. Rabiei[5]

[1]Argonne National Laboratory, Lemont, IL, USA
[2]Rensselaer Polytechnic Institute, Troy, NY, USA
[3]Northern Illinois University, DeKalb, IL, USA
[4]Fermi National Accelerator Laboratory, Batavia, IL, USA
[5]Partow Technologies LLC, Carlsbad, CA, USA

Abstract

Accurately capturing the longitudinal profile of electron bunches is a critical diagnostic for wakefield accelerators, particularly those employing shaped bunches to enhance transformer ratios. Electro-optic sampling of terahertz fields produced by ps-duration electron bunches offers a non-destructive approach for this purpose. To enable future characterization experiments, the Argonne Wakefield Accelerator (AWA) test facility has recently installed a 1550-nm laser system, along with the necessary support infrastructure to synchronize it with the photoinjector nominal laser system operating at 81.25 MHz. This paper reports on the successful installation and initial synchronization demonstrations, paving the way for advanced diagnostics R&D at AWA.

INTRODUCTION

Over the past two decades, electro-optic (EO) sampling of transient electric fields associated with relativistic electron bunches has proven to be a reliable and effective approach for measuring ultrashort bunches in linacs [1–3] and characterizing instabilities in electron storage rings [4]. The development of stable, synchronized lasers has further extended EO-based methods to serve as beam-arrival monitors with unprecedented sub-10-fs resolution. Recent advancements in EO techniques, such as the phase-diversity approach [5], have enabled precise measurements of beam current profiles with femtosecond resolution.

Given these developments and the Argonne Wakefield Accelerator Test Facility (AWA)'s research focus on beam manipulation—particularly the current profile—to enhance the performance and efficiency of beam-driven wakefield acceleration, AWA is actively considering the adoption of these techniques in its beamline [6]. Additionally, a recent collaborator-driven experiment, supported by the BeamNetUS consortium [7], focused on testing a fiber-coupled thin-film lithium-niobate (TFLN) EO electron beam sensor [8–10]. The current TFLN EO sensor design is optimized to operate with a 1550-nm laser pulse.

In light of these research interests, we recently deployed a fiber-laser system, on loan from collaborators at Fermilab, at the AWA facility. The system is an erbium-doped fiber laser, C-FIBER MENLOSYSTEMS, operating at 81.25 MHz and providing two fiber-coupled outputs with ~ 100 mW average power and ~ 70-fs pulses at $\lambda = 1550$ nm.

SYNCHRONIZATION & CONTROL

The C-FIBER laser operates at the 16th subharmonic of the AWA master clock and linac system ($f_0 = 1300$ MHz), matching the repetition rate of the nominal photocathode seed laser (VITARA-T system from COHERENT) used to generate electron bunches via photoemission from a photocathode located in a 1.5-cell 1.3-GHz RF gun. The laser needs to be phase-locked to the $f_0/16 = 81.25$-MHz reference signal derived from the master clock and used to synchronize the VITARA-T system. In addition the C-FIBER laser needs to have a programmable delay (ie, a phase shift) with respect to the VITARA-T laser. In its nominal implementation, the VITARA-T laser phase is controlled by shifting the phase of its 81.25-MHz reference signal. Due to limitations in the electronics, the phase shift is restricted to $\delta\phi \in [0°, 90°]$ at 81.25 MHz, which is sufficient for nominal operation as it corresponds to a 1.3-GHz phase shift of $\delta\phi_0 = 16\delta\phi$. However, to enable EO-sampling diagnostics, it is necessary

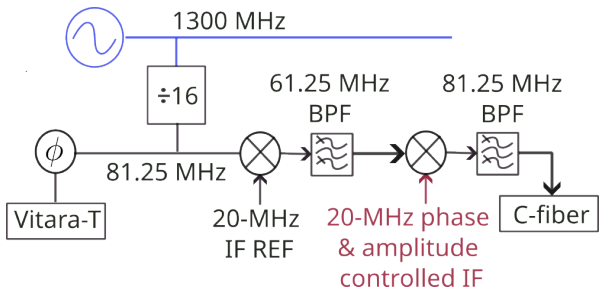


Figure 1: Block diagram of the LLRF system to control the C-FIBER laser phase. Note that both laser are phase-locked using their respective synchronization boxes.

* This work was supported by the U.S. Department of Energy, Office of Science, High Energy Physics, through the BeamNetUS program under Contract No. DE-AC02-06CH11357 with Argonne National Laboratory.
† aody@anl.gov

Content from this work may be used under the terms of the CC BY 4.0 licence (© 2022). Any distribution of this work must maintain attribution to the author(s), title of the work, publisher, and DOI.

ISBN: 978-3-95450-261-5 ISSN: 2673-7000 doi: 10.18429/JACoW-NAPAC2025-MOP050

IMPROVE BEAM BRIGHTNESS WITH BAYESIAN OPTIMIZATION AT THE AGS BOOSTER INJECTION AT BNL*

W. Lin[1,†], P. Adams[1], K. A. Brown[1], X. Gu[1], L. Hajdu[1], V. Schoefer[1], E. Hamwi[2], G. H. Hoffstaetter de Torquat[1,2]
[1]Collider-Accelerator Department, Brookhaven National Laboratory, Upton, NY, USA
[2]CLASSE, Cornell University, Ithaca, NY, USA

Abstract

Alternating Gradient Synchrotron (AGS) and its Booster serve as part of the injector compound for RHIC and the future EIC at Brookhaven National Laboratory. Injection and early acceleration processes set maximum beam brightness for the collider rings. Such processes have many control parameters and are traditionally optimized empirically by operators. In an effort to streamline the injection processes with machine learning (ML) techniques, we develop and test a Bayesian Optimization (BO) algorithm to automatically tune the Linac to Booster (LtB) transfer line magnets to maximize beam brightness after injection into the Booster. We present experimental results that demonstrate BO can be applied to optimize Booster injection efficiency.

INTRODUCTION

For polarized proton operation at the Relativistic Heavy Ion Collider (RHIC), 200 MeV H^- beam is created in the Linac and transported to the Booster through the Linac to Booster (LtB) transfer line. The LtB line is 114 feet in length and includes three main sections [1]. The first section starts from the Linac High Energy Beam Transport (HEBT) line to the 126° bend region. The second section is the 126° bend region with four identical dipoles. The third section starts from the exit of the last 126° dipole and continues into the Booster through the backleg iron of the C5 main ring dipole. H^- particles are fully stripped to protons at a carbon foil after the C5 magnet. Figure 1 shows the layout of the Booster injection region, with the LtB line outlined in red.

Proton beam in the Booster is scraped in both planes to reduce the emittance and intensity to RHIC requirements. The operation efficiency of Booster injection is characterized by three quantities: the input intensity, the early intensity, and the late intensity. The input intensity is measured when beam leaves the Linac, and this value usually stays relatively constant throughout normal operations. The early intensity is measured when beam first enters the Booster, and the late intensity is measured right before extraction to the AGS, after acceleration and scraping in the Booster. Figure 2 shows how beam changes during a typical Booster acceleration cycle. Timestamps when early and late intensities are measured are shown with red arrows.

* Work supported by Brookhaven Science Associates, LLC under Contract No. DE-SC0012704 with the U.S. Department of Energy and by DOE-NP No. DE SC-0024287.

† wlin1@bnl.gov

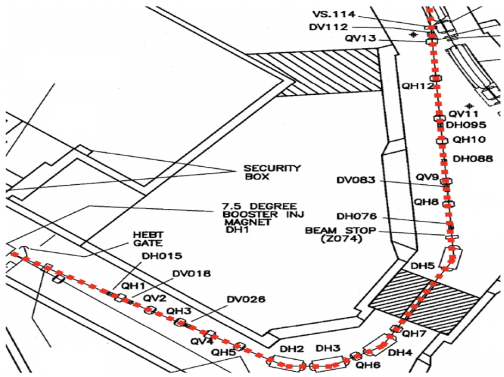


Figure 1: Layout of the Linac to Booster (LtB) transfer line (outlined with red dashed line).

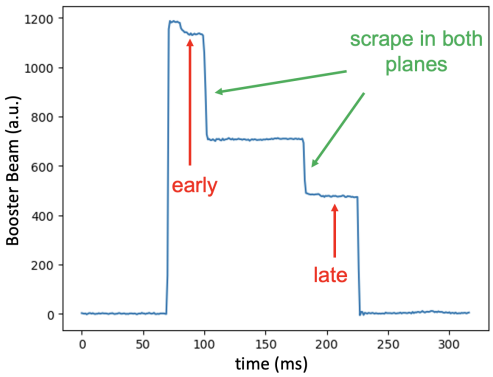


Figure 2: Booster beam intensity in one Booster cycle. Horizontal and vertical scrapings are visible as sharp decreases.

There are 13 quadrupoles and 16 correctors in the LtB line used to optically match the incoming beam both at the entrance of the 126° bend region and into the Booster ring. Traditionally Booster injection is hand tuned by experienced operators to increase the Booster early and late intensities.

In this work, we use Bayesian optimization (BO) to optimize Booster injection efficiency. BO has been widely implemented to solve complex particle accelerator control problems [2], because it is sample efficient and needs no existing model. Accurate models for transfer lines are difficult to construct due to their complicated geometry, so we choose BO for fast real-time optimization.

SIMULATION RESULTS

In order to study the sensitivity of injection efficiency to the correctors, a corrector scan was performed where all 16 correctors were changed individually until the Booster late intensity dropped by 50 %. Figures 3 and 4 show the

Content from this work may be used under the terms of the CC BY 4.0 licence (© 2022). Any distribution of this work must maintain attribution to the author(s), title of the work, publisher, and DOI.

ISBN: 978-3-95450-261-5 ISSN: 2673-7000 doi: 10.18429/JACoW-NAPAC2025-MOP051

INSTRUMENTATION FOR A PROTOTYPE FUSION PROPULSION SYSTEM

G.E. Bittlingmaier[1], G.P. Jackson[2], A.S. Lee[1]
[1]Beam Alpha Incorporated, West Chicago, IL, USA
[2]Hbar Technologies, LLC, West Chicago, IL, USA

Content from this work may be used under the terms of the CC BY 4.0 licence (© 2022). Any distribution of this work must maintain attribution to the author(s), title of the work, publisher, and DOI.

Abstract

A prototype colliding beam accelerator has been fabricated for the study of a fusion-based propulsion concept for interplanetary exploration. The purpose of this prototype is to demonstrate collider luminosities commensurate with the requirements of this application. While fusion fuels such as p/Li7 and He3/He3 would generate the required thrust characteristics, this prototype currently employs deuterium. Because neutrons are produced via DD fusion with a peak cross section of 0.1 barns, even modest initial luminosities yield event rates suitable for real-time measurements and lifetime monitoring. The proposed luminosity monitor is based on neutron moderation and absorption and subsequent gamma-ray detection. Sodium chloride serves as the moderator, with most neutrons absorbed by chlorine-35 nuclei having a thermal neutron absorption cross section of 43.6 barns. The collider is a linear device employing electrostatic axial confinement and radial focusing. A combination of destructive and nondestructive sensors are employed to monitor various beam parameters such as intensity, energy spectrum, transverse tunes and halo density distribution.

TERRESTIAL APPARATUS

The fusion reactor architecture used in the proposed propulsion system [1] consists of an electrostatic charged particle trap [2-4] that brings two ion beams into collision with equal and opposite momentum. The terrestrial prototype apparatus utilizes deuteron beams confined both radially and axially by an array of electrostatic electrodes. A picture of the apparatus exterior is displayed in Fig. 1. The dark spots along the side of the white tube are the vacuum electrical feedthroughs to each electrode. Visible on the left side are vacuum pumps and related equipment along with vacuum feedthroughs to a Faraday cup.



Figure 1: Picture of the prototype fusion propulsion apparatus used to understand and improve luminosity performance.

The internal geometry of the collider, along with the axial potential, are illustrated in Fig. 2. The radial aperture of the electrodes increases linearly with distance from the central collision region. On one side of the array is the deuteron ion source, while on the opposite side is a set of destructive beam instrumentation such as the Faraday cup.

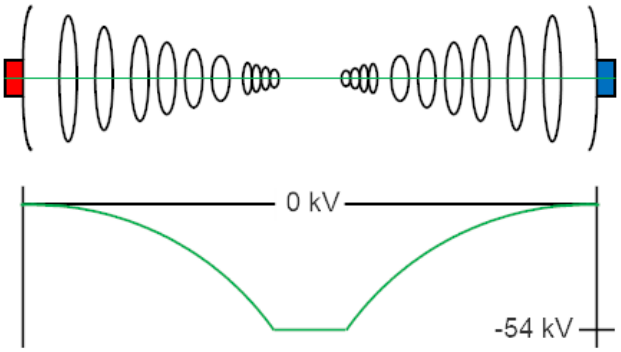


Figure 2: Illustration of the electrostatic electrode array of the fusion collider (top) and the axial potential (bottom).

The axial potential is imposed by applying specific voltages to each electrode in the array. Maintaining even axial symmetry about the center, networks of resistors and capacitors pictured in Fig. 3 are used to distribute the appropriate electrode voltages from a single high-voltage power supply. While the end electrodes are set to zero volts to simplify instrumentation connections, the central collision region is set to an axial potential of -54 kV.

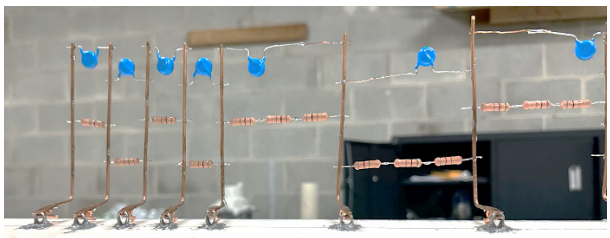


Figure 3: Picture of a portion of the network of resistors and capacitors used to set the voltages of the individual electrodes.

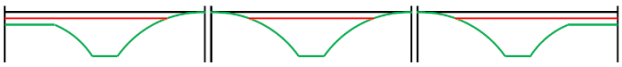


Figure 4: Illustrations of beam injection (left), storage (center), and extraction (right) via modification of the axial potential. The total (kinetic plus potential) energy of the beam is indicated with the red line.

Beam injection and extraction is accomplished with high-speed high-voltage switches that lower the axial potential during each of these events. Illustrations of these operations are sketched in Fig. 4. This enables deuteron injection from ion source on the left side with finite kinetic energy. Before bouncing back to the left side, the axial potential is returned to the storage configuration in the center (and shown in Fig. 2). Arbitrary beam collision kinetic energies less than 54 keV are achievable.

ISBN: 978-3-95450-261-5 ISSN: 2673-7000 doi: 10.18429/JACoW-NAPAC2025-MOP052

DESIGN OF A BPM PICK-UP FOR THE EIC ELECTRON STORAGE RING*

M. Sangroula†, J. Bellon, A. Blednykh, D. Gassner, C. Hetzel, C. Liu, I. Pinayev, M. Wendt
Brookhaven National Laboratory, Upton, NY, USA

Abstract

A new beam position monitor (BPM) pick-up, compatible to operate reliably with the high current electron beams foreseen in the 5 - 18 GeV Electron Storage Ring (ESR) of the Electron-Ion Collider (EIC) project, is presented. We discuss a few design options for this button-style BPM pick-up with a focus on output signal levels, position characteristic, and wakefield effects. Regarding the octagonal cross-section geometry of the ESR vacuum chamber, the BPM pick-up analysis relies on numerical methods, here performed using the CST Studio software.

INTRODUCTION

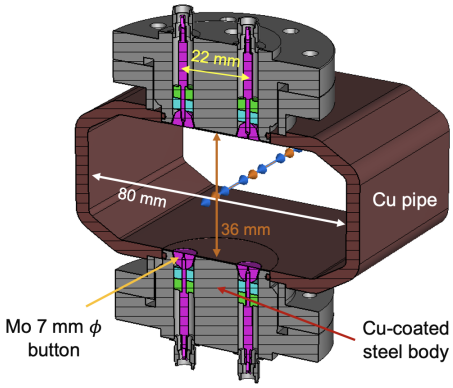
The Electron-Ion Collider (EIC) [1–4], presently in the design phase, will enable collisions between polarized electron and hadron beams at center-of-mass energies ranging from 30 to 140 GeV/nucleon. The collider consists of two main rings, an Electron Storage Ring (ESR) and a Hadron Storage Ring (HSR), both reside in RHIC tunnel having a 3.8 km circumference. The vacuum chamber of the ESR is made of copper and has an octagonal cross-section shape with 80 mm (horizontal) × 36 mm (vertical) aperture. While operating with the highest beam current, up to 2.5 A, comprised of short electron bunches (σ = 7 mm), refer to Table 1, in the ESR poses several design challenges for the 220 beam position monitors (BPMs). These challenges include elevated beam-induced resistive wall (RW) heating, achieving acceptable beam-coupling impedance to ensure beam stability, and providing sufficient position measurement resolution, accuracy and reproducibility, all required to achieve high luminosity and preserve polarization.

Table 1: ESR Beam Parameters for the Highest RW Heating

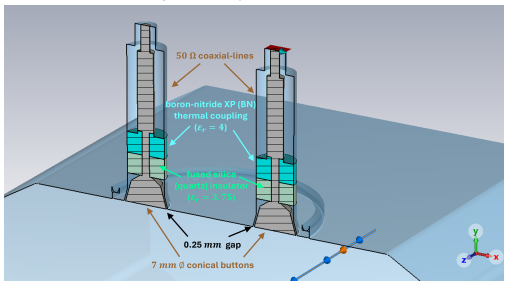
Parameters	Value	Unit
Bunch length (σ_{rms})	7	mm
Average beam current	2.5	A
Charge per bunch (Q_b)	27.6	nC
Number of bunches (N_b)	1160	
Beam energy	5 & 10	GeV

THE ESR BUTTON BPM PICK-UP

Button BPMs are the most popular and cost-effective type of pick-up to monitor the beam centroids of short electron bunches in electron storage rings. We will use button BPMs throughout all the EIC accelerator complex, including the EIC Electron Storage Ring (ESR). Figure 1 (a) illustrates the geometry of the ESR button BPM pick-up mounted to the octagonal shaped copper vacuum chamber. It consists of two flanges - top and bottom - each housing two molybdenum button electrodes of 7 mm diameter, are housed as pairs, separated by 22 mm in two 304L stainless-steel flanges mounted on top and bottom of the vacuum pipe (cooling channels not shown). While we used the detailed geometry, Fig. 1 (a), for the numerical analysis of the BPM including the losses in the metals, we used a simplified model, Fig. 1 (b), to find the relevant details to analyze the position characteristic and the geometric wakefield effects. For the simulation setup, we used *normal* (vacuum: $\varepsilon_r = 1,\ \mu_r = 1$) background in the former case, and *perfect electric conductor* (PEC) in the later lossless analysis.



(a) ESR BPM geometry with materials indicated



(b) Simplified model for the loss free analysis

Figure 1: Cross-section view of the ESR BPM pick-up assembly.

An alternative button electrode with simple cylindrical button shape instead of conical, and with the same button diameter, and other dimensions, see Fig. 2, was used for a comparative lossless study. Due to the octagonal cross-section of the vacuum chamber, analytical methods are not feasible for this button BPM design. Therefore, numerical

* Work supported by Brookhaven Science Associates, LLC under Contract No. DE-SC0012704 with the U.S. Department of Energy.

† msangroul@bnl.gov

Content from this work may be used under the terms of the CC BY 4.0 licence (© 2022). Any distribution of this work must maintain attribution to the author(s), title of the work, publisher, and DOI.

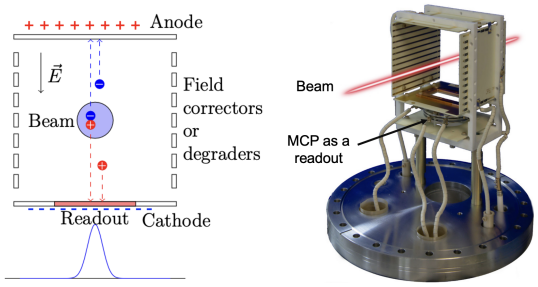
ISBN: 978-3-95450-261-5 ISSN: 2673-7000 doi: 10.18429/JACoW-NAPAC2025-MOP053

INVESTIGATION OF IPM PROFILE CHANGES WITH VARIATIONS IN THE APPLIED ELECTRIC FIELD*

M. Sangroula†, D. Gassner, S. Hafeez, C. Liu
Brookhaven National Laboratory, Upton, NY, USA

Abstract

Variations in the applied electric field in the Ionization Profile Monitor (IPM) affects the time of flight for the ionized particles (primarily electrons) which could affect the measured transverse beam profile. In addition, the applied electric field may affect the space charge of the ionized electrons inside the IPM. In this paper, we present an experimental beam study of RHIC IPM profiles, examining the effect of varying applied electric fields. Such a beam study will be helpful to enhance the design of the future IPMs for the Electron-Ion Collider. We analyzed horizontal and vertical profiles of gold and proton beams, comparing measured data with simulations along with the procedure we used for measurement. Potential causes for discrepancies between measured and simulated results are also discussed.



(a) Working principle (b) IPM internal view

Figure 1: Schematic of the IPM working principle (left) and a photograph of its internal components (right), reproduced from Ref. [1].

INTRODUCTION

The Ionization Profile Monitor (IPM) is a non-invasive diagnostic tool commonly used to measure the transverse profile of high-intensity hadron or heavy-ion beams. Unlike wire scanners, which are suitable for low-intensity beams, IPMs are essential for high-intensity operations where the destructive nature of the beam can damage invasive diagnostics. As each IPM provides profile information in a single transverse plane, two orthogonally oriented IPMs are typically employed to obtain both horizontal and vertical beam profiles.

The IPM reconstructs the transverse beam profile by detecting particles generated through beam-induced ionization of residual gas molecules in the vacuum chamber. As the beam traverses the chamber, it ionizes a small fraction of these gas molecules, producing electrons and ions. An external electric field, applied via high-voltage electrodes, extracts the ionized particles toward opposing directions due to their opposite charges. A sufficiently strong electric field is required to efficiently collect the ionized particles without significantly distorting the spatial distribution, thereby enabling accurate profile reconstruction. A schematic representation of this principle is shown in Fig. 1(a), where the electrons and ions are observed drifting toward opposite electrodes under the influence of the applied field.

The accuracy of the transverse beam profile measured by an IPM is influenced by several factors, including beam velocity (which relates to space charge), bunch intensity, and the uniformity of the applied electromagnetic fields. To preserve the spatial distribution of the extracted electrons as they drift toward the micro-channel plate (MCP) or readout plate, it is critical to maintain a highly uniform extraction electric field. This is achieved through the use of field correctors, as illustrated in Fig. 1(a), which minimize field distortions near the beam path. Furthermore, a transverse magnetic field is often superimposed to constrain the electron trajectories along the drift direction, thereby suppressing electron divergence due to beam-induced space-charge forces [2, 3].

Historically, both ion-collecting and electron-collecting IPMs have been used. However, recent studies show that ion-collecting IPMs are highly sensitive to space-charge effects from the circulating beam, causing significant variations in the measured beam profile [4]. In contrast, electron-collecting IPMs are less affected by space-charge effects and therefore provide more reliable measurements. Another investigation on the effect of space charge on IPM profiles can be found in Ref. [5].

The number of ionized particles generated by a heavy ion beam is smaller as we maintain an ultra-high vacuum inside the beam pipe. To amplify the number density of the electrons, we use a MCP. When a particle hits the MCP hole entrance, secondary electrons are emitted. Due to the potential difference, these electrons are accelerated toward the channel output, striking the hole walls and generating additional secondary electrons in a cascading effect [1].

A position-sensitive detector, typically composed of conductive strips (or a phosphor screen, which converts electrons into visible photons), is placed on the detection plane to detect the electrons flowing via each strips. The ionization current flowing through these strips is recorded to determine the spatial distribution and reconstruct the transverse beam profile. One of the pioneering papers on beam detection using residual gas ionization can be found in Ref. [6].

* Work supported by Brookhaven Science Associates, LLC under Contract No. DE-SC0012704 with the U.S. Department of Energy.
† msangroul@bnl.gov

Content from this work may be used under the terms of the CC BY 4.0 licence (© 2022). Any distribution of this work must maintain attribution to the author(s), title of the work, publisher, and DOI.

ISBN: 978-3-95450-261-5 ISSN: 2673-7000 doi: 10.18429/JACoW-NAPAC2025-MOP054

LIFETIME EXTENSION OF LEGACY CEBAF LLRF HARDWARE

M. Geesaman†, J. Latshaw
Thomas Jefferson National Accelerator Facility, Newport News, VA, USA

Abstract

A significant portion of the Low-Level Radio Frequency (LLRF) hardware in Jefferson Lab's CEBAF is from the original construction of the facility using 1980's CAMAC technology. Of the fifty-three zones in CEBAF, thirty-six of them are legacy hardware. The age of the legacy system has led to difficulties in maintaining the hardware due to parts going obsolete without suitable drop-in replacements. Continued operation of the legacy system is required as the installation of LLRF 3.0 systems is costly and cannot be completed in a short period of time with the available resources. The most pressing failure in the legacy system was a failing buffer card, which is responsible for communication between the EPICs network and individual RF control modules. A new buffer card was designed as a transparent, drop in, replacement so that upgrades are simply a matter of swapping the existing legacy hardware. This buffer card upgrades a single point failure component and promises to extend the operable lifetime of CEBAF's legacy systems.

LLRF 1.0

As it currently stands, over two thirds of the LLRF system in JLab's CEBAF is original hardware. Communication between the RF Control Modules (RFCM) and the Experimental Physics and Industrial Control System (EPICS) is facilitated through the Computer Aided Measurement And Control (CAMAC) system [1]. Each RFCM is connected to its own Buffer Card inside the CAMAC crate, for a total of eight Buffer Cards per zone [1]. With thirty-six zones still using legacy hardware, this brings the total number of buffer cards in the machine to 288. These buffer cards use a now obsolete PEEL173 complex programmable logic device (CPLD), to decode read/write instructions from the CAMAC backplane. Due to the age of the PEEL's, the memory is failing, rendering the buffer cards non-functional. These failures cause intermittent issues in the operation of the zones. Whilst some LLRF 1.0 systems are being upgraded to LLRF 3.0, the upgrade process is multi-year and the current plan is not to replace all the 1.0 zones with 3.0 due to numerous constraints. The memory failures, the inability to obtain replacement components and the need to keep the LLRF 1.0 systems operational, necessitated the development of a drop-in replacement for the Buffer Card using new hardware.

LLRF 2.0/3.0

JLab's CEBAF currently contains seventeen zones equipped with either LLRF 2.0 or 3.0 systems. These new systems eliminate the need for buffer cards in the zones they are installed in as each field control chassis (FCC) communicates directly over the network [2]. These systems bring improved control of the superconducting cavities and reduce trip recovery time [2]. Upgrading all of the zones in CEBAF would be ideal, however due to resource constraints this path is not currently feasible.

CONCEPTUAL DESIGN

Multiple options were explored for the replacement controller during the development process. Current CPLDs, FPGAs and microcontrollers were all considered for use. We decided to use a microcontroller for the new revision of the buffer card due to a combination of the ease of use, availability and cost as compared to the other options. The selected microcontroller is part of the PIC18 family of devices. The PIC18F57Q43 was selected for its 8 Configurable Logic Cells (CLC), 5V operation and pin count. Updated buffer chips were selected, reducing the risk of components going obsolete in the near future and reducing the overall part count. The CLCs are programmed with the requisite logic functions to decode the read/write instructions from the CAMAC backplane, this allows the commands to be interpreted and executed in hardware leaving the microprocessor available for other operations (Fig. 1). A RS232 interface was added to the board to enable the display of additional diagnostic information.

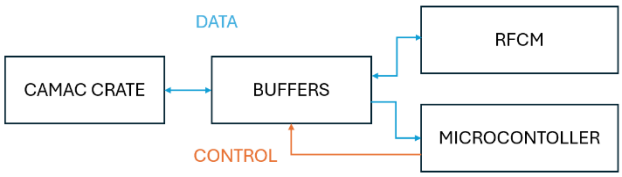


Figure 1: Operational Diagram.

CODE SIMPLIFICATION

The original code is made up of multiple independent sub-functions which make up the read, write and acknowledge functions (Fig. 2). These functions are larger than necessary, as such they were simplified using Boolean algebra, allowing the logic to fit on the available CLCs (Fig. 3).

Authored by JSA, LLC under U.S. DOE Contract DE-AC05-06OR23177 and DE-SC0005264. The U.S. Govt. retains a non-exclusive, paid-up, irrevocable, worldwide license to publish or reproduce this for U.S. Govt. purposes.

† geesaman@jlab.org

Content from this work may be used under the terms of the CC BY 4.0 licence (© 2022). Any distribution of this work must maintain attribution to the author(s), title of the work, publisher, and DOI.

ISBN: 978-3-95450-261-5 ISSN: 2673-7000 doi: 10.18429/JACoW-NAPAC2025-MOP055

LOW-CHARGE, HIGH-RESOLUTION BEAMLINE PREPARATION FOR THE NANOPATTERNED MICROBUNCHING EXPERIMENT AT ARGONNE WAKEFIELD ACCELERATOR *

R. Margraf-O'Neal[1†], A. Ody[1], J. Power[1], J. Hlavenka[1], B. N. Temizel Ozdemir[1,2], G. Andonian[3], B. Carlsten[4], A. DeSimone[1,2], G. Ha[1,2], A. Halavanau[5], H. Xu[4], N. Majernik[5], J. M. Maxson[6], A. Parrack[3], R. Ryne[7], M. Yadav[3,8], N. Yampolsky[4], J. Rosenzweig[3]

[1] Argonne National Laboratory, Lemont, IL, USA
[2] Northern Illinois University, DeKalb, IL, USA
[3] University of California - Los Angeles, Los Angeles, CA, USA
[4] Los Alamos National Laboratory, Los Alamos, NM, USA
[5] SLAC National Accelerator Laboratory, Menlo Park, CA, USA
[6] Cornell University, Ithaca, NY, USA
[7] Lawrence Berkeley National Laboratory, Berkeley, CA, USA
[8] Old Dominion University, Norfolk, VA, USA

Abstract

The emittance exchange (EEX) beamline at the Argonne Wakefield Accelerator (AWA) is designed to transfer properties of an electron beam phase space between the transverse and longitudinal planes. Recently, it has been proposed this beamline could be used to convert a microscale transverse modulation created by a TEM grid into a microbunch train in the longitudinal plane. Such a technique would be useful for obtaining nano-scale microbunching that does not rely on the sensitive process of FEL gain. This new approach has been proposed to enable development of a compact free-electron laser at Arizona State, greatly reducing size and cost compared with existing short wavelength FELs. To perform an exploratory demonstration of this concept at AWA, this experiment requires low normalized emittance ($\approx$50 nm $\cdot$ rad), low charge ($\approx$1 pC) electron bunches, and transverse diagnostics with high-resolution (1 - 3 µm) and high-light-collection to resolve the modulation on the electron beam. This report will give a progress update on preparing the necessary beams and diagnostics at AWA for an emittance exchange experiment that would produce 100s of nm scale microbunches.

INTRODUCTION

X-Ray free-electron lasers (XFELs) rely on microbunching to produce exponential gain of short-wavelength X-ray radiation. This is most commonly done using a self-amplified spontaneous emission (SASE) process [1–6], where microbunches originate from noise, requiring a long undulator to build up microbunches. There are also many schemes that have been developed and implemented for seeded XFELs [7–10] and proposals for cavity-based XFELs [11, 12]. A recent proposal at Arizona State University [13, 14] described a method of FEL seeding by transforming transverse beamlets into longitudinal microbunches. This technique promises a highly efficient and compact method for generating microbunches, but is very sensitive to beam emittance, and collective effects such as space charge. Thus, the nanopatterned microbunching collaboration has been formed to perform a proof-of-principle experiment of this mechanism at the Argonne Wakefield Accelerator (AWA).

As depicted in Fig. 1, the nanopatterned microbunching experiment will produce beamlets by scattering on a 12.5 µm period grating. These will be demagnified using a quadrupole lattice to 3 µm, then transformed into 800 nm microbunches via an emittance exchange lattice. While 800 nm is too long of a wavelength to yet be useful for XFELs, this experiment will provide a proof of principle achievable within the constraints of the AWA facility that will be extendable to shorter wavelengths with higher energy beams where space charge effects are less dominant.

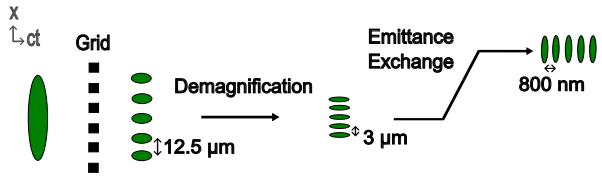


Figure 1: Overview of the nanopatterned microbunching experiment. Beamlets are created in the transverse plane using a TEM grid, demagnified to a 3 µm period using a quadrupole lattice, then transformed into longitudinal microbunches at 800 nm with an emittance exchange beamline.

The nanopatterned microbunching experiment has several requirements on the AWA facility that are outside of its normal operating range. AWA is tuneable within a large charge range (1 pC - 400 nC), but optimized for high charge (100s of nC) bunch trains to drive structure wakefield acceleration [15, 16]. However, to mitigate collective effects, the nanopatterned microbunching experiment must operate at

* This work is supported by the U. S. Department of Energy, under contract No. DE-AC02-06CH11357.

† rmargrafoneal@anl.gov

Content from this work may be used under the terms of the CC BY 4.0 licence (© 2022). Any distribution of this work must maintain attribution to the author(s), title of the work, publisher, and DOI.

ISBN: 978-3-95450-261-5 ISSN: 2673-7000 doi: 10.18429/JACoW-NAPAC2025-MOP056

MACHINE LEARNING ASSISTED BAYESIAN CALIBRATION OF ACCELERATOR DIGITAL TWIN FROM ORBIT RESPONSE DATA*

W. Lin[1,†], K. A. Brown[1], G. H. Hoffstaetter de Torquat[1,2], C. Kelly[3], N. Urban[4]
[1]Collider-Accelerator Department, Brookhaven National Laboratory, Upton, NY, USA
[2]CLASSE, Cornell University, Ithaca, NY, USA
[3]Computational Science Department, Brookhaven National Laboratory, Upton, NY, USA
[4]Applied Mathematics Department, Brookhaven National Laboratory, Upton, NY, USA

Abstract

Digital twins of particle accelerators are used to plan and control operations and to design data collection campaigns. Accurate modeling typically requires knowledge of quantities that are hard to measure directly, e.g., magnet alignments, power supply transfer functions, magnet nonlinearities, and stray fields. In this work we introduce multiplicative nuisance parameters to the quadrupole transfer functions to parametrize these effects and use Bayesian methods to probabilistically estimate their values and uncertainties by calibrating the Bmad digital twin to beam measurements performed at the AGS Booster at Brookhaven National Laboratory. The inference is computationally accelerated using a machine learning emulator of the physical accelerator digital twin trained to a perturbed-parameter ensemble of Bmad simulations. The result is a joint posterior distribution over the nuisance parameters constrained by the data and taking into account beam monitor errors. Incorporating estimates of the nuisance parameters into the digital twin is shown to result in a significant improvement in the quality of the model and provides error bars on the model parameters and predictions.

INTRODUCTION

The Alternating Gradient Synchrotron (AGS) Booster acts as the pre-injector for the AGS, increasing the AGS injection energy from 200 MeV to 1.5 GeV [1]. It also serves as a heavy-ion source for the NASA Space Radiation Laboratory. As one of the most upstream components in the acceleration chain, accurate control of beam properties in the Booster is indispensable to providing high quality beams to both the Relativistic Heavy Ion Collider (RHIC) and the future Electron Ion Collider (EIC).

A good understanding of magnet properties in the Booster is essential for better beam control. A comparison of measured and simulated orbit response data reveals that the current Booster digital twin is inaccurate at the level of several percent. The overarching goal of our research is to utilize Bayesian uncertainty quantification (UQ) techniques to identify and model the sources of these discrepancies.

As a first step in this direction, we focus on the uncertainties associated with the 48 quadrupole magnets, as these are expected to play a dominant role. We introduce magnet-dependent nuisance parameters to the transfer function that relates the magnetic field to the power supply current, allowing the unknown sources of error to individually affect the magnet's impact on the beam orbit.

The values of these nuisance parameters are constrained using experimental data via Bayesian UQ. The resulting posterior distribution provides data-constrained values for the nuisance parameters that are then incorporated into the digital twin to improve the modeling.

ORBIT RESPONSE MEASUREMENT

To collect suitable data from the Booster we developed a script [2] that sets each corrector in turn to three settings: zero kick (baseline value), positive kick, and negative kick, while leaving all other correctors in their baseline setting. After setting the corrector, live beam position monitor (BPM) data and all the magnet settings are saved. The script work flow is outlined in Fig. 1.

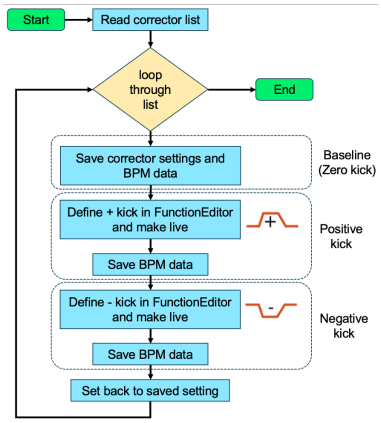


Figure 1: Work flow of orbit response measurement script.

The script was applied to both the 24 horizontal and 24 vertical correctors in the Booster. Each corrector was set to ±22 A between 50 and 110 milliseconds during the Booster magnet cycle. In this work we utilize only the data collected at a flat-top time of 92 ms. For each setting, between 2 and 5 (typically 3) repeated measurements were taken over different cycles, for a total of 224 and 113 measurements for the horizontal and vertical correctors, respectively.

The data collected comprises both orbit data and all magnet current settings in the Booster, including dipoles, quadrupoles, sextupoles, and all correctors. These settings

* Work supported by Brookhaven Science Associates, LLC under Contract No. DE-SC0012704 with the U.S. Department of Energy and by DOE-NP No. DE SC-0024287.

† wlin1@bnl.gov

Content from this work may be used under the terms of the CC BY 4.0 licence (© 2022). Any distribution of this work must maintain attribution to the author(s), title of the work, publisher, and DOI.

ISBN: 978-3-95450-261-5 ISSN: 2673-7000 doi: 10.18429/JACoW-NAPAC2025-MOP057

MACHINE LEARNING AT THE SPALLATION NEUTRON SOURCE ACCELERATOR AND TARGET*

W. Blokland†,[1], A. Kasparian[2], K. Rajput[2], A. Raj[1], M. Schram[2], D. Winder[1], S. Zhukov[1]
[1]Oak Ridge National Laboratory, Oak Ridge, TN, USA
[2]Thomas Jefferson National Accelerator Facility, Newport News, VA, USA

Abstract

We describe the ongoing efforts to apply Machine Learning techniques to improve the performance of our accelerator and target. Specially, we are looking to minimize halo beam losses in the absence of a proper physics model, automatically detect and log anomalies in the target support systems such as cooling, and detect and prevent errant beam pulses in the linac. We also describe the infrastructure we use to acquire and stream data to the GPU cluster for training, our code development cycle, and edge computing for model inference. To minimize halo beam losses, we use a Reinforcement Learning technique tested on a virtual accelerator. The target anomaly detection is trained on archived data using unsupervised learning and is made part of the existing target reporting system. The errant beam prevention analyses beam current and beam phase waveforms as well as accelerator configuration data to predict errant pulses. We also develop continual learning to adapt to changes in the accelerator.

INTRODUCTION

A review of the existing ML applications in particle accelerator applications can be found in Refs. [1, 2]. It shows that most ML solutions do not reach deployment in operational settings. We aim to not only research how Machine Learning (ML) can improve operations but to also integrate ML into Operations Spallation Neutron Source (SNS). To demonstrate our approach, we select problems that, when solved, have a chance to improve accelerator or target performance gains within a reasonable timescale. Previously, we found that ML can do prognostics, e.g. determining that a high-power supply is going to fail, but fixing the power supply is as time consuming as waiting for the equipment to fail. Thus, it is not a good use-case for improving performance. Based on previous experience, we applied the following criteria to select use-cases:

- Data must be available early in the project.
- The ML model, trained on data from the past, must function in the future.
- There must be an acceptable false positive rate.
- The result must be actionable.

*This work was supported by the DOE Office of Science, United States under Grant No. DE-SC0009915 (Office of Basic Energy Sciences, Scientific User Facilities Program). This manuscript has been authored by UT-Battelle, LLC, under Contract DE-AC05-00OR22725 with the US Department of Energy (DOE). The Jefferson Science Associates (JSA) operates the Thomas Jefferson National Accelerator Facility for the U.S. Department of Energy under Contract No. DE-AC05-06OR23177. This research used resources at the SNS, a DOE Office of Science User Facility operated by the ORNL.
†blokland@ornl.gov

The selected use-cases based on these criteria are:

- Errant Beam Prognostics: ML aborts the accelerator before an errant beam pulse causes beam loss or damages the accelerator.
- Automatic and fast optimization of beam orbit to reduce beam losses: our goal is to halve the tune-up time which can last from an hour to a day.
- Detect and predict anomalies in the target support cooling and mercury loops: report anomalies in time for intervention.

We must add infrastructure for ML applications as it requires larger data streams and data storage than a typical accelerator control system. ML requires large data sets and significant computing power, especially GPUs, for training. The ML infrastructure needs to be within the accelerator network because even if the network needs to be air gapped, the ML applications must still be able to operate.

USE-CASES

Errant Beam Prognostics

The Differential Beam Current monitor supplies most of the data for the Errant Beam Prognostics (EPB). Previous studies [3] showed that precursors of errant beam were hidden in this data. This is important as we want to abort before the errant beam pulse is issued and not during to prevent the damage or radioactivation from happening. Our goal is to show that we can abort beam pulses before the errant beam pulse occurs.

We look at the True Positive Rate (TPR) at a very low False Positive Rate (FPR) < 0.5% to avoid unnecessarily abort beam. On a static dataset, we had implemented uncertainty aware Machine Learning model and achieved about a 60% TPR [1, 4]. We found that the TPR is roughly 30% for a non-static set (aka during Operations).

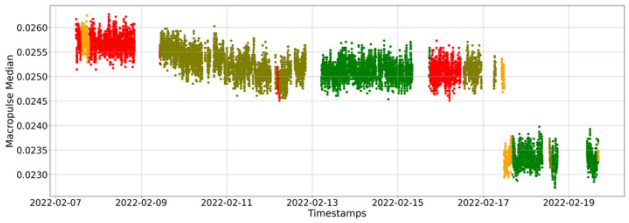


Figure 1: Changes in the beam current. Different colors represent data from different beam settings configuration.

The main challenge for operations is that we can only train on historical data and must infer during operations when the accelerator data varies both due to configuration changes and due to drift and the data changes (see Fig. 1). A configuration change is when the operators change a

Content from this work may be used under the terms of the CC BY 4.0 licence (© 2022). Any distribution of this work must maintain attribution to the author(s), title of the work, publisher, and DOI.

ISBN: 978-3-95450-261-5 ISSN: 2673-7000 doi: 10.18429/JACoW-NAPAC2025-MOP059

MACHINE LEARNING-ENHANCED INFRARED IMAGING FOR TEMPERATURE ANOMALY DETECTION IN POWER SUPPLIES *

O. Mohsen†, M. Borland, Y.Sun Argonne National Laboratory, Lemont, IL, USA
I. Lobach, Brookhaven National Laboratory, Upton, NY, USA

Abstract

The performance of particle accelerators is critically dependent on the reliability of their power supplies, which can number in the thousands in many facilities. In this work, we present different methods for monitoring temperature anomalies in power supplies. By applying various machine learning algorithms to the obtained features, we develop a reliable anomaly detection system that can improve the uptime of accelerator facilities. This approach enables early detection of potential issues, facilitating predictive maintenance and enhancing overall operational efficiency.

INTRODUCTION

Most accelerator facilities use power supplies to control magnets. Depending on the size of the facility, these power supplies can be numbered in the thousands. For instance, the Advanced Photon Source Upgrade (APS-U) storage ring (SR) [1], which was recently commissioned [2], uses approximately 1300 power supplies of various types to control its magnets. Earlier data from the APS indicates that the average downtime due to power supply failure was about two hours [3]. Such downtime disrupts the operation of the dozens of beamlines operating at any time. Faults in power supplies can range from equipment failure to faults caused by nuisance trips. For most of the failures in the power supplies, the stored beam is lost. In this work, we use a power supply test stand to study temperature anomalies in power supplies. Specifically, we focus on bipolar type, fast-corrector power supplies [4]. These power supplies control the corrector magnets, which are used for orbit feedback.

First, we discuss the use of an infrared (IR) camera coupled with a Machine Learning (ML) model to record and predict temperature distribution inside a power supply. We follow the work of [5], which showed promising results of using an IR camera to predict temperature anomalies using analytical methods. We discuss scalability and issues with our ML model. Moreover, we discuss the results of a larger data training study that involved all the fast correctors in one sector of the SR. Finally, we discuss the future outlook for such a model and its application to APS-U operation.

EXPERIMENTAL SETUP

To investigate the use of different diagnostics and allow flexible data acquisition, a power supply test stand was set up; see Fig. 1. The test stand can host and control different types of power supplies independently of beam operation. The setup has a power supply controller, a resistive load, and several external sensors to record ambient temperature. The power supply top lid is open so that an IR camera located above the power supply can image temperature variation in the unit. The IR camera Seek Thermal Camera has a resolution of 320 x 240 pixels and is able to record images at a rate of 9 frames per second [6]. The setup has 2 independent relays that can turn on and off the power supply fans. This allows us to create synthetic anomalies by turning off a fan. Finally, a raspberry pi is used to facilitate data acquisition and host the related EPICS variables on the network.

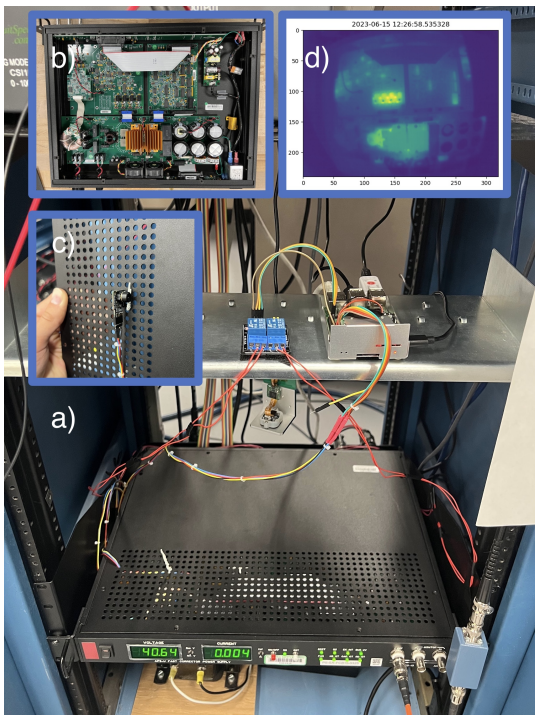


Figure 1: Power supply setup for data collection (a), the power supply test unit when the top lid is removed (b), IR camera (c) and the image obtained from the IR camera (d).

Data Collection and Processing

For all the models referenced in this work, data collection is performed over three days and then separated into three different categories: training, validation, and testing. Unlike the training and validation data, only the testing data contains synthetic anomalies, which are used to evaluate the model performance. The data used for the model consists of a series of current ramps that are generated using a pseudo-random number generator. The current $I(A)$ is varied at 1 Hz rate from -15 A to 15 A. The data from all the power supply

* The work is supported by the U.S. DOE Office of Science-Basic Energy Sciences, under Contract No. DE-AC02-06CH11357.
† omohsen@anl.gov

Content from this work may be used under the terms of the CC BY 4.0 licence (© 2022). Any distribution of this work must maintain attribution to the author(s), title of the work, publisher, and DOI.

ISBN: 978-3-95450-261-5 ISSN: 2673-7000 doi: 10.18429/JACoW-NAPAC2025-MOP061

MITIGATING IDVC THERMAL DEFORMATION WITH MECHANICAL CONSTRAINT FOR RELIABLE ID MINIMUM GAP OPERATION*

W. Li†, M. Qian, J. Liu, A. Donnelly, J. TerHAAR, Y. Piao, J. Xu
Argonne National Laboratory, Lemont, IL, USA

Abstract

Premature activation of the insertion device (ID) minimum-gap limit switches was observed during beamline commissioning at the Advanced Photon Source Upgrade (APSU). This was traced to vertical displacement of the insertion device vacuum chamber (IDVC), due to the temperature differences between the chamber and its strongback. Direct measurements of temperature and vertical displacement of the IDVC in a selected sector confirmed this effect, and simulations reproduced the underlying thermal deformation mechanism. To address this issue, we developed a simple mechanical constraint to limit the vertical displacement by adding an additional support stand. Post-installation tests successfully demonstrated its effectiveness, allowing the IDs to reach the minimum gap without activating the limit switches. This paper represents the investigation, simulation, and validation efforts to resolve this issue.

INTRODUCTION

Hybrid Permanent Magnet Undulators (HPMUs) are essential components of the Advanced Photon Source Upgrade (APSU) for generating high-brightness X-ray beams for the insertion device (ID) beamlines. Insertion devices are designed with different period lengths and minimum gaps to cover specific X-ray energy ranges [1]. The minimum magnetic gaps of most IDs are designed to be 8.5 mm [2], while the insertion device vacuum chamber (IDVC) is designed with an outer height of 7.5±0.3 mm [3, 4], leaving a very small clearance on either side of the IDVC.

Due to these tight spacing constraints, the IDVC must be aligned within ±50 µm vertically and the chamber straightness maintained within ±100 µm throughout the 5.4 m full length [4]. To meet these tolerances, a strongback beam with the same length as the IDVC is designed to serve as both a support structure and an alignment reference. They connect via five L-brackets, each with three adjustment bolts, giving 15 correction points in total [4], as shown in Fig. 1.

Since the commissioning of the storage ring in 2024, the electron beam current increased, and commissioning of ID beamlines began. However, some IDs experienced premature activation of their minimum-gap limit switches at high beam current before reaching their designed minimum gaps. This discrepancy between the operational and the designed minimum gaps, referred to as the minimum gap shift, shown in Fig. 2. The shift varies across devices and can reach several hundred micrometers. For example, the upstream ID (USID) in Sector 08 was limited to approximately 396 µm above its designed minimum gap of 8.5 mm. These issues do not occur when the ring is not filled with beam. A systematic study of the minimum gap shift was conducted for all IDs with a 200 mA beam stored in the ring, shown in Fig. 2. It is observed that all the USIDs had their downstream-top (DST) switches activated, and all the downstream IDs (DSIDs) triggered their upstream-top (UST) switches. The only exception was one USID that exhibited activation of both its DST and upstream-bottom (USB) limit switches.

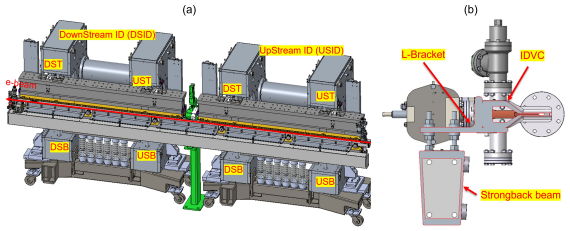


Figure 1: (a) Schematic of the IDVC and strongback in a sector with two IDs and an inline phase shifter. (b) Cross-sectional view of the IDVC mounted to the strongback.

Given the strong correlation of these events with beam current and that most activation events happened near the center of the IDVC, the most probable root cause is beam-induced thermal deformation of the IDVC. In this paper, we present our efforts investigating this issue and describe the solution developed to restore the operational minimum gaps for the IDs to the designed values.

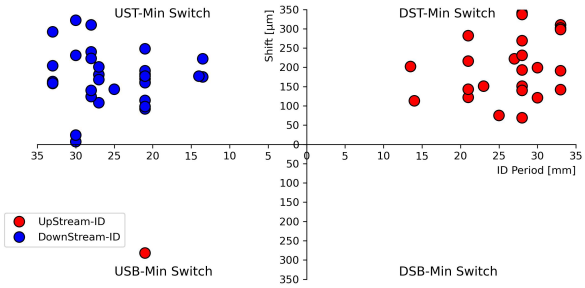


Figure 2: Minimum gap shifts relative to the designed values, measured with a 200-mA beam stored.

MEASUREMENT

Thermocouples and a potentiometer were installed to directly measure temperature changes and IDVC vertical displacement. Eight high-precision thermocouples, with a resolution of 0.1 °C, were installed on the Sector 08 IDVC,

* Work supported by U.S. Department of Energy, Office of Science, Office of Basic Energy Sciences, under Contract No. DE-AC02-06CH11357.
† liw@anl.gov

Content from this work may be used under the terms of the CC BY 4.0 licence (© 2022). Any distribution of this work must maintain attribution to the author(s), title of the work, publisher, and DOI.

ISBN: 978-3-95450-261-5 ISSN: 2673-7000 doi: 10.18429/JACoW-NAPAC2025-MOP064

ONLINE ACCELERATOR MODELING WITH TWO CONTROLS SYSTEMS AT FACET-II

Z. Buschmann*, M. Gibbs, N. Majernik, R. Loney, G. Yocky
SLAC National Accelerator Laboratory, Menlo Park, CA, USA

Abstract

FACET-II is a unique experimental facility housed in 1 km of the original Stanford Linear Accelerator tunnel. Multiple generations of hardware are still in use, as are two generations of software controls. A majority of subsystems (RF, magnets, timing, etc.) have their controls split across both ecosystems. Three software layers, including a newly-developed online modeling infrastructure, bridge this gap to form a unified high-level abstraction of the accelerator used for data analysis and as a foundation to develop control-room physics applications. We discuss the implementation of this infrastructure and some downstream programs.

ACCELERATOR CONTROLS

Electron beam system controls at FACET-II [1] are split across two systems. A legacy mainframe controls large sections of the main linac, while EPICS [2] is used for the photoinjector, early linac and two bunch compressors. The experiment beamline at the accelerator front-end has a mixture of devices controlled by both systems. Figure 1 shows the structure and approximate jurisdictions of these systems. Relevant legacy software is defined below.

SLC Control Program (SCP): Custom-built accelerator controls system [3], hosted by an openVMS mainframe called "MCC" (Main Control Computer), which communicates with an array of microcluster computers (or "micros") via a custom FM cable network called SLCNet to control accelerator hardware.

Accelerator Independent Data Access (AIDA-PVA): Java process on MCC that handles read and write requests to the SCP and MCC database over the SLAC controls network using the PVAccess protocol.

Channel Access Repeater: Java process on MCC that broadcasts a limited set of values for read-only access at up to 1 Hz using the Channel Access protocol.

LIVE MODEL ENGINE

Consistent accelerator operations depend on having access to a descriptive model of extant machine conditions. At SLAC, a number of programs have been written to read magnet and RF settings from the machine to update a model for performing calculations. With an API for communicating with accelerator controls, it is possible to write a script that will read current settings to update a model. In the SCP these computations were run directly on the mainframe by a model job.

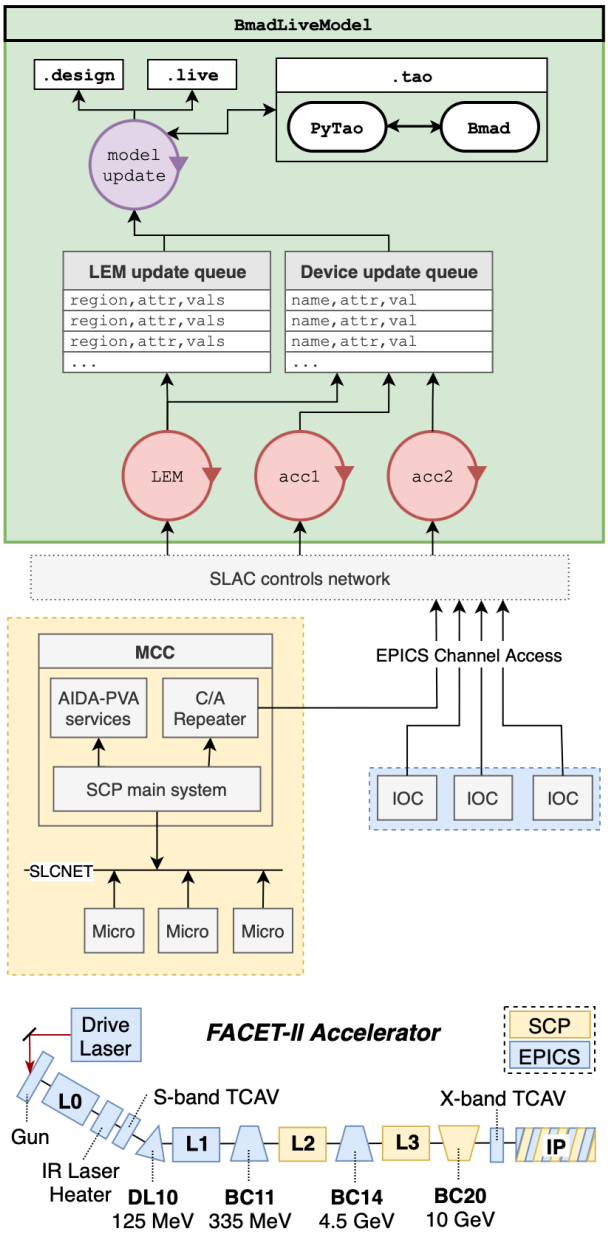


Figure 1: (Upper) Architecture of the BmadLiveModel class. (Lower) Schematic of the FACET-II accelerator and controls systems, with approximate jurisdictions labeled.

We have built a live modeling "engine" to solve this problem more generally that uses a thread-based architecture to collect accelerator controls system information and update a locally instanced modeling code. This system is portable, outperforms simpler scripts and is designed to streamline

* zack@slac.stanford.edu

Content from this work may be used under the terms of the CC BY 4.0 licence (© 2022). Any distribution of this work must maintain attribution to the author(s), title of the work, publisher, and DOI.

ISBN: 978-3-95450-261-5 ISSN: 2673-7000 doi: 10.18429/JACoW-NAPAC2025-MOP065

INTEGRATING SIMULATION AND MACHINE LEARNING FOR PROTON STORAGE RING BEAM ANALYSIS*

E.-C. Huang†, C. A. Leon, P. M. Anisimov, A. Scheinker
Los Alamos National Laboratory, Los Alamos, NM, USA

Content from this work may be used under the terms of the CC BY 4.0 licence (© 2022). Any distribution of this work must maintain attribution to the author(s), title of the work, publisher, and DOI.

Abstract

The Proton Storage Ring (PSR) at the Los Alamos Neutron Science Center (LANSCE) compresses a 625-μs-long proton beam into a 290-ns pulse for neutron production at the Lujan Center. The data-acquisition system for the Beam Position Monitors (BPMs) in the PSR was upgraded over the past year from a multiplexer system to independent readouts, significantly increasing the data output.

To leverage this improved capability, we developed a new analysis package based on existing MAD-X model to provide critical ring information like betatron tunes and injection offsets in real time. Furthermore, a Convolutional Neural Networks (CNN's) are trained on this simulation data to learn mappings between raw BPM signals and those key parameters for a more precise measurement. A combination of a physics-based fit with a CNN correction was found to produce the best results.

INTRODUCTION

The Proton Storage Ring (PSR) at the Los Alamos Neutron Science Center (LANSCE) is a critical component in the delivery of high-intensity proton pulses for neutron production. Designed for accumulation and compression, the PSR receives an 800-MeV H^- beam from the linac, strips the electrons via a thin foil, and accumulates the resulting protons over a 625-μs injection window. The accumulated beam is then extracted, forming a short pulse approximately 290 nanoseconds in duration base to base, which is directed to the Lujan Center spallation target. With a circumference of approximately 90 meters and a revolution time of ~360 ns, the PSR operates at a repetition rate of up to 20 Hz, delivering a nominal charge at 5 μC per pulse.

The PSR operates under high space-charge conditions, which introduces challenges in maintaining beam stability and minimizing losses. Effective tuning of the ring requires careful adjustment of beam optics parameters such as the betatron tune (ν_x, ν_y), closed orbit (CO), and injection offsets (x_0, x_0', y_0, y_0'). The initial injection offsets are critical as the production beam are painted vertically to minimize the number of foil hits from circulating beam. At the beginning of the run cycle, these quantities are measured and tuned up in the "single-shot" mode. The single-shot mode injects only one 290-ns-long (or shorter) minipulse into the PSR during the whole 625-μs accumulation window for the Beam Position Monitor (BPM) measurements. Furthermore, in the single-shot mode, the RF buncher and bump magnets for transverse painting are turned off.

* Work supported by LANL's LDRD program under 20250783MFR
† en-chuan@lanl.gov

The original BPM system is built upon a multiplexer system [1] that was only equipped with one readout each for the top, bottom, left, and right plates for all 20 BPMs. To measure beam positions for all BPMs, the system needs to cycle through each of the BPM. Procedures are built around this limitation to switch between turn-by-turn/time mode and azimuth mode for closed orbit measurements. One would also need to be careful in the BPM selections. The online analyses built for these procedures rely on linear approximations obtained from responses matrices with very limited visualization capabilities. As a result, the PSR tune-up process is often tedious and error prone.

Over the past year, LANSCE finally replaced the multiplexer system with an individual data acquisition (DAQ) system. With the new system, we can obtain the first 30 to 40 turns (the 201.25 MHz structure from the linac dissipates after 30 turns) of beam positions for all BPMs within a single pulse. This enables us to significantly improve our online analysis methods. In this proceeding, we will demonstrate the updated analysis package based on MAD-X [2] and the new ML-based method to even further improve the precision. The model-based method is heavily built upon the RingScan work [3], which automatically switches the multiplexer through all BPMs.

MADX-BASED ONLINE ANALYSIS

Figure 1 shows an example of the measurements of all BPMs over 40 turns from a sample dataset taken during the RingScan work. Oscillation patterns for each BPM (row) and the phase advance of the betatron oscillation are both apparent. In addition to the beam positions, the new DAQ also outputs the signal intensity and beam phases relative to reference 201.25-MHz signal.

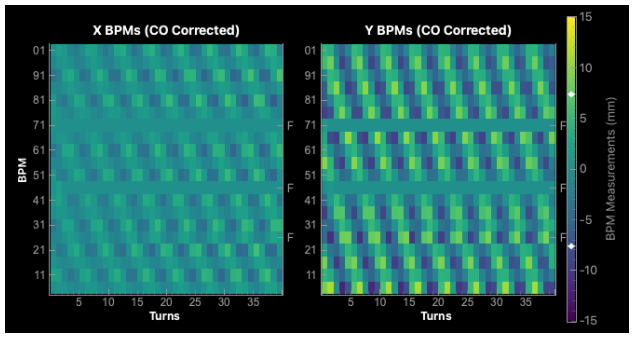


Figure 1: BPM measurements with closed-orbit corrections applied for all 20 BPMs over 40 turns.

To obtain the betatron tunes, x & y data from each BPM are fitted into a simple cosine function:

$$x_i(n) = A_i \cdot \cos\left(2\pi\nu_{x,i}n + \phi_{x,i}\right) + c_{x,i},$$

where i is the BPM number, A_i is the betatron oscillation amplitude, $\nu_{x,i}$ is the betatron tune measured at this BPM

ISBN: 978-3-95450-261-5 ISSN: 2673-7000 doi: 10.18429/JACoW-NAPAC2025-MOP066

ONLINE MULTI-OBJECTIVE BAYESIAN OPTIMIZATION OF INJECTION EFFICIENCY AND BEAM LIFETIME WITH SKEW QUADRUPOLES AT NSLS-II*

Y. Hidaka†, G. M. Wang, Y. Li, Brookhaven National Laboratory, Upton, NY, USA
N. Kuklev, L. Emery, Advanced Photon Source, Argonne National Laboratory, Lemont, IL, USA
R. Roussel, A. Edelen, SLAC National Accelerator Laboratory, Menlo Park, CA, USA

Abstract

At NSLS-II, the vertical emittance of electron beam is typically blown up to ~30 pm with a coupling wave to increase beam lifetime during user operation. As more and more insertion devices are added to the storage ring, injection efficiency to the ring drops noticeably in certain machine states, apparently due to degraded dynamic apertures. To help alleviate this issue, we have recently performed online multi-objective Bayesian optimization to increase injection efficiency while maintaining beam lifetime, by adjusting the strengths of 15 skew quadrupoles in non-dispersive sections. We report the results of this optimization effort.

INTRODUCTION

At storage rings like NSLS-II, it is common practice to increase the vertical beam size during beamline user operations to extend the beam lifetime. This mode of operation reduces the frequency of injections needed to maintain a constant beam current in the ring. The main benefits are threefold. First, it minimizes transient orbit disturbances during injections, enhancing orbit stability and enabling high-quality beamline experiments. Second, a longer beam lifetime results in reduced radiation from beam loss. Third, it decreases the load on injection-related equipment, thereby extending the equipment's operational lifespan.

The vertical beam size scales approximately with the square root of the vertical emittance. The two primary sources of vertical emittance are betatron coupling and vertical dispersion [1]. NSLS-II initially used coupling to increase vertical emittance. A coupling wave was introduced into the lattice by powering skew quadrupoles in non-dispersive sections of the ring, which typically raised the vertical emittance to about 30 pm. This method was effective in increasing the beam lifetime, but occasionally reduced injection efficiency, most likely because the large initial horizontal offset from off-axis injection was converted into large vertical oscillations, leading to beam loss at the small apertures of insertion devices (IDs).

To mitigate this issue, a vertical dispersion wave was employed to increase the vertical emittance. This approach has been shown to have a smaller impact on injection efficiency as well as beam lifetime (via the momentum aperture) compared to the coupling method, since it does not significantly affect the vertical oscillations of the injected beam [2, 3]. However, it was later discovered that, in this mode, the horizontally focused X-ray beam at the secondary source of beamline 17-ID-2 became rotated.

The resulting increase in the width of the projected beam at the sample position led to a loss of spatial resolution in certain beamline experiments for macromolecular crystallography, such as data collection from the smallest crystals and highly inhomogeneous crystals [4]. This issue forced us to revert to the coupling wave mode. Since then, we have been seeking ways to improve injection efficiency in this mode.

MULTI-OBJECTIVE BAYESIAN OPTIMIZATION

We recently conducted online multi-objective Bayesian optimization (MOBO) [5] to optimize the harmonic sextupoles at NSLS-II, using the Python package `apsopt` developed by APS-U [6, 7]. The goal was to maximize both injection efficiency and beam lifetime by adjusting the strengths of up to 23 harmonic sextupoles in the ring. This effort resulted in a significant improvement in both metrics within just 50 iterations.

Building on this success, we applied the same optimization technique to address the injection efficiency issue associated with the coupling wave currently used in operation, which had been arbitrarily chosen and never optimized, either online or offline, to reduce its adverse impact on nonlinear beam dynamics. The aim was to improve this wave by maintaining high injection efficiency while preserving, or potentially enhancing, beam lifetime by tuning the strengths of 15 skew quadrupoles (SQH family) located in the non-dispersive sections of the ring.

EXPERIMENTAL SETUP

All the IDs in the storage ring were set to their nominal operation gaps, except for all the in-vacuum undulators, which were set to their minimum gaps to represent the worst case scenario. The linear optics and coupling of the ring were then corrected, resulting in a vertical emittance of approximately 10 pm, as measured by an X-ray pinhole camera. The maximum power supply current limits for the skew quadrupoles are ±18 A, but some of this range is reserved for minimizing

* Work supported by U.S. DOE, Office of Science, Office of Basic Energy Sciences, under DOE Contract No. DE-AC02-76SF00515.
This information is controlled by the U.S. Department of Commerce Export Administration Regulations 15 CFR Parts 730-774 as EAR99 Technology.
† yhidaka@bnl.gov

Content from this work may be used under the terms of the CC BY 4.0 licence (© 2022). Any distribution of this work must maintain attribution to the author(s), title of the work, publisher, and DOI.

ISBN: 978-3-95450-261-5 ISSN: 2673-7000 doi: 10.18429/JACoW-NAPAC2025-MOP068

OSCILLATION DATA ANALYSIS DURING THE LCLS-II COMMISSIONING AT SLAC*

F.-J. Decker†, SLAC National Accelerator Laboratory, Menlo Park, CA, USA

Abstract

Analyzing the betatron oscillation of a beam is mainly used to find focusing errors in the lattice, like quadrupole errors. The generated trajectory differences can be compared with the design lattice or the current machine lattice where some magnets have been changed for different purposes or accidentally. Each method has different advantages and disadvantages like finding a quadrupole which got turned off by mistake won't be discovered with the current lattice method, while matching quadrupoles errors (which get tuned away from design) are harder to identify with the design lattice comparison. Besides lattice errors BPM (Beam Position Monitor) problems can be found too. Interpreting the data can have many pitfalls, some will be explained.

INTRODUCTION

Data Taking

The data taking is done by changing corrector magnets early in the beam path for a transverse trajectory in *x* and *y*, and RF (Radio Frequency) amplitude and phase for a longitudinal change, e.g. an energy *E* change. All BPMs (Beam Position Monitors) are recorded for a few (5) different settings. Since the phase advance between two correctors might be too small (or too close to a 180° phase advance) three *x* and three *y* correctors are used together with two energy changes generating a data set of 40 orbits (or trajectories to be correct) with around 175 BPMs taking about 3 minutes.

Data Analysis

To get the best signal to noise the difference orbit of the first and fifth corrector setting should be analysed. When there was any beam loss (or gain) involved, the data might be compromised near the loss area. This can be mitigated by choosing for instance the second and fifth corrector setting difference orbit. The raw difference orbits are often a good start to look for problems but are also often "messy" with coupled *x* and *y* behaviour. With good data five different orbits can be orthogonalized then at any chosen downstream location where there is only ONE of the five parameters (*x, x', y, y', E*) not equal to zero. There is no need for getting additional data further downstream. Figure 1 shows the orbit difference for the third parameter (Sample 3) for *y* being non-zero at the BPM # 110. From the corresponding *y*-kick θ a quadrupole error ΔQ is calculated via:

$$\theta = \frac{0.03}{E} \cdot \Delta Q \cdot y$$

with the energy *E* in GeV and the BPM *y*.

*Work supported by U.S. Department of Energy, Contract DE-AC02-76SF00515.

† Decker@SLAC.Stanford.edu

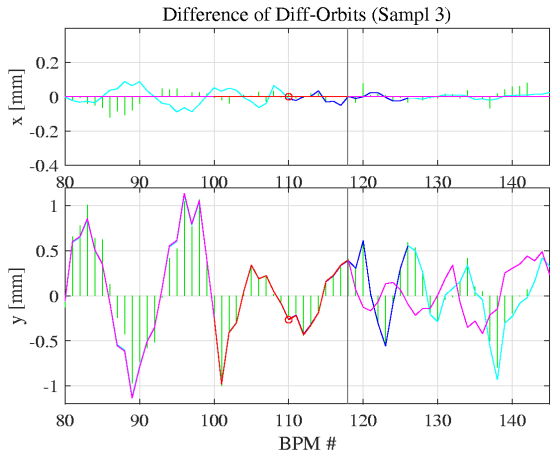


Figure 1: The data show the measured beam oscillations in green bars. It is a combination of a few orbits so there is only a y-offset at BPM # 110. In red is a fit which then extrapolates as magenta. Since it deviates near BPM # 118 (vertical line) a second fit including a kick at the nearest quadrupole is fitted in blue and extrapolated in cyan.

The quadrupole error was -66% of the quadrupole value making it three times weaker. The root cause was that the current transducer was configured for 300 A instead of 100 A.

IDENTIFYING PROBLEMS

More than ten problems were identified via this analysis, but often it was not as clear as in the case above. We go from the strong easy cases to the more complicated ones and discuss the signatures of the problems.

Easy Problems

The easiest were two -200% problems where the quadrupoles had just the wrong polarity. Then it looked we were down to 20% to 40% problems but suddenly two -100% cases occurred where a quadrupole was just off. One was where a quadrupole tripped before midnight, and the next crew saved a "SCORE" configuration which saves the current setup which then can be restored in the future. It stayed in there for about two months. Similar smaller variations are often not easily detected. The second one should have been found even quicker. The BDES (desired magnetic field *B*) had the right value, but the power supply was tripped and did not turn red indicating a wrong state.

Medium Problems

The 20% to 40% problems were in a location where we adjust quadrupoles to measure and match the beam's alpha and beta functions to the design lattice values. The same strong quadrupoles which are used for a 1500 MeV beam are also used where the beam energy is only 75 MeV or 20-

Content from this work may be used under the terms of the CC BY 4.0 licence (© 2022). Any distribution of this work must maintain attribution to the author(s), title of the work, publisher, and DOI.

ISBN: 978-3-95450-261-5 ISSN: 2673-7000 doi: 10.18429/JACoW-NAPAC2025-MOP069

NEW ACE3P CAPABILITIES AND CODE INTEGRATION OF ACE3P WITH GEANT4 AND LUME

D. Bizzozero†, L. Fowler, L. Ge, Z. Li, C.-K. Ng, M. Othman, S. Ramirez, H. Saleh, L. Xiao
SLAC National Accelerator Laboratory, Menlo Park, CA, USA

Abstract

The Advanced Computational Electromagnetic 3D Parallel simulation suite (ACE3P), developed by SLAC National Accelerator Laboratory, is a state-of-the-art multi-physics toolkit designed for virtual prototyping of accelerator and RF components. Leveraging over two decades of development, ACE3P integrates advanced physics modeling, including thermal and structural modelling, capabilities with scalable numerical algorithms to deliver cutting-edge simulations. The suite, comprised of seven application modules, utilizes high-order curved finite element methods to achieve high accuracy while enabling fast simulations for large-scale problems.

Two recent advancements include the integration with Geant4, for radiation studies and positron source generation, and the development of LUME-ACE3P, built on the Python framework of the LUME project, which streamlines parameter sweeps and optimization tasks. Furthermore, other code developments are presented here including more LUME-ACE3P functionality, dispersive material applications, and dynamic mode decomposition analysis.

INTRODUCTION

The multi-physics software toolkit Advanced Computational Electromagnetic 3D Parallel (ACE3P) has been developed at SLAC and has seen numerous improvements and added features over many years [1]. A recent ACE3P code workshop hosted at SLAC has noted an increasing interest in robust and efficient electromagnetic (EM) computations on HPC resources, especially for workflow management and code integration [2]. A brief list and overview of the various ACE3P code modules is given here:

- Omega3P – frequency-domain eigenmode solver
- S3P – frequency-domain S-parameter solver
- T3P – time-domain transient and wakefield solver
- Track3P – particle trajectory solver for multipacting
- Pic3P – particle-in-cell beam and space charge solver
- TEM3P – EM, thermal, and mechanical solver
- Gun3P – electrostatic field solver for DC guns

In this paper we will summarize various code integration efforts and new capabilities of the ACE3P code suite. We present an overview of recent efforts in code-integration of Geant4 with ACE3P for the study of dark currents [3] and a new python-based workflow based on the Lightsource Unified Modeling Environment (LUME) [4].

ACE3P-GEANT4 INTEGRATION

The particle and radiation transport code Geant4 enables the calculation of radiation dosage collected externally to accelerator components. This code integration was recently used to provide valuable insight into dark current radiation studies for a 56-cell accelerator structure at KEK [3]. An overview of the code workflow setup (Fig. 1) and results of the full integrated study are shown (Fig. 2).

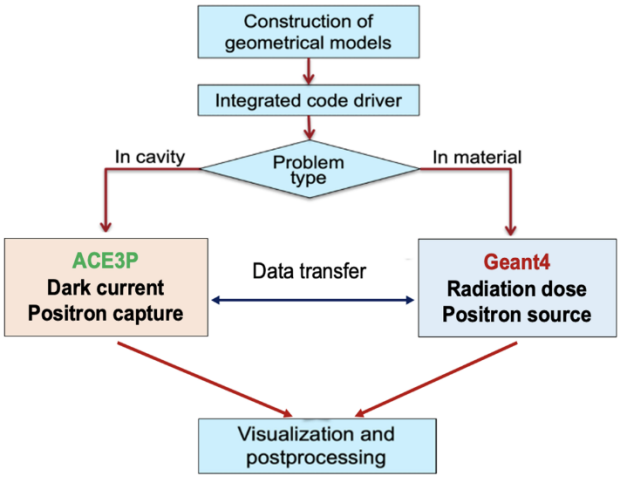


Figure 1: ACE3P-Geant4 code integration overview.

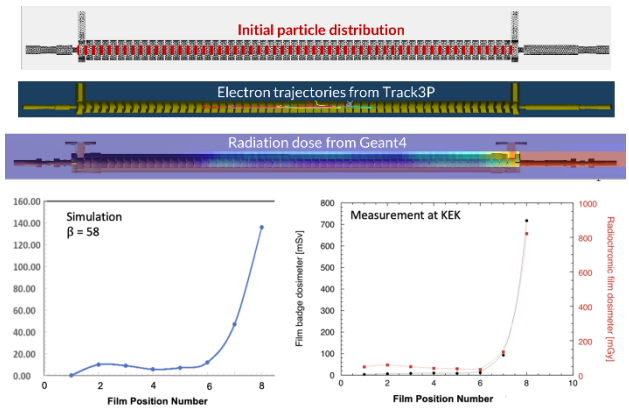


Figure 2: (Top) initial particle distribution, Track3P electron trajectories, and radiation pattern from Geant4. (Bottom) comparison of simulated radiation dose by monitor location and actual measurements taken from the monitors placed around the structure.

† dbizzoze@slac.stanford.edu

Content from this work may be used under the terms of the CC BY 4.0 licence (© 2022). Any distribution of this work must maintain attribution to the author(s), title of the work, publisher, and DOI.

ISBN: 978-3-95450-261-5 ISSN: 2673-7000 doi: 10.18429/JACoW-NAPAC2025-MOP070

PERFORMANCE OPTIMIZATION OF THE IOTA DUOPLASMATRON PROTON SOURCE

N. Banerjee*, D. Edstrom Jr., A. Romanov, M. Wallbank, Fermilab, Batavia, IL, USA
B. Simons, Northern Illinois University, DeKalb, IL, USA

Content from this work may be used under the terms of the CC BY 4.0 licence (© 2022). Any distribution of this work must maintain attribution to the author(s), title of the work, publisher, and DOI.

Abstract

We present results from online optimization studies of a duoplasmatron ion source designed to produce 50 keV protons for acceleration to 2.5 MeV and subsequent injection into the Integrable Optics Test Accelerator (IOTA) at Fermilab. Using a Bayesian exploration technique, we developed multi-parameter models of the source's proton current and employed these models to optimize its performance. Depending on the spectrometer configuration used to isolate the proton beam and the chosen optimization objective, we identified three candidate operating points, achieving normalized 50% emittances between 0.57 and 1.3 μm and a maximum proton current of 14.5 ± 0.6 mA.

INTRODUCTION

The Integrable Optics Test Accelerator (IOTA) [1] at Fermilab is transitioning to operations with 2.5 MeV protons in its upcoming run, with the goal of studying beam dynamics in the presence of intense space-charge [2–4] and a controlled impedance environment [5]. To support this, we are commissioning a new injector beamline [6] capable of producing proton beams with currents up to 8 mA, normalized rms transverse emittances of 0.3 – 0.5 μm, and a relative momentum spread of ~ 10^{-3}. Protons are extracted from a duoplasmatron source [7] at 50 keV, accelerated to 2.5 MeV using a 325 MHz normal-conducting Radio Frequency Quadrupole (RFQ) [8], and finally matched into IOTA for single-turn injection. This paper outlines the commissioning and optimization studies of the proton source aimed at achieving the injector's design requirements.

The duoplasmatron source, shown in Fig. 1, is a DC ion source in which hydrogen gas is ionized by a plasma discharge, and the resulting ions are extracted through a pinhole using an electrostatic field. The production of H^+, $H_2{}^+$, and $H_3{}^+$ ions in the plasma cup is driven by impact ionization of neutral hydrogen [9] by hot electrons, which are generated via thermionic emission from a specially coated tungsten filament. The electrons' mean free path and velocity distribution determine the resulting ion species populations. An external magnetic field, aligned with the direction of ion extraction, enhances ion production rates by confining the hot electrons through cyclotron motion. An extractor electrode held at an intermediate potential between ground and the anode is used to extract and focus the ion beam expelled from the pinhole. Because plasma generation in the duoplasmatron produces substantial heat, both the arc discharge and ion extraction are operated in short voltage pulses at a low duty cycle. Table 1 lists the relevant operating parameters of the source along with their acceptable ranges. To optimize proton production, while maintaining control over the beam's transverse phase space and temporal stability, we adjust the hydrogen pressure P_{H_2}, magnetic flux density (via I_{sol}), plasma arc current I_{arc}, and extractor potential.

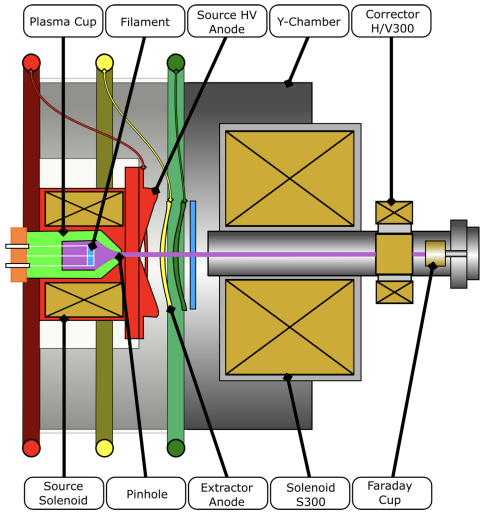


Figure 1: Schematic diagram of the duoplasmatron. The optimization knobs are hydrogen pressure, magnetic field created by the source solenoid, and current driven through the arc discharge inside the plasma cup.

Table 1: Parameter ranges of the IOTA duoplasmatron. The last three parameters are subject to optimization.

Parameter	Nominal	Range	Unit
Anode voltage	50	0 – 50	kV
Filament current	20.5	18 – 22	A
Repetition rate	1	—	Hz
Arc pulse length	80	—	μs
Extractor pulse delay	40	—	μs
Extractor pulse length	40	—	μs
Extractor voltage	10	0 – 10	kV
H_2 pressure (P_{H_2})	—	60 – 250	mTorr
Solenoid current (I_{sol})	—	0.8 – 1.2	A
Arc current (I_{arc})	—	4 – 12	A

In the next section, we describe the spectrometer beamline used to isolate 50 keV protons from the source and present results from a Bayesian exploration of beam current and jitter. We then measure the vertical phase-space

* nilanjan@fnal.gov

ISBN: 978-3-95450-261-5 ISSN: 2673-7000 doi: 10.18429/JACoW-NAPAC2025-MOP072

TRANSVERSE PHASE SPACE TOMOGRAPHY AT FACET-II

Yiheng Ye*, Spencer Gessner, SLAC National Accelerator Laboratory, Menlo Park, CA, USA

Content from this work may be used under the terms of the CC BY 4.0 licence (© 2022). Any distribution of this work must maintain attribution to the author(s), title of the work, publisher, and DOI.

Abstract

We present transverse phase space tomographic reconstruction of the two-bunch configuration at FACET-II. We demonstrate diagnosing two superimposed electron bunches with different transverse phase spaces using a single quadrupole scan. Tuning the bunch charge revealed unexpected space-charge-dominated dynamics.

INTRODUCTION

Emittance characterizes beam quality in accelerators and is typically measured via quadrupole scans: we scan a quadrupole magnet upstream and record beam sizes on a downstream screen, then quadratically fit beam sizes versus quadrupole strength to extract transverse emittance ϵ and Twiss parameters α, β, and γ (see e.g. [1]). This method assumes gaussian beam profiles, which often don't reflect actual operating conditions. With non-gaussian beams, this measurement technique may be inaccurate and provide minimal insights for accelerator tuning.

Transverse phase space reconstruction at FACET-II is based on tomography [2]: reconstructing n-dimensional objects from $(n-1)$-dimensional projections at different angles. In quadrupole scans, the $x(y)$-profile at the screen represents a projection of $x(y)$-phase space at a specific angle for each quadrupole setting. We use detailed screen profiles from quadrupole scans to reconstruct the complete transverse beam phase space.

The two-bunch mode at FACET-II is used to generate drive and trailing bunches for plasma wakefield experiments [3]. The injector laser is split into double pulses to generate driver-witness electron bunch pairs, which are then co-accelerated through the linac in the same rf bucket. In nominal operating mode, the driver-to-witness bunch charge ratio is 3:1 with a time separation of around 7 ps. Both the bunch charge and the time separation can be tuned to satisfy the needs of different experiments. The transverse phase spaces of the two bunches overlap, but are not identical. The combined two-bunch phase space is generally non-gaussian.

We have implemented tomographic measurements in the FACET-II injector in order to characterize the two-bunch phase space. Our implementation is based on references [4–6]. We scanned the bunch charge ratio to observe transverse space-charge dynamics in the injector and tuned the bunch separation to observe effects of bunch generation in different rf phases. Our experimental observations diverge from simulation results, indicating that follow-up studies will be required.

* yihengy@slac.stanford.edu

TRANSVERSE PHASE SPACE TOMOGRAPHY

Transverse tomography is carried out in FACET-II's injector beamline, using a quadruple and screen separated by 2.7 m as shown in Fig. 1. Given a quadruple strength k and the drift length d, we can calculate the transfer matrix $M(k)$ between the quadruple and the screen. The coordinates of an electron in the $x(y)$ phase space are given by

$$\begin{pmatrix} x_{\text{screen}} \\ x'_{\text{screen}} \end{pmatrix} = \begin{pmatrix} M_{1,1}(k) & M_{1,2}(k) \\ M_{2,1}(k) & M_{2,2}(k) \end{pmatrix} \begin{pmatrix} x_{\text{quad}} \\ x'_{\text{quad}} \end{pmatrix}. \quad (1)$$

The quadruple magnet both rotates and shears the phase space of the beam, such that in each plane the projection of the image on the screen is the projection of the phase space at angle θ, scaled by a factor of s, where θ and s are given by

$$\theta = \tan^{-1}\left(\frac{M_{1,1}(k)}{M_{1,2}(k)}\right),\ s = \sqrt{M_{1,1}^2(k) + M_{1,2}^2(k)}. \quad (2)$$

Projections of the beam image at the screen are stacked together to form a sinogram. Then it is rescaled and labeled according to Eq. (2). We reconstruct the phase space using Maximum Likelihood Expectation Maximization (MLEM) algorithm [7].

TWO BUNCH CONFIGURATION

In the two-bunch configuration, the default quad scan that fits scalar beam sizes provides limited information on the transverse phase space. The drive bunch and the witness bunch are co-accelerated in the same rf bucket at different rf phases determined by their separation in time. They may have different Twiss parameters at a given location because of the energy difference between the two bunches.

The nominal two bunch configuration for the plasma wakefield acceleration (PWFA) experiment consist of a 1.6 nC drive bunch and a 0.5 nC witness bunch. We did a quadruple scan in the injector to analyze the transverse phase space. Figure 2 (left) shows the tomographically reconstructed transverse phase spaces of the nominal two-bunch setting in the injector. We observe an X-shaped pattern in the horizontal phase space, which we interpret as the superposition of the two horizontal phases spaces of the individual bunches. This is confirmed by characterizing each bunch individually.

We set the laser pulse separation to 0 and observe the effect of bunch charges. Figure 2 (right) shows the "two bunch", "witness", and "drive" phase spaces. In this case, the "two bunch" is a single bunch with 2.1 nC of charge, while "witness" and "drive" bunch are approximately the same with equal phase and charge. In both plane, phase spaces are stretched out in the spatial direction. We can see

ISBN: 978-3-95450-261-5 ISSN: 2673-7000 doi: 10.18429/JACoW-NAPAC2025-MOP073

PHYSICS CONSIDERATIONS FOR A HARP SYSTEM DESIGN AT THE SECOND TARGET STATION OF THE SPALLATION NEUTRON SOURCE *

Y. Lee†, Oak Ridge National Laboratory, Oak Ridge, TN, USA

Abstract

A harp system is being developed for monitoring proton beam profile direct upstream of the proton beam window at the Second Target Station of the Spallation Neutron Source, Oak Ridge National Laboratory. It consists of two sensor planes which have arrays of thin conducting wires aligned vertically and horizontally, respectively. It monitors beam profiles in two transverse directions to the beam axis by measuring the net-charge depositions in the sensor wires, which are caused by ejection of secondary electrons and delta rays driven by electromagnetic interactions with high-energy protons. The net charge deposition in a sensing wire linearly correlates with the number of incident protons on it. This correlation is perturbed when the wire interacts with secondary electrons and delta rays originating from beam-matter interactions in neighboring wires, PBW and residual gases. In this paper, we analyze the physical phenomena that affects the measurement uncertainties of the harp using particle transport simulations.

INTRODUCTION

The target of the Second Target Station (STS) at the Spallation Neutron Source (SNS) of the Oak Ridge National Laboratory (ORNL) will receive 1.3 GeV protons at 700 kW beam power. The beam profile on the target has a super-Gaussian shape with sharp shoulders and > 90% of the protons will hit the rectangular area spanned by $\Delta x = 128$ mm and $\Delta y = 48$ mm. The thermo-mechanical stresses in the target affecting its operability is correlated with the peak current density. As higher beam current density could cause a premature failure of the target, it is important to have a capability of monitoring the beam profile on the target during operation.

The harp wires capture beam profile measuring the charge imbalance in each conductive wire that is caused by proton induced secondary and delta-ray electron emissions. However, it does not provide information about the momentum distribution of protons when they pass through the harp wires. Therefore, it is advantageous to place the harp system as close as possible to the target as the ratio of beam footprints on the target to that on the harp is close to unity. Close to the target, there are two locations where a harp system can be installed. The first is at the target viewing periscope (TVP) end port which is 105 cm upstream from the target and the other is 20 cm upstream from the proton beam window (PBW) which is 2.6 meters upstream from the target. The TVP port is inside the target core vessel which has either a 133 Pa rough vacuum or a slightly sub-atmospheric pressure helium. The upstream region of the PBW is in accelerator vacuum at an estimated pressure of maximum $6.12 \cdot 10^{-5}$ Pa.

At the TVP end-port location, the harp signal will be disturbed by secondary and delta ray electrons from the PBW, target, neighboring wires and discharge of the core vessel gases. Also, the positive ions from gas discharge will affect the harp signal. At the PBW location, the beam current signal of a harp system will be disturbed by secondary and delta electrons from the PBW, and neighboring wires. In this paper, we study the physics that contribute to anomalous harp signal readings.

ELECTRON EMISSIONS

The net-charge deposition in a harp wire is caused by emissions of secondary and delta-ray electrons due to incident protons. The emitted secondary electrons (SE) per proton, η_{SE} is described by Sternglass theory presented in Ref. [1],

$$\eta_{\mathrm{SE}} = \frac{P \cdot \delta_s}{E_i} \frac{dE}{dz}. \quad (1)$$

Here, $P = 0.5$ is the probability of an electron escaping, $\delta_s = 1$ nm is the average depth from which the secondaries arise, and $E_i = 25$ eV is the average kinetic energy lost by the incoming particle per ionization. Finally, dE/dz is the differential proton stopping power of the wire which depend on proton energy, which can be calculated by the Bethe-Bloch formula. Tungsten and silicon carbide (SiC) are considered for wire materials. For a 1.3 GeV proton beam at STS, the calculated dE/dz for tungsten and silicon carbide is given by 22.98 MeV·cm^{-1} and 5.44 MeV·cm^{-1} respectively. The calculated SE yields per proton η_{SE} in tungsten and SiC wires are summarized in Table 1.

To calculate the delta-ray electron (DE) yields in tungsten and SiC wires, particle transport simulations have been performed for a single wire with a diameter of 0.1 mm using FLUKA [2–4]. A rectangular shaped 1.3 GeV beam with a beam footprint defined by $\Delta x = \Delta y = 0.1$ mm was used. The calculated DE yields per proton η_δ in tungsten and SiC wires are summarized in Table 1. The net-charge deposition in the tungsten wire is higher than that in the SiC wire. This indicates that the signal strength from the tungsten wires is higher than SiC for the same beam intensity. On the other hand, tungsten has higher scattering cross section than SiC for a 1.3 Gev proton, which could lead to a higher beam loss

* Notice: This manuscript has been authored by UT-Battelle, LLC, under contract DE-AC05-00OR22725 with the US Department of Energy (DOE). The US government retains and the publisher, by accepting the article for publication, acknowledges that the US government retains a nonexclusive, paid-up, irrevocable, worldwide license to publish or reproduce the published form of this manuscript, or allow others to do so, for US government purposes. DOE will provide public access to these results of federally sponsored research in accordance with the DOE Public Access Plan (https://www.energy.gov/doe-public-access-plan).

† leey1@ornl.gov

Content from this work may be used under the terms of the CC BY 4.0 licence (© 2022). Any distribution of this work must maintain attribution to the author(s), title of the work, publisher, and DOI.

ISBN: 978-3-95450-261-5 ISSN: 2673-7000 doi: 10.18429/JACoW-NAPAC2025-MOP075

DETECTORS AND BEAM MONITORS BASED ON WIDE BANDGAP SEMICONDUCTORS AT CRYOGENIC TEMPERATURES*

S. V. Kuzikov†, Thomas Jefferson National Accelerator Facility, Newport News, VA, USA
G. Burrows, University of Kentucky, Lexington, KY, USA

Abstract

Wide-bandgap semiconductors, such as single-crystal diamond and sapphire, can be used to measure the flux of passing particles through a particle-induced conductivity effect. We recently demonstrated a diamond-based, electrodeless electron beam halo monitor. This monitor utilized a thin diamond blade placed within an open, high-quality microwave resonator. The blade partially intercepted the beam and changes in the RF properties of the resonator were used to infer beam parameters. To enhance the sensitivity of our semiconductor sensors, we propose two new techniques: (1) biasing the semiconductor sensor to support avalanche multiplication of free carriers, and (2) operating at cryogenic temperatures to reduce intrinsic semiconductor losses and increase the mobility of induced carriers. These techniques are applicable not only to particle beam diagnostics but also to the detection of various types of ionizing radiation.

INTRODUCTION

Wide-bandgap semiconductors, such as diamond and sapphire, can transit from dielectric to "metallic" states through photo- or beam-induced conductivity. When high-energy photons or beam particles strike the semiconductor, they generate secondary charge carriers (electrons and holes) in the conduction band, increasing the overall conductivity of the crystal. This phenomenon allows the measurement of primary photon or particle beam fluxes by detecting changes in the semiconductor's conductivity.

The proposed method involves placing a semiconductor sample inside an open, high-quality, critically coupled RF resonator, which is highly sensitive to changes in inserted losses (Fig. 1). Variations in the resonator's reflection coefficient—quantified by the S_{11} parameter—can be precisely measured.

The described principle was successfully implemented by Euclid Techlabs under a DoE SBIR grant [1–4]. Experiments conducted at Argonne Wakefield Accelerator (AWA) using a diamond beam halo monitor demonstrated greater sensitivity than traditional YAG screens and enabled two-dimensional mapping of the beam density distribution. By employing a novel nonlinear response processing method and multi-pixel beam image reconstruction, high space resolution was also achieved [4].

Additionally, an avalanche effect—previously observed in classical diamond sensors [4]—was discovered in this RF-based technology, significantly enhancing sensitivity. In this process, free carriers induced in diamond drift under a DC bias electric field and, through collisions, generate new secondary carriers. This chain reaction (or avalanche) results in a much higher concentration of carriers compared to the unbiased case, increasing detector sensitivity by up to two orders of magnitude.

A key advantage of this technique lies in the high-quality factor (Q-factor) of the RF resonator containing the semiconductor. For the best single-crystal diamond samples at room temperature, the loss tangent (10^{-3} to 10^{-4}) limits the Q-factor of the RF cavity. To overcome this limitation, we propose using an RF resonator incorporating a diamond or sapphire element cooled to cryogenic temperatures, which can increase detection sensitivity by several orders of magnitude.

RF MESUREMENT TECNIQUE

When exposed to beam particles or high-energy photons, the dielectric permittivity of wide bandgap semiconductors increases significantly in the imaginary component, indicating heightened conductivity due to the generation of secondary charge carriers:

$$\varepsilon = \varepsilon' + i\varepsilon' tan\delta + i\frac{4\pi\sigma}{\omega}, \quad (1)$$

where ε' is real part of permittivity, $tan\delta$ is loss tangent, ω is RF frequency, and σ is crystal conductivity induced by primary particles. The dielectric response of a semiconductor can be described by this complex permittivity consisting of three components. The first term corresponds to the real part of the dielectric constant, which is approximately 5.7 for diamond and 9.4 for sapphire. The second term represents the imaginary part, or the material's natural loss tangent, which varies with both frequency and temperature. The third term accounts for beam- or photon-induced conductivity and is proportional to the density of free secondary charge carriers (electrons and holes), denoted as N_e:

$$\sigma = eN_e(\mu_e + \mu_h). \quad (2)$$

Here, μ_e and μ_h represent the mobilities of electrons and holes in the conduction band, respectively. The induced free carrier density, N_e, is proportional to the density of the incident primary particles but also depends on their energy and depth of penetration into the material.

At cryogenic temperatures, both diamond and sapphire exhibit exceptional performance characteristics. Diamond possesses extraordinarily high mobilities for free carriers. At 10 K, the electron mobility in diamond reaches approximately 1×10^6 $cm^2V^{-1}\cdot s^{-1}$—three orders of magnitude higher than at room temperature (300 K) [5]. This enhanced mobility enables much higher induced conductivity at temperatures 70 K and below, and thus, significantly improved sensitivity to primary particle exposure (Fig. 2). In

*This material was supported by the U.S. Department of Energy, Office of Science, Office of Nuclear Physics (contract DE-AC05-06OR23177).
† kuzikov@jlab.org

Content from this work may be used under the terms of the CC BY 4.0 licence (© 2022). Any distribution of this work must maintain attribution to the author(s), title of the work, publisher, and DOI.

ISBN: 978-3-95450-261-5 ISSN: 2673-7000 doi: 10.18429/JACoW-NAPAC2025-MOP076

PRELIMINARY STUDY OF AUTO-DIFFERENTIATION ALGORITHM IN BEAM DYNAMICS WITH STOCHASTIC PROCESS*

C. T. Ratcliff†, Y. Hao, Facility for Rare Isotope Beams, East Lansing, MI, USA

Abstract

Modern particle accelerator optimization requires sophisticated computational methods to address the inherently stochastic nature of beam dynamics. This research develops a framework that applies AD to stochastic differential equations that specifically addresses beam dynamics challenges in particle accelerators, focusing on accurately modeling and optimizing beam behavior in regimes dominated by stochastic processes. By incorporating key physical phenomena such as synchrotron radiation, wakefield effects, and quantum excitation, the framework aims to provide auto-differentiation on the figure of merit of the phase space evolution and beam dynamics. The methodology will enable an effective optimization method in a dynamic system with stochastic process.

INTRODUCTION

Optimizing particle accelerator performance in the presence of stochastic processes—such as synchrotron radiation, intra-beam scattering, or other random effects—can be particularly challenging [1]. The system's equilibrium behavior is typically determined through complex simulations, which often yield only the expected value of the stochastic process. When gradients are estimated using finite differences across multiple simulations, the resulting derivatives tend to exhibit high variance, making optimization less efficient and less reliable.

Automatic differentiation (AD) has emerged as a powerful tool for optimization in machine learning and scientific computing [2]. However, extending AD to stochastic differential equations (SDEs) presents challenges. Advances in stochastic AD, particularly the development of stochastic triple methods, offer new possibilities for efficient gradient computation in stochastic systems [3].

This work presents a study of applying stochastic AD algorithms to beam dynamics simulations in electron storage rings. The approach uses longitudinal dynamics with synchrotron radiation damping and excitation as a benchmark to validate the accuracy of gradient computations in a controlled setting where analytical solutions provide ground truth comparisons [4].

STOCHASTIC TRIPLE METHODOLOGY

For a stochastic program $X(p)$ with parameter p, a stochastic triple takes the form:

$$\text{stochastic triple} = v + d \cdot \varepsilon + (j \text{ with probability } w \cdot \varepsilon) \quad (1)$$

where v represents the primal value, d is the dual component analogous to traditional automatic differentiation, j captures the jump value for discrete transitions, and w denotes the jump probability weight. The parameter ε represents an infinitesimal perturbation.

The derivative of the expected value is computed through the relationship:

$$\frac{dE[X(p)]}{dp} = E[\delta + w(Y - X(p))], \quad (2)$$

where δ represents the deterministic derivative component, w is the weight factor, and Y captures finite perturbations with infinitesimal probabilities.

This methodology handles both discrete random variables such as Bernoulli and binomial distributions and continuous distributions within a unified framework, accounting for jump processes common in accelerator physics simulations including quantum excitation events and discrete radiation emission processes. Unlike conventional automatic differentiation, stochastic triples can propagate derivative information through non-differentiable stochastic operations while preserving statistical properties of the underlying random processes. The primary advantage over finite difference methods lies in providing derivative information through single program execution rather than requiring multiple function evaluations, significantly reducing computational overhead while maintaining statistical rigor in derivative estimates.

A comparison between various stochastic triple methods and other derivative methods for a simple random walk with 100 steps can be seen in Fig. 1. It can be seen that, excluding the score function, all of them grow at similar rates, but the two stochastic triples have the least growth in the standard deviation of the derivative. The smoothed stochastic triple is a method that would not very applicable accelerator methodologies, but it is a potential draw of the package.

ELECTRON STORAGE RING SIMULATION

The validation framework employs an electron storage ring (ESR) configuration designed to achieve equilibrium distributions that approximate the Haissinski distribution [4]. This semi-analytical benchmark provides a test case for later validation of derivative accuracy because the equilibrium properties can be computed in a semi-theoretical method and compared against simulation results.

The simulation incorporates the physical processes governing electron beam evolution in storage rings [1]. RF cavity interactions provide longitudinal acceleration, while synchrotron radiation introduces both damping and quantum

* Work supported by the U.S. Department of Energy Office of Science under award number DE-SC0024170 and Cooperative Agreement DE-SC0023633, the State of Michigan, and Michigan State University.

† ratcliff@frib.msu.edu

Content from this work may be used under the terms of the CC BY 4.0 licence (© 2022). Any distribution of this work must maintain attribution to the author(s), title of the work, publisher, and DOI.

ISBN: 978-3-95450-261-5 ISSN: 2673-7000 doi: 10.18429/JACoW-NAPAC2025-MOP078

PROPOSAL TO MEASURE BUNCH LENGTHS USING A PULSE DILATION PHOTOMULTIPLIER TUBE*

K. P. Wootton†, Argonne National Laboratory, Lemont, IL, USA

Abstract

Electron bunches in storage rings are typically short (~100 ps) and separated by long periods of time (≥2 ns). A pulse dilation photomultiplier tube offers a new way of measuring high bandwidth optical pulses using low bandwidth oscilloscopes. Experiments performed by others have demonstrated a temporal resolution of 12 ps, meeting requirements for electron bunches expected for the Advanced Photon Source Upgrade. Compared to electrooptical streak cameras, we think that this may be a preferred technique for measuring the longitudinal profile of bunches in electron storage rings.

INTRODUCTION

Measurements of electron beam temporal profiles in storage rings are typically performed using streak cameras [1, 2]. We are interested in considering alternative techniques of measuring electron beam bunch length other than a streak camera. We have identified a novel diagnostic device that we feel could be usefully applied to measure bunch durations in electron storage rings: a Pulse Dilation Photo-Multiplier Tube (PD-PMT).

In the present work, we evaluate the PD-PMT for measurement of electron bunches in the APS-U storage ring. We introduce the properties of the PD-PMT, and its background of use for experiments at the National Ignition Facility (NIF). We summarise properties of the nominal APS-U electron bunch profile and storage ring fill patterns.

BACKGROUND

Photo-Multiplier Tubes (PMTs) have been used extensively to measure beams of synchrotron radiation [3–6]. PMTs are typically operated with a direct-current (DC) voltage between a photocathode and the first (and subsequent) dynodes. PMTs are available with fast time resolution, however the fastest tubes available have a time response ~100 ps [7].

But a time response on the order of ~100 ps is insufficient for measuring the temporal profile of electron bunches in the APS-U storage ring, with rms bunch lengths on the order of ~100 ps [8, 9]. Ordinarily, this temporal profile is measured by a streak camera [10, 11]. By way of example, a synchroscan streak image of the electron beam temporal profile in the APS-U storage ring is reproduced in Fig. 1.

In the special case of a PD-PMT, a long electron drift tube is positioned between the photocathode and the first dynode. By exciting the accelerating potential between the photocathode and dynode with an electrical pulse that falls in time, electrons departing the photocathode drift and are velocity-dispersed as they are accelerated towards the dynodes [16–19]. This is illustrated in Fig. 2 [19].

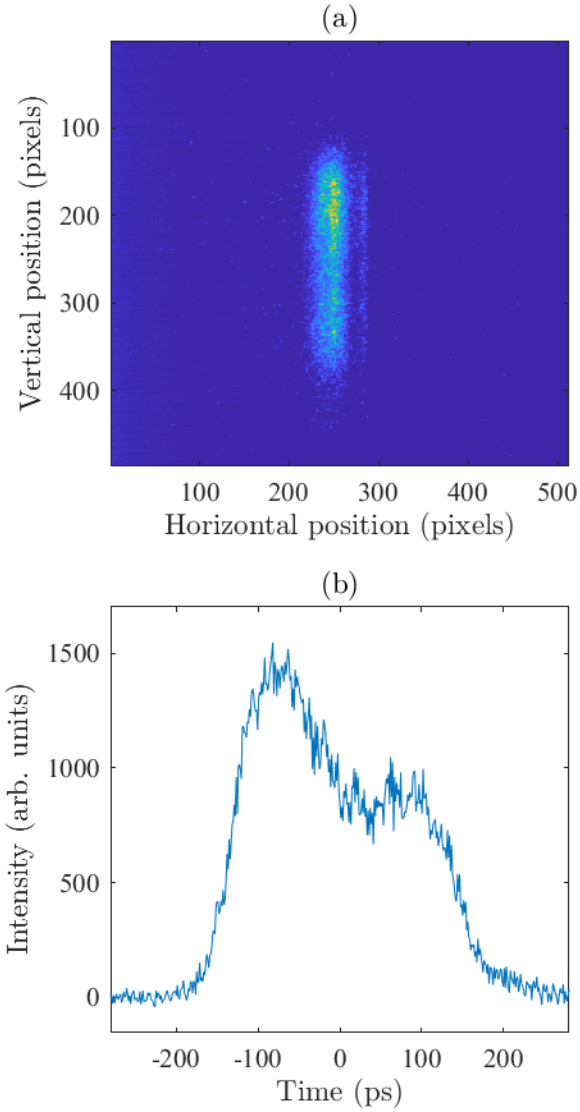


Figure 1: Measured electron beam temporal profile of bunches in the APS-U electron storage ring. A Hamamatsu C5680 dual sweep visible light streak camera was used at 35-BM beamline [12]. (a) Measured streak camera image. The beam was measured using a streak camera operating in synchroscan in the vertical direction, and unswept in the horizontal direction. The digitised image was acquired using a DataCube Max Video MV200 system [13–15]. (b) Measured temporal profile [projection of (a)].

* Work was supported by the U.S. DOE Office of Science-Basic Energy Sciences, under Contract No. DEAC02-06CH11357.

† kwootton@anl.gov

Content from this work may be used under the terms of the CC BY 4.0 licence (© 2022). Any distribution of this work must maintain attribution to the author(s), title of the work, publisher, and DOI.

ISBN: 978-3-95450-261-5 ISSN: 2673-7000 doi: 10.18429/JACoW-NAPAC2025-MOP079

PROPOSAL TO STREAK OPTICAL PULSES USING A SOLID STATE OPTICAL DEFLECTOR*

K. P. Wootton†, Argonne National Laboratory, Lemont, IL, USA
S. Lidia, T. Suzuki[1], Michigan State University, East Lansing, MI, USA
[1]also at Argonne National Laboratory, Lemont, IL, USA

Content from this work may be used under the terms of the CC BY 4.0 licence (© 2022). Any distribution of this work must maintain attribution to the author(s), title of the work, publisher, and DOI.

Abstract

Streak cameras are flexible cameras used to measure the temporal profile of optical pulses. Streak cameras have been employed to measure the longitudinal beam profile on accelerators around the world. In the present work, we highlight a potential alternative to a new streak camera. We consider particularly linear (Pockels) and quadratic (Kerr) electro-optical nonlinearity solid-state streaking systems. Of the possible solid state systems, we motivate the potential advantages of a potassium tantalum niobate ($KTa_{1-x}Nb_xO_3$) crystal as a photon beam deflector to measure the longitudinal profiles of electron beams in accelerators.

INTRODUCTION

We are interested in investigating alternatives to streak cameras for the measurement of electron beams in accelerators. Essentially, we were initially interested in the possibility of applying the rising or falling edge of a fast (~ns) voltage pulse to an electro-optical component such as a Pockels cell. This is illustrated schematically in Fig. 1. The falling edge would have the same effect: the important feature is that the gradient dV/dt is fast enough to streak bunches shorter than the time duration of the rising edge.

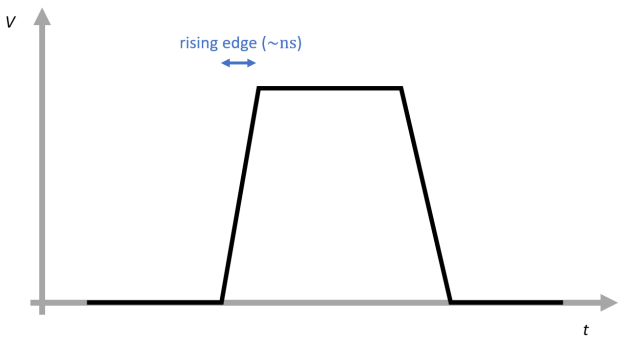


Figure 1: Schematic illustration of the rising edge of a fast (~ns) rising edge of a voltage pulse to streak a photon beam.

In the present work, we evaluate potential alternatives to a streak camera for the measurement of electron beam bunch length in particle accelerators. We consider particularly rotating mirror (mechanical) streaking systems, as well as linear (Pockels) and quadratic (Kerr) electro-optical nonlinearity solid-state streaking systems.

* Work was supported by the U.S. DOE Office of Science-Basic Energy Sciences, under Contract No. DEAC02-06CH11357.
† kwootton@anl.gov

EXISTING OPTICAL PULSE STREAKING TECHNIQUES

Rotating Mirror

Rotating mirrors have been employed to measure the temporal distribution of electron beams in storage rings [1]. It appears that rotating mirrors were the first (mechanical) streak cameras [2]. Rotating mirrors typically operate at a frequency rate of hundreds to thousands of rotations per second. Commercial rotating mirror streak cameras are available, with a mirror rotation speed 7500 revolutions per second and corresponding temporal resolution 0.65 ns pix^{-1} [3]. These sweep rates are similar to the slow time axis on a streak camera, but not comparable to the fast time axis.

Electro-Optical Streak Camera

Streak cameras were used to measure picosecond laser pulses in the early 1970s [4, 5], and were subsequently applied to measure the length of electron bunches in particle accelerators [6]. Streak cameras have since been used to measure short electron bunch lengths at many laboratories [7–10].

Streak cameras are still used to measure the shortest optical pulses [11], and especially on times scales <1 ps. However the technology of streak cameras is focussing on the ultrafast, ultrashort pulse community and diverging from the needs of some particle accelerators: electron bunches in rings are not getting shorter. A streak camera can measure the temporal profile of electron bunches in a ring, but the temporal resolution is unnecessary.

POTENTIAL NEW APPROACHES

We review several approaches for measuring short pulses in accelerators. We especially consider a few solid-state options for streaking optical beams.

Digital Deflection Using the Linear Electro-Optic (Pockels) Effect

Pockels cells are fast polarisation-switching units in regenerative amplifier lasers. Multiple variants on this idea were proposed and tested in the 1960s for computing using optical pulses [12], and also in the 1990s for solid state streak cameras [13].

We had initially considered essentially something similar to the apparatus of Ref. [14] (Fig. 1 therein). A KDP Pockels cell is followed by a Wollaston prism. This apparatus is also similar to that of Ref. [12]. Essentially, we consider an active

ISBN: 978-3-95450-261-5 ISSN: 2673-7000 doi: 10.18429/JACoW-NAPAC2025-MOP083

RESONANT CAVITY FOR QUADRUPOLE MOMENT MEASUREMENTS OF HEAVY ION BEAMS*

A. S. Plastun†, S. Cogan, K. Hwang, S. Lidia, T. Maruta, P. N. Ostroumov, S. Zhao, Q. Zhao
Facility for Rare Isotope Beams, Michigan State University, East Lansing, MI, USA

Content from this work may be used under the terms of the CC BY 4.0 licence (© 2022). Any distribution of this work must maintain attribution to the author(s), title of the work, publisher, and DOI.

Abstract

Non-invasive and fast beam emittance measurement is highly demanded for accelerated multi-charge-state heavy-ion beams. The driver linac of the Facility for Rare Isotope Beams is the first accelerator capable of accelerating multiple charge states of stripped heavy ion beams and delivering up to 400 kW to the isotope production target. Emittance measurements of, for example, five charge states of uranium beam using conventional wire profile monitors take more than an hour in one location and add up to a few hours throughout the linac. This work presents design studies for a resonant cavity monitor capable of instantaneous measurement of the quadrupole moment of the beam distribution. Coupling with the beam and signal acquisition system, the separation between monopole, dipole, and quadrupole modes of the cavity are discussed.

INTRODUCTION

The driver linac of the Facility for Rare Isotope Beams (FRIB) at Michigan State University is the first accelerator capable of accelerating multiple charge states of stripped heavy-ion beams and delivering up to 400 kW to the isotope production target. Setting up the linac for no-loss acceleration is a challenging problem involving transverse beam matching at several locations in the linac [1,2]. The matching procedure is as follows:

- The beam transverse profiles are measured with a conventional wire scanner for a few different optics settings providing underfocused, focused, and overfocused beam at the wire location, commonly referred to as quadrupole scan.
- Profiles are analyzed to extract the horizontal and vertical rms beam sizes σ_x and σ_y for each measurement.
- Twiss parameters at a given location are found by fitting the beam envelope to the measured data.
- Measurements and fitting are repeated for other charge states of the beam.
- Twiss parameters are loaded to the beam optics code to adjust the magnets' settings for the optimum matching for all charge states of the beam.

Currently, a single wire scan takes about 3 min, which adds up to 25 min for a single-charge-state scan, or 2 h for the five-charge-state uranium beam. Matching in several locations along the linac requires about 4 - 6 h. After implementation of the instant phase setting [3], transverse matching is now one of the most time-consuming procedures in the linac set-up. Since beam species are changed on average every two weeks, expediting the matching procedure is highly demanded at FRIB.

In recent years, we have been working on virtual diagnostics for fast and non-invasive measurements, and reconstruction of Twiss parameters from the beam position monitors' (BPM) data [4, 5]. The reconstruction is based on fitting the beam optics model into the quadrupole terms BPMQ, measured by several BPMs.

$$\mathrm{BPMQ} = G\frac{U_R + U_L - (U_T + U_B)}{U_R + U_L + U_T + U_B} - (x^2 - y^2) \approx \sigma_x^2 - \sigma_y^2, \quad (1)$$

where G is a geometric factor that depends on the BPM geometry, U_T, U_L, U_R and U_B are the induced signal at the top, left, right, and bottom pickups, x and y represent the horizontal and vertical beam centroids. As the primary role of the BPMs is to measure the beam position, the BPMQ is significantly weaker compared to the beam centroid signal. Consequently, small errors, such as calibration inaccuracies, can lead to substantial errors in the measurements. To address these issues, we have developed a machine learning model. Although this model showed a modest improvement over Eq. (1), prediction accuracy cannot exceed the quality of the original data.

The design studies presented in this paper are dedicated to the development of a resonant cavity for the quadrupole term measurements.

RESONANT CAVITY

Resonant beam position monitors are well-known instruments for beam position measurements [6–8]. Several designs have been proposed to measure the second moment of the beam [9]. The principle of resonant monitors is in accumulation of electromagnetic energy that carries the necessary information about the beam distribution by making the cavity resonate at a harmonic of the beam frequency. For example, for the BPMs, the dipole modes of the cavity, and for the second moment monitor, its quadrupole mode is set to resonate with a beam harmonic. The $n\omega_0$ beam current harmonic for Gaussian-shaped bunches of temporal rms length σ and bunch spacing $T = 2\pi/\omega_0$ is presented in Fig. 1 and described as follows [10]:

$$I_n = 2I_0 e^{-(n\omega_0)^2\sigma^2/2}, \quad (2)$$

where I_0 is the average beam current. Shorter bunches have wider spectra, allowing the use of higher harmonics and making the cavities more compact. In this project, we selected the 1288 MHz harmonic ($n = 32$) to be resonant with the quadrupole mode of the rectangular-shaped monitor cavity,

* Work supported by the U.S. Department of Energy, Office of Science, Office of Nuclear Physics under award number DE-SC0025531.

† plastun@frib.msu.edu

ISBN: 978-3-95450-261-5 ISSN: 2673-7000 doi: 10.18429/JACoW-NAPAC2025-MOP084

RF CHARACTERIZATION OF A CRYOGENIC X-BAND CAVITY BEAM POSITION MONITOR FOR SUPERCONDUCTING UNDULATOR APPLICATIONS AT SLAC*

K.O. Kruchinin†, A. Haase, B. Jacobson, E. M. Kraft, P. Krejcik,
E. A. Nanni, C. Nantista, M. Othman, X. Permanyer
SLAC National Accelerator Laboratory, Menlo Park, CA, USA

Content from this work may be used under the terms of the CC BY 4.0 licence (© 2022). Any distribution of this work must maintain attribution to the author(s), title of the work, publisher, and DOI.

Abstract

Superconducting undulators (SCUs) have gained significant interest due to their advantages over permanent magnet undulators, including the ability to achieve higher magnetic fields and shorter periods, leading to enhanced photon energy gain.As part of the SCU project at SLAC, an X-band cavity beam position monitor (BPM) has been designed and fabricated. This BPM plays a crucial role in the SCU assembly ensuring precise beam alignment with sub-micron resolution. The BPM incorporates two rectangular cavities for X- and Y-position measurements and a cylindrical reference cavity, all housed within a single copper block. Each cavity is separated by approximately 30 mm, which eliminates cross-talk between channels. The design of each cavity includes a single WR-75 waveguide port with a ceramic window as vacuum-air interface for out-coupling the EM field from the cavity to the external circuit. Additionally, each cavity is equipped with a tuner pin for resonant frequency adjustments. In this work, we report on the RF characterization of the BPM cavities conducted at both room and cryogenic temperatures. A consistent resonant frequency shift of approximately 37 MHz was observed when cooling the cavities from room temperature to 40 K, which is the nominal operating temperature within the undulator cryomodule. These measurements validate the predictions made during the BPM design phase through simulations. We also discuss future plans and possible applications beyond the SCU project.

INTRODUCTION

Precision alignment of components in the undulator beamline at the Linac Coherent Light Source (LCLS) is critical in achieving the desired performance of the X-ray Free Electron Laser (FEL). To ensure lasing, the X-ray photon beam must overlap with the electron beam across the entire beamline with micron-level accuracy. This alignment precision is attained only by using the electron beam itself as a reference in a procedure known as beam-based alignment [1]. A magnetic focusing quadrupole and BPM are mounted in each interspace region between the undulators on a micro-movable girder, together with each undulator, allowing the beam to be iteratively steered straight by moving each girder in X and Y directions. The success of this procedure relies upon BPMs to measure the beam trajectory on a single-shot basis with sub-micron resolution at the typical beam operating current. For this purpose, we have successfully used copper RF cavity BPMs operating at 11.424 GHz X-band frequency to achieve submicron resolution at 100 pC bunch charge [2]. Recently, we have been developing a new Superconducting Undulator (SCU) with superior performance capability than the existing Permanent Magnet Undulators (PMUs) to achieve shorter X-ray wavelengths and higher X-ray intensities [3]. The operation of the SCUs at cryogenic temperatures requires, in a compact design layout, that the RF cavity BPM is also located in the cryostat and cooled to cryogenic temperatures [4]. In this paper, we discuss the design challenges this poses and how we choose to overcome them. The copper cavity BPMs still operate in the normal conducting mode, but large changes in material properties must be accounted for at cryogenic operating temperatures. Large dimensional changes occur when the BPM is cooled from room temperature; the resistivity of the copper changes significantly, and consequently, the cavity resonant frequency, the cavity Q, and the cavity coupling ratio change. The cavity BPM is also no longer accessible once it is installed inside a cryomodule, so we had to rethink how the cavity would be tuned prior to installation and cooling. This led us to make conceptual changes in the design [5] where the single, cylindrical X and Y dipole mode cavity was replaced with two rectangular cavities to allow independent, uncoupled measurement of the X and Y dipole modes. The tuning of the new cavity design is much simpler and requires only one tuning pin in place of the four on the previous cylindrical cavity, and the tuning is now very repeatable, even after extended thermal cycling to cryogenic temperatures. The cavity BPM has also been made more mechanically robust by replacing the coaxial SMA vacuum feedthroughs with X-band waveguide windows, which are more tolerant to thermal cycling than the fragile coaxial feedthroughs. Waveguide-to-coax adapters allow cables to be easily attached to the BPM inside the cryomodule. RF measurements of the new BPM have been performed both at room temperature and cryogenic temperature to compare with RF design predictions. Installation on the LCLS beamline is being prepared so that we can compare the performance with the electron beam at room temperature with the existing BPMs before installing the new BPM inside the cryomodule.

* Work supported by U.S. Department of Energy under Contract Numbers DE-AC02-06CH11357.

† konkruz@slac.stanford.edu

ISBN: 978-3-95450-261-5 ISSN: 2673-7000 doi: 10.18429/JACoW-NAPAC2025-MOP086

SEM GRID TESTING AT NLCTA IN BEAMNETUS PROGRAM*

A. Baxter[1], A. Dhar[2], A. Gabriel[2], D. McCormick[2], E. Kendrick[1], E. Snively[2], G.A. Klinger[1], J. Cruz[2], N. Horiguchi[1], N. Samuel[1,2,†], S. Allen[1], W.H. Tan[2], D. Nembhard[1]
[1]Harvey Mudd College, Claremont, CA, USA
[2]SLAC National Accelerator Laboratory, Menlo Park, CA, USA

Content from this work may be used under the terms of the CC BY 4.0 licence (© 2022). Any distribution of this work must maintain attribution to the author(s), title of the work, publisher, and DOI.

Abstract

We report on the performance of a secondary electron monitor (SEM) grid used to measure the transverse profile of an MeV range electron beam tested at SLAC National Accelerator Laboratory's Next Linear Collider Test Accelerator (NLCTA) facility. When inserted into the path of the electron beam, secondary electron emission results in a measurable current on the wires that make up the grid. We present measurements using this technique to reconstruct the beam profile. The SEM grid was designed and manufactured by a team of undergraduate students at Harvey Mudd College (HMC) and was tested at SLAC's NLCTA facility in collaboration with NCLTA staff as part of the BeamNetUS program. Developed for real-time diagnostics of MeV-range electron beams, this SEM grid has potential applications in both industrial and medical contexts.

INTRODUCTION

Secondary electron emission monitors (SEM) grids are well-established devices for determining the transverse profile of particle beams. Examples include designs for use with proton beams at Fermilab [1], and for electron beams at DESY [2].

The SEM grid tested in this experiment was designed as part of an undergraduate engineering capstone project at Harvey Mudd College. The goal was to design a device to capture and transmit real-time data on the transverse profile of an electron beam for NorthStar Medical Radioisotopes, the capstone project sponsor. NorthStar is a radiopharmaceutical company who produces radioisotopes Actinium-225 and Copper-67 for cancer treatment [3]. These radioisotopes are produced through a process including irradiation of target materials with an IBA Rhodotron electron beam [4, 5].

One of the prototypes developed as part of this project was tested at SLAC National Laboratory's Next Linear Collider Test Accelerator (NLCTA) facility. The X-band Test Accelerator (XTA) at NLCTA provided a comparable electron beam energy to NorthStar's IBA Rhodotron but at a significantly lower power (< 1 W). At this low power, the functionality of the prototype could be tested without the challenges associated with excessive heating. The following sections describe general principles of SEM grids, the design of our specific prototype, the experimental setup and procedure, and the analysis and conclusions from the data.

*This work was supported by the U.S. Department of Energy, Accelerator R&D and Production Program, under Contract No. DE-AC02-76SF00515 as part of BeamNetUS.
†nsamuel@g.hmc.edu

SEM GRID BACKGROUND

SEM grids work by the phenomenon of secondary electron emission (SEE), which occurs when an incident particle beam imparts sufficient energy to a target material such that electrons escape the material entirely, leaving a charge behind [6–8]. In the case of an SEM grid setup, the target material of interest is one or two grids of wires which the beam is incident on. When the beam hits these wires, the energy transfer frees some electrons from the wires. This results in a measurable current in each of the wires, varying across the cross section of the beam and grid [9]. Biasing, the introduction of a large voltage to the setup, is often used to control the potential re-absorption of emitted electrons back into the wires [2, 6].

Based on the literature on SEM grids, we developed a prototype consisting of one vertical and one horizontal wire frame, and three biasing plates. The wire frames each had six tungsten wires, spaced approximately 0.2" apart. The wire diameter was less than a millimeter, and was chosen through thermal analysis.

EXPERIMENTAL PROCEDURE

The SEM grid set-up in the NLCTA beamline was configured for quick accessibility. The SEM grid and biasing plates were enclosed in a plastic box to make the device touch safe, as shown in Fig. 1 at left. The SEM grid was mounted on a two-axis translation stage in air at the end of the beamline. A DRZ screen [10], serving as an alternative beam profile monitor, was placed on the stage on top of the SEM grid prototype in the approximate plane of the wires, as seen in Fig. 1 at right. A smaller piece of DRZ was placed near the entrance to the SEM grid assembly to assist with initial alignment of the beam into the enclosure.

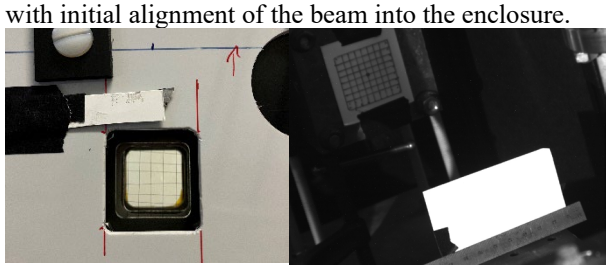


Figure 1: SEM grid with both wire grids visible through aperture in plastic enclosure, and alignment DRZ film above aperture (left) the DRZ film (bright white rectangle) illuminated on top of the plastic enclosure, in the same camera frame used to image the beam profile (right).

The electrical current signal from each individual wire of the SEM grid was passed through long BNC cabling out of the beam area to the control room and then to a SR750

ISBN: 978-3-95450-261-5 ISSN: 2673-7000 doi: 10.18429/JACoW-NAPAC2025-MOP087

STATUS OF LONGITUDINAL BUNCH-BY-BUNCH FEEDBACK SYSTEM AT THE UPGRADED ADVANCED PHOTON SOURCE*

P. Kallakuri†, A. Brill, W. Cheng, L. Emery, R. Lindberg, U. Wienands
Argonne National Laboratory, Lemont, IL, USA

Content from this work may be used under the terms of the CC BY 4.0 licence (© 2022). Any distribution of this work must maintain attribution to the author(s), title of the work, publisher, and DOI.

Abstract

The upgraded Advanced Photon Source (APS) is using twelve Radio Frequency (RF) cavities from the original APS RF system to compensate for beam energy loss. Undamped higher order modes (HOMs) from these cavities pose a risk of instability under the new APS conditions. Dimtel iGp12 processor-based bunch-by-bunch Longitudinal Feedback (LFB) system is developed to address longitudinal coupled-bunch instabilities caused by HOMs. These instabilities are exacerbated by the reduced synchrotron frequency and faster growth rates in presence of bunch lengthening system. The mitigation strategy involves initially reducing growth rates through precise cavity temperature tuning, followed by employing the LFB system to effectively manage residual growth rates. Resonance cavity temperatures of the HOMs have been characterized under APS conditions, providing a reference for tuning in the upgraded APS operation. The LFB system is designed to operate in both phase and energy sensing modes. This paper presents the feedback configuration, initial commissioning results with phase and energy sensing modes, and the feedback setup for operations.

INTRODUCTION

The upgraded Advanced Photon Source is using 12 RF cavities from the original APS 352 MHz RF system to make up the energy loss of the beam. Additionally, a 1408 MHz (4th-harmonic) superconducting Bunch Lengthening System (BLS) is installed to improve beam lifetime. The RF cavities have mostly undamped higher order modes, which may have instability growth rates greater than the radiation damping under the upgraded APS operating conditions. Design studies indicated the potential for longitudinal coupled-bunch instabilities driven by the HOMs of the RF cavities. Dimtel [1] bunch-by-bunch longitudinal feedback (LFB) system is installed to deal with the instabilities. The presence of the BLS introduces additional complexity, as instability growth rates increase with decreasing synchrotron frequency. Furthermore, the increased synchrotron frequency spread associated with the BLS makes feedback control more challenging. To address this, a dual mitigation strategy has been developed that combines precise RF cavity temperature tuning with the bunch-by-bunch feedback system. Temperature tuning of the HOM frequencies can effectively shift harmful modes away from synchrotron sidebands, significantly reducing growth rates and relaxing the requirements on the feedback system. After temperature tuning, the longitudinal feedback system can more effectively damp the remaining modest growth rates. The resonance temperatures of RF cavity HOMs have been characterized under APS operating conditions [2, 3]. The longitudinal feedback system's front-end has been utilized as a diagnostic tool to map the resonant cavity water temperatures corresponding to HOMs. Growth rates for each mode across 324 bunches were measured by selectively exciting individual modes. A comprehensive dataset of HOM resonance peaks over a wide range of cavity temperatures has been collected. This mapping serves as a reference for optimal cavity temperature tuning during upgraded APS operation, even with variations in the working RF frequency and cavity power.

Traditionally, longitudinal feedback systems rely on measured bunch phase for feedback corrections. However, the synchrotron period is longer with the higher harmonic cavity in operation, requiring faster detection and correction of unstable motion seeded by energy errors. Energy sensing is a suitable option in this scenario, as it detects energy errors based on the transverse offset of the beam in a dispersive region. The front-end of the LFB system has been designed to operate in both phase-sensing and energy-sensing configurations. This paper presents the architecture of the feedback system, initial commissioning results, and details of the user operation setup.

FEEDBACK SYSTEM ARCHITECTURE

General block diagram of the longitudinal bunch by bunch feedback system is shown in Fig. 1. Beam position monitor (BPM) is used for beam pickup. Phase sensing uses sum signal from a non dispersive BPM and energy sensing uses ΔX signal from a dispersive BPM. Front-end electronics provide baseband signal to the controller on iGp12 processor which computes correction signals, and back-end processes the signal to provide an analog output to RF power amplifiers.

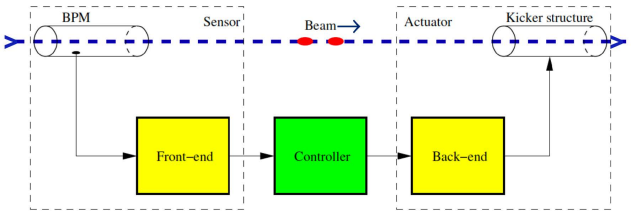


Figure 1: Block diagram of the closed loop feedback configuration

Physical layout of the longitudinal feedback system at upgraded APS is shown in Fig. 2. Sampling Rate of the feedback processor is 352.055 MHz, max. damping rate is 500/s, and back-end 3 dB bandwidth is 60 MHz. Two

* This work was supported by the U.S. Department of Energy, Office of Science, under Contract No. DE-ACO2-O6CH11357.

† pkallakuri@anl.gov

ISBN: 978-3-95450-261-5 ISSN: 2673-7000 doi: 10.18429/JACoW-NAPAC2025-MOP089

SURROGATE MODEL FOR THIRD-INTEGER RESONANCE EXTRACTION AT THE FERMILAB DELIVERY RING*

A. Narayanan†, J. Berlioz, K. Danison-Fieldhouse, K. Hazelwood, M. Khan,
J. St. John, N. Tran, A. Whitbeck, Fermilab, Batavia, IL, USA
J. Ji, M. Walter, Toyota Technical Institute of Chicago, Chicago, IL, USA

Abstract

We present an ongoing work in which a surrogate model is being developed to reproduce the response dynamics of the third-integer resonant extraction process in the Delivery Ring (DR) at Fermilab. This effort is in pursuit of smoothly extracting circulating beam to the Mu2e Experiment's production target, wherein the goal is to extract a uniform slice of the circulating $1e12$ protons in the DR over 25,000 turns (43 ms). The DR contains 3 harmonic sextupoles which excite a third-integer resonance as well as three fast, tune-ramping quadrupole magnets which drive the horizontal tune towards the $29/3$ resonance. In our initial work the surrogate model trains on a semi-analytical simulation provided in the same format as live data. Using Reinforcement Learning (and other potential ML methods), the trained surrogate acts as the "environment" in which a simple ML control agent could learn to dynamically adjust the quadrupole ramp at 430 break points within the 43 microsecond spill window. The control agent will be hosted on a dedicated Arria 10 FPGA, introducing its own requirements on control agent architecture. In this work we report the accuracy and fidelity of surrogate models in comparison to the response dynamics of the physics simulator.

THE MU2E EXPERIMENT AND BEAM REQUIREMENT

Mu2e is an upcoming experiment [1] at Fermi National Accelerator Laboratory (Fermilab) that intends to look for beyond-standard-model (BSM) physics through charged lepton flavor violation. Mu2e will heavily suppress large systematic effects such as RPC background [2] by using a pulsed muon beam (from a pulsed proton beam) and delaying the detector live window, enabling a clean measurement of muon-converted electrons.

The pulsed proton beam (see Table 1) (directed to the muon production target) will be produced using a third-integer resonant extraction process at Fermilab's Delivery Ring (DR). The goal is to inject $1e12$ protons into the DR and uniformly extract equal slices of the circulating proton beam, sending these micropulses to the production target. A Spill Regulation System (SRS) [3] is commissioning in order to facilitate the uniformity of the spill by achieving a Spill Duty Factor (SDF) of 60% or greater.

Table 1: Some Main Parameters Pertinent to Resonant Extraction

Parameter	Value
Beam kinetic energy	8 GeV
Spill Duration	43 ms
Number of spills per super cycle	8
Number of bunches per spill	1
Initial proton intensity	10^{12} protons
# of protons extracted per turn	$< 4 \times 10^7$ protons
Time between proton micropulses	1.695 µs
Normalized Emittance (95%) ϵ_x	16 π mm-mrad
Spill Duty Factor (SDF)	> 60 %
Reset time between spills	5 ms

PHYSICS ENVIRONMENT

To simulate the 3rd integer resonant extraction, the most accurate choice of simulation would be to perform particle tracking. However, even simulating an intensity of 1e12 protons with 1e7 macroparticles over 25,000 turns would be very computationally expensive. A semi-analytical model was built to simulate of the 3rd integer resonant extraction, consisting of following components.

Noise in spill rate The modeling of the spill, for the purposes of Fast Regulation, assumes a *perfect* extraction in the absence of any instantaneous noises in the system, with the assumption that a logarithmic quad ramp curve would result in ideal extraction rate. The physics simulator generates random log-normal points at 1 kHz rate and interpolates the generated points to provide smooth noise data for over 430 time steps (since the maximum SRS design bandwidth is 10 kHz), with each time step constituting 100 µs (or equivalently ≈60 turns). The expectation value of the spill rate is normalized to 1, and the log-normal generated noise is added to 1 to give us a noise profile for every spill.

PID Control Loop Once the noise in the spill rate is generated, and the error in the spill rate known, it is sequentially fed to the PID control loop, with the three gain values of the PID controller passed as an argument. The PID function inputs the gain values, the spill rate data, and computes the control signal for each of the time steps, given by Eq. (1):

$$u(t) = G_p e(t) + G_I \int_0^t e(\tau)\,\mathrm{d}\tau + G_d \frac{\mathrm{d}}{\mathrm{d}t} e(t), \qquad (1)$$

* This work was produced by Fermi Forward Discovery Group, LLC under Contract No. 89243024CSC000002 with the U.S. Department of Energy, Office of Science, Office of High Energy Physics.

† aakaashn@fnal.gov

Content from this work may be used under the terms of the CC BY 4.0 licence (© 2022). Any distribution of this work must maintain attribution to the author(s), title of the work, publisher, and DOI.

ISBN: 978-3-95450-261-5 ISSN: 2673-7000 doi: 10.18429/JACoW-NAPAC2025-MOP090

SYNCHROTRON FREQUENCY MEASUREMENTS USING BUNCH BY BUNCH LONGITUDINAL FEEDBACK SYSTEM IN A STORAGE-RING WITH HIGHER HARMONIC CAVITY *

P. Kallakuri†, W. Cheng, L. Emery
Advanced Photon Source, Argonne National Lab, Lemont, IL, USA

Abstract

The upgraded Advanced Photon Source (APS) features a 1408 MHz superconducting Bunch Lengthening System (BLS) to improve beam lifetime. The main RF system is significantly affected by ambient 60 Hz-harmonics noise, complicating the measurement of synchrotron frequency under varying higher harmonic cavity conditions. To address this, using Dimtel iGp12 processor-based longitudinal feedback system we developed two methods to measure synchrotron frequency effectively. Our approach involves driving multi-bunch beam modes by considering a span for synchrotron frequency sideband and analyzing mode amplitude changes across the sweep frequency range. The "slow" method scans fixed drive frequencies within a range, recording the beam response at each frequency. The "fast" approach drives the beam with a broadband chirp signal and analyzes the resulting single mode spectrum data. Both methods are tested during beam studies. Synchrotron frequency changes are measured in two setups: First, adjusting BLS voltage manually while keeping beam current constant. Second, BLS voltage varying as a function of decaying beam current. This paper presents, details of the measurement procedure and results from the beam-based machine studies.

INTRODUCTION

The upgraded Advanced Photon Source incorporates a bunch lengthening system [1] featuring a 1408 MHz superconducting 4th harmonic passive cavity to enhance beam lifetime. The beam dynamics will change with harmonic cavity voltage, which affects the synchrotron frequency (F_s) of longitudinal higher-order modes (HOMs). The natural frequency of coupled bunch mode zero remains insensitive to changes in the BLS voltage and is influenced by beam loading effects. To characterize the longitudinal properties of the beam, it is essential to reliably measure the synchrotron frequencies of mode zero and higher-order modes under varying operational conditions, including changes in RF gap voltage, BLS voltage, and beam current. However, the main 352 MHz RF system is significantly affected by ambient 60 Hz harmonic noise, which complicates synchrotron frequency measurements. The bunch spectrum is dominated by peaks at the 60 Hz harmonics, making it challenging to isolate the synchrotron frequency signal. To address this issue, we developed two methods for effective synchrotron frequency measurement within the framework of the longitudinal feedback (LFB) system, which are designed to operate in the presence of ambient RF noise.

The bunch-by-bunch longitudinal feedback system is based on the Dimtel integrated Gigasample processor (iGp) [2], which has been installed in the upgraded APS storage ring for operational use. The beam signal is captured using a button-type beam position monitor (BPM). Front-end electronics detect and convert it into a baseband signal suitable for feedback computations. The iGp12 processor performs real-time feedback calculations and generates correction signals. Back-end electronics process the correction signal generated by the feedback controller. The processed signal is sent to the RF amplifiers, which drive the LFB kickers to apply corrective forces to the beam on a bunch-by-bunch basis.

Synchrotron tune measurements can be realized using an active longitudinal feedback system, since it can generate a signal, drive the beam, and detect the corresponding response. Our approach involves driving multi-bunch beam modes by considering a span of synchrotron sidebands and analyzing mode amplitude changes across the sweep frequency range. The slow method involves scanning the beam response by applying fixed drive frequencies within a predefined range, and recording the beam response at each frequency. The fast method employs a broadband chirp signal to excite the beam across a wide frequency range simultaneously. The next sections present detailed descriptions of the slow and fast methods, along with experimental results from beam studies conducted at the upgraded APS.

SYNCHROTRON FREQUENCY MEASUREMENT PROCEDURE

Drive and data acquisition options available in Dimtel processor are used to develop the synchrotron tune measurement procedures. Drive pattern generator provides the means to generate an excitation signal on a bunch-by-bunch basis. We can drive the beam with a single frequency sine signal or sine-sweep with a span. Drive signal parameters can be changed using the options: amplitude, frequency, span and period. Input frequency is computed using mode number, revolution frequency, and synchrotron sideband. Span is zero for sine signal and non zero for chirp drive. SRAM data acquisition engine collects and postprocesses the beam signal data in the real-time and generates averaged bunch spectrum, single mode spectrum, and modal amplitudes of all multi-bunch modes.

* This work was supported by the U.S. Department of Energy, Office of Science, under Contract No. DE-ACO2-O6CH11357
† pkallakuri@anl.gov

Content from this work may be used under the terms of the CC BY 4.0 licence (© 2022). Any distribution of this work must maintain attribution to the author(s), title of the work, publisher, and DOI.

ISBN: 978-3-95450-261-5 ISSN: 2673-7000 doi: 10.18429/JACoW-NAPAC2025-MOP091

THE BEAMLINE STEERING SOFTWARE FOR THE APS UPGRADE (APS-U) ACCELERATOR STORAGE RING*

Hairong Shang†, Louis Emery, Martin Smith, Siniša Veseli
Argonne National Laboratory, Lemont, IL, USA

Content from this work may be used under the terms of the CC BY 4.0 licence (© 2022). Any distribution of this work must maintain attribution to the author(s), title of the work, publisher, and DOI.

Abstract

A new beamline steering software system has been developed for the Advanced Photon Source Upgrade (APS-U) accelerator storage ring. This system comprises three main components: the main steering server, which performs the actual beamline steering; the beamline steering server, which monitors user steering requests and forwards them to the main steering server; and an operational steering application. The underlying steering functionality is managed by the APS Data Acquisition (DAQ) PV Group (PVG) module. This new software offers significant improvements over the previous system, including parallelization capabilities and enhanced efficiency, and is compatible with any kind of global orbit correction running independently.

INTRODUCTION

Historically, the APS provided steering through a relatively slow protocol that involved manual interactions through floor coordinators and operators, resulting in substantial delays. The initial improvements introduced a web-based steering request interface [1], which reduced response times to a few minutes.

The APS-U steering software significantly advances these protocols by integrating real-time control and automation using EPICS [2,3] through the Python-based DAQ PV Group module [4], facilitating immediate steering response and improved accuracy.

APS-U steering software includes the steering server and user steering interface, which is operated by the MCR team on a daily basis. To enhance user convenience, a beamline steering tool has also been developed. This tool includes a beamline steering server to monitor users' steering requests and MEDM screens for users to input steering requests. The actual steering is performed by the steering server.

The APS-U Steering Server is a crucial innovation, centralizing control via a graphical user interface (GUI) with dedicated tabs for insertion device (ID), bending magnet (BM), and canted undulator (CU) steering. This system provides:

- **Sector-specific server management**, to allow efficient allocation of computational resources.
- **Integrated Channel Access (CA) [5] connections** for efficient communication with steering process variables (PVs).
- **Automated limit-checking mechanisms** to ensure operations remain within predefined safe ranges.
- **Comprehensive Save-Compare-Restore (SCR) file management**, to provide robust data archiving for user-specific steering configurations.

The server performs detailed checks to ensure operational safety, including verifying beam position monitor (BPM) limits, corrector limits, and potential operational conflicts. It also provides real-time feedback and notifications to both beamline personnel and operators.

DAQ PV GROUP

The DAQ PV Group [4] is a Python package that enables efficient management and monitoring of a set of related EPICS Channel Access (CA) Process Variables (PVs). The software uses PvaPy [6] for communicating with EPICS PVs and for hosting EPICS PV Access (PVA) servers. The PVG package can be used via its Python APIs or through included command-line interfaces (CLIs).

The PVG *create* command uses a list of PVs and other group parameters specified either on the command line or via the input SDDS [7] configuration file, which will be described in more details in the next section in the context of the steering server. The *create* command starts the PVG controller process responsible for controlling the group PVs. The controller process establishes CA monitors for all group PVs, and it starts EPICS PVA [8] and remote procedure call (RPC) servers that enable interaction with users. Optionally, it can also start a local EPICS IOC hosting several designated control PVs that can be used for setting the group PV values and reporting the group status. The PVA server is used for hosting a channel containing values of all group PVs, as well as various other group information and metadata. The PVA group channel can be accessed using standard PVA command-line tools and APIs. The custom PVG RPC channel can be accessed using the provided Python API and command-line interfaces. Those interfaces offer users the ability to retrieve and set group PVs, retrieve group status and performance information, change group configuration at runtime, and send the shutdown signal to the group controller. For user convenience, a limited set of control and monitoring features is also offered via a set of control and configuration Channel Access PVs that can be hosted locally by the PVG controller or by a remote IOC. This allows users to set group PV values, update and read the most frequently used group settings by direct CA put and get operations, and use any of the standard EPICS CLI and API tools.

* Work supported by the U.S. Department of Energy, Office of Science, Office of Basic Energy Sciences, under Contract No. DE-AC02-06CH11357.

† shang@anl.gov

ISBN: 978-3-95450-261-5 ISSN: 2673-7000 doi: 10.18429/JACoW-NAPAC2025-MOP092

THE CONTROL AND MONITORING SYSTEM FOR THE APS-U FRONT-END XBPM*

S. Xu†, H. Shang, B. X. Yang, Argonne National Laboratory, Lemont, IL, USA

Abstract

The Advanced Photon Source Upgrade (APS-U) project aims to enhance the performance and capabilities of the APS, delivering brighter and more coherent x-ray beams to support cutting-edge scientific research. A critical component of this upgrade is the front-end X-ray Beam Position Monitor (XBPM) system, which plays a vital role in ensuring beam stability and precision. This paper presents the design and implementation of the control and monitoring system for the APS-U front-end XBPM. The system integrates advanced hardware and software solutions to achieve real-time monitoring of x-ray beam position. Key features include high-resolution data acquisition, robust signal processing algorithms, and seamless integration with the APS-U control architecture. The system utilizes the Experimental Physics and Industrial Control System (EPICS) input/output controllers (IOCs) to interface with front-end instruments. By leveraging EPICS IOCs, the system achieves high reliability and flexibility.

INTRODUCTION

The original APS XBPM system relied on a commercial VME-based DSP card to acquire and process X-ray blade signals for determining beam position for both bending magnet (BM) and insertion device (ID) beamlines. It also processed position data from narrowband RF BPMs adjacent to each insertion device, integrating with the storage-ring fast-feedback system and providing filtered data to both the feedback system and the EPICS control system [1].

Figure 1 shows the original XBPM system diagram. This system served reliably for over 20 years.

The APS-U project introduced significant upgrades to front-end and insertion devices to handle increased power. Two new types of insertion device front ends were implemented:

- High heat load front end (HHLFE) for dual inline undulator sources.
- Canted front end (CFE) for two canted undulators with a cant angle of 1 mrad [2].

These front ends employ novel XBPMs—HHLFE-XBPM and CFE-XBPM—to monitor beam stability. All ID front ends now feature these XBPMs to ensure long-term beamline stability, while BM front ends were minimally modified and reused. The upgraded XBPM front-end electronics provide Ethernet interfaces, delivering beam position information to EPICS IOCs for further processing.

* Work supported by the U. S. Department of Energy, Office of Science, Office of Basic Energy Sciences, under Contract No. DE-AC02-06CH11357

† xusf@anl.gov

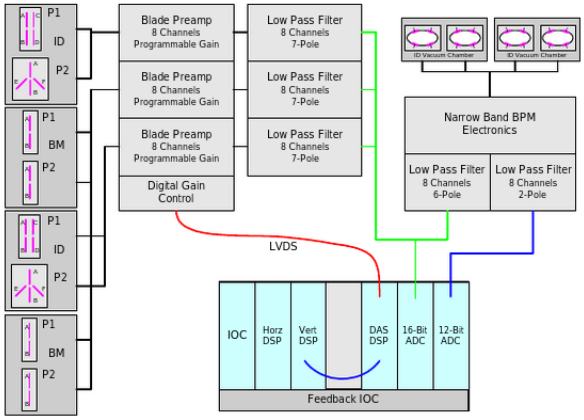


Figure 1: Original APS XBPM system diagram.

CONTROL SYSTEM OVERVIEW

ID Front-End XBPMs

The APS-U ID front-end features two X-ray beam position monitor assemblies:

- XBPM1: Uses array detectors to detect X-ray beam and calculate the X-ray beam position. Figure 2 shows the concept.
- XBPM2: Utilizes X-ray fluorescence from the exit mask to read out the beam position at the mask.

For the CFE, XBPM2 monitors beam positions of both upstream (US) and downstream (DS) undulator beams.

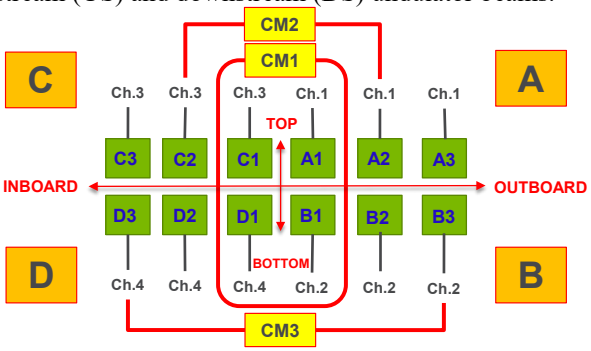


Figure 2: Concept of XBPM1 with array detectors.

BM Front-End XBPMs

The BM front end has two X-ray beam position monitors, each equipped with molybdenum photoemission blades.

Typically:

- Each ID XBPM1 uses three picoammeters.
- Each ID XBPM2 uses one picoammeter.
- Each BM XBPM uses one picoammeter.

Content from this work may be used under the terms of the CC BY 4.0 licence (© 2022). Any distribution of this work must maintain attribution to the author(s), title of the work, publisher, and DOI.

ISBN: 978-3-95450-261-5 ISSN: 2673-7000 doi: 10.18429/JACoW-NAPAC2025-MOP093

TOWARDS ACCURATE BEAM SIGMA MATRIX DETERMINATION IN A TRANSPORT LINE USING DIFFERENTIABLE SIMULATION*

C. Xu†, M. Borland, L. Emery, O. Mohsen, Y. Sun, Argonne National Laboratory, Lemont, IL, USA
R. Roussel, SLAC National Accelerator Laboratory, Menlo Park, CA, USA

Content from this work may be used under the terms of the CC BY 4.0 licence (© 2022). Any distribution of this work must maintain attribution to the author(s), title of the work, publisher, and DOI.

Abstract

Precise characterization of the beam distribution is essential for matching the incoming beam and optimizing injection into storage rings. We present a method to efficiently reconstruct the full 5×5 beam sigma matrix (excluding the time coordinates) at the booster-to-storage-ring (BTS) transport line at the Advanced Photon Source Upgrade (APS-U). Earlier works demonstrated that the beam sigma matrix can be accurately reconstructed using linear transport matrices under the assumption of negligible chromatic effects. However, the presence of chromaticity introduced significant non-linearities and leads to discrepancies from the linear approaches. In this work, we demonstrate a novel approach leveraging Cheetah, a differentiable beam dynamics simulation framework, to enable direct gradient-based optimization of the beam matrix. Initial results shows efficient and accurate reconstruction under both linear and second-order tracking models, providing improved robustness in simulation studies. This method offers a scalable, interpretable, and computationally efficient alternative to black-box methods for beam matrix reconstruction in transport lines in presence of complex effects.

INTRODUCTION

A standard method for characterizing the beam properties in a transport line is the quadrupole scan. By varying the strengths of multiple quadrupoles and observing the transverse beam sizes on a downstream screen, we could measure the emittances or the transverse 4×4 beam sigma matrix [1]. When the quadrupole magnets are placed at locations with non-zero dispersion, the resulted transverse beam profile further depends on the beam momentum. As such, it allows the determination of 5×5 beam sigma matrix, excluding the temporal part. Relying on the linear transport matrices, the output beam moments can be expressed as a linear equation system of the initial beam sigma matrix, which can be solved to obtain the incoming beam properties [2, 3]. While this method works well for linear systems, the discrepancies increase when the system cannot be sufficiently approximated by first order transport matrices, for example due to strong chromatic effects. As a result, the linear solution needs to be further adjusted to accurately determine the beam properties. This can be achieved using black box optimization methods like genetic algorithms. However, as the problem has high-dimensionality and is non-convex, the fitting requires many sample evaluations, often taking hours. In recent years, several differentiable beam dynamics simulation codes were developed, including the PyTorch-based package Cheetah [4, 5], Bmad-Julia [6], and JuTrack [7]. They utilize the auto-differentiation (AD) technique which allow automatic calculation of derivatives alongside of the particle tracking. In this paper, we describe using Cheetah for gradient-based optimization of the initial 5×5 beam sigma matrix. This approach resembles the generative phase space reconstruction (GPSR) [8, 9] method, which leverages differentiable simulation to reconstruct the 6-dimensional phase space distribution from a small number of transverse beam images by scanning quadrupoles, a transverse-deflecting cavity, and a dipole spectrometer.

* The work is supported by the U.S. DOE Office of Science-Basic Energy Sciences, under Contract No. DE-AC02-06CH11357.

† chenran.xu@anl.gov

GRADIENT-BASED OPTIMIZATION OF BEAM SIGMA MATRIX

We start with the initial particles $\boldsymbol{x}_0 = (x, p_x, y, p_y, \tau, \delta)$ distributed according to the design settings. The unknown beam distribution at the entrance of the transport line is represented by a matrix which transforms the initial particles by

$$\boldsymbol{x}_t = \boldsymbol{x}_0 R_{\boldsymbol{\theta}}^T, \tag{1}$$

with $\{R_{ij}, i, j \neq 5\}$ being the non-temporal components to be determined. The transformed particles $\boldsymbol{x}_t$ are further tracked through the transport line up to second order with the transfer function

$$\boldsymbol{x}_f = f(\boldsymbol{x}_t | \boldsymbol{k}_Q), \tag{2}$$

which depends on the quadrupole strengths $\boldsymbol{k}_Q = (k_{Q_1}, \ldots, k_{Q_j})$. The screen images are simulated from the phase space coordinates of the output macroparticles using the kernel density estimation (KDE) method, allowing the gradients to be propagated $Y_f = \mathrm{KDE}(\boldsymbol{x}_f)$. By evaluating different quadrupole settings $\boldsymbol{k}_Q^{1,\ldots,n}$, a set of n screen images are generated. A loss function can be calculated between the simulated and target screen images

$$l = \sum_{i=1,\ldots,n} \mathrm{Loss}(Y_f^i - Y_{\mathrm{target}}^i). \tag{3}$$

As such, the goal is to minimize the differences between the simulated and the target images by finding the best initial transform matrix

$$\min_{\boldsymbol{\theta}} l(Y_{\mathrm{target}}, Y_f(\boldsymbol{\theta})), \ \boldsymbol{\theta} \in \mathbb{R}^{5\times5}. \tag{4}$$

When tracking the particles with a differentiable simulation code such as Cheetah [4], we automatically obtain the gradient of the loss function with respect to the unknown

ISBN: 978-3-95450-261-5 ISSN: 2673-7000 doi: 10.18429/JACoW-NAPAC2025-MOP094

TWO-STAGE CONSTRAINED BAYESIAN OPTIMIZATION FOR PARTICLE ACCELERATOR TUNING *

Fuhao Ji†, Zihan Zhu, Ryan Roussel, Lee Zucker-Murray[1], Mianzhen Mo, Yusong Liu, Patrick Kramer, Frederick (Erik) Cropp, Sara Miskovich, Indranil Nayak, Stephen Weathersby, Zhe Zhang, Sean Gasiorowski, Alexander Reid, Daniel Ratner, Auralee Edelen, Robert Joel England
SLAC National Accelerator Laboratory, Menlo Park, CA, USA
[1]also at University of California, Los Angeles, CA, USA

Content from this work may be used under the terms of the CC BY 4.0 licence (© 2022). Any distribution of this work must maintain attribution to the author(s), title of the work, publisher, and DOI.

Abstract

Particle accelerators are highly complex, non-linear systems that require rapid tuning during operation to meet requirements on beam qualities for applications in different scientific disciplines. Multi-objective Bayesian Optimization (MOBO) has been recently demonstrated at SLAC MeV-UED facility for speeding up online electron beam tunings and obtaining Pareto Fronts giving trade-offs between key beam properties of interest. One challenge in algorithm-based tuning is the alignments of beam through the collimators, screens and timing diagnostics under different system working points. This usually requires trial-and-error based hand tunings and strongly limits the data taking efficiency. Here, we utilize two-stage constrained Bayesian optimizations (CBE-MOBO) for beam tunings at MeV-UED. Instead of directly optimizing objectives of interest, beam property constraints are first modeled in the input space using constrained Bayesian exploration. Based on the information learned, MOBO is then used to efficiently search the parameter space and resulted in dramatically improved valid data efficiency. Our results show potential of CBE-MOBO for autonomous tunings of particle accelerators under various constraints.

INTRODUCTION

Artificial intelligence and machine learning (AI/ML) have recently reached sufficient maturity for applications in real-world tasks, including natural language processing [1], autonomous driving, protein folding prediction [2] and fusion reactor control [3]. Speeding up and aiding online optimizations of complex particle accelerators is one of the key areas where AI/ML can make substantial contributions [5–13]. Bayesian Optimization (BO) with Gaussian processes (GPs) represents a class of ML algorithms in which a probabilistic model and its uncertainty at each measurement step are used to select the optimal next observation point. BO-based optimization methods have been widely applied by the accelerator physics community in recent years due to its advantages in addressing complex optimization tasks, especially for online accelerator tunings and computational expensive simulations [10]. At SLAC MeV-UED [4], Multi-objective Bayesian Optimization (MOBO) [14] has been recently demonstrated for speeding up online electron beam tunings and obtaining Pareto Fronts (PFs) giving trade-offs between key beam properties of interest [13]. Practically, one challenge in online accelerator tuning is the alignments of beam through the collimators, screens and timing diagnostics under different system working points. This often requires extensive hand tunings based on a trial-and-error approach and strongly limits the data taking efficiency of MOBO. To this end, we utilize two-stage constrained Bayesian optimizations for automating beam tunings at MeV-UED. Instead of directly optimizing objectives of interest, constrained Bayesian Exploration (CBE) [11] is first conducted for constructing Gaussian Processes (GPs) to model the beam property constraints in the input domain. Based on the information learned using CBE, constrained MOBO is then conducted to efficiently search the parameter space and optimize the PF. The CBE-MOBO approach results in dramatically improved valid data efficiency with minimal human inputs, and show potential of autonomous tunings of complex, correlated particle accelerators under various beam property constraints.

TWO-STAGE CONSTRAINED MULTI-OBJECTIVE BAYESIAN OPTIMIZATION

Practically, accelerator tunings often require meeting constraints such as transmission through collimators or apertures, as well as alignments through diagnostic elements. CBE treats each unknown constraint function $c_i(\mathbf{x})$ as an independent GP [15], and uses those models to bias exploration toward regions where each constraint exceeds a required threshold Q_i. Given a set of N observations:$D_N = \{(\mathbf{x}_1, \mathbf{y}_1), (\mathbf{x}_2, \mathbf{y}_2), ..., (\mathbf{x}_N, \mathbf{y}_N)\}$, The objective and constraint functions can be models as:

$$f(\mathbf{x}) \sim \mathcal{GP}\big(\mu_f(\mathbf{x}),\, k_f(\mathbf{x}, \mathbf{x}')\big) \tag{1}$$

$$c_i(\mathbf{x}) \sim \mathcal{GP}\big(\mu_{c_i}(\mathbf{x}),\, k_{c_i}(\mathbf{x}, \mathbf{x}')\big) \tag{2}$$

For a "$> Q_i$" constraint, the probability that c_i is satisfied at $\mathbf{x}$ is

$$P_i(\mathbf{x}) = P\big(c_i(\mathbf{x}) > Q_i\big) = \Phi\Big(\frac{\mu_{c_i}(\mathbf{x}) - Q_i}{\sigma_{c_i}(\mathbf{x})}\Big) \tag{3}$$

* Work supported by U.S. Department of Energy Office of Science, Basic Energy Sciences under Contract No. DE-AC02-76SF00515

† Corresponding author: fuhaoji@slac.stanford.edu

ISBN: 978-3-95450-261-5 ISSN: 2673-7000 doi: 10.18429/JACoW-NAPAC2025-MOP095

ULTRA-FAST SWITCHING UTILIZING AN IVA TOPOLOGY FOR CHOPPER APPLICATIONS*

K. A. Hansz[1], H. J. Gaus III, A. M. Chrysler, H. R. Patel
Los Alamos National Laboratory, Los Alamos, NM, USA
[1]also at Texas Tech University Pulsed Power Laboratory, Lubbock, TX, USA

Content from this work may be used under the terms of the CC BY 4.0 licence (© 2022). Any distribution of this work must maintain attribution to the author(s), title of the work, publisher, and DOI.

Abstract

Recent trends in power electronics indicate increasing demand for fast response switching networks with sub nanosecond switching speed at a variety of voltages. Gate driving networks meet the desired switching speeds using COTS (Commercial Off-The Shelf) parts. This work describes an IVA (Inductive Voltage Adder) system capable of producing a rise and fall time in the single digits of ns with a projected voltage output of 2 kV, using a gate driving topology to drive GaN (Gallium Nitride) HEMTs (High Electron Mobility Transistor). These rapid switching systems are proposed to be used in the LAMP (LANSCE Accelerator Modernization Project) chopper by enabling effective production of clean beam to select target stations, producing the necessary output.

INTRODUCTION

Fast response switching circuits provide the necessary rise and fall time that ordinary switching circuits can't withstand. Whereas the automotive industry, for example, can average between 10s to 100s of nanoseconds for their required rise and fall times. Fast response switching circuits that are incorporated in high efficiency pulsed power systems, such as high-powered accelerators, require faster turn on times that fall in the single digits of nanoseconds.

With the required voltage being 2 kV and the GaN devices' limit being 650 V, the addition of an IVA topology was utilized to electrically add the outputs of the GaN devices in series. With the use of 4, 1:1, pulse transformers, representing the IVA in the system, the output of each GaN device gets electromagnetically coupled to the secondary side of the transformer, then added up with the rest of signals.

IVA CONCEPT

Fundamentals

IVAs are systems that inductively add multiple pulse forming network outputs through a network of transformers with their secondaries connected in series. Each of these stages are coupled with its respective stage with a 1:1 transformer allowing the voltage pulse to travel through the transformer, theoretically undisrupted [1]. These series connections of 1:1 transformers output the addition of each stage in the IVA and supply an external load with the added signals.

Most IVAs are designed using metal rings connected to the input signal, the primary in this case, and a metal stalk that acts as the secondary. This stalk and core design produces the required inductive values but adds on a level of complexity that is eliminated with the use of the pulse transformers.

Design Specifications

An IVA typically has a metal ring and core [stalk], creating inductive values on the IVA, the IVA used here implements the use of a 1:1 pulse transformer to recreate the ring and stalk. The use of a 1:1 pulse transformer, compared to a ring and stalk, allows for the same inductive reaction to take place, but with less complexity due to the less complex nature of the design requirements of this project.

With the design of these boards having a maximum voltage output of 650 Volts, due to the GaN FETs internal limitation, the addition of an IVA effectively replaces the need for a higher voltage and more complex board. The IVA inductively adds the outputs of each stage allowing, for example, 4 separate 500-Volt stages to have a final output of 2 kV. Due to the magnetic properties of the transformer core, the voltage pulse is inductively coupled to the secondary winding, enabling the voltage from each stage to combine constructively at the IVA output.

OVERALL SYSTEM DESIGN

The overall system design of this project utilizes a 4 stage IVA design, with each stage producing an output wave of 500 V. One PCB holds all 4 driving networks and the multi staged IVA.

Gate Driver Network Design and Analysis

The gate driver network utilizes the properties of the LMG1020 gate driver and added embedded networks. An EZDrive and RL peaking circuit are utilized to meet the requirements for the output waveforms of the IVA system.

The LMG1020 has a low propagation delay for its turn-on and turn-off time, 2.5 and 2.6 ns respectively, and an ultra-fast output rise and fall time, 375 and 350 ps respectively. These fast turn on and off times allow the LMG1020 to comfortably produce the needed drive allowing the GaN FETs to output these single digits turn on times.

The EZDrive circuit is a level shift network used to help control slew rate and optimize the output signals leading into the gate of a FET. The network has a high impedance resistor, recommended value of 10 kΩ, to keep driving voltage steady and a capacitor in parallel, recommended value of 47 nf, to hold negative voltage for when the FET turns off. Along with the above components there is a Zener diode clamping network used to clamp the positive and negative gate voltage, connected from the output of the resistor and to the Kelvin source of the FET [2]. The EZDrive circuit and its values are shown in Fig. 1.

ISBN: 978-3-95450-261-5 ISSN: 2673-7000 doi: 10.18429/JACoW-NAPAC2025-MOP096

UPGRADE TO FIXED AND TRANSLATING SCINTILLATION-BASED LOSS DETECTOR SYSTEM IN THE FERMILAB DRIFT TUBE LINAC*

E. V. Chen†, A. L. Saewert, R. V. Sharankova
Fermi National Accelerator Laboratory, Batavia, IL, USA

Abstract

The closed-off structure of the Fermilab Drift Tube Linac precludes a robust array of instrumentation from directly monitoring the H^- beam that is accelerated from 750 keV to 116 MeV. To improve beam tuning and operational assessment of Drift Tube Linac performance, scintillator-based loss monitors were previously installed along the exterior of the first two accelerating cavities to assess low energy beam losses. Here we present a recent upgrade to the loss monitor system, including significant improvements in analog signal processing to address baseline-interfering noise; digitization of the signals to enable regular operational use and tuning; and a new remote operation upgrade of the translating loss monitor with precise positioning of the loss monitor along its nine-foot track. Data from the fixed and translating detectors collected under varying beam conditions validate the utility of the upgrade.

INTRODUCTION

The Fermilab Drift Tube Linac (DTL) accelerates H^- ions from 750 keV to 116 MeV using five 201 MHz cavities. The DTL has a ~92% transmission efficiency, making it the section of the linac with the highest beam loss. Given the lack of diagnostics within the cavities and the known misalignments of the drift tubes, especially in the vertical direction [1], it is difficult to tune the DTL effectively.

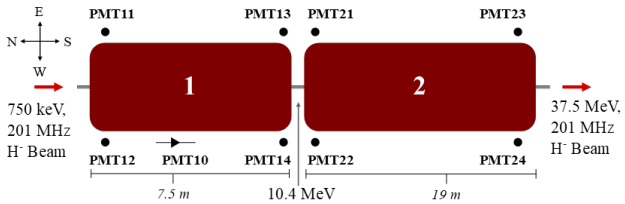


Figure 1: Schematic of the first two DTL cavities and the arrangement of scintillator detectors around the cavities, labelled PMTmn, where m refers to the cavity number and n refers to the position. Circle markers and triangle markers indicate stationary and translating detectors, respectively.

Previously, we demonstrated the ability of scintillator-based detectors to quantify products of beam loss when installed outside of the DTL cavities [2], using a translating detector (PMT10) and two stationary detectors (PMT23, PMT24). The detectors are composed of a scintillator (EJ-208 or NE102), light guide, and photomultiplier tube. At the first two DTL cavities (750 keV to 37.5 MeV), we expect the scintillators to detect x-rays and gamma rays generated from beam loss and RF cavity emissions.

* This manuscript has been authored by Fermi Forward Discovery Group, LLC under Contract No. 89243024CSC000002 with the U.S. Department of Energy, Office of Science, Office of High Energy Physics.
† erinchen@fnal.gov

This work describes an upgrade to the scintillator-based detector system along the first two DTL cavities, bringing it to an operational-ready state for use in quadrupole magnet tuning and DTL alignment, and an initial investigation in beam loss patterns.

DETECTOR UPGRADES

The upgrade involves the installation of six additional stationary detectors (PMT11, PMT12, PMT13, PMT14, PMT21, and PMT22) along the sides of the first two DTL cavities (Fig. 1); digitization of the detector signals for integration with Fermilab's accelerator control system; improved signal processing and amplification of the detector signals; and an upgrade to the translating detector system for remote control and greater detector position precision.

Installation of the new detectors involved tuning the photomultiplier tube supply voltage to yield acceptable signal-to-noise and avoid saturation in the photomultiplier tube. Detectors are not absolutely calibrated and supply voltages range from 600 to 1100 V.

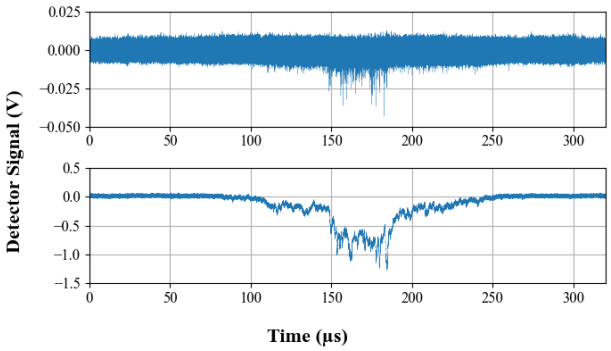


Figure 2: Signal from the PMT14 stationary detector. Raw data (top) and data processed with the amplification and filtering module (bottom) are shown from different 35.64 μs pulses, beginning at ~150 μs. More negative signal corresponds to greater beam loss.

Signal Amplification, Filtering, and Digitization

NIM modules were developed to amplify and filter the raw detector signal for digitization (Fig. 2). The modules contain three amplification stages, one non-inverting and two inverting, with an overall gain of 28 μA/V and a bandwidth from DC to 350 kHz. This bandwidth provides integration of the PMT pulses for the 10 MHz, ±5 V digitizers and reduces the 201 MHz Linac gallery RF noise by over 100 dB. A common-mode choke is used at each channel before the amplifier/filter stages to eliminate the ~500 Hz baseline wavelet noise produced by quadrupole power supplies. The choke was made from a compact nanocrystalline core for high permeability, with inductance per square turn

Content from this work may be used under the terms of the CC BY 4.0 licence (© 2022). Any distribution of this work must maintain attribution to the author(s), title of the work, publisher, and DOI.

ISBN: 978-3-95450-261-5 ISSN: 2673-7000 doi: 10.18429/JACoW-NAPAC2025-MOP097

MACHINE LEARNING-DRIVEN COMPUTATIONS OF 3D COHERENT SYNCHROTRON RADIATION *

C. Leon †, P. M. Anisimov, N. Yampolsky, A. Scheinker
Los Alamos National Laboratory, Los Alamos, NM, USA

Abstract

As electrons are accelerated, for instance, along curved paths in a magnetic field within a particle accelerator, they emit synchrotron radiation. When the wavelength of this radiation exceeds the bunch length, it becomes coherent, leading to significant alterations in the phase space distribution of the electrons. Simulating the effects of coherent synchrotron radiation is a highly resource-intensive task in accelerator physics. In this work, we demonstrate the application of a modified U-Net model to generate 3D wakefields from electron distributions. Our results demonstrate that the machine learning model can generate accurate wakefields much faster than traditional methods, while also effectively generalizing beyond its training dataset.

INTRODUCTION

Coherent Synchrotron Radiation (CSR) can substantially modify the electron distribution in circular orbits, as observed in systems like electron storage rings or bunch compressors. When the emitted wavelength, λ, is much larger than the bunch size, the bunch appears as a point source at λ-resolution, with all N_e electrons exhibiting nearly identical motion. As a result, the emitted radiation from these electrons is roughly in phase, leading to coherent addition of the radiation and an intensity scaling as $\mathcal{O}(N_e^2)$. This coherence effect can significantly alter the phase space distribution of the bunch. In the ultra-relativistic regime, this primarily manifests as energy loss in the tail and center of the bunch, while the head gains energy, contributing to an increase in the overall emittance.

The force experienced by an electron due to radiation emitted by other electrons in the past is termed the wakefield, $\mathrm{W}(\mathrm{r}, t)$. To calculate this wakefield, one must integrate the Lorentz force, $\mathrm{F}(\mathrm{r}, t)$, derived from the Liénard-Wiechert fields, over the past light cone:

$$\mathrm{W}(\mathrm{r}) = \int_{\triangle} d^3\mathrm{r}'\,\lambda(\mathrm{r}', t')\mathrm{F}(\mathrm{r}', t')\Big|_{ret.} . \qquad (1)$$

Here, $\triangle$ denotes the past light cone, the time variable in the integrand corresponds to the retarded time, and $\lambda(\mathrm{r}', t')$ represents the particle density. The computational burden of handling retarded time evaluations, along with the $\mathcal{O}(N_e^2)$ interactions (where N_e typically reaches 10^{10}), makes performing CSR calculations extremely resource-intensive. This challenge has led to the use of approximations, such as the 1D model [1]. However, even under the 1D approximation, incorporating CSR into simulations can increase processing time by a factor of ten [2]. As a result, traditional simulation methods often become too slow for certain use cases, particularly when optimizing accelerator designs through comprehensive parameter space exploration. Given the trend toward smaller bunch sizes in modern accelerators, the need for fast and precise 3D CSR modeling has become increasingly important, as this becomes important in constraints, shown in Table 1.

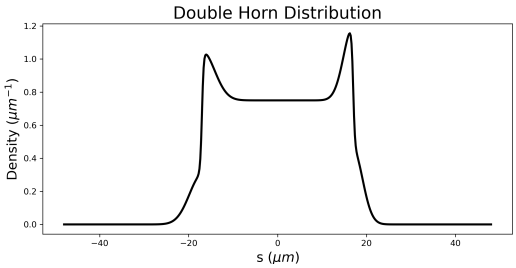


Figure 1: Double-Horn 1D Profile.

Machine learning (ML) can speed up simulations to provide real-time virtual diagnostics which can be used for real-time adaptive beam control. For example, in [3] the first approach to adaptive ML was demonstrated combining a deep learning with adaptive feedback [4] for automatic control of the longitudinal phase space of the LCLS FEL electron beam. They can also be used to speed up accelerator simulations [5, 6]. Convolutional neural network (CNN) computations utilize matrix multiplications and several parallelized operations and with modern GPU's, which are optimized for such tasks, can be performed rapidly. Hence, a CNN trained on CSR simulations data can lead to very fast computations.

Here, we take previous a CNN model trained to predict the fully 3D wakefields generated by electrons at steady-state [7] and see its generalization ability. Specifically, we investigate at how well it performs on multi-Gaussian in the test set. In addition, we test how well it performs on out of distribution

Table 1: Characteristics of Dataset

	Multi-Gaussian Dataset
Physical Range	$x_i \in (-48, 48)$ μm $i = s, x, y$
Distribution Attributes	Sum of 2 to 25 Gaussians $\mu_i \in (-12, 12)$ μm $\sigma_i \in (2, 12)$ μm

* Work was supported by the Los Alamos National Laboratory Laboratory Directed Research and Development (LDRD) DR project 20220074DR.
† cleon@lanl.gov

Content from this work may be used under the terms of the CC BY 4.0 licence (© 2022). Any distribution of this work must maintain attribution to the author(s), title of the work, publisher, and DOI.

ISBN: 978-3-95450-261-5 ISSN: 2673-7000 doi: 10.18429/JACoW-NAPAC2025-MOP099

X-RAY INSPECTION FOR NON-INVASIVE REAL-TIME BEAM DETECTION*

P. K. Roy†, Z. R. Harvey, E. Albin, S. Upadhyayula, S. G. Heppelmann
PLS directorate, Lawrence Livermore National Laboratory, Livermore, CA, USA

Abstract

We introduce a novel non-destructive X-ray diagnostic technique for real-time proton beam profile monitoring. The method utilizes high-energy X-ray photons (120–180 keV) in the Compton-dominated regime to probe the halo or electron environment surrounding the proton beam. Applied X-rays undergo Klein-Nishina Compton scattering with electrons from the beam-induced ionization and ambient gas, then pass through the beam pipe window to reach a position-sensitive detector. The scattered X-ray intensity distribution directly maps the spatial electron density, providing real-time proton beam profile and halo structure information.

INTRODUCTION

Conventional methods for measuring lower-energy charged particle beams—including Faraday cups [1,2], moving wire scanners [3], and scintillators [4,5]—are invasive techniques that become impractical for higher-energy beams exceeding material damage thresholds due to excessive heat deposition and radiation damage. Proton beams present unique detection challenges due to their large electromagnetic interaction cross-sections [6,7], characteristic energy deposition patterns (Bragg peak [8]), and distinct angular scattering distributions upon material interaction. The situation becomes more complex when beam halo [9,10] is present and the beam passes through varying vacuum conditions in a long transport beamline [11].

Alternative beam detection techniques using spill radiation monitoring [12,13] or beam position monitors [14–16] generate unwanted secondary particles [17,18] and present significant challenges for particle species identification. An established non invasive method—a laser wire scanner [19]—has been successfully employed to profile high energy beams by detecting up-scattered Compton photons off electrons as a laser is scanned across the beam. In this study, we investigate a new non-invasive X-ray inspection counterpart [20–22] as a novel approach for proton beam characterization. X-ray photons exhibit exceptional radiation hardness [23–25], offering substantial advantages over conventional optical or electronic detectors that suffer radiation damage [26–28] when exposed to high-intensity proton beams. However, X-ray scattering cross-sections for protons are significantly smaller than for electrons. In this work, X-ray interaction events are simulated to develop a comprehensive proton beam profile monitoring system.

CONCEPTUAL EXPERIMENTAL SETUP

Figure 1 illustrates the conceptual experimental configuration for non-invasive proton beam diagnostics. A bremsstrahlung X-ray source is positioned external to the vacuum beam tube, generating incident photons that interact with the stainless steel wall through photoelectric absorption and Compton scattering mechanisms. At X-ray energies above 100 keV, Compton scattering becomes the dominant interaction process since the photon energies significantly exceed the K-edge binding energies of steel constituents (Fe: 7.1 keV, Cr: 6.0 keV, Ni: 8.3 keV).

The dominant interaction regime is characterized by the dimensionless energy parameter $\alpha = E_\gamma/(m_e c^2)$, where E_γ is the photon energy and $m_e c^2 = 511\,\text{keV}$ represents the electron rest mass energy. Figure 2 illustrates the calculated dominance boundaries between different scattering mechanisms. In the classical regime ($\alpha < 0.1$, corresponding to $E_\gamma < 51\,\text{keV}$), the photoelectric effect dominates due to its strong energy dependence. The photoelectric cross-section scales [29] approximately as $\sigma_{\text{pe}} \propto Z^{4-5}/E_\gamma^{3-3.5}$, making it particularly significant for low-energy photons interacting with high-Z materials.

The transition regime ($0.1 \geq \alpha < 1$) is characterized by Compton scattering dominance, where the interaction probability becomes relatively independent of atomic number and depends primarily on electron density. At higher energies ($\alpha > 2$, corresponding to $E_\gamma > 1.02\,\text{MeV}$), pair production becomes energetically accessible and eventually dominates the interaction cross-section.

For effective penetration of the steel beam pipe, an X-ray source with energies exceeding 100 keV is required to operate within the Compton-dominated regime. The photon flux must be sufficiently high to ensure adequate interaction statistics for reliable measurements. Critical design parameters include detector placement distance, spatial resolution, and detection efficiency, which directly influence system sensitivity and measurement precision. These parameters have been studied through preliminary simulation.

X-RAY SCATTERING PHYSICS

When higher-energy X-rays are applied to conducting metals, the X-rays readily photo-ionize K-shell electrons from all constituent elements, resulting in strong X-ray absorption and the production of characteristic fluorescence X-rays from these elements. However, a significant portion of the primary X-rays (I_0) can still be transmitted through steel, depending on thickness as described by the Beer-Lambert law ($I = I_0 e^{-\mu x}$, where μ is the linear attenuation coefficient

* LLNL-PROC-2009413
† roy28@llnl.gov

Content from this work may be used under the terms of the CC BY 4.0 licence (© 2022). Any distribution of this work must maintain attribution to the author(s), title of the work, publisher, and DOI.

ISBN: 978-3-95450-261-5 ISSN: 2673-7000 doi: 10.18429/JACoW-NAPAC2025-MOP100

FIRST RESULTS OF THE SXMAP CAVITY FIELD EMISSION DETECTION SYSTEM FROM INSIDE A CRYOMODULE

P. Pizzol†, R. Afanador, J. D. Mammosser, D. Vandygriff, D Vandygriff, S. Gold
Oak Ridge National Laboratory, Oak Ridge, TN, USA

Abstract

Field emission (FE) has been one of the limiting factors in achieving high gradients in superconducting RF cavities. While the causes for FE are mostly known (contaminants on the inner cavity surface, dust, gases adsorbed…), identifying the exact location of field emitters has been a challenge. A detection system developed by Kyoto University has been developed to address this task, the sXmap system. This diagnostic device is made of inexpensive sensor strips that wrap around the iris of a multi cell SRF cavity that sense x-rays generated by FE. In this paper we will present the results obtained from a naked 6 cell SRF cavity in a vertical test configuration, and – for the first time – the results obtained from applying the sensor strips to an SRF cavity already installed inside a cryomodule in our test cave at ORNL – SNS.

INTRODUCTION

Field emission is widely considered one of the limiting factors in achieving high accelerating gradients in superconducting radio frequency cavities. As the demand for more powerful or more compact particle accelerators increases, so does the need to achieve higher gradients, and therefore the need to control and minimize field emission.

State of the art cavities technology nowadays is capable of minimizing field emission to a satisfactory level [1, 2], at least during cavity qualification in vertical tests. During the cavities installation in cryomodules though, the challenge has been preventing the field emission onset from shifting to a gradient below target specification, which reduces the overall total gradient of a LINAC.

After extensive beam operation, the field emission threshold for a cavity may shift due to contamination or degradation, also reducing the overall performance of the cryomodule by interacting with the surrounding cavities.

Since SNS has been operational since the late 2010s, new tools to quantify the degradation of cavity performance will be useful to help us plan for future machine intervention, both to preserve performance and beam availability for the user facilities. One of such tools, the sXmap system, is being deployed to better understand SNS cavity field emission and to validate our internal cavity reprocessing facilities [3, 4].

EXPERIMENTAL

The sXmap system was previously tested at ORNL on a 6 cells unjacketed single cavity. The lack of titanium jacket allowed us to install 7 sXmap strips, one for each iris of the cavity. As shown in [3], the strips were slid under the cavity stiffening rings.

This is of course not possible on a jacketed cavity, since the stiffening rings are inaccessible, limiting our test to the use of just 2 sXmap strips. The strips were positioned at each end of one of the cavities inside a high β SNS spare cryomodule. The specific cavity (cavity B) was chosen due to its history of poor performance and high field emission detected at ~8 MV/m. Figure 1 shows the strips wrapped around the beampipe as reasonably close as possible to the cavity under investigation.

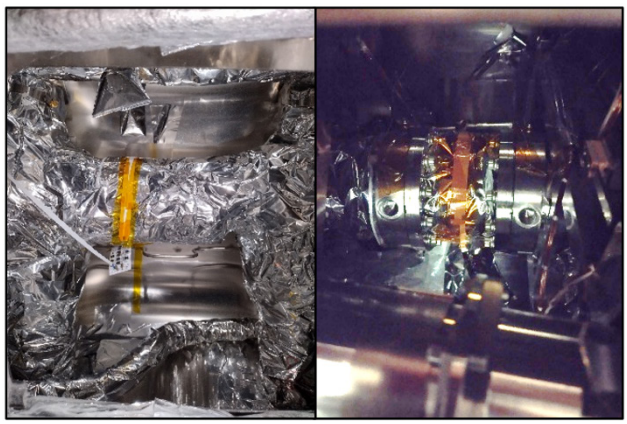


Figure 1: sXmap strips installed on spare cryomodule.

Due to limitations in the SNS cryomodule test cave RF system that doesn't allow to power multiple cavities at once, the cavity was individually energized – which proved beneficial in ruling out potential field emission being generated by other cavities in the cryomodule.

The cavity was tested up to a gradient of 10 MV/m, when the test was stopped due to the field emission reaching administrative limits for our test cave. It is worth noting that the cavity has a design specification of 15.5 MV/m, which it is not able to achieve. While the test was running, the sXmap system was logging data as shown in Fig. 2.

RESULTS

High β Cryomodule Cavity Test Results

Figure 2 shows the data collected by the sXmap system strips during the cavity test at different accelerating gradients. The data related to gradients below 5.5 MV/m are not reported due to the lack of x-ray emission. sX-01 identifies the strip placed downstream of the cavity in respect to the beam direction, while sX-02 identifies the strip upstream.

† pizzolp@ornl.gov

Content from this work may be used under the terms of the CC BY 4.0 licence (© 2022). Any distribution of this work must maintain attribution to the author(s), title of the work, publisher, and DOI.

ISBN: 978-3-95450-261-5 ISSN: 2673-7000 doi: 10.18429/JACoW-NAPAC2025-MOP102

IMPEDANCE MODELING OF IN-VACUUM UNDULATOR WITH GAUSSIAN PROCESS

Minghao Song*, Aamna Khan, Victor Smaluk, Guimei Wang, Michael Seegitz
Brookhaven National Laboratory, Upton, NY, USA

Content from this work may be used under the terms of the CC BY 4.0 licence (© 2022). Any distribution of this work must maintain attribution to the author(s), title of the work, publisher, and DOI.

Abstract

The impedance of in-vacuum undulators (IVUs) significantly affect the broadband impedance and, consequently, the beam dynamics in storage rings. During the IVU design phase, numerous iterative discussions between physicists and engineers are required, often involving extensive simulations of the complete 3D geometry, a few meters long, using limited computational resources. In this paper, we propose training a Gaussian process model with limited simulation data to emulate the physical model. We compare the predictions of the trained model to the simulation data and explore its application in optimizing the IVU design.

INTRODUCTION

In-vacuum undulator (IVU) [1], in which magnet arrays are placed inside the vacuum chamber, is a key component for producing high-brightness photon beams in storage ring light sources [2–4]. By placing the undulator inside the vacuum, it allows a smaller vertical gap and more periods to generate shorter wavelength radiation and higher photon flux. However, a smaller gap will significantly influence the total coupling impedance of the storage ring [5], resulting in instabilities in the motion of the electron beam. Therefore, the design of an IVU needs to be optimized to minimize the impedance effects.

The IVU exhibits a complex geometry including tapers and transitions between cross sections. Due to its structural complexity, there are generally no accurate analytical theories to calculate its contribution to total impedance. As a result, it usually computes impedance through a comprehensive 3D simulation, which requires very expensive computation resources, including many number of working nodes, long processor time, and extensive computation memories. In particular, more computation is required when simulating the wakefields induced by short (e.g., a few millimeters) electron bunches.

The conventional way to design an IVU involves many back-and-forth conversations between engineers and accelerator physicists. For example, accelerator physicists calculate the impedance and provide feedback to engineers to make necessary changes to IVU geometry. Consequently, due to the expensive simulated computation and file exchange between engineers and accelerator physicists, it usually takes a long time before the structure of IVU is finalized. In addition, because the impedance of the IVU is affected by multiple parameters, therefore, it is difficult to find the best structure by manually changing the size of the IVU.

* msong1@bnl.gov

In this work, we propose a machine learning-based surrogate model to replace the computationally expensive IVU model, enabling significantly faster impedance calculations under varying IVU geometries. In this study, Gaussian process regression is used for model training due to the limited availability of data.

IN-VACUUM UNDULATOR

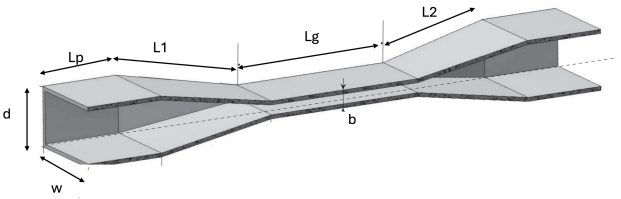


Figure 1: Simplified geometry of closed gap in-vacuum undulator.

Figure 1 shows the simplified geometry of the closed-gap in-vacuum undulator. The simplified IVU features a taper transition from the center to the ends, introducing additional complexity to the impedance computation. Table 1 summarizes the parameters that determine the simplified IVU and their valid ranges. To train the surrogate model, a total of 100 data points are randomly sampled from the parameter space, each parameter being constrained to integer values within its specified range due to engineering considerations. These data points serve as input features for the model.

Consequently, the output used for the model training is the kick factor, which quantifies the magnitude of the transverse kick experienced by the beam. Given the transverse wake function, the kick factor is defined as follows [5]:

$$k_y = \frac{1}{\sqrt{2\pi}\sigma_s} \int_{-\infty}^{\infty} W_y(s) e^{-s^2/2\sigma_s^2} ds, \qquad (1)$$

where σ_s is the rms length of a Gaussian electron bunch, and $W_y(s)$ is the vertical wake potential.

Table 1: Parameters of the Simplified IVU and Their Valid Ranges

Parameters	Range (mm)
b	5-25
d	20-30
w	50-100
L_p	50-100
L1, L2	150-300
L_g	500-800

ISBN: 978-3-95450-261-5 ISSN: 2673-7000 doi: 10.18429/JACoW-NAPAC2025-MOP103

ONLINE OPTIMIZATIONS OF NSLS-II LINAC AND LINAC-TO-BOOSTER BEAM LINES USING MACHINE LEARNING METHODS

Minghao Song*, Guimei Wang, Yoshiteru Hidaka, Xi Yang
Brookhaven National Laboratory, Upton, NY, USA

Content from this work may be used under the terms of the CC BY 4.0 licence (© 2022). Any distribution of this work must maintain attribution to the author(s), title of the work, publisher, and DOI.

Abstract

The NSLS-II is a cutting-edge 3 GeV storage ring light source in the world. The electron beam is initially accelerated in a linear accelerator to an energy of 170 MeV and subsequently accelerated in a booster synchrotron to a beam energy of 3 GeV. Therefore, the performance of the Linac and the Linac-to-Booster beam lines is imperative for good beam injection to the booster. Online optimization is an effective solution to improve accelerator performance when there is degradation. This paper presents the results of online optimization employing a machine learning method.

INTRODUCTION

Linear accelerators (Linacs), Linac-to-booster transport lines, upstream boosters, and storage rings are essential components in modern synchrotron radiation facilities. Achieving optimal injection performance from the Linac to the booster requires precise control of many machine parameters, including buncher phase, RF phases and amplitudes, and corrector magnet strengths. However, because of the lack of accurate physics models for the Linac and Linac-to-booster beamlines, along with the effects of drifts and environmental disturbances, it is often difficult for simulations to accurately reflect the real behavior of the machine. Therefore, a practical method for improving the performance of the actual machine is needed.

Online optimization has been increasingly used in the accelerator community to improve machine performance. These optimization algorithms adjust machine parameters in real time based on direct measurements from the accelerator, allowing performance improvements to be made directly and efficiently.

Traditional algorithms, such as robust simplex [1], robust conjugate direction search (RCDS) [2], non-dominated sorting genetic algorithm II (NSGA-II) [3], and particle swarm optimization (PSO) [4], have been widely used for online accelerator tuning [5, 6]. However, due to their stochastic nature, these algorithms are often inefficient, requiring a large number of objective function evaluations to reach the global optimum. This inefficiency arises because the trial solutions generated by these methods do not fully utilize the information contained in the previously sampled data from the parameter space.

In this study, we used the multi-generation Gaussian process optimizer (MG-GPO) [7] for online optimization of problems with complex parameter spaces. MG-GPO was originally developed for design optimization, which uses posterior Gaussian process regression models [8] to filter for good trial solutions in an iterative process similar to NSGA-II [3] or PSO [4]. It has been successfully applied to storage ring nonlinear lattice design optimization [9] and online accelerator optimization [10]. This method can significantly reduce the tuning time and improve operational reliability.

* msong1@bnl.gov

OPTIMIZATION METHODS

Particle Swarm Optimization

In particle swarm optimization, each solution is represented by a particle's position, $\mathbf{x}_i(t)$, which is updated by adding a velocity increment, $\mathbf{v}_i(t+1)$. The iterative update process is described in more detail by the following equations [4]:

$$\mathbf{x}_i(t+1) = \mathbf{x}_i(t) + \mathbf{v}_i(t+1), \quad (1)$$

$$\mathbf{v}_i(t+1) = \omega\,\mathbf{v}_i(t) + c_1 r_1 \left(\mathbf{pbest}_i(t) - \mathbf{x}_i(t)\right) + c_2 r_2 \left(\mathbf{gbest}(t) - \mathbf{x}_i(t)\right), \quad (2)$$

where $\mathbf{x}_i(t)$ and $\mathbf{x}_i(t+1)$ represent the positions of ith particle at generation t and $t+1$, respectively. The parameter $\mathbf{v}_i(t+1)$ is the velocity-based correction that determines the change in position between two successive generations. According to Eq. (2), the velocity update is influenced by three terms. The first term, known as the inertia influence, is scaled by the inertia weight ω, which determines the contribution rate from the previous velocity. The second term, referred to as the cognitive influence, depends on the distance between a particle's personal best position **"pbest"** and its current position. The third term, called the social influence, reflects the distance between the global best position **"gbest"** found by the swarm and the current position. The coefficients c_1 and c_2 are called the cognitive and the social learning factors, respectively. In addition to the hyper-parameters ω, c_1 and c_2, the random variables r_1 and r_2 also have an impact on the optimization results.

Multi-Generation Gaussian Process Optimizer

The multi-generation Gaussian process optimizer (MG-GPO) updates a population with a fixed number of solutions from generation to generation. Compared to traditional stochastic optimization algorithms such as NSGA-II [3] and PSO [4], MG-GPO enables the pre-selection of candidates from a large set of trial solutions using Gaussian process (GP) models, which is less expensive for evaluations and could guarantee the offspring solutions outperform the previous ones [7]. As a result, MG-GPO can be effectively used for online optimization problems where beam study time is limited and the objective evaluation can be time consuming.

ISBN: 978-3-95450-261-5 ISSN: 2673-7000 doi: 10.18429/JACoW-NAPAC2025-TUYD01

LASER ASSISTED CHARGE EXCHANGE INJECTION AT THE SPALLATION NEUTRON SOURCE*

F. Lin†, A. Aleksandrov, S. Cousineau, N. Evans, T. Gorlov, Y. Liu, A. Menshov, A. Oguz, A. Shishlo, A. Zhukov, Oak Ridge National Laboratory, Oak Ridge, TN, USA
Luke Chapman, Tennessee Tech University, Cookeville, TN, USA

Content from this work may be used under the terms of the CC BY 4.0 licence (© 2022). Any distribution of this work must maintain attribution to the author(s), title of the work, publisher, and DOI.

Abstract

Laser Assisted Charge Exchange (LACE) technology is being developed to replace foil-based charge exchange injection in high power H^- accelerators. Replacing the foil with field-stripping has the potential to significantly reduce injection losses, making LACE a promising solution for future high-intensity multi-megawatt power H^- beams. While the LACE technique has been successfully demonstrated, it has not yet been implemented in a configuration suitable for beam injection into a ring. This paper will present recent progress on evaluation of High Energy Beam Transport (HEBT) optics for providing required beam for LACE, design of LACE for the Spallation Neutron Source (SNS) ring injection and simulation of LACE-produced circulating beam in the SNS ring to explore the beam dynamics.

INTRODUCTION

A Laser Assisted Charge Exchange (LACE) injection [1-3] has been under development in the SNS in the past two decades. In this concept, negative ions of hydrogen H^- are stripped of their electrons, $H^- \rightarrow p^+ + 2e^-$, through relatively strong magnetic fields and powerful lasers. A three-step LACE scheme is as shown in Fig. 1. H^- beam is stripped of one electron due to its small binding energy, $H^- \rightarrow H^0 + e^-$, through the first magnet. A laser with an exact wavelength is utilized to excite the remaining electron from the ground state to an excited state, $H^0 \rightarrow H^{0*}$. Then H^{0*} is stripped of the second electron when it passes through the second magnet. Early proof-of-principle experiments have been carried out on the experimental stand in the SNS LINAC and demonstrated high stripping efficiency of ~90% for a single pass beam with a duration of ns to us [4-6].

With the recent successful commission of Proton Power Upgrade (PPU) in the SNS, the H^- beam energy has been upgraded from 1 GeV to 1.3 GeV. This energy upgrade offers new opportunities to optimize the configurations of laser and beam, and their parameters achieve high stripping efficiency with reduced laser power requirements. A new experimental vessel has been fabricated and installed in the HEBT line in the SNS for testing three choices of laser light, UV, green-green and green-IR. Preparation for the ongoing LACE experiments have been discussed in [7].

Along with the ongoing experimental optimization of laser and beam parameters for LACE, progress has also been made in several related areas: evaluating the capability of HEBT to deliver the desired beam parameters for LACE, designing the LACE injection system for the SNS ring, and performing simulations of LACE-produced beam in the SNS to study its dynamics. This paper presents our recent results in each of these areas.

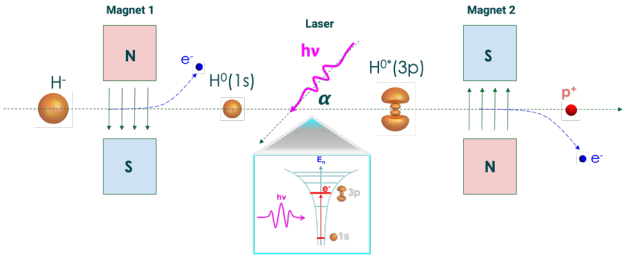


Figure 1: Scheme of a three-step LACE concept.

LACE INJECTION DESIGN

The SNS ring injection region is designed to accommodates foil charge exchange injection and consists of four chicane dipole magnets along with four sets of horizontal and vertical kicker magnets for a turn-by-turn painting injection. The injection region layout after the SNS Proton Power Upgrade (PPU) is shown in Fig. 2, with only about 63 cm available space for a LACE injection scheme. Figure 3 shows a schematic drawing of the injection region, where the foil has been replaced by the LACE system. The following sections provide a detailed description of recent progress in integrating the LACE system into the SNS ring injection region.

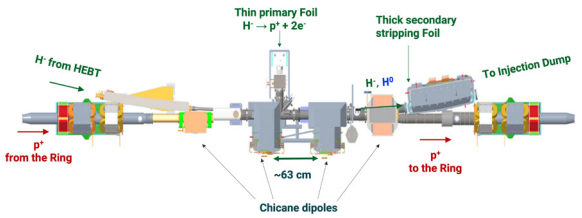


Figure 2: Layout of the SNS injection region after the PPU project.

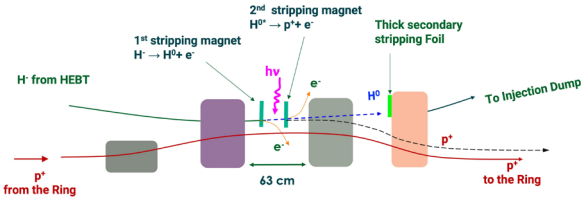


Figure 3: Schematic drawing of the SNS injection region with a LACE system.

ISBN: 978-3-95450-261-5 ISSN: 2673-7000 doi: 10.18429/JACoW-NAPAC2025-TUBD01

SNS SECOND TARGET STATION PROTON ACCELERATOR SHIELDING DESIGN AND ACCIDENT SCENARIO EVALUATION*

W. C. de Wet†, J. H. McLaurin
Oak Ridge National Laboratory, Oak Ridge, TN, USA

Content from this work may be used under the terms of the CC BY 4.0 licence (© 2022). Any distribution of this work must maintain attribution to the author(s), title of the work, publisher, and DOI.

Abstract

Design of the Second Target Station (STS) for Oak Ridge National Laboratory's (ORNL) world-class Spallation Neutron Source (SNS) Facility is underway. The STS will provide an optimized high-brightness cold neutron source for up to 18 new beamlines, both expanding and complementing the current neutron science capabilities at ORNL. The Ring-to-Second-Target beam Transport (RTST) will deliver a 700 kW beam of 1.3 GeV protons at 15 Hz to a rotating target composed of individual water-cooled tungsten wedge segments. Spanning roughly 220 m, the RTST will consist of 56 quadrupole focusing magnets and 15 dipole bending magnets. Installation and maintenance of large beamline components will be facilitated via a truck access tunnel. While the proton accelerator is in operation, the truck access tunnel entrance is shielded by an arrangement of stacked steel shielding blocks. This shielding design must account for both normal operating conditions as well as design-basis accident scenarios. Provided in this work is an analysis of the accelerator truck access tunnel shielding design for a worst-case full beam loss accident scenario.

INTRODUCTION

The STS is a planned upgrade to the SNS at ORNL that will provide a high-brightness cold neutron source for up to 18 new beamlines. A 1.3 GeV, 700 kW proton beam will be delivered from the SNS accumulator ring via the 220 m RTST line, which incorporates focusing and bending magnets as well as extensive shielding. A dedicated truck access tunnel allows installation and removal of large components; during operations its entrance is shielded by stacked steel blocks, concrete bookends, and an overhead lintel to limit radiation streaming.

The most severe design-basis accident considered is a dipole magnet failure near the tunnel opening, directing the full proton beam into the RTST tunnel wall. Although the credited Personnel Protection System (PPS) will terminate the beam within 2 s [1], the shielding must ensure that potential radiation exposures in accessible areas remain below the 11 mrem design criterion.

This work presents a radiation transport analysis of the truck access tunnel shielding for the RTST under the worst-case full-beam-loss accident scenario. The analysis evaluates the labyrinth geometry, stacked steel shielding, and concrete structures using Monte Carlo transport methods to predict effective dose rates in the surrounding accessible areas. The results are intended to verify compliance with the STS radiation safety design goals and to inform any necessary design refinements prior to construction.

SHIELDING DESIGN CRITERIA

The RTST truck access tunnel, labyrinth, and stacked steel shield block design is being evaluated for a full beam loss accident. The design objective is that the ensemble of shielding design components mitigates human radiation exposures in generally accessible areas to less than 11 mrem over a period of 2 s [1, 2].

METHODOLOGY

In this analysis, a geometry representative of the RTST truck access tunnel was constructed. Radiation transport calculations were then performed to propagate a loss-of-beam source term throughout this geometry. Variance reduction methods were employed to converge the expected radiation exposure quantities in the vicinity of the RTST truck access tunnel labyrinth and the stacked configuration of steel shielding blocks.

Geometry

The geometry for this work is built using constructive solid geometry (CSG) format. The major components included in this geometry are the RTST tunnel, truck access tunnel, the labyrinth, the stacked steel shielding blocks (see Fig. 1).

The RTST tunnel contains the beamline and magnet components. The truck access tunnel branches from the RTST tunnel and opens to the exterior of the main shielding berm structure. A labyrinth between the end of the truck access tunnel and the exterior of the primary berm shielding structure facilitates personnel access to the RTST.

Directly outside of the truck access tunnel sits a collection of large, stacked steel blocks that shield the exterior environment from the radiation produced within the RTST tunnel. The steel shielding blocks are accompanied by two poured-in-place concrete bookends as well as a lintel overhead (see Fig. 2). The bookends and lintel mitigate radiation streaming from the gap between the stacked shielding and the exterior face of the truck access tunnel. The steel shielding blocks are in place during beam operations and is removable to bring equipment into the RTST tunnel.

* This manuscript has been authored by UT-Battelle, LLC, under contract DE-AC05-00OR22725 with the US Department of Energy (DOE). The US government retains and the publisher, by accepting the article for publication, acknowledges that the US government retains a nonexclusive, paid-up, irrevocable, worldwide license to publish or reproduce the published form of this manuscript, or allow others to do so, for US government purposes. DOE will provide public access to these results of federally sponsored research in accordance with the DOE Public Access Plan (http://energy.gov/downloads/doe-public-access-plan).
† dewetwc@ornl.gov

ISBN: 978-3-95450-261-5 ISSN: 2673-7000 doi: 10.18429/JACoW-NAPAC2025-TUBD02

DRAMATICALLY REDUCING BEAM LOSSES AT BNL 200 MeV H- LINAC*

D. Raparia†, G. Atoian, T. Lehn, V. Lodestro, J. Ritter
Brookhaven National Laboratory, Upton, NY, USA

Abstract

The Brookhaven National Laboratory (BNL) 200 MeV Drift Tube Linac (DTL) operates at 6.67 Hz, delivering H^- beams for both the polarized proton program at RHIC and isotope production at BLIP. Over the past two decades, targeted upgrades—especially within the low-energy and medium-energy beam transport (LEBT and MEBT) sections—have dramatically enhanced linac performance. Beam transmission for high-current isotope production has improved by more than 100%, while transverse emittance has been halved for polarized proton operation. Moreover, beam losses have been reduced by three orders of magnitude, significantly lowering radiation levels and enabling higher current delivery. These upgrades translate into increased beam intensity to BLIP and superior quality and stability to RHIC, marking a transformative step for the linac's long-term operational reliability and scientific output.

INTRODUCTION

The Brookhaven National Laboratory (BNL) 200 MeV Drift Tube Linac (DTL) has been in continuous operation since its commissioning in November 1970. Originally designed for 100 mA peak current, 200 μs pulse lengths, and 10 Hz repetition rate, the linac has undergone extensive upgrades over five decades to meet the evolving demands of the BNL accelerator complex. [1] Today, the linac delivers H^- beams at 6.67 Hz and 200 MeV in support of two primary programs: the polarized proton program at the Relativistic Heavy Ion Collider (RHIC) and the Brookhaven Linac Isotope Production (BLIP) facility. These programs impose distinct operational requirements: **RHIC Program:** 200 MeV energy, ~400 μA current, 300 μs pulse length; primary goals are to maximize polarization and minimize transverse emittance. **BLIP Program:** 66- 200 MeV energy range, ~600 μs pulse length, beam current up to 60 mA; emphasis is on uniform beam delivery to the target with minimal beam losses. This paper highlights the beam loss performance of the linac, emphasizing recent upgrades that have enabled high-current, low-loss operation critical for both scientific research and medical isotope production.

BNL 200 MeV LINAC HISTORY

Initially designed for 100 mA proton beams with low emittance, early designs used a 750 keV C-W pre-injector and an 8.5 m beamline with eight triplets and two bunchers. Particle simulations revealed that matching and quadrupole focusing were critical in limiting emittance growth, primarily occurring in the first tank (10 MeV). Capture efficiency was ~65-70%. [2,].

In 1982 switching to H^- operation increased the intensity in the AGS, while decreasing the linac output.

With the RFQ integration in 1989, the new LEBT and 7 m MEBT introduced choppers, diagnostics, and dipoles for polarized beam handling. However, beam quality suffered due to constraints on longitudinal beam size, which expanded to ±120° near the bunchers. This led to sensitivity to RF amplitude/phase at 200 MeV, although no clear transmission improvement was observed. [3, 4]

The 1996 linac RF and power systems were upgraded to 7.5 Hz, 550 μs pulses [5]. The LEBT was shortened, and solenoids repositioned to better match into the RFQ. These changes improved RFQ transmission by 10% and reduced emittance by 20%. To address MEBT matching issues, a PMQ was added at the RFQ flange. Combined with repositioned diagnostics and quadrupoles, this led to 50% better transmission and 45% lower emittance, though Tank 1 still exhibited ~40% beam losses [6].

In 2000, the OPPIS polarized source was integrated, and the MEBT dipole replaced with a spin rotator [7]. In 2008, a major reconfiguration reduced MEBT to 70 cm and adjusted the LEBT to ~4.5 m [8]. This included collimators, choppers, neutralization via Xe gas, and additional steerers and solenoids. Resulting losses dropped to ~30-35%, and transverse emittance was reduced by 65% [9].

A 2010 redesign shifted the high-intensity source upstream with a 45° bend. The new 2 m LEBT included two solenoids, quadrupoles, steerers, a dipole, and a chopper. Transmission improved by 30%, raising BLIP average current from 80 to 110 μA [10, 11]. A second source was added in 2019 at -45° [12].

These upgrades yielded a 25% reduction in RHIC emittance at collision energy and widespread loss reduction. Figure 1 shows the present layout of the LEBT and MEBT, two unpolarized and polarized source sending beam to single RFQ. source can be change at rate of 10 Hz.

Now linac is delivering the highest average current to BLIP while maintaining minimum losses since it was built in 1970. Figure 2 summarizes maximum average intensity of the BNL H^- linac over 55 years.

Figure 3 shows a comparison of the beam footprint at the BLIP target before and after the upgrade after 2010. Radiation due to beam losses has been reduced everywhere, compared to before the upgrade.

*Work supported by U.S. Department of Energy
†raparia@bnl.gov

Content from this work may be used under the terms of the CC BY 4.0 licence (© 2022). Any distribution of this work must maintain attribution to the author(s), title of the work, publisher, and DOI.

ISBN: 978-3-95450-261-5 ISSN: 2673-7000 doi: 10.18429/JACoW-NAPAC2025-TUBD03

SIMULATION MODELING OF FIRST-TURN LOSSES FOR THE LANSCE PROTON STORAGE RING (PSR)

J. T. Yoskowitz*, A. Alexander, E. Henestroza, E.-C. Huang, J. W. Lewellen, C. E. Taylor, H. Xu
Los Alamos National Laboratory, Los Alamos, NM, USA

Content from this work may be used under the terms of the CC BY 4.0 licence (© 2022). Any distribution of this work must maintain attribution to the author(s), title of the work, publisher, and DOI.

Abstract

The LANSCE proton storage ring (PSR) accumulates 795 MeV protons into a short, 290 ns pulse over 625 µs, or about 1745 turns. One of the primary limitations for maximum proton pulse intensity is beam loss between the stripper foil and the first dipole magnet downstream of the foil. One of the major beam losses in this region, referred to as "first-turn losses," are due to incomplete stripping of the injected H^- beam into H^+ during the injection process. H^- that foil strip into H^0 can either pass through the first dipole magnet to the injection beam dump, or get Lorentz stripped by the magnetic field of the dipole or the defocusing quadrupole magnet between the foil and dipole. First-turn losses not only result in a lower extracted proton pulse intensity but can also result in longer maintenance periods following beam runs due to the activation of PSR components, which require "cooling down" prior to any hands-on maintenance. In this work, a detailed particle-tracking model of the PSR injection system was created using the simulation package General Particle Tracer (GPT) using three C++ custom elements created to simulate foil scattering, foil stripping, and Lorentz stripping. The simulation model will be described, and the simulation results will be presented at the conference.

INTRODUCTION

The LANSCE PSR is a 90.2 m accumulator ring that delivers intense, 290 ns proton pulses at 795 MeV to the Manuel Lujan Neutron Scattering Center and the Weapons Neutron Research (WNR) Facility for spallation neutron experiments [1]. These experiments require the proton pulses to have high intensity to optimize the signal-to-noise ratio [2,3]. Historically, the intensity of the proton pulses has been on the order of 10^{13} protons/pulse [4]. However, the maximum intensity achievable by the PSR is limited primarily by beam loss. The main sources of beam loss include first-turn losses — losses during PSR injection [5], emittance growth (i.e., beam scraping) [6,7], losses during extraction [4], and beam instabilities [8].

First-turn losses occur due to incomplete foil stripping of the injected H^- beam. If H^- strip into H^0 instead of H^+, or if the H^- miss the foil entirely, they are either transported to the injection beam dump or are Lorentz stripped by the B-field and are lost. These losses have been estimated to account for about half of the total losses in the ring and therefore are of primary concern [4]. Beam losses can cause equipment damage and the activation of beamline components, which lead to long maintenance periods following beam operations. Several upgrades to the PSR have been proposed to reduce first-turn losses, such as introducing a magnetic field to Lorentz strip H^0 immediately after the foil [9], or modifying the foil material to improve its stripping efficiency [10, 11]. However, predicting the effectiveness of these mitigation techniques requires a detailed simulation model.

In this work, particle-tracking simulations of the PSR injection system were created within the framework of the simulation package General Particle Tracer (GPT) [12]. To model foil stripping, foil scattering, and Lorentz stripping, C++ custom elements were developed and implemented in the simulations. The GPT model and the simulation results are described in the following sections.

PSR INJECTION SYSTEM AND FIRST-TURN LOSSES

The injection system of the PSR is shown in Fig. 1. A 795 MeV H^- beam composed of 625 µs pulses, each of which are composed of 290 ns "minipulses," are injected into the PSR at 20 Hz. A 6.8° dipole magnet bends the H^- beam such that it joins with the recirculating H^+ beam at the foil. The H^- undergoes foil scattering and foil stripping into H^0 and H^+. When the H^-, H^0, and H^+ reach the first of two 16.2° dipole magnets there are several possibilities:

1. H^- that miss the foil are Lorentz stripped into H^0 or H^+ and are lost on the beam pipe.
2. H^0 in the ground state (n=1) or first excited state (n=2) pass straight through the two dipole magnets and are transported to a beam dump.
3. H^0 in higher excited states (n>2) can undergo Lorentz stripping within the dipole magnet into H^+. Because these H^+ are sufficiently displaced from the recirculating H^+ beam to be outside the PSR acceptance region, they are lost [13].
4. H^+ are bent towards the PSR and begin recirculation around the ring.

Beam losses due to #1-3 comprise first-turn losses and account for about 2-3% of the injected beam.

FIRST-TURN LOSS SIMULATIONS

To explain and predict the effect of using different stripper foil parameters on first-turn losses, a simulation model of the PSR injection system was created using GPT. In each simulation, a 795 MeV H^- pulse, representing the injected H^- beam, is tracked from 0.1 m upstream of the stripper foil to 2 m past the two 16.2° dipoles, modeled using magnetic field maps, after the foil. The H^- pulse is composed of 10^4

* jty@lanl.gov

ISBN: 978-3-95450-261-5 ISSN: 2673-7000 doi: 10.18429/JACoW-NAPAC2025-TUBN01

FLAT BEAM PWFA THEORY AND EXPERIMENT AT AWA

P. Manwani*, Y. Kang, J. Mann, G. Andonian, B. Naranjo, J. B. Rosenzweig
UCLA, Los Angeles, CA, USA
A. Ody, P. Piot, D. Scott, E. Wisniewski, W. Liu, J. Power
Argonne National Laboratory, Lemont, IL, USA
N. Majernik, SLAC National Accelerator Laboratory, Menlo Park, CA, USA
K. Huang, Kansai Institute for Photon Science, Kizugawa-city, Kyoto, Japan

Content from this work may be used under the terms of the CC BY 4.0 licence (© 2022). Any distribution of this work must maintain attribution to the author(s), title of the work, publisher, and DOI.

Abstract

In plasma wakefield acceleration, when the driver beam is denser than the plasma, there is an expulsion of the plasma electrons from the beam channel, resulting in an ion filled cavity. This cavity is called a bubble and has been well studied for round beams which result in an axisymmetric bubble. However, transversely asymmetric (flat) beams create elliptical bubbles, which have key differences. They offer asymmetric but linear focusing, with non-uniform acceleration, which is distinct from the axisymmetric case. We discuss the theory on beam-plasma interaction and present an experimental study in the context of the Argonne Wakefield Accelerator (AWA) which has capabilities for flat beams.

INTRODUCTION

Particle beams with asymmetric transverse emittances and profiles can be used to drive asymmetric plasma wakefields. The axisymmetric blowout regime has been extensively studied in the context of plasma wakefield acceleration [1–3]. Here, we discuss the formalism for the elliptical blowout created by the beam and show that the focusing forces that are transversely asymmetric. We utilize the ellipticity of the plasma ion cavity to model the beam evolution of the flat beam driver in a plasma capillary (developed at UCLA) [4], in preparation for the flat beam plasma wakefield acceleration (PWFA) experiment at the AWA. [5, 6].

FLAT BEAM PWFA INTERACTION

The theory of elliptical blowouts, created when the flat beam driver is denser than the plasma density, has been documented in detail in Ref. [7], which shows that the transverse wakefields are linear and depend on the semi major (a_p) and minor axes (b_p) of the transverse ellipse. We can write down the transverse wakefields as

$$\begin{aligned} W_x &= E_x - B_y = x\left(\frac{b_p^2}{a_p^2+b_p^2}\right) = x\left(\frac{1}{\alpha_p^2+1}\right) \\ W_y &= E_y + B_x = y\left(\frac{a_p^2}{a_p^2+b_p^2}\right) = y\left(\frac{\alpha_p^2}{\alpha_p^2+1}\right). \end{aligned} \tag{1}$$

Here we define $\alpha_p = a_p/b_p$ as the ellipticity of the blowout, where a_p and b_p are the semi-major and semi-minor axes of the ion cavity, respectively. In contrast to the axisymmetric case ($\alpha_p = 1$), the transverse focusing forces differ in the x and y directions, resulting in distinct betatron wavenumbers in each plane. This asymmetry modifies the beam-matching conditions that are needed for emittance preservation [8], requiring that the beam sizes and divergences be adjusted in the two transverse directions to maintain matched propagation through the plasma. The new matched beta functions are

$$\beta_x = \sqrt{(1+\alpha_p^2)\gamma}\,k_p^{-1} \tag{2}$$

$$\beta_y = \sqrt{\left(1+\frac{1}{\alpha_p^2}\right)\gamma}\,k_p^{-1}, \tag{3}$$

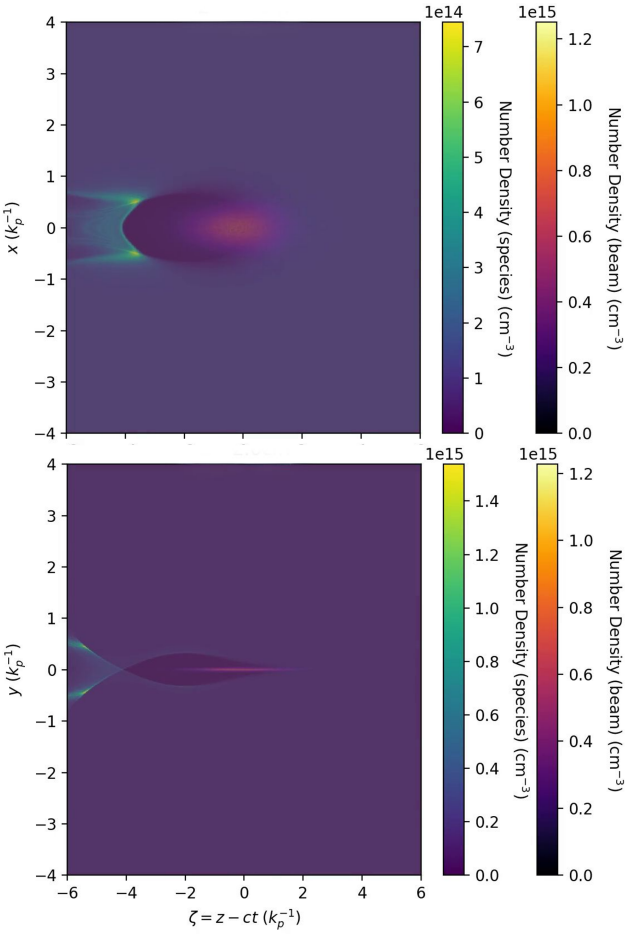


Figure 1: Asymmetric plasma blowout created by the flat beam driver, using the parameters in Table 1.

* pkmanwani@gmail.com

ISBN: 978-3-95450-261-5 ISSN: 2673-7000 doi: 10.18429/JACoW-NAPAC2025-TUBN03

PICOMETER-SCALE EMITTANCE AND SPACE CHARGE EFFECTS IN NANOSTRUCTURED PHOTOCATHODES

A. Ullattuparambil*, M. M. Rizi, P. P. Owusu, S. Karkare
Arizona State University, Tempe, AZ, USA
M. Kaemingk, Los Alamos National Laboratory, Los Alamos, NM, USA
A. Bartnik, M. Gordon, C. Abbamonte, S. Levenson, J. Maxson
Cornell University, Ithaca, NY, USA

Abstract

Generation of ultra-low emittance electron beams with high brightness is critical for several applications such as ultrafast electron diffraction, microscopy, and advanced accelerator techniques. By leveraging the differences in work function and electronic structure between different materials, we enabled spatially localized photoemission, resulting in picometer-scale emittance from a flat photocathode. We also investigated space charge effects by measuring how the emission spot size, as measured in a photoemission electron microscope, changes with the number of electrons emitted per laser pulse. When more than one electron is emitted simultaneously, Coulomb repulsion causes a substantial broadening of the observed source size, enabling us to investigate the limitations imposed by vacuum space charge forces during pulsed photoemission. Our results highlight the potential of nanoscale photoemitters as high-brightness electron sources and offer new insights into electron correlations that emerge after ultra-fast photoemission.

INTRODUCTION

Femtosecond-scale pulsed electron sources are indispensable for probing atomic motion with sub-ångström spatial resolution in ultrafast electron diffraction and microscopy (UED/UEM) [1–4]. The normalized transverse emittance sets the fundamental limit on the attainable spatial resolution in these applications, motivating ongoing efforts to achieve picometer-level emittance directly at the photocathode. Although field-emission cathodes can deliver sub-picometer emittance, they operate in continuous mode and suffer from poor survivability under the high electric fields of modern accelerator structures. Consequently, photoemission remains the most viable approach for generating high-brightness, ultrafast electron pulses compatible with high-field accelerator environments.

The normalized transverse emittance of an electron bunch is given by [5]:

$$\varepsilon_{n,x} = \sigma_x \sqrt{\frac{\mathrm{MTE}}{m_e c^2}} \tag{1}$$

where σ_x is the root-mean-square (RMS) emission area and MTE is the mean transverse energy of the emitted electrons. This expression illustrates that the emittance can be reduced by minimizing either the MTE or the emission spot size.

The MTE reflects the transverse momentum spread of the photoemitted electrons and is mainly determined by the photocathode material, its band structure, physical and chemical roughness, and the photon energy of excitation light. According to the Dowell-Schmerge model, the MTE of emitted electrons varies linearly with the excess energy, that is, the difference between the photon energy and the material's work function [6]—and approaches the thermal limit as the photon energy approaches the work function [7]. Atomically ordered surfaces have demonstrated ultra-low mean transverse energies (MTEs), further minimized by operation near the photoemission threshold at low temperatures [8].

For applications like stroboscopic UED/UEM where single to few electrons per bunch are sufficient, the smallest possible emission area is typically governed by the smallest possible laser spot size, which is restricted to the few micrometer scale due to the diffraction limit of light. Reducing this size below the diffraction limit of light requires alternative strategies to produce sub-micron-sized electron beams.

Recent advancements include nano-localized linear photoemission from a Schottky emitter, which enabled transverse emittances as low as 13.25 pm·rad [9]. Nonetheless, these emitters face limitations such as reduced operational lifetime at high electric fields and undesirable dark current due to field emission, making them unsuitable for RF gun environments. Other efforts have employed plasmonic interference to confine emission, achieving a record emittance of 40 pm·rad from flat photocathodes via nonlinear photoemission using circularly polarized light [10]. However, the higher MTE and energy spread associated with nonlinear emission limit the achievable emittance [11].

In this work, we demonstrate a novel photocathode concept that simultaneously addresses both MTE and emission area reduction using a geometrically flat photocathode, as shown in Fig 1. By patterning a circular region of low work function material on a high work function background, and by operating the photocathode at a photon energy between the two work functions, we spatially confine the photoemission to a sub-um scale area while maintaining low MTE. We achieved a low rms emission area of 106 nm from a gold photocathode fabricated on Silicon. Additionally, we demonstrate spatially confined photoemission from a metal-on-metal photocathode comprising platinum dots patterned

* aullattu@asu.edu

Content from this work may be used under the terms of the CC BY 4.0 licence (© 2022). Any distribution of this work must maintain attribution to the author(s), title of the work, publisher, and DOI.

ISBN: 978-3-95450-261-5 ISSN: 2673-7000 doi: 10.18429/JACoW-NAPAC2025-TUZN01

HIGH-DIMENSIONAL MAXIMUM-ENTROPY PHASE SPACE TOMOGRAPHY*

A. Hoover†, Oak Ridge National Laboratory, Oak Ridge, TN, USA

Abstract

Reconstructing 4D or 6D phase space distributions from 1D or 2D measurements is a challenging inverse problem encountered in particle accelerators. Entropy maximization is an established method to incorporate prior information in the reconstruction, but it is typically infeasible in high-dimensional spaces. In this paper, I review two recent approaches to high-dimensional entropy maximization. The first approach utilizes differentiable simulations and a class of generative models known as *normalizing flows*, whereas the second approach employs the method of Lagrange multipliers and Markov Chain Monte Carlo (MCMC) sampling. My aim is to provide a short explanation of each method using a common notation. I conclude by mentioning several unsolved problems in phase space tomography.

INTRODUCTION

Phase space density measurements enable model-based prediction and control of charged particle beams in particle accelerators. This paper focuses on indirect measurements in which the density is *inferred* from partial information in the form of low-dimensional projections. Such measurements are especially challenging when the phase space is high-dimensional [1]. One challenge is to search the space of distribution functions. Simple models may not be able to capture the full complexity of the real distribution, while complicated representations may require too many parameters to fit to the data [2]. The second challenge is that the data do not identify a unique distribution; rather, they carve out a set of *feasible* distributions, each of which is compatible with the data to within the desired precision.

Here, I focus on the method of maximum entropy (MaxEnt) to select a distribution from the feasible set. After describing the reconstruction problem and MaxEnt strategy, I review two recent approaches to high-dimensional MaxEnt. The first approach leverages advances in differentiable simulations and generative modeling to find approximate maximum-entropy distributions. The second approach is an extension of the MENT algorithm, which uses the method of Lagrange Multipliers to find an exact constrained maximum entropy distribution. My aim is to provide a short explanation of each method using a common notation, rather then to provide a comprehensive literature review. I conclude by mentioning several unsolved problems in phase space tomography, including the preservation of dynamic range, the inclusion of self-forces in the forward model, and robust uncertainty quantification (UQ). I do not discuss experimental design—a separate but equally important problem.[1]

MAXIMUM-ENTROPY METHODS FOR PHASE SPACE RECONSTRUCTION

We begin by describing the generic reconstruction problem. Let $p(x)$ be the probability density at location $x \in \mathbb{R}^N$ in phase space, where $N \in \{2, 4, 6\}$ is the dimension of the phase space. Let s be the distance along the accelerator, with the reconstruction location at $s = 0$. Let $\boldsymbol{\phi}$ be a vector of accelerator parameters, such as quadrupole strengths, which determines the single particle dynamics between reconstruction and measurement location. For measurement indices $k = 1, \ldots, K$, we select accelerator parameters $\boldsymbol{\phi}_k$ and tracking distance s_k. These choices define a set of symplectic transformations from input coordinates $x \equiv x_0$ to output coordinates x_k:

$$x_k = \mathscr{M}_k(x). \tag{1}$$

We measure the projection of the transformed distribution onto a plane $x_{k_\parallel} \in \mathbb{R}^M$, where $1 < M < N$. Here, $x_{k_\parallel}$ identifies the observed coordinates on the measurement axis, while $x_{k_\perp}$ identifies the unobserved coordinates. With these definitions, the projection is written as

$$g_k(x_{k_\parallel}) = \int p(\mathscr{M}_k^{-1}(x_k))dx_{k_\perp}. \tag{2}$$

This setup is illustrated in Fig. 1. We wish to recover the initial distribution $p(x)$.

The data do not, in general, identify a unique distribution; the size of the solution space depends on the chosen coordinate transformations $\mathscr{M}_k$, the dimension of the phase space, and the dimension of the measurements. Rather than exploring the full solution space, let us instead search for a single distribution compatible with the data. Consider a *prior* distribution $p_*(x)$ over the phase space coordinates; how should we update this prior in light of new information? We will perform the update by maximizing an entropy functional $S[p(x), p_*(s)]$ subject to the measurement constraints:

$$\max_{p(x)} S[p(x), p_*(x)] \quad \text{s.t.} \quad G_k[p(x)] = 0, \tag{3}$$

where

$$G_k[p(x)] = g_k(x_{k_\parallel}) - \tilde{g}_k(x_{k_\parallel}) = 0 \tag{4}$$

* This manuscript has been authored by UT-Battelle, LLC, under Contract No. DE-AC05-00OR22725 with the U.S. Department of Energy. The United States Government retains, and the publisher, by accepting the article for publication, acknowledges that the United States Government retains a non-exclusive, paid-up, irrevocable, world-wide license to publish or reproduce the published form of this manuscript, or allow others to do so, for United States Government purposes. The Department of Energy will provide public access to these results of federally sponsored research in accordance with the DOE Public Access Plan (http://energy.gov/downloads/doe-public-access-plan)

† hooveram@ornl.gov

[1] Implementations of the methods described here, along with example applications, are found in software repositories [3,4] and data repositories [5–7] linked to the corresponding papers [8–10].

Content from this work may be used under the terms of the CC BY 4.0 licence (© 2022). Any distribution of this work must maintain attribution to the author(s), title of the work, publisher, and DOI.

ISBN: 978-3-95450-261-5 ISSN: 2673-7000 doi: 10.18429/JACoW-NAPAC2025-TUCD03

OPERATION AND R&D OF LIQUID LITHIUM CHARGE STRIPPER AT FRIB

R. Iwai*, S. Cogan, S. Draeger, K. Hotton, T. Kanemura, M. LaVere, F. Marti, T. Maruta, Y. Momozaki[1], P.N. Ostroumov, A.S. Plastun, B. Strunk, J. Wei, L. Zampieri, T. Zhang, Q. Zhao, Q. Zhong, Facility for Rare Isotope Beams, East Lansing, Michigan, USA
[1]also at Argonne National Laboratory, Lemont, Illinois, USA

Abstract

Charge stripping is essential for the efficient acceleration of heavy-ions. The Facility for Rare Isotope Beams (FRIB) utilizes the Liquid Lithium Charge Stripper (LLCS) to produce the world's most powerful heavy-ion beams. This paper summarizes experiences of the LLCS after three years operation and ongoing R&D efforts including new method to form the liquid lithium film jet.

INTRODUCTION

The Facility for Rare Isotope Beams (FRIB) is a scientific user facility operated by the U.S. Department of Energy Office of Science [1]. FRIB operates the world's most powerful heavy-ion accelerator for stable ions from ^{16}O to ^{238}U. So far, the beam power has been demonstrated up to 20 kW with 200 MeV/u energy including ^{238}U, and it will ultimately ramp-up to 400 kW in the future. In the high-power heavy-ion accelerators, charge stripping is a key technology used to strip electrons and produce highly charged ions for efficient acceleration.

LIQUID LITHIUM CHARGE STRIPPER

Conventionally, a thin carbon foil has been used for charge stripping. However, with high-power heavy-ion beams, the lifetime of the foil is limited due to significant energy deposition and radiation damage on the material. To overcome this technical issue, FRIB utilizes the Liquid Lithium Charge Stripper (LLCS) [2]. In this device, a free-surface liquid metal film jet is used to strip the electrons from the beams. Compared to solid-based methods, flowing a liquid metal is more compatible with harsh environments characterized by extreme thermal loads and radiation. Particularly, liquid lithium has a good thermal performance due to its relatively low melting point, high heat capacity and, low vapor pressure. The free-surface flow allows greater flexibility in dimensions with minimal mechanical support structures. In addition, low atomic number lithium offers physical advantages: the low electron capture cross-section of swift heavy-ions with respect to the lithium atom yields high charge stripping efficiency [3], while minimizing energy straggling and multiple scattering of the penetrating beam.

OPERATION EXPERIENCE

The LLCS is operated at the Folding Segment 1 (FS1), an early stage of the driver linac following the Linac Segment 1 (LS1), where the beam energy is 17-20 MeV/u (Fig. 1, top). For a case of the ^{238}U beam, the charge state of the beam is $Q = 35$ before stripping, and distributed around $Q = 75$ after stripping. Through subsequent acceleration in Linac Segments 2 and 3 (LS2 and LS3), up to five charge states ($Q = 73 - 77$) are accelerated and delivered to the rare isotope production target [4]. The other unused charge states ($Q < 73$ and $Q > 77$) are selected by a bending magnetic field and intercepted by a water cooled Glidcop jaws (charge selector).

A leaf-shaped liquid lithium film flowing at 50 m/s is produced by impinging a round jet (500 µm diameter) onto a deflector (Fig. 1, bottom left). The typical thickness of the film is 1.0 mg/cm^2 or approximately 20 µm corresponding to typical energy deposition of about 0.5 MeV/u. The bottom right panel of Fig. 1 shows an image of the lithium film during 20 kW beam power operation with a ^{238}U beam. The incident beam power is approximately 2 kW, corresponding

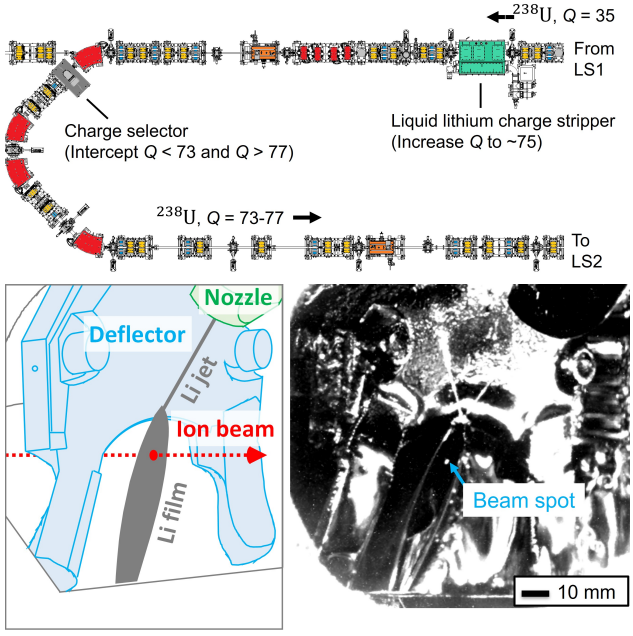


Figure 1: Top: Schematic view of the FS1. Charge states of the ^{238}U beam are indicated. Bottom left: Sketch of the film formation scheme reproduced from [2]. Bottom right: Picture of the liquid lithium filmed operated with the 20 kW ^{238}U beam. The beam spot on the film is indicated. Note that the poor quality of the image is due to radiation damages on the camera.

* iwai@frib.msu.edu

Content from this work may be used under the terms of the CC BY 4.0 licence (© 2022). Any distribution of this work must maintain attribution to the author(s), title of the work, publisher, and DOI.

ISBN: 978-3-95450-261-5 ISSN: 2673-7000 doi: 10.18429/JACoW-NAPAC2025-TUCN02

ELECTRO-OPTIC SAMPLING BEAM POSITIONING MONITOR FOR RELATIVISTIC ELECTRON BEAMS

E. L. Ros, M. L. Litos, A. Knetsch, B. O'Shea, C. Hansel, D. Matteo, G. Andonian, M. Hogan, R. Ariniello, S. Meng, T. Hodgetts, V. Lee
University of Colorado Boulder, Boulder, CO, USA

Abstract

Non-destructive diagnostics able to resolve transverse offsets and longitudinal separation of ultra-relativistic, two-bunch electron beams are necessary for a variety of applications including the ion channel laser (ICL) and other plasma wakefield (PWFA) experiments. A prototype electro-optic beam positioning monitor (EOS-BPM) utilizing two independent laser pulses traveling through a pair of EO crystals has been installed at the SLAC National Accelerator Laboratory FACET-II facility. This system is capable of order 10 fs temporal resolution and order 100 μm transverse position resolution. To achieve better transverse resolution we introduce a new design using an axicon lens to create a donut beam and a multi-crystal structure placed around the axis of propagation of the electron beam. Experimental results of the prototype EOS-BPM along with the simulated response of the new EOS-BPM design to the ultra-relativistic, two-bunch electron beam used for PWFA experiments at FACET-II will be presented.

INTRODUCTION

Plasma wakefield accelerated (PWFA) beams are extremely sensitive to transverse and longitudinal offsets. The primary motivation for the Electro-Optic Sampling Beam Positioning Monitor (EOS BPM) is to improve the alignment of the beams for PWFA. For this we require independent transverse and longitudinal measurements of the drive and witness beams. The beams must have precise transverse alignment to avoid chromatic phase spreading in the witness beam [1]. This occurs when the witness beam is transversely offset from the wake created by the drive beam causing emittance growth. PWFA beams are also sensitive to longitudinal separation. Precise alignment of longitudinal separation is required for optimal beam loading which minimizes energy spread and maximizes the acceleration efficiency. We also require the precise transverse and longitudinal resolution the EOS BPM will provide for the Ion Channel Laser (ICL) [2] which relies on the transverse offset of the witness beam to create FEL-like coherent radiation.

For both PWFA and ICL applications we require a shot by shot non-destructive diagnostic able to resolve fs timescales and μm scale transverse beam offsets. Traditional electronic beam positioning monitors (BPMs) are unable to resolve shorter than ns time scales, resulting in single measurement of the charge-averaged transverse position of the two bunches. Another commonly available diagnostic, the transverse deflecting cavity (TCAV), is able to measure the longitudinal separation between the bunches, but only by destructively streaking the beams onto a screen downstream. The use of ultra fast optics to encode fs/μm scale information into a laser pulse with electro-optic sampling is a well proven method to resolve time of arrival and longitudinal separation between bunches. The EOS BPM builds on this technique to also resolve transverse beam offsets on the length scales required for PWFA experiments.

METHODOLOGY

We employ a cross polarization electro-optic sampling scheme depicted in Fig. 1 part a). As a relativistic electron beam passes by an electro optic (EO) crystal changing the birefringent properties of the crystal at the instant the electron beam passes by [3, 4]. The polarization of a laser pulse passing through the crystal at that instant has its polarization rotated. For this design, the laser goes through a polarizer before the crystal such that only horizontally polarized light enters the crystal. Another polarizer is then placed after the crystal to filter out the un-rotated part of the laser pulse such that the signal viewed by the camera corresponds only to the vertical component of the polarization rotated portion of the laser pulse. When the probe laser enters the crystal at an angle we are able to map the temporal information of the electron beam to the transverse profile of the laser pulse. This method is able to resolve on the order of 10s of fs bunch separations between the drive and witness beams and has been used at FELs and other accelerator facilities to measure the electron beam time of arrival.

The University of Colorado Boulder Wakefield Acceleration and Radiation Generation (WARG) group along with Radiabeam Technologies have implemented a two crystal electro optic sampling beam positioning monitor (EOS BPM) Mk.1 design at FACET-II [6, 7]. We leverage the correlation between electron beam location with respect to the EO crystal and detected signal strength. This is similar to the method used by traditional electronic BPMs. A rough schematic of this design is shown in Fig. 1 part b), depicting two probe lasers entering the EO crystals which are oriented on either side of the axis of propagation of the electron beam.The strength of the signal—that is, the degree of the polarization rotation—is correlated with the distance between the signal encoded region of the laser pulse and the transverse position of the electron beam. With this we are able to independently measure the 3D centroid position of both the drive and witness beam.

We have conducted experiments testing the EOS BPM Mk.1's capabilities at FACET-II. Some results are shown in Fig. 2, the top and bottom plot represent the calculated

Content from this work may be used under the terms of the CC BY 4.0 licence (© 2022). Any distribution of this work must maintain attribution to the author(s), title of the work, publisher, and DOI.

ISBN: 978-3-95450-261-5 ISSN: 2673-7000 doi: 10.18429/JACoW-NAPAC2025-TUCN03

SRF CAVITY INSTABILITY DETECTION WITH MACHINE LEARNING AT CEBAF*

D. Turner†, R. Bachimanchi, A. Carpenter, H. Ferguson[1],
J. Latshaw, C. Tennant, D. Thomas
Thomas Jefferson National Accelerator Facility, Newport News, VA, USA
[1]Old Dominion University, Norfolk, VA, USA

Abstract

During the operation of the Continuous Electron Beam Accelerator Facility (CEBAF), one or more unstable superconducting radio-frequency (SRF) cavities often cause beam loss trips while the unstable cavities themselves do not necessarily trip off. The present RF controls for the legacy cavities report at only 1 Hz, which is too slow to detect fast transient instabilities during these trip events. These challenges make the identification of an unstable cavity out of the hundreds installed at CEBAF a difficult and time-consuming task. To tackle these issues, a fast data acquisition system (DAQ) for the legacy SRF cavities has been developed, which records the sample at 5 kHz. An unsupervised learning framework has been developed to identify anomalous SRF cavity behavior. We will discuss the present status of the DAQ system and our framework, along with recent successes in detecting anomalous cavity behavior. Overall, our method offers a practical solution for identifying unstable SRF cavities, contributing to increased beam availability and machine reliability.

INTRODUCTION

CEBAF is a 5.5-pass, 12 GeV continuous wave (CW) electron accelerator [1]. CEBAF is comprised of two anti-parallel SRF linacs connected by two sets of recirculation arcs, enabling the acceleration of electron beams for delivery to up to four experimental halls (Figure 1).

Each linac is comprised of 200 SRF cavities, plus 18 cavities in the injector, which provide electron beam acceleration. During the operation of CEBAF, any one unstable SRF cavity can cause beam loss trips while the unstable cavities themselves do not necessarily trip off or present a fault.

The existing tools and diagnostics for identifying unstable SRF cavities at CEBAF are presently rather limited. Out of the 418 SRF cavities at CEBAF, 288 are of the original legacy CEBAF design which lacks the fast data acquisition capabilities of the newer cavities. The legacy cavity diagnostics are limited to what is presented to the EPICS [2] control system which is limited to a data rate of 1 Hz, which is not fast enough to capture transient instabilities. Also, simply the number of cavities in the machine makes the search for instabilities time consuming. Work described in [3] addresses fault classification for the newer SRF cavities at CEBAF. This work addresses identifying unstable cavities of the legacy design.

To address these problems, a new fast data acquisition (DAQ) system has been designed and is being installed on the legacy SRF cavities at CEBAF, along with an anomaly detection model based on Principal Component Analysis (PCA).

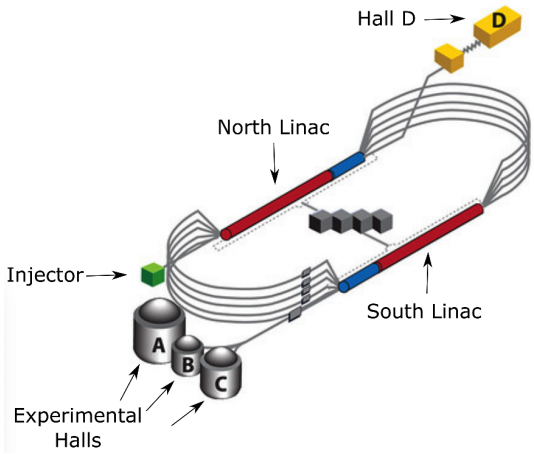


Figure 1: 12 GeV CEBAF overview. The legacy SRF cavities comprise most of the red regions of the linacs.

FAST DATA ACQUISITION SYSTEM

Each legacy SRF cavity has four analog outputs on its control module:

- GMES: Measured Gradient. Should mirror the GSET value in EPICS and should be stable to within 0.044 % during normal operations. Has DC and AC components.
- PMES: Measured Phase. This is the phase in the cavity measured against the absolute 70 MHz reference. This also should mirror PSET in EPICS and should be varying less than ±0.3°.
- GASK: Gradient Drive. The change in klystron incident power needed to maintain the GMES value within specifications. This signal will change in response to beam detuning or beam loading.

* Notice: Authored by Jefferson Science Associates, LLC under U.S. DOE Contract No. DE-AC05-06OR23177. The U.S. Government retains a non-exclusive, paid-up, irrevocable, world-wide license to publish or reproduce this manuscript for U.S. Government purposes.

† dturner@jlab.org

Content from this work may be used under the terms of the CC BY 4.0 licence (© 2022). Any distribution of this work must maintain attribution to the author(s), title of the work, publisher, and DOI.

ISBN: 978-3-95450-261-5 ISSN: 2673-7000 doi: 10.18429/JACoW-NAPAC2025-TUP001

2D PHASE SPACE TOMOGRAPHY WITH SciBmad TRACKING

X. Yang[1], M. G. Signorelli[1], D. Sagan[1], D. Abell[2], G. Hoffstaetter[1]
[1]CLASSE, Cornell University, Ithaca, NY, USA
[2]RadiaSoft LLC, Boulder, CO, USA

Abstract

This paper presents the application of `BeamTracking.jl`, a key package in the Julia based SciBmad software ecosystem for differentiable accelerator physics simulations. This study demonstrates the use of phase space tomography to reconstruct the 2D phase space distribution of a particle beam. Using the SciBmad tracking package `BeamTracking.jl`, the phase space distribution of the beam can be constructed from the beam's projections after being transported through a quadrupole and a drift. This result showcases the utility of SciBmad and highlights its potential for studying and optimizing injection, transport, and beam acceleration.

INTRODUCTION

SciBmad is a new, open-source, differentiable accelerator physics code designed to provide modular, high-performance tools for simulations, lattice design, analysis, and machine learning [1,2]. The `BeamTracking.jl` package in the SciBmad ecosystem provides universally polymorphic, portable, and parallelized routines for simulating charged-particle beams [3]. Its integrators, which include Yoshida's second, fourth, sixth, and eighth order methods with drift-kick and "thick"-kick (quadrupole-kick, solenoid-kick, bend-kick) splits, are differentiable and GPU compatible for a wide variety of hardwares. In this paper, we demonstrate 2D phase space tomography using `BeamTracking.jl`, comparing real and reconstructed distributions.

BEAMTRACKING.JL

The `BeamTracking.jl` package provides forward, reverse, and Taylor-mode differentiable tracking routines, making it easy to compute (high order) derivatives of arbitrary quantities with respect to initial particle coordinates and/or beamline parameters, e.g. quadrupole strengths. This is achieved through compatibility with registered automatic differentiation (AD) packages in the Julia ecosystem, including `GTPSA.jl` (Generalized Truncated Power Series Algebra), another package in the SciBmad ecosystem [4, 5]. Paired with SciBmad's fully polymorphic and differentiable lattice definition package `Beamlines.jl` [6], SciBmad provides a natural environment to compute things such as how the phase space depends on parameters, how the Twiss parameters depend on parameters, and much more.

`BeamTracking.jl`'s tracking routines are also GPU compatible via the `KernelAbstractions.jl` package, supporting parallel execution across various hardwares including NVIDIA CUDA, AMD ROCm, Apple Metal, and Intel oneAPI [7]. This enables GPU acceleration of particle tracking using the same tracking API as on the CPU.

2D PHASE SPACE TOMOGRAPHY

We employed a standard tomography technique to reconstruct the two-dimensional phase space distribution of a particle beam from a series of projections. Tomographic reconstruction is commonly used for beam diagnostics to extract parameters such as emittance, correlations, and beam shape under various lattice configurations. By recording the images of the cross sections of a beam as it propagates through a lattice, the phase space distribution of the initial beam can be reconstructed using standard algorithms.

In a typical setup for beam tomography, a section of the beamline controls the beam distribution with a known transformation. As a beam passes through that section, the phase space distribution of the beam changes accordingly. Placing a screen along the beam path in a downstream position z_1 will produce a spatial projection of this beam distribution $g(x, y)$. With multiple projections at position z_1, we will be able to reconstruct the phase space distribution of the beam bunch at z_0, as described in Ref. [8].

The standard tomography methods assume uncoupled, linear dynamics, where the phase space coordinates from z_0 to z_1 are related to the transfer matrix by

$$\begin{pmatrix} x_1 \\ x_1' \end{pmatrix} = \begin{pmatrix} M_{11} & M_{12} \\ M_{21} & M_{22} \end{pmatrix} \cdot \begin{pmatrix} x_0 \\ x_0' \end{pmatrix}.$$

Under such linear transformation, the projection of the beam distribution onto the screen plane remains a straight line, but its orientation and scaling changes. In our setup, we simulate a lattice consisting of a quadrupole followed by a drift. By adjusting the quadrupole strength, we effectively rotate the phase space distribution, thereby obtaining the projection profiles at different rotation angles.

The projection angle can be found by

$$\tan\theta = \frac{M_{12}}{M_{11}}.$$

To generate multiple projection angles, we varied the quadrupole strength and tracked the beam through a lattice defined using `Beamlines.jl`, consisting of a quadrupole of length 0.172 m and a drift of length 0.1228 m. The transport matrix for each setting is obtained through `GTPSA.jl` after tracking with `BeamTracking.jl` . For this study, we simulated 150 different quadrupole strengths, producing 150 projection angles evenly spaced between 0 and π.

For each setting, the beam is propagated from the longitudinal position z_0 to z_1. The transformed coordinates x

Content from this work may be used under the terms of the CC BY 4.0 licence (© 2022). Any distribution of this work must maintain attribution to the author(s), title of the work, publisher, and DOI.

ISBN: 978-3-95450-261-5 ISSN: 2673-7000 doi: 10.18429/JACoW-NAPAC2025-TUP002

A BEAM CHOPPING SCHEME CONCEPT FOR THE NEW LAMP MEBT *

S. Sosa Guitron†, K. Bishofberger, G.E. Dale, D.A. Dimitrov, D. Gorelov, S. Kurennoy, J.W. Lewellen, L. Rybarcyk, J. Upadhyay, H. Xu
Los Alamos National Laboratory, Los Alamos, NM, USA

Content from this work may be used under the terms of the CC BY 4.0 licence (© 2022). Any distribution of this work must maintain attribution to the author(s), title of the work, publisher, and DOI.

Abstract

As part of the LANSCE Accelerator Modernization Project (LAMP), the two existing 750-keV Cockcroft Waltons are planned to be replaced by a single radio-frequency quadrupole (RFQ). The new LAMP front-end needs to deliver beams with similar timing patterns to what is currently delivered to the multiple target stations. To accomplish this, the 3-MeV Medium Energy Beam Transport (MEBT) is designed with two choppers that help produce the beam timing patterns required by the experimental user facilities. The new RFQ will introduce satellite bunches around the single high-intensity bunch that is required by the users. These satellite bunches need to be removed in the MEBT. This contribution describes the design of LAMP MEBT with a beam chopping scheme and presents simulation results.

INTRODUCTION

The Los Alamos Neutron Science Center (LANSCE) accelerator facility at Los Alamos National Laboratory (LANL) delivers high-intensity beams for multiple nuclear and neutron experiments: H^+ beam is delivered to the Isotope Production Facility (IPF), two H^- beams with different timing structures are delivered to the Lujan Center and to the Weapons Neutron Research (WNR) target, single-shot trains of H^- beam are also delivered for proton radiography (pRAD) and Ultracold Neutron (UCN) experiments.

The LANSCE Accelerator Modernization Project (LAMP) is planning to upgrade the front-end of LANSCE to ensure that beams can be delivered reliably to experimental facilities in years to come [1]. A major upgrade being considered is the replacement of two 750-keV Cockcroft Walton (CW) generators for a single Radiofrequency Quadrupole (RFQ) capable of accelerating dual-species beams to 3 MeV. A MEBT will then transport and help tailor the beam before injection into a new 100 MeV Drift Tube Linac (DTL). We developed a physics model of the LAMP front-end that meets the project requirements [2]. This paper describes the current state of the MEBT design and the adopted beam chopping scheme required to remove satellite bunches in the WNR beam.

The beam to WNR is unique and challenging to produce under intense low-energy space charge effects. It consists of a high intensity rf bunch separated every 1.8 μs over the length of a 625 μs macro-pulse. Two major requirements are called out by the experiment; a high-intensity bunch with at least 115 pC at target, and an empty gap with beam intensity less than 10^{-5} that of the main bunch, this is referred to as dark current at target. The MEBT chopper scheme in LAMP is designed to remove the satellite bunches produced during the high-intensity bunch formation.

Shaping of WNR Pulse in LAMP

In the LAMP conceptual design, the WNR beam is produced through beam manipulations in the Low Energy Beam Transport (LEBT) and the MEBT. High current H- beam, 35 mA, is produced at the source and propagates to the LEBT chopper. From the source to the chopper, we assume the beam to have space charge compensation of 90%. The chopper produces an initial 25-ns short pulse, and no further space charge compensation is assumed from this point. The initial pulse at the chopper is shown in Fig. 1. The chopper finite rise and fall times produce tails at the front and the back of the pulse. Here we assumed a linear ramp and a chopped pulse with 5 ns rise/fall time and 15 ns flat top.

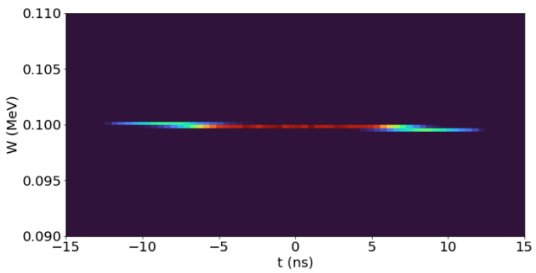


Figure 1: Beam pulse produced by LEBT chopper with 5-ns rise, 15-ns flat and 5-ns fall times.

The chopped pulse is then transported into a low frequency buncher (LFB). The LFB consists of two gaps separated by $\beta\lambda/2$ and operates at a sub-harmonic of the DTL frequency, 16.77 MHz. The electric fields across the gaps introduce velocity modulation of the beam, resulting in compression of the chopped pulse into the central 4.96-ns of the pulse, the 201.25 MHz rf period. Figure 2 shows the resulting compressed beam at the entrance of the RFQ.

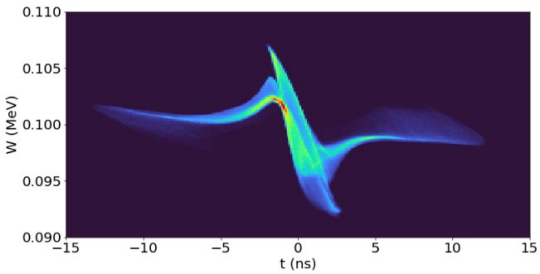


Figure 2: Beam pulse at the RFQ entrance with high charge accumulation at the center resulting from the LFB effect.

* This work benefitted from the use of the LANSCE accelerator facility. Work was performed under the auspices of the US Department of Energy by Triad National Security under contract 89233218CNA000001.
† salvador@lanl.gov

ISBN: 978-3-95450-261-5 ISSN: 2673-7000 doi: 10.18429/JACoW-NAPAC2025-TUP003

ACCELERATOR PHYSICS REQUIREMENTS AND CHALLENGES OF RF BASED ELECTRON COOLER FOR EIC INJECTION ENERGY*

A.V. Fedotov†, Y. Jing, D. Kayran, J. Kewisch, S. Seletskiy, G. Wang
Brookhaven National Laboratory, Upton, NY, USA

Abstract

Cooling of hadrons in Electron Ion Collider (EIC) at the injection energy is critical to achieving EIC design parameters. A 13 MeV electron cooler fit for the task is presently under design. This cooler will use RF-accelerated electron bunches and will provide strong cooling of the hadrons having energy of 24 GeV/nucleon. The paper describes optimization of the cooling performance, taking into account space charge, IBS and other effects, and provides physics requirements for the cooler.

INTRODUCTION

The Electron-Ion Collider (EIC) is a partnership project between Brookhaven National Laboratory (BNL) and Thomas Jefferson National Accelerator Facility (TJNAF) to be constructed at BNL, using much of the existing infrastructure of the Relativistic Heavy Ion Collider (RHIC); a layout of the EIC is shown in Fig. 1. Collisions occur between the hadrons in the Hadron Storage Ring (HSR) and the electrons in the Electron Storage Ring (ESR) [1].

In order to achieve the design emittances of the hadron beam, hadron beams are injected into the HSR and cooled to the target emittances at injection energy of protons of 23.8 GeV. After the target emittances are achieved, the HSR is ramped to the collision energy.

Cooling of protons at 23.8 GeV will be done using conventional electron cooling technique which requires 13 MeV electron accelerator. The design of such Low-Energy Cooler (LEC) is based on the RF-accelerated electron bunches, similar to the LEReC [2] approach, but scaled to higher energy.

COOLER REQUIREMENTS

The LEC design is based on the non-magnetized cooling approach with zero magnetic field on the cathode and no magnetic field in the cooling region [2]. The layout of the LEC accelerator is shown in Fig. 2.

The friction force acting on the ion with charge number Z inside a non-magnetized electron beam with velocity distribution function $f(v_e)$ is

$$\vec{F} = -\frac{4\pi n_e e^4 Z^2}{m}\int \ln\left(\frac{\rho_{\max}}{\rho_{\min}}\right)\frac{\vec{V}_i - \vec{v}_e}{\left|\vec{V}_i - \vec{v}_e\right|^3} f(v_e)\,d^3 v_e \quad , (1)$$

where e and m are the electron charge and mass, V and v_e are the ion and electron velocities respectively, and n_e is electron density in the particle rest frame (PRF).

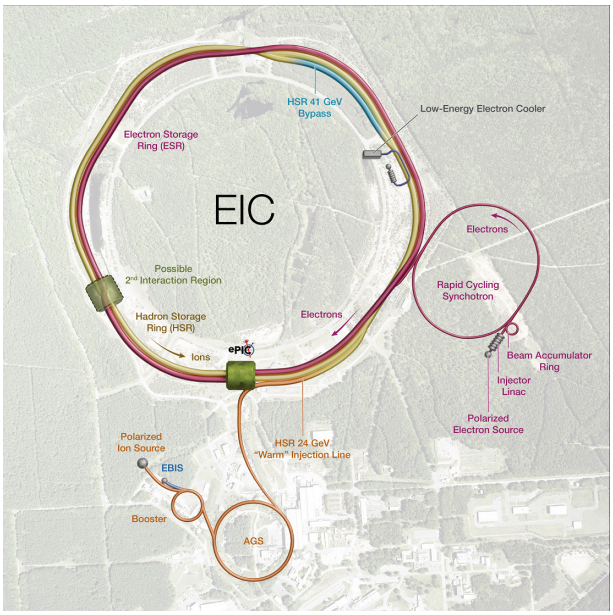


Figure 1: The layout of the Electron-Ion Collider (EIC). The Hadron Storage Ring (HSR), Electron Storage Ring (ESR), and the Rapid Cycling Synchrotron (RCS) labels are color-coded to their respective rings; the current and proposed IRs are shown at IR6 and IR8, with the Low-Energy Cooling (LEC) system located in IR2.

To maximize the cooling power and to preserve transverse distribution of hadrons under cooling, the electron beam rms velocity spreads are chosen close to those of the hadron beam. At injection energy in the EIC with γ=25.4, the proton beam with bunch intensities $N=2.8\times10^{11}$ will have rms longitudinal momentum spread of about $\sigma_p=7\times10^{-4}$. The requirement for the rms momentum spread of electron beam are $< 4\times10^{-4}$. For the rms normalized emittance of the proton beam around 2 μm and 150 m minimum beta function in the cooling section, the hadron beam rms angular spread in the lab frame is 0.023 mrad. This gives the requirement for the total electrons angular spread in the cooling section to be around 0.025 mrad.

The total angular spread of electrons in the cooling section has several contributions, with the dominant contributions coming from electron beam emittance and electron beam space charge. As a result, special efforts are being made to develop proper electron beam transport to and through the cooling section to ensure that requirements on angular spread are satisfied.

*Work supported by the US Department of Energy under contract No. DE-AC02-98CH10886.
†fedotov@bnl.gov

Content from this work may be used under the terms of the CC BY 4.0 licence (© 2022). Any distribution of this work must maintain attribution to the author(s), title of the work, publisher, and DOI.

ISBN: 978-3-95450-261-5 ISSN: 2673-7000 doi: 10.18429/JACoW-NAPAC2025-TUP004

A COMMUNITY EFFORT TOWARD A PARTICLE ACCELERATOR LATTICE STANDARD (PALS)*

C. Mitchell†, J-L. Vay, E. Zoni, A. Huebl, J. Qiang, LBNL, Berkeley, CA, USA
D. Sagan and M. G. Signorelli, Cornell University, Ithaca, NY, USA
C. Mayes, xLight, Inc., Palo Alto, CA, USA
D. Bruhwiler, RadiaSoft LLC, Boulder, CO, USA
D. Kallendorf, GSI Helmholtzzentrum für Schwerionenforschung, Darmstadt, Germany
Yue Hao, FRIB, Michigan State University, East Lansing, MI, USA
D. Winklehner, Physics Dept., Massachusetts Institute of Technology, MA, USA

Content from this work may be used under the terms of the CC BY 4.0 licence (© 2022). Any distribution of this work must maintain attribution to the author(s), title of the work, publisher, and DOI.

Abstract

A major obstacle to collaboration on accelerator projects has been the sharing of lattice description files among modeling codes. To address this problem, a standardized lattice description called the Particle Accelerator Lattice Standard (PALS) is being developed. PALS development is a community-wide international effort involving accelerator physicists from multiple institutions. Along with the standard, interface packages written in commonly used languages will be developed.

The importance for developing PALS is due to the increase in scale and complexity of new machines bringing an ever greater need for global collaboration, as well as interfacing with the data-driven activities using artificial intelligence and machine learning.

The proposed Particle Accelerator Lattice Standard aims to promote: (i) portability between applications, (ii) a unified open-access description for scientific data (publishing and archiving), (iii) a unified description for post-processing, visualization and analysis. We present an introduction to the effort, an overview of the standard, a simple example, and discuss plans and future involvements from the community.

INTRODUCTION

Multi-institutional collaboration on accelerator projects that involve beam dynamics modeling, lattice design optimization, and numerical code benchmarking are challenging in part because of differing conventions among beam dynamics codes, variations in file format, and differences in implementation details. Community standardization of user-facing code inputs, outputs, and workflows provides an effective and manageable approach to mitigate these difficulties [1].

There is now an increasing need for standardization due to the scale and complexity of new machines (which typically require the integrated use of multiple simulation codes during the design stage) and the need to connect codes to AI/ML and data science ecosystems through common application programming interfaces (APIs).

The Particle Accelerator Lattice Standard (PALS) aims to define a schema for the sharing of lattice information to describe particle accelerators and storage rings [2]. While past efforts at lattice standardization [3,4] have met with partial or limited success, new factors now include the support of an international collaboration, widespread community adoption of open-source version control software such as `git`, and successful examples of other efforts toward particle accelerator community standards. These efforts include the Open Standard for Particle-Mesh Data (openPMD), a metadata standard for scalable I/O and exchange of particle and mesh-based data [5], and the Particle-In-Cell Modeling Interface (PICMI), defining conventions for the naming and structuring of input files for PIC simulations [6].

OVERVIEW OF PALS

PALS is a standard for describing the physical layout and properties of an accelerator lattice, providing a schema that defines the names of various lattice element kinds, how to organize lattice elements into lines (that beams of particles or photons can move through), and how various branches consisting of lines and elements are interconnected to form an accelerator complex (Fig. 1). The aim of a PALS based lattice is to hold all the information about an entire machine complex, from beam creation to dump lines, enabling a single lattice file to be used as the basis of start-to-end simulations, as well as design, construction and operation.

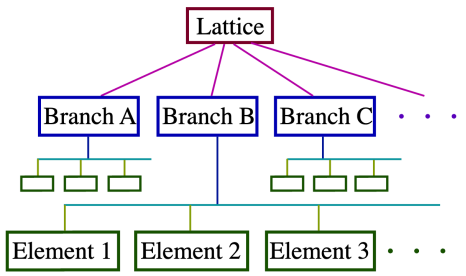


Figure 1: An expanded lattice contains a set of branches (not necessarily in an array) and each branch holds an ordered array of lattice elements.

The PALS standard does *not* describe how particles are to be tracked through a lattice. An effort has been made to separate the physical lattice description from the beam dynamics details, as far as such a separation is possible

* Contributed on behalf of the PALS collaboration.
† ChadMitchell@lbl.gov

ISBN: 978-3-95450-261-5 ISSN: 2673-7000 doi: 10.18429/JACoW-NAPAC2025-TUP006

A HIGHER MOMENTUM APERTURE LATTICE PROPOSED FOR THE sPHENIX BACKGROUND PROBLEM*

C. Liu†, G. Robert-Demolaize, Y. Luo, X. Gu, K.A. Drees
Collider Accelerator Department, Brookhaven National Lab, Upton, NY, USA

Content from this work may be used under the terms of the CC BY 4.0 licence (© 2022). Any distribution of this work must maintain attribution to the author(s), title of the work, publisher, and DOI.

Abstract

During the 2024 Au+Au 100 GeV physics run, the sPHENIX MVTX detector experienced background issues originating from the Yellow beam, leading to frequent auto-recoveries during streaming mode operation. One hypothesis attributes the background to the loss of off-momentum particles. An evaluation of the momentum apertures in both RHIC rings revealed that the Yellow ring had a worse momentum acceptance compared to the Blue ring. To address this, a new lattice design with a reduced W-function was proposed. This report presents the momentum aperture comparison between the two rings, the proposed new lattice design considering additional constraints, and the resulting momentum and dynamic apertures.

INTRODUCTION

The Monolithic Vertex Tracker (MVTX) is a crucial component located at the center of the sPHENIX detector, designed to provide high-precision vertex tracking. The MVTX 1 consists of 48 staves arranged in three layers (Fig. 1), all centered at the interaction point (IP) and extending ±13.5 cm along the beam axis. If any of the staves become overloaded with charge, the entire stave enters an auto-recovery mode, initiating a 20-second reboot process to reset and reinitialize the system. During this period, no data is recorded, leading to a temporary loss of tracking information. The primary source of excessive charge deposition is the Yellow beam [1], which generates significantly higher hit rates compared to the Blue beam. The MVTX auto-recovery display is shown Fig. 1 where the red triangles correspond to staves in auto-recovery state.

STUDY OF THE MOMENTUM APERTURE

Off-momentum particle losses were hypothesized to be the primary source of the observed background [2]. However, a notable asymmetry was present, with the Yellow ring exhibiting significantly higher losses than the Blue ring. This raises the question: from an accelerator physics perspective, why is the momentum aperture substantially more limited in the Yellow ring?

The momentum aperture is evaluated in Mad-X [3] without implementing the physical aperture. The method is to scan the momentum deviation and check beam stability. When the beam is unstable, Mad-X would fail to find Twiss parameters, and in the following plot, the tune stays at an initial value, while the tune would vary in the stable region.

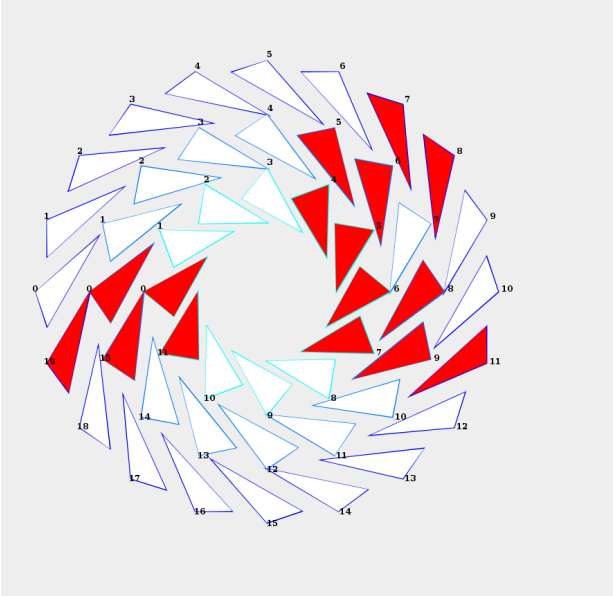


Figure 1: : The cross-section of the MVTX detector. Each triangle represents one stave. The red triangles are the staves in auto-recovery mode, which takes 20 seconds before the stave can take data.

As shown in Fig. 2, the Yellow ring lattice has a narrower stable region, therefore a smaller momentum aperture.

Higher-order chromaticity—specifically, second- and third-order components—is intrinsically linked to the momentum aperture. Generally, increased higher-order chromaticity corresponds to a reduced momentum aperture. Nevertheless, direct measurements of chromaticity did not reveal a significant difference in higher-order terms between the two rings.

An alternative approach to quantifying chromatic nonlinearities is through the chromatic beta-beating, characterized by the W function [4]. A lower value of the W function indicates reduced chromatic distortion and, consequently, improved dynamic performance.

The W-function of the two RHIC rings (Blue vs Yellow) is shown in Fig. 3.

One approach is to employ sextupole magnets not only for linear chromaticity correction but also for optimizing the W function. Alternatively, the lattice can be designed such that the chromatic contributions from the two interaction regions (IRs)—which are the dominant sources—effectively cancel each other [5]. The latter strategy is adopted in this study.

* Work supported by Brookhaven Science Associates, LLC under Contract No. DE-SC0012704 with the U.S. Department of Energy.
† cliu1@bnl.gov

ISBN: 978-3-95450-261-5 ISSN: 2673-7000 doi: 10.18429/JACoW-NAPAC2025-TUP007

A MULTI-HARMONIC CAVITY SYSTEM FOR BUNCH LENGTHENING FOR THE NSLS-II UPGRADE

G. Bassi*, A. Khan, V. Smaluk, F. Gao, J. Rose
Brookhaven National Laboratory, Upton, NY, USA

Abstract

In the next generation of light sources, to improve the beam lifetime of the bunches and mitigate collective effects such as intrabeam scattering, Higher-Harmonic Cavity (HHC) systems are commonly used to increase the equilibrium bunch length without an increase of the energy spread. Present HHC systems are based on HHCs of the same order. To increase the bunch lengthening factor induced by the HHC system, we investigate a scheme based on the combination of HHCs of different order. In the present contribution we investigate bunch lengthening conditions for a multi-harmonic cavity system consisting of a passive third order harmonic cavity and an active fifth harmonic cavity. Numerical simulations are performed with Vlasov-Fokker-Planck solver SPACE, with parameters of the NSLS-II upgrade.

INTRODUCTION

We investigate a multi-Harmonic Cavity (multi-HC) system to increase the bunch length in the low-emittance rings. In this contribution we consider a passive normal conducting cavity of order three combined with an active normal conducting cavity of order five. With parameters of the NSLSII-U [1], we show that a bunch lengthening factor $u \approx 10$ is theoretically possible. Conditions for normal conducting cavities are determined. The case of a combined active multi-HC system of order m and n has been investigated in [2], while the case of a multi-HC system using a passive superconducting third harmonic cavity will be studied in a future work.

BUNCH LENGTHENING CONDITIONS

Sextic Potential (Passive HC of Order m and Active of Order n)

In the case of equally spaced stationary bunches, the total voltage induced by a passive harmonic cavity of order m and an active cavity of order n reads

$$\begin{aligned} V(\tau) &= V_{rf}\sin(\omega_{rf}\tau + \phi_s) \\ &\quad - i_m R_m \cos\psi_m \cos(m\omega_{rf}\tau + \psi_m) \\ &\quad + rV_{rf}\sin(n\omega_{rf}\tau + \psi_n) - V_{rf}\sin\phi_{s0}, \qquad (1) \\ \sin\phi_{s0} &= \frac{U_0}{eV_{rf}} \end{aligned}$$

where $i_m = 2I_0\tilde{\lambda}(m\omega_{rf})$ and $\tilde{\lambda}(\omega) = e^{-\frac{1}{2}(m\omega_{rf}\sigma_t)^2}$, and where we used a Gaussian approximation for $\tilde{\lambda}(\omega)$. The total potential reads therefore

$$\begin{aligned} U(\tau) = \frac{eV_{rf}}{T_0E_0\omega_{rf}}\Big[&\cos(\omega_{rf}\tau + \phi_s) - \cos\phi_s \\ &+ \frac{r}{n}(\cos\psi_n - \cos(n\omega_{rf}\tau + \psi_n)) \\ &+ i_m R_m \frac{\cos\psi_m}{m\omega_{rf}}(\sin(m\omega_{rf}\tau + \psi_m) - \sin\psi_m) \\ &+ \omega_{rf}\tau\sin\phi_{s0}\Big]. \qquad (2) \end{aligned}$$

Small Oscillations ($\tau \ll 1$) Performing a Taylor series expansion, we obtain a sextic potential via setting to zero the coefficient of the expansion up to order five. Solving for ϕ_s, R_m, ψ_m, r and ψ_n we obtain

$$\begin{aligned} \sin\phi_s &= \frac{m^2n^2}{a_{mn}}\sin\phi_{s0}, \\ R_m &= -\frac{V_{rf}a_{mn}(n^2-1) + m^2n^4\sin^2\phi_{s0}}{i_m m^2n^2(m^2-n^2)\sin\phi_{s0}}, \\ r &= \frac{\sqrt{a_{mn}(m^2-1) - n^2m^4\sin^2\phi_{s0}}}{n(m^2-n^2)\sqrt{n^2-1}}, \\ \tan\phi_m &= \sqrt{(m^2-1)(a_{mn}(n^2-1) - m^2n^4\sin^2\phi_{s0})} \\ &\quad \times \frac{\sqrt{-a_{mn}^2 + m^4n^4\sin^2\phi_{s0}}}{mn^2\sin\phi_{s0}\sqrt{-(a_{mn}^2 + (m^2-1)m^2n^4\sin^2\phi_{s0})}}, \\ \tan\phi_n &= \frac{m^2n\sin\phi_{s0}(a_{mn}^2 - (m^2-1)m^2n^4\sin^2\phi_{s0})}{\sqrt{-(m^2-1)^2(a_{mn}(n^2-1) - m^2n^4\sin^2\phi_{s0})^2}} \\ &\quad \times \frac{1}{\sqrt{-a_{mn}^2 + m^4n^4\sin^2\phi_{s0}}}, \qquad (3) \end{aligned}$$

where $a_{mn} = (m^2-1)(n^2-1)$.

Bunch Lengthening Factor

The bunch lengthening factor u for a sextic potential reads [2]:

$$\begin{aligned} u &:= \frac{\sigma_\tau}{\sigma_{\tau 0}} \qquad (4) \\ &= \sqrt{\frac{\Gamma(1/2)}{\Gamma(1/6)}}\left(\frac{720\cos\phi_{s0}}{(a_{mn} - 2(m^2-1))\omega_{rf}^4\cos\phi_s}\right)^{1/6}\frac{1}{\sigma_{\tau 0}^{\frac{2}{3}}}. \end{aligned}$$

BUNCH LENGTHENING IN THE NSLS-II-U

With parameters of the NSLS-II-U, as shown in Table 1, we determine the conditions for operating a combined passive third order and active fifth order HC system. Numerical

* gbassi@bnl.gov

Content from this work may be used under the terms of the CC BY 4.0 licence (© 2022). Any distribution of this work must maintain attribution to the author(s), title of the work, publisher, and DOI.

ISBN: 978-3-95450-261-5 ISSN: 2673-7000 doi: 10.18429/JACoW-NAPAC2025-TUP008

ANALYSIS OF THE ELLIPTIC INTEGRABLE NON-LINEAR SYSTEM IN IOTA USING TRACKING OF A SINGLE ELECTRON*

A. Romanov†, G. Stancari, J. Santucci, J. Jarvis
Fermi National Accelerator Laboratory, Batavia, IL, USA

Abstract

Integrable nonlinear lattices that can be realized in practical accelerators are of great interest, as they offer the potential to support high-intensity beams via Landau damping of collective instabilities. One such system, based on an elliptic potential, has been extensively studied at the IOTA storage ring at Fermilab. The analysis of strongly nonlinear dynamics with multi-particle bunches is challenging due to the rapid decoherence of kicked beams. IOTA has the capability to track single electrons using linear multi-anode photomultiplier tubes for simultaneously measuring transverse coordinates and arrival times of synchrotron-radiation pulses. This technology enables the full reconstruction of turn-by-turn positions and momenta in all three planes for a single particle. Using this apparatus, we measured the dependence of small-amplitude tunes on the strength of the nonlinear magnet, as well as tunes dependence on oscillations amplitudes.

INTRODUCTION

This paper presents one of the first application cases of beam diagnostics based on single-electron tracking [1, 2] at the Integrable Optics Test Accelerator (IOTA, [3]). The ability to track an electron in all six phase-space dimensions allows researchers to avoid a fundamental problem of multi-particle bunches – the smearing of collective signals due to decoherence. Nonlinear systems, such as the elliptical integrable system studied at IOTA, exacerbate decoherence, reducing the useful number of observable turns after a beam kick to only a few tens when the nonlinear insert is strongly excited.

The IOTA lattice must satisfy several conditions: zero dispersion in the nonlinear insert, and an equivalent of an axially symmetric thin focusing lens with predefined strength for the section outside the nonlinear insert. The nominal tunes must lie on the coupling resonance; however, for diagnostic purposes, a controlled distortion was introduced in the case of a disabled nonlinear insert. This adjustment was necessary to distinguish between vertical and horizontal modes. The parameters of the bare lattice and the beam sizes are given in Table 1 and Fig. 1. A comparison of the beta functions for the lattice with the nonlinear insert disabled and with strength $t = 0.45$ is shown in Fig. 2.

Table 1: IOTA Parameters During the Experiment

Parameter	Value
Perimeter	39.96 m
Momentum	150 MeV/c
Bunch intensity	1 e^-
RF frequency	30 MHz
RF voltage	350 V
Betatron tunes, (ν_x, ν_y)	(5.3, 5.3)
Synchrotron tune, ν_s	3.5×10^{-4}
Damping times, (τ_x, τ_y, τ_s)	(2.08, 0.65, 0.24) s
Horizontal emittance, ϵ_x	127 nm
Momentum spread, $\Delta p/p$, RMS	1.3×10^{-4}
Momentum compaction, α_p	0.083
Natural chromaticity C_x, C_y	-10.9, -9.4
Compensated chromaticity C_x, C_y	0.0, 0.0

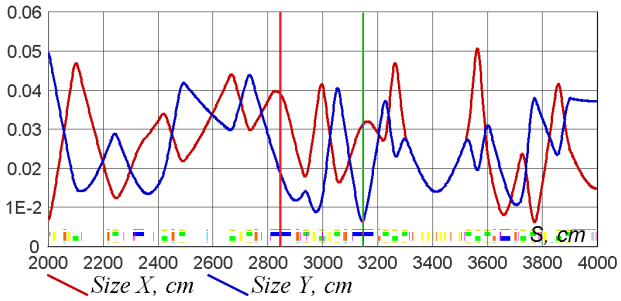


Figure 1: Horizontal and vertical beam sizes in the second half of IOTA. The vertical lines show locations of the detector at M3L (red) and M2L (green) dipoles.

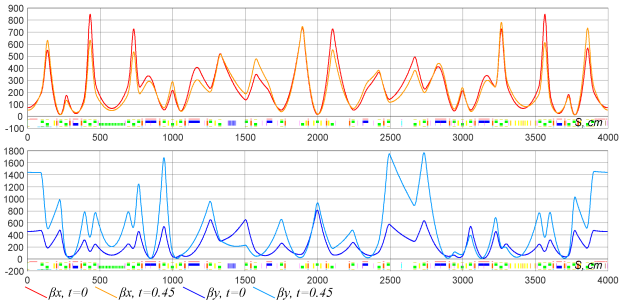


Figure 2: Horizontal and vertical beta-functions for the bare IOTA lattice and for t=0.45, which is close to the integer resonance in the vertical plane.

The first-order effect of the nonlinear insert is equivalent to that of a quadrupole. The dependence of the small-amplitude oscillation tunes on the insert's dimensionless scaling parameter t is given by [4]:

* This work was produced by FermiForward Discovery Group, LLC under Contract No. 89243024CSC000002 with the U.S. Department of Energy, Office of Science, Office of High Energy Physics and by Fermilab's Laboratory Directed Research and Development grant FNAL-LDRD-2022-041.

† aromanov@fnal.gov

Content from this work may be used under the terms of the CC BY 4.0 licence (© 2022). Any distribution of this work must maintain attribution to the author(s), title of the work, publisher, and DOI.

ISBN: 978-3-95450-261-5 ISSN: 2673-7000 doi: 10.18429/JACoW-NAPAC2025-TUP009

AN EXTENDED FROISSART-STORA FORMULA FOR CHANGING CROSSING SPEED

J. P. Devlin*,[1], G. H. Hoffstaetter[1,2], and D. P. Barber[3]
[1]CLASSE, Cornell University, Ithaca, NY, USA
[2]Brookhaven National Laboratory, Upton, NY, USA
[3]Dept. of Mathematics and Statistics, University of New Mexico, Albuquerque, NM, USA

Content from this work may be used under the terms of the CC BY 4.0 licence (© 2022). Any distribution of this work must maintain attribution to the author(s), title of the work, publisher, and DOI.

Abstract

When the closed-orbit spin tune is ramped linearly through an isolated spin-orbit resonance, the asymptotic polarization loss is well-approximated by the Froissart-Stora formula. However, it is often observed in accelerator simulations that the crossing speed, defined as the slope of the amplitude-dependent spin tune with respect to the machine azimuth, changes at the moment of resonance crossing. For example, the behavior of the amplitude-dependent spin tune in the vicinity of a higher-order spin-orbit resonance can often be reasonably approximated by such a piecewise-linear function. In this paper, we derive an extension to the Froissart-Stora formula which describes the asymptotic polarization loss in the case of changing crossing speed. We then demonstrate that this formula provides a good estimate of the polarization lost when crossing a higher-order spin-orbit resonance in both a toy model and simulations of RHIC.

INTRODUCTION

In polarized hadron colliders, such as the Relativistic Heavy Ion Collider (RHIC) at Brookhaven National Laboratory, the primary obstacles in the way of high polarization are spin-orbit resonances [1]. At low energy, the dominant resonances are first-order spin-orbit resonances, for which it is well-known that the degree of depolarization encountered upon resonance crossing can be approximated using the Froissart-Stora formula [2]. At high energy, polarization can only be maintained if Siberian snakes are introduced to eliminate all first-order resonances, leaving higher-order resonances as the dominant effect. It is not well-known that the Froissart-Stora formula can be applied to some higher-order resonances as well [3]. In this paper, the Froissart-Stora formula is extended to apply to a larger class of higher-order resonances.

THE SINGLE-RESONANCE MODEL

First-order spin-orbit resonances are usually studied in the context of a toy model known as the single-resonance model (SRM) [4]. In this model, only one Fourier term is retained in the spin-precession vector, leading to the equation of motion:

$$\begin{aligned}\boldsymbol{S}'(\theta) &= [\boldsymbol{\Omega}_0(\theta) + \boldsymbol{\omega}(z(\theta),\theta)] \times \boldsymbol{S}(\theta),\\ \boldsymbol{\Omega}_0(\theta) &= \nu_0 \boldsymbol{n}_0(\theta),\\ \boldsymbol{\omega}(z(\theta),\theta) &= \epsilon[\cos(\kappa\theta+\phi)\boldsymbol{m}(\theta) + \sin(\kappa\theta+\phi)\boldsymbol{l}(\theta)].\end{aligned} \tag{1}$$

Here, ν_0 is the closed-orbit spin tune, $(\boldsymbol{m}, \boldsymbol{l}, \boldsymbol{n}_0)$ is a periodic coordinate system in which spins on the closed orbit rotate uniformly around $\boldsymbol{n}_0$ with frequency ν_0, ϵ is the resonance strength, ϕ is the resonance phase, and $\kappa = k_0 + \boldsymbol{k}\cdot\boldsymbol{Q}$, where $(k_0, \boldsymbol{k}) \in \mathbb{Z}^4$ and $\boldsymbol{Q}$ contains the orbital tunes.

This model's name derives from the fact that it contains a single spin-orbit resonance located at $\nu_0 = \kappa$. Froissart and Stora found that, in the case of a linear resonance crossing, i.e., $\nu_0(\theta) = \kappa + \alpha\theta$, the asymptotic polarization loss could be derived analytically [2]. With the initial condition $s_3(-\theta_0) = 1$ ($s_3 \equiv \boldsymbol{S}\cdot\boldsymbol{n}_0$), their result (the Froissart-Stora formula) is:

$$\lim_{\theta_0\to\infty} s_3(\theta_0) = 2\exp\left(-\frac{\pi\epsilon^2}{2\alpha}\right) - 1. \tag{2}$$

The Froissart-Stora formula can be generalized to higher-order resonances with the substitutions $s_3 \to J_S \equiv \boldsymbol{S}\cdot\boldsymbol{n}$ (the spin action) and $\alpha \to \mathrm{d}\nu/\mathrm{d}\theta$, where $\boldsymbol{n}$ is the invariant spin field (ISF) and ν is the amplitude-dependent spin tune (ADST) [3, 5, 6]. The problem with this idea is that the variation of ν with the reference energy can be very complicated so that ν does not vary linearly with θ even when the reference energy is ramped linearly.

In simulations of real accelerators, it is often found that ν is almost piecewise linear as a function of θ, with the slope changing at the moment of resonance crossing. Hence, one way to generalize the Froissart-Stora formula is to instead use:

$$\nu(\theta) = \begin{cases}\kappa + \alpha_1\theta, & \theta < 0\\ \kappa + \alpha_2\theta, & \theta \geq 0.\end{cases} \tag{3}$$

After a calculation similar to that of Froissart and Stora with the initial condition $J_S(-\theta_0) = 1$, this leads to:

$$\begin{aligned}\lim_{\theta_0\to\infty} J_S(\theta_0) = 2\exp&\left[-\frac{\pi\epsilon^2}{8}\left(\frac{1}{\alpha_1}+\frac{1}{\alpha_2}\right)\right]\\ &\times\left|\frac{\Gamma\left(\frac{1}{2}+\frac{i\epsilon^2}{8\alpha_2}\right)}{\Gamma\left(\frac{1}{2}+\frac{i\epsilon^2}{8\alpha_1}\right)}\cosh\left(\frac{\pi\epsilon^2}{8\alpha_2}\right)\right.\\ &\left.-\sqrt{\frac{\alpha_2}{\alpha_1}}\frac{\Gamma\left(1+\frac{i\epsilon^2}{8\alpha_2}\right)}{\Gamma\left(1+\frac{i\epsilon^2}{8\alpha_1}\right)}\sinh\left(\frac{\pi\epsilon^2}{8\alpha_2}\right)\right|^2 - 1.\end{aligned} \tag{4}$$

The derivation is to be published elsewhere.

* jpd285@cornell.edu

ISBN: 978-3-95450-261-5 ISSN: 2673-7000 doi: 10.18429/JACoW-NAPAC2025-TUP011

ASPECTS OF STROBOSCOPIC AVERAGING FOR THE INVARIANT SPIN FIELD

E. Hamwi*[1], J. P. Devlin[1], M. G. Signorelli[1], and G. H. Hoffstaetter[1,2]

[1]CLASSE, Cornell University, Ithaca, New York, USA
[2]Brookhaven National Laboratory, Upton, New York, USA

Content from this work may be used under the terms of the CC BY 4.0 licence (© 2022). Any distribution of this work must maintain attribution to the author(s), title of the work, publisher, and DOI.

Abstract

A new method is formulated for calculating the invariant spin field (ISF) at a phase space point by leveraging the property that spins which are distributed along the ISF achieve maximum time-averaged polarization. To quantify this, we construct the time-average of spin rotation matrices beginning at a certain phase space point. It is recognized that the ISF vector at that point achieves the matrix-norm, meaning that the ISF corresponds to the first right-singular vector of that matrix. We show the relation of this method with traditional stroboscopic averaging, such that these methods are two sides of the same coin. This approach offers a new perspective in invariant spin field calculations.

INTRODUCTION

The semi-classical spin dynamics used in accelerator physics is described by the Thomas-Bargmann-Michel-Telegdi (T-BMT) equation [1–3]. For purely magnetic fields, it is

$$\frac{\mathrm{d}\boldsymbol{S}}{\mathrm{d}t} = -\frac{q}{m\gamma}\left[(1+G\gamma)\boldsymbol{B}_\perp + (1+G)\boldsymbol{B}_\parallel\right]\times\boldsymbol{S}, \quad (1)$$

where G is the anomalous gyromagnetic ratio, γ is the Lorentz factor, $\boldsymbol{B}_\parallel$ is the component of the magnetic field parallel to the particle velocity, and $\boldsymbol{B}_\perp = \boldsymbol{B} - \boldsymbol{B}_\parallel$. In a circular accelerator, the static magnetic fields along the co-moving coordinate system are periodic in space with the ring's circumference C:

$$\boldsymbol{B}(x, y, s + C) = \boldsymbol{B}(x, y, s). \quad (2)$$

However, in general, the fields along a particle's trajectory are not periodic with the circumference because the trajectory itself is not periodic. Therefore, except for a particle traveling on the closed orbit, the spin motion is not periodic. However, if the T-BMT equation is expressed in action-angle coordinates, it becomes evident that the spin motion is quasiperiodic in the orbital phases and in the azimuth θ around the ring [4]. As in Floquet's theorem, the solution can then be written as

$$\boldsymbol{S}(\theta) = U_{\boldsymbol{J}}(\theta, \boldsymbol{\phi}(\theta))\ \exp(\boldsymbol{\mathcal{J}}\nu_{\boldsymbol{J}}\theta)\ U_{\boldsymbol{J}}(0, \boldsymbol{\phi}(0))^{\mathrm{T}}\,\boldsymbol{S}(0) \quad (3)$$

where $\boldsymbol{\mathcal{J}}$ is the generator of rotations around the third axis, $\nu_{\boldsymbol{J}}$ is an *amplitude-dependent spin tune* (ADST), and $U_{\boldsymbol{J}} = [\boldsymbol{u}_1, \boldsymbol{u}_2, \boldsymbol{n}]_{\boldsymbol{J}}$ is an *invariant frame field* (IFF). There are situations where an ADST and/or an IFF do not exist, such as when the beam is sitting on an orbital resonance. We restrict further discussion to situations where an ADST and an IFF both exist. The inverse matrix of the IFF in the above equation transports the initial spin coordinates into a system in which the spin rotates around the third axis with uniform frequency ν. Then, the IFF transports the spin back into the accelerator's coordinate system. For spin dynamics, the IFF is therefore analogous to a normal-form transformation of the orbital motion.

The axis around which the spin rotates in the IFF is $\boldsymbol{n}$, known as the *invariant spin field* (ISF). The projection of a particle's spin vector onto the ISF, $J_S \equiv \boldsymbol{S}\cdot\boldsymbol{n}$, has been shown to be an adiabatic invariant of spin motion [5]. It is the non-adiabatic change of this quantity that is responsible for beam depolarization. The computation of the ISF in accelerator simulations is therefore of great interest, and that subject is the topic of this paper.

STROBOSCOPIC AVERAGING

The first non-perturbative algorithm available for efficiently computing the ISF with three-dimensional orbital motion was *stroboscopic averaging* [6]. To begin, we define a spin field as a function $\boldsymbol{f} : \mathbb{R}^6 \times \mathbb{R} \to S^2$ satisfying the T-BMT equation along any orbital trajectory, where S^2 is the unit sphere in $\mathbb{R}^3$. The ISF is a spin field which is 2π-periodic in the azimuth, i.e., $\boldsymbol{n}(\boldsymbol{z}, \theta + 2\pi) = \boldsymbol{n}(\boldsymbol{z}, \theta)$ with $\boldsymbol{z} = (\boldsymbol{J}, \boldsymbol{\phi})$. If the orbital motion is integrable and an IFF exists, any sufficiently-smooth spin field $\boldsymbol{f}$ satisfies

$$\begin{aligned}\lim_{N\to\infty}\frac{1}{N+1}\sum_{j=0}^{N}\boldsymbol{f}(\boldsymbol{J}_0, \boldsymbol{\phi}_0, \theta_0 + 2\pi j)\\ = \langle \boldsymbol{f}(\boldsymbol{J}_0, \boldsymbol{\phi}, \theta_0)\cdot\boldsymbol{n}(\boldsymbol{J}_0, \boldsymbol{\phi}, \theta_0)\rangle_{\boldsymbol{\phi}}\,\boldsymbol{n}(\boldsymbol{J}_0, \boldsymbol{\phi}_0, \theta_0).\end{aligned} \quad (4)$$

As long as the expectation value is not zero, this property can be used to recover an approximate ISF by choosing a large N.

The intuitive derivation of this method is that shifting θ_0 by an integer multiple of 2π does not affect the average in the limit $N \to \infty$, so the result must be 2π-periodic in the azimuth. Additionally, by the linearity of the T-BMT equation, the average in Eq. (4) is also a solution of the T-BMT equation. Hence, the result is either zero or parallel to an ISF.

For simplicity, the spin field $\boldsymbol{f}$ is usually chosen to be constant across phase space at the starting azimuth, i.e.,

* eh652@cornell.edu

ISBN: 978-3-95450-261-5 ISSN: 2673-7000 doi: 10.18429/JACoW-NAPAC2025-TUP012

BEAM-BASED MEASUREMENT OF LCLS-II INJECTOR SOLENOID MISALIGNMENTS*

A. Osman†, T. Maxwell, F. Zhou
SLAC National Accelerator Laboratory, Menlo Park, CA, USA

Abstract

Solenoid focusing is commonly used in accelerators for electron-beam containment and to compensate for space-charge induced emittance growth at low beam energies. However, misalignment between the solenoid field and the beam trajectory can result in degraded emittance compensation due to orbit kicks, dispersive effects, and non-linearities in the magnetic field profile. This paper presents a technique for beam-based measurement of solenoid misalignments, using expressions derived from a hard-edged solenoid linear transfer matrix with known beam parameters. The results of measurements conducted at the LCLS-II injector are presented as a validation of this method, along with simulation studies that estimate the impact of solenoid misalignments on emittance growth.

INTRODUCTION

The LCLS-II injector features a low-power RF photocathode gun, two solenoids, and an RF buncher (see Fig. 1), which prepare the electron beam for injection into the main linear accelerator [1]. At these early stages, the low energy beam is particularly susceptible to emittance growth due to space-charge forces. Solenoid magnets are used both to confine the beam and to compensate for emittance growth [2, 3].

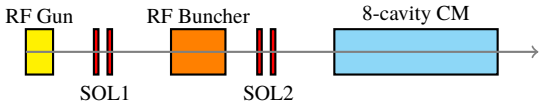


Figure 1: Schematic of injector layout showing RF gun, solenoids (SOL1, SOL2), buncher, and 8-cavity SRF cryomodule.

Table 1: Beam and Solenoid Parameters (Hard-Edged)

Parameter	Value
Beam momentum (p)	1.03 MeV/c
Maximum B_0	0.074 T
Effective length (L)	0.21 m
Larmor rotation angle (θ_L)	2.26 rad
Effective focal length (f)	41 mm

Precise alignment of the beam trajectory through the solenoids is crucial to achieving low final emittance. Misalignments introduce orbit kicks and dispersive effects that compromise beam quality. The effects of higher-order magnetic field terms, commonly referred to as geometric aberration, also become more pronounced at larger radial distances from the magnetic axis [3-5].

In this paper, we develop a beam-based method for measuring solenoid misalignments. By fitting the beam deflection at a downstream beam position monitor (BPM) as a function of solenoid field, we extract the transverse offsets and angles of the incoming beam relative to the solenoid magnetic axis. This requires knowledge of the beam energy, drift length to the measurement BPM, and accurate magnetic measurements of the solenoid.

We also present simulation results that estimate the impact of solenoid misalignments on transverse emittance growth in the LCLS-II injector.

SOLENOID MODELING AND TRANSFER MATRIX FORMALISM

The LCLS-II injector solenoids exhibit approximately Gaussian on-axis magnetic field profiles, as shown in Fig. 2. Nonetheless, the effect of the solenoid on the trajectory of the beam can be effectively modeled using a hard-edged solenoid transfer matrix. Spatial separation between the solenoid and RF fields is important for this approximation, although in principle this limitation can be overcome with further modeling (see Ref. [5]).

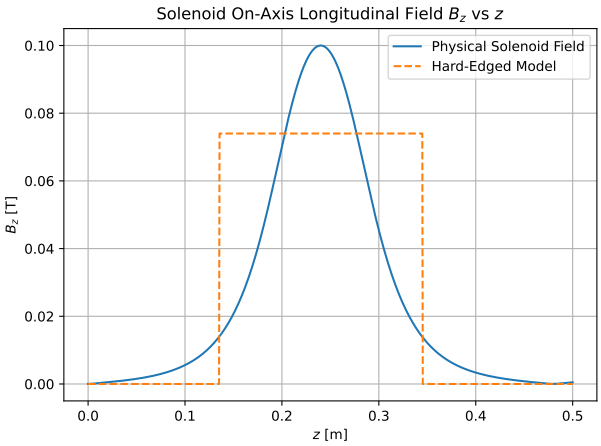


Figure 2: Comparison of measured solenoid field profile with equivalent hard-edge model used for linear beam dynamics modeling.

The transfer matrix for an ideal hard-edged solenoid of length L and a uniform longitudinal field B_0, acting on a particle with momentum p, can be expressed as [6]:

* Work supported in part by US Department of Energy contract number DE-AC02-76SF00515.
† aosman@slac.stanford.edu

Content from this work may be used under the terms of the CC BY 4.0 licence (© 2022). Any distribution of this work must maintain attribution to the author(s), title of the work, publisher, and DOI.

ISBN: 978-3-95450-261-5 ISSN: 2673-7000 doi: 10.18429/JACoW-NAPAC2025-TUP014

BEAM-BEAM LIMITATION TOWARD 10^{34} cm^{-2} s^{-1} LUMINOSITY FOR ELECTRON-ION COLLIDER*

Derong Xu†, William Bergan, Yun Luo, Brookhaven National Laboratory, Upton, NY, USA

Abstract

Achieving the design luminosity of in the Electron-Ion Collider (EIC) requires a deep understanding of beam-beam interaction limits in a weak-strong collision regime with flat hadron beams. This contribution presents recent studies of synchro-betatron resonances — particularly the coupling resonance $2\nu_x - 2\nu_y + p\nu_z = 0$ — that can induce emittance transfer between the horizontal and vertical planes and limit luminosity performance. We identify the hourglass effect, caused by the proton bunch length being comparable to the vertical beta functions of both beams at the interaction point (IP), as the dominant source driving this resonance. We further investigate how physical noise, such as intra-beam scattering and fluctuations in the electron orbit and beam size, couples with the beam-beam interaction to amplify emittance growth and reduce luminosity. Mitigation strategies are also discussed. These studies provide important guidance for future EIC operation and inform strategies for potential upgrades.

INTRODUCTION

The Electron-Ion Collider (EIC) is poised to operate in a novel regime of beam dynamics that pushes beyond current collider experience. Achieving high luminosity is a fundamental objective for all modern colliders, as it directly determines the event rate for physics processes of interest. At the EIC, this goal must be balanced against complex beam dynamics effects, particularly those arising from intense beam-beam interactions and the geometric configurations imposed by the collider design.

The beam-beam interaction, a nonlinear electromagnetic force exerted between colliding bunches, is intrinsically six-dimensional and strongly influences beam quality. In lepton colliders, a well-defined empirical beam-beam limit has been established, with typical beam-beam parameters on the order of $0.10 \sim 0.15$ [1–3]. In contrast, hadron colliders operate with beam-beam parameters approximately one order of magnitude lower due to the absence of radiation damping [4]. The EIC enters uncharted territory by simultaneously operating with beam-beam parameters comparable to those achieved in high-performance lepton and hadron colliders — a combination never before realized in a single machine.

To accommodate detector constraints and suppress parasitic collisions, the EIC employs a large crossing angle at the interaction point (IP). This geometry is compensated by crab cavities, which restore effective head-on collision through transverse RF kicks that tilt the bunches in the horizontal-longitudinal plane. Crab crossing was successfully demonstrated in KEKB through collisions of crabbing electron and positron bunches, leading to record luminosities [5]. Crabbing of proton bunches has been experimentally demonstrated at CERN's SPS [6]. As a result, crab cavities have become an essential component in the design of next-generation colliders, including the HL-LHC [7] and the EIC [8].

A key innovation in the EIC design is the use of flat hadron beams, in which the vertical emittance is an order of magnitude smaller than the horizontal [9]. While flat beams are naturally produced in electron storage rings, they are nontrivial to achieve in hadron storage rings due to the lack of damping mechanisms. Given the flatness at the IP characterized by the aspect ratio $\kappa = \sigma_y^*/\sigma_x^*$, the luminosity and beam-beam parameters scales as:

$$L \propto \frac{1}{\kappa}, \quad \xi_x \propto \frac{\beta_x^*}{1+\kappa}, \quad \xi_y \propto \frac{\beta_y^*}{\kappa(1+\kappa)} \tag{1}$$

By adjusting the beta functions β_x^* and β_y^* accordingly, one can boost luminosity without increasing the beam-beam parameters beyond acceptable limits.

Together, these design features, strong beam-beam interactions, crab crossing, and flat hadron beams, define a challenging yet promising regime for collider design. They also necessitate detailed simulation studies to understand their interplay and identify potential limitations in integrated luminosity, which this work seeks to address.

SYNCHRO-BETATRON RESONANCE

In the presence of crab cavities, the finite bunch length introduces a significant coupling between the transverse and longitudinal dynamics. The transverse kick from the crab cavity depends sinusoidally on the longitudinal position z, and for the hadron bunch parameters of the EIC, the condition $|k_c z| \sim 1$ is met, where k_c is the wave number of the crab cavity. This leads to nonlinear crabbing, where the induced offset at the IP contains cubic terms in z. This nonlinearity couples the transverse betatron motion with the synchrotron oscillation, giving rise to synchro-betatron resonances.

Frequency map analysis reveals two families of resonances:

$$m\nu_x + p\nu_z = 1, \tag{2}$$

$$2\nu_x - 2\nu_y + p\nu_z = 1 \tag{3}$$

where m and p are integers, and $\nu_{x,y,z}$ are horizontal, vertical, and longitudinal tunes, respectively.

While the first family appears only in the presence of crab crossing, the second exists even for head-on collisions due

* Work supported by Brookhaven Science Associates, LLC under Contract No. DE-SC0012704 with the U.S. Department of Energy.

† dxu@bnl.gov

Content from this work may be used under the terms of the CC BY 4.0 licence (© 2022). Any distribution of this work must maintain attribution to the author(s), title of the work, publisher, and DOI.

ISBN: 978-3-95450-261-5 ISSN: 2673-7000 doi: 10.18429/JACoW-NAPAC2025-TUP015

BEAM HALO FORMATION WITH DIFFERENT CATHODE DISTRIBUTIONS*

I. Neththikumara†, K. Deitrick, B. R. Gamage, R. Rimmer, T. Satogata, N. Sereno, S. Setiniyaz
Thomas Jefferson National Accelerator Facility, Newport News, VA, USA
W. Bergan, E. Wang, Brookhaven National Lab, Upton, NY, USA
N. Wang, Cornell University, Ithaca, NY, USA

Abstract

Beam halo is the low-density distribution of particles extending beyond the beam core, and its generation and mitigation are important topics in particle accelerator design. In particular, effective mitigation of beam halo is essential for the hadron cooler design based on Energy Recovery Linac (ERL), which is being developed to suppress emittance growth in high energy proton beams in the Electron-Ion Collider. The ERL is required to deliver an electron beam with average beam current of 100 mA and a bunch charge of 1 nC. In the ERL injector and booster-linac, space charge effects are stronger due to the relatively low beam energy (6 MeV). Additionally, the longer bunch length of approximately 100 ps in this regime *vs* the RF period of 5.08 ns makes the formation of beam halos more likely. Therefore, effective collimation of beam halo is critical for maintaining the required beam parameters. To design an effective collimation scheme, several halo distributions were generated at the cathode and used to study halo formation within the injector-merger. This paper presents different halo distributions and halo formation, providing insights on halo collimation strategy.

INTRODUCTION

A Strong Hadron Cooler (SHC) based on an Energy Recovery Linac (ERL) is a possible solution to cool high energy proton beams in the U.S. Electron-Ion Collider (EIC), with the goal of mitigating emittance growth and meeting high-luminosity requirements of the EIC. This ERL cooler is designed to operate in two distinct modes (modes A & B), to cool down hadron beams with energies 100 GeV and 275 GeV. Electron beam of an average current 100 mA is used with peak bunch currents of 10 A and 13 A for mode A and mode B, respectively. Electron beam energies at the entrance to the cooling section are 55 MeV and 150 MeV so that the velocities of both hadrons and co-propagating electrons are equal. A schematic of the SHC-ERL is given in Fig. 1 [1, 2].

Cooling effectiveness depends on maintaining the quality of the intense, high current electron beam as it transported through the SHC-ERL towards the cooling sections. Higher current beams tend to create beam halo due to intense space charge fields, magnet misalignment and imperfections, orbit misalignment and steering errors and RF errors. Beam halo is usually defined as the low-density particle distribution formed around the denser beam core. These halos create problems in maintaining quality beam transport and could cause radiation damage to beamline equipment. Mitigation of halo formation and propagation is critical for machine protection, while maintaining proper beam transport.

HALO FORMATION AT CATHODE

Halo formation at the cathode occurs due to multiple reasons, creating halo in both transverse and longitudinal phase space.

- Larger cathode response time resulting longer tails, eventually contributes to formation of beam halo [3].
- Degradation of cathode material leads surface imperfections, affecting its quantum efficiency (QE). This could lead to increased thermal emittance or non-uniform electron emission that could eventually create beam halo.
- Mismatch of the cathode spot size influences create beam halo as this strongly affects important beam properties such as beam brightness, emittance, energy spread and space charge effects [4].

If the density functions of the core and halo are given by ρ_1 and ρ_2, then the beam density with halo is expressed as

$$\rho(r) = \rho_1 \exp\left(\frac{r}{\sigma_1\sqrt{2}}\right)^2 + \rho_2 \exp\left(\frac{r}{\sigma_2\sqrt{2}}\right)^2, \quad (1)$$

where $\rho_2 \leq \rho_1$ and $\sigma_2 \geq \sigma_1$ [9]. Here $\rho_{(1,2)}$ define the amplitudes of the two density profiles, while r denotes the radius.

Beam halo studies in the SHC-ERL is limited to the beam dynamics during its design phase. We used Distgen package [5] to generate the distributions and Bmad [6] for tracking studies and implementing collimation scheme.

Core Beam

The core beam used in SHC-ERL tracking studies has a radially truncated, beer-can-shaped distribution with a total charge of 1 nC, as illustrated in Fig. 2. The mean transverse energy is 130 meV. The beam accelerates to approximately 400 keV at the injector gun, with an average beam current of 100 mA. The transverse distribution is Gaussian with a

* This work is supported by Jefferson Science Associates, LLC under U.S. DOE Contract DE-AC05-06OR23177 and Brookhaven Science Associates, LLC, Contract DESC0012704

† isurunh@jlab.org

Content from this work may be used under the terms of the CC BY 4.0 licence (© 2022). Any distribution of this work must maintain attribution to the author(s), title of the work, publisher, and DOI.

ISBN: 978-3-95450-261-5 ISSN: 2673-7000 doi: 10.18429/JACoW-NAPAC2025-TUP016

BEAM TILT CHARACTERIZATION USING PASSIVE STREAKING STRUCTURES

T. Xu*, A. A. Lutman, A. Halavanau
SLAC National Accelerator Laboratory, Menlo Park, CA, USA

Abstract

Passive wakefield devices such as corrugated structures have demonstrated great potential for longitudinal phase space control and diagnostics in FELs. In this paper, we will discuss the application of corrugated structures in beam tilt characterization. We show that a tilted beam experiences asymmetric kicks when passing through corrugated metal jaws and the asymmetry of streaked profiles is related to the degree of tilt. Practical implementation of beam tilt correction is discussed.

INTRODUCTION

Passive streaking devices, such as corrugated structures, have emerged as powerful tools for longitudinal beam diagnostics in free-electron lasers (FEL), enabling precise measurements of the temporal beam profile through time-dependent wakefield kicks [1–4]. These devices allow reconstruction of the electron bunch length and longitudinal phase space in FEL beamlines and are critical for optimizing FEL performance. Recent studies have further demonstrated their utility in tailoring longitudinal phase space via wakefield interaction [5–7], underscoring their versatility in beam manipulation and diagnostics. While longitudinal diagnostics are well-established, the characterization of spatiotemporal correlations, particularly beam tilt (X-Z correlation), remains a significant challenge. Such tilts arise in high-brightness beams due to transverse-longitudinal coupling from wakefield effects in accelerating structures or coherent synchrotron radiation (CSR)-induced energy spread during strong compression [8]. These correlations degrade beam quality, leading to suboptimal FEL gain, and are difficult to diagnose with conventional methods.

In this work, we propose a method to characterize beam tilt using corrugated structures. We show that when a tilted beam traverses different corrugated jaws, it experiences asymmetric transverse kicks, producing a corresponding asymmetry in the streaked image. By comparing the streaked profiles from opposing jaws, one can extract information about the tilt magnitude and direction. As a proof of concept, we simulate a tilt correction procedure based on minimizing this asymmetry and demonstrate effective reduction of the beam tilt through upstream optical tuning.

WAKEFIELD OF CORRUGATED STRUCTURES

As most beam tilt occurs in the X-Z plane, we will consider wakefields of a beam with X-Z tilt in a vertical dechirper that streaks horizontally. The dipole and quadrupole wake functions near the single jaw of a vertical dechirper are given by [9]

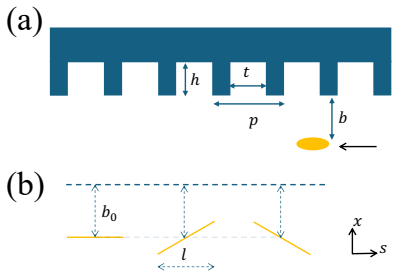


Figure 1: (a) Cartoon of an e-beam near a single plate corrugated structure. (b) Beams with different tilt orientation. $\mu = 0$ (left), $\mu > 0$ (middle), and $\mu < 0$ (right).

$$w_{xd}(s) = \frac{2}{b^3} s_{0x} \left[1 - \left(1 + \sqrt{\frac{s}{s_{0x}}} \right) e^{-\sqrt{\frac{s}{s_{0x}}}} \right] \quad (1)$$

$$w_{xq}(s) = \frac{3}{b^4} s_{0x} \left[1 - \left(1 + \sqrt{\frac{s}{s_{0x}}} \right) e^{-\sqrt{\frac{s}{s_{0x}}}} \right] \quad (2)$$

where s is the bunch longitudinal coordinate with head at $s = 0$ m, b is the particle offset from dechirper plate, $s_{0x} = \frac{8b^2 t}{9\pi\alpha^2 p^2}$, p and t are the period and longitudinal gap of the structure (see Fig. 1), $\alpha = 1 - 0.465\sqrt{t/p} - 0.07(t/p)$.

The dipole and quadrupole wake potential are given by

$$W_d(s) = \int_{-\infty}^{s} \mathrm{d}s' \int_{-\infty}^{\infty} \mathrm{d}b'\, w_{xd}(s - s', b')\rho(s', b') \quad (3)$$

$$W_q(s) = \int_{-\infty}^{s} \mathrm{d}s' \int_{-\infty}^{\infty} \mathrm{d}b' \Delta b\, w_{xq}(s - s', b')\rho(s', b') \quad (4)$$

here s' and b' are the longitudinal coordinate and offset of the source particle, ρ is the spatiotemporal profile of the beam, Δb is the horizontal offset between source and probe particle and depends on the form of $\rho(s', b')$. Consider a pencil beam with bunch length l, where its horizontal coordinate x and longitudinal coordinate s are related by $x = \mu(s - l/2)$. Here μ denotes the tilt in the x-s space [8]. As illustrated in Fig. 1(b), the local offset b is then $b = -\mu(s - l/2) + b_0$, where b_0 is the nominal offset of beam centroid to jaw. To model the effect of beam tilt on wakefield kicks, we calculate the dipole and quadrupole wake voltage for a bunch with charge Q passing near a single vertical dechirper plate of length L using the following beam and structure parameters: $l = 60\,\mu$m, $Q = 250$ pC, $L = 2$ m, $p = 500\,\mu$m, $t = 250\,\mu$m, $b_0 = 500\,\mu$m. The results are shown in Fig. 2. For a fixed centroid offset b_0, beams with different tilt values experience different transverse kicks due to the variation in local offset along the bunch. This leads to an asymmetric wakefield

* txu@slac.stanford.edu

Content from this work may be used under the terms of the CC BY 4.0 licence (© 2022). Any distribution of this work must maintain attribution to the author(s), title of the work, publisher, and DOI.

ISBN: 978-3-95450-261-5 ISSN: 2673-7000 doi: 10.18429/JACoW-NAPAC2025-TUP017

REALISTIC SIMULATION OF THE 76-INCH CYCLOTRON: COMSOL MAGNETIC-FIELD EXPORT INTEGRATED WITH AN OPAL PARTICLE-TRACKING MODEL

S.-C. Pai*, M. Backfish, E. Prebys, University of California Davis, Davis, CA, USA

Abstract

Accurate studies of particle behavior in accelerator chambers require precise magnetic field maps with regard to the iron geometry. We generated a realistic magnetic-field map for the 76-inch cyclotron at Crocker Nuclear Lab using COMSOL Multiphysics, then imported it into the OPAL (Object-Oriented Parallel Accelerator Library) software to model particle trajectories. It accurately simulates beam dynamics, provides reliable validation against measured data, and establishes a foundation for future cyclotron optimization and upgrades.

INTRODUCTION

Our facility at UC Davis's Crocker Nuclear Lab (CNL) operates a 76-inch cyclotron, which is based on the design of the Oak Ridge Isochronous Cyclotron (ORIC) and has been operating since 1966. Despite its age and the removal of certain components, such as the valley and harmonic coils, the cyclotron continues operation. Unfortunately, historical data and some detailed documentation for our cyclotron have been lost, which means that although we know how to operate the machine, we know very little about the internal particle dynamics during operations. Scientists used to measure the magnetic field map by using a Hall probe with two-axis statistical analysis [1–3]. Unfortunately, we cannot open the chamber and spend a few weeks measuring the field. In order to get correct data, we have adopted finite element simulation of the magnetic field from COMSOL and use OPAL (Object Oriented Parallel Accelerator Library) [4] to analyze and predict particle behavior inside the machine, which will allow us to effectively analyze and predict particle behavior, including particle trajectories and tunes. This simulation will allow us to optimize performance and potentially plan upgrades without significant operational disruption.

PARTICLE-IN-CELL SIMULATION, OPAL

OPAL is a particle-in-cell (PIC) code for charged particle optics in linear, ring accelerator, cyclotron, etc. It has multiple flavors, such as OPAL-cycl, OPAL-t, and OPAL-map; each can only be applied to specific features. In our work, we used OPAL-cycl to model our structure. The goal of this study is to model particle behavior numerically within the cyclotron and accurately predict beam trajectories, which would result in more effective diagnostics for machine tuning and for planning upgrades.

* pai@ucdavis.edu

OPAL Structure

To model the particle trajectories with OPAL, the system requires the magnetic field in a specific format. Generally, the magnetic field can be expressed by

$$\frac{d\mathbf{p}(t)}{dt} = q\left(c\beta \times \mathbf{B} + \mathbf{E}\right), \tag{1}$$

which comes with rest mass, charge, and Lorentz factor. Our 76-inch cyclotron is designed to be isochronous, and we need to consider that the loss of isochronism due to the relativistic increase in mass limits the energy reach of a classical cyclotron. The momentum p per particle can be denoted in 3D Cartesian coordinates with normalization by m_0c as:

$$\begin{aligned}
\frac{dp_x}{dt} &= \frac{q}{m_0c}E_x + \frac{q}{\gamma m_0}(p_yB_z - p_zB_y),\\
\frac{dp_y}{dt} &= \frac{q}{m_0c}E_y + \frac{q}{\gamma m_0}(p_zB_x - p_xB_z),\\
\frac{dp_z}{dt} &= \frac{q}{m_0c}E_z + \frac{q}{\gamma m_0}(p_xB_y - p_yB_x).
\end{aligned} \tag{2}$$

To simplify the model. We start with a single-particle tracking mode. The charged particle is only affected by the electric field E and the magnetic field B, which both are superpositions of external field and self-field.

$$\begin{aligned}
\mathbf{E} &= \mathbf{E}_{\text{ext}} + \mathbf{E}_{\text{self}}\\
\mathbf{B} &= \mathbf{B}_{\text{ext}} + \mathbf{B}_{\text{self}}\,.
\end{aligned} \tag{3}$$

For given E and B values, we could explicitly calculate each particle with the equation of motion of a charged particle in an electromagnetic field. We could also solve for E_{self} B_{self} numerically as a function of time. With the appropriate Lorentz Transformation L

The modeling capability of OPAL-cycl [5] is solving the Vlasov-Poisson equation system in the cyclotron with an external static magnetic field and fixed-frequency RF field. In modeling a high-intensity isochronous cyclotron, space charge effects should be considered not only in a single bunch but also in the mutual interactions of neighboring multiple bunches in the radial direction [6].

The magnetic field map at the center plane is read from an ASCII file. Instead of Cartesian coordinates, the system required a spherical coordinate frame. In this case, we could only consider two situations: whether the B-Field is at vertical axis $Z = 0$ or $Z \neq 0$

In most cyclotrons, we only measure the median plane B-field ($Z = 0$) by Gaussmeter. The magnetic field outside the median plane needs to be expanded along the Z axis.

Content from this work may be used under the terms of the CC BY 4.0 licence (© 2022). Any distribution of this work must maintain attribution to the author(s), title of the work, publisher, and DOI.

ISBN: 978-3-95450-261-5 ISSN: 2673-7000 doi: 10.18429/JACoW-NAPAC2025-TUP019

POWER LOSS INDUCED BY WELDING BEADS IN THE HSR BEAM SCREEN OF THE ELECTRON-ION COLLIDER*

G. Wang†, A. Blednykh, M. Sangroula, S. Verdú-Andrés
Brookhaven National Laboratory, Upton, NY, USA

Abstract

In this paper, we present GdfidL-based simulations of resistive wall wake potential and power loss in the beam screen of the Hadron Storage Ring (HSR) of the Electron-Ion Collider (EIC). The resistive wall power loss is calculated from the wake potential computed in the finite-difference 3D electromagnetic code GdfidL. The study includes benchmarking against analytical results and comparison with CST simulations.

INTRODUCTION

The proton beam in the EIC HSR will operate with more than twofold increase in bunch numbers, each with a tenfold shorter bunch length compared to those in RHIC, as shown in Table 1. Consequently, the heating induced by the circulating beam in the vacuum components presents a significant challenge to the cryogenic system. An accurate calculation of the resistive wall heating induced by the beam is crucial for the proper design of the vacuum components.

Table 1: Compare Proton Beam Parameters Between RHIC and HSR (High E_{CM} Mode Operation)

	Number of bunches	R.M.S. bunch length
RHIC	111	60 cm
HSR	290	6 cm

In the past, CST has been used to calculate the resistive wall heating in the beam screen [1,2] by integrating the surface current over the resistive wall of the beam screen. In this work, we use GdfidL [3]to calculate the longitudinal wake potential and the loss factor due to the resistive wall of the screen. The heating power is obtained from the loss factor and compared with what was previously obtained from the CST.

BENCHMARKING GDFIDL WITH ANALYTICAL RESULTS

To ensure that the simulation code, GdfidL, is properly set up for calculating the resistive wall wake potential, we benchmarked its results with the analytical formula. For a beam pipe with circular cross section, the resistive wall wake potential can be calculated from the expression [4]:

$$W_{||} = \frac{\Delta E}{eQ_{bunch}} = \frac{Lc}{2^{3/2}\pi^2 a\sigma_z^{3/2}}\sqrt{\frac{Z_0}{\sigma}}\,G\left(\frac{z}{\sigma_z}\right), \qquad (1)$$

where:

$$G(x) = -\int_{-x}^{\infty}\frac{ye^{-\frac{y^2}{2}}dy}{\sqrt{y+x}},$$

a is the radius of the beam pipe, L is the length of the beam pipe, σ_z is the R.M.S. bunch length, σ is the conductivity of the beam pipe and $Z_0 \approx 377\Omega$ is the impedance of the free space. To benchmark GdfidL with the analytical results of eq. (1), we assume that the beam pipe is made of copper with conductivity of $5.8 \times 10^7\ S/m$ and its dimension is as shown in Fig. 1.

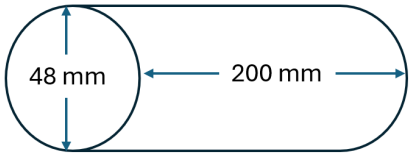


Figure 1: A schematic diagram showing the dimension of cylindrical beam pipe used to benchmark with GdfidL simulation.

As shown in Fig.2, the longitudinal wake potential calculated by GdfidL with the window wake method perfectly agrees with that obtained from the analytical expression of Eq. (1). However, the window wake method is very slow when calculating results with long wake range and fine mesh. Consequently, we use the FDTD method when a fine mesh is needed for the GdfidL simulation.

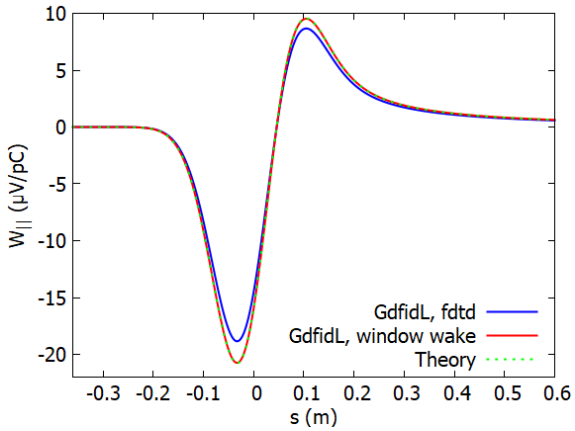


Figure 2: The longitudinal wake potential induced by a proton bunch with the R.M.S. bunch length of 6 cm in a circular copper beam pipe with the dimension shown in Fig. 1. The green dashed curve is obtained from the analytical results, i.e. Eq. (1). The blue solid curve is computed from GdfidL with finite difference time domain (FDTD) method and the red solid curve is computed from the window wake method in GdfidL.

* Work supported by Brookhaven Science Associates, LLC under Contract No. DE-SC0012704 with the U.S. Department of Energy.
† gawang@bnl.gov

Content from this work may be used under the terms of the CC BY 4.0 licence (© 2022). Any distribution of this work must maintain attribution to the author(s), title of the work, publisher, and DOI.

ISBN: 978-3-95450-261-5 ISSN: 2673-7000 doi: 10.18429/JACoW-NAPAC2025-TUP021

BeamNetUS PILOT YEAR REPORT: ENABLING ACCESS TO BEAM TEST FACILITIES*

C. Clarke†, M. Hogan, I. Rajkovic, E. Snively
SLAC National Accelerator Laboratory, Menlo Park, CA, USA
S. Doran, P. Piot, J. Power
Argonne National Laboratory, Lemont, IL, USA
M. Ilardi, K. Kusche, A. Lueangaramwong, W. Li, M. Palmer, I. Pogorelsky, N. Ramistella
Brookhaven National Laboratory, Upton, NY, USA
J. Jarvis, A. Valishev, M. Wallbank
Fermi National Accelerator Laboratory, Batavia, IL, USA
S. Barber, Q. Ji, W. Liu, J. Osterhoff, J. van Tilborg
Lawrence Berkeley National Laboratory, Berkeley, CA, USA
N. Vafaei-Najafabadi
Stony Brook University, Stony Brook, NY, USA
M. Poelker, A. Seryi
Thomas Jefferson National Accelerator Facility, Newport News, VA, USA

Content from this work may be used under the terms of the CC BY 4.0 licence (© 2022). Any distribution of this work must maintain attribution to the author(s), title of the work, publisher, and DOI.

Abstract

BeamNetUS is a network of facilities united in a common mission to advance accelerator research and applications of accelerator technology through improving awareness and access to these unique facilities. For its pilot campaign, the network includes facilities at Argonne National Laboratory (ANL), Brookhaven National Laboratory (BNL), Fermi National Accelerator Laboratory (FNAL), Lawrence Berkeley National Laboratory (LBNL), SLAC National Accelerator Laboratory, and Thomas Jefferson National Accelerator Facility (JLab). These facilities provide complementary capabilities enabling research in plasma physics, beam physics, material science, radiofrequency sources and structures, nuclear physics and electron beam irradiation. In 2025, BeamNetUS awarded time at the facilities through a competitive review process with a remit towards creating new, productive engagements. User awards were given to universities, industry and other laboratories. At NAPAC25 in a satellite meeting, we reflect on the BeamNetUS experience in its pilot year and plans for the future.

INTRODUCTION

The Department of Energy (DOE) National Laboratories represent immense investment into basic research facilities. The ten DOE Office of Science National Laboratories operate 13 User Facilities based around accelerators, serving more than 16,800 users each year, researching topics in physics, chemistry, material science and biology.

Less well known are the R&D facilities where the accelerator technologies and new applications are first developed. The National Laboratories build and run these facilities for R&D when they have a need, such as the NLCTA which originated for R&D for the "Next Linear Collider", or HiRES which was originally a novel gun technology demonstration, or UITF which was first used by NASA to study space radiation effects on materials.

These facilities are hidden gems of the National Laboratory system with unique equipment and experts. Raising awareness of their existence and facilitating external access to them is BeamNetUS's core mission.

The initial BeamNetUS network formed in 2024 (Fig. 1 and Table 1). Representatives from nine beam test facilities spanning six National Laboratories started the network with a mission to:

- Advance accelerator research and applications of accelerator technology;
- Provide access to unique accelerator and accelerator component resources;
- Foster collaboration to exchange ideas, skills and resources.

The network meets its mission by:

- Coordinating outreach and targeting communities not currently engaged in research at the facilities;
- Executing a program for external user engagements.

IMPROVING ACCESS AND AWARENESS

The main barrier to outside-use of the beam facilities at the National Laboratories is a lack of awareness of facilities' capabilities and availability. The Lab Partnering Service is a resource that lists facilities and expertise at the National Laboratories [1], however, it has a broad remit to cover all capabilities and lacks details of the beam test facilities.

BeamNetUS seeks to become the established brand for those looking for beam test facilities in the US, to simplify the process to find the best fit for the research. BeamNetUS launched a website [2] in 2024 that summarizes the facilities and provides a point of contact at each facility for direct

* BeamNetUS is supported by the U.S. Department of Energy, Office of Science, Accelerator Stewardship Program
† cclarke@slac.stanford.edu

ISBN: 978-3-95450-261-5 ISSN: 2673-7000 doi: 10.18429/JACoW-NAPAC2025-TUP022

COMMISSIONING OF A FUSION COLLIDER FOR INTERSTELLAR PROPULSION

G.P. Jackson[2], G.E. Bittlingmaier[1]
[1]Beam Alpha Incorporated, West Chicago, IL, USA
[2]Hbar Technologies, LLC, West Chicago, IL, USA

Content from this work may be used under the terms of the CC BY 4.0 licence (© 2022). Any distribution of this work must maintain attribution to the author(s), title of the work, publisher, and DOI.

Abstract

A prototype colliding beam accelerator has been fabricated for the study of a fusion-based propulsion concept for interplanetary exploration. The purpose of this prototype is to demonstrate collider luminosities commensurate with the requirements of this application. Direct emission of fusion daughters generates the exhaust velocities required for spacecraft speeds in excess of 1% of the speed of light. Past attempts at nuclear fusion energy production with colliding beams have been limited by Coulomb scattering, a deficiency overcome in this collider architecture. Instead of using fusion fuels such as p/Li7 and He3/He3 capable of generating the required thrust characteristics, this prototype employs deuterons. DD fusion produces neutrons that provide a convenient luminosity detection channel. The commissioning campaign described in this paper operates the collider at a peak beam kinetic energy of 54 keV at the interaction point. Axial confinement and radial focusing are achieved electrostatically. Proposed analysis of imminent beam measurements of axial (longitudinal) and radial (transverse) beam dynamics and beam lifetime are presented.

LOW LUMINOSITY COLLIDER

The fusion reactor architecture used in the proposed propulsion system [1] consists of an electrostatic charged particle trap [2-4] that brings two ion beams into collision with equal and opposite momentum. The goal is to directly emit a focussed flux of fusion daughters as an exhaust stream capable of generating a spacecraft velocity change of at least 4.6% of the speed of light [5].

Given the current state of accelerator physics, increasing collider luminosity by several orders of magnitude is the greatest challenge. A terrestrial prototype collider has been designed and built in order to begin the experimental process of increasing the achievable luminosity of this architecture. Instead of using appropriate fusion fuels for propulsion, this terrestrial prototype collides deuterons. By measuring luminosity [6] from the flux of emitted neutrons, and adapting the operations and technologies employed, the goal is to gradually achieve the required luminosity.

Many unique physics and technology issues arise from the proposed collider architecture. At a fundamental level, it makes no sense to concentrate on increasing luminosity if the single particle optics and beam dynamics are not already well understood. For this purpose, a second apparatus was designed and fabricated. Figure 1 contains a photograph of this "Lifetime Demonstrator" while it was un-dergoing vacuum cleaning via a controlled gas discharge.

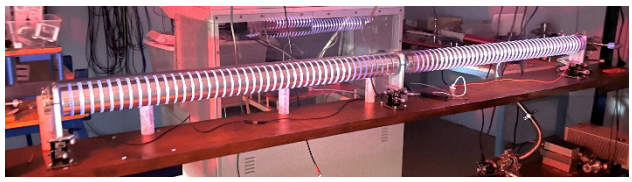


Figure 1: Luminosity Demonstrator apparatus while undergoing a gas discharge vacuum cleaning.

The physical structure of this is sketched in Fig. 2. Two quartz tubes (central green rectangles) are sealed at the center and ends by O-rings compressed by custom-fabricated stainless steel fittings. A future iteration of the apparatu will replace the O-rings with vacuum epoxy. The central fitting is 18' in length, and each quartz tube is 48" long. On either side of this structure exists various vacuum gauges, pumps, and valves. While on one side a destructive Faraday cup is used measure deuteron intensity, the other side is connected to the deuteron source. The axis formed by this structure is referred to as the axial direction, similar in some ways to the longitudinal coordinate in circular accelerators.

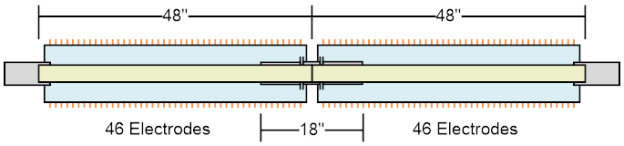


Figure 2: Illustration of the structure of the Lifetime Demonstrator apparatus.

Given the absence of steering magnets or other comparable devices in the radial (perpendicular to axial) direction, precise relative alignment of the three stainless steel fittings is employed. Figure 3 contains a picture of the commercial translation stages employed under each fitting.

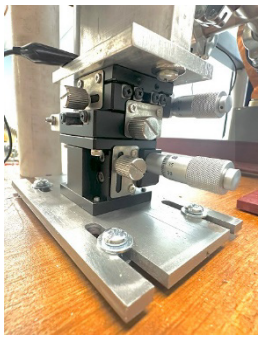


Figure 3: Picture of the commercial translation stages employed to align the center and axial edges of the structure in Fig. 2.

ISBN: 978-3-95450-261-5 ISSN: 2673-7000 doi: 10.18429/JACoW-NAPAC2025-TUP023

CONCEPTUAL DESIGN OF THE ELECTRON-ION COLLIDER (EIC) ELECTRON STORAGE RING (ESR) BEAM ABORT SYSTEMS*

H. Oh†, E. Aschenauer, B. Bhandari, K. A. Drees, M. Esposito, C. Hetzel, D. Holmes, R. Lambiase, C. Liu, C. Montag, D. Marx, S. Tepikian, S. Trabocchi, V. Ptitsyn, E. Skordis, N. Tsoupas, F. Willeke, M. Wendt
Brookhaven National Laboratory, Upton, New York, USA

Abstract

Two possible solutions for the electron beam abort system of the Electron Storage Ring (ESR) in the Electron-Ion Collider (EIC) are devised and discussed. The first, the *Septum Extraction Abort System* will use fast rising kicker magnets with a rectangular pulse form and a new DC septum magnet to extract the beam into the extraction beamline. The second, the *Resonant Orbit Abort System* utilizes AC dipoles to generate resonant closed orbit bumps and disposes the beam on the beam dump integrated within the ESR beam pipe aperture. A comparison of the candidates will support the selection of the ESR beam abort system.

ESR BEAM ABORT REQUIREMENTS

The Electron Storage Ring (ESR) is a vital part of the Electron-Ion Collider (EIC) that will provide polarized electron beams of various energies: 5 GeV, 10 GeV, and 18 GeV. The beams of electron synchrotrons at these energy scales can be hazardous and can damage the equipment, because of synchrotron radiation and beam power. A resilient and reliable beam abort system must be implemented for machine protection. The 10 GeV configuration with a beam current of 2.5 A will impose the highest stored beam energy of 320 kJ; and a beam dump must withstand at least 320 kJ within a single turn, over not more than ~20 μs. The ESR abort gap is 1 μs. See Table 1 and the EIC Conceptual Design Report [1].

Table 1: ESR Electron Beam Energy

Energy	Total Intensity	Stored Energy
5 GeV	2.00e+14 e-	159.83 kJ
10 GeV	2.00e+14 e-	319.67 kJ
18 GeV	1.80e+13 e-	51.85 kJ

BEAM ABORT SYSTEM LOCATION

The installation location of the beam abort system is foreseen at the IR2 Straight Section of ESR. The selection of this location is justified by the sufficient space availability, with multiple vacant 12.36 m drift sections. The *Resonant Orbit Abort System* and its beam dump will be integrated within these drift sections. The other scheme that will extract the beam from the ESR circulating ring via a kicker and a septum magnet will deposit the beam in the *stub-tunnel* in the IR2. The *stub-tunnel* was once built for the BNL ISABELLE project. The tunnel has been unoccupied since the RHIC project.

SEPTUM EXTRACTION ABORT SYSTEM

Fast extraction kickers with the total kick strength of 1.085 mrad is required to offset the beam from the ESR circulating ring orbit to the septum entrance. This kick strength shall be distributed among six kickers to increase operational redundancy. The kickers must respond in a fast manner, such that they meet the criteria shown in Table 2.

Table 2: Fast Extraction Kicker Requirements

Extraction Kicker	Parameter
Abort Gap	1 μs
Flattop Field Length	13 μs
Number of Kickers	6
Septum Kick Strength	1.085 mrad

The Septum Extraction Abort System will require a new septum magnet for the beam extraction from the ESR. The location of the septum magnet along the IR2 straight section was determined in such a way that the bend trajectory will guide the beam into the *stub-tunnel* requiring minimal kicker strength, while avoiding physical interference with other beamline elements. The horizontally elongated design of the ESR beampipe (inner radius of 40mm) provides sufficient clearance for the extracted beam to propagate towards the septum entrance.

The septum magnet design used herein features a 4 m long effective magnet length to provide the required 38 mrad bending angle. The septum extraction beam trajectory will require an opposing bend to guide the trajectory towards the *stub-tunnel*. Two existing dipole magnets (dismantled dipoles from the APS) have been secured to accomplish this inward bend. Each magnet is 3 m long with a bending radius of 40 m at 7 GeV. This is equivalent to a bending angle of 29 mrad at 18 GeV. This geometry will require the bend angle to be -22.124 mrad for each dipole.

* Work supported by U.S. Department of Energy (USDOE) Contract No.DE-SC0012704, Nuclear Physics
† moh@bnl.gov

Content from this work may be used under the terms of the CC BY 4.0 licence (© 2022). Any distribution of this work must maintain attribution to the author(s), title of the work, publisher, and DOI.

ISBN: 978-3-95450-261-5 ISSN: 2673-7000 doi: 10.18429/JACoW-NAPAC2025-TUP025

CST SIMULATION AND RF POWER FOR AN EQUIVALENT SCL CAVITY AT LANSCE

J. A. Valladares†, J. T. Bradley, T. Tajima, J. L. Castellano
Los Alamos National Laboratory, Los Alamos, NM, USA

Content from this work may be used under the terms of the CC BY 4.0 licence (© 2022). Any distribution of this work must maintain attribution to the author(s), title of the work, publisher, and DOI.

Abstract

Superconducting LINAC (SCL) technology has been a mature option for several years. The SCL option has been studied in the past. This option has the potential to improve beam availability to the LANSCE facility users by allowing the RF system to partially migrate to a modern RF power solution such as the Spallation Neutron Source (SNS) or the European Spallation Source (ESS) klystron modulators. Due to the higher RF efficiency of the SC cavity, the use of recent advances in Solid-State Power Amplifiers (SSPA) becomes a possibility as an adequate substitute for the RF power plant. Another important aspect of the SCL option is that the partial removal of the Coupled Cavity LINAC (CCL) at β=0.78 and implementing high-gradient SC cavities provides a technically sound solution to reach beam energy of more than 1 GeV within the already existing beam tunnel, making this available for the users at LANSCE. In addition, the current capability of 800 MeV beam can be maintained by choosing a dynamic mode of operation where only the needed SC RF structures are operated. This would allow continued use of the Proton Storage Ring (PSR) without requiring an upgrade, while providing the >1 GeV option for other users on demand.

THE HIGH BETTA SECTION

The 805 MHz LANSCE CCL cavity LINAC is composed of 44 modules. The CCL has been in operation for over 50 years. The extended life is due to the robustness of the original CCL design. The last cavity in the chain of modules can be used under normal operation for fine tune of the proton beam. That is, the last cavity can be utilized to either accelerate or decelerate the beam for optimal operation. This last module is powered by a full-sized klystron tube rated at 1.25 MW of RF power.

For the high-beta sections, the length of the LANSCE CCL is comparable to that of the SNS SCL [1, 2], with approximately 15.3 meters for the CCL module, and 7.7 meters for the SCL cryomodule, respectively. Thus, replacing a CCL module at LANSCE with an SNS SCL would consume only half the linear length of the existing linac section, leaving space open for future needs [3].

The CCL at LANSCE averages 1 MV/m of acceleration, and according to initial design reports the SNS cavities were qualified at the Tesla Test Facility (TTF) at a gradient of 11.9 MV/m. The design energy gain of the last module in CCL 16.9 MeV. The high beta cryomodule in contrast has four, six-cell cavities, with each SCL cavity averaging 8 MeV of design energy gain. This results in 24 MeV energy gain per SCL cryomodule at the design gradient.

SC CAVITY SIMULATION

A CST simulation was run to verify cavity parameters and required performance of the RF power amplifier. The unloaded Q of the cavity simulation is 1.12E6, which can be considered low by modern standards. A parametrized tunning check was done for field flatness. Although further geometry tunning needs to be performed for optimal cavity design (insert quote here), this was used for a first order calculation of the expected RF power and beam energy gain through the cavity. The length of the model is of 0.84 meters. The cavity from Fig. 1 parameters of Table 1 from the simulation are found in Table 1.

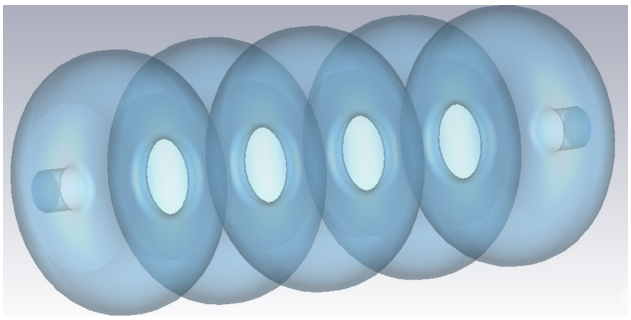


Figure 1: CST model cavity model.

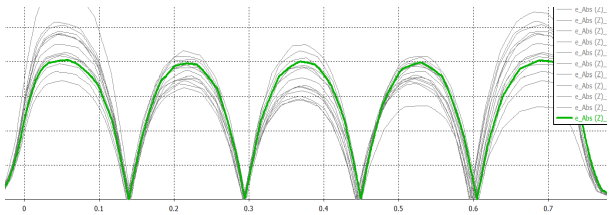


Figure 2: Tunning iterations for field flatness.

RF POWER CALCS

Currently, the RF power system at LANSCE feeds the CCL and most of the power is spent in the Copper establishing the required field gradient for acceleration. On average the LANSCE cavities use up to 300 kW for peak beam loading. The CCL can drive up to 15 mA of beam, the remainder of the RF power from the 1.25 MW available from each klystron is spent in the Cu cavity. Since a SCL cavity option has higher efficiency than the CCL, most of the RF power would be available for proton beam acceleration.

The equations from Ref. [4] for steady state conditions, and appropriate scaling were used to find the required

† chuy@lanl.gov

ISBN: 978-3-95450-261-5 ISSN: 2673-7000 doi: 10.18429/JACoW-NAPAC2025-TUP026

CURRENT STATUS OF THE ELECTRON TRANSPORT LINE FROM RCS TO ESR: RTE LINE*

I. Neththikumara†, K. Deitrick, B. R. Gamage, T. Satogata, N. Sereno, S. Setiniyaz
Thomas Jefferson National Accelerator Facility, Newport News, VA, USA
B. Bhandari, C. Montag, V. Ranjbar, N. Tsoupas, W. Bergan, E. Wang
Brookhaven National Lab, Upton, NY, USA

Abstract

The electron injection system of the U.S. Electron-Ion Collider (EIC) is located outside of the RHIC tunnel. Electron beams accelerated by the Rapid Cycling Synchrotron (RCS) must be transported to the Electron Storage Ring (ESR), which resides within the RHIC tunnel. To accomplish this, a dedicated beam transport line, referred to as RTE (RCS-to-ESR) line is being designed. The proposed conceptual design comprises three main sections; RCS extraction, a vertical bend and dispersion suppression region, and ESR injection matching. The extraction section uses pulsed kickers and septum magnets to achieve a total deflection angle of 3°. To align the injection section with ESR, the beamline must provide a vertical elevation of 1.68 m, and an array of FODO cells is used to suppress the vertical dispersion. The total length of the RTE line is approximately 133 m, and this paper presents the current design status and considerations for this transport line.

INTRODUCTION

The U.S. Electron-Ion Collider (EIC) complex is being designed to be built at Brookhaven National Lab (BNL), New York, as a collaborative effort in between BNL and Jefferson Lab (JLab). Figure 1 provides a bird eye view of the EIC complex. The Hadron Storage Ring (HSR) and Electron Storage Ring (ESR) are housed within the existing RHIC tunnel, while the electron injection system—consisting of an injector linac, Beam Accumulator Ring (BAR), and Rapid Cycling Synchrotron (RCS)—has been relocated to a dedicated tunnel outside the RHIC enclosure.

Polarized electrons are injected from the electron injector and pre-accelerated by the linac. The electron bunch charge exiting the linac is 1.1 nC with a repetition frequency of 30 Hz. The beam then enters the BAR ring, where the charge is accumulated to 28 nC at extraction [1–3]. These high charge electron bunches then are transported to the RCS, where the beam is accelerated to one of three different energies: 5 , 10 or 18 GeV, before being transported to and injected into the ESR ring at IP 4 [4].

Electron bunches are extracted from the RCS at a rate of up to 1 Hz for injection into the ESR. A single-bunch, on-axis extraction scheme is employed in the horizontal plane. The RTE line is divided into three sections: the RCS extraction segment, a vertical bend achromat to accommodate the elevation change, and the ESR injection segment [4].

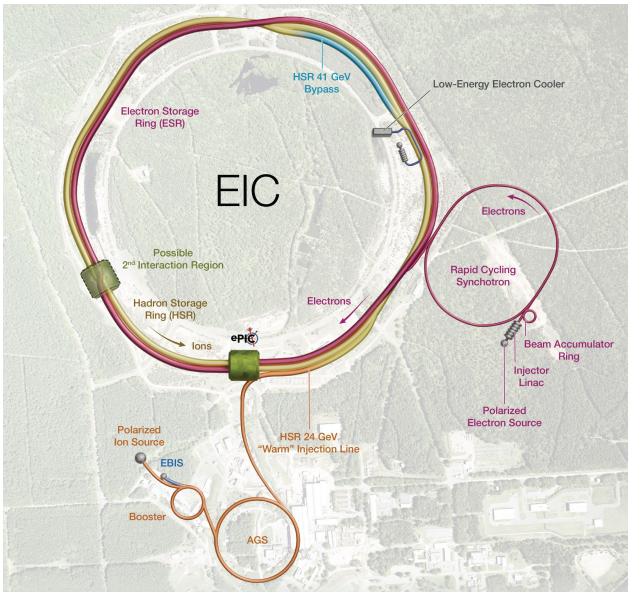


Figure 1: Layout of the current EIC design, HSR and ESR rings inside the RHIC tunnel, Electron and hadron injector complexes are outside of it.

In the conceptual design of the RTE line, three kicker magnets, each 0.8 m long, and two septum magnets—a thin septum (1.5 m) and a thick septum (2 m)—are used to achieve a net extraction angle of 52.36 mrad (3°) [4]. Since the two rings are located at different elevations, the RTE line incorporates a vertical drop of 1.68 m before ESR injection. The vertical bend section consists of two 3 m long vertical dipole magnets, and nine quadrupole magnets placed between them to suppress vertical dispersion, forming an achromatic bend. The matching quadrupoles are 0.3 m length with aperture 0.02 m radius, forming 4.5 FODO cells [4]. Figure 2 shows optics of this conceptual design.

The beta functions remain reasonable and well below 70 m. However, interference between the RTE beam pipe and the downstream RCS quadrupole (MQD21) magnet is observed, as shown in Fig. 3. To resolve this issue, the spacing between the MDQF21 and MQD21 quadrupole magnets must be increased. Therefore, the injection pulsed magnet beamline layout must be modified to accommodate the updated RCS lattice.

* This work is supported by Jefferson Science Associates, LLC under U.S. DOE Contract DE-AC05-06OR23177 and Brookhaven Science Associates, LLC, Contract DESC0012704

† isurunh@jlab.org

Content from this work may be used under the terms of the CC BY 4.0 licence (© 2022). Any distribution of this work must maintain attribution to the author(s), title of the work, publisher, and DOI.

ISBN: 978-3-95450-261-5 ISSN: 2673-7000 doi: 10.18429/JACoW-NAPAC2025-TUP027

DERIVATION OF CONDITIONS UNDER WHICH BOUSSARD'S CRITERION FOR THE MICROWAVE INSTABILITY MAY APPLY*

R. Lindberg, ANL, Argonne, IL, USA

Content from this work may be used under the terms of the CC BY 4.0 licence (© 2022). Any distribution of this work must maintain attribution to the author(s), title of the work, publisher, and DOI.

Abstract

The microwave instability is typically driven by perturbations whose characteristic wavelength is much shorter than the bunch. In this case, Boussard argued that the microwave instability threshold can be found using the predictions of an infinite (coasting) beam, with the average current replaced by the peak current. We revisit this problem, and theoretically show that Boussard's hypothesis holds provided 1) the longitudinal ring impedance is dominated by frequencies much shorter that the inverse bunch length; 2) the single-particle wakefield is much shorter than the bunch length, or, equivalently, the impedance is slowly varying over frequencies longer than the inverse bunch length; 3) the resulting instability has a sudden onset with growth rate of the order of the synchrotron frequency. The first two conditions imply that perturbations are localized within distances much less than the bunch length, while the last condition means that the instability experiences significant growth before the particles can make one synchrotron oscillation. While these conditions may be "obvious" in retrospect, we believe that the last two have not been clearly stated or widely appreciated.

INTRODUCTION

The microwave instability is a classic single bunch instability in which collective longitudinal wakefields drive small-scale density perturbations. Its signature is a sudden increase in the energy spread when the beam current is above a threshold value. The microwave instability is naturally self-limiting; in some cases the final state is a seemingly stable beam with inflated energy spread [1–4], while in other cases one observes "saw-tooth" or "bursting" behavior in which the energy spread periodically grows to a large value followed by a slow damping towards equilibrium [5–8].

The standard theoretical treatment of the microwave instability applies to a coasting beam with constant current. We suppose our ring has a circumference C_R, slip factor η_s, and longitudinal impedance $Z_\parallel(k)$, and we wish to consider the linear stability of perturbations whose wavelength $\lambda = 2\pi/k$. For a coasting beam with average current I, energy γmc^2, and Gaussian energy distribution with rms width σ_δ, the complex frequency Ω describing the stability of such perturbations satisfies the dispersion relation [9, 10]

$$1 = \frac{eI}{\eta_s\sigma_\delta^2\gamma mc^2}\frac{Z_\parallel(k)}{ikC_R} \times\left[1+\hat{\Omega}\frac{e^{-\hat{\Omega}^2/2}}{\sqrt{2/\pi}}\left(i\,\mathrm{sgn}(\eta_s)-\mathrm{erfi}(\hat{\Omega}/\sqrt{2})\right)\right]. \quad (1)$$

* Work supported by the U.S. Department of Energy, Office of Science, Office of Basic Energy Sciences, under Contract No. DE-AC02-06CH11357.

Here, the scaled frequency $\hat{\Omega} = \Omega/(ck\eta_s\sigma_\delta)$ with $\Im(\Omega) > 0$ implying instability, $\mathrm{sgn}(x)$ picks the sign of x, while the imaginary error function $\mathrm{erfi}(x) = 2/\sqrt{\pi}\int_0^x dt\; e^{t^2}$.

Since the microwave instability is typically driven by fine-scale perturbations, Boussard suggested that the longitudinal stability of bunched beams may also be governed by a dispersion relation analogous to Eq. (1), only with the average current being replaced by the peak current [11]; for a Gaussian current profile of rms width σ_z this means that the microwave instability is given by Eq. (1) but with $I \to (C_R/\sqrt{2\pi}\sigma_z)I$. The goal of this paper is to determine in detail under what conditions Boussard's hypothesis applies.

THEORY

Our analysis considers the Vlasov equation of a bunched beam under the assumption that the rf potential is quadratic in z. In this case the zero-current motion is simple harmonic with frequency $\omega_{s0} = |\eta_s|\,\sigma_\delta c/\sigma_z$, and we therefore transform longitudinal coordinates to the harmonic oscillator action-angle variables $(\Phi, \mathcal{I})$ by replacing the position $z = \sigma_z\sqrt{2\mathcal{I}/\sigma_z\sigma_\delta}\cos\Phi$, and the energy deviation with $(\gamma/\gamma_0 - 1) = \mathrm{sgn}(\eta_s)\sigma_\delta\sqrt{2\mathcal{I}/\sigma_z\sigma_\delta}\sin\Phi$. To the unperturbed, simple harmonic dynamics we add the longitudinal collective forces derived from the wakefield potential

$$V_\mathrm{w}(z) = i\chi\sigma_\delta^2\,|\eta_s|\int d\hat{\mathcal{I}}\,d\hat{\Phi}\;F(\hat{\mathcal{I}},\hat{\Phi})\int d\kappa\;\frac{Z_\parallel(\kappa)}{2\pi\kappa}e^{i\kappa(z-\hat{z})},$$

where $\chi = eI/(\eta_s\sigma_\delta^2\gamma mc^2)$ and $F(\Phi, \mathcal{I}; s)$ denotes the single particle distribution function. The latter then satisfies the following Vlasov equation

$$0 = \frac{\partial F}{\partial s} + \frac{\omega_{s0}}{c}\frac{\partial F}{\partial\Phi} + \frac{|\eta_s|}{\eta_s}\left[\frac{\partial V_\mathrm{w}}{\partial\mathcal{I}}\frac{\partial F}{\partial\Phi} - \frac{\partial V_\mathrm{w}}{\partial\Phi}\frac{\partial F}{\partial\mathcal{I}}\right]. \quad (2)$$

We consider linear stability by dividing the distribution function into its equilibrium and perturbation,

$$F(\Phi,\mathcal{I};s) = F_0(\mathcal{I}) + f(\Phi,\mathcal{I};\Omega)e^{-i\Omega s/c}, \quad (3)$$

and assume that $|F_0| \gg |f|$. The static contribution $(\partial V_\mathrm{w}/\partial\Phi)(\partial F_0/\partial\mathcal{I})$ where the V_w is driven by F_0 accounts for the "potential well distortion," in which the impedance perturbs the harmonic potential and alters the equilibrium current profile from a Gaussian. We will approximate the perturbed potential as a quadratic function in z, and partially account for potential well distortion [12] by setting $\omega_{s0} \to \omega_s = |\eta_s|\,\sigma_\delta c/\sigma_z$, with σ_z the self-consistent (Haissinski) rms bunch length. In other words, we allow the impedance to stretch (or shorten) the bunch, but model

ISBN: 978-3-95450-261-5 ISSN: 2673-7000 doi: 10.18429/JACoW-NAPAC2025-TUP028

DESIGN OF FLAT-TO-ROUND (VORTEX) BEAM ADAPTER WITH STRONG SPACE CHARGE*

S. Bernal†, D. Abell, B. Beaudoin, I. Haber, L. Pocher,
D. Sutter, S. Wang, T. Antonsen, P. G. O'Shea
IREAP, University of Maryland, College Park, MD, USA

Content from this work may be used under the terms of the CC BY 4.0 licence (© 2022). Any distribution of this work must maintain attribution to the author(s), title of the work, publisher, and DOI.

Abstract

We describe the design of a symmetrical skew-quadrupole triplet and associated four-quadrupole matching section for a flat-to-round (vortex) (FTR) beam transformation in a low-energy, high-current electron experiment at the University of Maryland. We review the basic principles involved, from the Courant-Snyder parameters, beam (sigma) matrix, conservation of canonical angular momentum and emittances, to the evolution of the beam envelopes, with emphasis in practical aspects of the design. The initial optimization involves the use of TRACE 3-D, a classic sigma- matrix code that can include direct space-charge effects. Particle-in-cell (PIC) computer simulations and preliminary results from experiments are presented in an accompanying paper.

INTRODUCTION

The manipulation of phase space of charged-particle beams is an active area of research in the science and technology of particle accelerators and related devices. An important example is the transformation of angular-momentum-dominated beams ("vortex" beams) into flat beams and vice versa. These beam transformers find applications in electron cooling of hadron beams, linear colliders, and space-charge compensation, among others. Typically, in a round-to-flat transformer (RTF), an electron beam is generated in a photocathode that is immersed in a strong axial field (0.5 – 200 kG), accelerated to 10 – 500 MeV and then passed through a triplet of skew quadrupoles to remove the coupling between space and velocity coordinates. The flat beam that results normally has a high emittance ratio of the order of 100:1 (horizontal to vertical).

Interestingly, the optics of high-energy, high B-field, beam transformers can be scaled to low-energy, low B-field systems, which facilitate parametric studies, while possibly introducing significant space-charge effects. At the University of Maryland Long-Solenoid Experiment (LSE), we are investigating the detailed beam dynamics in a FTR transformer with the parameters summarized in Table 1.

The key parameter for the FTR design is the Larmor β function, or β_L (Table 1); it corresponds to the inverse of the focusing constant of a matched solenoid following the FTR triplet, for *zero* beam current. Furthermore, β_L sets a *length scale* for the FTR, 0.3 m in our case [1].

The tabulated effective emittances for the flat beam are 4RMS, unnormalized values. These emittances are obtained with a 10:1 mm (horizontal:vertical) slit housed in the chamber that follows the two short solenoids, as shown in Fig. 1. The slit intercepts a 19 mA round beam that is focused to near a beam waist by the solenoids. The average angular momentum is normalized with the linear momentum p_z. The 2RMS beam radius at the solenoid includes the effect of direct space charge, obtained from smooth-approximation calculations discussed below. The laminarity parameters measure the ratio of space charge to emittance terms in the $X - Y$ coupled Kapchinskij–Vladimirskij (K-V) envelope equations [2].

Table 1: Basic Parameters for Beam Transformer

Parameter	LSE FTR
Energy	5 keV
Magnetic Rigidity, $B\rho$	2.39×10^{-4} Tm
Magnetic Field, B_S	15 G, at solenoid
$\beta_L = 2(B\rho)/B_S$	0.319 m
Charge	0.049 nC
Peak Current (Slit 1)	0.49 mA
Beam Perveance, K	2.1×10^{-5}
2RMS Beam Radius @ Solenoid	2.3 mm
Flat Beam Eff. Emitt., $(\varepsilon_X, \varepsilon_Y)$	(23.2, 2.23) μm
Norm. Avg. Angular Momentum	$\varepsilon_X - \varepsilon_Y = 21$ μm
Flat Beam Laminarity Par., S_X, S_Y	0.44, 1.4

FLAT AND VORTEX BEAM MATRICES

The matrix representing a *flat* beam with $\alpha_X = 0 = \alpha_Y$, that is, at a beam waist, is given by

$$\mathbf{\Sigma}_{Flat} = \begin{bmatrix} \beta_L\varepsilon_X & 0 & 0 & 0 \\ 0 & \varepsilon_X/\beta_L & 0 & 0 \\ 0 & 0 & \beta_L\varepsilon_Y & 0 \\ 0 & 0 & 0 & \varepsilon_Y/\beta_L \end{bmatrix}. \quad (1)$$

This matrix is transformed by the transport matrix of a symmetrical triplet of skew *thin* quadrupoles into the matrix representing a round *and vortex* beam, Eq. (2).

From Eq. (2), the 2RMS beam radius of the vortex beam at the output of the FTR is $\sqrt{2\beta_L(\varepsilon_X + \varepsilon_Y)}$, while the normalized average angular momentum at the output is $(\varepsilon_X - \varepsilon_Y)$. We emphasize that these results are valid for a zero-current beam. Space-charge effects will be discussed later.

LATTICE DESIGN

There are four main components in the LSE experiment: the two-solenoid and slit aperture plate, the skew quadrupole

* Work supported by the U.S. Department of Energy, Office of High Energy Physics, under contract number DE-SC0022009.

† sabern@umd.edu

ISBN: 978-3-95450-261-5 ISSN: 2673-7000 doi: 10.18429/JACoW-NAPAC2025-TUP029

DESIGN UPDATE ON THE TRANSITION BEAMLINE FOR THE CEBAF ENERGY UPGRADE*

B.R. Gamage†, J. Benesch, R.M. Bodenstein, S.A. Bogacz, K.E. Deitrick, R. Kazimi, D. Khan, G.A. Krafft, E. Nissen, Y.R. Roblin, T. Satogata, A. Seryi
Jefferson Lab, Newport News, VA, USA
V.S. Morozov, Oak Ridge National Lab, Oak Ridge, TN, USA
J.S. Berg, S.J. Brooks, D. Trbojevic
Brookhaven National Lab, Upton, NY, USA

Abstract

For Jefferson Lab's 22 GeV upgrade, two new fixed field alternating gradient (FFA) permanent magnet arcs will be integrated to serve the accelerator's six highest-energy recirculation passes. Connecting these FFA arcs to the existing linear accelerator (linac) requires a carefully engineered transition section. The current design has two parts where the first part adiabatically matches the beam dispersion and orbit trajectories, while the second part aligns the Twiss parameters (alpha and beta functions) with those at the linac entrance. Given the tight spatial constraints and multiple matching requirements, a genetic algorithm is being explored to optimize beam optic matching. This paper presents current progress in developing and optimizing this transition.

INTRODUCTION

Jefferson Lab is evaluating an upgrade to the Continuous Electron Beam Accelerator Facility (CEBAF) that would approximately double the number of beam acceleration passes through its superconducting linacs [1]. Due to spatial constraints within the existing tunnel, a conventional expansion of recirculating arcs is not feasible. Instead, the proposed design introduces two new Fixed-Field Alternating Gradient (FFA) arcs, using permanent magnet technology [2], to accommodate the additional passes (see Fig. 1).

In the current CEBAF layout, each beam pass is directed through a unique electromagnetic (EM) arc. A recombination system then merges beams of differing energies into a common trajectory before returning to the linac. In the proposed upgrade, the FFA arcs transport all new passes within a single plane, which allows their recombination with existing EM arcs via a fixed magnetic chicane. However, this chicane does not provide independent control of optics for each energy pass. To achieve proper optical matching between the FFA arcs and the linac, a dedicated transition section is required. Although separating the FFA passes into multiple beamlines for individual matching would offer greater flexibility, it was not practical due to space constraints of the existing CEBAF facilities. Therefore, a combined matching strategy where all high-energies passes are simultaneously matched within a single FFA transport line is being worked on.

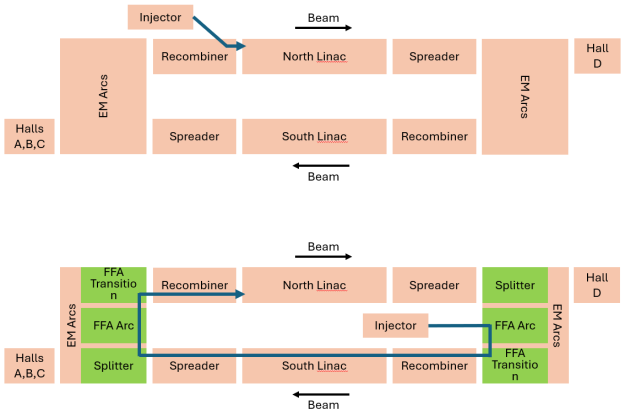


Figure 1: A block diagram illustrating the existing CEBAF layout (top) and the proposed configuration for the energy upgrade (bottom) is shown. In the upgraded design, the new FFA arc replaces the current lowest-energy electromagnetic arc and is positioned beneath the remaining arcs. To integrate this FFA arc into the CEBAF, a dedicated transition and splitter [3] sections for the high energy passes will be added, as shown. Extraction [4] is integrated into the splitter section.

It is worth noting that the CEBAF linac provides virtually no focusing for high-energy passes and that favors large betas with small alphas, which is challenging to reach for all passes simultaneously in the limited space available while maintaining the beam size reasonably small.

TRANSITION BEAMLINE LAYOUT

In the previous design [5], a single beamline section was used to simultaneously suppress dispersion and orbit offsets while matching the Twiss parameters for all energy passes. However, this combined approach has shown to be suboptimal due to emerging issues (to be detailed later), which complicate achieving both objectives effectively within the same section. To address this, we are now exploring a two-stage transition scheme. In the first stage, the focus is solely on eliminating orbit deviations and dispersion across all energies. Once these are adequately corrected, the second stage performs the Twiss function matching required for

* This material is based upon work supported by Jefferson Science Associates, LLC under Contract No. DE-AC05-06OR23177, Brookhaven Science Associates, LLC under Contract No. DE-SC0012704 and UT-Battelle, LLC, under contract No. DE-AC05-00OR22725 with the U.S. Department of Energy.

† randika@jlab.org

Content from this work may be used under the terms of the CC BY 4.0 licence (© 2022). Any distribution of this work must maintain attribution to the author(s), title of the work, publisher, and DOI.

ISBN: 978-3-95450-261-5 ISSN: 2673-7000 doi: 10.18429/JACoW-NAPAC2025-TUP030

DENSITY FUNCTIONAL THEORY APPROACH FOR CALCULATING ELECTRONIC BAND STRUCTURE PARAMETERS FOR MONTE CARLO SIMULATIONS OF PHOTOEMISSION

J. O. Mendez*, J. Callahan, O. Chubenko, Northern Illinois University, DeKalb, IL, USA
L. Cultrera, Brookhaven National Laboratory, Upton, NY, USA
S. Karkare, Arizona State University, Tempe, AZ, USA
R. Palai, University of Puerto Rico Rio Piedras, San Juan, PR, USA

Content from this work may be used under the terms of the CC BY 4.0 licence (© 2022). Any distribution of this work must maintain attribution to the author(s), title of the work, publisher, and DOI.

Abstract

Monte Carlo simulations are a powerful tool for modeling photoemission from photocathodes, enabling the prediction of key parameters, such as quantum efficiency, mean transverse energy, electron spin polarization, and photocathode response time. However, these simulations require material band structure parameters, which are not always available from experiments. This work aims to establish a reliable framework for calculating electronic band structure parameters using Density Functional Theory (DFT). Specifically, we apply this framework to investigate the effects of lattice strain and temperature on the electronic band structure and electron transport in GaAs. This approach will be further extended to explore band structure modifications in heavily *p*-doped semiconductors and to calculate electronic band structures of novel spin-polarized photocathode materials.

INTRODUCTION

GaAs based photocathodes are widely used in accelerator science due to their ability to produce spin-polarized electrons with high brightness. While strained superlattices [1] can enhance polarization, their quantum efficiency (QE) is often reduced and fabrication is costly. Moreover, activation with cesium remains necessary and vulnerable to ion bombardment. The search for alternative materials and structures with improved properties is ongoing [2–5], but experimental investigations remain time-intensive.

Computational modeling, particularly density functional theory (DFT) in combination with Monte Carlo (MC) simulations, offers a cost-effective and quick method to explore new materials under different operating conditions for advanced photocathodes. The goal of this work is to develop a robust framework in which temperature and strain dependent material parameters derived from DFT can be reliably used in MC simulations [6] of electron transport and photoemission. We use bulk GaAs as a benchmark material due to the availability of extensive experimental data.

METHODS

Electronic structure calculations were performed using Quantum ESPRESSO with fully relativistic norm-conserving pseudopotentials and with Perdew Burke Erzenhof (PBE) exchange-correlation functional [7–9]. To address the known underestimation of the GaAs band gap from DFT [10, 11], we employed the DFT+U correction method, tuning the Hubbard U parameter to reproduce an intrinsic band gap of 1.52 eV at 2 K [12], and up to 1.42 eV at room temperature (293 K) [12]. The procedure for testing different values of U involved calculating the electronic band gap energy as well as the static and high frequency dielectric constants. The U was applied to the arsenic ranging from 0 eV to 10 eV in steps of 0.5 eV, and for gallium the range was from 0 eV to 20 eV with the same step value. Applying the U to arsenic resulted in greater change of the parameters than applying it to Gallium. Figures 1 and 2 demonstrate how choosing a U value that provides good agreement for all parameters might be difficult as each parameter is affected differently by the Hubbard correction. Ultimately, the above-mentioned approach of applying different values of U for different temperatures only to arsenic was chosen to ensure that the intrinsic band gap closely matches the value given by the equation $E_g = 1.522 - 5.8 \times 10^{-4}(\frac{T^2}{T+300})$ [12].

Temperature effects were incorporated via thermal expansion coefficient using experimentally measured coefficients, while strain was modeled by transforming the zincblende unit cell to an orthorhombic face centered to emulate pseudomorphic growth under biaxial compression. From these calculations, we extracted effective masses, non-parabolicity factors, static and high frequency dielectrics, phonon dispersion, and optical transmission and reflectivity as a function of temperature and strain. These parameters were used in a spin-resolved MC transport model [6] simulating drift velocity as a function of electric field strength. The model includes scattering and spin-relaxation effects essential to spin-polarized photoemission.

RESULTS

Tables 1 and 2 summarize the results from the DFT calculations. The parameter that is closest to their reference value is the intrinsic band gap due to the applied Hubbard Correction (Fig. 3). The calculated band gap increases with applied in-plane compressive strain, rising from 1.42 eV to 1.55 eV at −5.0 % strain, which can be observed in Fig. 4. Additionally the loss of degeneracy of the light and heavy hole bands due to the strain was able to be observed with the strain, and not at different temperatures as seen in Fig. 3. Experimental data for the high frequency dielectric constant show that it increases as the temperature increases [13]. We observed this trend in the DFT results when the the Hubbard correction was not applied or when it was not change for every temperature.

* z2044141@students.niu.edu

ISBN: 978-3-95450-261-5 ISSN: 2673-7000 doi: 10.18429/JACoW-NAPAC2025-TUP031

DYNAMIC APERTURE CORRECTION FOR RING ELECTRON COOLER*

J. Unger†, G. H. Hoffstaetter, Cornell University, Ithaca, NY, USA
A. Fedotov, J. Kewisch, S. Seletskiy, Brookhaven National Laboratory, Upton, NY, USA

Content from this work may be used under the terms of the CC BY 4.0 licence (© 2022). Any distribution of this work must maintain attribution to the author(s), title of the work, publisher, and DOI.

Abstract

The Ring Electron Cooler is one option to provide cooling to the Electron Ion Collider's 275 GeV proton bunches. Using traditional electron cooling this racetrack shaped storage ring uses one straight section to cool the protons and the other one to enhance the radiation damping of the electrons using 2.4 T wigglers. These sections comprise the majority of the ring and are connected by short arcs. Space for sextupoles and octupoles is made in short straight sections between the wigglers. The strong wigglers and limited space for correction magnets create challenges in finding a suitable dynamic aperture correction. In this paper, we outline the challenges present in rings of this type and present a correction scheme that meets the aperture requirements of the design.

INTRODUCTION

The Ring Electron Cooler (REC), is under design as a possible solution to the cooling need for the Electron Ion Collider's (EIC) Hadron Storage Ring (HSR) at its top energy of 275GeV.

In order to counteract emittance growth in the HSR, the REC design uses electron cooling [1] with a multi-turn ring. The electron bunches will be reused for cooling on many turns. To counteract the growth of electrons emittance and energy spread, caused by intra-beam scattering (IBS) and proton-electron beam-beam scattering, substantial radiation damping is needed. The cooling of electrons through radiation damping is facilitated by dedicated wigglers, with the parameters important for cooling and dynamic aperture shown in Table 1.

The wiggler section contains 18 wigglers alternating with short sections housing quadrupoles and sextupoles. These are arranged in 17 alternating wiggler blocks. Each of these wigglers have a 2.4T main field and are 4.2m long, and are responsible for the majority of the electron damping [2].

Another consideration in a ring based cooler is the need to maintain a dynamic aperture sufficient to obtain the beam lifetime needed for the desired cooling. This was determined to lead to a requirement of 5σ for the transverse and momentum apertures.

LATTICE OVERVIEW

The lattice has the approximate layout of a short and long trapezoid, with the cooling section on the top which overlaps with the HSR, and the bottom housing the wiggler section. The two short straight sections on the sides are to be used for injection and RF systems. Short arcs connect the sides as shown in Fig. 1.

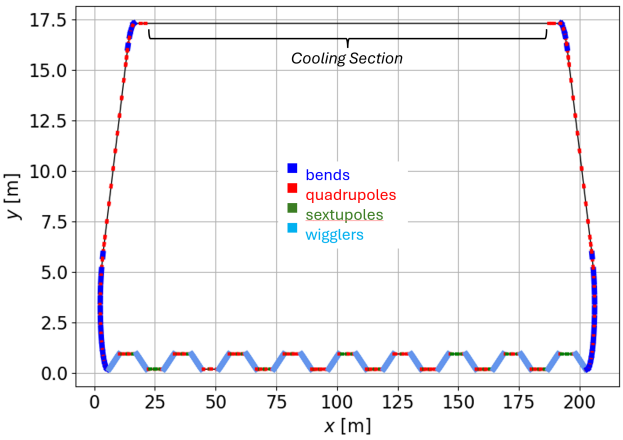


Figure 1: REC layout.

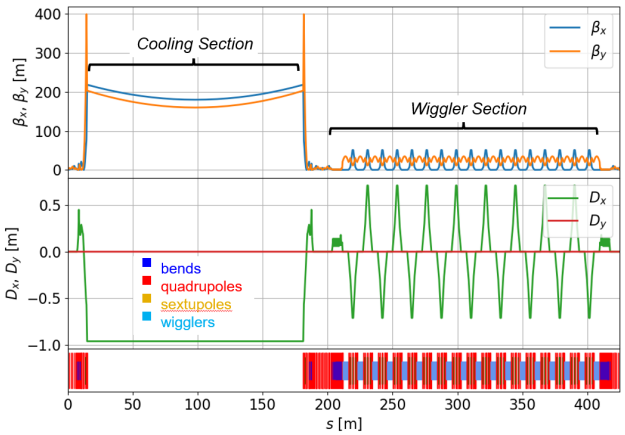


Figure 2: REC optics and lattice.

In order to reduce emittance growth due to IBS, the optics in the wigglers are desired to minimize the function:

$$\mathcal{H}_x = \gamma_x \eta_x^2 + 2\alpha_x \eta_x \eta_x' + \beta_x \eta_x'^2. \quad (1)$$

Inside the wigglers, the periodic dispersion is small, leading to the first term in $\mathcal{H}_x$ to have small contribution. The derivative of dispersion (η_x') is large in the wigglers, leading to the need to reduce β_x. This is accomplished by adding horizontal focusing in the wigglers, resulting in the optics in Fig. 2.

There are multiple choices of wiggler fields that can achieve similar focusing, however the non-linear effects of these fields on dynamic aperture can vary significantly. The conceptually simplest choice of fields is a wiggler with a superimposed quadrupole field. Unfortunately, this field configuration was shown to cause large chromaticity for the

* Work supported by Brookhaven Science Associates, LLC under Contract No. DE-SC0012704 with the U.S. Department of Energy.
† jeu8@cornell.edu

ISBN: 978-3-95450-261-5 ISSN: 2673-7000 doi: 10.18429/JACoW-NAPAC2025-TUP032

DYNAMIC APERTURE STUDIES AT THE FERMILAB RECYCLER RING

C. Gonzalez-Ortiz*, R. Ainsworth
Fermi National Accelerator Laboratory, Batavia, IL, USA

Abstract

As part of the Proton Improvement Plan II (PIP-II), Fermilab aims to increase beam intensity delivered to neutrino experiments. In this context, higher intensity injection into the Recycler Ring enhances space charge effects, pushing operations closer to third-order resonances. These resonances reduce the Dynamic Aperture (DA), leading to increased beam loss. This study presents simulations of DA as a function of tune in the Recycler Ring, incorporating chaos indicators such as the Reversibility Error Method (REM). The effectiveness of existing resonance mitigation strategies is evaluated by quantifying their ability to delay DA degradation. Additionally, the study examines how space charge detuning and DA limitations dictate viable operational tune points for the Recycler Ring.

INTRODUCTION

The dynamic aperture (DA) is defined as the region of phase space where stable motion occurs. Third-order betatron resonances reduce the Dynamic Aperture (DA) of circular accelerators, particularly when the machine operates near resonance lines in tune space. In high-intensity regimes, this leads to increased beam losses and decreased transmission efficiency. As part of the Proton Improvement Plan II (PIP-II) [1], the Fermilab Recycler Ring is expected to handle higher intensity beams, which makes understanding and mitigating these resonances critical to successful operation.

The Recycler Ring (RR) is a permanent magnet storage ring located in the Fermilab Accelerator Complex. RR is a machine operating at a fixed momentum of 8.835 GeV/c, equivalent to an energy of 8 GeV. Figure 1 shows the approximate nominal tunes for the bare machine, i.e., with all tune control magnets turned off [2]. As the Recycler Ring starts to deal with higher intensities and larger tune spreads, it is important to study how its Dynamic Aperture (DA) behaves close to neighboring third order resonances. Figure 1 also shows approximate space charge tune shifts for nominal PIP-II parameters.

The following work explores how third order resonances decrease available dynamic aperture in the Fermilab Recycler Ring. This is done through tracking simulations using Xsuite [3]. In particular, the nominal transverse tunes in the lattice are swept while recording Dynamic Aperture region and Reversibility Error Method (REM) chaos indicators. Furthermore, this works investigates how dynamic aperture behaves along the space charge detuning direction.

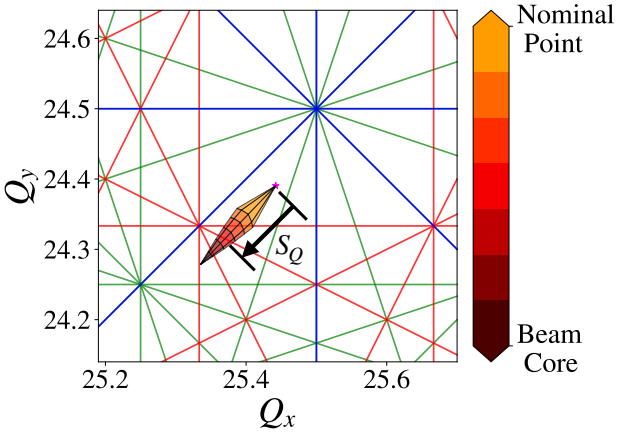


Figure 1: Tune diagram for the Recycler Ring with approximate tune spread due to space charge forces from nominal set point to beam core calculated using PySCRDT [4, 5]. The space charge detuning S_Q is illustrated.

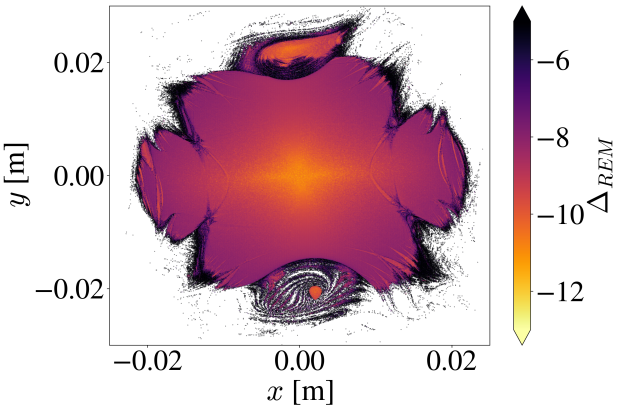


Figure 2: Dynamic aperture (DA) of the Fermilab Recycler Ring for the bare machine, using the Reversibility Error Method (REM) as a chaos indicator.

DYNAMIC APERTURE SIMULATIONS

In order to get dynamic aperture calculations, tracking simulations through the lattice model were done using Xsuite [3]. Xsuite is a modular, Python-based accelerator simulation tool developed at CERN, capable of high-performance multi-particle tracking on GPU contexts. For this study, the full Recycler Ring lattice was imported from MAD-X into Xsuite, and 2.5×10^6 particles were tracked over 2048 turns for a grid of initial transverse amplitudes. A physical aperture ten times the size of the real aperture was introduced in order to capture the entire region of stability.

* gonza839@fnal.gov

Content from this work may be used under the terms of the CC BY 4.0 licence (© 2022). Any distribution of this work must maintain attribution to the author(s), title of the work, publisher, and DOI.

ISBN: 978-3-95450-261-5 ISSN: 2673-7000 doi: 10.18429/JACoW-NAPAC2025-TUP033

EFFICIENT PHASE SPACE DENSITY CONSTRUCTION VIA TRANSFER OPERATORS*

V. B. Tembo†, D. T. Abell, I. Haber, T. M. Antonsen
University of Maryland, College Park, MD, USA

Abstract

Finding invariant phase space level curves for large ensembles of particle trajectories is a core challenge for studying systems subject to complex Hamiltonian or weakly dissipative dynamics, such as beam and accelerator physics. These curves characterize long-term system behaviour and are critical for assessing stability, confinement, and matched beam transport. Direct methods rely on expensive particle pushing and tracking. We developed a fast, transfer-operator-based approach for finding invariant phase space surfaces that leverages sparse matrix computation to construct approximate invariant densities directly from trajectory data, enabling efficient level curve discovery while integrating with existing codes.

INTRODUCTION

We can understand the long-term behaviour of dynamical systems if we can characterize their invariant density distributions. Direct approaches involve pushing large ensembles of particles over long distances to accumulate sufficient information to approximate the invariant measure. While conceptually straightforward, this approach becomes computationally prohibitive for these systems. A way around this is to use transfer operators that encode the essential dynamical information without requiring exhaustive trajectory integration. The key is that the information needed to determine invariant densities lies in the local transition probabilities between different regions of phase space, rather than in the detailed long-term evolution of individual trajectories.

METHODOLOGY

The procedure we employ has two steps. First, data is collected describing in detail the trajectories in phase space over a finite distance or time. Typically, this data will come from a simulation code. However, in this paper, we use a map to generate the data. Then, instead of continuing the detailed simulation over longer periods of time to determine the asymptotic phase space density, a transfer operator is constructed based on the collected data that efficiently advances the phase space density directly. A similar method has been used to characterize magnetic flux surfaces in 3D plasma confinement configurations [1].

In the first step, phase space is discretized into an array of bins, with each bin labelled by an integer index i. For each particle in the data set, we record its starting and ending bin number. Then a sparse transfer matrix F_{ij} is constructed by recording the fraction of trajectories that begin in bin i and terminate in bin j after one iteration. Trajectories that exit the phase space domain are discarded, and the corresponding matrix entries F_{ij} for out-of-bounds destinations are set to zero.

The invariant density distribution is obtained through iterative evolution of a density field using the constructed transfer matrix. At each iteration n, the density in bin j, d_n^j is updated according to:

$$d_{n+1}^j = \frac{1}{2}\left(d_n^j + \sum_i F_{ij} d_n^i \right) . \quad (1)$$

This evolution equation is a weighted average between the previous density and the density predicted by the transfer matrix, with equal weighting factors of 1/2 chosen to provide numerical stability by damping high-frequency oscillations in the density field.

Following each matrix evolution step, numerical diffusion may be applied to account for the inherently dissipative nature of the physical system and to compensate for discretization effects. The diffusion scheme employs nearest-neighbour averaging, where each bin transfers a fraction of its density (determined by a diffusion strength parameter) to its four neighbouring bins. We note that the process of binning the density introduces a numerical diffusion, as there is often more than one receiving bin-j for a given sending bin-i. While the diffusion is artificial, it has been found in another application [2] to be advantageous. After diffusion, the density field is renormalized to maintain the constraint $\sum_j d_n^j = 1$.

RESULTS: APPLICATION TO THE STANDARD MAP

We take as our system the standard map. Trajectories in the (p, θ) plane are advanced according to:

$$p_{n+1} = p_n + \Delta \sin \theta_n$$
$$\theta_{n+1} = \theta_n + p_{n+1}$$

Although the mapping is periodic in both variables, we take a trajectory for which p_n falls outside the interval $|p| < \pi$ to be out of bounds. The initial density is taken to be independent of θ and peaked at $p = 0$. The results of a sample calculation are shown in Fig. 1. Pictured in color is the converged density map on a square grid of 500x500 bins. Overlaying the density plot is a trajectory generated by iterating the standard map 250 times. On the right, is a line plot of the density as a function of p evaluated at $\theta = \pi$.

There are two issues of convergence that we have addressed. The first is the convergence of the density with

* This work supported in part by the US Department of Energy, Office of Science, Office of High Energy Physics, under Grant #DE-SC-0025277
† vtembo@umd.edu

Content from this work may be used under the terms of the CC BY 4.0 licence (© 2022). Any distribution of this work must maintain attribution to the author(s), title of the work, publisher, and DOI.

ISBN: 978-3-95450-261-5 ISSN: 2673-7000 doi: 10.18429/JACoW-NAPAC2025-TUP036

EMITTANCE MISMATCHING OF ELECTRON INJECTION FOR THE ELECTRON STORAGE RING OF THE ELECTRON-ION COLLIDER*

Y. Luo†, V. Ranjbar, M. Blaskiewicz, C. Montag, S. Nagaitsev, V. Ptitsyn, D. Xu
Brookhaven National Laboratory, Upton, NY, USA

Abstract

The Electron-Ion Collider (EIC), to be constructed at Brookhaven National Laboratory, will collide polarized high-energy electron beams with polarized proton and ion beams, achieving peak luminosities of up to $1 \times 10^{34}\text{cm}^{-2}\text{s}^{-1}$ in the center-of-mass energy range of 20-140 GeV. The EIC consists of two storage rings: the Hadron Storage Ring (HSR) and the Electron Storage Ring (ESR). Due to the short polarization lifetime of the electron beam, a swap-out injection scheme is adopted for the ESR. In this article, we estimate the injection emittance mismatch tolerances for electron bunches transferred from the Rapid Cycling Synchrotron (RCS) into the ESR. These studies are based on strong-strong beam-beam simulations. The resulting tolerances for injection emittance mismatch in the ESR are presented.

INTRODUCTION

There are several collision modes involving highly polarized electrons colliding with protons or ions in the EIC [1,2]. In this article, we study the emittance mismatch during electron bunch injection from the Rapid Cycling Synchrotron (RCS) into the Electron Storage Ring (ESR). The electron beam energies in the ESR can be 5 GeV, 10 GeV, or 18 GeV. To maintain an average polarization above 70%, electron bunches must be periodically swapped out and replaced with freshly polarized bunches. For instance, at 18 GeV, the electron bunch must be replaced approximately every three minutes.

In contrast, proton bunches remain in the Hadron Storage Ring (HSR) for the entire physics store, which can last several hours. A key concern is the potential increase in proton emittance during the repeated electron bunch swap-out process, particularly due to injection emittance mismatch between the RCS and ESR. Since the injected electron bunch collides with the circulating proton bunch immediately upon injection, any mismatch can lead to proton emittance growth. The emittance of the injected electron bunch is mainly determined by the linac performance and synchrotron radiation damping in the RCS.

In the following sections, we perform strong-strong beam-beam simulations [3] to study the impact of electron injection emittance mismatch during the swap-out process. Our goal is to limit the proton emittance growth from each individual electron bunch injection to less than 1%, ensuring that the cumulative emittance increase remains below 20% over a typical 9-hour store. Based on this criterion, we determine the acceptable tolerances for injection emittance mismatch.

Table 1: Electron Beam Design Parameters for the ESR

Emittances	5 GeV	10 GeV	18 GeV
ϵ_x (nm)	20	20	24
ϵ_y (nm)	1.8	1.1	2.0
Bunch length (cm)	0.7	0.7	0.9
RMS dp/p_0 (10^{-4})	6.8	5.8	10.9
ϵ_L (10^{-4} eVs)	0.8	1.35	5.8

Table 2: Equilibrium Electron Parameters for the RCS

Emittances	5 GeV	10 GeV	18 GeV
ϵ_x (nm)	3.87	15.51	50.2
ϵ_y (nm)	~ 0	~ 0	~ 0
Bunch length (cm)	(0.46)	(1.08)	(1.33)
RMS dp/p_0 (10^{-4})	4.49	8.96	16.1
ϵ_L (10^{-4} eVs)	(0.35)	(3.22)	(12.65)

EMITTANCE MISMATCH

In this article, we focus on three electron–proton collision modes: (1) 5 GeV electrons colliding with 100 GeV protons, (2) 10 GeV electrons with 275 GeV protons, and (3) 18 GeV electrons with 275 GeV protons. Table 1 lists the main design parameters for the electron bunches in the ESR. The design parameters for the latter two collision modes are already well optimized. However, for the first mode between 5 GeV electrons and 100 GeV protons, we must reduce the electron bunch intensity by 30% from the value presented in the EIC Conceptual Design Report (CDR) in order to stabilize the proton beam under beam-beam interaction. The proton beam-beam parameters for the three collision modes are approximately 0.01, 0.012, and 0.004, respectively.

The original plan was to place the RCS inside the RHIC tunnel, sharing the same space with both the HSR and ESR. However, due to extremely tight installation constraints, it was recently decided to relocate the RCS outside of the RHIC tunnel [2]. Based on preliminary calculations, Table 2 lists the electron emittances, bunch lengths, and relative momentum spreads $(\delta p/p_0)_{\text{rms}}$ at the three extraction energies [4]. The values for bunch length and longitudinal emittance listed in brackets are derived from the calculated momentum spread, assuming matched longitudinal phase space profiles between the RCS and ESR.

* Work supported by the U.S. Department of Energy, Office of Science under contracts DE-SC0012704 and DE-AC05-06OR23177

† yluo@bnl.gov

Content from this work may be used under the terms of the CC BY 4.0 licence (© 2022). Any distribution of this work must maintain attribution to the author(s), title of the work, publisher, and DOI.

ISBN: 978-3-95450-261-5 ISSN: 2673-7000 doi: 10.18429/JACoW-NAPAC2025-TUP037

ENHANCING RECIPROCAL SPACE RESOLUTION IN MEV ULTRAFAST ELECTRON DIFFRACTION WITH PERMANENT MAGNET LENSES

C. J. R. Duncan*, T. Xu, R. J. England
SLAC National Accelerator Laboratory, Menlo Park, CA, USA
B. Guzelturk, Argonne National Laboratory, Lemont, IL, USA
P. Denham, P. Musumeci, University of California, Los Angeles, Los Angeles, CA, USA

Abstract

Ultrafast electron diffraction (UED) probes structural dynamics on femtosecond timescales and angstrom spatial scales. Artificial crystals are a novel experimental target for UED beams. Typically composed of lattice-mismatched atomic layers, the repeating atomic patterns in artificial crystals can have periods several nanometers in length, which produces intricate satellite features in the electron diffraction pattern. Resolving fascinating satellite diffraction peaks in a compact UED beamline requires high angular magnification. In this work, we describe the implementation of post-sample angular magnification using a pair of compact permanent magnet solenoid lenses. Configured as an objective-eyepiece pair, these lenses achieve a camera length of 50 meters, i.e., the lens system is equivalent to extending the beamline drift length by a factor 15. We demonstrate the advantages of this scheme with data that resolves satellite diffraction peaks in a heterostructure sample.

INTRODUCTION

The dominant features in electron diffraction from single-crystal samples are typically the Bragg peaks corresponding to the few-Angstrom size of the crystal unit cell. More subtle features of particular scientific interest are caused by periodic distortions in the crystal lattice (PLD). These distortions can be intrinsic to a material, e.g., charge-density waves [1], and also engineered via interfacial strain in stacked heterostructures, the latter being especially significant in samples consisting of only a few atomic layers [2].

The period of PLD can extend to several nanometers [2], and thus measuring the diffraction peaks corresponding to PLD requires especially fine reciprocal space resolution [3]. While the ultimate physical limit on reciprocal space resolution is set by the brightness of the electron beam source, the detector point-spread-function and pixel size are an important practical contraint that can be overcome by magnifying the diffraction pattern on the detector. Angular magnification can be characterized by the *camera length L*, defined,

$$L = \frac{dr}{d\theta}, \tag{1}$$

where θ is the scattering angle (or other deflection) at the sample plane and r is the transverse position of the scattered (deflected) beam on the detector plane. When imaging system is simply a drift section of the beamline, L is the drift length.

* cjduncan@slac.stanford.edu

An angular magnification lens doublet implemented at the SLAC Megaelectronvolt UED facility is shown in Fig. 1. A permanent magnet solenoid (PMS) objective lens with a focal length of 62 cm at the 3.1 MeV primary energy of the beam forms a virtual image of the sample diffraction pattern that is further magnified by a 3 cm focal length eyepiece. The short focal length PMS is further described in Table 1, and described in more detail in [4, 5].

Table 1: Permanent Magnet Solenoid Parameters

Remanence	1.32 T
Inner radius	0.6 cm
Outer radius	3.5 cm
Length of single ring	1.6 cm
Focal length (single ring, 3.1 MeV)	5.0 cm
Focal length (double ring, 3.1 MeV)	2.7 cm

RESULTS

To demonstrate the improvement in reciprocal space resolutuion, Fig. 2 shows an example static diffraction pattern from a strontium titanate / lead zirconate (STO/PZO) heterostructure without (a) and with (b) the angular-magnification lens system. Knowing the STO lattice constant and beam energy determines $d\theta$ in Eq. (1), from which the camera length is calculated to be 50 m, a factor 15 longer than the physical distance from source to detector.

Lineouts shown in Fig. 2(c) and (d) are fit to the function $I(x)$:

$$\begin{aligned} &I(x; A_1, \mu_1, \sigma_1, \gamma_1, A_2, \mu_2, \sigma_2, \gamma_2) \\ &= A_1 V(x - \mu_1; \sigma_1, \gamma_1) + A_2 V(x - \mu_2; \sigma_2, \gamma_2), \end{aligned} \tag{2}$$

where $V(x; \sigma, \gamma)$ is the Voigt profile, a convolution of a normalized gaussian with r.m.s. size σ and a normalized lorentzian with f.w.h.m. of γ [6]. The fits demonstrate that with angular magnification (panel (d)), the measured width of the diffraction peak is reduced by a factor two compared to without (panel (c)). The residual peak width in the magnified case is explained by the coherence length of the illuminating beam and the crystallinity of the sample.

Figure 3(a) zooms in on the diffraction feature at Miller index (0,-2), plotting contours of equal diffraction intensity. These contours reveal the presence of satellite features associated with the interfacial strain between the STO and PZO, which have mismatched lattice constants. The satellites are

Content from this work may be used under the terms of the CC BY 4.0 licence (© 2022). Any distribution of this work must maintain attribution to the author(s), title of the work, publisher, and DOI.

ISBN: 978-3-95450-261-5 ISSN: 2673-7000 doi: 10.18429/JACoW-NAPAC2025-TUP038

ESTIMATION OF THE WAKEFIELD RESONANT FREQUENCY USING DIFFERENT SIMULATION TOOLS *

M.A. Unutmaz, V. Dolgashev, P. Krejcik, C. Nantista, M. Othman
SLAC National Accelerator Laboratory, Menlo Park, CA, USA

Content from this work may be used under the terms of the CC BY 4.0 licence (© 2022). Any distribution of this work must maintain attribution to the author(s), title of the work, publisher, and DOI.

Abstract

Reliable and fast wakefield calculations are important for beam dynamics and THz generation in accelerators. We compare approaches and limitations with different available simulation tools and compare results. As an example, we analyse a cylindrical corrugated waveguide with narrower and wider radii of 5 and 6 mm, and aperture width and periodicity of 1 and 2 mm using ABCI by KEK and ANSYS HFSS simulation software. First, ABCI was used to determine the resonant frequency of the cylindrical corrugated waveguide with different lengths. The corresponding results were taken as a reference to examine the simulation method in the ANSYS HFSS environment. The eigenmode solver of ANSYS HFSS was used to determine different resonant frequencies. This was followed by examining a cylindrical corrugated waveguide that was implemented having a length of 17 mm for different conductor settings. The corresponding waveguide was fed by a plane wave having a resonant frequency that satisfies the intersection of the light line and dispersion curve of the corresponding mode. The analysis showed that the maximum loss factor was achieved at 39.20 and 40.07 GHz using ANSYS HFSS simulation data for different conductors, whereas ABCI resulted in 38.50 GHz. The talk will present the results gathered by different simulation setups implemented in ANSYS HFSS.

INTRODUCTION

Terahertz technology has become increasingly important for accelerators, charged particle beam manipulation and the measurement of relativistic electron beam properties. Terahertz structures can be operated at much higher gradients than conventional RF accelerating structures, reaching GeV/m, and they are well-matched to operating with extremely short bunches, and can be built in compact size [1]. Likewise, extremely short bunches generate wakefields at THz frequencies, which can either be disruptive to the beam propagation if not taken into proper consideration or can be exploited as a powerful diagnostic tool for measuring the longitudinal distribution of the ultrashort bunches [2].

The dimensions of the accelerating structures scale with wavelength, so that in many cases the structures resemble corrugated waveguides. We seek new computational tools to analyse the properties and performance of these structures.

When comparing different numerical tools, we take the generalized case of a corrugated cylindrical waveguide with a standard set of dimensions. The solutions are complex as the waveguide can be excited by a large number of waveguide modes over a range of frequencies limited only by the cutoff frequencies of the pipe. These modes may have both longitudinal and transverse field components that can interact with the beam.

A powerful tool exists in the ABCI program [3] for calculating the wakefields excited by an electron bunch in a cylindrical waveguide. Since we are also interested in rectangular and parallel plate structures, we have also investigated 3D numerical software such as ANSYS HFSS.

However, HFSS calculates the electromagnetic field propagation in waveguides and does not implicitly include the field from a relativistic bunch. Nonetheless, the resonant eigenmodes calculated by HFSS can all be excited by the relativistic bunch. The challenge investigated in this paper is to identify which eigenmodes can interact with the electron bunch and are therefore generated as wakefields in the structure. The electron bunch will couple its energy into those waveguide modes with the greatest loss factor. Secondly, the field will only couple to the bunch if the phase velocity of the waveguide mode satisfies the $v{=}c$ condition.

We also take the opportunity to examine the influence of different material properties on the numerical calculations, such as the conductivity and the surface roughness of the waveguide.

METHOLOGY AND RESULTS

A 2-dimensional wakefield simulation software, ABCI [3], was used to figure out the resonant frequency of the strongest wakefield of a corrugated cylindrical waveguide. The structure of the waveguide was selected to have a narrower and wider radii of 5 and 6 mm, respectively. The period and aperture width of the corrugations were set as 2 and 1 mm, respectively. The waveguide was analysed for different lengths in ABCI environment. The resonant frequency of the wakefield was determined to be 38.50 GHz by using ABCI. By taking ABCI solution as reference, the same waveguide was examined in commercially available ANSYS HFSS environment using a similar methodology to one that is presented in [4]. The simulations were done for perfect electric conductor (PEC) and a finite conductivity boundary with Huray model surface rough model [5]. First, ANSYS HFSS eigenmode solver was utilized to determine the possible resonant frequencies of wakefields that can be generated by a travelling electron bunch. A single period of the corrugated waveguide was implemented to collect dispersion curves of both PEC- and Huray surface roughness model-implemented waveguides. The dispersion curves of both PEC and Huray surface roughness model cases are given in Fig. 1. The eigenmode solver was set to solve the first twenty modes. The results show that both eigenmode solver simulations setups result in very close dispersion curves. Hence, the intersections of the

ISBN: 978-3-95450-261-5 ISSN: 2673-7000 doi: 10.18429/JACoW-NAPAC2025-TUP040

EXPLICIT SYMPLECTIC REPRESENTATIONS OF NONLINEAR DIPOLE FRINGE FIELD MAPS

C. E. Mitchell*, Lawrence Berkeley National Laboratory, Berkeley, CA, USA
K. Hwang, Facility for Rare Isotope Beams, Michigan State University, East Lansing, MI, USA

Abstract

The representation of beam transport through magnetic dipole fringe fields using effective "thin" maps has a long history. More recent work has extended the second-order Taylor model of Brown by providing Lie generators for symplectic maps that capture effects at higher order, expressed in terms of field integrals. These maps can be cumbersome to evaluate in an explicit symplectic form appropriate for particle tracking codes, and existing approaches often require additional approximations. We show how such maps can be recovered in a simple, explicit form as rational symplectic functions using a mixed-variable generating function approach.

INTRODUCTION

Second-order models for "thin" maps describing the dynamical effects of dipole fringe fields are well-known [1–3]. Recent works [4, 5] extend these models to capture additional effects, such as closed orbit deviation, octupole-like focusing effects, and quadrupole or sextupole content in the magnet body. The result is a symplectic map $\mathscr{M}_F$ defined by:

$$\mathscr{M}_F = e^{:\Omega_M:}, \tag{1}$$

where Ω_M is approximated (through third or fourth-order terms) in the phase space variables and the magnetic gap. Approaches to express this map in an explicit form include: i) extracting the corresponding Taylor map, sacrificing symplecticity, or ii) splitting Ω_M into exactly-solvable terms, which requires ingenuity, approximates Eq. (1) in the size of Ω_M, and results in complicated expressions.

We describe how to bring Eq. (1) into an explicit form by constructing a mixed-variable generating function directly from the generator Ω_M. Maps obtained from mixed-variable generating functions are always symplectic, but they are typically implicit. However, in the cases of interest the Lie generator is (at most) linear in the momenta p_x and p_y, and this feature allows for a complete treatment [6, 7]. The result is an explicit, rational symplectic map that agrees with the underlying model to the same order of approximation.

HAMILTONIANS AT MOST LINEAR IN THE MOMENTA

Consider a Hamiltonian of the following general form:

$$H(q,p,\bar{q},\bar{p}) = p \cdot f(q,\bar{p}) + h(q,\bar{p}), \tag{2}$$

where we have a vector of coordinates $q = (q_1, \ldots, q_d)$ with a corresponding vector of momenta $p = (p_1, \ldots, p_d)$, and an additional vector of coordinates $\bar{q}$, not appearing on the right-hand side of Eq. (2), with a corresponding vector of momenta $\bar{p}$. [Here we can take $q = (x, y)$, $p = (p_x, p_y)$, $\bar{q} = z$, and $\bar{p} = \delta$.]

The differential equations for the variables q and $\bar{p}$ form a system that is decoupled from the remaining variables. Let $Q(t, q, \bar{p})$ denote the unique solution of this system with the initial condition q at $t = 0$, so explicitly:

$$\frac{dQ(t,q,\bar{p})}{dt} = f(Q(t,q,\bar{p}),\bar{p}), \qquad Q(0,q,\bar{p}) = q. \tag{3}$$

The momenta $\bar{p}$ are invariant, and may be treated as fixed parameters in the solution of Eq. (3).

If the solution $Q(t, q, \bar{p})$ of Eq. (3) is exactly known, then the solution of the entire system for Eq. (2) follows [6, 7].

Mixed-variable Generating Function

For each value of the independent variable t, we define a mixed-variable generating function F_t given by:

$$F_t(q,P,\bar{q},\bar{P}) = \bar{P}\cdot\bar{q} + P \cdot Q(t,q,\bar{P}) + \int_0^t h(Q(s,q,\bar{P}),\bar{P})ds. \tag{4}$$

The expression Eq. (4) yields a symplectic map of the form $(q, p, \bar{q}, \bar{p}) \mapsto (Q, P, \bar{Q}, \bar{P})$, which is defined by the implicit relations:

$$Q_j = \frac{\partial F_t(q,P,\bar{q},\bar{P})}{\partial P_j}, \quad p_j = \frac{\partial F_t(q,P,\bar{q},\bar{P})}{\partial q_j}, \tag{5a}$$

$$\bar{Q}_k = \frac{\partial F_t(q,P,\bar{q},\bar{P})}{\partial \bar{P}_k}, \quad \bar{p}_k = \frac{\partial F_t(q,P,\bar{q},\bar{P})}{\partial \bar{q}_k}. \tag{5b}$$

Because of the simple, linear dependence on the momenta P appearing in Eq. (4), the relations Eq. (5) can be explicitly inverted [8].

We claim that the map $(q, p, \bar{q}, \bar{p}) \mapsto (Q, P, \bar{Q}, \bar{P})$ describes the time evolution $0 \mapsto t$ generated by the Hamiltonian Eq. (2). It is sufficient to show that the mixed-variable generating function F_t satisfies the following Hamilton-Jacobi equation [9]:

$$\frac{\partial F_t}{\partial t} = H\left(\frac{\partial F_t}{\partial P}, P, \frac{\partial F_t}{\partial \bar{P}}, \bar{P}\right), \tag{6a}$$

$$F_0(q,P,\bar{q},\bar{P}) = P\cdot q + \bar{P}\cdot\bar{q}, \tag{6b}$$

where the initial condition Eq. (6b) states simply that F_0 generates the identity map. This initial condition is easily checked by setting $t = 0$ in Eq. (4). The left-hand side of Eq. (6a) becomes:

$$\frac{\partial F_t}{\partial t} = P\cdot\frac{\partial Q}{\partial t}(t,q,\bar{P}) + h(Q(t,q,\bar{P}),\bar{P}) = P\cdot f(Q(t,q,\bar{P}),\bar{P}) + h(Q(t,q,\bar{P}),\bar{P}), \tag{7}$$

* ChadMitchell@lbl.gov

Content from this work may be used under the terms of the CC BY 4.0 licence (© 2022). Any distribution of this work must maintain attribution to the author(s), title of the work, publisher, and DOI.

ISBN: 978-3-95450-261-5 ISSN: 2673-7000 doi: 10.18429/JACoW-NAPAC2025-TUP041

EXPLORING SPACE CHARGE MITIGATION WITH EIGENPAINTING AT THE SNS*

N. J. Evans†, A. Hoover, T. Gorlov, V. Morozov, Oak Ridge National Lab, Oak Ridge, TN, USA

Abstract

Building on recent work developing the method of eigenpainting to preferentially fill one non-planar mode of coupled optics in the Spallation Neutron Soruce ring via phase space paining, we present plans for future experiments. Our plans focus on experimentally producing several beam distributions prepared in non-planar modes, including gaussian, hollow, and Danilov (a special case of the KV). We lay out plans for experiments in the SNS, describe the available hardware, and propose a new technique for probing space charge in non-planar modes.

INTRODUCTION

A major challenge to the operation of high-intensity hadron accelerators is the effect of space charge on beam dynamics. Dependent on the details of the distribution of particles, space charge is generally non-linear, complicating the design, and operation of high-power accelerators. Perturbative treatments predict nonlinear particle-core resonances which drive particles from dense inner regions of phase space to a sparsely populated "halo" surrounding the beam [1]. Non-perturbative treatments reveal collective instabilities which can dramatically change the distribution, leading to growth in effective phase space volume [2]. Finally, in circular accelerators, space charge introduces a frequency spread in the beam which can effectively broaden single-particle resonance stopbands driven by nonlinear external forces [3]. All these effects can contribute to beam degradation and loss at high intensities. The standard limiting figure for beam loss in high power accelerators is 1 W/m, less than 1 part per million for MW scale machines such as the Spallation Neutron Source. Such stringent limits require a deep understanding of space charge dynamics to plan and operate the next generation of high-power accelerators.

One standard technique to increase the intensity of an accelerator complex is to increase the energy before injection, due to the advantageous scaling of space charge effects with energy. However, this is expensive, and other techniques have also been proposed to mitigate space charge effects, including controlling the shape of the distribution to manage the space charge force. Here we consider non-planar beam distributions as method of mitigating space charge.

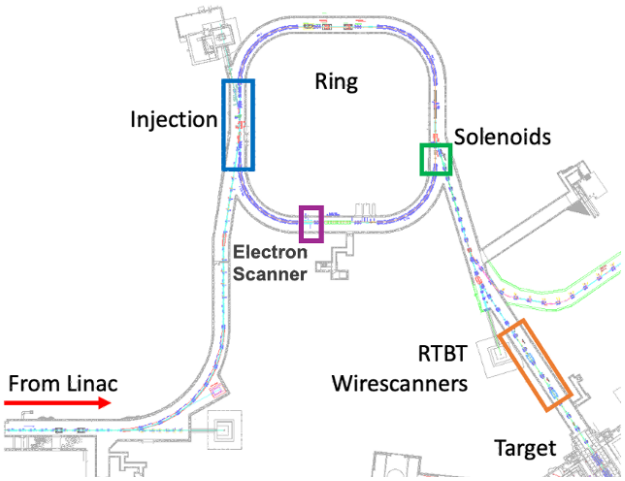


Figure 1: The SNS ring with location of key diagnostics and insertions indicated.

Exploiting the fact that transverse motion takes place in 4D phase space, but space charge only depends on the distribution in the x-y plane, non-planar modes maintain beam brightness, while reducing the effects of space charge. Additional mitigation is gained by phase-space painting—precisely placing small "beamlets" into the ring in a controlled way to construct a desired distribution. As of recent upgrades to the ring optics to allow non-planar beams, SNS is the only facility capable of both supporting non-planar beams, and phase space painting with control of position and angle in both transverse planes. In previous work we have developed a technique to paint exclusively into a single non-planar mode we call 'eigenpainting'. Eigenpainting offers direct control over the full four-dimensional phase space density in a fully-coupled ring, offering new ways to mitigate collective effects during accumulation. Compared to other methods of space charge mitigation painting non-planar beams may offer a cost-effective solution based on standard optics that could be retrofitted at existing facilities with minor disturbance to existing programs.

In addition to other applications non-planar modes have been proposed as a mitigation for space charge [4, 5]. However, no one has undertaken a systematic, experimental study of this method in a high-intensity hadron ring. This is largely due to the lack of available facilities. SNS is currently the only high-intensity ring equipped with both a flexible phase space painting system, and the optics necessary to produce non-planar modes. Figure 1 shows the layout of the ring and downstream Ring to Target Beam Transport (RTBT) line

* This manuscript has been authored by UT-Battelle, LLC, under Contract No. DE-AC05-00OR22725 with the U.S. Department of Energy. The United States Government retains, and the publisher, by accepting the article for publication, acknowledges that the United States Government retains a non-exclusive, paid-up, irrevocable, world-wide license to publish or reproduce the published form of this manuscript, or allow others to do so, for United States Government purposes. The Department of Energy will provide public access to these results of federally sponsored research in accordance with the DOE Public Access Plan (http://energy.gov/downloads/doe-public-access-plan).

† nhe@ornl.gov

Content from this work may be used under the terms of the CC BY 4.0 licence (© 2022). Any distribution of this work must maintain attribution to the author(s), title of the work, publisher, and DOI.

ISBN: 978-3-95450-261-5 ISSN: 2673-7000 doi: 10.18429/JACoW-NAPAC2025-TUP042

EXTRACTING SYMPLECTIC MAPS FOR SPACE CHARGE DOMINATED BEAMS

N. Bachhawat*, V. N. Litvinenko†,1, Stony Brook University, Stony Brook, NY, USA
[1]also at Brookhaven National Laboratory, Upton, NY, USA

Abstract

Symplecticity of transfer maps is important for reliable evaluation of space-charge dominated beams in accelerators. Unfortunately, most simulation codes that include collective effects, such as space charge, do not use canonical phase-space variables and therefore are not symplectic in the presence of electromagnetic fields. In this paper, we present a numerical method to extract local linear symplectic transfer maps using particle tracking simulation code IMPACT-T for space-charge dominated beams. We demonstrate this method for the photo-injector (113 MHz SRF gun) section of the Coherent electron Cooling (CeC) Proof of Principle (POP) experiment.

INTRODUCTION

There is a need for rigorous analytical methods to study beam dynamics in accelerator lattices, which frequently involve solving 3D Maxwell-Vlasov equation [1]. Symplecticity of the local linearized maps is critically important for finding analytically tractable solution (i.e. linear integral equation) for microscopic instabilities, which could be otherwise missed even by the most sophisticated codes. An example of this is the discovery of Plasma Cascade instability (PCI), which was first seen experimentally [2, 3], but was not observed in IMPACT-T simulation data. The analytical treatment of PCI [4] , subsequently allowed the IMPACT-T model to be updated and to correctly reproduce this phenomenon.

However, most of the commonly used particle codes which include collective effects (CE), including popular Particle-In-Cell (PIC) codes such as IMPACT-T [5], WARP [6], ASTRA [7] and PARMELA [8], track mechanical momenta instead of canonical momenta and generate accurate but non-symplectic transfer maps.

Since most CE particle-tracking codes are non-symplectic and symplectic tracking codes usually have limited functionality for start-to-end simulation that include guns and injectors, we propose a general numerical post-processing method to extract local linear symplectic maps (in the vicinity of a chosen phase-space trajectory) from any non-symplectic particle tracking codes.

METHOD

For codes using time as the independent variable, the extraction of symplectic transfer maps requires knowledge of the geometric transfer map, M_g as well as the vector potential at both initial and final times[1]. Then, we can solve the r.h.s. equation:

$$\{\vec{r}(t), \vec{p}(t)\} = M_g : \{\vec{r}(t_0), \vec{p}(t_0)\}, \tag{1}$$

where, $\vec{p}(t) = \vec{P}(t) - \frac{e}{c}\vec{A}(t, \vec{r}(t))$. A solution can be found by linearization of the map around the phase-space trajectories. Let us introduce 6-vectors to denote mechanical (Y) and canonical (X) phase-space coordinates:

$$Y = \begin{bmatrix} \vec{r} \\ \vec{p} \end{bmatrix} \Rightarrow Y(t) = \mathbf{M}_g : Y(t_0);$$
$$X = \begin{bmatrix} \vec{r} \\ \vec{P} \end{bmatrix} = Y + \frac{e}{c} \cdot \begin{bmatrix} 0 \\ \vec{A}^{\,T}(t, \vec{r}) \end{bmatrix} \Rightarrow X(t) = \mathbf{M}_s : X(t_0), \tag{2}$$

where $\mathbf{M}_s$ is the desirable, but unknown, symplectic transfer map. Let us pick one of the allowed space-phase trajectories (indicated by the subscript o):

$$Y_o(t) \equiv \begin{bmatrix} \vec{r}_o(t) \\ \vec{p}_o(t) \end{bmatrix} = \mathbf{M}_g : Y_o(t_0), \tag{3}$$

and expand map around it,

$$Y = Y_o + \nu;\ \nu = \begin{bmatrix} \vec{\rho} \\ \vec{\pi} \end{bmatrix};\ \nu(t) = \mathbb{M}_g \cdot \nu(t_0) + O(|\nu|^2);$$
$$\mathbb{M}_g = \left.\frac{\partial(\mathbf{M}_g : Y)}{\partial Y}\right|_{Y=Y_o(t)};$$
$$X = X_o + \xi; \quad \xi = \begin{bmatrix} \vec{\rho} \\ \vec{\Pi} \end{bmatrix};\ \xi(t) = \mathbb{M}_s \cdot \xi(t_0) + O(|\xi|^2);$$
$$\vec{\Pi} = \vec{\pi} + \mathbf{V}(t) \cdot \vec{\rho};\ \mathbf{V}(t) = \frac{e}{c} \cdot \left.\frac{\partial(\vec{A}(t, \vec{r}))}{\partial \vec{r}}\right|_{r=r_o(t)} \tag{4}$$

where the local 6×6 matrix $\mathbb{M}_g$ is defined by the geometric transfer map M_g and the chosen trajectory. The 3×3 matrix $\mathbf{V}$ is defined by the vector potential, and the symplectic 6×6 matrix, $\mathbb{M}_s$, still needs to be determined. For the rest of the paper, we will also neglect higher order terms identified as $O(\varepsilon^2)$, where ε is the expansion parameter.

Unfortunately, particle tracking codes typically do not provide full information about the vector potential, including self-field contributions, and the user needs to define the necessary components of the EM 4-potential themselves.

* nikhil.bachhawat@stonybrook.edu
† vladimir.litvinenko@stonybrook.edu

[1] For codes using coordinates along the reference trajectory, s, one would need to know transverse components of the vector potential and scalar potential at initial and final azimuth to extract symplectic transfer map for (x,y,-ct, Px,Py, H/c). While technically it is different for the above description, the idea of the method is the same.

Content from this work may be used under the terms of the CC BY 4.0 licence (© 2022). Any distribution of this work must maintain attribution to the author(s), title of the work, publisher, and DOI.

ISBN: 978-3-95450-261-5 ISSN: 2673-7000 doi: 10.18429/JACoW-NAPAC2025-TUP046

FAST SPIN TRACKING USING A MAGNUS EXPANSION

J. P. Devlin*,1, E. Hamwi[1], G. H. Hoffstaetter[1,2]
[1]CLASSE, Cornell University, Ithaca, New York, USA
[2]Brookhaven National Laboratory, Upton, New York, USA

Abstract

Spin motion in particle accelerators obeys the Thomas-Bargmann-Michel-Telegdi (T-BMT) equation. Due to the structure of the T-BMT equation, the spin-transfer quaternion of a magnet is generally a nonlinear function of the entrance coordinates even if the phase-space motion is linear. This nonlinear function can be written as a Dyson expansion, for example as employed in the program Sprint, which normalized the first-order expansion of the spin-transfer quaternion. Alternatively, this nonlinear function can be written as a Magnus expansion. This paper points out that in cases where the phase-space coordinates change little, as is generally the case for accelerator elements, the Magnus expansion is a much more appropriate method to describe the nonlinear spin motion because this expansion terminates after the first term when the phase-space coordinates are constant. We will demonstrate, with several examples, that an approximation based on the Magnus expansion leads to very good agreement with time-consuming numerical integration, and to significantly better agreement than obtained with historical codes like Sprint.

INTRODUCTION

Despite the ubiquity of matrices in accelerator physics, the reality is that even the simplest magnetic field configurations lead to nonlinear transfer maps. This is exemplified by the fact that the motion through a drift space is nonlinear, which one can trace back to the square root in the relativistic energy-momentum relation [1]. As a consequence, for most magnets, the full transfer map can only be obtained through numerical integration. Nevertheless, matrices are useful in that they are fast and, in many cases, provide an adequate approximation of the transfer map. It would be useful if an analogous concept existed for spin motion, i.e., a method to track spins which avoided expensive numerical integration but still retained reasonable accuracy.

The equation of spin motion in a purely magnetic field is a special case of the Thomas-Bargmann-Michel-Telegdi (T-BMT) equation and takes the form [2, 3]

$$\begin{aligned} \boldsymbol{S}'(s) &= \left[\boldsymbol{\Omega}(z(s),s) + g\boldsymbol{e}_y\right] \times \boldsymbol{S}(s), \\ \boldsymbol{\Omega}(z,s) &= -\frac{q}{p_0}\frac{1+gx}{\sqrt{(1+p_z)^2 - p_x^2 - p_y^2}} \\ &\quad \times \left[(1+G\gamma)\boldsymbol{B}_\perp(z,s) + (1+G)\boldsymbol{B}_\parallel(z,s)\right]. \end{aligned} \tag{1}$$

Here, $\boldsymbol{B}_\perp$ (resp. $\boldsymbol{B}_\parallel$) represents the magnetic field perpendicular (resp. parallel) to the particle velocity, z contains the canonical coordinates, g is the horizontal curvature of the reference trajectory, and s denotes the arc length along the reference trajectory. The coordinate system and canonical coordinates used here are taken from Bmad, where the transverse momenta are normalized by the reference momentum p_0 and $p_z = (p - p_0)/p_0$ [4]. Given that the cross product is a linear operation, it is often useful to rewrite Eq. (1) in the form

$$\boldsymbol{S}'(s) = \mathbf{A}(z(s),s)\boldsymbol{S}(s), \tag{2}$$

where $\mathbf{A}(z,s)$ is a skew-symmetric matrix.

Even if the orbital motion is propagated using a matrix (i.e., z is a linear function of the initial coordinates z_0) and the magnetic field is a linear function of z, it is clear from Eq. (1) that $\boldsymbol{S}'$ is a nonlinear function of z_0. This is the first indication that the spin motion is quite complicated, especially in light of the fact that the linearity of z is merely an approximation. Another fact of note is that when $\mathbf{A}$ commutes with itself, i.e.,

$$[\mathbf{A}(z(s_1),s_1), \mathbf{A}(z(s_2),s_2)] = 0 \tag{3}$$

for any s_1 and s_2 with the matrix commutator $[\cdot,\cdot]$, the flow of Eq. (2) is given by

$$\mathbf{R}(z_0,s;s_0) = \exp\left(\int_{s_0}^{s} \mathbf{A}(z(\sigma),\sigma)\,\mathrm{d}\sigma\right). \tag{4}$$

The exponential will generally contain all orders of z_0 even if $\mathbf{A}(z,s)$ is approximated by a linear function of z.

PERTURBATION THEORY

Two ways to extend Eq. (4) to the case of noncommuting $\mathbf{A}$ are the Dyson expansion and the Magnus expansion. The leading-order Dyson expansion is

$$\mathbf{R}(z_0,s;s_0) \approx \mathbf{1} + \int_{s_0}^{s} \mathbf{A}(z(\sigma),\sigma)\,\mathrm{d}\sigma\,, \tag{5}$$

which is just the linear expansion of Eq. (4) [5]. The leading-order Magnus expansion is [6, 7]

$$\mathbf{R}(z_0,s;s_0) \approx \exp\left(\int_{s_0}^{s} \mathbf{A}(z(\sigma),\sigma)\,\mathrm{d}\sigma\right). \tag{6}$$

Of course, this is a good approximation when the noncommutativity of $\mathbf{A}$ perturbs the flow negligibly.

The Magnus expansion has some advantages over the Dyson expansion. To begin, note that when $\mathbf{A}(z,s)$ belongs to a Lie algebra $\mathfrak{g}$, the flow of Eq. (2) belongs to the corresponding Lie group G. The approximate flow provided by the leading-order Magnus expansion also belongs to G, while that of the Dyson expansion in general does not. In spin dynamics, the case of interest is $G = \mathrm{SO}(3)$ (although it is more efficient to use unit quaternions in numerical simulations) [8, 9]. For this reason, use of the Dyson expansion usually leads to an undesirable change in the length of spins.

* jpd285@cornell.edu

Content from this work may be used under the terms of the CC BY 4.0 licence (© 2022). Any distribution of this work must maintain attribution to the author(s), title of the work, publisher, and DOI.

ISBN: 978-3-95450-261-5 ISSN: 2673-7000 doi: 10.18429/JACoW-NAPAC2025-TUP048

GENERATION OF LOW-EMITTANCE BUNCHES WITH SELECTIVE COLLIMATION AT THE ARGONNE WAKEFIELD ACCELERATOR

E. Frame*, O. Chubenko, Northern Illinois University, DeKalb, IL, USA
S. Doran, P. Piot, J.G. Power, E.E. Wisniewski, Argonne National Laboratory, Lemont, IL, USA

Abstract

The Argonne Wakefield Accelerator (AWA) facility's drive-beam linear accelerator can generate electron bunches at a wide range of charge - from 100 pC to 100 nC. This provides a unique opportunity to study selective transverse collimation as a method to increase beam brightness by selecting the core of the beam using various initial bunch charges. This paper presents numerical modeling of the scheme. Simulations were performed to explore the impact of a collimating aperture on emittance, scraping the outermost electrons and retaining only the inner core of the beam with the goal of maximizing the beam brightness for a 100-pC electron beam. An optimization of various beamline parameters, including the initial bunch charge, was done to produce possible operating points that generate the lowest emittance. These simulations inform an experimental campaign that is also discussed.

INTRODUCTION

Bright electron beams have enabled critical developments in accelerator applications, including X-ray free-electron lasers and ultrafast electron microscopy and diffraction. One limiting factor to the generation of high-brightness beams is the beam emittance, with the reduced 5-dimensional brightness given by

$$B_5 \equiv \frac{\hat{I}}{\varepsilon_\perp^2}, \tag{1}$$

where $\hat{I}$ represents the beam's peak current and $\varepsilon_\perp$ represents the beam emittance in the transverse direction [1].

The minimum achievable emittance (sometimes called the intrinsic or thermal emittance) is fundamentally set by the electron source. For photocathodes, it is determined by the mean transverse energy (MTE) of the emitted electrons and the emission area, both of which are governed by the material's intrinsic electronic properties and surface conditions. Generally, due to the disproportionate contribution of halo particles to the transverse phase space, the experimental emittance scales with the fraction of the beam considered. Consequently, removing the outer halo can help reduce the beam emittance. This work investigates the use of a collimating aperture as a method for emittance minimization. The technique was proposed in Ref. [2] as a way to use the beam's peripheral particles to compensate for slice-emittance growth in high brightness photoinjectors. The numerical simulations of this method are presented, as well as the details of an upcoming experimental campaign guided by the results.

Specifically, we study the generation of a higher-charge initial beam scraped down to 100 pC with the goal of maximizing the beam brightness by emittance reduction using the Argonne Wakefield Accelerator's (AWA) drive-beam linear accelerator. The drive-beam linac operates at a wide range of charge - 100 pC to 100 nC - which enables the exploration of selective collimation for a wide range of initial charge values.

The drive-beam photoinjector consists of a 1.3-GHz $1+\frac{1}{2}$ cells RF cavity with a high-quantum efficiency photocathode; see Fig. 1. The electron bunches are generated via photoemission triggered by 292-nm ultraviolet (UV) laser pulses impinging on a Cs_2Te photocathode. Nominally, the laser is transversely uniform with a 400-fs Gaussian termporal distribution. The Gaussian pulse can be replicated and stacked to produce a plateau-like flat-top distribution with a duration of 6 ps.

As can be seen in Fig. 1, the RF gun is surrounded by three solenoids (LB, LF, and LM) to control the transverse emittance at production and match the beam into the first linear accelerating cavity. Six 1.3-GHz traveling wave linac cavities (C1 - C6) accelerate the beam to energies nearing 70 MeV. Additional solenoids (LS1 - LS3) focus the beam downstream of the gun. Four quadrupoles located just upstream of the aperture can be used for an emittance measurement.

NUMERICAL METHODS

This paper uses multi-objective optimization to investigate the impact of various beamline parameters on minimizing transverse emittance $\varepsilon_\perp$ and bunch duration σ_t. As a result of the optimization, a Pareto front is generated, which shows the tradeoff between the two objectives by creating a curve composed of the non-dominated solutions; these are solutions where further improvement in one objective degrades another [3]. The optimization framework DEAP [4] is integrated with the particle tracking algorithm ASTRA [5] to generate these tradeoff curves. ASTRA takes as input the on-axis electromagnetic fields and expands them radially, assuming cylindrical symmetry. The beamline parameters varied in the optimization are listed in Table 1, along with their range of values (as a note, the value of the peak B field for the bucking solenoid used in the simulations is calculated by multiplying the setting number with the focusing solenoid peak field value, and taking the opposite). Additionally, the two different laser pulse profiles were studied, as well as

* z1902539@students.niu.edu

Content from this work may be used under the terms of the CC BY 4.0 licence (© 2022). Any distribution of this work must maintain attribution to the author(s), title of the work, publisher, and DOI.

ISBN: 978-3-95450-261-5 ISSN: 2673-7000 doi: 10.18429/JACoW-NAPAC2025-TUP049

HIGH DC INJECTION VOLTAGE PHOTOCATHODE E-BEAM SOURCES

B. L. Beaudoin[1], R. B. True[1], P. G. O'Shea[1], J. Petillo[2], H. P. Freund[1], M. V. Fazio[3]
[1]Institute for Research in Electronics and Applied Physics, University of Maryland, College Park, MD, USA
[2]Leidos, Acton, MA, USA
[3]SLAC National Accelerator Laboratory, Menlo Park, CA, USA

Content from this work may be used under the terms of the CC BY 4.0 licence (© 2022). Any distribution of this work must maintain attribution to the author(s), title of the work, publisher, and DOI.

Abstract

Laser switched photocathode sources are typically used to produce trains of polarized electron bunches for high performance accelerators. This paper considers two high brightness, high charge-per-bunch, e-beam injector approaches that utilize laser gated cathodes followed by DC beam acceleration sections comprised of 1-3 grading electrodes. The use of grading electrodes provides reliable high voltage standoff between the plates themselves and ground. In the rectilinear beam source case in particular, we found that the uniformity of the emitted current density can have a major effect on final beam emittance and brightness.

CONVERGENT BEAM

The first approach is based upon one of the thermionic sources in [1, 2] for use in 1 THz high-power FELs. A plot of this source is shown in Fig. 1.

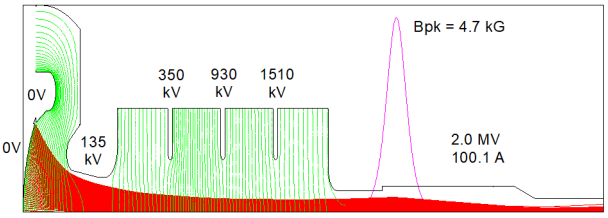


Figure 1: Simulation of 2 MV, 100.1 A, 0.0354 μperv electron beam 1 THz FEL source.

The beam optical design was developed using the DEMEOS code [3] whereas the self-consistent fields solution results from this code are in exact agreement with those from MICHELLE [4].

Next, MICHELLE was utilized in the transient mode to model the case in which 10ps long pulses are emitted from the cathode. Sample results from the movie of the evolving beam in the cathode region are shown in Fig. 2.

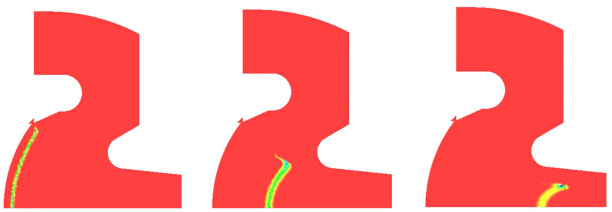


Figure 2: MICHELLE transient simulation of gun in Fig. 1 for 10 picosecond pulse emission.

Figure 3 shows the pulse of emitted current downstream from the movie of the transient simulation.



Figure 3: Current pulse downstream in the MICHELLE transient simulation of the source of Fig. 1 for the 10 ps pulse emission case.

The high voltage structure in Fig. 1 was designed for 2 μsec pulse standoff. In operation, a train of 10 ps pulses would lie within each 2us macro pulse.

For DC standoff operation, all the voltages must be scaled by a factor of approximately 0.4. Hence, at a body voltage of 800 kV, for constant perveance, the beam current will be 25.3 A.

Another point with this design is the challenge of full illumination of the cathode with the drive laser. This aspect is the subject of further study.

CYLINDRICAL BEAM

The second approach is a planar cathode rectilinear beam gun followed by a set of acceleration electrodes as shown in Fig. 4. The design is configured to reliably stand off the voltages DC.

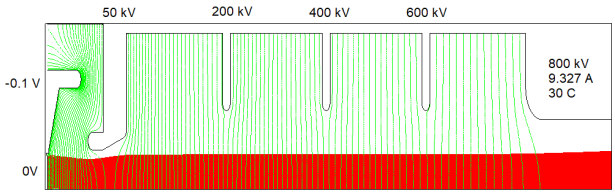


Figure 4: Simulation of 800 kV DC beam voltage, 9.327 A, 0.0130 μperv cylindrical beam source (Photo1sc).

The case in the plot assumes the cathode at room temperature or 30°C. The appearance of the beam is essentially the same for the nonthermal beam case, and for the 1100°C case. Near the problem exit at 21.0 cm, the normalized rms emittance for the cold beam is 1.619 μm, at 30°C true it is 1.848 μm, and at 1100°C it is 2.250 μm. These numbers are all outstanding. Further, normalized brightness can be obtained from Eq. (3.22) in [5]. For the 30°C case, it is 3.6E+10A/(m-rad)^2 a very high value.

The photocathode design work of this section has drawn heavily from the excellent article by Wang, et al. [6]. In their design, the DC voltage was 350 kV, current 4.5 A, perveance 0.0217 μperv. And normalized RMS emittance

ISBN: 978-3-95450-261-5 ISSN: 2673-7000 doi: 10.18429/JACoW-NAPAC2025-TUP050

IMPACT OF ELECTRON BEAM SIZE RIPPLE ON PROTON EMITTANCE GROWTH FOR EIC*

D. Xu†, Y.-K. Kan, Y. Luo, B. Podobedov
Brookhaven National Laboratory, Upton, NY, USA

Abstract

The Electron-Ion Collider (EIC) employs a flat hadron beam to achieve high luminosity, with the proton beam's vertical emittance being an order of magnitude smaller than its horizontal one. The smaller vertical emittance is sensitive to external noise. This study examines electron beam size ripple, which comes from power supply fluctuations. Through beam-beam interaction, the electron size ripple contributes to vertical emittance growth. Mitigation strategies are discussed to preserve the flat beam aspect ratio.

INTRODUCTION

The Electron-Ion Collider (EIC) is a next-generation facility to be constructed at Brookhaven National Laboratory (BNL) [1]. The EIC employs flat hadron beam to achieve high luminosity [2], in which the vertical emittance of the proton beam is ten times smaller than the horizontal one.

This configuration introduces sensitivities to external noise, particularly in the vertical plane. One such concern is the electron beam size ripple. Due to the nonlinear beam-beam interactions, fluctuations in the electron beam size can induce a time-varying beam-beam force on the protons. When this force resonates with the betatron or synchro-betatron motion of the proton beam, it can drive vertical emittance growth, compromising the flatness of the hadron beam.

This paper investigates the impact of electron beam size ripple on proton emittance evolution using weak-strong beam-beam simulations. The ripple modeling and simulation setup follow our previous study on electron orbit ripple [3], with the key distinction that the fluctuation is applied to the RMS beam size of the strong beam rather than its centroid position. Simulation results show that even small ripples can cause cumulative emittance growth, depending on their frequency and amplitude. Possible mitigation strategies are discussed to reduce the vertical emittance growth.

FULL RANGE SCAN OF CENTER FREQUENCY

Figure 1 presents the results of a frequency scan with an electron beam size ripple of 0.5%. The ripple amplitude is defined as the RMS variation of the electron beam size, normalized to the nominal beam sizes at the interaction point (IP). The proton working point is $\nu_x = 0.228$, $\nu_y = 0.210$, and $\nu_z = -0.01$. The ripple is modeled as narrow-band noise with a bandwidth of 1000 Hz, which is slightly larger than the beam-beam tune spread. The center frequency of this ripple is scanned from 0 up to half the revolution frequency.

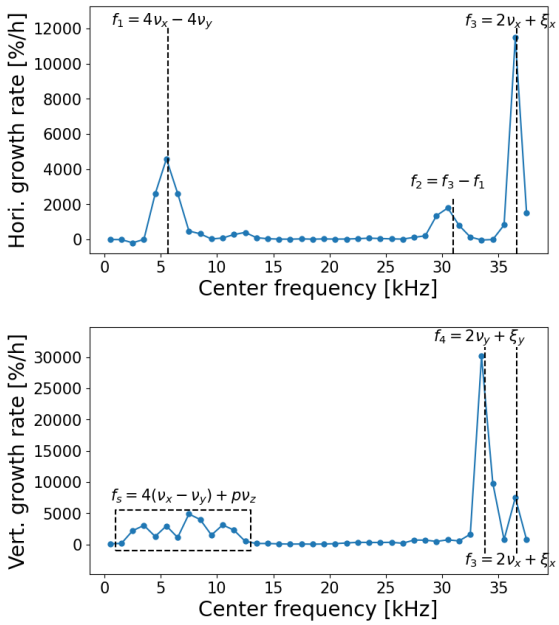


Figure 1: Proton horizontal (top) and vertical (bottom) emittance growth rates as a function of ripple frequency, with a fixed electron size ripple amplitude of $0.5\%\sigma_{x,y}$. The vertical lines and labeled numbers indicate resonance conditions (frequencies normalized by the revolution frequency). Simulations are tracked for 10^6 turns.

In the horizontal plane, the dominant peak appears at $f_3 = 2\nu_x$, corresponding to envelope oscillations of the proton beam. Due to the beam-beam tune spread $\xi_x \sim 0.1$, this peak spans from $2\nu_x$ to $2\nu_x + 2\xi_x$. This resonance occurs because the external ripple frequency aligns with the envelope oscillation frequency of the proton beam, which is twice the horizontal betatron frequency.

The second strongest peak occurs at $f_1 = 4\nu_x - 4\nu_y$, which is interpreted as a harmonic of the cross-plane coupling resonance $2\nu_x - 2\nu_y$. Since the beam-beam potential is an even function of transverse coordinates $V_{bb} = V(x^2, y^2)$, and the size ripple drives envelope oscillations at twice the betatron frequency, this resonance drives a large emittance growth when the external frequency coincides with it.

The third peak, located at $f_2 = f_3 - f_1$, may correspond to a sideband arising from the interference between the primary envelope mode and the nonlinear coupling mode.

Similarly, in the vertical plane, the highest peak appears at twice the vertical betatron frequency, $f_4 = 2\nu_y$, corresponding to vertical envelope oscillations. Since the verti-

* Work supported by Brookhaven Science Associates, LLC under Contract No. DE-SC0012704 with the U.S. Department of Energy.
† dxu@bnl.gov

Content from this work may be used under the terms of the CC BY 4.0 licence (© 2022). Any distribution of this work must maintain attribution to the author(s), title of the work, publisher, and DOI.

ISBN: 978-3-95450-261-5 ISSN: 2673-7000 doi: 10.18429/JACoW-NAPAC2025-TUP051

IMPEDANCE AND WAKEFIELD STUDIES OF THE EIC RCS 591 MHz FIVE-CELL CAVITY

S. Setiniyaz[1*], N. Sereno[1], I. Neththikumara[1], K. Deitrick[1], Z. A. Conway[1], T. Satogata[1], J. Guo[1], R. Rimmer[1], A. Blednykh[2], G. Wang[2], W. Xu[2]
[1]Jefferson Lab, Newport News, VA, USA
[2]Brookhaven National Laboratory, Upton, NY, USA

Abstract

The Electron-Ion Collider (EIC) is a next-generation accelerator complex designed to enable high-luminosity collisions between highly polarized electrons and ions. A central component of its Electron Injection System (EIS) is the Rapid Cycling Synchrotron (RCS), which accelerates electron bunches from 750 MeV to 5, 10, or 18 GeV using a total of eight 591 MHz 5-cell superconducting RF cavities. To ensure stable acceleration of high-charge bunches, we conducted detailed impedance and wakefield studies of the cavity structure using both frequency- and time-domain methods. Wakefield solvers (ECHO3D, ECHOz1, ECHOz2, CST), eigenmode analysis, and multi-particle tracking with ELEGANT were employed to evaluate longitudinal and transverse impedance effects and to determine instability thresholds. These studies provide critical input for the cavity design and operating parameters required to preserve beam quality and stability in the RCS.

INTRODUCTION

As illustrated in Fig. 1, the Electron–Ion Collider's Electron Injection System (EIS) relies on a Rapid Cycling Synchrotron (RCS) (see Fig. 2) to accelerate a single 28 nC bunch from 750 MeV to 5, 10, and an 11 nC bunch to 18 GeV [1]. A central element of this lattice is the eight 591 MHz, 5-cell superconducting RF cavities. Ensuring beam stability against both impedance-driven and wakefield-induced effects is therefore critical. In this paper, we present a comprehensive suite of impedance studies—encompassing wakefield calculations, eigenmode analyses, and multi-particle beam-tracking simulations—to assess stability risks.

CAVITY GEOMETRY

The initial design derives from the BNL 650 MHz 5-cell cavity, scaled to 591 MHz [2], with the HOM coupler removed to simplify the model, as shown in Fig. 3(a). The modified configuration in Fig. 3(b) employs a standard beam-pipe diameter of 274 mm, extended to 800 mm in length to accommodate a future Beam Line Absorber (BLA). Because the BLA absorbs HOM power and consequently heats up, it must be positioned sufficiently far from the cryogenic cavity to avoid thermal loading. A 500 mm-long taper transitions the 274 mm section down to a 36.32 mm inner-diameter pipe. The iris diameter between cavity cells is 178.2 mm, while that between the cavity and the beam pipe is 182.6 mm.

* saitiniy@jlab.org

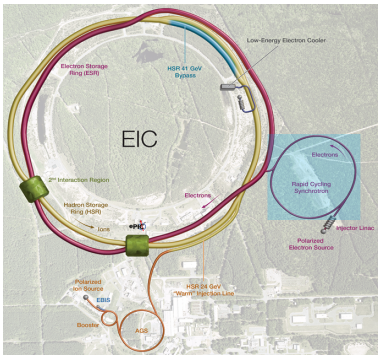


Figure 1: EIC top view with RCS highlighted in blue.

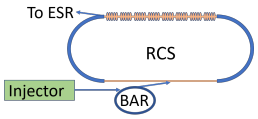
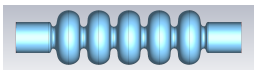
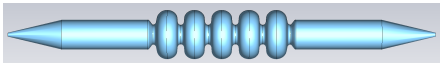


Figure 2: Schematic layout of the RCS, the Beam Accumulator Ring (BAR), and the Injector Linac.



(a) Scaled cavity model (V1).



(b) Scaled and modified cavity model (V3).

Figure 3: 5-cell 591 MHz cavity models.

Note: Neither the V1 nor V3 cavity and taper designs are final; they're intended solely for impedance-target studies.

WAKEFIELD SIMULATIONS

Benchmarking

Wakefield simulations were carried out using ECHO3D [3] for the scaled cavity model. The results were cross-checked and benchmarked against GdfidL [4] and CST [5] for short-range wakes with a 7 mm RMS bunch length. Loss factors are listed in Table 1, and wake potentials are plotted in Fig. 4.

Additionally, loss factors were computed from the eigenmode simulation data via Eq. (1) for monopole modes

Content from this work may be used under the terms of the CC BY 4.0 licence (© 2022). Any distribution of this work must maintain attribution to the author(s), title of the work, publisher, and DOI.

ISBN: 978-3-95450-261-5 ISSN: 2673-7000 doi: 10.18429/JACoW-NAPAC2025-TUP052

IMPLEMENTATION OF ADJOINT SENSITIVITY ANALYSIS IN WARP*

D. T. Abell†, V. B. Tembo, I. Haber, T. M. Antonsen, University of Maryland, College Park, MD, USA

Abstract

The design of accelerator lattices involves evaluating and optimizing Figures of Merit (FoMs) that characterize a beam's properties. These properties—hence the FoMs—depend on the many parameters that describe a lattice, including the strengths, locations, and possible misalignments of focusing elements. Often what is required is the gradient of the FoM with respect to each of the parameters. For systems that require numerical simulation, a naïve computation of a gradient requires one simulation for the "base case", plus one additional simulation for each parameter of interest—a daunting effort in the case of computationally demanding simulations with many parameters. Adjoint techniques allow one to extract gradient information from one base-case simulation plus an additional one or two carefully prepared simulations. We demonstrate these techniques using the accelerator simulation code WARP, and we present our proof-of-concept results using several different FoMs as the basis for adjoint analyses of a simple beamline with multiple parameters.

INTRODUCTION

The design of all accelerator systems today uses sophisticated, computationally intensive, numerical models. An essential element of the design process is a determination of how various performance metrics vary with respect to the many parameters that define an accelerator lattice. A determination of this dependence has at least two benefits: (i) It establishes the gradient of a given metric in parameter space, which facilitates design optimization using steepest descent. (ii) It yields the sensitivity of a particular design to errors in the lattice, and hence enables designers to set construction tolerances.

Adjoint methods provide a dramatically more efficient way to calculate parameter dependencies than straightforward parameter differencing, which requires a separate simulation run for each parameter being varied [1]. As an indication of the power of adjoint methods, we point out that adjoint techniques are used in the engineering community in a variety of contexts to compute sensitivities and gradients. The adjoint approach has previously been applied in circuit theory [2], electromagnetics [3], aerodynamics [4], plasma confinement [5–7], as well as in many other fields. They have been used to optimize the design of three-dimensional magnetohydrodynamic equilibria in stellarators [6, 7]. In the context of accelerators, we have recently deployed adjoint methods to optimize electrostatic [8] and magnetic [9] focusing systems, as well as to optimize the combination of quadrupole and solenoid magnetic fields needed to transform—in the presence of strong space charge—a flat beam to a round, angular-momentum-dominated beam [1].

A HAMILTONIAN ADJOINT RELATION

Lots of analysis and algebra (as sketched in the appendix) leads to the following *adjoint relation*, which involves two types of perturbations—true and adjoint, denoted respectively by superscripts (T) and (A):

$$\sum_j \frac{I_j}{I}\left(\delta p_j^{(T)}\cdot\delta x_j^{(A)} - \delta p_j^{(A)}\cdot\delta x_j^{(T)}\right)\Big|_0^L = \int_0^L \mathrm{d}z \int \mathrm{d}^2x_\perp \frac{q}{I}\Big\{ \left[-\delta\rho^{(A)}\,\delta\phi^{(T)} + \delta J^{(A)}\cdot\delta A^{(T)}\right] - \left[A \leftrightarrow T\right]\Big\}, \quad (1)$$

where j indexes particles in the beam, and $[A \leftrightarrow T]$ denotes the previous expression in square brackets with the superscripts (T) and (A) reversed. On the left-hand side (LHS), we have a net change in the symplectic area separating the trajectories of two different perturbed solutions. On the right-hand side (RHS), we see a space-time integral over mixed—(A) and (T)—products of charge and current density perturbations with, respectively, scalar and vector potential perturbations.

The utility of the adjoint relation derives from the freedom we have to assign the adjoint perturbations on the LHS: We shall assign them so as to make the LHS become the change in some relevant FoM. This constitutes the *difficult-to-compute* quantity of interest. The RHS we can evaluate using an additional pair of carefully instrumented simulations. This constitutes the *easy-to-compute* quantity that yields the change we seek to determine in the FoM of interest. Moreover, we can use the linearity of integration to accumulate individual contributions to the RHS, and compute thus—with just the one additional pair of simulations—the FoM *gradient* with respect to as many parameters as we deem relevant.

We focus on FoMs F that measure some aspect(s) of the particle phase-space distribution at the exit plane $z = L$. We write our F in the generic form

$$F = \sum_j \frac{I_j}{I} f(x_{\perp j}, p_{\perp j})\Big|_{z=L}. \quad (2)$$

To make the LHS of Eq. (1) look like a change in the FoM, we assume the True solution has no perturbations to the particle phase-space coördinates at the lattice entrance, $z = 0$, and we assume the Adjoint solution has particle perturbations at the lattice exit, $z = L$, given by the rules

$$\delta x_j^{(A)} = \frac{\partial f}{\partial p_j}\Delta, \quad \delta p_j^{(A)} = -\frac{\partial f}{\partial x_j}\Delta, \quad (3a)$$

* This work supported in part by the US Department of Energy, Office of Science, Office of High Energy Physics, under Grant #DE-SC-0025277.

† dabell@umd.edu

Content from this work may be used under the terms of the CC BY 4.0 licence (© 2022). Any distribution of this work must maintain attribution to the author(s), title of the work, publisher, and DOI.

ISBN: 978-3-95450-261-5 ISSN: 2673-7000 doi: 10.18429/JACoW-NAPAC2025-TUP053

INSTABILITY THRESHOLD MEASUREMENTS IN THE IOTA RING AT FERMILAB*

M.K. Duncan†, Y.K. Kim[1], University of Chicago, Chicago, IL, USA
R. Ainsworth, N. Eddy, Fermi National Accelerator Laboratory, Batavia, IL, USA
[1]also at Fermi National Accelerator Laboratory, Batavia, IL, USA

Abstract

Nonlinear focusing elements enhance the stability of particle beams in high-energy colliders via Landau Damping, a phenomenon which acts through the tune spread these elements introduce. Our experiment at Fermilab's Integrable Optics Test Accelerator (IOTA) aims to investigate the influence of nonlinear focusing elements on transverse beam stability by using a novel method to directly measure the strength of Landau Damping, employing an active transverse feedback as a controlled source of impedance. The resulting motion of the beam can then be used to directly measure the stability diagram, a threshold that maps the stability conditions of the system. A proof-of-principle experiment of this measurement method was first explored at the LHC, where the experiment at IOTA aims to map out the entirety of the stability diagram and obtain the beam distribution function from the stability diagram, a procedure never done before. Here, we present our simulation results, initial data analysis, and plans for further investigation.

MOTIVATION

A major challenge facing many particle accelerators is maintaining high beam intensity. Factors limiting intensity include collective instabilities, which not only reduce beam intensity but produce losses, irradiate components, and generate other negative effects.

Our group approaches the challenge of intensity by directly studying beam stability at the Integrable Optics Test Accelerator (IOTA) at Fermilab. IOTA is an easily reconfigurable 40 m storage ring designed to run both electrons and protons at energies of 150 MeV and 2.5 MeV, respectively. This experiment is concerned with electrons circulating the ring.

One phenomena studied in understanding beam stability is Landau Damping (LD), which damps collective oscillation modes and acts as a defense against collective instabilities. LD relies on particle betatron frequency spread and works through the energy transfer between coherent and incoherent oscillation modes [1]. Studies on the strength of LD are often approached via Stability Diagram (SD) Theory, which depends on the dispersion relation between the beam's coherent tune shift from an external excitation and the resulting tune of the mode. The dispersion relation for a coherent vertical degree of freedom is shown in Eq. (1):

$$\Delta\omega_y = -1/\int \frac{J_y \partial F/\partial J_y}{\nu - \delta\omega(J_x, J_y) + io}\, dJ_x dJ_y \qquad (1)$$

Where $\Delta\omega_y$ is the coherent tune shift, ν is the tune of the mode, J_y and J_x are the actions in the x and y planes, F is the bunch distribution function, $\delta\omega$ is the oscillating particle frequency shift, and io is a vanishingly small term introduced in derivation to avoid singularities. The distribution function is meant to be normalized: $\int\int F(J_x, J_y) dJ_x dJ_y = 1$ [2].

Given a coherent tune shift, one can use Eq. (1) to find the tune of the mode. To find ν, one would traditionally solve Eq. (1) for all $\Delta\omega$. By mapping $\mathrm{Im}[\nu] = 0$ onto the complex plane of $\Delta\omega$, one obtains a SD, the threshold separating the bunch's stable and unstable states. There currently exist techniques to obtain stability diagrams, although they have limitations as they do not perform direct measurements of SDs [3]. We therefore investigate an alternative method to directly measure stability diagrams. In this method, the polarity of a transverse feedback is reversed, creating an 'antidamper' which excites a coherent mode in the beam, producing a coupling impedance:

$$Z(\omega) \propto Ge^{i\phi}\delta(\omega) \qquad (2)$$

Where G is the gain and ϕ is the phase advance between the pickup and the kick. The $\delta(\omega)$ shows that the antidamper kicks the bunch as a whole. The coupling impedance produces a coherent tune shift:

$$\Delta\omega = ge^{i\phi} \qquad (3)$$

Where g is the growth rate of the beam's centroid position. The gain and phase can be independently changed, making a source of controlled impedance and enabling one to observe at what tune shifts the beam becomes unstable. For the experimental setup at IOTA, the antidamper excitation acts in the y-plane, where the nonlinearity acts in the x-plane. With these conditions, Eq. (1) reduces to:

$$\Delta\omega_y = \left[\int \frac{F_x(J_x)}{\nu - \delta\omega(J_x, J_y) + io} dJ_x\right]^{-1} \qquad (4)$$

With octupoles acting as the source of nonlinearity in the x-plane: $\delta\omega = k\epsilon J_x$, where k is the octupole nonlinearity coefficient and ϵ is the x-plane rms emittance. Our group is working with gaussian beams, where the normalized distribution function is: $F_x(J_x) = e^{-J_x}$. The normalized stability diagram for this distribution is shown in Fig.1. To experimentally obtain Fig.1, G and ϕ are scanned, changing $\Delta\omega$. The top-right subfigure of Fig. 1 shows the beam centroid

* Work supported by the NSF and the Center for Bright Beams
† mbossard@uchicago.edu

Content from this work may be used under the terms of the CC BY 4.0 licence (© 2022). Any distribution of this work must maintain attribution to the author(s), title of the work, publisher, and DOI.

ISBN: 978-3-95450-261-5 ISSN: 2673-7000 doi: 10.18429/JACoW-NAPAC2025-TUP054

INTERACTIONS BETWEEN THE CIRCULATING BEAM AND THE INJECTION FOIL AT THE PROTON STORAGE RING OF LANSCE*

E.-C. Huang†, A. M. Alexander, M. J. Kay, J. W. Lewellen,
C. E. Taylor, R. T. Thornton, J. T. Yoskowitz
Los Alamos National Laboratory, Los Alamos, NM, USA

Abstract

At the Los Alamos Neutron Science Center (LANSCE), the Proton Storage Ring (PSR) utilizes charge-exchange injection via a carbon stripper foil to convert H^- ions into circulating protons. While beam loss due to partially stripped neutrals is a well-known concern, interactions between the circulating beam and the injection foil also play a significant role in limiting beam quality and foil lifetime. Simulations indicate that each stored proton typically interacts with the foil around 30 times during accumulation. These repeated encounters result in large-angle scattering, which becomes a dominant loss mechanism. To reduce the number of foil traversals, a set of bump magnets is employed to move the closed orbit away from the foil over time. In this study, we benchmark foil scattering models in PyORBIT against Monte Carlo simulations using MCNP and Geant4, evaluate different bumping schemes, quantify sensitivities to injection offsets, generate spatial distribution of beam-foil interactions on the foil, and assess the impact of different injected beam distributions. The results inform both operational optimization and future upgrade paths for foil injection systems in high-intensity proton rings.

INTRODUCTION

The Proton Storage Ring (PSR) at LANSCE accumulates protons from an 800 MeV H^- linac via charge exchange injection at a Hybrid-Boron-Carbon (HBC) stripper foil [1]. Charge-exchange injection using a thin stripper foil is a fundamental technique in high-intensity proton rings, including the PSR. During injection, H^- ions from the linac are stripped of their electrons, converting them to protons which are then accumulated in the PSR. However, two of the three main sources of the beam losses are related to the stripper foil: Lorentz stripping from partially stripped excited H^0 at injection and the nuclear scattering between the injection foil, while the third main source of the ring losses come from extraction [2]. In this work, we are trying to improve our simulation capability for the foil-related losses. In [3] at this conference, J. Yoskowitz will present the simulation effort to understand the partially stripped H^0 and its corresponding loss location.

In this paper, we will focus on improving our simulation capability on the interactions between the stripper foil and the circulating beam. Figure 1 shows that loss level along the PSR decreases when the foil thickness in the model decreases, showing the importance of the foil's contribution to ring losses. Note that the loss contribution at 0.083% for the stored beam with the nominal foil thickness at 450 μg/cm^2 is slightly lower than 0.11-0.17% estimated in [1]. To understand the interplay between the circulating beam and the foil, we focus on two major items: (1) the comparison of different simulation models on the nuclear scattering and (2) the number of interactions between each proton and the foil.

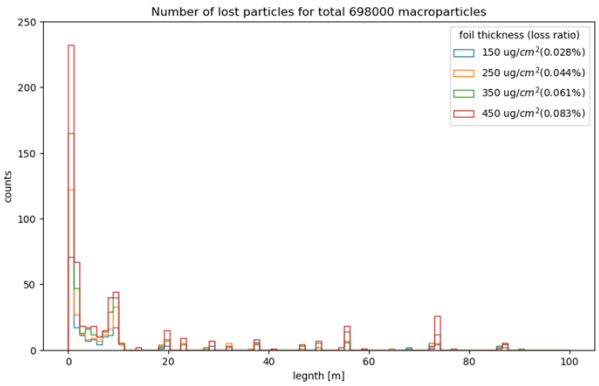


Figure 1: Simulated loss level across the PSR with different foil thickness using PyORBIT. For this simulation, the losses due to partially stripped H^0 are not considered; the simulation directly starts with a H^+ beam. Therefore, the losses centered right after the foil (at x=0) demonstrate the losses due to nuclear scattering.

NUCLEAR SCATTERING

Since the nuclear scattering effect contributes almost 50% of the losses from the earlier estimate [2], it is critical for us to benchmark the performance of the simulation code. Specifically, we'd like to compare beam dynamics codes like PyORBIT [4] and Xsuite [5] (xcoll [6], particularly for the material interaction) against high-fidelity Monte Carlo code like MCNP [7] and BDSIM [8] (based on Geant4 [9]). We used 1M random particle distribution generated by MCNP according to the injection design Twiss parameters and the nominal 800 MeV kinetic energy for protons. Each code assumes that the foil is composed of 100% carbon at a thickness 450 mg/cm2, 1000x of the nominal thickness at thickness 450 μg/cm2 for operation), while each code adopts its own definition of the carbon material, and therefore, calculate its thickness in length. The difference in calculated lengths (~mm) should be negligible for the outcome.

Figure 2 and Table 1 show the comparison between the codes for x', y' and energy loss, while x and y are virtually the same so we will ignore them. Our analysis reveals that the Monte Carlo codes demonstrate consistent results between coordinates. The energy loss modeling shows

* Work supported by the LANSCE Modernization Project (LAMP)
† en-chuan@lanl.gov

Content from this work may be used under the terms of the CC BY 4.0 licence (© 2022). Any distribution of this work must maintain attribution to the author(s), title of the work, publisher, and DOI.

ISBN: 978-3-95450-261-5 ISSN: 2673-7000 doi: 10.18429/JACoW-NAPAC2025-TUP055

IOTA EXPERIMENT FOR PROTON PULSE COMPRESSION AT EXTREME SPACE-CHARGE

B. Simons[1]*, N. Banerjee[2], J. Eldred[2], V. Shiltsev[1]
[1]Department of Physics, Northern Illinois University, DeKalb, IL, USA
[2]Fermi National Accelerator Laboratory, Batavia, IL, USA

Abstract

The longitudinal compression of intense proton bunches with strong space-charge force is an essential component of a proton driver for a muon collider. We propose a proton bunch compression experiment at the Integrable Optics Test Accelerator (IOTA) storage ring at Fermilab to explore optimal radio frequency (RF) cavity and lattice configurations. IOTA is a compact fixed-energy storage ring circulating 2.5-MeV protons with extreme space-charge. Using ImpactX and its 3D space-charge solver, simulations indicate that bunch length can be rapidly reduced by a factor of at least two, without appreciable degradation in transverse beam quality, even under strong space-charge conditions. Optimization of bunch compression under such conditions is discussed.

INTRODUCTION

In the wake of the most recent P5 report [1], the vision for the future of HEP programs includes charting a realistic path to a 10 TeV parton center-of-momentum (pCM) collider. A Muon Collider (MuC) is a compelling option for a 10 TeV pCM collider, with Fermilab considered as a potential host facility for MuC R&D projects as well as the collider itself. Fermilab is currently studying the core parameters of the proton driverfor the production of the muon beams, which is required to deliver extremely intense 1-3 ns bunches.

Space-charge is a major constraint for a 2–4-MW proton driver with 8-GeV protons compressed into nanosecond-scale pulses [2, 3]. Accelerator R&D for these short, intense proton pulses, while critical for realizing a future MuC, has applications for many next-generation High Energy Physics (HEP) experiments including dark sector searches, neutrino physics, and flavor physics [4, 5]. This work will develop a new experimental proposal for bunch compression at Fermilab's Integrable Optics Test Accelerator (IOTA) [6] storage ring during its upcoming proton runs.

FAST/IOTA is the only US dedicated facility for intensity frontier accelerator R&D and due to this, its portfolio of R&D interests include techniques for mitigating coherent instabilities and space-charge effects, such as nonlinear integrable optics (NIO) [7] and electron lenses [8]. This includes compressing that intense proton beam into the short bunches required for next-generation HEP experiments.

The IOTA ring itself, shown in Fig. 1 along with the proton injector line, is a compact fixed-energy storage ring that can circulate a 2.5 MeV proton beam with a beam current of up to

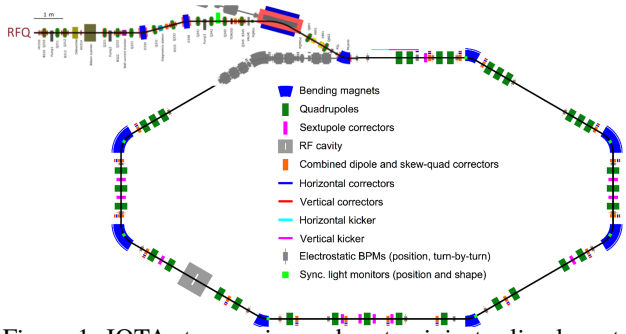


Figure 1: IOTA storage ring and proton injector line layout.

8 mA [6] and a corresponding incoherent space-charge tune shift ($|\Delta Q_{sc}|$) of up to 0.5. The proposed accelerator R&D program will incorporate factor of two bunch compression to extend the space-charge regime.

THE EXPERIMENT

The R&D program, called the FAST/IOTA Bunch Rotation Experiment (FIBRE), would be an upgrade to the existing capabilities of the IOTA ring, allowing the intense proton beams to be compressed into shorter pulses through an RF manipulation called snap bunch rotation. The IOTA proton injector (IPI) is currently being commissioned [9] for the upcoming proton runs slated to start at the end of 2025. As discussed in [10], the RF cavity in the DR section of IOTA contains two RF gaps operating at harmonic numbers $h = 4$ (2.19 MHz) to fully bunch the proton beam, and $h = 56$ (30.6 MHz) to introduce longitudinal modulation for instrumentation. Table 1 shows design parameters, and various RF parameters are discussed in later sections.

The voltage of the 2.19 MHz RF gap is limited to 1 kV based on the maximum power available from the existing high-level RF configuration. This voltage limit encouraged a search for determining the requirements of possible replacement, or additional, RF cavities that would benefit not only this experiment, but the operations of the IOTA ring and its future research program as a whole.

Specifically for this experiment, more voltage is required to successfully perform the snap bunch rotation. Along with more voltage, the new cavity would require a new power supply that could provide enough power for the increase in voltage to be obtained in just a few revolutions. Within the list of currently operational RF cavities at Fermilab, a compatible RF cavity design has been identified and its performance will be discussed in a future paper.

* bsimons1@niu.edu

Content from this work may be used under the terms of the CC BY 4.0 licence (© 2022). Any distribution of this work must maintain attribution to the author(s), title of the work, publisher, and DOI.

ISBN: 978-3-95450-261-5 ISSN: 2673-7000 doi: 10.18429/JACoW-NAPAC2025-TUP056

JUTRACK, A JULIA-BASED AUTO-DIFFERENTIABLE ACCELERATOR SIMULATION CODE FOR ADVANCED DYNAMICS, SCIENTIFIC MACHINE LEARNING AND OPTIMIZATION*

Jinyu Wan†, Helena Alamprese, Christian Ratcliff, Yue Hao,
Facility for Rare Isotope Beams, Michigan State University, East Lansing, MI, USA
Ji Qiang, Lawrence Berkeley National Laboratory, Berkeley, CA, USA

Content from this work may be used under the terms of the CC BY 4.0 licence (© 2022). Any distribution of this work must maintain attribution to the author(s), title of the work, publisher, and DOI.

Abstract

JuTrack is a high-performance accelerator modeling and particle tracking package developed in the Julia programming language. With compiler-level automatic differentiation (AD), JuTrack enables fast and precise derivative computations for arbitrary differentiable simulation functions. It supports efficient modeling of complex collective effects such as space-charge forces, wakefields, and beam-beam interactions. Beyond conventional tracking simulations, JuTrack also incorporates a machine learning–based module for self-field modeling and convenience interface that brings data-driven and physics-driven model together. In this paper, we demonstrate the capability and performance of JuTrack through a broad set of beam dynamics applications and optimization across various accelerator types, including a synchrotron light source, a heavy-ion linear accelerator, and the colliders. Built on Julia's high-performance architecture and user-friendly syntax, JuTrack provides a powerful tool for beam dynamics studies and accelerator design optimization.

INTRODUCTION

Automatic differentiation (AD) is a computational technique for evaluating derivatives of functions implemented in computer programs. By decomposing a function into elementary operations and applying the chain rule sequentially, AD delivers machine-precision derivatives while avoiding the complexity and overhead of symbolic differentiation. It has long been a foundational tool in fields such as machine learning and numerical optimization.

Recently, AD has attracted growing interest in the accelerator physics community. AD-enabled simulation codes, such as JuTrack [1], Cheetah [2], BMAD [3], and MAD-NG [4], have emerged. JuTrack is a high-performance accelerator modeling and tracking package written in Julia. With compiler-level AD, it enables rapid and accurate derivative evaluations for arbitrary differentiable functions. In this paper, we present the capability and performance of JuTrack in a broad set of beam dynamics and optimization tasks, including collective effects studies based on machine learning, gradient-based optimization for a synchrotron light source, multicharge state particle tracking in a heavy-ion linac, and dynamic aperture analysis of a collider using the convergence map method.

* Work supported by DOE Office of Science, with award number DE-SC0024170. J. Q.'s work was supported by the U.S. Department of Energy under Contract No. DE-AC02-05CH11231.

† wan@frib.msu.edu

NONLINEAR BEAM DYNAMICS OPTIMIZATION

One of the primary motivations for integrating AD into accelerator modeling is to optimize the design parameters to meet specific beam objectives, such as minimizing natural emittance, maximizing the dynamic aperture, and improving overall stability. With derivatives, many complex optimization tasks become straightforward gradient descent problems.

As an example, for the Stanford Positron Electron Asymmetric Ring (SPEAR3), a third-generation synchrotron light source, its geometric resonance driving terms (RDTs) such as h_{21000}, h_{10110}, h_{30000}, h_{10200}, and h_{10020}, can be evaluated with JuTrack. These RDTs are key indicators of dynamic aperture and reducing them tends to enlarge the dynamic aperture.

To minimize the RDTs, a simple test is performed in which two sextupole families in the ring are varied. Here we just tune the two sextupole families to demonstrate the effectiveness of the AD gradients in beam dynamics optimization. In real optimization processes, additional constraints, such as preserving the chromaticity of the ring, should be considered. Figure 1 shows that after roughly 500 iterations, the gradient-descent algorithm converges to a local minimum, with the gradients for both sextupole strengths approaching zero. This shows that one can effectively suppress the RDTs with the AD gradients.

MULTI-CHARGE-STATE PARTICLE TRACKING

Most tracking codes handle only a single species of charged beam, while the Facility for Rare Isotope Beams (FRIB) accelerates multiple charge states simultaneously after stripping, creating a distinctive challenge for particle tracking simulation.

To address this specific requirement, JuTrack has been extended to track multiple charge states while preserving full differentiability. Figure 2 shows the concurrent tracking of three charge states, $^{124}Xe^{49+}$, $^{124}Xe^{50+}$ and $^{124}Xe^{51+}$. The JuTrack tracking results were compared with FLAME, a fast envelope tracking code used for daily operation at FRIB. With the same lattice configurations and initial conditions, the JuTrack results show great agreement with FLAME, suggesting the precision of the multi-charge state tracking capability [5].

ISBN: 978-3-95450-261-5 ISSN: 2673-7000 doi: 10.18429/JACoW-NAPAC2025-TUP057

LANSCE BEAM TRANSPORT MODEL ENHANCEMENT AND VALIDATION

C.- M. Alvinerie†, C.E. Taylor, E.-C. Huang
Los Alamos National Laboratory, Los Alamos, NM, USA

Abstract

At the Los Alamos Neutron Science Center (LANSCE), accurate beam transport modelling is essential to understand the nature of beam instabilities and losses. The model analysis enables significant improvement in beam transport tuning. It is critical to ensure the beam envelope remains constrained and that the bunch structure is preserved as it traverses the distance from the 800-MeV Linac to the target downstream. Historically, all the high-energy beamlines (HEBT) have been simulated using the TRANSPORT code. Enhanced beamline models are developed in more modern accelerator physics codes such as MAD-X or elegant, which enable more detailed particle tracking and include some space-charge effects. These models may help us better understand the beam parameters during transport to the targets. This work presents the beamlines and their associated simulation models and, where applicable, comparison with experimental beam measurements.

INTRODUCTION

The Los Alamos Neutron Science Center (LANSCE), illustrated in Fig. 1, is a major experimental science facility that provides a high intensity and broad energy spectrum of neutron to multiple targets to study various materials.

Beams with two distinct energies are produced at LANSCE depending on target requirements. The Isotope Production Facility (IPF) receives a 100 MeV H+ beam while the four other user stations, namely, Proton Radiography (pRad), Ultra-Cold Neutrons (UCN), Lujan Center and the Weapons Neutrons Research (WNR) take the 800-MeV H- beam with various timing patterns. The beam is accelerated up to 800-MeV by two accelerating sections: the 201.25 MHz Drift Tube Linac (DTL) to bring the beam energy from 0.75 MeV to 100 MeV and the 805 MHz Side Coupled-Cavity Linac (CCL) from 100 MeV to 800 MeV.

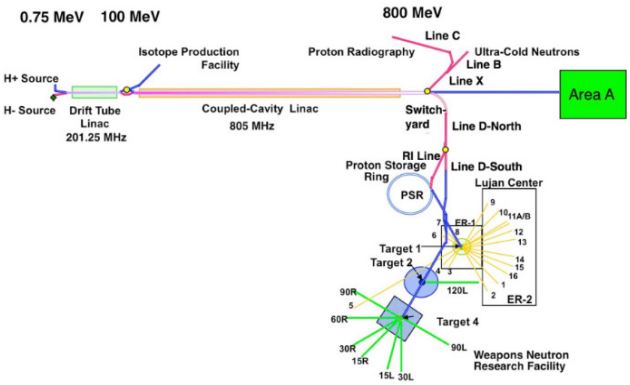


Figure 1: Overview of the LANSCE facility [1].

† calvinerie@lanl.gov

The high-energy beamlines downstream of the CCL transport the 800-MeV beam to the Proton Storage Ring (PSR) and the experimental areas. These beamlines are historically simulated with the TRANSPORT [2] code. Enhancing the modelling of the beamlines in modern beam dynamics codes such as MAD-X [3] or elegant [4] is necessary to better understand the beam transport and losses.

This contribution presents the beam transport model enhancement and validation of the beamlines downstream, especially north of the Linac: Line B and Line C. First, we introduce succinctly the beamlines. Then, we will describe the modelling of the beamlines and compare the simulation results with experimental data.

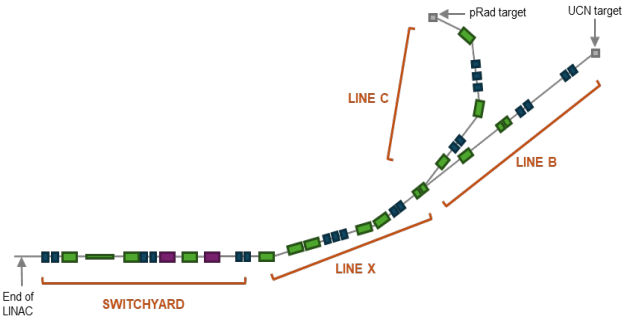


Figure 2: Layout of the Lines B and C with their main sections: joint Switchyard and Line X and the specific Line B and Line C. The quadrupoles are represented in blue, the bending magnets in green and the kicker magnets in violet.

DESCRIPTION OF LINES B AND C

The Lines B and C are defined as the beamlines from the end of the Linac to, respectively, the UCN target and the pRad target (Fig. 2).

The Switchyard receives the 800 MeV H- beam and guides it to the Line X with bending magnets. Two quadrupole doublets focus the beam. The final kicker magnet diverts a portion of the beam to the north.

Then, the beam enters the Line X, which consists of seven quadrupoles and seven bending magnets. The beam is directed in the north direction with its size constrained. The last bending magnet performs a left bend to Line C or a right bend to Line B.

Finally, the two beamlines, Line B and Line C, direct the beam to two different targets, respectively the UCN target and the pRad target. The Line B goes straight to the target. The beam shape and size are controlled by two quadrupole doublets. For the Line C, three bending magnets guide the beam left to the pRad target and five quadrupoles constrain the beam.

Content from this work may be used under the terms of the CC BY 4.0 licence (© 2022). Any distribution of this work must maintain attribution to the author(s), title of the work, publisher, and DOI.

ISBN: 978-3-95450-261-5 ISSN: 2673-7000 doi: 10.18429/JACoW-NAPAC2025-TUP059

LATTICE DESIGN FOR LOW ENERGY COOLING IN EIC HSR-IR2*

Derong Xu†, J. Scott Berg, Stephen G. Peggs, Vadim Ptitsyn
Brookhaven National Laboratory, Upton, NY, USA

Abstract

Insertion Region at two o'clock (IR2) of the Relativistic Heavy Ion Collider will be modified to provide effective cooling for the Electron-Ion Collider (EIC). This paper summarizes the update of the HSR-IR2 lattice design to meet the evolving requirements of the EIC. The geometry has been redesigned to satisfy the yellow-to-yellow configuration. The injection optics is optimized to satisfy the Low Energy Cooling requirements and physical aperture.

INTRODUCTION

The EIC, under construction at Brookhaven National Laboratory, will collide polarized electron and hadron beams over a broad energy and species range. It targets a peak luminosity of 10^{34} cm^{-2}s^{-1} and average polarization of $\sim$ 70 % [1]. As shown in Fig. 1, the EIC includes multiple key components: the Hadron Storage Ring (HSR), the Electron Storage Ring (ESR), a new injector complex, and two interaction regions.

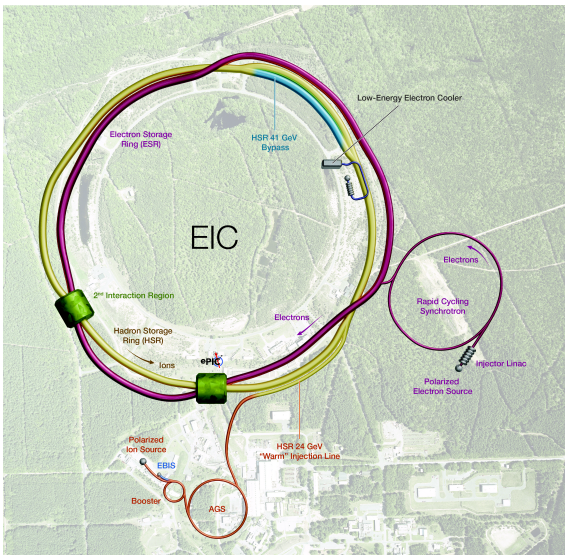


Figure 1: Conceptual layout of the EIC, showing key components including the HSR, ESR, injector complex, and interaction regions. IR2 serves as the cooling section for generating flat hadron beams and probably support high-energy cooling in future upgrades.

The HSR, upgraded from Relativistic Heavy Ion Collider (RHIC), will store highly polarized hadron beams with a flat profile, where vertical emittance ten times smaller than horizontal. Six helical Siberian Snakes [2] will preserve polarization during acceleration and storage. The Insertion Region at two o'clock (IR2) will serve as the cooling section to generate flat beams at injection energy and potentially provide high-energy cooling. It will also host one Siberian Snake.

This work serves as a follow-up study to our previously accepted paper [3], which investigated how to construct a smooth ramping path from the injection to top-energy optics. Since that study, the design requirements have evolved, necessitating rematching of the beam optics. In response to these changes, the current paper applies the methods developed in our previous work, providing updated results and insights that align with the revised specifications.

EIC COOLING STRATEGY AND CONSTRAINTS

The EIC leverages a flat hadron beam to maximize peak luminosity, with the vertical emittance an order of magnitude smaller than the horizontal. Unlike lepton machines, synchrotron radiation damping is negligible in the HSR due to the large rest mass. As a result, the hadron beam emittance is set by the ion source, which naturally produces round beams. External beam cooling is therefore essential to achieve the desired flatness. This concept has been experimentally demonstrated at RHIC using stochastic cooling techniques [4]. In the EIC, electron cooling will be applied at the injection energy to generate a flat beam, which will then be ramped to the top energy while preserving its emittance ratio.

To achieve optimal cooling performance, a long drift section is required in which electrons co-propagate with protons at the same velocity. During this interaction, both the Twiss and dispersion functions must be carefully controlled to ensure effective electron-hadron cooling. Detailed parameter table is shown in [3].

A major design change after April 2025 was to use electron cooling for gold beams as well, since stochastic cooling cannot achieve the target emittance ratio in a short time. Due to gold's lower charge-to-mass ratio, its injection energy is approximately 2.4 times lower than that of protons, resulting in a larger geometric emittance at injection. This poses a more stringent challenge: the Twiss parameters required for efficient electron cooling are now in tension with the injection aperture constraints, which demand physical aperture to accommodate 7σ horizontally and 6σ vertically.

As a result, a warm doublet is inserted at both sides of the long drift to provide flexibility to control beam sizes at injection energy, as shown in Fig. 2.

* Work supported by Brookhaven Science Associates, LLC under Contract No. DE-SC0012704 with the U.S. Department of Energy

† dxu@bnl.gov

Content from this work may be used under the terms of the CC BY 4.0 licence (© 2022). Any distribution of this work must maintain attribution to the author(s), title of the work, publisher, and DOI.

ISBN: 978-3-95450-261-5 ISSN: 2673-7000 doi: 10.18429/JACoW-NAPAC2025-TUP060

LATTICE REFINEMENTS FOR NONLINEAR INTEGRABLE OPTICS IN IOTA *

J. Wieland†,1, A. Romanov, Fermilab, Batavia, IL, USA
[1]also at Michigan State University, East Lansing, MI

Abstract

Nonlinear integrable optics of the type proposed by Danilov and Nagaitsev place strict constraints on the lattice parameters in the matching section outside of the nonlinear insert. In particular, the effects of energy spread in the beam have significant effects on the stability of the system. Typical chromatic compensation using sextupoles has significant perturbative effects on the dynamics but is operationally necessary to suppress fast losses. Fast decoherence of kicked beam measurements limits the available signal for studies. Refinements to the IOTA lattice parameters based on this experience with electron beam operation are presented.

INTRODUCTION

The Integrable Optics Test Accelerator (IOTA) is a research and development storage ring dedicated to beam dynamics studies [1]. The namesake experiment at IOTA is an implementation of nonlinear integrable optics (NIO) of the type proposed by Danilov and Nagaitsev [2]. The NIO Hamiltonian combines strong amplitude dependent tune shift with bounded single particle trajectories, and is a promising system for intense beams. The NIO in IOTA consists of a unique string of magnets as a 1.8 m, 18 magnet insert into a 40 m typical linear storage ring, referred to as the matching lattice. The previous experiments in IOTA have been conducted with a 150 MeV electron beam [3, 4]. This beam has a short damping time and low emittance from synchrotron radiation and is used as a probe of the phase space of the system. In particular, turn-by-turn measurements of kicked beam are used for studies of the underlying dynamics. Some lattice related experimental shortcomings experienced and a series of simulation studies addressing them are presented.

EXPERIMENTAL SHORTCOMINGS

Operational experience with IOTA operations during the last runs has indicated a few deficiencies with the current matching lattice. The NIO system is designed around the matching lattice as an effective thin lens. With nonzero energy spread, this suggests zero dispersion and zero chromaticity through the NIO insert. Further studies [5] indicated that zeroing dispersion in the insert and matching chromaticities in the matching lattice was a sufficient condition. During previous experiments, the chromaticity was fully compensated with sextupoles for this condition, and to increase the coherence time of kicked bunch measurements in the lattice without NIO excitation.

Additionally, without chromatic correction, significant losses were encountered while ramping the nonlinear insert. Figure 1 shows the comparison of circulating current as the nonlinear insert strength (t parameter) is ramped before and after compensation. Practically, this made the chromatic correction necessary to access higher nonlinear insert strengths.

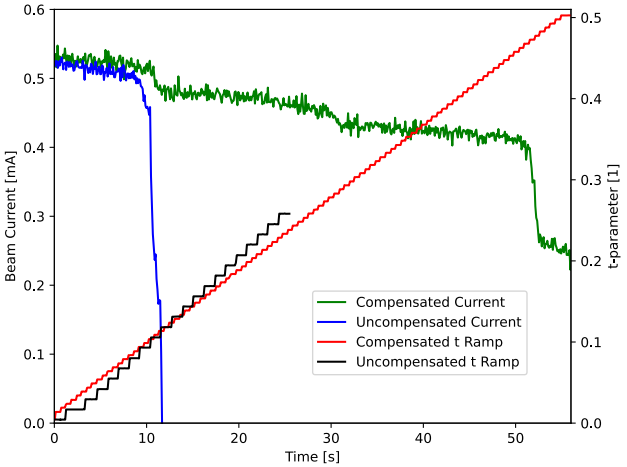


Figure 1: Experimental beam loss with and without chromatic compensation.

Kicked bunch measurements with the NIO insert exhibited fast decoherence, limiting the available signal for tune measurements and momentum reconstruction for studies. This stems from the tune footprint of the bunch at equilibrium emittance.

The basic transverse lattice requirements of the NIO system require 6 degrees of freedom to fully match. With the addition of dispersion suppression, this brings us to 7 degrees of freedom (assuming no coupling). IOTA is usually tuned to be mirror symmetric for convenience, which gives 20 quadrupole knobs, so there is available flexibility in the lattice for significant adjustments. The above shortcomings and available flexibility motivated considering adjustments to the IOTA linear lattice design for future experiments.

CHROMATICITY IMPACT ON INVARIANTS

As the chromaticity has demonstrated impacts on the integrability of the system, this was directly compared to a few different lattice configurations. Select configurations that were considered are presented in Fig. 2 as ImpactX [6] tracking simulations of tune dependence on energy offest. In two

* This research was supported by the ASET Traineeship and the FRIB laboratory at the Michigan State University under DOE award numbers DE-SC0018362 and DE-SC0023633.

† wielan22@msu.edu

Content from this work may be used under the terms of the CC BY 4.0 licence (© 2022). Any distribution of this work must maintain attribution to the author(s), title of the work, publisher, and DOI.

ISBN: 978-3-95450-261-5 ISSN: 2673-7000 doi: 10.18429/JACoW-NAPAC2025-TUP061

LINAC TO BAR/RCS TRANSFER LINE DESIGN FOR EIC ELECTRON INJECTION SYSTEM*

B.R. Gamage†, K.E. Deitrick, T. Satogata, N. Sereno
Thomas Jefferson National Accelerator Facility, Newport News, VA, USA
B. Bhandari, Q. Wu, Brookhaven National Laboratory, Upton, NY, USA

Content from this work may be used under the terms of the CC BY 4.0 licence (© 2022). Any distribution of this work must maintain attribution to the author(s), title of the work, publisher, and DOI.

Abstract

A transfer line has been designed for the Electron-Ion Collider (EIC) [1] to transport electron bunches from the linac to the Rapid Cycling Synchrotron (RCS). In its initial operational stage, the line accommodates 1 nC electron bunches directly from the linac. To support a future upgrade involving a Beam Accumulator Ring (BAR), which will stack individual bunches to form high-charge 28 nC bunches, the design incorporates two switching dipoles enabling injection into and extraction from the BAR. In addition, a beam dump has been included for operational flexibility and safety. The final segment of the line interfaces with the RCS through a modified Penner bend, preserving beam quality while satisfying geometric constraints. This layout ensures compatibility with both current and future operational modes of the EIC injection system.

INTRODUCTION

The Electron Injector is a pulsed accelerator chain designed to generate, accumulate, and accelerate polarized electron bunches for injection into the Electron Storage Ring (ESR). It supports both initial ring filling and periodic single-bunch replacements during collisions, a key feature for maintaining average polarization and luminosity throughout EIC operation. The system is optimized for high-repetition rate performance, minimal beam loss, and precise control of polarization preservation at each stage. A schematic of the machine layout with the new electron injector complex is shown in Fig. 1.

To achieve these goals, the injector complex consists of two sequential accelerators, a storage ring for bunch accumulation, and a network of connecting transfer lines. The front end, referred to as the Preinjector, includes a polarized electron source followed by a normal conducting S-band linear accelerator that delivers bunches at 750 MeV. Downstream of the linac, the Beam Accumulator Ring (BAR) enables the stacking of multiple low-charge pulses to produce high-intensity bunches, while also allowing for phase space damping and emittance equilibrium. These high-charge bunches are then transferred to the Rapid Cycling Synchrotron (RCS), which ramps the beam to GeV scale energies suitable for ESR injection, operating at a nominal repetition rate of 1 Hz.

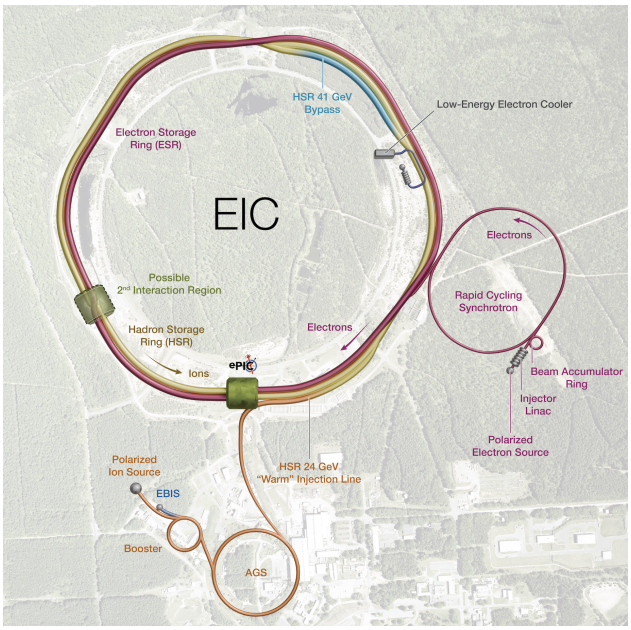


Figure 1: Layout of the EIC complex indicating the hadron storage ring (HSR), electron storage ring (ESR) and electron injector (RCS). The new electron injector complex is shown in purple, placed in the middle right side of the RHIC tunnel.

The synchrotron lattice is specifically designed to preserve polarization throughout the acceleration cycle.

This paper focuses on the design of the transport line connecting the preinjector Linac To the RCS (LTR). In the baseline configuration, electron bunches with a charge of approximately 1.1 nC are transported directly from the linac to the RCS, where they are accelerated to 5 , 10 , or 18 GeV before injection into the ESR at 4 o-clock region. A future upgrade will enable longitudinal stacking in the BAR to achieve bunch charges of up to 28 nC. To support this, the transfer line includes a branching section that allows beam transport into and out of the BAR using two switching dipoles. This adaptable configuration supports two operational modes: direct transport of low-charge bunches from the linac to the RCS, used during commissioning and reduced intensity operation and high-charge accumulation via the BAR for full intensity injection. Table 1 shows the incoming beam parameters from the linac.

DESIGN

The upstream portion of the Linac to RCS (LTR) transport line focuses on eliminating the horizontal dispersion coming from the linac prior to the first switching dipole (D1). A

* This material is based upon work supported by Jefferson Science Associates, LLC under Contract No. DE-AC05-06OR23177, Brookhaven Science Associates, LLC under Contract No. DE-SC0012704 with the U.S. Department of Energy.

† randika@jlab.org

ISBN: 978-3-95450-261-5 ISSN: 2673-7000 doi: 10.18429/JACoW-NAPAC2025-TUP062

MATCHING THE BEAM FROM AGS TO THE EIC HADRON STORAGE RING WITH EXCELLENT EMITTANCE PRESERVATION*

A. Jiang[1], L. He[1], C. Liu[†2], M. Oh[2], N. Tsoupas[2], S. Peggs[2], W. Lin[2]

[1]Ward Melville High School, East Setauket, NY, USA
[2]Collider Accelerator Department, Brookhaven National Lab, Upton, NY, USA

Abstract

The Electron-Ion Collider (EIC), a next-generation accelerator facility, is being jointly developed by Brookhaven National Laboratory (BNL) and Jefferson Lab (JLab), and will be constructed at BNL. The EIC design builds on the existing RHIC heavy-ion infrastructure, transforming the RHIC rings into the Hadron Storage Ring (HSR) with necessary modifications. To ensure optimal performance, it is critical to accurately match the beam from the injectors to the HSR in a six-dimensional phase space, in addition to the match of positions and angles. Inadequate matching can lead to emittance growth, which negatively impacts the achievable luminosity of the collider. This report outlines the key constraints involved in the matching process and presents a systematic approach to achieving high-fidelity beam matching while preserving emittance quality.

EIC OVERVIEW

The Electron-Ion Collider (EIC) [1] is a planned particle accelerator designed to study the internal structure of protons and nuclei. It will collide proton/heavy ion beams with energy up to 275 GeV with electron beam up to 18 GeV with an average spin polarization of 70% and 80% respectively. The ultimate luminosity to be delivered is of the order of $10^{34}\,\mathrm{cm}^{-2}\mathrm{s}^{-1}$. The layout of EIC is shown in Fig. 1.

In addition to the existing Relativistic Heavy Ion Collider (RHIC) [2] facility, electron injectors and a storage ring will be added with the storage ring located in the same RHIC tunnel. A 740 MeV linear accelerator will generate an electron beam with a bunch charge from 1 to 1.7 nC for injection into a Bunch Accumulation Ring (BAR). The output bunch charge for the BAR is up to 28 nC. The electron bunches will be accelerated in the Rapid Cycling Synchrotron (RCS) before being sent to the Electron Storage Ring (ESR).

The RHIC rings will be modified and reconfigured [3] to become the Hadron Storage Ring (HSR) to provide proton and heavy ions for the EIC facility. Its modification includes, but not limited to, a straight section modification to allow an energy upgrade to 275 GeV, an injection system upgrade for the injection of 290 bunches, the insertion of beam screens in the superconducting magnet beampipe for three times more beam current, the addition of electric cooling, the upgrade of RF and the instrumentation system. The HSR mostly

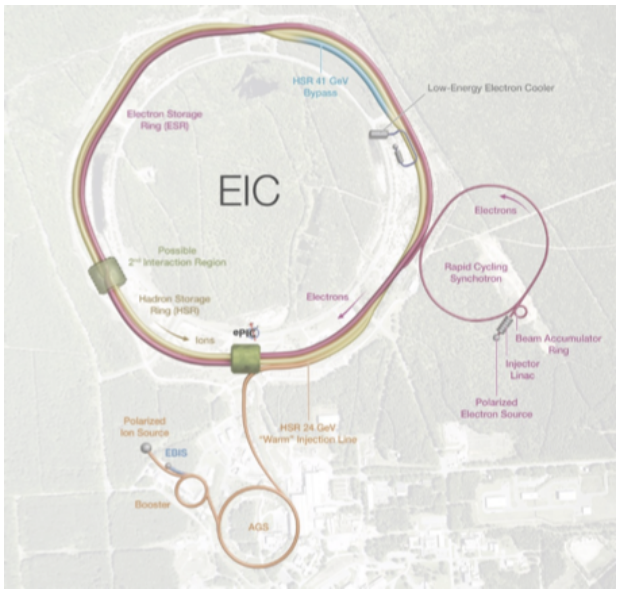


Figure 1: The Electron-Ion Collider layout. The RHIC facility, with modifications to the RHIC rings, will provide hadron beams. The electron Linac, Bunch Accumulation Ring, the Rapid Cycling Synchrotron and the Electron Storage Ring will be added as the electron facility to provide polarized electron up to 18 GeV.

comprises the yellow RHIC ring plus one sector of the blue ring for the operation of 41 GeV.

The HSR injection system, which includes a transfer line, septum magnets, and injection kickers, is required to inject 290 bunches into the HSR. Therefore, the rising time of the kickers is much shorter (7 ns) compared to that of the current RHIC injection kicker, which would require a stripline design. To provide enough kicker strength, 20 1-meter long kickers are required. Therefore, the location of IR4 is chosen to accommodate these devices since IR8 is reserved for a potential second experimental area. To bring the beam from the end of the ATR line to IR4 we have decided to use warm transfer line. The main purpose of this paper is to design this transfer line with a perfect match of the transverse phase space.

HADRON STORAGE RING (HSR) INJECTION LINE

The HSR injection line consists of the upstream matching section (UP), the periodical cells (CELL) and the down-

* Work supported by Brookhaven Science Associates, LLC under Contract No. DE-SC0012704 with the U.S. Department of Energy.
† cliu1@bnl.gov

Content from this work may be used under the terms of the CC BY 4.0 licence (© 2022). Any distribution of this work must maintain attribution to the author(s), title of the work, publisher, and DOI.

ISBN: 978-3-95450-261-5 ISSN: 2673-7000 doi: 10.18429/JACoW-NAPAC2025-TUP063

MEASUREMENTS AND SIMULATIONS OF INTRABEAM SCATTERING EFFECTS AT NSLS-II

A. Khan*, G. Bassi, V. Smaluk, B. Bacha
BNL, NSLS-II, Upton, NY, USA

Content from this work may be used under the terms of the CC BY 4.0 licence (© 2022). Any distribution of this work must maintain attribution to the author(s), title of the work, publisher, and DOI.

Abstract

In this study, we present recent measurements of intrabeam scattering effects at NSLS-II and compare them with particle tracking simulations using ELEGANT. The evolution of bunch length, energy spread, and horizontal and vertical emittances is studied as a function of single-bunch current. Simulations incorporating intrabeam scattering and longitudinal impedance using a broadband resonator model—are used to interpret the measurement observations.

INTRODUCTION

The National Synchrotron Light Source II (NSLS-II) is a 3 GeV third-generation light source delivering high-brightness photon beams for a wide range of user experiments. Table 1 summarizes key beam parameters for both the bare lattice and the operational configuration with all insertion devices (IDs).

Collective effects such as intrabeam scattering (IBS) and impedance-induced instabilities play a central role in determining the equilibrium beam quality in low-emittance storage rings [1]. In particular, the bare lattice—characterized by reduced radiation damping and shorter natural bunch length—exhibits stronger sensitivity to IBS and a lower microwave instability threshold. On the other hand, impedance-induced bunch lengthening increases with current and leads to reduced charge density, partially mitigating IBS effects. A proper interpretation of measured emittance growth therefore requires self-consistent modeling of both IBS and impedance effects.

In this study, we present systematic measurements of bunch length, energy spread, and transverse emittances as a function of single-bunch current for both the bare and operational NSLS-II lattices. The results are compared to simulations using ELEGANT [2], incorporating broadband longitudinal impedance and intrabeam scattering to interpret the observed trends.

MEASUREMENTS AND SIMULATIONS

This section describes the experimental setup, simulation methods, and results used to study the interplay between intrabeam scattering and impedance effects in NSLS-II.

Measurement Setup

Measurements of bunch length (σ_z), energy spread (σ_δ), and transverse emittances (ε_x, ε_y) as a function of single-bunch current were performed using dedicated diagnostics at NSLS-II. Bunch length was measured using a streak camera system viewing visible synchrotron radiation from a bending magnet. The horizontal beam size was measured with the BM-A X-ray pinhole camera, located in a region of negligible dispersion ($\eta_x \approx 0$), allowing direct extraction of ε_x using the known β_x function. The vertical beam size and energy spread were obtained from the 3PW X-ray pinhole camera in Cell-22, which lies in a dispersive region ($\eta_x \approx 0.17$ m). Vertical emittance was determined from the vertical beam size using the nominal β_y value, while σ_δ was extracted by combining horizontal beam size measurements from both BM-A and 3PW locations and solving $\sigma_x^2 = \beta_x \varepsilon_x + (\eta_x \sigma_\delta)^2$.

Table 1: NSLS-II Storage Ring Parameters for the Bare Lattice and Operational Lattice With All IDs

Parameter	Symbol	Value	Unit
Circumference	C	792	m
Beam energy	E	3	GeV
Average current	I_{av}	500	mA
RF voltage	V_{rf}	3.6	MV
Harmonic number	h	1320	
Bare Lattice			
Energy loss per turn	U_0	286.4	keV
Natural energy spread	σ_δ	5.1×10^{-4}	
Bunch length	σ_s	8.2	ps
Horizontal emittance	ε_x	2086	pm
Operational lattice			
Energy loss per turn	U_0	799.3	keV
Natural energy spread	σ_δ	7.9×10^{-4}	
Bunch length	σ_s	12.7	ps
Horizontal emittance	ε_x	746	pm

A single bunch was injected at approximately 1.5 mA and then slowly scraped down to lower currents using vertical collimators. Beam properties were recorded at each current level during this controlled decay to capture the full current dependence.

Simulations Approach

Bunch length and energy spread were first modeled using a broadband resonator impedance, with parameters tuned to reproduce both the measured bunch length and the observed microwave instability threshold. For the bare lattice, the model achieving the best agreement used $R_s = 18$ kΩ, $f = 30$ GHz, and $Q = 1$. The resulting equilibrium longitudinal parameters were then used as input for IBS simulations.

Particle tracking simulations were performed using ELEGANT, employing element-by-element tracking with the

* akhan1@bnl.gov

ISBN: 978-3-95450-261-5 ISSN: 2673-7000 doi: 10.18429/JACoW-NAPAC2025-TUP065

MEASUREMENTS OF THE BEAM LONGITUDINAL PROPERTIES IN THE FERMILAB LINAC*

R. Sharankova†, J-P. Carneiro, E. Chen, A. Shemyakin
Fermi National Accelerator Laboratory, Batavia, IL, USA

Abstract

The Fermilab Linac delivers 400MeV, 25mA H^- beam. The longitudinal bunch parameters are reconstructed using a Bunch Shape Monitor (BSM) installed in the middle of the Linac. For that, the bunch length is measured as a function of the phase of an upstream cavity and fitted to simulations. The cavity gradient and its phase with respect to the beam are recovered from readings of Beam Position Monitors (BPMs). Since the cavity provides a significant transverse defocusing, the BSM measurements are correlated with transverse beam size measurements by a wire scanner (WS). Simulations connect these three types of measurements, allowing to deduce the longitudinal emittance and Courant-Snyder parameters.

INTRODUCTION

The Fermilab Linac consists of a drift-tube Linac (DTL) and a side-coupled Linac (SCL) with a Transition section between them. The DTL is made up of 5 Alvarez RF cavities with 201.49 MHz resonant frequency which accelerate beam to 116.5 MeV design energy. The SCL consists of 7 RF cavities, operates at 805 MHz resonant frequency and accelerates beam to 401.5 MeV design energy. The transition section has two bunching cavities and is responsible for matching the DTL and SCL sections in all planes. It is well instrumented with diagnostics and is thus well-suited for extracting emittance measurements in the longitudinal and transverse planes. Transverse parameter reconstruction is described in Ref. [1, 2], and this paper focuses on the longitudinal properties.

The Linac Transition Section

Figure 1 shows a schematic of the Transition section. The beamline components in the section include 3 wire scanners (WS, shown in black), 4 quadrupole magnets in a FODO configuration (dark green), 2 bunching RF cavities (the larger Buncher followed by the smaller Vernier, in blue), 1 bunch shape monitor (BSM, brown), and 3 beam position monitors (BPMs) (not shown explicitly). D_{ij} in an element name indicate location as shown in Fig. 1.



Figure 1: A schematic of the Transition section and the beginning of SCL. Star indicates elements used in the measurements discussed in this work.

* This work was produced by FermiForward Discovery Group, LLC under Contract No. 89243024CSC000002 with the U.S. Department of Energy, Office of Science, Office of High Energy Physics.
† Email address: rshara01@fnal.gov

Beam Position Monitors

The Transition section has 4 two-planes stripline BPMs located in the aperture of every quadrupole magnet. Beside horizontal and vertical position of the beam centroid, the BPMs measure relative phase w.r.t. the RF reference line. The BPMs operate at the second beam harmonic of 402.5 MHz. Reported phase is not absolutely calibrated for cable and electronics delay, so it is only used in relative measurements.

Wire Scanners

The Linac employs wire scanners with 3 wires (horizontal, vertical and 45 degrees) fixed to a frame which runs through beam at a constant speed to record beam profiles in the horizontal (x), vertical (y) and 45-degree (u) planes. More details on the wire scanners can be found in [1].

Bunch Shape Monitor

The bunch shape monitor (BSM) [3] is a device that measures the longitudinal profile of the bunch. Figure 2 shows a schematic of the BSM working principle.

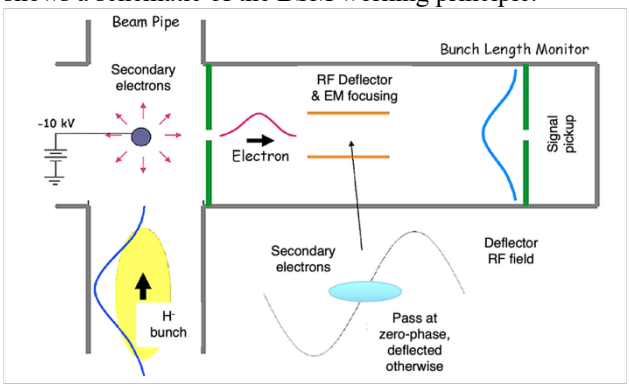


Figure 2: BSM working principle.

A tungsten wire at negative electrical potential is moved in the H- beam path. The ions hitting the wire produce secondary electrons which are repelled by the wire potential towards the primary collimator (slit). The secondary electrons carry the time (longitudinal) structure of the H- bunch. The electrons enter an RF deflector cavity where only those at zero-phase w.r.t. the cavity pass undeflected towards the secondary slit. Finally, the electrons are collected by an electron multiplier tube and recorded as electrical signals. The signal magnitude is proportional to the electron density, which in turns is proportional to bunch density. Scanning the RF phase of the deflector cavity allows to measure the electrons density along the time (longitudinal) dimension of the bunch.

Content from this work may be used under the terms of the CC BY 4.0 licence (© 2022). Any distribution of this work must maintain attribution to the author(s), title of the work, publisher, and DOI.

ISBN: 978-3-95450-261-5 ISSN: 2673-7000 doi: 10.18429/JACoW-NAPAC2025-TUP066

MINIMIZING DISPERSION THROUGH RESONANT EXTRACTION FOR BNL'S NSRL

E. Hamwi[1,*], P. Adams[2], K. A. Brown[2], B. Dhital[2],
G. H. Hoffstaetter[1,2], W. Lin[2], T. Olsen[2], D. Sagan[1]
[1]CLASSE, Cornell University, Ithaca, NY, USA
[2]Collider-Accelerator Department, Brookhaven National Laboratory, Upton, NY, USA

Abstract

Simulations, analysis, and measurements are performed on the BNL Booster's third integer resonance extraction to the NSRL line, which uses a constant optics slow extraction method. In this method, ring dipoles and quadrupoles are changed synchronously for a coasting beam, which aids in maintaining a fixed separatrix orientation through the spill. Simulations show that the outgoing beam has a very small dispersion, independent of the periodic dispersion value at the septum. We show using a first-order normal form approximation that transforms to the Kobayashi Hamiltonian, how the dynamics of such a spill lead to a dispersion-free outgoing beam, which is critical to the uniformity requirements of the NSRL. Finally, we measure the dispersion of the beam by varying the flattop energy of the coasting beam in the booster before engaging the spill and show that the magnitude of dispersion is reduced by over a factor of 5 from the periodic value in the ring.

INTRODUCTION

BNL's Booster ring uses a third-integer resonance to perform slow extraction of a coasting beam into the NSRL transfer line. Typical third-integer resonant extraction schemes manipulate tune or sextupole strength to shrink the stable area and drive particles into the unstable separatrix. In contrast, the Booster-to-NSRL extraction uses a constant optics scheme in which the working point remains fixed during the extraction [1]. Instead, the extraction ramp is driven by a slow reduction of dipole fields, leading to an adiabatic decrease in reference momentum ($B\rho$). Through large negative chromaticity, this reduces the average tune of the beam, bringing it into resonance. The key insight is that while the periodic dispersion at the septum may be nonzero, the outgoing particles—those that cross the separatrix—do so in such a way that their final trajectories are nearly independent of momentum deviation. This apparent cancellation of dispersion is central to meeting NSRL's stringent requirements on beam uniformity and position stability during slow spill delivery.

FIRST-ORDER RESONANT NORMAL FORM

Elliptical Fixed Point

To interpret the dynamics analytically, we simplify the motion by only focusing on the horizontal phase space, and perform a first-order normal form transformation around the dispersive *elliptical* fixed point of the third-integer resonance. The power of normal form transformations of truncated power series are enhanced when the map is close to the identity, so in the vicinity of $Q_x \approx m/3$ we transform to the co-moving reference frame that is the composition of 3 one-turn maps. The transformed tune is $\omega \equiv 6\pi\Delta Q_x$, where $3\Delta Q_x = 3Q_x - m$. After normalizing phase space coordinates into $(\tilde{x}, \tilde{p}_x)$ via the Twiss parameters, we write the phasor basis coordinates:

$$z = \sqrt{2J}e^{i\phi_x}, \quad 2J = z\bar{z} = \tilde{x}^2 + \tilde{p}_x^2, \quad \phi_x = \text{phase advance}.$$

While the RF cavities are not entirely off, the debunched beam is coasting with approximately constant energy. Thus, the individual particle tunes Q_x are parametrized through chromaticity by the fractional deviation between particle momentum p and the reference momentum p_0 of the dipole fields $\delta = \frac{p-p_0}{p_0}$. The amplitude-dependent tune shift is negligible in this ring since the highest multipoles are sextupoles whose effective tune shift only has nonlinear dependence on amplitude. Then to first order, $\mathbf{Q}(\delta) = \mathbf{Q}_0 + \delta\,\boldsymbol{\xi} + \mathcal{O}(\delta^2)$ and $\omega = 2\pi(3Q_{0,x} - m) + 6\pi\delta\xi_x$.

Continuing, we can write the transformed Hamiltonian to first order in sextupole strength a la Kobayashi [2, 3]:

$$H = \omega J - \frac{1}{8}\left(S_\mathrm{v} z^3 + \bar{S}_\mathrm{v}\bar{z}^3\right),$$

where S_v is the virtual sextupole/resonance strength [4]:

$$S_\mathrm{v} = \frac{1}{2}\sum_j \left[k_2 l\, \beta^{\frac{3}{2}}\, e^{3i\phi_x}\right]_j.$$

Here, k_{2j}, l_j, β_j, $\phi_{x,j}$ are the normalized strength, length, beta function, and phase advance at each sextupole location. This sum over sextupoles defines an effective coherent strength that governs the shape and orientation of the separatrix, which is given by the effective phase ψ of the virtual sextupole $3\psi \equiv \arg(S_\mathrm{v})$.

When $H = \frac{8\omega^3}{27|S_\mathrm{v}|^2}$, the Hamiltonian can be factored into a product of three lines forming an equilateral triangular

* eh652@cornell.edu

Content from this work may be used under the terms of the CC BY 4.0 licence (© 2022). Any distribution of this work must maintain attribution to the author(s), title of the work, publisher, and DOI.

ISBN: 978-3-95450-261-5 ISSN: 2673-7000 doi: 10.18429/JACoW-NAPAC2025-TUP067

MITIGATION OF COHERENT SYNCHROTRON RADIATION BY BUNCH PROFILE OPTIMIZATION AND SHIELDING

O. H. Ramachandran[1,2*], G. Ha[1,2], C.-K. Huang[3], X. Lu[1,2], J. Power[2], and J. Qiang[4]

[1]Northern Illinois University, DeKalb, IL, USA
[2]Argonne National Laboratory, Lemont, IL, USA
[3]Los Alamos National Laboratory, Los Alamos, NM, USA
[4]Lawrence Berkeley National Laboratory, Berkeley, CA, USA

Content from this work may be used under the terms of the CC BY 4.0 licence (© 2022). Any distribution of this work must maintain attribution to the author(s), title of the work, publisher, and DOI.

Abstract

The mitigation of the effects of coherent synchrotron radiation (CSR) is a key challenge in generating high brightness beams. Shielding by parallel plates installed in the dipole magnet vacuum chambers shows promise, both in simulation and experiment at small shielding gap separations. In this work, we investigate the combined use of longitudinal profile shaping and shielding to reduce CSR induced emittance growth in a 4 dipole chicane. The CSR wake is calculated using a 3D technique currently in development that represents the particle distribution with smooth 3D shape functions. Our results indicate current profiles that result in smaller emittance growth at separations larger than the scales at which shielding on a Gaussian beam causes effective CSR mitigation.

INTRODUCTION

Collective effects like Coherent Synchrotron Radiation (CSR) within a bunch represent a significant challenge in the generation of high brightness beams. In particular, for short bunches of high intensity propagating through a bend – as is required for X-ray free electron lasers (FELs) – the radiated CSR wake can have serious effects on the beam dynamics, such as the expansion of the transverse phase space [1] and the generation of microbunching instabilities [2]. Several mitigation strategies have been proposed in the literature, ranging from placing parallel plate shielding walls inside the vacuum chamber of the bending magnet [3], tuning of the overall optical lattice [4], and careful shaping of the longitudinal current profile to flatten out the CSR wake [5].

While the shielding effect has been experimentally observed to cancel out the CSR wake, the required length scales for the gap separation varies with the bunch length σ_z as $\sqrt[3]{R\sigma_z^2}$ for Gaussian beams [6], necessitating very small gaps for short bunches. In this work, we extend the method proposed in [5] and investigate the potential use of wall separations larger than the aforementioned length scale in conjunction with shaping of the initial beam profile.

We evaluate the CSR fields through direct integration of Jefimenko's equations with the charge and current distributions represented by smooth shape functions – in particular, we use products of Gaussians in the longitudinal and transverse dimensions whose widths and amplitudes can be tuned depending on the bunch being modeled. This forward evaluation is then used as part of a nonlinear minimization algorithm to obtain optimal initial profiles.

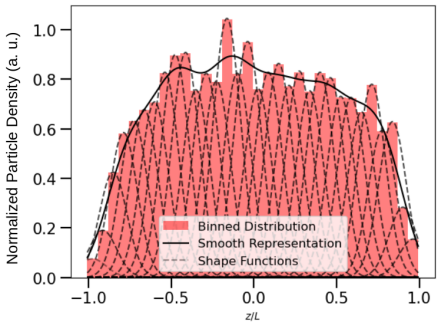


Figure 1: An example of constructing a smooth particle distribution from a binned macroparticle ensemble. z/L is the longitudinal position in relation to the bunch length. The shape functions are depicted before final normalization.

FORMULATION OF THE FORWARD PROBLEM

Our simulation approach computes the radiated electric fields by integrating Jefimenko's equation for a smooth bunch profile in 3D space:

$$\mathbf{E}(\mathbf{r},t) = \frac{1}{4\pi\epsilon_0}\int d\mathbf{r}'\left[\frac{\mathbf{R}}{|\mathbf{R}|^3}\rho(\mathbf{r}',t_r) + \frac{\mathbf{R}}{c|\mathbf{R}|^2}\frac{\partial}{\partial t}\rho(\mathbf{r}',t_r)\right] - \frac{1}{4\pi\epsilon_0}\int d\mathbf{r}'\frac{1}{c^2|\mathbf{R}|}\frac{\partial}{\partial t}\mathbf{J}(\mathbf{r}',t_r). \tag{1}$$

Here, $\mathbf{R} = \mathbf{r} - \mathbf{r}'$ and $c(t - t_r) = |\mathbf{R}|$ is the constraint satisfied by the retarded time t_r. The charge and current densities, ρ and $\mathbf{J}$ respectively, can be described using shape functions as follows:

$$\rho(\mathbf{r}',t) = Q_b\sum_i S_i\left(\mathbf{r}'(t)\right) \tag{2}$$

$$\mathbf{J}(\mathbf{r}',t) = Q_b\frac{\partial\mathbf{r}'(t)}{\partial t}\sum_i S_i\left(\mathbf{r}'(t)\right) \tag{3}$$

where, Q_b is the bunch charge and $S_i(\mathbf{r}')$ is a sufficiently smooth shape function in $\mathbb{R}^3$. Existing solution methods

* oramachandran@anl.gov

ISBN: 978-3-95450-261-5 ISSN: 2673-7000 doi: 10.18429/JACoW-NAPAC2025-TUP068

Mu2e RESONANT EXTRACTION REGULATION SYSTEM SIMULATION IN DELIVERY RING

A. Narayanan, Fermi National Accelerator Laboratory, Batavia, IL, USA *

Content from this work may be used under the terms of the CC BY 4.0 licence (© 2022). Any distribution of this work must maintain attribution to the author(s), title of the work, publisher, and DOI.

Abstract

Mu2e is an upcoming experiment at Fermilab that relies on the slowly extracted 8 GeV proton beam from the Delivery Ring. The experiment imposes strong requirements on the spill uniformity. To address these requirements, the fast spill regulations system is being developed and commissioned. To inform this development and optimize the system performance we are carrying out the detailed simulations of the regulation process. The simulation includes the effect of six harmonic sextupoles that excite the third-integer resonance and three fast ramping quadrupoles that drive the horizontal tune to 29/3. The components of spill regulation system are designed to mitigate long-term drifts in the beam, ensuring stable operation over extended timescales, as well as addresses rapid variations within single spill. In this study, we review the regulation system design, simulation of the slow regulation, and the fast regulation PID regulation to curtail random variations in the extraction rate that could occur within a single spill.

RESONANT EXTRACTION FOR Mu2e

Mu2e is an upcoming experiment at Fermilab that is designed to look for charged lepton flavor violation thorugh direct neutrino-less decay of muon to electron. To create the muons for the experiment, 8 GeV kinetic energy protons are to be bombarded to a muon production target. In order to suppress several background physics processes, Mu2e demands pulses muon beam, which is achieved by creating pulsed proton beam using resonantly extracted 8 GeV proton from Fermilab's Delivery Ring (DR). The 3rd integer resonant extraction is achieved in the machine by using 6 harmonic sextpoles that excite the third-integer resonance and three fast ramping quadrupoles that drive the machine tune close to a third-integer resonance. The goal is to inject 1e12 proton from the Fermilab Recycler Ring into the DR and resonantly extract the beam over 43 ms (which is about 25,000 turns). Other beam parameters can be found in Table 1.

Table 1: Some Key Beam Parameters Pertinent to Resonant Extraction

Parameter	Value
Beam kinetic energy	8 GeV
Spill Duration	43 ms
Number of spills per super cycle	8
Number of bunches per spill	1
Initial proton intensity	10^{12} protons
# of protons extracted per turn	$< 4 \times 10^7$ protons
Time between proton micropulses	1.695 μs
Normalized Emittance (95 %) ϵ_x	16 π·mm·mrad
Spill Duty Factor (SDF)	> 60 %
Reset time between spills	5 ms

SPILL REGULATION SYSTEM (SRS)

Mu2e imposes strict requirements on the intensity of the spill, quantified by spill duty factor, defined by

$$\mathrm{SDF} = \frac{1}{1+\sigma^2} \tag{1}$$

where σ is the standard deviation in the extraction rate. Mu2e requires an SDF of 60% or higher. To help achieve this SDF, a spill regulation system [1] is in place to ensure extraction uniformity. The Spill Regulation System primarily consists of three components: slow spill profile regulation, fast random ripple regulation and Harmonic ripple content suppressor.

In this paper, we shall go into the details of the slow regulation algorithm [2], look at particle tracking results for the fast regulation, and discuss future directions of potentially extending this framework to implementing Radio Frequency Knock-out (RFKO).

Slow Regulation

Some of the main characteristics of the beam, such as its horizontal size, injection emittance, beam steering error, etc., could vary slowly over time due to many factors. Apart from this, a slow drift in the accelerator components could reflect in the spill intensity profile as a low frequency deviation from the ideal spill rate. Given such a short spill time, this slow variation in the spill rate could be possibly span across multiple spill durations. A regulation loop is thus needed to keep the overall profile of the spill intensity as close to the ideal as possible, and this would be done using the Slow Regulation Loop (SRL).

The Slow Regulation Loop would not concern itself about any random fluctuations in the spill rate that could occur just within one spill, nor does it care about the high frequency noise components, either arising from the magnet power supplies or other wise, that could fluctuate the spill intensity within one spill.

In order to avoid correcting the random fluctuations in the spill rate that may occur just within one spill (but not repeat in the subsequent spills), the Slow Regulation Loop would work over *many* spills. The exact number of spills to average the spill rate data over could vary depending on the actual operation of the spill. But the main goal of the Slow

* This work was produced by Fermi Forward Discovery Group, LLC under Contract No. 89243024CSC000002 with the U.S. Department of Energy, Office of Science, Office of High Energy Physics.

ISBN: 978-3-95450-261-5 ISSN: 2673-7000 doi: 10.18429/JACoW-NAPAC2025-TUP069

MULTI-OBJECTIVE OPTIMIZATION OF STRONG HADRON COOLER ENERGY RECOVERY LINAC INJECTOR*

N. Wang†, G. H. Hoffstaetter de Torquat, Cornell University, Ithaca, New York, USA
K. Deitrick, I. Neththikumara, T. Satogata, N. Sereno, S. Setiniyaz
Thomas Jefferson National Accelerator Facility, Newport News, VA, USA
W. Bergan, E. Wang, Brookhaven National Lab, Upton, NY, USA

Abstract

The Strong Hadron Cooler (SHC) proposed for the Electron-Ion Collider (EIC) requires high-current, low-emittance electron bunches with minimal energy spread. The Energy Recovery Linac (ERL) injector plays a critical role in shaping the beam before acceleration. We present a multi-objective optimization study of the SHC ERL injector and merger using space charge tracking in Bmad and parallel genetic algorithm. The optimized configuration reduces the normalized transverse emittance by 62% and energy spread by 85% from the original configuration.

INTRODUCTION

The Electron-Ion Collider (EIC) at Brookhaven National Laboratory is a next-generation facility designed to explore the structure of protons and nuclei through high-luminosity electron-hadron collisions. To achieve its target luminosity of 10^{34} cm^{-2} s^{-1}, the EIC requires sustained low emittance in the hadron beam [1]. However, intrabeam scattering (IBS), beam-beam interactions, and other collective effects cause emittance growth, limiting performance.

To counteract these effects, a high-energy cooling system is required to achieve the luminosity and beam quality for hadron collisions. One proposed solution is the Strong Hadron Cooler (SHC), which utilizes a high-current, low-emittance Energy Recovery Linac (ERL) to deliver cooling electron beams at multiple energies.

A key challenge in delivering the required beam quality lies in the injector, where the beam is still at low energy and dominated by space charge effects. Accurate modeling of space charge and careful tuning of beamline elements are necessary to minimize transverse emittance and energy spread, while preserving the beam's uniformity and brightness.

To meet these requirements, we designed and optimized a DC gun-based injector using Bmad [2] for space charge simulation and Xopt [3] for multi-objective optimization. The optimization strategy using Non-dominated Sorting Genetic Algorithm (NSGA-II) [4] resulted in significant improvements in the transverse emittances and energy spread. This paper presents the injector and merger design, simulation framework, and results of the multi-objective optimization, demonstrating significant improvements in beam quality.

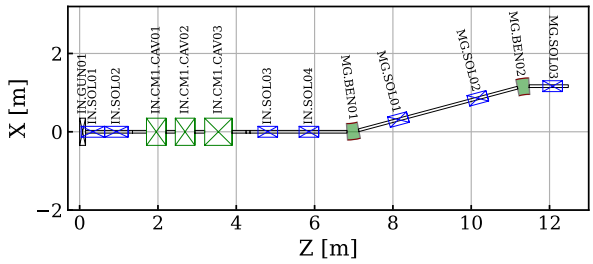


Figure 1: Layout of the ERL injector and merger used in this optimization study.

BEAMLINE MODEL AND SIMULATION

The injector and merger lattice, shown in Fig. 1, is designed to produce a high-quality 6 MeV electron beam for the Strong Hadron Cooler [5–10].

The system begins with a 400 kV DC gun that generates a 1 nC electron bunch. For this study, the initial particle distribution is a beer-can distribution generated using distgen [11]. It has a longitudinal 10th order SuperGaussian profile with $\sigma_t = 83$ ps. The transverse distribution is a Gaussian distribution of $\sigma_r = 3$ mm truncated at 1σ and the Mean Transverse Energy (MTE) is 130 meV. The injector section then accelerates the beam to approximately 6 MeV using two 197 MHz fundamental RF cavities and one 591 MHz third-harmonic cavity. The third-harmonic cavity is used to linearize the longitudinal phase space to counteract the energy chirp induced by strong space charge forces. Solenoids are placed along the injector to provide transverse focusing and control the beam size.

Following the injector, a merger section composed of dipoles and solenoids guides the beam onto the main ERL axis. This section is designed to be achromatic, with the goal of closing both horizontal and vertical dispersion at its exit to prepare the beam for downstream transport.

Beam dynamics are simulated using Bmad, which includes a 3D particle-in-cell algorithm to accurately model space charge effects [12, 13]. We track a distribution of

* This work was produced in part by Jefferson Science Associates, LLC under Contract No. DE-AC05-06OR23177 and Brookhaven Science Associates, LLC, under Contract DE-SC0012704 with the U.S. Department of Energy, and the Office of Science Graduate Student Research (SCGSR) Program.

† nw285@cornell.edu

Content from this work may be used under the terms of the CC BY 4.0 licence (© 2022). Any distribution of this work must maintain attribution to the author(s), title of the work, publisher, and DOI.

ISBN: 978-3-95450-261-5 ISSN: 2673-7000 doi: 10.18429/JACoW-NAPAC2025-TUP070

MULTIPLE INTERACTION POINTS IN GHOST COLLISIONS*

B.R. Gamage†, A. Hutton,
Thomas Jefferson National Accelerator Facility, Newport News, VA, USA

Abstract

The Ghost Collider makes use of unique "ghost" bunches, which are electrically neutral combinations of electrons and positrons within the same RF bucket, eliminates the beam-beam effects typically present at the interaction point (IP) in conventional colliders. This allows for the novel possibility of placing multiple interaction regions in series, achieving additive luminosity without introducing significant disruption. However, to obtain higher luminosity, the beta functions at the IP reaches the millimeter scale, which in turn adds significant chromatic contribution to the collider. Correcting these chromatic effects is essential to maintain beam stability and ensure high luminosity during collider operation. By carefully adjusting the phase advance between two IRs that are placed in series, it becomes possible to cancel chromaticity globally, enabling stable collider operation while preserving high luminosity. In this paper, we discuss the design of such IR/IRs to be used in a ghost collider.

INTRODUCTION

A Linear Collider vision statement [1], published in March 2025, reaffirmed the commitment of the global scientific community to develop a high-energy, high-luminosity Higgs factory [2]. The Ghost Collider has emerged as an early contender for such a facility. Its unique use of *ghost* bunches, which are charged particle bunches composed of equal numbers of electrons and positrons, eliminates the beam-beam effects typically present at the interaction point (IP) in conventional colliders. Because the net charge of the ghost bunches is zero, they are electromagnetically neutral as seen from the outside, allowing them to co-propagate through the accelerator and collide without experiencing mutual disruption.

Ghost bunches, illustrated in Fig. 1 offer unique possibilities that are challenging or impossible in conventional two-beam linear colliders. Without beam-beam disruption, ghost bunches can traverse multiple interaction regions (IRs) in series, allowing the collider to achieve additive luminosity for each IP, without requiring independent beam delivery systems that usually accompany bending which in turn requires crabbing to obtain maximum luminosity.

INTERACTION REGION DESIGN

In the Ghost Collider, electrons and positrons travel toward the interaction point (IP) from opposite directions and are focused using the same set of final focus quadrupoles.

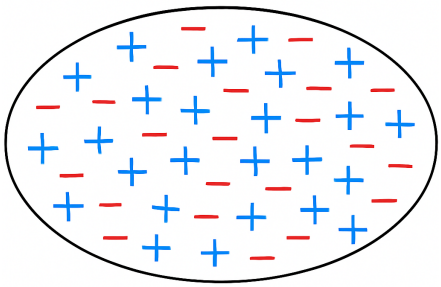


Figure 1: Conceptual illustration of a ghost bunch, composed of equal numbers of electrons and positrons occupying the same bunch.

This symmetric beam delivery scheme allows for a more compact and efficient optical design achieved by adopting equal horizontal and vertical beta functions at the IP: $\beta_x^* = \beta_x^* = 2$ mm [3]. Unlike traditional linear colliders such as the ILC, which require ultra-flat beams to mitigate beam-beam disruption ($\beta_x^* = 11$ mm, $\beta_x^* = 0.48$ mm), the Ghost Collider benefits from the absence of coherent beam-beam forces. As a result, round beams with equal transverse emittances can be used, significantly simplifying the interaction region optics.

Electrons and positrons arrive at the IR from both directions and are focused by a shared set of final focus quadrupoles (main triplet). And a secondary triplet adds the flexibility of having a symmetrical twiss parameter set at the starting end of the IR, which gives the possibility of having both positron and electrons to travel in both directions of the IR while maintaining the required spot size at the IP. This symmetric layout allows for compact interaction region designs and supports equal focusing conditions on both beams. Table 1 shows some chosen parameters for a linear ghost collider design currently in the design phase [3]. For a beam-pipe radius of 2 cm, the maximum field gradient

Table 1: A Parameters Set for a Linear Ghost Collider

Parameter	Value	units
Energy	275	GeV
Normalized emittance	6.5	mm−mrad
$\beta_{x,y}^*$	2	mm
Max $\beta_{x,y}$	64.9	km
Max $\sigma_{x,y}$	885	μm
Max quadrupole gradient	182	T−m

* This material is based upon work supported by Jefferson Science Associates, LLC under Contract No. DE-AC05-06OR23177 with the U.S. Department of Energy.

† randika@jlab.org

Content from this work may be used under the terms of the CC BY 4.0 licence (© 2022). Any distribution of this work must maintain attribution to the author(s), title of the work, publisher, and DOI.

ISBN: 978-3-95450-261-5 ISSN: 2673-7000 doi: 10.18429/JACoW-NAPAC2025-TUP071

NEW MEASUREMENT TECHNIQUES FOR GEAR-CHANGING RESEARCH USING DESIREE*

E. A. Nissen[1,†], A. Simonsson[2]
[1]Thomas Jefferson National Accelerator Facility, Newport News, VA, USA
[2]Stockholm University, Stockholm, Sweden

Abstract

In this work we cover some of the newer techniques developed to measure the effects of a gear changing system maintained in DESIREE at Stockholm University. Gear-changing is a collider synchronization method where two rings with different harmonic numbers in them maintain collisions through different velocities, pathlengths or a combination of the two. This system has been demonstrated using the low energy ion collider DESIREE at Stockholm university. We have not only continued our previous methods of studying the beam using a repeating pattern technique where one bucket in each ring is intentionally left empty, but we now also use recently installed pickups outside of the merger region to study the beams separately while they collide.

INTRODUCTION

This work is a continuation of the Direct Observations in DESIREE of Gear-changing Events (DODGE) program [1-3]. Gear-changing is a collider synchronization method that collides beams with different harmonic numbers, and thus different numbers of bunches, through a combination of different pathlengths and/or different particle velocities [4]. For example, in a 4 on 3 gear-changing system the beam with three bunches would move at 4/3 the velocity of the beam with 4 bunches. Gear-changing allows for more flexibility in colliding slower moving heavy ions in a collider without having to modify the pathlength of the machine. It can also allow the reuse of existing infrastructure for new types of experiments. Since each bunch in a machine interacts with each other bunch there is a reduction in systematic errors for an experiment. However, this can also lead to harmful resonances [5].

DESIREE is a small ion collider at Stockholm University in Sweden [6]. It can collide a variety of singly, oppositely charged, ions of up to 100 keV on up to 25 keV. It has a unique geometry where instead of colliding head-on the beams move with each other in the same direction. DESIREE was designed to study mutual neutralization reactions between ions to approximate reactions found in the interstellar medium. DESIREE's energy range allows us to "dial-in" relative velocities, making it an excellent test bed for gear-changing research. It was designed to have the beams move together at the same velocity for its mutual neutralization experiments, but since gear-changing requires different velocities there are still collisions in a moving reference frame.

Since 2020 we have performed multiple experiments to study gear-changing collisions using DESIREE. In this work we examine several of the techniques we have developed to set up and study gear-changing interactions. A diagram of DESIREE with its diagnostics highlighted is shown in Fig. 1. We developed a "missing bunch" method that allows us to set up our interactions, as well as measure the effects of the interactions over time. We had to adjust our measurement system so that we could extract the necessary data without worrying about spurious readings. In an attempt to measure the beam without using the missing bunch method we attempted to kick away one beam while measuring the other. Finally, we made use of expanded capabilities that came from an additional pair of beam position monitors that had been added to DESIREE to allow us to study the beams without early extraction or the missing bunch method.

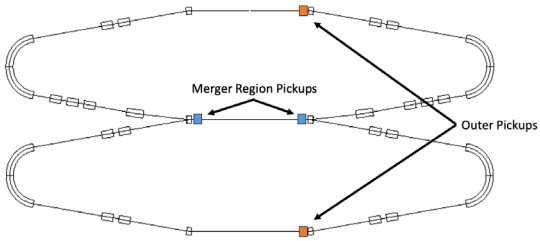


Figure 1: Outline of the DESIREE collider with instrumentation highlighted.

MISSING BUNCH METHOD

Since the beginning of the DODGE program, we understood the need to develop a way to quickly visualize and determine that gear-changing was happening. Early on we developed a "missing bunch method" which would leave one bucket empty in each ring. Thus, in a 4 on 3 gear-changing system, there would be three bunches colliding with two, with empty slots in each. While this method was initially created as a quick visual check, it quickly showed itself to be a very powerful method of setting up and measuring the beam-beam interactions. This type of method creates a repeating pattern with collisions, an empty section where the empty buckets both enter the merger region at the same time, and instances where one of the bunches collides with an empty bucket. An example of this is shown in Fig. 2.

* Supported by the U.S. Department of Energy, contract DE-AC05-06OR23177. Portions performed at the Swedish National Research Infrastructure, DESIREE (Swedish Research Council Contract No. 2017-00621)

† nissen@jlab.org

Content from this work may be used under the terms of the CC BY 4.0 licence (© 2022). Any distribution of this work must maintain attribution to the author(s), title of the work, publisher, and DOI.

ISBN: 978-3-95450-261-5 ISSN: 2673-7000 doi: 10.18429/JACoW-NAPAC2025-TUP073

OPTICAL PROPERTIES OF WIGGLERS WITH HIGH FIELD-TO-ENERGY RATIO *

S. Seletskiy†,[1], J. Kewisch[1], D. Kayran[1], J. Unger[2], G. Hoffstaetter[2]
[1]Brookhaven National Laboratory, Upton NY, USA
[2]Cornell University, Ithaca NY, USA

Abstract

One of the options to bring electron cooling to high energies is to employ an electron storage ring, which utilizes damping wigglers to counteract emittance growth of electron bunches used to cool hadrons. An example of such a cooler is the Ring Electron Cooler (REC) that can find potential future applications in Electron Ion Collider (EIC). The REC is designed to operate at 150 MeV and requires wigglers with peak field of 2.4 T. This unique combination a strong field wiggler operated at a relatively low energy results in unusual optical properties. In this paper we derive analytic formulas for focusing and chromaticity of different wiggler options and compare analytic and beam tracking results. While our analysis was used to optimize chromaticity in the REC, the derived formulas have a general applicability to wigglers with a high field-to-energy ratio.

INTRODUCTION

The Ring Electron Cooler [1] is designed to provide cooling of EIC protons at top energy ($\gamma = 273$).

The REC is a non-magnetized RF-based 150 MeV electron cooler, in which electrons are kept in the storage ring and re-utilized for multiple turns. The REC is equipped with 18 damping wigglers, which keep electrons' emittance constant by counteracting both electrons' IBS and a proton-electron beam-beam scattering. These wigglers operate at a relatively low energy but must have a rather high peak field B_0 =2.4 T to provide the required radiation cooling of electrons. As a result of this unique range of parameters, the wigglers' optics exhibits interesting features [2].

The REC design requires that throughout the wiggler horizontal β-function is $\beta_x = 29.5$ cm. Thus, a wiggler must produce a strong focusing in the wiggling direction.

Below we show that to limit contribution of the wigglers to the REC chromaticity while producing necessary horizontal focusing, a special field profile is required.

We consider wigglers with period $\lambda = 23.28$ cm, 2 cm gap and number of periods $N_p = 18$.

EQUATIONS OF MOTION

We consider motion in the wiggler's reference frame, with x-axis directed in the wiggling direction, y-axis orthogonal to the wiggling plane and z being in the direction along the wiggler's axis. The equations of motion in approximation of $x' \ll 1$ and $y' \ll 1$ are:

$$x'' = -\frac{B_y}{B\rho} + y'\frac{B_z}{B\rho};\; y'' = \frac{B_x}{B\rho} - x'\frac{B_z}{B\rho} \tag{1}$$

Quadratic Focusing

Consider the following representation of wiggler field:

$$\begin{aligned} B_x &= \frac{k_x}{k_y} B_0 \sinh(k_x x)\sinh(k_y y)\sin(kz) \\ B_y &= B_0 \cosh(k_x x)\cosh(k_y y)\sin(kz) \\ B_z &= \frac{k}{k_y} B_0 \cosh(k_x x)\sinh(k_y y)\cos(kz) \end{aligned} \tag{2}$$

where $k = \frac{2\pi}{\lambda} \approx 27$ m^{-1}, k_x and k_y are geometric parameters such that $k_x^2 + k_y^2 = k^2$.

In this wiggler the poles are shaped to produce a quadratic dependence of B_y on x near the axis and a focusing in x-direction is happening due to particles going with an offset through a sextupole-like field.

Substituting Eq. (2) into Eq. (1) we get:

$$\begin{aligned} x'' &= -b\cosh(k_x x)\cosh(k_y y)\sin(kz) + \\ &\quad + b\frac{k}{k_y} y' \cosh(k_x x)\sinh(k_y y)\cos(kz) \\ y'' &= b\frac{k_x}{k_y}\sinh(k_x x)\sinh(k_y y)\sin(kz) - \\ &\quad - b\frac{k}{k_y} x' \cosh(k_x x)\sinh(k_y y)\cos(kz) \end{aligned} \tag{3}$$

where $b = \frac{B_0}{B\rho}$.

An approximate solution of Eq. (3) is given by [2]:

$$\begin{aligned} x &= \frac{b}{k^2}\sin(kz) + x_0\cos\left(\frac{bk_x}{\sqrt{2}k}z\right) + \frac{\sqrt{2}k}{bk_x}\left(x_0' - \frac{b}{k}\right)\sin\left(\frac{bk_x}{\sqrt{2}k}z\right) \\ y &= y_0\cos\left(\frac{b\sqrt{k^2-k_x^2}}{\sqrt{2}k}z\right) + y_0'\frac{\sqrt{2}k}{b\sqrt{k^2-k_x^2}}\sin\left(\frac{b\sqrt{k^2-k_x^2}}{\sqrt{2}k}z\right) \end{aligned} \tag{4}$$

There is a good agreement between Eq. (4) and numerical integration of Eq. (3) (see Fig. 1).

Linear Focusing

An example of linear focusing is a wiggler immersed in a continuous quadrupole field (the assumption of continuous field simplifies equations, a periodic quadrupole field gives similar final results):

$$\begin{aligned} B_x &= B_0\,\cos(k_q x)\sinh(k_q y) \\ B_y &= B_0\cosh(ky)\sin(kz) + B_0\sin(k_q x)\cosh(k_q y) \\ B_z &= B_0\sinh(ky)\cos(kz) \end{aligned} \tag{5}$$

where k_q is a quadrupole parameter.

* Work supported by Brookhaven Science Associates, LLC under Contract No. DE-SC0012704 with the U.S. Department of Energy
† seletskiy@bnl.gov

Content from this work may be used under the terms of the CC BY 4.0 licence (© 2022). Any distribution of this work must maintain attribution to the author(s), title of the work, publisher, and DOI.

ISBN: 978-3-95450-261-5 ISSN: 2673-7000 doi: 10.18429/JACoW-NAPAC2025-TUP074

OPTICS RECONSTRUCTION IN THE SCL SECTION OF THE FNAL LINAC*

J.-P. Carneiro†, E. Chen, A. Pathak, R. Sharankova, A. Shemyakin
Fermi National Accelerator Laboratory, Batavia, IL, USA

Abstract

The Side-Coupled Linac (SCL) section of the FNAL linac accelerates the beam from 117 MeV to 401.5 MeV, operating at 22-24 mA beam current. Transverse focusing is performed by 32 quadrupoles, and the beam orbit is guided by 19 dipole correctors and measured by 29 BPMs. The bunch length is measured in a single location by a Bunch Shape Monitor (BSM). This paper presents a three-step reconstruction of the machine optics. First, the transverse and longitudinal Twiss parameters at the start of the SCL section are determined using quadrupole scans and BSM measurements at different settings of an upstream cavity. Second, the quadrupole calibrations are adjusted based on differential-trajectory measurements. Finally, the beam is propagated along the SCL linac using the code TraceWin. A comparison between TraceWin simulations and the beam envelope measured by the 12 wire scanners of the SCL linac is performed. Transverse and longitudinal beam parameters at the entrance of the transition section are reported.

INTRODUCTION

The front-end of the Fermilab linac [1] consists of an Ion Source producing 35 keV H^- beam and a Low Energy Beam Transport (LEBT) that matches the H^- beam produced by the source into a 4-rod RFQ operating at 201.25 MHz. The beam exits the RFQ with an energy of 750 keV and is matched into a Drift Tube Linac (DTL) by a Medium Energy Beam Transport (MEBT) made of two quadrupole doublets and one buncher. The DTL section operates at 201.25 MHz and consists of 207 drift tubes distributed over 5 DTL tanks. At the exit of the DTL Tank5, the H^- beam has an energy of 117 MeV. A 4-meter Transition section made of four quadrupoles and two 805 MHz cavities (the Buncher and the smaller Vernier) ensures proper matching between the DTL Tank5 and the Side Coupled Linac (SCL) section, which further accelerates the beam to 401.5 MeV. The SCL section consists of seven 805 MHz modules, with each module containing four Side-Coupled Cavities (SCC). Transverse focusing on the DTL, transition and SCL sections is made by quadrupoles.

Upon exiting the SCL section, the beam travels about 70 meters for injection into the 8 GeV Booster synchrotron. During daily operation, the linac outputs 22-24 mA beam in 35 μs long pulses at 15 Hz repetition rates.

In this paper, we present an attempt to reconstruct the Twiss parameters at the start of the Transition section, based on beam measurements and the beam dynamics code TraceWin [2]. In the second part of the paper, we describe a method based on differential trajectory method and the code Linac_Gen [3] for calibration of the Transition and SCL sections quadrupoles. Finally, we discuss the status of agreement between measured and reconstructed beam envelopes along the Transition and SCL sections.

TWISS RECONSTRUCTION

Figure 1 shows a schematic of the Transition section and the start of the SCL section (Module 1, Cavities 1 and 2). We attempted to reconstruct the Twiss at the Beam Position Monitor downstream of the DTL Tank5 (as shown in Fig. 1), for normal operation at 23.7 mA. A summary of the reconstructed Twiss parameters at this location is reported in Table 1.

Table 1: Reconstructed Beam Parameters at the Start of the Transition Section (BPM Downstream Tank5, See Fig. 1)

Beam Parameters	Values
Energy	117 MeV
Beam current	23.7 mA
Alpha X	-0.49
Beta X	9.03 mm/mrad
Emittance rms norm. X	0.9 mm-mrad
Alpha Y	0.35
Beta Y	1.89 mm/mrad
Emittance rms norm. Y	0.8 mm-mrad
Alpha Z	-0.5
Beta Z	8.0 mm/mrad
Emittance rms norm. Z	1.0 mm-mrad
Emittance rms norm. Z	0.45 deg-MeV

We first started the Twiss reconstruction by performing a calibration of the Buncher and the Vernier during nominal operation. The signals of the downstream BPMs are recorded as a function of the Buncher and Vernier phases. The BPM signals (recorded at the base frequency of 402.5 MHz) are then reconstructed with TraceWin which allowed us to estimate the operating effective gap voltages and synchronous phases of the Buncher and Vernier. We estimate from these BPM studies that the Buncher and Vernier are operating daily with an effective gap voltage of respectively $E_0T = 1.68$ MV/m and $E_0T = 2.95$ MV/m and that both cavities operate with a synchronous phase of -90 deg.

* Work produced by FermiForward Discovery Group, LLC under Contract No. 89243024CSC000002 with the U.S. Department of Energy, Office of Science, Office of High Energy Physics.
† carneiro@fnal.gov

Content from this work may be used under the terms of the CC BY 4.0 licence (© 2022). Any distribution of this work must maintain attribution to the author(s), title of the work, publisher, and DOI.

ISBN: 978-3-95450-261-5 ISSN: 2673-7000 doi: 10.18429/JACoW-NAPAC2025-TUP075

OPTIMIZING 4D EMITTANCE MEASUREMENTS USING THE PINHOLE SCAN TECHNIQUE

P. P. Owusu[†,1], C. Zhang[2], A. Bartnik[2], T. Kalpada[1], J. Anawalt[1], J. Maxson[2], S. Karkare[1]
[1]Arizona State University, Tempe, AZ, USA
[2]Cornell University, Ithaca, NY, USA

Abstract

Accurate measurement of electron beam emittance is essential for optimizing high-brightness electron sources. The Pinhole Scan Technique measures the 4D phase space and hence the emittance by measuring the beam profile after clipping the beam using a pinhole followed by a drift section and then scanning the beam over the pinhole. This technique has been implemented in low energy (< 200 keV) beamlines at both Cornell University and Arizona State University. However, the technique poses several practical challenges. In this work, we analyze and address key issues affecting the 4D phase space and emittance measurements using this technique. We identify and investigate sources of inaccuracies like the pinhole aspect ratio, beam divergence, position-momentum correlations in the phase space, and the point-spread-function of the detector and suggest techniques to minimize them. Our findings offer a pathway to more accurate 4D phase space characterization in advanced electron beam systems.

INTRODUCTION

A general figure of merit for electron beam quality is its transverse emittance, which characterizes its phase-space distribution. Precise emittance measurement and characterization of the 4D transvserse phase space of electron beams is thus vital for the refinement of electron sources in high-brightness applications. The pinhole scan technique is a powerful tool for characterizing the full 4D phase space of electron beams and obtaining the emittance. This technique has been implemented in the Cornell MEDUSA Beamline, the Cornell Photocathode Lab [1] and the ASU CryoGun Beamline [2, 3]. In this method, a small, precisely defined aperture (or "pinhole") is placed in the path of a focused electron beam to spatially select a tiny portion of the beam. The beam is then systematically scanned across this pinhole by varying the transverse beam position using dipole steering magnets. For each position of the beam relative to the pinhole, the transmitted electrons form a beamlet that travels through a drift space. The transverse distribution of this beamlet is recorded on a downstream detector, typically a scintillator screen coupled to a high-resolution camera. This transverse distribution represents the transverse momentum distribution in the beamlet. By collecting a series of these transmitted beamlet images as the beam is rastered across the aperture in both transverse directions, a detailed map of the beam's four-dimensional transverse phase space (x, x', y, y') can be reconstructed. Here, x and y represent the transverse spatial coordinates at the aperture plane, while x' and y' correspond to the transverse angles (or momenta) derived from the positions on the detector and the known drift length. This dataset allows for the calculation of the full four-dimensional beam covariance matrix as below:

$$\Sigma_{4D} = \begin{bmatrix} \langle xx \rangle & \langle xx' \rangle & \langle xy \rangle & \langle xy' \rangle \\ \langle x'x \rangle & \langle x'x' \rangle & \langle x'y \rangle & \langle x'y' \rangle \\ \langle yx \rangle & \langle yx' \rangle & \langle yy \rangle & \langle yy' \rangle \\ \langle y'x \rangle & \langle y'x' \rangle & \langle y'y \rangle & \langle y'y' \rangle \end{bmatrix} \quad (1)$$

from which the beam's 4D normalized transverse emittance is computed as:

$$\epsilon_{4D,n} = (\gamma\beta)^2 \sqrt{\det(\Sigma_{4D})} \quad (2)$$

where γ is the Lorentz factor, $\beta = v/c$, and $\det(\Sigma_{4D})$ is the determinant of the 4D beam matrix [1].

This method measures the full 4D phase space and captures correlations between transverse planes revealing subtle beam distortions caused by aberrations or space charge effects that degrade beam performance making it particularly useful for precise characterization and optimization of the electron beam.

Assuming the normalized transverse emittance is invariant in the beamline, it can then be used to extract the mean transverse energy (MTE) of the electrons emitted from the photocathode through the relation:

$$\text{MTE} = \frac{\epsilon_{4D,n}}{\sigma_i^2 m_0 c^2} \quad (3)$$

In this expression, σ_i is the RMS laser spot size at the photocathode, and m_0c^2 is the rest mass energy of the electron [2].

Despite its advantages, the pinhole scan technique presents inherent challenges that affect the accuracy of the emittance values obtained. In this work, we identify the key issues related to the pinhole aspect ratio, beam divergence, position-momentum correlations in the phase space, and the point-spread-function of the detector. We also outline the steps taken to resolve them in pursuit of improved measurement accuracy. All measurements presented here have been performed at very low bunch charges or with DC beams, making effects of space charge negligible.

FACTORS AFFECTING THE MEASUREMENT

The beamlines at Cornell and ASU in which this technique has been implemented consist of a DC gun followed by at least one solenoid that can be used to focus the beam

[†]ppowusu@asu.edu

Content from this work may be used under the terms of the CC BY 4.0 licence (© 2022). Any distribution of this work must maintain attribution to the author(s), title of the work, publisher, and DOI.

ISBN: 978-3-95450-261-5 ISSN: 2673-7000 doi: 10.18429/JACoW-NAPAC2025-TUP077

PHASE VARIATION FOR SNAKE MATCHING IN THE EIC'S HSR

E. Hamwi*,[1], G. H. Hoffstaetter[1,2], K. Hock[2], H. Huang[2]
[1]CLASSE, Cornell University, Ithaca, NY, USA
[2]Collider-Accelerator Department, Brookhaven National Laboratory, Upton, NY, USA

Abstract

The Hadron Storage Ring of the Electron-Ion Collider will feature 6 Siberian snakes placed at the start of each arc to coherently cancel spin precession from diametrically opposite arcs in the ring. To avoid spin-orbital resonances, the alternating sum of the rotation axes of all snakes is 90°, ensuring the closed-orbit spin tune is ½ and sufficiently far away from betatron tunes and integer tunes. This choice does not account for amplitude-dependent spin tune (ADST) shift, which introduces high-order spin orbit resonances in the vicinity of strong first-order resonances. By varying betatron phase advances across each of the 6 arcs, we minimize the strength of first-order spin-orbit resonances as well as ADST shift. In the case of uncooled helium-3, we find it is necessary to minimally vary the vertical orbital tune as well but are able to completely avoid depolarization throughout the ramp with time-dependent phase advances.

INTRODUCTION

The acceleration and preservation of polarization in high-energy hadron beams remains a central challenge in modern accelerator physics. Since first collisions at 255 GeV, the Relativistic Heavy Ion Collider (RHIC) has shown that > 50% proton polarization can be maintained through Siberian snakes and careful lattice symmetry [1, 2]. Building on this legacy, the Hadron Storage Ring (HSR) of the forthcoming Electron-Ion Collider (EIC) will push polarized protons to 275 GeV and, for the first time at comparable energies, accelerate polarized helions (^{3}He) to roughly 180 GeV per nucleon [3]. Although the HSR reuses much of RHIC's magnet infrastructure, its two-interaction-point optimization and storage-mode optics break the three-fold symmetry that underpinned RHIC's success.

Six Siberian snakes placed at the start of each arc can enforce a closed-orbit spin tune of $1/2$ when the alternating sum of their rotation axes totals 90°, thereby suppressing first-order imperfection and intrinsic resonances [4]. However, this design does not account for amplitude-dependent spin-tune (ADST) shifts, which seed a dense spectrum of higher-order spin–orbit resonances near strong first-order stopbands. In the absence of electron cooling, especially consequential for helions with large anomalous magnetic moment, these effects threaten depolarization during the energy ramp.

We show that deliberately detuning the betatron phase advances across the six arcs (and for uncooled ^{3}He, slightly adjusting the vertical tune) minimizes both first-order coupling and ADST-driven resonance strength. With time-dependent phase-advance modulation throughout the ramp, we achieve essentially lossless polarization transmission for the studied cases.

SPIN–ORBIT RESONANCES AND SNAKES

Spin Resonances

Closed-orbit spin precession is characterized by the spin tune $\nu_0 = G\gamma$. *Imperfection resonances* occur when $\nu_0 \in \mathbb{Z}$ due to closed-orbit errors, while vertical betatron motion drives *intrinsic resonances* when

$$\nu_0 \pm Q_y \in \mathbb{Z}. \tag{1}$$

In a linearized treatment, the one-turn effect of such resonant precession defines a *spin–orbit coupling* integral. Writing $\vec{\omega} = \vec{\Omega} - \vec{\Omega}_0$ and $\Psi(s) = \int_0^s \vec{\Omega}_0 \cdot \vec{n}_0 \, \mathrm{d}s$, the leading contribution reads

$$\begin{aligned} \Delta(s_x + i s_y) &\propto \oint [\vec{\omega}(s) \cdot (\hat{x} + i\hat{z})] \, e^{-i\Psi(s)} \, \mathrm{d}s \\ &\approx (G\gamma + 1) \oint k(s) \sqrt{\beta_y(s)} \, e^{\pm i \phi_y(s)} e^{-i\Psi(s)} \, \mathrm{d}s, \end{aligned} \tag{2}$$

where $k = (B\rho)^{-1} \mathrm{d}B_y/\mathrm{d}x$, and β_y, ϕ_y are the vertical lattice functions.

Snake Magnets

Conceived by Derbenev and Kondratenko [5, 6], Siberian snakes rotate the spin by 180° around a horizontal axis. With pairs of diametrically opposite snakes and vanishing net dipole-driven vertical precession, the closed-orbit spin tune is fixed at

$$\nu_0 = \tfrac{1}{2}, \tag{3}$$

independent of energy, thus eliminating first-order resonances.

INVARIANT SPIN FIELD

In stable motion there exists a generalized frame describing off-orbit spin precession, the *invariant frame field* [7]. The corresponding *invariant spin field* (ISF) $\vec{n}(\vec{z}, s)$ obeys

$$\vec{n}(M(\vec{z}), s) = R(\vec{z}, s) \, \vec{n}(\vec{z}, s), \tag{4}$$

with M the one-turn orbital map and R the one-turn spin rotation. The associated *amplitude-dependent spin tune* (ADST) ν generally differs from the closed-orbit value:

$$\nu \neq \nu_0 = \tfrac{1}{2}. \tag{5}$$

* eh652@cornell.edu

Content from this work may be used under the terms of the CC BY 4.0 licence (© 2022). Any distribution of this work must maintain attribution to the author(s), title of the work, publisher, and DOI.

ISBN: 978-3-95450-261-5 ISSN: 2673-7000 doi: 10.18429/JACoW-NAPAC2025-TUP078

FIRST OBSERVATIONS OF DISPERSIVE SHOCK WAVES FROM THE KDV EQUATION IN AN ELECTRON BEAM

H. McCright*, I. Haber, I. Abel, P. O'Shea, B. L. Beaudoin
University of Maryland, College Park, MD, USA

Content from this work may be used under the terms of the CC BY 4.0 licence (© 2022). Any distribution of this work must maintain attribution to the author(s), title of the work, publisher, and DOI.

Abstract

We present the first experimental observation of dispersive shock waves (DSWs) in an electron beam. Using the University of Maryland Electron Ring (UMER), a 10 keV electron beam was perturbed with a localized beam velocity dip. The resulting current profiles evolve into oscillatory structures consistent with dispersive shock behavior governed by the Korteweg–de Vries (KdV) equation. These results are predicted by particle-in-cell simulations using the WARP code. The observed dynamics open new avenues for studying nonlinear longitudinal phenomena in intense beam systems.

INTRODUCTION

Dispersive shock waves (DSWs) are nonlinear wave structures characterized by an expanding train of oscillations trailing a soliton-like leading edge. They arise when nonlinear wave steepening is balanced by dispersion, a phenomenon observed in a variety of physical contexts such as tidal bores and atmospheric "morning glory" waves [1], as well as laboratory experiments with plasmas [2–5], nonlinear optics [1, 6–8], classical fluids [9, 10], and superfluids [11, 12]. Despite the differing media, the defining feature remains consistent: nonlinear steepening modulated by dispersion leads to the formation of a characteristic wave train.

The Korteweg–de Vries (KdV) equation models the dynamics of weakly nonlinear, dispersive waves and admits solitary and cnoidal wave solutions [13]. For step-like initial conditions, it predicts the formation of a DSW, as demonstrated by Gurevich and Pitaevskii [14] and confirmed numerically by Fornberg and Whitham [15].

In charged particle beams, similar wave dynamics arise from the interplay of nonlinear space-charge forces and dispersive effects due to self-consistent electric fields. Under the assumptions of cold, intense beams with negligible longitudinal emittance, the beam fluid model reduces to a KdV-like equation [16]:

$$\frac{\partial u}{\partial t} + \alpha u \frac{\partial u}{\partial z} + \beta \frac{\partial^3 u}{\partial z^3} = 0, \tag{1}$$

where $u(z,t)$ represents a velocity or current perturbation, and α, β are coefficients describing nonlinearity and dispersion, respectively. Previous work has demonstrated soliton formation in beams triggered by positive perturbations, exhibiting characteristic linear relationships between velocity and amplitude as well as amplitude and width squared [16, 17].

* Email: hmccrigh@terpmail.umd.edu

In this study, we report the first experimental observation of DSWs in a recirculating electron beam using the University of Maryland Electron Ring (UMER). By introducing localized velocity perturbations, we observe expanding nonlinear structures consistent with DSWs, providing a controlled environment to validate theoretical predictions and simulations over multiple passes.

THEORY

The KdV equation captures the evolution of nonlinear waves in dispersive media. When initialized with a localized negative perturbation, the solution does not form a solitary wave but instead develops a modulated wave train characteristic of a dispersive shock wave.

Figure 1 shows a numerical solution of the KdV equation evolved from such a negative initial perturbation. Nonlinear steepening sharpens the wavefront until a gradient catastrophe occurs; subsequently, dispersion dominates, generating oscillations. The leading edge travels fastest and possesses the largest amplitude, a defining signature of a DSW.

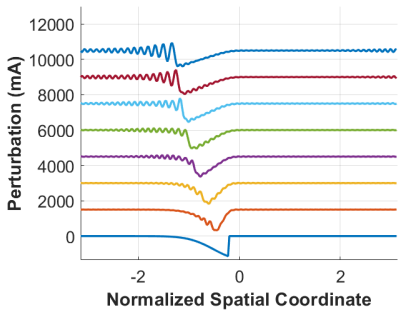


Figure 1: Numerical solution of the KdV equation on a periodic domain $x \in [-\pi, \pi]$, evolved using a pseudo-spectral method in space and a fourth-order Runge–Kutta scheme in time. Time increases vertically in steps of 100 μs. A negative initial perturbation develops into a dispersive wave train.

This theoretical evolution provides a template for the beam experiment: an initial negative velocity perturbation steepens and evolves into a dispersive shock structure with a leading soliton followed by dispersing oscillations, consistent with KdV dynamics.

PARTICLE-IN-CELL SIMULATIONS

To investigate DSW formation in an intense electron beam, we performed numerical modeling using the WARP particle-in-cell (PIC) code [18] in cylindrical (R–Z) geometry. The

ISBN: 978-3-95450-261-5 ISSN: 2673-7000 doi: 10.18429/JACoW-NAPAC2025-TUP080

PRELIMINARY STUDY OF SPACE CHARGE AND BEAM-BEAM INTERPLAY IN A COLLIDER RING *

H. Alamprese†, Y. Hao, Michigan State University, East Lansing, MI, USA
J. Qiang, Lawrence Berkeley National Laboratory, Berkeley, CA, USA

Content from this work may be used under the terms of the CC BY 4.0 licence (© 2022). Any distribution of this work must maintain attribution to the author(s), title of the work, publisher, and DOI.

Abstract

Hadron Collider Rings offer unprecedented opportunities to address fundamental scientific questions in particle and nuclear physics. To achieve these ambitious goals, the colliders must deliver exceptionally high levels of luminosity, hence require high intensity hadron beam in the ring, which leads to high beam-beam parameter, as well as comparable space charge effects. This study focuses on nonlinear effects that impact the beam dynamics within the hadron accelerator ring, including weak-strong beam-beam interactions and their interplay with space charge effects. Accurately predicting these non-linearities, particularly resonances arising during multi-turn acceleration, is critical for long beam lifetime and optimal accelerator performance. The current work presents an initial attempt to develop an optimized approach that integrates space charge effects across the entire ring length while incorporating localized beam-beam interactions at specific interaction points.

INTRODUCTION

It is well established that space charge forces, arising from the mutual Coulomb repulsion between charged particles in a high-intensity beam, must be carefully managed and, when necessary, actively compensated. The nonlinear nature of this force can lead to emittance growth, halo formation, and beam instabilities. These effects become particularly pronounced in scenarios where additional sources of nonlinearity—such as beam–beam interactions in colliders or synchrotron radiation damping and excitation in storage rings—are also present, potentially aggravating the degradation of beam quality and limiting machine performance [1, 2].

Therefore, recent literature highlights the critical need to accurately model nonlinear effects for predicting beam behavior, optimizing accelerator performance, and mitigating potential sources of instability.

This work is organized into two sections. The first presents the theory behind the transfer map that models momentum variation due to the space-charge force. The second part describes the implementation of this model in a weak-strong beam-beam tracking code. In this code, one hundred thousand macroparticles representing the proton beam are tracked over several thousand turns. The parameters used correspond to those of the Electron-Ion Collider (EIC) at Brookhaven National Laboratory.

* Work supported by the U.S. Department of Energy Office of Science under award number DE-SC0024170.

† alampres@msu.edu

TRANSVERSE MOMENTUM VARIATION FROM SPACE CHARGE EFFECTS

In high-intensity beams, space-charge forces often dominate the collective dynamics, significantly influencing beam stability and quality. In the beam's rest frame, each particle experiences the electromagnetic field produced by the surrounding charge distribution. This self-field imparts transverse momentum kicks, leading to betatron tune shifts and amplitude modulation. Under the 2D approach, the bunch is considered infinitely long and uniformly charged along the z-direction, reducing the problem to solving a purely transverse Poisson equation for the scalar potential. However, this approach neglects synchro-betatron coupling effects. To address this, a 2.5D model is adopted in this work, in which the longitudinal charge density follows a Gaussian distribution along the longitudinal direction (as shown in Eq. (1)), allowing the study and prediction of potential coupling resonances.

$$\lambda(z) = \frac{e^{-\frac{z^2}{2\sigma_z^2}}}{\sqrt{2\pi}\sigma_z} \tag{1}$$

The solution to the Poisson equation ($E_{x,y}$in Eq. (2)) is expressed using the Bassetti–Erskine formula [3]. The resulting transverse momentum kick is given by Eq. (2), where K denotes the perveance factor – defined as $K = 2r_0N/\beta^3/\gamma^3$ – in terms of classical radius r_0 and number of particles in the bunch N.

$$dp_{x,y} = \sum_{i=1}^{n} \lambda(z_i) \cdot K \cdot E_{x,y}(x_i, y_i; \sigma_x, \sigma_y) \cdot ds \tag{2}$$

The kick is applied at specific locations or interaction points (IPs) along the ring, which is divided into multiple segments. This segmentation enables the integration of the space-charge force over the length of each segment ds in Eq. (2). Moreover, the *frozen beam size* technique was applied in this preliminary study to reduce numerical errors [4]. As a result, the beam size is not directly influenced by the space-charge force but depends on the average value at the interaction point (IP).

IMPACT OF SPACE CHARGE AND BEAM–BEAM INTERACTIONS

The parameters used for the EIC simulations can be found in [5]. Synchro-betatron coupling resonances were studied using Frequency Map Analysis (FMA), performed with the NAFFlib Python library. The resulting color map illustrates the tune diffusion rate [6].

ISBN: 978-3-95450-261-5 ISSN: 2673-7000 doi: 10.18429/JACoW-NAPAC2025-TUP081

PROGRESS TOWARD DUAL-PULSE OPERATION AT THE PROTON STORAGE RING OF LANSCE*

E.-C. Huang†, B. Comiskey, E. Henestroza, H. Gaus, H. Patel, J. Upadhyay, J. Lyles, J. Bradley, J. Yoskowitz, M. Sanchez Barrueta, W. Hall, M. Kay
Los Alamos National Laboratory, Los Alamos, NM, USA

Content from this work may be used under the terms of the CC BY 4.0 licence (© 2022). Any distribution of this work must maintain attribution to the author(s), title of the work, publisher, and DOI.

Abstract

Significant progress has been made in both hardware development and simulation capability to shorten the proton bunch width delivered to the Lujan Center at LANSCE via the Proton Storage Ring (PSR). We have successfully demonstrated operation of the PSR RF buncher at 5.6 MHz, doubled from the standard running condition, in preparation to accumulate a shorter beam pulse. A quick switch between two modes is under consideration. To extract the beam properly, a prototype kicker test stand has been established, and the measurement of the pulse width, rise time, and charging time will be demonstrated. On the simulation front, beam dynamics models have been refined using both ELEGANT and pyORBIT codes to optimize dual-pulse stacking. We have performed detailed studies of longitudinal phase space evolution, space charge mitigation, and bunch separation fidelity, which guide ongoing design efforts and beamline integration. These advancements will be the foundation for future development of shorter pulses for the Lujan Center.

INTRODUCTION

The PSR delivers an intense, 290-ns-long proton beam that drives neutron scattering experiments at the Manuel Lujan Center user facility. The role of the PSR, which has a revolution time of 360 ns, is to "stack" a 625-μs-long train of 290-ns minipulses, each separated by a 70-ns gap to allow for extraction from the ring. Experiments relying on neutron time-of-flight (TOF) information benefit from the short pulse, as the TOF resolution depends on the duration of the proton pulse that creates the neutrons [1–4].

We have proposed a novel method of pulse stacking to generate two 120-ns pulses in the PSR, instead of a single 290-ns-long pulse [5]. The timing structures used to generate the 290-ns pulse and proposed dual 120-ns pulses are shown in Fig. 1. Achieving the dual pulse configuration requires efforts on three fronts: doubling the operating frequency of the RF buncher from 2.8 MHz to 5.6 MHz; modifying the timing structure of the extraction kickers; and investigating bunch compression techniques via simulation. An update on the status of work in each of these areas is reported in the following sections.

RF BUNCHER FREQUENCY DOUBLING

The PSR buncher currently operates at 2.8 MHz for 1 ms at a repetition rate of 20 Hz. The buncher cavity consists of a series inductor-capacitor-inductor, where the RF voltage is applied to the beam across the capacitor. The inductors are composed of a series of ferrite discs. The amplifier consists of two stages. The first is a Final Power Amplifier (FPA) in a cathode follower configuration, which minimizes the voltage induced by the high peak beam image current. The second is a tetrode Intermediate Power Amplifier (IPA), which enhances the input signal to the 16-kV AC signal required between the capacitor ends. The entire amplifier, IPA, FPA and cavity, shown in Fig. 2, was tested at 5.6 MHz and full voltage in 2023.

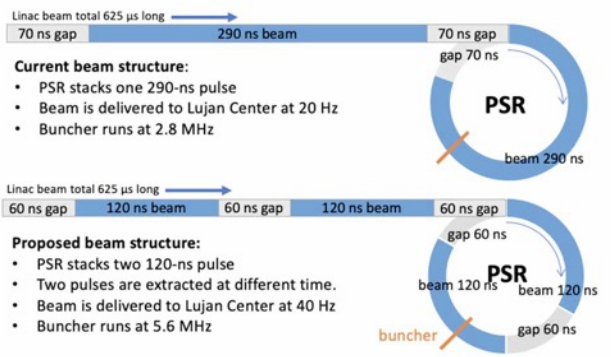


Figure 1: Timing structure for stacking one 290-ns pulse (top) and two 120-ns pulses (bottom), taken from [1].

The IPA is a tetrode-based amplifier with a tuned input circuit that matches the tetrode grid-cathode capacitance to the incoming 50-Ω line and produces 180° de-phased signals feeding each side of the amplifier. The output circuit similarly matches the tetrode output to 500-Ω coaxial lines feeding each final amplifier triode. The IPA requires changes to several capacitors and inductors of its input circuit (shown in Fig. 3) to produce equivalent tuning at 5.6 MHz. Additionally, the π-shaped capacitor-inductor-capacitor output

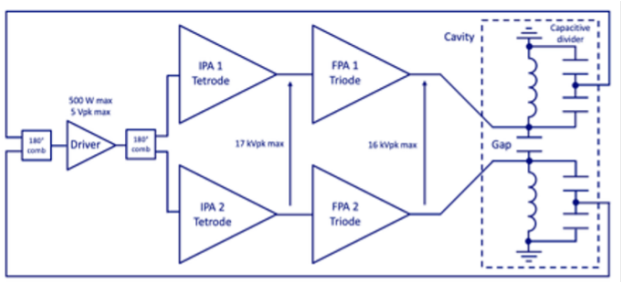


Figure 2: Schematic depicting the amplifier chain and connection to the buncher cavity.

* Work supported by Los Alamos National Laboratory's Laboratory Directed Research and Development (LDRD) program.

† en-chuan@lanl.gov

ISBN: 978-3-95450-261-5 ISSN: 2673-7000 doi: 10.18429/JACoW-NAPAC2025-TUP082

LATTICE DESIGN OF A PULSED SYNCHROTRON CHAIN FOR A MUON COLLIDER SITED AT FERMILAB*

K. G. Capobianco-Hogan†, Stony Brook University, Stony Brook, NY, USA
J. S. Berg, Brookhaven National Laboratory, Upton, NY, USA

Content from this work may be used under the terms of the CC BY 4.0 licence (© 2022). Any distribution of this work must maintain attribution to the author(s), title of the work, publisher, and DOI.

Abstract

We present preliminary lattices for a rapid cycling synchrotron (RCS) chain based on a bottom up design for a 10 TeV parton center-of-momentum (pCM) muon collider sited at Fermilab. The smallest RCS rings in this lattice are 6.28 km in circumference and the largest RCS ring fitting fully within the Fermilab site is 15.5 km. To reach 5 TeV per beam, a single tunnel containing up to two rings is allowed to exceed the 15.5 km limit. Each ring is either a conventional RCS or a hybrid RCS. A conventional RCS relies on only iron dominated, ramped field magnets while a hybrid RCS relies on a combination of interleaved ramped field and superconducting fixed field magnets to achieve higher average magnetic fields while maintaining the high ramp rates achievable with iron dominated magnets. A pair of 6.28 km RCS rings and a 15.5 km RCS ring accelerate beams from 63 GeV to 1.54 TeV. Three scenarios for acceleration from 1.54 TeV to 5 TeV using an off-site tunnel are presented.

INTRODUCTION

Our goal is to design a rapid cycling synchrotron (RCS) acceleration chain from 63 GeV to 5 TeV for muon and anti-muon beams as part of a Fermilab sited muon collider. Here, we present three preliminary designs to accomplish this using four to five RCS rings. All three scenarios rely on the same designs for the first three rings (which would fit within the Fermilab site) to reach an energy of 1.54 TeV. The scenarios differ in how they accelerate beams from 1.54 TeV to 5 TeV.

The existing Tevatron tunnel located on the Fermilab site has a circumference of 6.28 km. We use this as the circumference of the first two rings (RCS 1 and RCS 2), though further analysis is required to determine if the rings would in fact fit within the Tevatron tunnel. We estimate the maximum circumference that can fit on the Fermilab site to be 15.5 km, which we use for the third ring (RCS 3).[1] A single tunnel (containing one or two rings, depending on scenario) is allowed to go beyond the Fermilab site boundary to reach an energy of 5 TeV per beam, with the circumference of the final tunnel being optimized to do so.

Each ring is divided into either six or twelve superperiods. As shown in Fig. 1, each superperiod consists of a straight section, an arc section, and two dispersion suppressor sections (which connect the straight and arc sections). Straight section consists of n_{RF} straight cells containing RF cavities, with an additional two utility straight cells in six of the straight sections. Arc sections consist of n_{arc} arc cells. A half-bend dispersion suppressor scheme is used, with each dispersion suppressor section consisting of two dispersion suppressor cells — nominally, arc cells with bending fields reduced by approximately 50 %. We optimize the number of superperiods per ring, the number of arc cells per superperiod, and the number of RF straights per superperiod to maximize the extraction energy of each RCS while keeping other lattice parameters within reasonable limits.

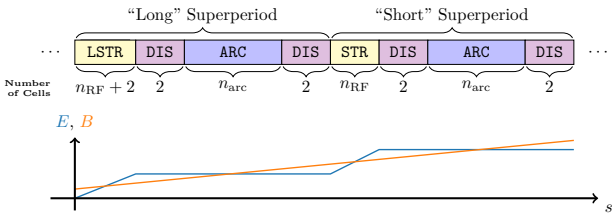


Figure 1: Above, a superperiod consists of either a "long" (`LSTR`) or "short" (`STR`) straight section, an arc section (`ARC`), and a pair of dispersion suppressor sections (`DIS`). Below, a sketch of intermittently ramped beam energy (blue) and continuously ramped magnetic field (orange) as a function of beam position depicts the mismatch between beam energy and ramped magnet field.

CONSTRAINTS AND ASSUMPTIONS

For our designs, we assume that ramped dipole bend magnets can reach fields of 1.75 T [1] and (following a "2/3 rule") that ramped quadrupole magnets can reach pole tip fields of 1.2 T. While these fields are sufficient for the lowest energy ring (RCS 1), they would result in excessively large rings at higher energies.[2] To limit the footprint of the RCS chain, fixed field superconducting magnets are interleaved with ramped magnets, achieving higher average fields, as shown in Fig. 2. Pole-tip field levels should be under 14 T for fixed field superconducting bend magnets and maximum pole tip fields of 12.5 T for fixed field superconducting quadrupoles [2].

A betatron phase advance per cell of 90° was chosen to facilitate the inclusion of sextupole magnets if chromatic corrections are necessary. Dispersion suppressor cells and the arc and straight cells adjacent to them are exempt from the 90° phase advance requirement as their quadrupole magnets are used for matching between the arc and straight sections.

* This manuscript has been authored by employees of Brookhaven Science Associates, LLC under Contract No. DE-SC0012704 with the U.S. Department of Energy.

† kyle.capobianco-hogan@stonybrook.edu

[1] In Scenario B, the fourth ring (RCS 4B, see Scenarios) shares the 15.5 km tunnel with RCS 3.

[2] Nearly 60 km of bending dipoles would be required for a ring to reach an energy of 5 TeV per beam.

ISBN: 978-3-95450-261-5 ISSN: 2673-7000 doi: 10.18429/JACoW-NAPAC2025-TUP084

RECENT PROGRESSES REGARDING ENCLOSED RF CAVITIES FOR FUTURE MUON COLLIDER COOLING CHANNEL

D. Merenich, X. Lu[1,*], Northern Illinois University, Dekalb, IL, USA
T. Luo[†], Lawrence Berkeley National Laboratory, Berkeley, CA, USA
[1]also at Argonne National Laboratory, Lemont, IL, USA

Content from this work may be used under the terms of the CC BY 4.0 licence (© 2022). Any distribution of this work must maintain attribution to the author(s), title of the work, publisher, and DOI.

Abstract

The muon collider (MuC) holds strong potential for reaching the 10 TeV energy frontier while introduces several technical challenges. Ionization cooling is essential to reduce beam emittance and achieve required luminosities. In this cooling process, as muons lose energy in absorbers, normal-conducting RF cavities restore it. However, strong magnetic fields—needed for beam focusing—increase the risk of RF cavity breakdowns. Thin beam windows are used to reduce breakdown probability and improve shunt impedance. In this paper, we present some recent studies on these cavities, including: 1) evaluating emittance growth due to particle scattering in the beam windows made of Be and Al by GEANT4, 2) calculating the beam loading effect in the presence of the beam windows with CST wakeifeld solver and Particle-In-Cell solver, 3) deriving the breakdown thresholds for different cavity materials in strong B fields based on a thermal-mechanical model.

INTRODUCTION

Collisions at a parton center-of-mass energy of 10 TeV promise both profound insights into the fundamental constituents of matter and technological advances, as highlighted by the Particle Physics Project Prioritization Panel [1]. To reach this energy, several colliders have been proposed, such as linear e^+e^- machines using wakefield techniques, or large-scale circular proton–proton colliders. A circular muon collider presents unique advantages. The muon's greater mass dramatically reduces synchrotron radiative losses compared to electrons, and—being an elementary particle—its collisions directly utilize the full center-of-mass energy compared to proton.

Although a muon collider's promise is high, it comes with its own set of technical challenges. Muons are created as offspring particles from a proton beam incident upon a target material, resulting in a large initial phase space that is not conducive to a high-luminosity collider. An ionization cooling method is adopted to reduce the muon beam emittance by 10^6 order with in the short muon lifetime. In this cooling process, RF cavities are needed to recover the longitudinal momentum lost in the absorbers. The surrounding large external magnetic fields have been shown to increase breakdown rates [2–4], which is a major challenge for such cavities. A thin, low-Z window is used to enclose the cavity to increase the shunt impedance and relieve the breakdown rates. These windows also cause scattering to the incident beam. In this work, the emittance dilution caused by scattering for Aluminum (Al) and Beryllium (Be) windows is presented. The effect of beam loading, which is crucial for the large bunch charge of the muon beam, is also investigated for the closed-window geometry. Lastly, the effects of breakdown enhanced by large magnetic fields are discussed for various window materials.

* xylu@niu.edu
† tluo@lbl.gov

EMITTANCE DILUTION DUE TO THIN BEAM WINDOWS

The thin, low-Z windows minimize muon loss and scattering but must be thick enough to resist thermo-mechanical deformation. Previous studies considered Be windows; however, handling and machinability issues have motivated exploring alternative materials. One possible choice is Al due to conductive properties similar to Be. Our GEANT4 simulations compared Al and Be windows [5], utilizing the FTFP_BERT package and Gaussian particle distributions. The window configurations are based on the latest 6D rectilinear cooling lattice design [6], which includes 4 pre-merging stages (A1-A4) and 10 post-merging stages (B1-B10). Space charge and external field effects, unrelated to scattering mechanisms, were neglected. Figure 1 shows relative normalized emittance changes for the first (A1) and last (B10) stages. Emittance dilution increases with thickness, remaining negligible until stage B6 due to large initial emittance. At later stages with significant cooling, dilution grows substantially. While single-window changes are small, cumulative effects across hundreds of multi-cell cavities could

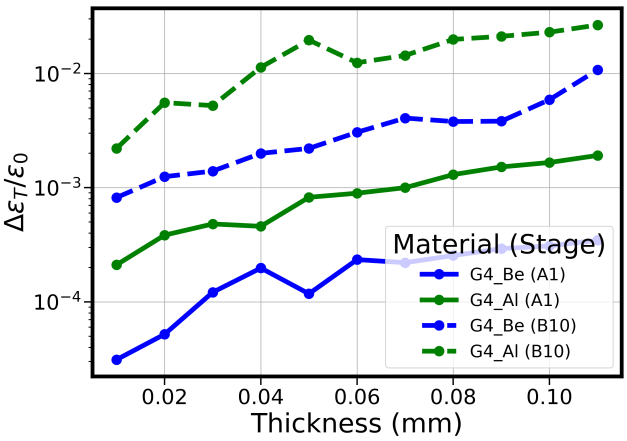


Figure 1: Relative emittance changes for Stages A1 and B10 in the muon collider cooling lattice.

ISBN: 978-3-95450-261-5 ISSN: 2673-7000 doi: 10.18429/JACoW-NAPAC2025-TUP086

SIMULATIONS OF CSR AND LSC INDUCED MICROBUNCHING IN THE PRESENCE OF A LASER HEATER*

S. Kladov†, Y.-K. Kim, University of Chicago, Chicago, IL, USA
C. Emma, Z. Huang, S. Gessner, SLAC National Accelerator Laboratory, Menlo Park, CA, USA

Content from this work may be used under the terms of the CC BY 4.0 licence (© 2022). Any distribution of this work must maintain attribution to the author(s), title of the work, publisher, and DOI.

Abstract

We present a study of microbunching instability in the FACET-II linac, in which the amplification and damping mechanisms are analyzed separately. Our simulations investigate the gain induced by Longitudinal Space Charge (LSC) and, critically, the damping caused by nonlinear terms in the beam transport transfer map. We show theoretically and through simulation that these nonlinear effects can produce damping several orders of magnitude stronger than predicted by linear theory.

Experimental evidence validates these findings. A quadrupole scan performed in the FACET-II dogleg reveals that an interaction between coherent betatron oscillations and transfer map nonlinearities shifts the point of minimal damping away from the expected linear condition of $R_{51} = 0$. The strong agreement between our simulations and the experimental data demonstrate that a thorough understanding of nonlinear dynamics is essential for high-brightness beam transport.

INTRODUCTION

Microbunching is defined as density modulations within a particle beam. Controlling and understanding the dynamics of the phenomenon is increasingly critical, as modern accelerator applications impose stringent limits on the amplitude of such modulations, particularly at short wavelengths. For example, Coherent Electron Cooling at the future Electron-Ion Collider [1] requires that modulations in the electron beam remain only slightly above the shot-noise level at wavelengths smaller than 10 µm [2–4]. Furthermore, for beams at moderate energies (300 MeV for electrons) with a transverse rms size smaller than 1 mm, the Space Charge (SC) impedance – a primary driver of the instability – shifts into the Near-Infrared (NIR) region (< 10 µm).

It is convenient to study the density modulations in the Fourier domain. The Fourier spectrum of the longitudinal distribution of the bunch is called "bunching factor" b [5]:

$$b(k) = \frac{1}{N}\sum_{j=1}^{N} \exp\left(-i\,k\,z_j\right), \tag{1}$$

where z_j is the position of the j particle at a given time, $k = 2\,\pi/\lambda$ is the wavenumber, and N is the total number of particles in the bunch.

The microbunching dynamics can be split into two parts: Gain and Damping. First, we will examine the Gain part induced by SC and CSR.

* Work supported by USDOE, Office of Science AC02-76SF00515.
† kladov@uchicago.edu

SC AND CSR INDUCED GAIN

The theoretical treatment of LSC-induced microbunching gain conceptually divides the lattice into sections: a "gain" section where SC induces an energy modulation, followed by an "R_{56}" section where this energy modulation is converted into a density modulation. For a system with multiple chicanes, the total gain is the product of the gains from each section.

The process begins with initial density modulations, $\Delta\rho(k)$, which may arise from sources such as imperfections at the cathode. These density fluctuations drive a proportional energy modulation, $\Delta\delta(k)$, where $\delta = (\gamma - \gamma_0)/\gamma_0$ is the relative energy deviation of a particle with relativistic factor γ from a reference particle with γ_0. The subsequent R_{56} section, typically a bunching chicane, then transforms this energy modulation into a longitudinal position shift via the linear transfer matrix element: $\Delta z = R_{56}\,\Delta\delta$. Consequently, the final bunching factor, $b_f(k_f)$, is proportional to the initial one, $b_0(k)$, such that $|b_f(k_f)| = |b_0(k)|\,G$. Here, G is the gain and k_f is the final wavenumber, accounting for the overall bunch compression. The Longitudinal SC (LSC) induced gain is well described in [6], and for a small initial modulation amplitude, it takes the form:

$$\begin{aligned} G &\approx \frac{I_0}{\gamma\,I_A}\left|k_f R_{56}\int_0^L \mathrm{d}s\,\frac{4\,\pi\,Z_{\mathrm{LSC}}(k_0;s)}{Z_0}\right| \mathrm{e}^{-\frac{1}{2}k_f^2\,R_{56}^2\,\sigma_{\delta,u}^2}, \\ Z_{\mathrm{LSC}}(k) &= \frac{i\,Z_0}{\pi\,k\,r_b^2}\left[1 - \frac{k\,r_b}{\gamma}K_1\left(\frac{k\,r_b}{\gamma}\right)\right], \end{aligned} \tag{2}$$

where I_0 is the peak bunch current, I_A is the Alfven current, L is the length of the gain section (without R_{56}), $Z_{\mathrm{LSC}}(k)$ is the SC impedance, Z_0 is the impedance of free space, r_b is the radius of the bunch (the transverse distribution is assumed uniform cylindrical), and $\sigma_{\delta,u}$ is the initial uncorrelated energy spread. The exponential term in Eq. (2), that represents the conventional damping from an initial uncorrelated energy spread, $\sigma_{\delta,u}$, was added for a clearer relation to the existing theories and comparison with simulations. The factorization of gain and damping is valid because the LSC-induced energy modulation does not depend on a particle's initial energy, as detailed in [7].

A comparison between the conventional SC gain theory and simulations for a section of the FACET-II lattice [8] is presented in Fig. 1. The simulations were performed using BMAD [9], focusing on the relevant lattice section shown in Fig. 2. To adhere to the theoretical assumptions, we analyze only the region from the end of the L1 accelerating section to the end of the BC11 chicane (PR11375). The drift (gain) section has a length of is $L = 0.77$ m, followed by a chicane with $R_{56} = -46$ mm. The bunch has a mean energy of $\gamma_0 = 655$, rms sizes of $\sigma_x = 0.27$ mm, $\sigma_y = 0.36$ mm, a

ISBN: 978-3-95450-261-5 ISSN: 2673-7000 doi: 10.18429/JACoW-NAPAC2025-TUP087

START-TO-END SIMULATIONS OF THE LAMP ACCELERATOR FRONT-END*

S. Sosa Guitron†, K. Bishofberger, G. E. Dale, D. A. Dimitrov, D. Gorelov,
S. Kurennoy, J. W. Lewellen, L. Rybarcyk, J. Upadhyay, H. Xu
Los Alamos National Laboratory, Los Alamos, NM, USA

Content from this work may be used under the terms of the CC BY 4.0 licence (© 2022). Any distribution of this work must maintain attribution to the author(s), title of the work, publisher, and DOI.

Abstract

The LANSCE Accelerator Modernization Project (LAMP) plans to replace the two existing 750-keV Cockcroft Waltons by a single radio-frequency quadrupole (RFQ), and to install a new 100-MeV drift-tube linac (DTL). LAMP will simultaneously produce H^+ and H^- beams with different timing patterns to serve multiple experimental facilities. A low energy beam transport (LEBT) is designed to transport H^+ and H^- beams from the ion sources into the 201.25 MHz RFQ, where the beams accelerate to 3 MeV. A medium energy beam transport (MEBT) is designed to transport the beam from the RFQ to the DTL. The DTL accelerates both beams to 100 MeV. The LEBT and MEBT designs include beam choppers and rf systems that imprint the multiple timing patterns required by experiments. Here we describe a concept of the LAMP front-end and present particle simulation results for multiple beams relevant to the facility.

INTRODUCTION

The LANSCE accelerator facility at LANL plays a crucial role in delivering high-intensity proton and neutron beams for a wide range of experiments with different intensity and time patterns. To maintain these LANL capabilities in the future, the LANSCE Accelerator Modernization Project (LAMP) plans to upgrade the LANSCE front-end by replacing the two 750-keV Cockcroft-Walton generators for a single, dual-species 3 MeV RFQ, and replacing the existing 100-MeV DTL [1]. These upgrades require a complete re-design of the front-end to accommodate for these major systems.

LANSCE is a pulsed accelerator with a 1-ms cycle. Different beams are produced and delivered during each machine cycle, usually a macro-pulse that is 625 μs long. Each beam has a different time structure [2]. Here we describe three beams, identified by their corresponding experimental target: the Lujan Center, the Weapons Neutron Research (WNR) and the Isotope Production Facility (IPF). The Lujan beam is the H^- beam used for accumulation in the Proton Storage Ring (PSR), it is formed by trains of 201.25 MHz rf bunches and is 270 ns long, this is a mini-pulse. Mini-pulses are separated by a 90 ns gap, necessary for PSR injection and extraction kickers to ramp-up. The beam repetition rate is 20 Hz. The WNR beam consists of high-intensity H^- bunches separated every 1.8 μs over the length of the macro-pulse. An empty gap between micro-pulses is required for accurate neutron time-of-flight studies. The beam repetition rate is 100 Hz. The IPF beam consists of H^+ rf bunches separated every 5 ns over the macro-pulse. The beam repetition rate is 100 Hz. The WNR and IPF beams share the same machine cycle, which means they are produced and transported at the same time. Single-shot beams are also delivered to proton-Radiography (pRad) and the Ultra-Cold Neutron (UCN) experiments. The new LAMP front-end design should be able to produce all the beams that LANSCE currently delivers.

A significant change is that LANSCE forms all beam patterns in the 750-keV LEBT. In the new front-end, all beams now need to be formed in the 100-keV LEBT and the 3-MeV MEBT [3]. In particular, the LEBT has significantly higher space charge forces acting on the beams, particularly in the WNR high-intensity beam.

We will describe design considerations on the transport lines and discuss start-to-end simulation results showing how the present design meets beam intensity require-ments for LAMP.

Low-Energy Beam Transport

A LEBT concept was designed to transport multiple beams from the ion sources to the RFQ. Figure 1 shows the layout of the LAMP LEBT. The Lujan and IPF beams are long pulses, and we expect a high degree of space charge neutralization, assumed 90%, can be achieved [4] from interaction with the background gas. For the WNR beam, the LEBT chopper produces an initial short pulse, 25-ns, that is spaced every 1.8 μs. No space charge neutralization can be assumed in this case.

The initial chopped pulse for WNR is compressed using a 16.77 MHz buncher [5] to increase the charge at the central 5-ns of the pulse, this high-intensity bunch formation scheme produces satellite bunches that need to be removed in the MEBT [6]. Under these conditions, together with the high-charge per pulse requirement at the WNR target, the LEBT is designed to maximize the transmission of the 35-mA short pulse for WNR beam. The WNR beam then sets the magnet settings on most of the LEBT magnets. The RFQ matched beam parameters are calculated for the Lujan and the IPF beams, and backpropagated through the LEBT. The independent Lujan and IPF beamlines provide sufficient variables to match the beams at the merging locations. The IPF beam merges at a 9° magnet, and the Lujan beam gets kicked into the WNR line upstream of the chopper.

* This work benefitted from the use of the LANSCE accelerator facility. Work was performed under the auspices of the US Department of Energy by Triad National Security under contract 89233218CNA000001.
† salvador@lanl.gov

ISBN: 978-3-95450-261-5 ISSN: 2673-7000 doi: 10.18429/JACoW-NAPAC2025-TUP088

PASSIVE HIGHER-HARMONIC RF CAVITY SIMULATIONS FOR BUNCH LENGTHENING IN THE NSLSII-U

Aamna Khan*, Gabriele Bassi, Victor Smaluk
BNL, NSLS-II, Upton, NY, USA

Abstract

Higher-harmonic cavities (HHCs) are commonly employed in modern synchrotron light sources to lengthen electron bunches without increasing the natural energy spread. This approach effectively reduces intrabeam scattering and enhances Touschek lifetime. Accurate simulations are essential for predicting beam dynamics, particularly the impact of cavity detuning on beam stability and performance. Simulations are performed with the particle-tracking code ELEGANT, and key uniform-fill results are verified with the Vlasov–Fokker–Planck solver SPACE.

INTRODUCTION

Achieving extremely low electron beam emittance is critical for advancing the capabilities of modern synchrotron light sources. However, ultra-low emittance operation often results in high particle density, which implies shorter bunch lengths and enhances collective effects such as intrabeam scattering (IBS) and impedance-induced effects [1, 2]. This leads to emittance growth and reduced beam lifetime, particularly at higher beam currents. To mitigate these effects, passive higher-harmonic cavities (HHCs) are employed to lengthen the bunch while preserving the natural energy spread. This reduces the strength of IBS and provides Landau damping for suppressing longitudinal instabilities [3].

The NSLSII-U is a proposed upgrade to NSLS-II, designed to operate at 4 GeV with a complex-bend achromat lattice [4]. As part of its intensity and stability enhancement strategy, the design includes a passive superconducting third-harmonic cavity (3HC). Table 1 summarizes the primary design parameters. In passive mode, the 3HC is detuned from the third harmonic of the main RF frequency, enabling beam-induced voltage to flatten the total RF waveform and lengthen the bunch. Although a multi-harmonic RF system combining multiple cavity orders is under consideration for NSLSII-U to further increase bunch lengthening and improve beam stability [5], this study focuses on the impact of a single 3HC. Uniform-fill simulations were carried out with the particle-tracking code ELEGANT; key results were cross-validated against the Vlasov–Fokker–Planck solver SPACE to confirm consistency.

Table 1: NSLSII-U High-Brightness Storage Ring Parameters for Complex-Bend Lattice

Parameters	Symbol	Value	Unit
Circumference	C	791.72	m
Beam energy	E	4	GeV
Average current	I_{av}	400	mA
Momentum compaction	α	6.67	10^{-5}
Natural energy spread	σ_δ	1.10	10^{-3}
RF Voltage	V_{rf}	4.8	MV
RF frequency	f_{rf}	499.8	MHz
Harmonic number	h	1320	
Bunch length	$\sigma_{\tau 0}$	7.87	ps
Energy loss per turn	U_0	1940	keV
Main RF shunt impedance	$R_{s,\mathrm{main}}$	33375	MΩ
Main RF quality factor	Q_{main}	7.5×10^8	—
HHC shunt impedance	R_H	8800	MΩ
HHC quality factor	Q_H	1.0×10^8	—
Detuning scan range	Δf	31–35	kHz

THEORETICAL MODEL

For passive HHC operation, the total RF voltage experienced by a particle at longitudinal coordinate τ is the combination of the main RF cavity voltage and the beam-induced voltage in the harmonic cavity [3]:

$$V(\tau) = V_{\mathrm{rf}} \sin(\omega_{\mathrm{rf}}\tau + \phi_s) - i_m R_H \cos\psi_m \cos(m\omega_{\mathrm{rf}}\tau + \psi_m), \quad (1)$$

where V_{rf} and ω_{rf} are the amplitude and angular frequency of the main RF cavity, respectively, ϕ_s is the synchronous phase, m is the harmonic number of the HHC, R_H is the shunt impedance of the HHC, and ψ_m is the cavity detuning angle. The beam-induced current component at the harmonic frequency $m\omega_{\mathrm{rf}}$ for an approx. Gaussian bunch of rms length σ_τ is given by $i_m = 2I_0 \exp\left[-\frac{1}{2}(m\omega_{\mathrm{rf}}\sigma_\tau)^2\right]$, where I_0 is the average stored beam current.

The detuning angle ψ_m is determined by the cavity's frequency offset from the exact harmonic multiple of the main RF frequency as:

$$\tan\psi_m = 2Q_H \frac{\omega_m - m\omega_{\mathrm{rf}}}{m\omega_{\mathrm{rf}}}, \quad (2)$$

with Q_H and ω_m being the quality factor and resonant angular frequency of the superconducting harmonic cavity, respectively.

For superconducting HHC operation in the NSLSII-U storage ring, the cavity shunt impedance R_H is significantly higher than the ideal value required for passive operation. This large impedance value forces the cavity to operate at a detuning angle ψ_m close to $\pi/2$. Under these conditions, the optimal operating points satisfy $V(0) = V'(0) = 0$, leading to the relationships:

$$\sin\phi_s = \sin\phi_{s0}, \quad \cos\psi_m = -\frac{V_{\mathrm{rf}}\cos\phi_s}{i_m m R_H}, \quad (3)$$

* akhan1@bnl.gov

Content from this work may be used under the terms of the CC BY 4.0 licence (© 2022). Any distribution of this work must maintain attribution to the author(s), title of the work, publisher, and DOI.

ISBN: 978-3-95450-261-5 ISSN: 2673-7000 doi: 10.18429/JACoW-NAPAC2025-TUP090

SINGLE-BUNCH INSTABILITIES DRIVEN BY SPACE CHARGE DURING LOW-ENERGY COOLING AT INJECTION IN THE EIC HADRON STORAGE RING

P. Baxevanis, A. Blednykh, M. Blaskiewicz
Brookhaven National Laboratory, Upton, NY, USA

Abstract

This paper presents a simulation-based study of single-bunch dynamics at the injection energy of 23.8 GeV for protons in the EIC hadron storage ring, focusing on the impact of space-charge–driven instabilities. The analysis demonstrates that at this energy, the proton bunch experiences significant transverse space-charge forces, which can reduce the stability margin in the presence of the geometric and resistive wall impedance. Various collective effects were considered, with particular attention to the nonlinear nature of the transverse space charge. To stabilize the beam, high chromaticity and octupoles were introduced and their effects analyzed using the ELEGANT code. The results provide a quantitative assessment of the stability thresholds and offer guidance for the machine design and operational strategy at injection.

TRANSVERSE BEAM DYNAMICS

At injection energy (23.8 GeV for protons), a single bunch in the EIC hadron storage ring experiences a relatively strong space charge field that can facilitate the onset of deleterious instabilities, particularly in the transverse plane, in conjunction with other wake sources. In order to guard against this possibility, a systematic study of the underlying beam dynamics under the influence of the relevant collective effects is required. In particular, special emphasis needs to be placed on the impact of the transverse component of the space charge force, which is intrinsically nonlinear in character and can potentially reduce the stability margin for a given machine impedance. In what follows, we present the outline of a short, simulation-based study of the above-mentioned effects, with the aim of clarifying the fundamental single-bunch stability behavior of the protons.

To start with, a straightforward means of quantifying the impact of (linear) wakefields upon the transverse dynamics of the hadrons is through the familiar concept of the transverse impedance. The latter quantity includes both dipole and quadrupole-type contributions, signifying dependence of the corresponding wake with respect to the transverse coordinates of the leading and trailing particles (respectively). Assuming a Gaussian transverse profile for the beam, it can be shown that, for the case of linear transverse space charge, the beam-induced component of the dipole impedance per unit length is given by [1]

$$\hat{Z}^{(d)}_{x,y}(\omega) = Z^{(d)}_{x,y}/L_R = -\frac{Z_0}{4\pi\gamma_0^2\Sigma^2_{x,y}}\,, \tag{1}$$

where $Z_0 \approx 377\,\Omega$ is the vacuum impedance, L_R is the ring circumference, γ_0 is the average relativistic factor and $\Sigma_{x,y} = (\sigma_{x,y}(\sigma_x + \sigma_y)/2)^{1/2}$ - with $\sigma_{x,y}$ being the proton beam transverse sizes, assumed constant in the simplified, smooth focusing model under consideration. As far as the corresponding quadrupole impedance per unit length is concerned, it is simply given by $\hat{Z}^{(q)}_{x,y}(\omega) = -\hat{Z}^{(d)}_{x,y}(\omega)$. An additional, but sometimes overlooked, source of dipole space charge impedance can be visualized by considering the image charges induced by an off-axis hadron beam upon the vacuum chamber, which (because of their asymmetrical distribution) cause a net deflection to an on-axis test particle. The relevant contribution to the dipole impedance is expressed by

$$\hat{Z}^{(d,i)}_{x,y}(\omega) = \frac{Z_0}{2\pi\gamma_0^2 b^2}\,, \tag{2}$$

where b is the vacuum chamber radius. Both the dipole and the quadrupole contributions to the transverse impedance can be fed directly into a particle tracking code such as ELEGANT [2]. Specifically, the latter code facilitates a transverse impedance input by means of the intrinsic ZTRANSVERSE element.

The dynamics impact of the above-described linear space charge impedances can be elucidated by means of the corresponding tune shifts, which are given by

$$\Delta\nu^{\text{linear}}_{x,y} = -\nu_{x,y}\beta^2_{x,y}\frac{Ne^2cZ_0\lambda(z)}{8\pi\gamma_0^3 m_h c^2\Sigma^2_{x,y}}\,, \tag{3}$$

where $\nu_{x,y} = L_R/(2\pi\beta_{x,y})$ are the original tunes of the ring, $\beta_{x,y}$ are the (constant) beta function values, Ze and m_h the charge and mass of the hadrons (respectively), N is the total number of hadrons and $\lambda(z)$ is the scaled longitudinal profile of the beam (normalized according to $\int dz\lambda(z) = 1$, where z is the position within the bunch). As expected for the defocusing space charge force, the tune shifts are negative and vary along the bunch according to the local current value.

All the results mentioned so far have assumed that the transverse space charge force is linear in nature. However, for the Gaussian model under consideration, this is merely an approximation. A more rigorous analysis reveals that the effect of the neglected nonlinear terms is to add a dependence of the particles tunes with respect to the transverse action variables $J_{x,y}$, so that the tune shifts now become $\Delta\nu_{x,y} = \Delta\nu^{\text{linear}}_{x,y}F(J_x, J_y)$. In fact, the modification factor F is such that the transverse actions only *reduce the absolute value of the tune shifts*. Moreover, it can be shown that the action-averaged values of the tune shifts can be approximated by $\langle\Delta\nu_{x,y}\rangle \approx 0.5\Delta\nu^{\text{linear}}_{x,y}$ [3]. Accordingly, one can

Content from this work may be used under the terms of the CC BY 4.0 licence (© 2022). Any distribution of this work must maintain attribution to the author(s), title of the work, publisher, and DOI.

ISBN: 978-3-95450-261-5 ISSN: 2673-7000 doi: 10.18429/JACoW-NAPAC2025-TUP091

SPACE CHARGE STUDIES ON STRONG HADRON COOLER ENERGY RECOVERY LINAC*

I. Neththikumara†, K. Deitrick, B. R. Gamage, T. Satogata, N. Sereno, S. Setiniyaz
Thomas Jefferson National Accelerator Facility, Newport News, VA, USA
W. Bergan, E. Wang, Brookhaven National Lab, Upton, NY, USA
N. Wang, Cornell University, Ithaca, NY, USA

Content from this work may be used under the terms of the CC BY 4.0 licence (© 2022). Any distribution of this work must maintain attribution to the author(s), title of the work, publisher, and DOI.

Abstract

An Energy Recovery Linac (ERL) based cooler, using Coherent electron Cooling (CeC) is being designed for cooling hadron beams of the Electron-Ion Collider (EIC). The ERL design utilizes high current, high-brightness electron beams with low emittance and a uniform longitudinal distribution for efficient hadron cooling. In order to cool 275 GeV and 100 GeV protons, this is designed to operate with 150 MeV and 55 MeV electrons, in both cases with an average current of 100 mA and 1 nC bunch charge. With these parameters, the space charge effects become significant in this ERL design due to the low beam energy and high beam current. In this paper, we discuss strategies for including space charge effects in the optics design and implementation of an interface for space charge dominated and non-dominated regions of this ERL lattice.

INTRODUCTION

The U. S. Electron-Ion Collider (EIC) is planned to be build at the Brookhaven National Laboratory (BNL) in New York. Higher luminosity achievement is challenging for the EIC as maintaining a lower beam emittance throughout the long beam storage times. Intra-beam scattering, collective effects and beam-beam effects tend to increase hadron beam emittance, hence a proper cooling mechanism is required to achieve low emittance hadron beams, to achieve design luminosity requirement in the order of 10^{34} cm^{-2}s^{-1} [1]. A coherent electron cooling based energy recovery linac is being designed to serve as the strong hadron cooling source for the EIC complex.

This Strong Hadron Cooling (SHC)-ERL design incorporates a high voltage DC photocathode gun at the injector and is capable of delivering electron beam with a charge of 1 nC. The ERL design intends to cool hadrons beams at two different energies; 100 GeV and 275 GeV. To support this, design allows operating in two distinct modes; mode A and mode B, with corresponding electron beam energies of 55 MeV and 150 MeV, respectively [2, 3]. A detailed schematic of the SHC-ERL complex is given in Fig. 1.

The electron injector consists with two 197 MHz quarter wave resonator (QWR) cavities and one 591 MHz cavity. Solenoids integrated into the injector and dog-leg merger are used to control the beam size in this low energy regime. The electron beam exits the injector at 6 MeV, and is further accelerated up to 13 MeV within the booster, which includes four 197 MHz cavities and two 591 MHz cavities. Electron beam then goes through the PX bunch compressor and proceeds to the main linac, where it is accelerated to the energy corresponding to its operating mode. The main linac consist of eight 5-cell 591 MHz cavities and four 5-cell 1773 MHz cavities. Third harmonic cavities are used to linearize the longitudinal phase space of the electron beam [4].

PARTICLE TRACKING WITH SPACE CHARGE

Electron beam energy is relatively low until the main linac, hence the space charge fields play a dominant role affecting the quality of this high current electron beam. Preserving low beam emittance and low energy spread is crucial for effective hadron cooling. Therefore, careful measures must be taken throughout this low-energy regime to mitigate space charge effects and maintain electron beam quality.

Particle tracking including space charge fields was performed using the Bmad toolkit. Bmad's Integrated Green's Function (IGF) algorithm was employed to accurately model the electron beam dynamics under the influence of space charge fields [5, 6]. A sensitivity analysis was carried out on mesh size and particle count to ensure the robustness and accuracy of the tracking simulation [7]. In a prior study, beam shaping at the cathode was investigated as a strategy to mitigate strong space charge effects at the electron gun. The resulting optimized beam profile is used to suppress emittance growth and minimize beam energy spread within the downstream beamline where space charge effects dominate [8]. An interface point is defined in the ERL lattice to achieve a Twiss match between space-charge-dominated and non-space-charge regimes. Matching Twiss parameters at this transition is essential for maintaining electron beam quality and enabling effective transport through the following sections of the lattice.

Injector and Merger Optimization

The initial electron distribution at the cathode is radially Gaussian, truncated at 2.33 mm with a σ_r = 1.98 mm. Longitudinally, this distribution follows a 10^{th} order super-Gaussian profile, σ_t = 82.87 ps. The beam has a mean thermal energy of 130 meV and a bunch charge of 1 nC [7]. Beamline optimization utilized Xopt, with the continuous NSGA-II algorithm [9, 10]. The primary objective of injector and merger optimization is to minimize beam emittance

* This work is supported by Jefferson Science Associates, LLC under U.S. DOE Contract DE-AC05-06OR23177 and Brookhaven Science Associates, LLC, Contract DESC0012704

† isurunh@jlab.org

ISBN: 978-3-95450-261-5 ISSN: 2673-7000 doi: 10.18429/JACoW-NAPAC2025-TUP092

START-TO-END SIMULATIONS OF NANOMETER-EMITTANCE BEAM TRANSPORT THROUGH AN EMITTANCE EXCHANGE BEAMLINE

B. N. Temizel Ozdemir*, G. Ha, Northern Illinois University, DeKalb, IL, USA

Content from this work may be used under the terms of the CC BY 4.0 licence (© 2022). Any distribution of this work must maintain attribution to the author(s), title of the work, publisher, and DOI.

Abstract

We present start-to-end simulation study of the transport of a few pico-Coulomb, nanometer-emittance beam through an emittance exchange (EEX) beamline. EEX with nanometer-emittance beams has potential to enable research opportunities utilizing tunable and high quality attosecond bunches and nanometer-scale longitudinal bunch trains. To account future possibility of experimental demonstrations, the simulation implemented existing EEX beamline at Argonne Wakefield Accelerator (AWA) facility. Simulation was conducted using General Particle Tracer (GPT) and ELEGANT code.

INTRODUCTION

A recent simulation study demonstrated the feasibility of generating sub-micron-scale longitudinal density modulation via an asymmetric emittance exchange (EEX) beamline [1]. In this study, an idealized 6D Gausssian beam was transported through an asymmetric EEX beamline, and the initial transverse modulation with periods of both 1 µm and 3 µm was successfully converted into longitudinal modulations with periods of 800 nm and 230 nm, respectively. While the conversion was successful, the 6D Gaussian beam model ignores various characteristics typically present in photoinjector beams. Here, we explore whether a realistic beam from a photoinjector can still achieve longitudinal modulations comparable to those obtained from a 6D Gaussian beam. Injector simulations were carried out using General Particle Tracer (GPT) [2] and the following asymmetric EEX beamline was simulated using Elegant [3]. Argonne Wakefield Accelerator facility (AWA) and its EEX beamline are modeled.

BEAMLINE LAYOUT

The beamline layout is provided in Fig. 1. The downstream of the linac will be redesigned for experimental demonstrations. The following will be considered in the simulation study to generate nano-scale modulations. A transmission electron microscopy (TEM) grid will be placed after the last accelerating cavity to scatter a portion of the beam and produce transverse density modulations with a period of 12.5 microns. The modulation produced by the TEM grid will then be adjusted in the following demagnification section to produce 3 micron modulations while meeting other beam requirements at the entrance of the asymmetric EEX beamline. Requirements are provided in Ref. [1].

The asymmetric EEX beamline consists of two doglegs with different bending angles and a transverse deflecting cavity (TDC) placed between them. To mitigate aberrations, a fundamental mode cavity (FMC) and five sextupole magnets are included in the beamline [1]. The EEX beamline is also illustrated in Fig. 1, and relevant parameters are summarized in Ref. [1].

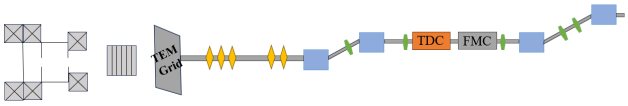


Figure 1: Beamline Layout.

INJECTOR SIMULATIONS

A multi-variable scan was performed using GPT [2] to identify operational points that satisfy the beam requirements for generating nanometer-scale modulations. As outlined in Ref. [1], the normalized transverse emittance must be on the order of tens of nanometers to preserve nano-scale modulations. We performed various injector scans for a 1 pC charge, as chosen in Ref. [1].

Several important behaviors were observed from the results. To satisfy the emittance requirement, the laser spot diameter must be below 300 µm. The laser pulse length should be in the range of 5-6 ps to produce an rms bunch length of approximately 400 µm, which meets the length requirement. Another notable observation is that the matching solenoid current does not significantly affect the projected transverse emittance. Unlike photoinjectors operating at O(100) pC or higher, the emittance varied by only 5 nm over the scan range as shown in Fig. 2. Therefore, it can be used primarily as a beam size controller.

The laser diameter was set to 180 µm, which corresponds to a normalized emittance of approximately 60 nm. To count the loss from a TEM grid, we raised the charge to 2 pC and scanned bucking-focusing (BF) solenoid current and gun phase. The laser pulse was set to a flat-top profile with a length of 6.4 ps FWHM. Transverse beam size at the TEM grid needs to be set to 400 µm, so the matching solenoid current was set to 175 A.

The new scan results are shown in Fig. 3. The optimal operating point was found at gun phase of 24° and BF solenoid current of 475 A, providing a horizontal rms beam size ($\sigma_{x,i}$) of 413.84 µm, and rms bunch length ($\sigma_{z,i}$) of 403.74 µm, a normalized transverse emittance ($\varepsilon_{nx,i}$) of 75.32 nm. The linac phase was set to + 3.6° from the crest to minimize the energy spread.

DENSITY MODULATION AND QUADRUPOLE DEMAGNIFIER

A 2 pC electron beam is used for density modulation generation so that the remaining charge can be a 1 pC. We used

* Z1972381@students.niu.edu

ISBN: 978-3-95450-261-5 ISSN: 2673-7000 doi: 10.18429/JACoW-NAPAC2025-TUP093

START-TO-END SIMULATION STUDY FOR TRANSVERSE WIGGLER-BASED MANIPULATION EXPERIMENT

G. Ha* and D. Sinha, Northern Illinois University, DeKalb, USA

Content from this work may be used under the terms of the CC BY 4.0 licence (© 2022). Any distribution of this work must maintain attribution to the author(s), title of the work, publisher, and DOI.

Abstract

We present a simulation study to support the planning of experimental demonstrations of transverse wiggler-based correlation control. While previous simulations confirmed the feasibility of this approach, they did not incorporate realistic field maps of the transverse wigglers. In addition, the impact of various jitter and error sources—key concerns for experimental implementation—has not been analyzed. In this study, wiggler fields are generated through magnetostatic simulations and incorporated into start-to-end particle tracking simulations. The phase space responses to different jitter and error sources are also evaluated.

INTRODUCTION

Authors recently proposed a concept for tailoring phase space correlations for various applications [1]. The proposed method utilizes cosine modulation that can be generated by various tools, such as transverse wiggler [2], wakefield structure, or laser. Unlike conventional methods using multipole magnets, which provide a polynomial approximation of the desired correlation, this approach approximates the correlation using cosines, which significantly improves the quality and expands capability. Several simulations have been carried out to confirm the feasibility of the method and its applications [1, 3–6].

Later, we studied the expected side effects of a transverse wiggler [7], which could significantly limit its applicability to high-energy beams or other particles (e.g., protons or muons). This work considered three major limiting factors: (1) transverse wiggler thickness, (2) the dependence of B_y field on the particle's vertical position, and (3) the B_x field along the horizontal direction. The study concluded that (1) and (3) are negligible unless the manipulation requires extreme conditions. Also, a vertical beam size of 3-5% of the wavelength can almost eliminate the impact of (2).

As the next step toward preparing an experimental demonstration, we performed another simulation study to examine the manipulation method's sensitivity to errors. We discuss issues found during start-to-end simulations, as well as the sensitivity of the manipulation to transverse wiggler parameters and injector parameters.

START-TO-END SIMULATION

The simulation was performed using the General Particle Tracer GPT code [8]. The Argonne Wakefield Accelerator facility [9] was modeled in GPT, and four accelerating columns were used to produce a 44-MeV electron beam. The layout of the beamline and corresponding beam envelope are shown in in Fig. 1. The bunch charge was set to 1 nC for the simulation. The downstream of the linac includes two sets of quadrupole triplet followed by transverse wigglers. To minimize the impact from $B_y(y)$ field components, vertical focusing is necessary while the horizontal beam size should be enlarged to avoid the use of short-period wigglers. Two sets were originally prepared to enable both shaping to a doorstep profile and linearization of the phase space downstream. The transverse wigglers placed at position **A** were optimized to generate a doorstep profile at position **B**. We ignore the linearization part in this paper.

Seven wigglers were used to optimize the phase space for generating the doorstep profile. A differential evolution algorithm was employed to search for optimal period combinations while the corresponding amplitudes and phases were calculated via linear regression. This combined approach can significantly reduce optimization time from a few days to a few hours. However, further R&D on the optimization and online tuning is necessary [10]. The periods and wiggler gaps are summarized in Table 1. For simplicity, cube magnets with dimensions of $\lambda/4 \times \lambda/4 \times \lambda/4$ were assumed to form a Halbach array [11].

Table 1: Transverse Wiggler Parameters

Wiggler index	Periods (mm)	Gap (mm)
1	29.60	15.96
2	21.20	14.03
3	13.30	31.61
4	10.40	10.89
5	7.10	11.00
6	6.30	10.07
7	5.60	21.92

Figure 2 shows the horizontal phase spaces before and after the transverse wigglers, as well as after transport to position **B**. This calculation assumes ideal kicks from the transverse wigglers. The resulting horizontal phase space at position **B** shows the designed doorstep profile, which starts at +5 mm and ends at -5 mm with a rectangular step spanning from +3.5 mm to +5.0 mm.

We also simulated the transverse wigglers with imported 3D field maps. Figure 3 shows a comparison of horizontal phase spaces at both positions and the corresponding profiles at the end. Panel (a) shows that the result obtained with 3D field maps resembles the ideal case. However, the result from the 3D field map also contains numerous artifacts originating from simulation accuracy and possibly harmonics components. These artifacts introduce significant deformation in the density profile as shown in Fig. 3 (b). Follow-up studies will be conducted.

* gha@niu.edu

ISBN: 978-3-95450-261-5 ISSN: 2673-7000 doi: 10.18429/JACoW-NAPAC2025-TUP094

STATUS OF CONCEPTUAL HORIZONTAL SPLITTER DESIGN FOR FFA@CEBAF ENERGY UPGRADE*

R.M. Bodenstein†, J.F. Benesch, A.M. Coxe‡, K.E. Deitrick,
B. Freeman, B.R. Gamage, R. Kazimi, D.Z. Khan, K.E. Price
Thomas Jefferson National Accelerator Facility, Newport News, VA, USA

Content from this work may be used under the terms of the CC BY 4.0 licence (© 2022). Any distribution of this work must maintain attribution to the author(s), title of the work, publisher, and DOI.

Abstract

Jefferson Lab's Continuous Electron Beam Accelerator Facility (CEBAF) is currently investigating the feasibility of upgrading its maximum operating energy using Fixed-Field Alternating-gradient (FFA) recirculating arcs to increase the total number of recirculations the beam through the pair of LINACs. These FFA arcs will be composed of permanent magnets, with small Panofsky-style multipole correctors. Horizontal splitters are needed to control the beam parameters through these FFA arcs. The geometrical and physical constraints, as well as the beam matching requirements are very restrictive, complicating the design. This work will show the current status of the most mature design, which includes matching solutions, as well as options for extraction of the beam.

INTRODUCTION

As part of the FFA@CEBAF energy upgrade [1], CEBAF's current ARC9 (after nine LINAC traversals) and ARCA (after ten LINAC traversals) will be replaced by new FFA arcs. These arcs will use permanent magnets to guide up to six beam passes through a single shared vacuum chamber. The baseline design incorporates one six-pass FFA arc in each main arc, resulting in four electromagnetic (EM) passes and six FFA passes during operation.

The FFA arcs will employ Halbach arrays [2, 3] with Panofsky-style correctors [4–8], but will otherwise be non-adjustable. Strict matching is required to transport multiple passes through the FFA arcs. Additionally, because the FFA design omits doglegs, time-of-flight (ToF) adjustments must be performed separately.

Drawing on experience from CBETA [9], horizontal Splitters are being developed for this upgrade [10–14]. These Splitters must independently control the optics of each pass, horizontally separating up to six beams after vertical separation by a spreader (which also routes the EM passes into their respective arcs). The combined FFA beam ensemble enters the Splitter, where it is separated onto independent lines, each with dedicated magnets. Each line must precisely match Twiss parameters (α, β), dispersion and dispersion prime (η, η'), horizontal coordinates (x, x'), ToF, and R_{56}. Inside the FFA arcs, the passes are no longer co-linear, each following a trajectory that corresponds to its energy.

* Authored by Jefferson Science Associates, LLC under U.S. DOE Contract No. DE-AC05-06OR23177.

† ryanmb@jlab.org
‡ Now at Virginia Commonwealth University

Design Rationale

The design approach is deliberately conservative, prioritizing **flexibility** and **operational robustness**. Wherever possible, pessimistic boundary conditions were chosen based on realistic constraints. Novel technologies such as multi-function or permanent magnets are avoided in this stage but may be added later if beneficial.

All electromagnets are either currently in use at CEBAF or derived from existing designs [15–24]. The quadrupoles are in present operation, while the dipoles have been conservatively designed with transverse dimensions intentionally larger than necessary to preserve future flexibility. All dipoles are 3 m long and 0.5 m wide (full width), except for four shorter 1.5 m dipoles of the same width and six extraction septa/dipoles, which are 0.3 m wide in the horizontal plane.

As noted in previous reports, some assumptions have been made regarding beam transport through these magnets. For example, certain beam trajectories may fall outside the magnets' good-field regions. While these issues are expected to be minor and correctable, they are noted here for transparency and future review.

CONSTRAINTS

Since they have been detailed in previous reports [10–13], only a brief summary of the relevant constraints is provided here. The design must fit within the existing CEBAF tunnel while meeting health, safety, and equipment access requirements, particularly for large components. The longitudinal and transverse space constraints are summarized in Table 1 and illustrated in Figure 1.

Table 1: Splitter Physical Geometrical Constraints

Name	Value
Wall to Beamline Center	1.3716 m
Beamline Center to Clearance Limit	1.5665 m
Total Available Transverse Space	2.939 m
Beamline Center Height	LINAC Height
Total Length in Z	92 m

The Splitters must match the beam into the FFA arc, including the required horizontal offsets (x, x') for each pass. Additionally, they should provide a mechanism to extract higher-energy passes, as no other system currently exists for this function.

ISBN: 978-3-95450-261-5 ISSN: 2673-7000 doi: 10.18429/JACoW-NAPAC2025-TUP097

THE IMPLEMENTATION OF ADAPTIVE STEP SIZE RUNGE KUTTA INTEGRATOR IN ZGOUBI

Jonathan Lee, Stony Brook University, Stony Brook, NY, USA
Bhawin Dhital, Haixin Huang, François Méot, Brookhaven National Laboratory, Upton, NY, USA

Content from this work may be used under the terms of the CC BY 4.0 licence (© 2022). Any distribution of this work must maintain attribution to the author(s), title of the work, publisher, and DOI.

Abstract

The Zgoubi simulation code for beam and spin dynamics employs a numerical method based on Taylor series to integrate the Lorentz and Thomas-BMT equations, optimizing computational efficiency while ensuring high accuracy and robust preservation of motion invariants. In this work, we developed and implemented an adaptive step-size Runge-Kutta (RK) integrator for implementation into Zgoubi to tackle growing computational demands in accelerator physics simulations. This new integrator complements Zgoubi's default solver, offering users the flexibility to choose between integration methods based on specific simulation requirements. We demonstrated that the adaptive step-size RK integrator achieves the necessary accuracy and performance for integrating the Lorentz and Thomas-BMT equations effectively. A key advantage of Zgoubi lies in its wide optical elements library, featuring over 60 accelerator components and variants, which the new adaptive step-size RK integrator can seamlessly utilize. Developed and rigorously tested over decades across numerous projects, this library provides a high degree of confidence in the code's reliability. The same advantage holds about ancillary computations such as synchrotron radiation, space charge, decay in flight, etc. The implementation of the adaptive step-size RK integrator supports Zgoubi's adaptability, enabling simulations of complex beam and spin dynamics with a trusted and well-established computational framework.

INTRODUCTION

In numerical analysis, solving ordinary differential equations (ODEs) is a critical task that requires methods balancing accuracy and computational efficiency. ODEs typically take the form:

$$\frac{dy}{dt} = f(t, y), \quad y(t_0) = y_0, \tag{1}$$

where $f(t, y)$ defines the dynamics, and $y(t_0) = y_0$ is the initial condition. Among the most prominent techniques for approximating solutions are the Runge-Kutta methods, a family of iterative algorithms. Adaptive step size methods address the inefficiencies of fixed-step integrators by dynamically adjusting the integration step size h based on the local behavior of the solution. These methods estimate the error at each step and modify the step size to keep the error within a specified tolerance. A common approach is to use embedded Runge-Kutta pairs, where two methods of different orders (e.g., 4th and 5th) share function evaluations. The difference between their solutions provides an estimate of the local truncation error, enabling step size adjustment.

The storage ring proton Electric Dipole Moment (srpEDM) experiment leverages a novel symmetric-hybrid, frozen-spin storage ring design using radial electric bending and magnetic focusing, enabling precise measurement of the vertical rotation of the polarization of a highly-polarized stored proton beam, targeting a sensitivity of $10^{-29}\, e{\cdot}$cm [1]. A primary challenge lies in achieving high integration accuracy in electric (or combined electric and magnetic) fields, where varying rigidity complicates simulations. To address this challenge and the increasing computational demands in accelerator physics, we developed and implemented an adaptive step-size Runge-Kutta integrator (Tsit5 method) within the Zgoubi framework [2, 3], enhancing the precision of simulations in electric and combined E-B fields.

TSIT 5TH ORDER ADAPTIVE STEP SIZE RUNGE KUTTA SOLVER

The Tsit5 method [4], developed by Tsitouras, is a sophisticated 5th-order Runge-Kutta integrator with an embedded 4th-order method, often denoted as a 5(4) pair. This design allows Tsit5 to compute a 5th-order accurate solution while simultaneously producing a 4th-order solution for error estimation, all with shared function evaluations for efficiency. Unlike RK4, Tsit5 adapts the step size h at each iteration, reducing it in regions of high curvature and increasing it where the solution is smooth. This adaptability enhances both accuracy and computational efficiency, making Tsit5 particularly well-suited for ODEs with varying dynamics. Its construction, detailed in a Butcher tableau, specifies the coefficients for its stages, but the key advantage lies in its ability to maintain high-order accuracy while optimizing performance across diverse applications.

The Tsit5 method advances the solution from t_n to $t_{n+1} = t_n + h$ using the following scheme:

$$y_{n+1} = y_n + h \sum_{i=1}^{6} b_i k_i, \tag{2}$$

and an embedded 4th-order estimate:

$$\hat{y}_{n+1} = y_n + h \sum_{i=1}^{6} \hat{b}_i k_i, \tag{3}$$

where the stages k_i are computed as:

$$\begin{aligned}
k_1 &= f(t_n, y_n), \\
k_2 &= f(t_n + c_2 h, y_n + h a_{21} k_1), \\
k_3 &= f(t_n + c_3 h, y_n + h(a_{31} k_1 + a_{32} k_2)), \\
k_4 &= f(t_n + c_4 h, y_n + h(a_{41} k_1 + a_{42} k_2 + a_{43} k_3)), \\
k_5 &= f(t_n + c_5 h, y_n + h(a_{51} k_1 + a_{52} k_2 + a_{53} k_3 + a_{54} k_4)), \\
k_6 &= f(t_n + c_6 h, y_n + h(a_{61} k_1 + a_{62} k_2 + a_{63} k_3 + a_{64} k_4 + a_{65} k_5)).
\end{aligned}$$

ISBN: 978-3-95450-261-5 ISSN: 2673-7000 doi: 10.18429/JACoW-NAPAC2025-TUP098

THIRD INTEGER RESONANT EXTRACTION TRANSIT TIME SIMULATION STUDIES

A. Narayanan
Fermi National Accelerator Laboratory, Batavia, IL USA

Content from this work may be used under the terms of the CC BY 4.0 licence (© 2022). Any distribution of this work must maintain attribution to the author(s), title of the work, publisher, and DOI.

Abstract

In this work, we present the investigation of transit time of particles in the non-linear third-integer resonant extraction process. Transit time is defined as the number of turns a particle takes to get extracted once it is in the unstable region in the phase space, i.e., outside the triangular separatrix in case of third-integer resonance. The study of transit time is important because transit time directly contributes to the beam response time during resonant extraction and thus knowing it apriori would be practically useful in designing of the extraction system. In this work, we shall investigate the analytical derivation of the transit time of particles (to the first order Kobayashi Hamiltonian) in different parts of the phase space distribution and compare against the analytical results. We also compare the simulation result of the transit time of particles (with higher statistics) for the static as well as dynamic extraction conditions cases, particularly in the context of resonant extraction parameters for Mu2e experiment at Fermilab.

HAMILTONIAN FORMALISM

The equation of a particle after every three turns in the presence of sextupole, and assuming that the horizontal tune goes very close to third-integer tune (29/3 in the case of Mu2e resonant extraction), turns out to be,

$$\Delta X_3 = \ 6\pi\delta Q X_0' + \frac{3}{2} S X_0 X_0' \tag{1}$$

$$\Delta X_3' = -6\pi\delta Q X_0' + \frac{3}{4} S (X_0^2 - X_0'^2) \tag{2}$$

where X_3 and X_3' are normalized phase space coordinates, δQ is the tune distance to a third-integer tune, and (X_0, X_0') are the initial normalized phase space coordinates of the particle. Since the spill duration (43 ms) is much larger than the one-turn revolution time ($\approx 1.69\ \mu$s) of the particles, it is reasonable to consider three-turns as the basic unit of time instead of one-turn.

We can derive the Hamiltonian of this system (also known as Kobayashi hamiltonian [1]) by integrating the above equations of motion,

$$H = \underbrace{3\pi\delta Q\Big(X^2 + X'^2\Big)}_{\text{First term}} + \underbrace{\frac{S}{4}\Big(3XX'^2 - X^3\Big)}_{\text{Second term}} \tag{3}$$

The first term of the Hamiltonian represents the linear motion in the accelerator, and the second term, caused by the presence of the sextupole element, introduces non-linearity in the particle dynamics. It is worthy to note that this Hamiltonian is true to the first order and ignores higher order terms in δQ and S.

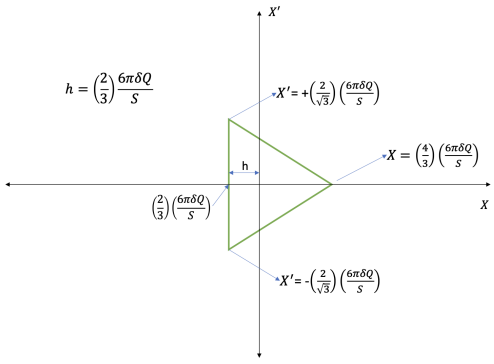


Figure 1: Triangular separatrix due to 3rd integer resonant excitation.

This non-linearity introduces a triangular stable region in the phase space (as shown in Fig. 1). Particles inside the stable region execute stable motion and are bound inside it, never venturing out. But the particles outside the stable region start to increase their amplitude with every turn, with their horizontal position eventually surpassing and jumping past the septum position. Once the particle is past the septum, it experiences an instantaneous horizontal kick to be sent to the extraction beam line and to the desired final location.

TRANSIT TIME EXPRESSION - STATIC CASE

One strategy [2] to derive the transit time of particles is to solve for the evolution of the particle's position as and when it reaches the electrostatic septum in the horizontal plane and solve back for the time step for the particle to reach the septum location. It is algebraically convenient to shift the coordinate system of the normalized phase space such that one of the vertices of the triangluar separatrix is in the origin. The translated Hamiltonian turns out to be $H_{\text{tran.}} = \frac{S}{4}(3hX^2 + 3h^3 + 3XX'^2 + 6\sqrt{3}XX'h - X^3 + 3X^2h + h^3)$.

We are now interested in the particle dynamics with the newly translated coordinates. We obtain them from the usual Hamilton's equations of motion,

$$\frac{\mathrm{d}X}{\mathrm{d}n} = \frac{\partial H}{\partial X'} = \frac{6SX}{4}\Big(\sqrt{3}h + X'\Big) \tag{4}$$

(5)

Similarly, for the evolution of X', we have,

$$\frac{\mathrm{d}X'}{\mathrm{d}n} = -\frac{\partial H}{\partial X} = -\frac{3S}{4}\Big(4hX + 2\sqrt{3}X'h + X'^2 - X^2\Big) \tag{6}$$

ISBN: 978-3-95450-261-5 ISSN: 2673-7000 doi: 10.18429/JACoW-NAPAC2025-TUP099

TIMING OF ULTRAFAST ELECTRON AND LASER PULSES WITH NARROWBAND THz INTERFEROMETRY FOR ULTRAFAST ELECTRON DIFFRACTION*

S. Weathersby†,1, T. K. Do[2], V. Dolgashev[1], C. Duncan[1], J. England[1], P. Kramer[1], M. Othman[1], D. Palmer[1]
[1]SLAC National Accelerator Laboratory, Menlo Park, CA, USA
[2]San Jose State University, San Jose, CA, USA

Abstract

Ultimately, accurate time of arrival determination of laser pump and electron beam probe will determine the temporal resolution of the SLAC MeV-Ultrafast Electron Diffraction* (MeV-UED) instrument, and therefore methods to achieve this at femto-second scales is an ultrafast science enabler. Interferometry of THz based e-beam and pump laser THz signals is a natural path towards this goal. As a first step, a detection scheme will be developed in a lab using laser pulses. The second step involves extracting the electron beam signal from a 100 GHz accelerating structure. Subsequently, both pump and electron beam signals are combined, filtered, amplified, and a temporal analysis can be performed. This proposal is for experimental detection and characterization of such signals, which arises from electron beam wakefield excitation of electromagnetic fields in a 100/200 GHz accelerating structure combined with a laser pump derived signal.

INTRODUCTION

The MeV-UED facility at SLAC provides short (100 fs), low charge (5-20 fC) bunches of 4 MeV electrons for pump probe experiments on a wide variety of material samples [1]. The pump is often a short (60 fs) laser pulse of predetermined wavelength precribed to excite particular photo-dynamics in the sample of interest. The pump laser is temporally delayed with respect to the electron bunch by a controlled path length, and delay-correlated electron probe diffraction images are captured to infer atomic dynamics. These events occur at fs-ps time scales. The progress towards characterization of this temporal resolution is the subject of this study. Measurements based on known dynamics, ie thin films of Bismuth, indicate instrument resolution at 150 fs rms [2]. Other well known methods can be used to derive e-beam and pump laser pulse length separately, but require lengthy and invasive set-up.

MOTIVATION

Temporal resolution places important limits on the understanding of photo-excited states of matter. Leveraging both optical and rf characterization, laser and electron beam signals can be distilled to electronic pulses and mixed, the mixed product signal containing the temporal resolution information. This is performed in the millimeter-wavelength range, where THz optical techniques and w-band rf electronics can be leveraged simultaneously. Fig. 2 shows a schematic description of a potential setup. The MeV-UED laser source is 12 mJ of 800 nm from a commercial chirped pulse amplified Ti:Sapphire system. Compressed 800 nm is split to drive the UV rf photo-electron gun and the sample optical pump. Pump laser can be split or temporarily diverted to the setup. The laser pulse is rectified using non-linear optical rectification. Periodically polled Lithium-Niobate (PPLN) [5] is available to enhance 100 GHz spectral components of the laser pulse. The rectified laser pulse is captured by a w-band mm-wave horn antenna and directed into a band-pass filter, centered at 100 GHz with 4 GHz of bandwidth. This filtered signal is incident in one arm of a w-band magic tee, to be combined with an electron beam signal incident in another arm. The electron beam signal results from electromagnetic modes (wakefields) excited in a metal 100 GHz resonant traveling wave rf structure by the electron beam [4]. The structure is depicted in a test setup in Fig. 1.

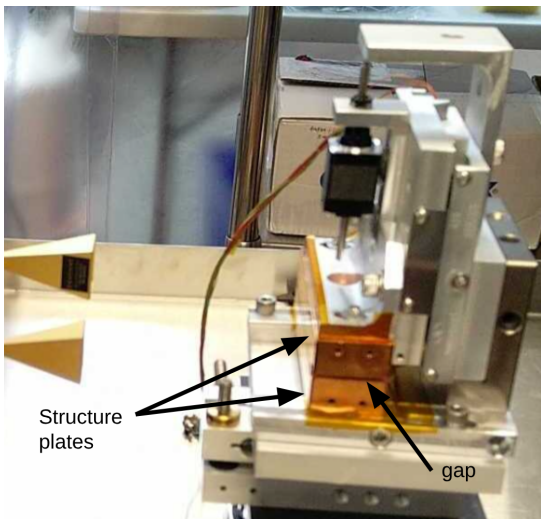


Figure 1: Copper rf structures in a test setup.

SIGNAL TO NOISE

The 100 GHz signals levels are expected to be low, 30 uW peak power for the 5 fC electrons. Depending on the details of the pump laser rectification, only a small fraction of the spectrum falls into the 100 GHz domain.

* Work supported by U.S. Department of Energy Office of Science, Basic Energy Sciences Under Contract No. DE-AC02-76SF00515
† spw@slac.stanford.edu

Content from this work may be used under the terms of the CC BY 4.0 licence (© 2022). Any distribution of this work must maintain attribution to the author(s), title of the work, publisher, and DOI.

ISBN: 978-3-95450-261-5 ISSN: 2673-7000 doi: 10.18429/JACoW-NAPAC2025-TUP100

TOLERANCES OF RF PHASE AND VOLTAGE NOISES WITH BEAM-BEAM INTERACTION IN THE ELECTRON-ION COLLIDER*

Y. Luo†, J.S. Berg, M. Blaskiewicz, Y. Kan, C. Montag, V. Ptitsyn, D. Xu
Brookhaven National Laboratory, Upton, NY, USA

Content from this work may be used under the terms of the CC BY 4.0 licence (© 2022). Any distribution of this work must maintain attribution to the author(s), title of the work, publisher, and DOI.

Abstract

The Electron-Ion Collider (EIC), to be constructed at Brookhaven National Laboratory, will collide polarized high-energy electron beams with polarized proton and ion beams, achieving peak luminosities of up to 1×10^{34} cm^{-2}s^{-1} in the center-of-mass energy range of 20-140 GeV. In this article, we present recent simulation studies focused on the effects of phase and voltage noise originating from the storage RF cavities in both the Electron Storage Ring (ESR) and the Hadron Storage Ring (HSR). The goal of this study is to determine acceptable tolerances for RF phase and voltage noise in the EIC storage rings and to provide critical input for the RF engineering design of the collider.

INTRODUCTION

The Electron-Ion Collider (EIC), to be constructed at Brookhaven National Laboratory, will collide polarized high-energy electron beams with polarized proton and ion beams, achieving peak luminosities of up to 1×10^{34}cm^{-2}s^{-1} in the center-of-mass energy range of 20-140 GeV [1, 2]. To achieve such high luminosities, the EIC employs high bunch intensities for both beams, small and flat transverse beam sizes at the interaction point (IP), and a large 25 mrad crossing angle in the interaction region (IR) to accommodate more than one thousand bunches in each storage ring.

In previous studies, we examined the impact of position and beam size fluctuations at the IP due to magnet power supply current ripples in the Electron Storage Ring (ESR) [3], as well as the phase and voltage noise introduced by the crab cavities in the Hadron Storage Ring (HSR) [4]. These studies showed that proton emittance growth is primarily driven by synchro-betatron resonances, which are enhanced by the flat-beam collision configuration of the EIC.

In this article, we extend our study to include the effects of phase and voltage noise from the storage RF cavities in both the ESR and HSR. A weak-strong beam-beam simulation is used to detect subtle beam size growth over one million tracking turns. The objective is to determine tolerances for RF phase and voltage noise, which will serve as critical input for the RF cavity engineering design of the EIC.

SIMULATION SETUP

In the current EIC design, the typical physics store duration with electron–proton collisions is expected to be about 4-5 hours without strong hadron cooling at collision energies. To preserve beam quality, the goal is to limit proton emittance growth from non-intrabeam scattering (non-IBS) sources to less than 20% per hour, or equivalently, a proton beam size growth rate of less than 10% per hour. Non-IBS sources of proton emittance growth include beam–beam interactions, power supply current ripples, noise from crab and storage cavities, ground vibrations, beam instabilities, and other machine-induced perturbations.

To detect small proton beam size growth rates on the order of a few percent per hour, we employ a weak–strong beam–beam simulation model. Unlike the electron beam, the proton beam does not benefit from synchrotron radiation damping, making it more susceptible to emittance growth, particularly in the vertical plane. In our model, the proton beam is represented by macro-particles, while the electron bunch is modeled as a rigid six-dimensional Gaussian charge distribution. The proton ring is modeled using a 6D linear uncoupled matrix. Simulations typically track the protons for up to one million turns.

For the RF phase and voltage noise spectra, we assume white noise, with a uniform power spectral density over the chosen frequency range. The revolution frequency of the EIC storage rings is approximately 78 kHz. Noise signals are generated in the frequency domain and then transformed to the time domain using inverse FFT to produce turn-by-turn noise profiles. The RMS value of the time-domain signal is used to characterize the phase noise strength, while for voltage noise, we use the RMS value of the relative voltage variation.

Table 1 summarizes the beam parameters used in this study. We adopt the parameters corresponding to the highest peak luminosity collision mode: 10 GeV electrons colliding with 275 GeV protons. In this configuration, both beams reach their maximum beam-beam parameters in the EIC. As shown in the table, the vertical beam size at the IP is approximately 11 times smaller than the horizontal one, making it particularly vulnerable to beam–beam perturbations and machine noise.

SIMULATION WITH ESR RF NOISES

As mentioned earlier, in our weak–strong simulation model, the electron bunch is assumed to be rigid, and the simulation code does not support explicit modeling of RF cavities. Instead, we simulate the effects of RF noise by applying random perturbations to the electron bunch's arrival time and bunch length at the interaction point (IP). Phase noise in the RF cavities leads to arrival time jitter of the electron bunch at the IP, while voltage noise affects the bunch length. We are currently developing an analytical framework to map the electron bunch arrival time jitter and bunch

* Work supported by the U.S. Department of Energy, Office of Science under contracts DE-SC0012704 and DE-AC05-06OR23177

† yluo@bnl.gov

ISBN: 978-3-95450-261-5 ISSN: 2673-7000 doi: 10.18429/JACoW-NAPAC2025-TUP101

TOWARDS DIFFERENTIABLE BEAM DYNAMICS MODELING IN BLAST/IMPACTX*

A. Huebl†, C.E. Mitchell, R. Lehe, A. Formenti, G. Charleux, A. Myers, W. Zhang, J. Qiang, J.-L. Vay, Lawrence Berkeley National Laboratory, Berkeley, CA, USA
J. Kaiser, C. Hespe, Deutsches Elektronen-Synchrotron DESY, Hamburg, Germany
J.P. Gonzalez-Aguilera, University of Chicago, Chicago, IL, USA
C. Xu, Argonne National Laboratory, Lemont, IL, USA
A. Santamaria Garcia, University of Liverpool, Liverpool, United Kingdom
R. Roussel, A. Edelen, SLAC National Accelerator Laboratory, Menlo Park, CA, USA
W.S. Moses, University of Illinois Urbana-Champaign, Champaign, IL, USA

Content from this work may be used under the terms of the CC BY 4.0 licence (© 2022). Any distribution of this work must maintain attribution to the author(s), title of the work, publisher, and DOI.

Abstract

Differentiable beam dynamics simulations are in demand, e.g., to solve inverse and optimization problems in accelerator and beam physics. Here, the two modern open source codes Cheetah and ImpactX are compared in their approach to performance-portable programming and automatic differentiation. A first auto-differentiable prototype of ImpactX explores how the C++ codes in the Beam, Plasma & Accelerator Simulation Toolkit (BLAST) could introduce differentiable modeling.

INTRODUCTION

Differentiable simulations are in demand in accelerator physics, demonstrating order-of-magnitude improvements for complex tasks such as many-parameter optimization for beamline calibrations [1, 2], reconstruction of hard-to-measure quantities [3–6], or uncertainty quantification.

Calculating gradients in simulations with respect to inputs requires more calculations and memory than commonly used, gradient-free simulations. At present, it is an open question which programming approach might be most effective and performant to implement the many advanced numerical methods of a (differentiable) beam dynamics simulation. Desirable is an approach where the physics models only need to be implemented once ("single-source") and automation ensures gradient-calculations (auto-differentiation) and performance on various computing platforms (CPU/GPU).

This work makes use of - and enhances - two fast, modern codes: ImpactX (25.08) [7] and Cheetah (0.7.5) [1, 2]. Both codes are actively developed in open source, well documented and support CPUs and GPUs. Historically, Cheetah implemented only linear tracking models [1], but recently added nonlinear paraxial methods from merging with the BMAD-X [2] code. ImpactX implements linear, nonlinear paraxial and exact Hamiltonian element models. Both codes implement the same 3D space charge model [8].

* Supported by the CAMPA collaboration, a project of the U.S. DOE, Office of Science SciDAC program. Supported by the LDRD Program of LBNL under U.S. DOE Contract No. DE-AC02-05CH11231. This research used resources of NERSC, a U.S. DOE Office of Science User Facility located at LBNL, using NERSC award HEP-ERCAP0031191.

† axelhuebl@lbl.gov

ImpactX approaches accelerator modeling from a need for symplectic modeling with collective effects, supporting high-order, multi-node scalable, long-term stable, simulations. It is written in C++ with Python bindings and reuses modular exascale methods from the WarpX [7, 9] code. Cheetah follows a differentiability-first approach, implementing exclusively on the PyTorch (2.7.1) library in its auto-differentiable array ("tensor") programming model [10]. Cheetah is limited to a single compute node (shared-memory system).

This paper is organized in two parts. First, we investigate the latest performance in an anecdotal example, where both codes have functional overlap – gradient-free modeling of chromatic element models with up to few-million particles per bunch and 3D space charge effects. Second, we show progress in introducing single-source differentiability in ImpactX using a modern compiler plugin, producing executables for gradient-based and gradient-free modeling without a rewrite away from performant C++.

GRADIENT-FREE BENCHMARKS

Achieving high performance for nonlinear beam dynamics simulations is a moving target, because programming languages, compilation techniques and hardware evolve constantly. The two codes in this paper use a modern approach of portable, "single-source" programming, where a generalized implementation of computational routines aims to perform well on CPUs and at least three different vendors of GPUs. While both codes approach accelerator modeling from different needs and implementations, comparing a snapshot of performance can be an instructive exercise to inform future implementations.

This section compares and tunes performance of commonly used, gradient-free nonlinear paraxial particle tracking and 3D space charge on a single node. Not studied here are features exclusively in ImpactX, e.g., exact Hamiltonian models or distributed-memory scalability, or only in Cheetah, e.g., concurrent runs of multiple small, independent simulations. The performance baseline in this paper is the current state-of-the-art performance, see comparisons in Refs. [1, 2]. Benchmarks use 1 node of the NERSC Perlmutter machine with and AMD EPYC 7763 CPU and Nvidia A100 80 GB GPU. The best-of-5 measurements is shown.

ISBN: 978-3-95450-261-5 ISSN: 2673-7000 doi: 10.18429/JACoW-NAPAC2025-TUP102

TRANSVERSE BEAM DYNAMICS STUDIES IN THE FRIB ACCELERATING CRYOMODULES

A. Gonzalez*, J. Wan, K. Fukushima, T. Maruta, P. N. Ostroumov, A. S. Plastun
Facility for Rare Isotope Beams, Michigan State University, East Lansing, MI, USA

Content from this work may be used under the terms of the CC BY 4.0 licence (© 2022). Any distribution of this work must maintain attribution to the author(s), title of the work, publisher, and DOI.

Abstract

The accelerating segments in the Facility for Rare Isotope Beams (FRIB) linac contain superconducting RF (SRF) cavities accelerating the beam and superconducting solenoids providing transverse focusing. We have studied the transverse emittance growth in the post-stripper linear accelerating segment of the FRIB linac. To understand the cause of the emittance growth we employ a macroparticle tracking code to simulate 3D beam dynamics in this segment of the linac. The model is being developed and validated by beam measurements. The measurements are focused on the response of the transverse beam position along the segment after the beam is kicked by dipole steering magnets at the entrance to this segment. The results of the studies with various beam species and energies will be presented.

INTRODUCTION

The FRIB linac contains three linear accelerating segments, shown in Fig. 1. The studies presented focus on the second linear accelerating segment, LS2. LS2 contains 168 SRF cavities distributed across 24 cryomodules. The initial beam energy is between 16 and 20 MeV/nucleon, and the final beam energy is typically greater than 150 MeV/nucleon. A superconducting solenoid is located at the center of each cryomodule to provide transverse focusing. As shown in Fig. 2, each of the solenoids has both horizontal and vertical steering coils to provide trajectory correction to compensate for misalignments.

Emittance Growth Control

Significant transverse emittance growth has been observed in LS2 [1]. This emittance growth is sensitive to slight changes in beam rigidity. For a $^{48}Ca^{19+,20+}$ beam, emittance growth was measured for 20+, but not 19+. The magnetic fields in the LS2 solenoids are set to have alternating sign, which has been previously shown to reduce emittance growth. The transverse phase advance per period provided by the solenoid was high (120 degrees) in the first cryomodule and descended irregularly along LS2. New solenoid field settings were calculated so that the phase advance began at 90 degrees and descended smoothly to 35 degrees in the last cryomodule of LS2. After applying the new solenoid settings, the emittance growth was mitigated. We could not reproduce the emittance growth in our simulations, which motivated the studies presented in this paper, as we seek to increase our understanding of the transverse dynamics in LS2.

* gonzalea@frib.msu.edu

Trajectory Response Studies

We performed measurements to calculate misalignments and observe the behavior of the beam through LS2. As displayed in Fig. 3, the four quadrupoles upstream of the LS2 entrance were included in this study. These quadrupoles are used to match the Courant-Snyder (CS) parameters of the beam to LS2.

The measurements were performed by doing "corrector scans", incrementally changing the current in a dipole steering magnet located upstream of the LS2 entrance. At each current setting, we used the downstream BPMs to measure the transverse beam position response. Multiple correctors were scanned in both the horizontal and vertical directions. The scans were performed using a 19.82 MeV/u $^{82}Se^{32+}$ beam and a 16.52 MeV/u $^{238}U^{75+}$ beam. For the uranium beam, LS2 was set up as normal, with all 168 SRF cavities providing acceleration. For the selenium beam, the LS2 cavities were deactivated and the solenoids were set to transport the 19.82 MeV/u beam with no acceleration.

MISALIGNMENTS

If the entrance of an element is misaligned horizontally by a distance Δ_i and the exit of the element is misaligned by Δ_e, then the phase space coordinates of the beam transform at the entrance of the misaligned element change as:

$$\begin{pmatrix} \tilde{x_i} \\ \tilde{x_i'} \end{pmatrix} = \begin{pmatrix} x_i \\ x_i' \end{pmatrix} - \begin{pmatrix} \Delta_i \\ 2\Delta_t/L \end{pmatrix} \quad (1)$$

where L is the length of the element and Δ_t is defined as $(\Delta_e - \Delta_i)/2$ [2]. Likewise, at the exit of the element, the coordinates transform as:

$$\begin{pmatrix} \tilde{x_e} \\ \tilde{x_e'} \end{pmatrix} = \begin{pmatrix} x_e \\ x_e' \end{pmatrix} - \begin{pmatrix} \Delta_e \\ 2\Delta_t/L \end{pmatrix} \quad (2)$$

We apply these transformations in our simulation codes to calculate misalignments of elements in the FRIB accelerator in both the horizontal and vertical direction.

Quadrupoles

Four quadrupoles directly upstream of the LS2 entrance were used in this study. As seen in Fig. 3, there are three BPMs in this area. The first is immediately downstream of the corrector being scanned, allowing us to use its measurements to determine proper initial conditions for our simulations. There are two quadrupoles in between each BPM, meaning the measurements from the second BPM were used to calculate misalignments of the first two quadrupoles, and

ISBN: 978-3-95450-261-5 ISSN: 2673-7000 doi: 10.18429/JACoW-NAPAC2025-TUP104

VERTICAL EMITTANCE GROWTH FROM IBS DIFFUSION VIA BEAM-BEAM COUPLING IN THE EIC*

Derong Xu†, Yi-Kai Kan, Yun Luo, Brookhaven National Laboratory, Upton, NY, USA

Abstract

We investigate vertical emittance growth in the Electron-Ion Collider (EIC) arising from intrabeam scattering (IBS) diffusion through beam-beam interactions. Using weak-strong simulations, we demonstrate that when horizontal noise is introduced, vertical emittance increases even in the absence of direct vertical diffusion. This behavior is attributed to resonance streaming around the synchro-betatron resonance $2\nu_x - 2\nu_y + p\nu_z = 0$, which enables unidirectional emittance transfer from the horizontal to the vertical plane. We further show that horizontal cooling alone cannot suppress the vertical growth, confirming that dedicated vertical cooling is essential for preserving the flat beam profile in high-luminosity EIC operation.

INTRODUCTION

Intra-beam scattering (IBS) refers to a diffusion process arising from multiple small-angle Coulomb scatterings between particles within the same beam [1]. While small emittances are essential for achieving high luminosity, the high phase space density of hadron beams makes them particularly susceptible to IBS-induced emittance growth. As a result, IBS is a major performance limitation in hadron colliders.

The Electron-Ion Collider (EIC), currently under construction at Brookhaven National Laboratory (BNL), is designed to probe the internal structure of protons and nuclei with high precision [2]. To maximize luminosity, the EIC will be the first collider to employ flat hadron beams, where the vertical emittance is ten times smaller than the horizontal [3]. However, this flat-beam configuration presents new challenges. The EIC will operate above transition energy, where IBS drives unbounded growth in all transverse and longitudinal emittances in the absence of effective cooling. This makes it difficult to preserve the large aspect ratio between vertical and horizontal emittance.

High energy cooling is the most direct method to counteract IBS-induced diffusion. However, practical implementation of cooling for high energy hadron beams remains under development. Consequently, top energy cooling is not included in the current EIC baseline design.

According to existing IBS formalisms for Gaussian beams, diffusion primarily occurs in the horizontal and longitudinal planes due to the presence of horizontal dispersion. In contrast, vertical emittance growth is typically much smaller, as vertical dispersion is absent in a planar storage ring [4].

This paper focuses on the additional vertical emittance growth induced by the beam-beam interaction in the presence of IBS diffusion. The beam-beam force is highly nonlinear, and the hourglass effect introduces a dependence on the longitudinal position, making synchro-betatron resonances unavoidable [5]. We study how horizontal and longitudinal diffusion driven by IBS can couple into the vertical plane through these resonances, leading to vertical emittance growth and potential degradation of the flat-beam configuration.

IBS MODELING

We employ a custom-developed weak strong simulation code to study the interplay between beam-beam interaction and IBS diffusion. The strong electron beam is modeled as a rigid Gaussian distribution, while the weak proton beam is represented by dynamically evolving macro-particles subject to beam-beam kicks and external perturbations. The beam parameters used in the simulation are consistent with the EIC design values in [2]. Further details of the beam-beam simulation framework are described in [6].

In our simulations, particles are tracked for one million turns, corresponding to approximately 12.8 seconds. Over this timescale, it is reasonable to assume that the IBS growth and cooling times remain constant. Therefore, the IBS diffusion and potential cooling effects are modeled using a lumped element located at the interaction point (IP), analogous to the radiation damping and excitation models used in other beam beam simulation codes [7].

$$\lambda_u = \exp\left(-\frac{-T_{\text{rev}}}{\tau_u}\right), \tag{1}$$

$$u_{n+1} = \lambda_u u_n + R_u \sigma_u \sqrt{1-\lambda_u^2}. \tag{2}$$

By turning off cooling, the diffusion equations simplify further:

$$u_{n+1} = u_n + R_u \sigma_u \sqrt{1-\lambda_u^2} \approx u_n + \frac{T_{\text{rev}}}{\tau_u} \sigma_u R_u, \tag{3}$$

where $u = x, p_x, y, p_y, z, p_z$ represents the phase space coordinate, T_{rev} the revolution time, τ_u the characteristics time of IBS diffusion, σ_u the RMS size of corresponding dimension, and R_u the random number following standard Gaussian distribution.

Alternatively, the IBS kick can be applied solely to the momentum components of the particles, with the kick strength scaled proportionally to the local particle density, as proposed in [8]. This density-dependent model offers a more localized description of diffusion and will be benchmarked in future studies.

* Work supported by Brookhaven Science Associates, LLC under Contract No. DE-SC0012704 with the U.S. Department of Energy

† dxu@bnl.gov

Content from this work may be used under the terms of the CC BY 4.0 licence (© 2022). Any distribution of this work must maintain attribution to the author(s), title of the work, publisher, and DOI.

ISBN: 978-3-95450-261-5 ISSN: 2673-7000 doi: 10.18429/JACoW-NAPAC2025-WEXN01

ACCELERATOR WORKFORCE DEVELOPMENT*

C. Clarke†, M. Bai, J. Schmerge
SLAC National Accelerator Laboratory, Menlo Park, USA
P. Piot, W. Wittmer, Argonne National Laboratory, Lemont, USA
E. Arenholz, L. Lari, M. Minty, M. Palmer, Brookhaven National Laboratory, Upton, USA
A. Stolz, J. Wei, Facility for Rare Isotope Beams, Michigan State University, East Lansing, USA
S. Gourlay, M. Kaducak, S. Posen, A. Valishev
Fermi National Accelerator Laboratory, Batavia, USA
C.G.R. Geddes, L. Phair, Lawrence Berkeley National Laboratory, Berkeley, USA
B. Carlsten, Los Alamos National Laboratory, Los Alamos, USA
G. Johns, F. Pilat, Oak Ridge National Laboratory, Oak Ridge, USA
T.I. Meyer, Princeton Plasma Physics Laboratory, Princeton, USA
E. Pozdeyev, A. Seryi, V. Ziemann
Thomas Jefferson National Accelerator Facility, Newport News, USA

Abstract

Accelerator science has been hugely influential, contributing to physics Nobel Prize-winning research every three years. The U.S. Department of Energy (DOE) Office of Science invests in accelerator science to sustain America's excellence, and constructs and operates large-scale scientific user facilities to be vital tools of discovery.

Developing the next breakthroughs in accelerator science, and designing, building, and operating user facilities, requires a large, highly skilled workforce of accelerator scientists, engineers, and technical (AS&E) staff. Some portions of the AS&E workforce are best planned with a long-term, national perspective in mind.

A round table meeting, involving nine DOE National Laboratories and one Office of Science Nuclear Physics User Facility, assessed their current accelerator workforce projected workforce needs. Critical and endangered skill sets were identified and best practices for workforce development were shared. Future expansion of participation to universities and industry is planned for future round table meetings.

ACCELERATOR SCIENCE AND ENGINEERING WORKFORCE CENSUS AND 10-YEAR PROJECTION

A January 2025 census surveyed over 4,100 individuals in accelerator-specific occupations across ten laboratories, comprising nine Department of Energy (DOE) National Laboratories and the Office of Science Nuclear Physics User Facility Facility for Rare Isotope Beams (FRIB), at Michigan State University (MSU). This workforce operates 14 National User Facilities based on accelerators, is involved in the construction or upgrade of eight large accelerators, and performs accelerator technology research and development. It also includes some workforce required for the upgrade to and operations of the primary fusion experiment at Princeton Plasma Physics Laboratory (PPPL), recognizing that the accelerator workforce is increasingly involved in providing magnet and RF expertise to the growing fusion sector.

To support the census, the round table participants developed a taxonomy, based on the Common Occupational Classification System [1]. This defined unique accelerator occupations and specialisms in a hierarchal structure under broad categories such as engineer, scientist, and manager [2].

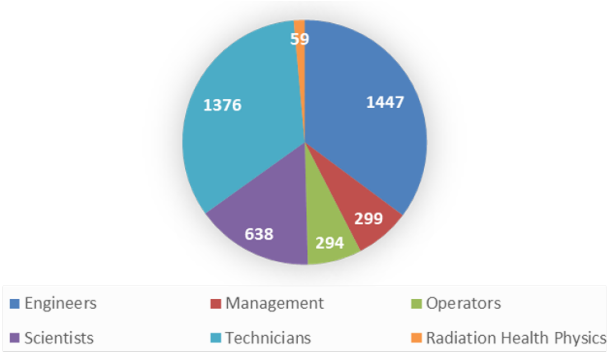


Figure 1: The breakdown of the accelerator workforce between the occupation classes.

The census shows that the accelerator workforce comprises approximately one-third engineers, one-third technicians, and one-sixth scientists, with the remainder in management, operations and health physics (Fig. 1). Electrical engineers (14% of the total accelerator workforce) and mechanical engineers (9%) engineers were prominent with key engineering specialisms including RF and pulsed power, instruments and controls, cryogenics, superconducting RF, safety credited controls engineering, vacuum engineering and accelerator systems integration. Scientists were predominantly physicists (11% of the total accelerator workforce) mainly specializing in accelerator and beam physics. Technicians were predominantly engineering technicians (17%)

* This material is based upon work supported by the U.S. Department of Energy, Office of Science.
† cclarke@slac.stanford.edu

Content from this work may be used under the terms of the CC BY 4.0 licence (© 2022). Any distribution of this work must maintain attribution to the author(s), title of the work, publisher, and DOI.

ISBN: 978-3-95450-261-5 ISSN: 2673-7000 doi: 10.18429/JACoW-NAPAC2025-WEAN02

STATUS OF PERMANENT MAGNET RADIATION RESILIENCY STUDIES AT CEBAF*

R. M. Bodenstein†, C. Decker, K. E. Deitrick, B. R. Gamage, J. F. Gubeli, D. Hamlette, M. Janak, K. Jordan, S. Lee, J. Meyers, B. Mosbrucker, I. Neththikumara, E. Nissen, V. Okey-Ejiowhor, J. Samari, S. Shriner, M. Smith, N. Wilson
Thomas Jefferson National Accelerator Facility, Newport News, VA, USA
S. J. Brooks, Brookhaven National Lab, Upton, NY, USA
S. Boogert, Cockcroft Institute, Daresbury, UK
W. Shields, Royal Holloway University London, Egham, UK
B. Shepherd, STFC, Daresbury, UK
L. Nevay, CERN, Meyrin, Switzerland

Content from this work may be used under the terms of the CC BY 4.0 licence (© 2022). Any distribution of this work must maintain attribution to the author(s), title of the work, publisher, and DOI.

Abstract

An ongoing investigation for the future of Jefferson Lab's Continuous Electron Beam Accelerator Facility (CEBAF) lies in upgrading its maximum nominal energy using Fixed-Field Alternating-gradient (FFA) technology for its recirculating arcs, using permanent magnets for the FFA arcs. A common concern among the community is the degradation of these permanent magnets during operation due to the radiation environment in which they will be present. This work, funded by a Laboratory Directed R&D grant, aims to measure the permanent magnet degradation in the CEBAF tunnel enclosure, and extrapolate to the energies expected from the upgrade. We present the latest results of this study, as well as plans moving forward.

BACKGROUND

The FFA@CEBAF energy upgrade feasibility study aims to increase the CEBAF electron beam energy from 12 GeV to over 20 GeV using Fixed Field, Alternating gradient (FFA) permanent magnet arcs [1]. The proposed permanent magnets have not yet been tested in a radiation environment comparable to that of CEBAF at these higher energies. To address this, samples of several magnet materials were placed in thirty different radiation regions of the operational 12 GeV CEBAF. Data from these tests, combined with simulations, external studies, and calculations, will inform assessments of radiation hardness and material lifetime for the FFA arcs.

This Laboratory Directed R&D (LDRD) project provides critical input into the FFA magnet design prior to manufacture and procurement. While previous studies have explored related issues [2], many have covered only limited portions of the relevant parameter space. Our work offers essential data on the performance of permanent magnets in conditions closely matching those expected in the upgraded CEBAF, contributing both to the FFA@CEBAF design effort and to broader research on radiation-induced magnet degradation.

* Authored by Jefferson Science Associates, LLC under U.S. DOE Contract No. DE-AC05-06OR23177. The research described in this work was conducted under the Laboratory Directed Research and Development Program at Thomas Jefferson National Accelerator Facility for the U.S. Department of Energy.

† ryanmb@jlab.org

METHODOLOGY

Hardware and Measurements

After placing dosimetry (optichromic rods and optically stimulated luminescence (OSL) area monitors) to map expected dose ranges throughout the CEBAF enclosure [3, 4], thirty locations were selected with suitable neutron and gamma radiation levels for this study. Site requirements included a range of doses, regular accessibility, and minimal risk of dosimeter saturation. In high-dose areas, locations near live-readback systems, such as the lab's Neutron Dose Rate Meter with Extended Capabilities (NDX) [5], were prioritized to provide dose estimates if passive dosimeters saturate. Calibration dosimetry was deployed with RF on but before beam operations to identify systematic offsets for error analysis.

Neodymium Iron Boron (NdFeB) and Samarium Cobalt (SmCo) are the primary permanent magnet materials used in accelerators. Brookhaven has assumed NdFeB grade N42EH for the prototype FFA magnet design [6]. For comparative studies, we selected N42EH, N52SH, SmCo33H, and SmCo35. Sample details and rationale are provided in [4].

Given the small expected changes between measurements, high-precision equipment is required. Point measurements use a Teslameter (Senis 3MH6 with a C-type, three-component Hall probe [7]) with 0.005% digital accuracy. For integrated field measurements, a precision Helmholtz coil system (Magnetic Instrumentation Model HCP with Rotator and Model 2130 Digital Fluxmeter [8]) is used. Both systems are mounted on portable lab carts for in-situ measurements during accelerator downtimes, ensuring no activated materials leave the enclosure.

To improve reproducibility, we developed 3D printed mounts for both the magnet samples and the Teslameter probe [9, 10]. These mounts ensure consistent sample placement and probe alignment, reducing human error and aiding data organization.

Demagnetization in Halbach assemblies is affected by interactions between magnet wedges [6, 11]. The key factor

ISBN: 978-3-95450-261-5 ISSN: 2673-7000 doi: 10.18429/JACoW-NAPAC2025-WEAN03

PMQ RADIATION TESTING AT THE NSLS-II IFE

T. Roff, R. Dos Santos Agusto, M. Johanson, M. Seegitz, T. Shaftan, S. Sharma,
T. Tanabe, R. Todd
Brookhaven National Laboratory, Upton, NY, USA

Content from this work may be used under the terms of the CC BY 4.0 licence (© 2022). Any distribution of this work must maintain attribution to the author(s), title of the work, publisher, and DOI.

Abstract

A new lattice for NSLS-II upgrade is likely to use high strength (> 100 T/m) Permanent Magnet Quadrupoles (PMQs). An ID beam exiting through these quadrupoles will place highly intense x-rays very close (~ 1mm) to the permanent-magnet material. In these tests the PMQs will be placed in the IFE (Instrumentation Front End) front end to assess any degradation of their field strengths and field quality due to long term exposure to an ID beam. The IFE beamline was recently commissioned at NSLS-II and is dedicated for testing mechanical properties of accelerator materials and components. The description of the source and experimental setup will be given.

INTRODUCTION

NSLS-II is based on the well-established double-bend achromat, commissioned with first light in 2014, it was the last synchrotron based on this lattice. Since then, new and upgraded synchrotrons have moved towards various forms of multi-bend achromats in an effort to reduce horizontal emittance. The goal of NSLSII-U is to select a lattice with world-leading emittance and brightness. To realize this goal, lattice designs using the complex-bend principle are being investigated. A promising lattice is the triple complex-bend achromat (TCBA) which utilizes three bending regions in each cell comprised of PMQ focusing and defocusing regions with magnetic aperture as little as 16mm. These constraints will impose significant radiation challenges to the permanent magnets from both synchrotron radiation at absorber and extraction regions as well as radiation generated from electron beam loss and gas interaction. Furthermore, the machine upgrade will be accompanied by a boost in beam energy from 3GeV to 4GeV and the anticipated vacuum chamber material will be thin ~2 mm wall aluminium providing little shielding. The small aperture (11 mm ID) vacuum chamber and close proximity (0.5 mm) to the permanent magnets, are seen in the recently completed full-scale complex-bend prototype (Fig. 1).

Demagnetization of Nd-Fe-B rare-earth magnets used within insertion devices have been observed at numerous third generation light sources such as ESRF and APS [1]. However, reduced field strength in magnets used to preserve electron orbit have far greater implications. Investing in such a design requires strong confidence in long term stability of the field strength and magnetic fidelity of the Sm_2Co_{17} permanent magnets. While it has been shown Sm-Co magnets have superior thermal stability and radiation resistance over Nd-Fe-B magnets, quantitative measurements are an important undertaking to gain confidence [2,3]. Installing the PMQ in close proximity to the circulating -e beam was not an option due to aperture and beam influence. However, the recently commissioned IFE at NSLSII is an excellent alternative to make long-term radiation hardness assessment of the PMQ prototype.

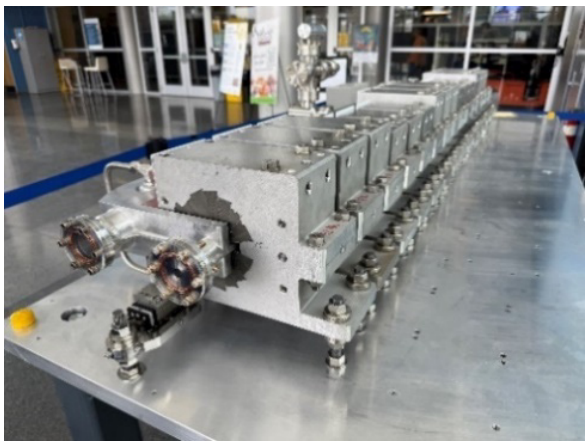


Figure 1: Full-scale complex-bend assembly.

EXPERIMENTAL

The IFE is dedicated to the study of accelerator materials and advanced diagnostics development for existing and future synchrotrons shown in Fig. 2.

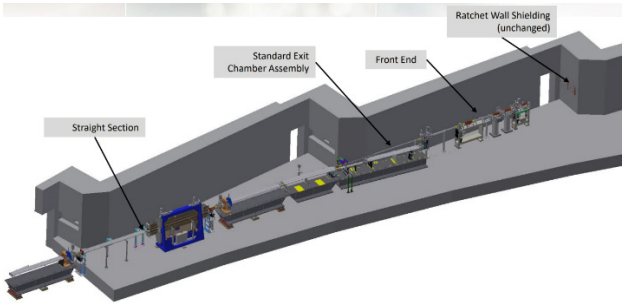


Figure 2: General arrangement of the IFE.

This tool, commissioned in 2023, has been used extensively to test and characterize thermal properties of CuCrZr absorber materials and configurations. The source, shown in Fig. 3, is the U68 Undulator acquired from Argonne National Lab and refurbished. It is capable of providing ~16 kW/mrad^2, with a total power of ~5.2 kW at 500 mA of beam. While low power compared to modern IDs, it is quite sufficient for thermal fatigue testing accelerator materials.

The beamline Instrumentation and Control system runs on EPICS architecture with comprehensive PV (process variable) monitoring and logging.

The IFE consists of a fixed mask, X-Y slits with prototype XBPMs, x-ray flag and endstation. There is also a fast-valve as well as drift pipe region(s) for additional testing

ISBN: 978-3-95450-261-5 ISSN: 2673-7000 doi: 10.18429/JACoW-NAPAC2025-WEYD01

A PLAN TO REVITALIZE THE DOMESTIC SUPERCONDUCTING RADIO-FREQUENCY INDUSTRY*

G. Ciovati† [1], M. Schuchman, Jefferson Lab, Newport News, VA, USA
W. Donaldson, Christopher Newport University, Newport News, VA, USA
A. Murokh, RadiaBeam Technologies, Santa Monica, CA, USA
M. Naughton, ATI Specialty Alloys & Components, Albany, OR, USA
D. Osha, C. F. Roark Welding & Engineering Co., Brownsburg, IN, USA
D. Packard, General Atomics, San Diego, CA, USA
J. Rathke, TechSource, Los Alamos, NM, USA
A. Todd, AMMTodd Consulting, Princeton Junction, NJ, USA
[1]also at Center for Accelerator Science, Old Dominion University, Norfolk, VA, USA

Abstract

Superconducting radio-frequency (SRF) cavities are essential building blocks of modern particle accelerators for scientific research, and they offer unique capabilities that could be transformative for commercial applications. Growth of the domestic SRF industry in North America has faced several challenges over the past decades, as most of the international demand for cavities was supplied by European vendors. This contribution provides a brief review of the domestic industrial vendor space, an outlook of the global demand for SRF cavities and an outline of the challenges leading to this supply chain deficiency. One of the main challenges towards establishing a robust domestic SRF industry has been the large uncertainty in the demand. Meanwhile, research and development activities to raise technical readiness of SRF accelerators for industrial use have continued and several potential markets are emerging that may offer a consistent and growing demand for SRF cavities. Finally, reasons and means of establishing and sustaining competitive domestic suppliers are described.

INTRODUCTION

Superconducting radio-frequency (SRF) cavities are essential components of modern particle accelerators. The standard material used for the fabrication of SRF cavities is high-purity, fine-grain Nb sheets. The cavities' shape and size depend largely on the operating frequency of the accelerator and the type of particles being accelerated. The target beam energy of the accelerator determines the number of cavities required.

A detailed description of the industrialization of SRF technology can be found in Ref. [1]. The industrialization of SRF technology in the U.S. has a long history, with several companies becoming interested in the technology in the past 30 years. However, there is currently no U.S. vendor capable of producing fully assembled, ready-to-test SRF cavities. As a result, government-sponsored SRF accelerator projects in the U.S. rely on European vendors for the cavity supply.

A 1-year project was carried out to review the history of domestic SRF industrial production, to identify new potential market opportunities for the SRF technology and to outline a business plan for establishing a robust, domestic industry supporting SRF technology demonstration and deployment. Information was gathered through:

- An extensive literature review.
- Bi-weekly meetings among the authors.
- A survey distributed to scientists, engineers, industry professionals, lab operations, procurement, and technology transfer professionals.
- A 1-day workshop held at Jefferson Lab on March 2024.
- Discovery and follow-up interviews conducted after the workshop.

This contribution represents a shortened version of a more extensive report which was submitted to the Department of Energy in January 2025 [2].

EVOLUTION OF DOMESTIC SRF INDUSTRY

Niobium Sheet Production

Currently, the two major suppliers of high-purity Nb sheets for SRF cavity production are Ningxia Orient Tantalum Industry Co. (OTIC), in China, and Tokyo Denkai in Japan. In the U.S., ATI Specialty Alloys & Components is a longstanding producer of high-purity Nb sheets. Increased competition from international sources, as well as increases in non-high-purity niobium and niobium-titanium demand related to superconducting industries, result in this U.S. vendor being priced out of the SRF Nb supplier competition, with unattractive lead times further straining its ability to provide high-purity Nb to U.S. projects. In the past, Fansteel and Cabot in the U.S. were suppliers of high-purity Nb in the 1990s, but they have both ceased operation. Supply chain issues related to the high-purity Nb sheets for SRF cavity fabrication were clearly identified in a recent DOE report [3].

* Work supported by the U.S. DOE Office of Accelerator R&D and Production through Jefferson Science Associates, LLC under U.S. DOE Contract No. DE-AC05-06OR23177.

† gciovati@jlab.org

Content from this work may be used under the terms of the CC BY 4.0 licence (© 2022). Any distribution of this work must maintain attribution to the author(s), title of the work, publisher, and DOI.

ISBN: 978-3-95450-261-5 ISSN: 2673-7000 doi: 10.18429/JACoW-NAPAC2025-WEYD02

ACCELERATOR-BASED MEDICAL ISOTOPE PRODUCTION: AN OVERVIEW OF EMERGING TRENDS AND NOVEL INITIATIVES

K. Gagnon†, Nusano, Salt Lake City, UT, USA

Abstract

Recent advances in drug development and radionuclide research have notably expanded the role of nuclear medicine in treating cancer over the past decade. Throughout such research and development efforts, the list of drug moieties and cancer types under investigation is paralleled by a similarly expansive list of radionuclides. This is because the suitability of a radionuclide for a therapeutic radiopharmaceutical application will depend on many factors including, but not limited to, the decay mode (e.g. α- vs β-emitter), the particle emission range, the matching of its half-life to the pharmacokinetics of the drug, and the co-emission of gamma rays of appropriate energy for imaging. Moreover, the successful adoption into clinical practice hinges on sustained, reliable, and cost-effective access to these radionuclides – a task which is not trivial. To this end, this work provides an overview of emerging trends in radionuclides, alongside novel initiatives for accelerator-based production strategies.

INTRODUCTION & NUCLIDE TRENDS

The application of radionuclides to theranostics, i.e. the combination of diagnostics and therapeutic nuclides emerged in the 1940s using radioiodine for imaging and treatment of thyroid cancer [1]. In the past decade theranostics has, however, made an inflection point with significant increase in the research and clinical implementation of radionuclide theranostic pairs for several clinical indications. Two notable examples include the approvals of ^{68}Ga- and ^{177}Lu-based radiopharmaceuticals for diagnosis and therapy (respectively) of neuroendocrine tumors and prostate cancer [2, 3]. Clinical trials with ^{68}Ga and ^{177}Lu expand, however, beyond these applications with the numbers of clinical trials using these nuclides increasing ~5 and 10-fold, respectively, in the past decade (Fig. 1).

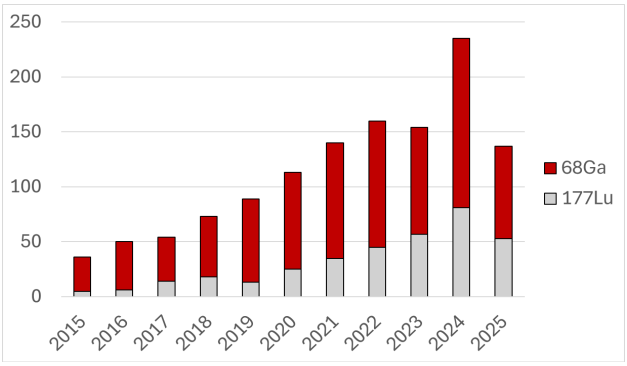


Figure 1: Number of clinical trials by starting year as reported on clinicaltrials.gov [4] for ^{68}Ga and ^{177}Lu search terms (accessed August 3, 2025).

^{68}Ga and ^{177}Lu are not, however, "magic bullet" nuclides for all applications. Instead, the decay characteristics of the nuclides must be considered in conjunction with the application (e.g. tracer kinetics, physical tumor characteristics, targeting properties, radiolabeling strategies, etc.). As such, and accompanied by new technologies for nuclide production, it is of no surprise that the "menu" of candidate nuclides of interest is ever-expanding. To this end, Fig. 2 highlights the growth of clinical trials using emerging radionuclides, while Fig. 3 summarizes select decay and chemical characteristics of these nuclides.

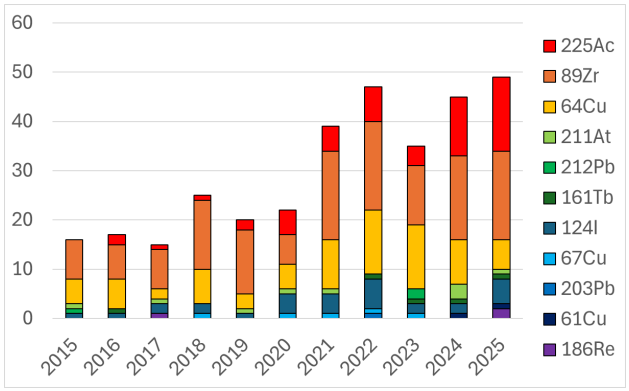


Figure 2: Number of clinical trials by starting year as reported on `clinicaltrials.gov` [4] for select theranostic nuclide search terms (accessed August 3, 2025).

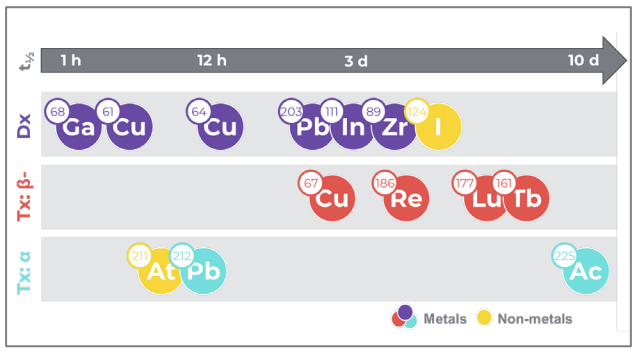


Figure 3: Properties of select theranostic nuclides based on half-life ($t_{½}$), diagnostic (Dx) or therapeutic (Tx) primary application, α- vs β-emitter, and considerations for radiolabeling (e.g. metal/non-metal).

NUCLIDE PRODUCTION

Translating this growing menu of nuclides of interest from research into widespread use requires a reliable and cost-effective supply chain of these nuclides. Although select nuclides (e.g. ^{177}Lu) require a nuclear reactor for large-scale production, many nuclides (i.e. the majority outlined in Fig. 2) require an accelerator.

† katie.gagnon@nusano.com

Content from this work may be used under the terms of the CC BY 4.0 licence (© 2022). Any distribution of this work must maintain attribution to the author(s), title of the work, publisher, and DOI.

ISBN: 978-3-95450-261-5 ISSN: 2673-7000 doi: 10.18429/JACoW-NAPAC2025-WEYN01

MACHINE LEARNING ENHANCED DETERMINISTIC FEEDBACK CONTROLS IN LASERS AND ACCELERATORS*

D. Wang†, Q. Du, A. Amodio, C. Berger, H. Tsai, S. Barber,
J. van Tilborg, A. Picksley, Z. Eisentraut, N. R. Vora,
M. Logantha, T. Zhou, A. Gonsalves, R. Wilcox
Lawrence Berkeley National Laboratory, Berkeley, CA, USA

Content from this work may be used under the terms of the CC BY 4.0 licence (© 2022). Any distribution of this work must maintain attribution to the author(s), title of the work, publisher, and DOI.

Abstract

Modern laser and accelerator systems require fast, precise, and scalable multi-input multi-output (MIMO) feedback control. As performance demands grow, particularly in high-repetition-rate and nonlinear regimes, traditional strategies face increasing limitations in speed and adaptability. This paper summarizes two application cases of machine learning (ML)-enhanced deterministic feedback control. In both cases, ML models trained on experimental or simulated data provide rapid predictions to support real-time decision-making. Integrated with conventional feedback loops, these models improve response time and robustness across operating conditions. At Lawrence Berkeley National Laboratory, ML feedback enabled the first preemptive pointing stabilization at the BELLA Petawatt beamline, achieving a ~60% reduction in jitter, and reduced response time in a coherent beam combining system by nearly an order of magnitude. These results show that ML can increase speed, stability, and adaptability without compromising determinism, opening new opportunities for intelligent control in next-generation facilities.

INTRODUCTION

High-energy particle accelerators and high-power laser systems are among the most complex scientific instruments in use today, supporting research from fundamental physics to materials science. These systems are challenging to control due to tight tolerance requirements, numerous tunable parameters, environmental disturbances, and nonlinear, cross-coupled responses [1, 2]. Feedback control is widely used to maintain stability and optimize performance [3]. In this work, we present a concise summary of two ML-enhanced deterministic feedback applications, laser pointing stabilization at the BELLA Petawatt beamline [4] and coherent beam combining (CBC) of fiber lasers [5–7], highlighting key methods and results without repeating all details from the original publications.

Feedback control is a foundational technique widely employed in both accelerator and laser systems [3]. As illustrated in Fig. 1, a typical feedback loop consists of sensors that provide measurements of system behavior, a controller that adjusts system variables in response, and a feedback algorithm, effectively the "brain" of the loop, that interprets the sensor data to compute correction signals. The goal is to maintain system stability or optimize performance despite disturbances and drift. Depending on the application, the measured signals can include laser beam pointing [4, 8], spatial diffraction patterns [5–7], magnetic quench indicators, RF waveforms, or accelerator beam trajectories derived from beam-position monitors.

Traditionally, feedback algorithms have relied on two broad approaches: model-based control, where a physics-based reverse model is used to compute corrections [9], and black-box methods such as dither-and-search, which iteratively optimize system performance without explicit models [10, 11]. In this work, we extend these paradigms by integrating data-driven machine learning (ML) models into the feedback loop. These ML-enhanced algorithms maintain deterministic behavior while enabling faster control [12]. We demonstrate this approach in two challenging applications: real-time laser alignment and coherent laser beam combining, showing how ML can improve precision and response time beyond the limits of conventional methods.

ML-ENHANCED REAL-TIME CONTROL IN LASER POINTING STABILIZATION AT BELLA PETAWATT/1Hz BEAMLINE

Requirements and Control Challenges

High-power lasers have enabled major advances in areas such as particle acceleration, advanced imaging, and future energy technologies. Among these, laser-plasma accelerators (LPAs) stand out for their potential to significantly reduce the size and cost of high-energy accelerators. However, LPAs are extremely sensitive to laser pointing stability, micron-scale shifts in the laser axis can cause substantial errors in the electron beam trajectory. For future applications like X-ray free-electron lasers or collider-grade LPAs, pointing stability on the order of microradians is required.

Passive stabilization techniques help mitigate slow drifts but are insufficient on their own, as thermal effects, mechanical vibrations, and other environmental factors can introduce long-term instabilities. Active feedback systems are needed to compensate for these disturbances, but they are fundamentally limited by the repetition rate of the high-power laser system, which is often too low to support rapid corrections.

* This work is supported by the Office of Science, Office of High Energy Physics, of the U.S. Department of Energy, and the Laboratory Directed Research and Development Program of Lawrence Berkeley National Laboratory under contract no. DE-AC02-05CH11231.

† dwang2@lbl.gov

ISBN: 978-3-95450-261-5 ISSN: 2673-7000 doi: 10.18429/JACoW-NAPAC2025-WEYN02

SAFE EXTREMUM SEEKING FOR REAL-TIME ADAPTIVE ACCELERATOR CONTROL*

A. Williams†, A. Scheinker ‡, Los Alamos National Laboratory, Los Alamos, NM, USA

Content from this work may be used under the terms of the CC BY 4.0 licence (© 2022). Any distribution of this work must maintain attribution to the author(s), title of the work, publisher, and DOI.

Abstract

This paper presents Safe Extremum Seeking (Safe ES), a robust n-dimensional adaptive control method, applied to automatic tuning and optimization tasks of accelerators while guaranteeing that the system remains within safe operating conditions. A key strength of Safe ES is its ability to handle safety measures that are analytically unknown. For instance, the algorithm can adaptively tune quadrupole magnets to achieve a desired beam profile while maintaining safety by keeping beam losses below a user-defined threshold.

The presentation provides a comprehensive technical overview of this optimization technique, highlighting its theoretical foundations and practical applications. It includes simulation studies demonstrating its effectiveness for accelerator systems, as well as results from an in-hardware demonstration conducted on the LANSCE accelerator at LANL. Also, the talk explores how Safe ES can be integrated with generative machine learning models to enable adaptive machine learning.

INTRODUCTION

Particle accelerators present a uniquely difficult challenge for both control and estimation. On the control side, performance must be optimized in real time on systems with thousands of coupled components, all subject to slow drift, high dimensionality, and unknown dynamics. At the same time, safety is critical—beam loss not only reduces performance, but can cause irreversible damage to equipment and create hazardous conditions for maintenance. On the estimation side, diagnostic measurements that fully characterize the six-dimensional (6D) phase space of charged particle beams are either invasive (destructive to the beam) or so slow as to be unusable in feedback. These two challenges—fast, safe control and non-invasive high-dimensional inference—demand adaptive methods that can operate directly on measured signals, without relying on analytical models or full state access.

Extremum seeking (ES) methods, see Ref. [1] for a general review, particularly in their recent constrained forms, offer a powerful solution to this dual problem. A constrained ES algorithm, Safe ES, uses a control barrier function (CBF)-inspired law to enforce safety constraints while optimizing unknown objectives in real time, using only measurements [2–4]. These methods have been applied experimentally on live accelerator systems at LANSCE, performing multivariable tuning of magnets while maintaining beam current constraints. Beyond control, Safe ES has also inspired new methods for estimation, including a physics-informed neural networks (PINNs) [5] method and an adaptive latent space tuning method for generative models [6], utilizing a bounded form of ES [7]. Recent advances even extend this paradigm to diffusion-based generative AI, using conditional latent diffusion to infer full 2D projections of a beam's 6D phase space from simple non-invasive diagnostics like beam current monitors [8]. This paper surveys reviews advances in constrained forms of ES and ES-inspired methods for accelerator control and machine learning, highlighting theory and experiment.

A variety of model-free, online optimization methods have been successfully applied to real particle accelerators. These include Bayesian optimization approaches for maximizing beam performance using surrogate models [9], as well as safe variants designed to operate under strict machine protection constraints [10]. Evolutionary algorithms, such as genetic algorithms combined with dimensionality reduction, have been used for multi-objective tuning in storage rings [11], while local direct-search methods like robust conjugate direction search (RCDS) have been deployed for real-time luminosity optimization [12]. More recently, reinforcement learning has been explored for autonomous accelerator control, with agents trained in high-fidelity simulations and targeted for deployment on hardware [13]. These methods represent a rich and growing body of work focused on real-time. Our approach contributes to this area by introducing a safety-aware, model-free optimization technique that operates entirely on live measurements. We also show use cases in which this technique can be combined with physics-informed models and generative machine learning for estimation.

SAFE EXTREMUM SEEKING

We begin our discussion with the work of Ref. [2]. This work, termed *Safe ES*, introduces an ES algorithm that solves the constrained optimization problem:

$$\min_{\theta\in\mathbb{R}^n} J(\theta) \quad \text{subject to} \quad h(\theta) \geq 0, \tag{1}$$

where both the objective $J(\theta) : \mathbb{R}^n \to \mathbb{R}$ and the CBF $h(\theta) : \mathbb{R}^n \to \mathbb{R}$, are unknown and only measurable, with unknown gradients. The parameters available to tune are given by θ.

To enforce safety during optimization, the algorithm incorporates a quadratic program (QP)-style CBF filter into the parameter update law. The dynamics of the idealized

* This work was supported by the Los Alamos National Laboratory (LANL) LDRD Program Directed Research (DR) project 20220074DR.

† awilliams@lanl.gov

‡ ascheink@lanl.gov

ISBN: 978-3-95450-261-5 ISSN: 2673-7000 doi: 10.18429/JACoW-NAPAC2025-WEYN03

MEASUREMENTS OF ULTRALOW EMITTANCE AND TRANSVERSE COHERENCE AT THE ADVANCED PHOTON SOURCE UPGRADE STORAGE RING*

K. P. Wootton†, X. Shi, Argonne National Laboratory, Lemont, IL, USA

Content from this work may be used under the terms of the CC BY 4.0 licence (© 2022). Any distribution of this work must maintain attribution to the author(s), title of the work, publisher, and DOI.

Abstract

Recent electron storage ring light sources continue to push towards increasingly lower electron beam sizes. In the present work, we report on the measurements of the electron beam emittance (sub 50 pm rad) achieved at the Advanced Photon Source Upgrade (APS–U), as well as its standing among electron storage ring light sources. We include a brief status update on the beam size monitor beamline at the APS–U. We conclude with a survey of measurement techniques and recent results across multiple laboratories.

INTRODUCTION

The Advanced Photon Source Upgrade (APS-U) project is a major upgrade to the Advanced Photon Source synchrotron light source facility [1]. With the completion of installation and commissioning of the electron storage ring [2], the goal of the present work was the characterisation of the electron beam size and emittance in the storage ring.

In the present work, we outline three measurement techniques performed during different stages of accelerator commissioning of the APS-U electron storage ring. We describe measurements using a white-beam pinhole camera, monochromatic hard X-ray coherence, and monochromatic soft X-ray undulator radiation characterisation. We outline the status of the beam size monitor beamline, and compare with other recent results from similar laboratories.

EXPERIMENTS

X-ray Pinhole Camera Measurements

During commissioning of the storage ring for the APS-U, the nominal 38-AM beam size monitor beamline was unavailable. The principal long-term purpose of the 35-BM X-ray beamline configuration is to preserve X-ray beam transport from the 35-BM-A through to 35-BM-C hutches, for use with the bunch purity monitor diagnostic [3, 4]. However the beamline can also be used as-configured for an X-ray pinhole camera for beam size measurements. We propose to measure the electron beam size using a polychromatic X-ray pinhole camera at the 35-BM beamline [5].

In the present work, we outline the components of the pinhole camera used to measure electron beam size at 35-BM [6]. We summarise the results of beam size measurements, and calculate a value for the horizontal emittance.

* Work was supported by the U.S. DOE Office of Science-Basic Energy Sciences, under Contract No. DEAC02-06CH11357.

† kwootton@anl.gov

The root-mean-square (RMS) transverse dimension of the electron beam σ_{i} can be expressed by:

$$\sigma_{\mathrm{i}} = \sqrt{\beta_{\mathrm{i}}\varepsilon_{\mathrm{i}} + \eta_{\mathrm{i}}^2 \left(\frac{\Delta E}{E}\right)^2}, \quad (1)$$

where β_{i} is the beta function, ε_{i} the emittance, η_{i} the dispersion in the coordinate plane i, and $\frac{\Delta E}{E}$ the electron beam energy spread. Parameters of the electron beam and pinhole camera in the horizontal plane are summarised in Table 1.

Table 1: Design 35-BM Pinhole Camera Parameters

Parameter	Symbol	Value
Beta function	β_x	0.84 m
Emittance	ε_x	42 pm rad
Energy spread	$\frac{\Delta E}{E}$	0.156%
Dispersion	η_x	3.67 mm
Beam size (source)	σ_x	8.3 µm
Pinhole magnification	M	0.832
Beam size (scintillator)	Σ_x	6.9 µm

Four blades of white-beam slits ($z = 25.0$ m) can be closed to form a rectangular pinhole aperture. A scintillator and optical microscope can be positioned near the end of the beamline ($z = 45.8$ m) in order to image the electron beam in the APS-U storage ring with an X-ray pinhole magnification $20.8/25.0 = 0.832$.

We anticipate that the spatial resolution needed to image an X-ray spot size of Gaussian distribution $\Sigma_x = 6.9\,\mu$m is challenging, but not beyond technical feasibility. For the temporary pinhole camera at 35-BM, we used an Optique Peter white beam x-ray optical microscope system. The key components of the optical microscope included:

- Thin Lutetium Aluminium Garnet - LuAG(Ce) scintillator crystal (~25 µm),
- Optique Peter long working-distance microscope,
- FLIR Blackfly S Digital Camera.

Using this FLIR digital camera (4.8 µm detector pixel pitch), we measured the effective pixel size at the position of the scintillator to be 0.47 µm in both the horizontal and vertical directions.

During early commissioning in 2024, the smallest beam size was measured on May 31, 2024. The accelerator was operated in swap-out mode, maintaining a stored beam current of ~30 mA. The measured and fitted beam profile is plotted

ISBN: 978-3-95450-261-5 ISSN: 2673-7000 doi: 10.18429/JACoW-NAPAC2025-WEZN01

DESIGN PROGRESS FOR THE 22 GeV CEBAF ENERGY UPGRADE*

E. A. Nissen†, R. M. Bodenstein, S.A. Bogacz, A.M. Coxe, K.E. Deitrick, B. R. Gamage, R. Kazimi, D. Khan, I. Neththikumara, S. Ogur, Y. R. Roblin, R. Ruber, T. Satogata, N. Sereno, A. Seryi, Thomas Jefferson National Accelerator Facility, Newport News, VA, USA
J.S. Berg, S.J. Brooks, D. Trbojevic, Brookhaven National Laboratory, Brookhaven, NY, USA
V.S. Morozov, Oak Ridge National Laboratory, Oak Ridge, TN, USA
G. H. Hoffstaetter, Cornell University, Ithaca, NY, USA

Content from this work may be used under the terms of the CC BY 4.0 licence (© 2022). Any distribution of this work must maintain attribution to the author(s), title of the work, publisher, and DOI.

Abstract

In this work we examine the progress made in the design of the proposed FFA upgrade to the Continuous Electron Beam Accelerator Facility (CEBAF). This proposed upgrade will double the number of passes through the two linacs by replacing the two highest energy arcs with new Fixed Field Alternating Gradient (FFA) arcs, roughly doubling the energy. These FFA arcs will use permanent magnets in a Halbach configuration to shape their fields. The design involves new optics for the linacs and remaining electromagnetic arcs, as well as new electromagnetic separators. These feed into the permanent magnet FFA arcs. We also report on ongoing studies of the dynamics of the beams, and an experiment to measure the effects of radiation on the permanent magnets.

THE CEBAF ACCELERATOR

Since 1994 Jefferson lab has operated the Continuous Electron Beam Accelerator Facility (CEBAF) [1]. CEBAF is a five-pass recirculating linac, which initially had a top energy of 6 GeV. These 6 GeV electron beams would then collide with fixed targets in three experimental halls, A, B, and C. Starting in 2015 the lab doubled its top energy to 12.1 GeV by adding 10 new cryomodules (five in each linac) which added an extra 1 GeV in acceleration per pass [2]. An experimental hall was also added with an extra half pass of acceleration. This upgrade was completed in 2017 and has been operating since. A diagram of CEBAF is shown in Fig. 1.

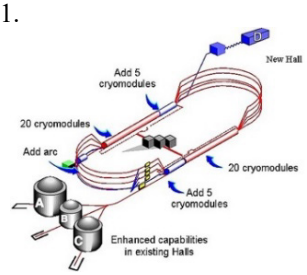


Figure 1: CEBAF after the 12 GeV upgrade.

Looking forward the lab is investigating future upgrades to CEBAF, the two we are focusing on are positrons and an energy upgrade [3,4,5].

* This material is based upon work supported by the U.S. Department of Energy, Office of Science, Office of Nuclear Physics under contract DE-AC05-06OR23177. Some of the work described in this paper was conducted under the Laboratory Directed Research and Development Program at Thomas Jefferson National Accelerator Facility for the U.S. Department of Energy.

† nissen@jlab.org

THE 22 GEV UPGRADE

The previous energy upgrade involved adding more acceleration capacity to the linacs of CEBAF, this was possible since there was empty space already planned in for future expansion. Increasing the amount of superconducting acceleration also required an increase in the cryogenic capacity of the lab as a whole. Due to the expense of adding more acceleration, the current plan for an energy upgrade will increase the number of passes through each linac, instead of increasing the acceleration of each linac.

In order to fit five additional passes into the existing tunnel we plan to replace the highest energy arcs on each side with Fixed Field Alternating Gradient (FFA) arcs each of which will be able to accommodate 6 passes of beam within a single beam pipe. FFAs date back to the 1950s [6], and there have been examples that are rings [7] and that are recirculating linacs [8].

In order to make sure the highest 6 passes through the FFA arcs have the proper beam parameters, we are adding horizontal splitters that will adjust the envelope functions, pathlength, and M_{56} to the proper values. We will also be adding an FFA based transition section to bring the beams back to being colinear as they enter the linacs. We also have initial designs for an extraction system to send the beam to the various halls, as well as a new injector that would make use of our existing Low Energy Recirculator Facility (LERF) [9]. A block diagram of the current upgrade baseline is shown in Fig. 2.

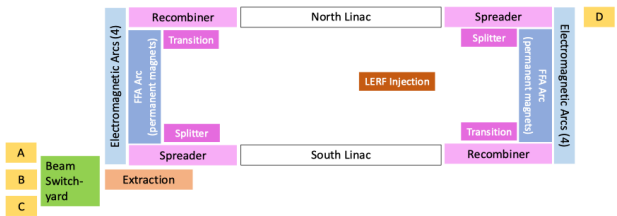


Figure 2: The plan for the proposed upgrade of CEBAF. Darker colors denote new additions to existing CEBAF infrastructure.

Linac Optics

While the current plan for the 22 GeV upgrade is to use the same accelerating cavities that are currently used in CEBAF, the optics will have to change. The lattice that keeps the beam focused and under control during acceleration tends to have diminishing effectiveness with each subsequent pass the electron beam takes, in the current 12 GeV machine the final pass almost acts like a drift from

ISBN: 978-3-95450-261-5 ISSN: 2673-7000 doi: 10.18429/JACoW-NAPAC2025-WECD01

SIMULATIONS OF IBS THROUGH ELECTRIC FIELD FLUCTUATIONS*

S. Kladov†, Y.-K. Kim, University of Chicago, Chicago, IL, USA
G. Stupakov, Z. Huang, SLAC National Accelerator Laboratory, Menlo Park, CA, USA

Content from this work may be used under the terms of the CC BY 4.0 licence (© 2022). Any distribution of this work must maintain attribution to the author(s), title of the work, publisher, and DOI.

Abstract

We present a study of intra-beam scattering (IBS) in high-brightness electron beams, incorporating a recent theory that accounts for enhanced temporal correlations of electric field fluctuations. These correlations, absent in conventional binary-collision models, arise from the periodic betatron motion of particles within the beam. To enable direct verification of the theoretical calculations, we perform simulations in a computer code specifically written for that purpose. In the code, the particle distribution is preserved over time, ensuring conditions compatible with theoretical assumptions, and the IBS is neatly separated from the conventional Space Charge (SC) effect.

The simulations, benchmarked against an exactly solvable case of an infinite isotropic uniform plasma, show good agreement with both uncorrelated models, such as Piwinski's, and the new correlation-based theory, across various bunch distributions and dynamical regimes. This validates the simulation approach and highlights the role of time-correlated fields in accurate IBS modeling.

INTRODUCTION

Space Charge (SC) is the effect of Coulomb's forces acting on the particles in a bunch. These forces are considered to be produced from a smooth distribution function, not taking the discreetness of particles into account. The effect of the difference between the full Coulomb's fields and the fields from a smooth function is called the Intra Beam Scattering (IBS). The IBS has been first studied by Piwinski [1] and by Bjorken and Mtingwa [2]. Estimates of IBS for an x-ray FEL driver can be found in Ref. [3].

All these papers consider the IBS as a result of binary collisions between the particles in the beam, averaged by time. Recently, a new treatment was proposed in Ref. [4] that derives the IBS from the interaction of particles with the fluctuating electromagnetic fields in the beam on the microscopic scales. For perfect periodic orbits with no longitudinal motion, it was obtained that the energy spread squared σ_η^2 grows quadratically with time. And if the longitudinal motion is included, the IBS growth rate was shown to saturate to a value higher than the Piwinski predictions.

In this paper, we carry out simulations of IBS within the framework of the fluctuating fields using a computer code written for that purpose. To test the code, we compare the results of our simulations for a uniform plasma with the plasma collision integral and find a good agreement. We also compare our simulations with the Piwinski formula, and the new theory from Ref. [4].

* Work supported by USDOE, Office of Science AC02-76SF00515.
† kladov@uchicago.edu

THEORY

In this paper, we study only the axially symmetrical beams of electrons and positrons, and are interested only in the energy spread growth $\mathrm{d}\sigma_\eta^2/\mathrm{d}t$. Here η denotes the relative energy deviation of the particle and σ_η is the rms energy spread in the beam. For simplicity, in this paper we present all the results in the beam frame, using the longitudinal velocity spread $\sigma_v' = c\,\sigma_\eta$, where prime means the parameter in the moving frame and v is the longitudinal velocity. The primes are omitted in what follows. The theory results are transformed accordingly. The conventional Piwinski theory for a three dimensional gaussian spatial distribution and two dimensional gaussian velocity distribution (with no longitudinal velocity spread at $t = 0$) gives [3]

$$\sigma_v^2(t) = t\,\frac{r_e^2\,c^4\,N\,\Lambda}{4\,\sigma_x^2\,\sigma_z\,\sigma_{v_x}}, \tag{1}$$

where N is the number of particles in the bunch, r_e is the classical electron radius, σ_x and σ_z are the rms bunch transverse and longitudinal sizes, σ_{v_x} is the rms transverse velocity spread, and $\Lambda = \ln(r_{\max}/r_{\min})$ is the Coulomb's logarithm. The $r_{\max}$ and $r_{\min}$ are the maximum and minimum impact parameters in a single scattering event [1].

For simplicity of the analysis and comparison with simulations we define a dimensionless parameter A with the meaning of the average growth rate across the time period t:

$$\sigma_v^2(t) = t\,A(t)\,\frac{r_e^2\,c^4\,N}{\sigma_x^2\,\sigma_z\,\sigma_{v_x}}. \tag{2}$$

For the case defined above, $A(t) = \frac{1}{4}\,\Lambda$. It is straightforward to see that the function $A(t)$ is a constant for all the averaging theories. For the same bunch, but with uniform longitudinal distribution instead of gaussian, $A(t) = (\sqrt{\pi}/4\sqrt{3})\,\Lambda$ [5].

Betatron Motion

Equation (35) in Ref. [4] gives a general answer for a beam with gaussian distributions by x, v_x, y, v_y and v (in this paper it is longitudinal velocity), and infinite uniform distribution by z. Particles execute transverse betatron motion (constant focusing) and uniform longitudinal motion.

$$A(\phi) = \int_0^\infty \mathrm{d}\kappa \int_0^\infty \mathrm{d}\kappa' \int_0^\phi \mathrm{d}\phi_2 \int_0^{\phi_2} \mathrm{d}\phi_1 \times \int_{-\infty}^\infty \mathrm{d}q_z F(\kappa, \kappa', \phi_1, q_z), \tag{3}$$

with

$$F = \frac{2\kappa\kappa'}{\pi\phi\sqrt{3}} \exp\left[-(\kappa^2+\kappa'^2)^2\right] I_0(2\kappa\kappa'\cos\phi_1) \times \frac{q_z^2 \exp\left[-\tau\,q_z^2\,\phi^2\right]}{(\kappa^2+q_z^2)(\kappa'^2+q_z^2)},$$

ISBN: 978-3-95450-261-5 ISSN: 2673-7000 doi: 10.18429/JACoW-NAPAC2025-WECD02

COMPUTING SPIN-POLARIZATION IN ELECTRON STORAGE RINGS BY MACHINE LEARNING VIA RANDOMIZED FOURIER NEURAL NETWORKS*

J. M. Agudelo Velez†, K. Heinemann‡, M. Motamed§, J.A. Ellison¶,
The University of New Mexico, Albuquerque, NM, USA

Abstract

Our work addresses the challenge of estimating spin polarization in high-energy electron and positron storage rings, such as the Electron Storage Ring (ESR) of the Electron-Ion Collider (EIC) at Brookhaven National Lab (BNL) and those in the electron/positron Future Circular Collider (FCC-ee) at CERN. We model the spin and orbital motion of particle bunches using the recently introduced spin-orbit Fokker-Planck (SOFP) equation, a linear time-evolution partial differential equation (PDE). In this paper, we propose a novel machine learning (ML) approach leveraging a randomized Fourier neural network (rFNN) framework, specifically designed to solve linear PDEs. We will discuss the SOFP highlight its relevance to spin polarization studies, and share preliminary results demonstrating the network's performance on the Poisson problem.

INTRODUCTION

In this article, we present our work in two parts: The modeling of orbital and spin dynamics of electron beams via the associated Ito stochastic differential equation (SDE) system of the SOFP in lab frame (LF) from [1], and the development of rFNNs for PDEs as applied to the multidimensional Poisson problem. The long-term goal of our project is to apply the rFNN theory to general Fokker-Planck (FP) systems and apply it to our SOFP in the beam frame (BF), where the BF is defined in [2]. It is thus useful to view our project as two independent problems, one in beam dynamics and the other in ML, with the understanding that we will eventually apply the theory from the latter to the former.

With regard to the beam dynamics portion of our project, the history of our method begins in 1975 with the derivation of Debenev and Kondratenko's (DK) orbital FP and Bloch equations in [3] for phase-space and polarization densities, respectively. This comprehensive model takes into account the Thomas-BMT spin precession effect, the Sokolov-Ternov effect along with the Baier-Katkov correction, and the kinetic polarization and radiative depolarization effects. Though comprehensive, the complexity of the orbital FP and Bloch equations makes it so that in the fifty years since the models introduction, it has yet to be fully implemented. A workaround reduced Bloch model has been implemented; it however only accounts for the radiative depolarization effect. Hence a full realization of the DK model is desired, as it will give a more precise estimate for the phase-space and polarization densities for high-energy accelerators. Fortunately, via the work done in [4] and [1], we may replace the problem of solving the two PDEs from [3] by solving the SOFP from [1]. The SOFP has an associated system of SDEs which we transform into the BF defined in [2].

From the standpoint of accelerator physics, the motivation of our project is to solve the SOFP. We aim to extend the theory developed in [5] on rFNNs to linear time evolution PDEs, such as the SOFP. This task is also motivated from the standpoint of applied mathematics where we seek to leverage the qualities of the rFNN approach in [5] to ideally build a serviceable solver for the FP. Specifically, we highlight a training methodology unrelated to traditional global optimization schemes seen in standard feed-forward networks. This is a "block-by-block" training approach that theoretically guarantees convergence depending on the type of target function.

ELECTRON BEAM DYNAMICS

The two PDEs seen in [3] have been transformed to the single 9-D SOFP in LF, as discussed in detail in [6]. It is preferable to analyze the SOFP in a BF based on the Frenet-Serret formalism on a design orbit, where analysis is easier and effects are more clearly seen, as is standard in accelerator physics. In addition, transforming SDE systems like ours is more convenient than transforming the corresponding FP equation. Thus, we move from the LF SOFP to the equivalent LF SDE system (written below) and do the transformations to BF. The BF SOFP follows immediately from the BF SDE and is ready for our analytical and numerical studies. We note that the LF SDE is transformed through several steps, as was outlined in the Handbook article for the orbital dynamics [2]. What we do now is an extension to include the spin dynamics. Further details into these transformations may be found in the slides accompanying this paper in these proceedings.

The LF System of SDEs

In the LF, the SDE system for position $\vec{R}$, momentum $\vec{\Pi}$, and spin $\vec{\Xi}$ of a single particle are given by Eq. (1)-(3) where $Q = (\vec{R}, \vec{\Pi})$. Here e, m denote the charge and mass of the electron, γ is the Lorenz factor, $\vec{E}, \vec{B}$ are the electric and magnetic fields due to the accelerator, $\vec{\mathcal{F}}_{rad}$ encompasses the radiation forces on the electron, $\vec{\mathcal{B}}_{\vec{\pi}}, \vec{\mathcal{B}}_{\vec{\xi}}$ together give kinetic polarization. $\vec{\Omega}$ gives the Thomas-BMT effect and

* Work supported by U.S. Department of Energy, Office of Science, under Award Numbers DE-SC0018008 and DE-SC0025476

† joseagudelo@unm.edu
‡ heineman@math.unm.edu
§ motamed@unm.edu
¶ ellison@math.unm.edu

Content from this work may be used under the terms of the CC BY 4.0 licence (© 2022). Any distribution of this work must maintain attribution to the author(s), title of the work, publisher, and DOI.

ISBN: 978-3-95450-261-5 ISSN: 2673-7000 doi: 10.18429/JACoW-NAPAC2025-WECD03

SINGLE-BUNCH INSTABILITIES AT THE FERMILAB RECYCLER RING

C. Gonzalez-Ortiz*, R. Ainsworth
Fermi National Accelerator Laboratory, Batavia, IL, USA

Abstract

Understanding and characterizing collective instabilities is critical for high-intensity operation at the Fermilab Recycler Ring. This work presents an application of the the Nested Head-Tail (NHT) formalism for modeling single-bunch transverse instabilities, incorporating analytical solutions to the resistive wall impedances in the absence of space charge. Predicted growth rates and mode structures are benchmarked against PyHEADTAIL simulations and ongoing experimental measurements. The experimental program includes studies of bare-machine instabilities at different machine parameters. These results support the understanding of naturally-occurring instabilities in the Recycler and contribute to the development of predictive tools for beam stability in future high-intensity configurations.

INTRODUCTION

As intensity is increased for the machines in the Fermilab Accelerator Complex, there are several physics phenomena that need to be better understood. This work focuses on one accelerator in the complex which is the Recycler Ring (RR). The Recycler Ring is permanent-magnet circular accelerator operating at an energy of 8 GeV. Specifically for RR, single bunch instabilities generated by collective effects in the bunch need to be better understood.

A single bunch instability refers to collective processes that affect an individual particle bunch within a particle accelerator. These instabilities arise from the interaction of the particles with the electromagnetic wakefields produced when the bunch interacts with the surrounding environment [1]. All along the accelerator, including the beam pipe itself, there will be impedance elements that will interact with the beam and create such wakefields. This type of instabilities exhibit an exponential growth of the beam oscillation, just at it is shown Fig. 1. Single bunch instabilities are a significant concern in high-intensity beam operations as they can lead to deterioration of beam quality, including emittance growth and particle loss, and can limit the achievable beam intensity.

The following work compares theoretical predictions and simulations against experimental data of single bunch instabilities. The theoretical predictions are done under the Nested Head-Tail (NHT) framework [2]. On the other hand, the simulations were done using PyHEADTAIL. In both cases, no space charge was modeled. Table 1 shows the nominal parameters used in the calculations.

* gonza839@fnal.gov

Table 1: Nominal Recycler Ring properties for beam used in instability experiments, theoretical calculations and PyHEADTAIL simulations.

Parameter	Value	Unit
Circumference C	3319.4	m
Machine Mean Radius R_0	528.30	m
Momentum	8.835	GeV/c
Relativistic Factor γ	9.47	
Revolution Period T_0	11.1	μs
Revolution Frequency f_0	89.8	kHz
RF Frequency	2.5	MHz
RF Voltage	80	kV
Synchrotron Tune Q_s	0.000595	
Slip Factor η	-8.6×10^{-3}	
Superperiodicity	2	
Horizontal Tune Q_x	25.4601	
Vertical Tune Q_y	24.412	
Horizontal Chromaticity ξ_x	0	
Vertical Chromaticity ξ_y	0	
95% Normalized Emittance	15	π mm mrad
Bunch Length σ_z	9	m
95% Longitudinal Emittance	3.64	eV·s
Beam Pipe Major Axis a	47.625	mm
Beam Pipe Minor Axis b	22.225	mm
Conductivity (SS) σ	1.4×10^6	S/m
Dipole Yokoya X G_{1x}	0.4501	
Dipole Yokoya Y G_{1y}	0.8369	

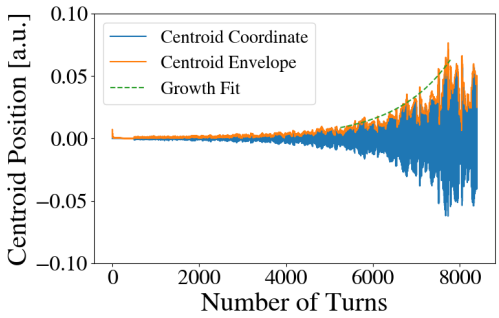


Figure 1: Measurement of a single bunch instability in the Recycler Ring with corresponding envelope used for fitting exponential trend.

NHT THEORY

The Nested Head-Tail (NHT) model, developed by A. Burov [2], is a Vlasov solver used to study transverse oscillations in bunched beams, taking into account factors such as impedance, feedback, and beam-beam interactions without taking into account any space-charge effects.

Content from this work may be used under the terms of the CC BY 4.0 licence (© 2022). Any distribution of this work must maintain attribution to the author(s), title of the work, publisher, and DOI.

ISBN: 978-3-95450-261-5 ISSN: 2673-7000 doi: 10.18429/JACoW-NAPAC2025-WECN01

LCLS-II INJECTOR OPERATIONAL CHALLENGES AND RECENT DEVELOPMENTS*

F. Zhou†, A. Brachmann, D. Cesar, W. Colocho, Y. Ding, D. Dowell, G. Just, A. Osman, N. Sudar, J. Tang, T. Vecchione, Z. Zhang, C. Zimmer
SLAC National Accelerator Laboratory, Menlo Park, CA, USA

Content from this work may be used under the terms of the CC BY 4.0 licence (© 2022). Any distribution of this work must maintain attribution to the author(s), title of the work, publisher, and DOI.

Abstract

The Linac Coherent Light Source II (LCLS-II) has been in user operations since 2023 and has successfully ramped up the beam repetition rate to 93 kHz. The LCLS-II photoinjector has demonstrated the ability to deliver a high-brightness, low-emittance electron beam at high repetition rates, meeting key performance targets. However, several operational challenges have emerged during commissioning and user operation. These include substantial gun dark current, degradation of cathode quantum efficiency (QE) manifesting as QE craters, unexpected electron beam splitting, significant emittance growth through the laser heater chicane, complications during laser heater commissioning, and the presence of beam halos. This paper provides an overview of these challenges and highlights recent efforts to address these outstanding issues.

INTRODUCTION

Continuous-wave (CW) free-electron laser (FEL) facilities such as LCLS-II impose stringent requirements on the photoinjector to deliver high-brightness, low-emittance, and reliable electron beams. The LCLS-II 1 MeV electron source was successfully commissioned between 2018 and 2020, following the resolution of several significant technical challenges [1]. In 2022, the full-scale >70 MeV injector was commissioned, and its beam performance was then characterized and optimized. Figure 1 presents a schematic layout of the complete injector system.

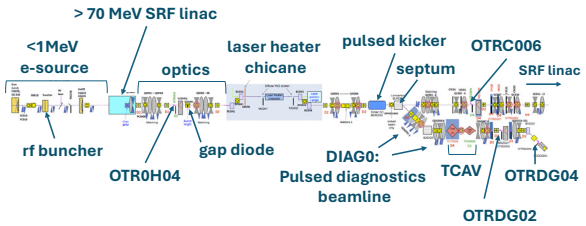


Figure 1: Schematic of the LCLS-II injector layout.

The injector consists of the 1 MeV electron source, a >70 MeV standard cryomodule (CM01), a laser heater chicane, and multiple diagnostic stations. These include the first emittance station (OTR0H04) and a gap diode for relative bunch length measurements, both located before the laser heater chicane; a second emittance station (OTRC006) located downstream of the chicane; and a dedicated off-axis diagnostics station equipped with a transverse deflecting cavity (TCAV) for absolute bunch length measurement, along with an additional emittance measurement station.

Since the start of FEL user operations in 2023, a variety of operational challenges have been encountered in the injector system. This paper discusses the key issues and the corresponding efforts toward their resolutions, including:

- A steady gun vacuum pressure rise over the time.
- Large gun dark current, which has led to frequent damages to downstream camera electronics, formation of localized hot spots, and beam loss events that trigger full machine trips.
- The formation of quantum efficiency (QE) crater on the photocathode after just a few days of operation, resulting in spatial and charge instability in the beam.
- Nonlinear magnetic fields in the laser heater chicane, contributing to significant emittance growth.
- Lessons learned from commissioning the laser heater.
- The presence and mitigation of beam halos.

OPERATIONAL CHALLENGES AND RECENT DEVELOPMENTS

The following sub-sections present an overview of each operational challenge and the systematic efforts undertaken to diagnose and resolve them.

CW Gun Operational Improvement

Figure 2 shows the gun vacuum gradually degraded over time, increasing from 8×10^{-10} Torr in 2023 to 2×10^{-9} Torr by 2024. In October 2024, a small step-like increase in vacuum pressure was observed; however, the source of this change remained unidentified until December 2024, when a vacuum leak was discovered on one of two RF windows. Following the identification of the leak, the faulty window was replaced, and the entire gun assembly was baked at 150–170 °C.

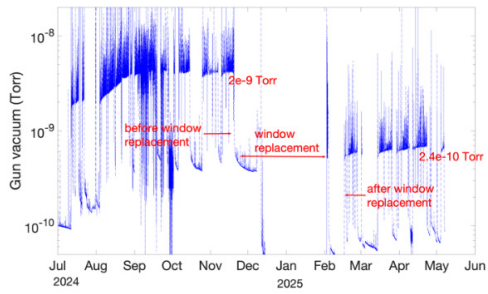


Figure 2: Gun vacuum trends before and after gun window replacement.

Historically, during RF power processing of the gun, we would 'jump' over the multipacting barriers by rapidly

* Work supported by DOE contract # DE-AC02-76SF00515
† zhoufeng@slac.stanford.edu

ISBN: 978-3-95450-261-5 ISSN: 2673-7000 doi: 10.18429/JACoW-NAPAC2025-WECN02

EFFECTS OF BEAM CONDITIONS ON ACHIEVING COMPACT LONGITUDINAL DE-CHIRPING USING TRANSVERSE DEFLECTING CAVITIES

A. DeSimone*, G.Ha, Northern Illinois University, DeKalb, IL, USA
S. Doran, W. Liu, J. Power, E. Wisniewski[1], Argonne National Laboratory, Lemont, IL, USA
Q. Marksteiner, H. Xu, N. Yampolsky, Los Alamos National Laboratory, Los Alamos, NM, USA
[1]also at Illinois Institute of Technology, Chicago, IL, USA

Abstract

It has been shown that a transverse deflecting cavity (TDC)-based de-chirper can be made by altering the drift sections in a TDC-based chirper to form negative drifts. While five appropriately configured quadrupole magnets can form such negative drifts, this approach is limited by spatial and experimental constraints. In this study, we investigate an alternative configuration that uses three quadrupole magnets to form a negative identity transport section between the TDCs instead of a negative drift. To assess the robustness of this proposed design, a computational study has been conducted on initial beam conditions to determine operational limitations. This includes the effects of space charge and initial transverse beam conditions, such as beam size and divergence, on the resulting transverse emittance.

INTRODUCTION

A common method for imparting longitudinal chirp to an electron beam is off-crest acceleration in linear accelerator. Slightly off-crest operation causes the head and tail of the bunch to experience different accelerations, which manifests as a longitudinal chirp. Although this method is simple and effective, it inevitably reduces acceleration efficiency, which leads to a lower central beam energy. A novel method was proposed to address this issue so that imparting the chirp does not involve operating the linac off-crest [1].

This method utilizes transverse deflecting cavities (TDCs). TDC, operating at TM_{110} mode, provides a transverse kick based on particles' longitudinal positions and accelerates particles longitudinally based on their transverse positions. Thus, the first TDC introduces a tilt in $z - x$ phase space, then the following TDC provides acceleration based on the horizontal positions of particles, which are correlated to z. In this way, it is possible to impart longitudinal chirp, and the third TDC is introduced to remove remaining unwanted correlations. It is important to note that this configuration only provides negative chirping—head loses energy while tail gains energy—as $\Delta h = R_{65} \propto -\kappa^2$. Ref. [1] also proposed a modification of the beamline to enable dechirping. It could be accomplished by adding five quadrupoles, forming a negative drift section, between TDCs.

Recently a collaboration was initiated to demonstrate the TDC-based chirping and dechirping. While the chirping configuration can be installed at the Argonne Wakefield Accelerator facility [**conde-2017-a**], there is not enough space to accommodate a total of ten quadrupole magnets forming two negative drift sections. Thus, we proposed a new form factor using three quadrupoles forming a negative identity drift [2]. This previous study showed its feasibility. Thus, in this paper, we primarily discuss preliminary study results on limiting factors.

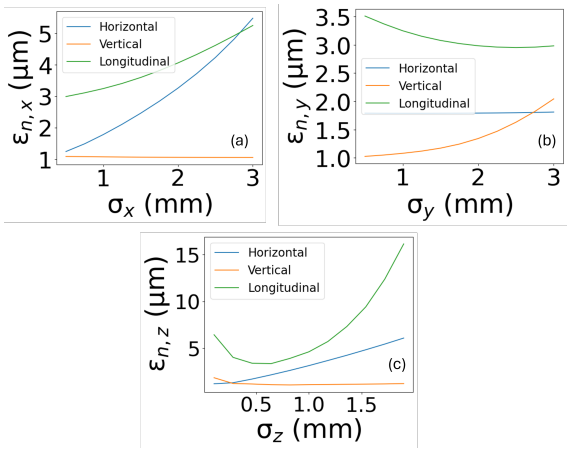


Figure 1: 1D beam size scans.

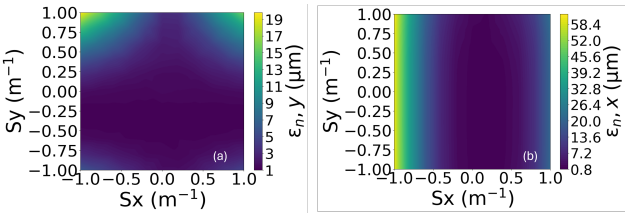


Figure 2: Slope scan results. The phase space slope is defined as $S_x = -\frac{\alpha_x}{\beta_x} = \frac{\langle xx' \rangle}{\langle x^2 \rangle}$.

SIMULATION SETUP

To characterize the beamline's response to various limiting factors, 6D-Gaussian beams were produced and transported in the General Particle Tracer (GPT) code [3]. We scanned beam's second moments at the entrance to find optimal condition minimizing emittance growth and identify

* z2035090@students.niu.edu

Content from this work may be used under the terms of the CC BY 4.0 licence (© 2022). Any distribution of this work must maintain attribution to the author(s), title of the work, publisher, and DOI.

ISBN: 978-3-95450-261-5 ISSN: 2673-7000 doi: 10.18429/JACoW-NAPAC2025-WECN03

MULTI–OBJECTIVE BAYESIAN OPTIMIZATION OF AN ELECTRON INJECTOR LINAC FOR 4TH GENERATION LIGHT SOURCES: A COMPARATIVE STUDY WITH MOGA

C. S. Park*, Korea University, Sejong, South Korea

Abstract

The performance of electron injector linear accelerators (linacs) critically influences the beam brightness and stability in 4th generation light sources. In this study, we employ a multi-objective Bayesian optimization (MOBO) framework to optimize the injector linac design, targeting the simultaneous minimization of transverse emittances and energy spread at the linac exit. This data-efficient approach leverages Gaussian process regression and acquisition functions to navigate the high-dimensional design space with significantly fewer simulations than conventional methods. We compare the results of MOBO with those obtained from the well-established Multi-Objective Genetic Algorithm (MOGA), highlighting differences in convergence speed, solution diversity, and computational efficiency. Our findings demonstrate that MOBO achieves comparable or superior optimization outcomes with reduced computational cost, offering a powerful alternative for accelerator design and tuning in next-generation light source facilities.

INTRODUCTION

Fourth–generation synchrotron and FEL facilities require injector beams with ultra–low transverse emittance and also tightly controlled relative energy spread [1–3] For Korea–4GSR, the injector linac must minimize end–of–linac $\mathbf{f} = [\varepsilon_{n,x}, \varepsilon_{n,y}, \sigma_\delta]$ while meeting limits on beam size/divergence, bunch length, mean energy, and transmission [4]. This is challenging because the space–charge–dominated gun region couples strongly to downstream optics and RF phasing, so small changes in early knobs can propagate nonlinearly.

Multi–objective optimization (MOO) is well suited to expose these trade–offs via a Pareto set. Genetic algorithms (e.g., NSGA–II [5]) provide robust coverage on nonconvex fronts but typically require many high–fidelity simulations, which is costly when each evaluation is a 3D space–charge model.

Bayesian optimization (BO) offers a sample–efficient alternative by learning a probabilistic surrogate (Gaussian Process) and selecting new evaluations via an acquisition function that balances improvement and uncertainty [6]. While true MOBO methods based on expected hypervolume improvement exist, a practical route is to *scalarize* the objectives with normalized weights and run BO on the resulting single objective, $J(\mathbf{w}) = \sum_i w_i \tilde{f}_i$ with $\tilde{f}_i = f_i / f_{i,\mathrm{ref}}$.

In this work we study the Korea–4GSR injector with both approaches: NSGA–II as a high–quality Pareto baseline, and scalarized BO across nine weight triplets to reconstruct knees and extremes. The decision variables are eight operational knobs—solenoid field B_{sol}, focusing/defocusing quadrupoles $k_{\mathrm{QF}}, k_{\mathrm{QD}}$, gun phase ϕ_{gun}, and four cavity phases $\phi_{1..4}$—all evaluated at the linac end. BO uses GP surrogate and batched acquisition (qEI/qNEI).

Table 1: Decision Variables, Bounds, and Units Used in the Optimization

Variable	Range	Units
B_{sol}	[0.10, 0.30]	T
k_{QF}	[0, 10]	T/m
k_{QD}	[−10, 0]	T/m
ϕ_{gun}	[0, 360]	deg
ϕ_1, ϕ_2	[0, 360]	deg
ϕ_3, ϕ_4	[0, 360]	deg

INJECTOR AND OPTIMIZATION PROBLEM

Injector Overview and Evaluation Plane

The Korea–4GSR injector is a normal–conducting RF gun followed by a solenoid, four accelerating modules, and a short matching section with a focusing (QF) and defocusing (QD) quadrupole. The optimization is performed against high-fidelity 3D space–charge simulations (ASTRA [7]) and all figures of merit are evaluated at the end–of–linac diagnostics plane ($s \simeq 16.2$ m). Throughout this paper emittances are *normalized rms* and the energy spread is the rms fractional quantity $\sigma_\delta = \sigma_E / \langle E \rangle$.

Decision Variables

The decision vector $\mathbf{x} \in \mathbb{R}^8$ comprises eight operational knobs that are routinely accessible during tuning:

$$\mathbf{x} = [B_{\mathrm{sol}},\ k_{\mathrm{QF}},\ k_{\mathrm{QD}},\ \phi_{\mathrm{gun}},\ \phi_1,\ \phi_2,\ \phi_3,\ \phi_4].$$

Here B_{sol} is the on-axis solenoid field, $k_{\mathrm{QF/QD}}$ are the integrated gradients of the quadrupoles, and $\phi_{\mathrm{gun}}, \phi_{1\ldots4}$ are the RF phases of the gun and four downstream cavities (degrees). Hardware-realistic bounds are enforced.

Objectives

We target simultaneous reduction of the three end-of-linac objectives

$$\mathbf{f}(\mathbf{x}) = [\varepsilon_{n,x}(\mathbf{x}),\ \varepsilon_{n,y}(\mathbf{x}),\ \sigma_\delta(\mathbf{x})],$$

Content from this work may be used under the terms of the CC BY 4.0 licence (© 2022). Any distribution of this work must maintain attribution to the author(s), title of the work, publisher, and DOI.

* kuphy@korea.ac.kr

ISBN: 978-3-95450-261-5 ISSN: 2673-7000 doi: 10.18429/JACoW-NAPAC2025-WEP005

A COMPACT TOP-OFF INJECTION WITH CASCADED NONLINEAR KICKERS FOR DIFFRACTION LIMITED STORAGE RINGS*

X. Yang†, H. Dave, Y. Li, P. N'Gotta, T. Shaftan, V. Smaluk, M. Song, R. Todd, G. Wang
National Synchrotron Light Source II, Brookhaven National Laboratory, Upton, NY, USA

Content from this work may be used under the terms of the CC BY 4.0 licence (© 2022). Any distribution of this work must maintain attribution to the author(s), title of the work, publisher, and DOI.

Abstract

To address the stringent dynamic aperture (DA) constraints of diffraction-limited storage rings, we propose a compact top-off injection scheme based on cascaded nonlinear kickers (NLKs) strategically placed near the injection point. By optimizing phase advances and distributing kicks across multiple NLKs, the injected beam oscillations are effectively suppressed within a fraction of a turn. The NLK design preserves a field-free on-axis region, ensuring minimal perturbation to the stored beam and enabling transparent injection. A novel NLK geometry can reduce the peak field distance to the beam orbit from greater than 7 mm to less than 5 mm, improving injection efficiency and reducing stored-beam distortion. Particle tracking simulations using Accelerator Toolbox, incorporating realistic field maps, alignment tolerances, and injected beam errors, confirm >90% injection efficiency and support a relaxed DA requirement of 5 mm for the NSLS-II upgrade lattice.

INTRODUCTION

Next-generation synchrotron light sources (NG-SLSs), such as NSLS-IIU, use multi-bend achromat lattices to achieve ultra-low emittance. While this improves brightness, it drastically reduces the dynamic aperture (DA)—from ~15 mm in third-generation rings to as little as 1-2 mm in advanced upgrades like ALS-U [1, 2]—challenging conventional off-axis injection.

On-axis swap-out injection, used in APS-U and ALS-U [3, 4], addresses this by replacing full bunches but demands major injector upgrades, increasing cost and complexity. We propose an alternative: a compact, scalable top-off injection scheme using cascaded nonlinear kickers (NLKs) that enable off-axis injection even in tight DA and physical aperture (PA) conditions.

The NLK scheme uses sequential, phase-matched kickers to suppress oscillations within a turn. Two innovations enable this: a novel NLK geometry reducing field-to-beam distance (~5 mm), and a cascaded layout distributing moderate kicks to minimize orbit disturbance. Particle tracking simulations validate greater than 90% efficiency within the 5 mm DA in the NSLS-IIU lattice. A prototype is under development at NSLS-II under LDRD funding with the goal of establishing a robust, low-impact injection technique for future diffraction-limited storage rings in alignment with Basic Energy Sciences Advisory Committee (BESAC) – 24 priorities [5].

*This manuscript has been authored by Brookhaven Science Associates, LLC under Contract No. DE-SC0012704 with the U.S. Department of Energy. This information is controlled by the U.S. Department of Commerce Export Administration Regulations 15 CFR Parts 730-774 as EAR99 Technology.

† xiyang@bnl.gov

SIMULATION AND RESULTS

Simulation

Simulations show that sequential NLKs can suppress injected beam oscillations within one turn while preserving a field-free on-axis region for the stored beam. This results in negligible perturbations to the beamlines. By distributing kicks across two NLKs, residual oscillations are reduced by a factor of 10 when using moderate magnetic fields.

Using Accelerator Toolbox (AT) [6], we placed NLK1 and NLK2 in adjacent straight sections (cells 1 and 2) of the NSLS-IIU lattice (see Fig. 1a). Simulated magnetic fields of 0.021 T and 0.014 T over 0.3 m were optimized for rapid oscillation damping and transparency. DA (Fig. 1d) and misalignment errors were incorporated into the analysis, confirming robustness down to 5 mm.

Figures 1 and 2 illustrate the phased kick sequence, beam envelope comparisons, and kicker field profiles. As shown in Fig. 2c, the peak of NLK2 cannot occur at 0.3 mm off-axis; therefore, the kick θ_2 from NLK2 follows the magnetic field slope. The close alignment of the stored and injected beam trajectories, with only small offsets observed in Fig. 2a, confirms that the operation has minimal impact.

Feasibility and Optimization

Design feasibility was evaluated through multi-turn tracking, considering injection offsets, field tolerances, and kicker placement. Optimized kick angles (θ_1, θ_2) were selected via a 2D scan (Fig. 3) to minimize residual beam motion. Results reveal a clear operating point that balances damping effectiveness with manageable field strength.

The modular simulation framework also supports adaptive optimization. If one kicker fails, remaining elements can be re-optimized to maintain performance—offering a resilient and scalable design for future upgrades.

Injection Efficiency and Sensitivity

Efficiency was evaluated based on a ±5 mm horizontal and vertical acceptance, using realistic beam emittances. The injected electron beam had horizontal and vertical emittances of 60 nm·rad and 6 nm·rad, respectively. Simulations showed 100% injection efficiency under ideal conditions. With position and angle errors, injection efficiency becomes highly sensitive, especially to angular offsets (Fig. 4) and position deviations that distort angular kicks due to NLK field gradients. These effects the importance of placing the injected beam at the off-axis field peak. Therefore, precise alignment and trajectory control are crucial for optimal performance.

ISBN: 978-3-95450-261-5 ISSN: 2673-7000 doi: 10.18429/JACoW-NAPAC2025-WEP006

APPLICATION OF LOW-COST SENSORS AND DEEP AUTOENCODERS FOR MONITORING WATER PUMPS IN PARTICLE ACCELERATORS*

R. Sainju†, O. Mohsen, M. Borland, Y. Sun
Advanced Photon Source, Argonne National Laboratory, Lemont, IL, USA

Abstract

In particle accelerator facilities, cooling-water pumps play a critical role in removing substantial amounts (megawatts) of waste heat from numerous high-power accelerator components (e.g., magnets, radio frequency structures, power supplies) and beamline components. Despite their role in daily operations, inspecting hundreds of water pumps is labor-intensive and performed only occasionally. Unexpected pump failures can lead to degradation of beam quality, hardware damage, and costly unplanned downtime. This study introduces an innovative method for real-time monitoring of water pump vibrations to identify anomalies that signal potential mechanical failures. Our approach integrates (i) affordable vibration sensors, which will continuously sample pump vibration data and transmit it to a (ii) deep autoencoder model for detecting anomalies. The planned model will recognize the normal vibration patterns of each pump and identify subtle variations. This developmental monitoring system will help facilitate proactive maintenance by enabling early detection of anomalies, enhancing pump reliability, lowering maintenance expenses, and minimizing costly downtimes.

INTRODUCTION

Cooling-water pumps at the Advanced Photon Source (APS) remove several megawatts of waste heat from accelerator magnets, radio frequency (RF) structures, power supplies, and beamline components. An unplanned pump failure can lead to beam loss and unexpected interruptions. Historical cases at accelerator facilities show that bearing wear or shaft misalignment, undetected between quarterly inspections has led to costly downtimes [1]. Recent advances in low-cost MEMS accelerometers achieving sub-mg resolution and kilohertz (kHz) bandwidth, enable continuous, on-site vibration monitoring at a fraction of the cost of commercial systems [2]. In parallel, transformer-based deep-learning architectures have emerged as powerful tool for modelling long-range temporal dependencies in time-series data, providing improved fault detection over traditional methods [3]. A major barrier to training such models is lack of labelled failure data. To address this, we developed physics-based methods to inject synthetic anomalies into vibration data, creating a ground-truth dataset for training. This paper explores the potential of using affordable sensors, synthetic anomaly generation, and dual-domain (time and frequency) anomaly detection to create low-cost, scalable condition monitoring framework for APS water pumps at Argonne National Laboratory.

* The work is supported by the U.S. DOE, Office of Science-Basic Energy Sciences, under contract No. DE-AC02-06CH11357
† rsainju@anl.gov

METHODS

Low-Cost Vibration Sensor and Data Acquisition

We employed a 3-axis IIS3DWB MEMS accelerometer (STMicroelectronics) housed in an STWIN.box development kit. The sensor, costing approximately $120, offers a wide bandwidth (up to 6 kHz) and low intrinsic noise. Figures 1a-b show the installation on the pump coupler end. An acquisition sampling rate of 10 kHz was chosen to effectively capture relevant high-frequency signals while minimizing noise. The Raspberry Pi edge node stores data locally and forwards it for model training and inference (see Fig. 1c). Representative time-domain acceleration signals in X, Y, and Z under normal operation are shown in Fig. 2a. Since vibration data is routinely analysed in the harmonic orders domain, an in-house FFT-based algorithm automatically detects the fundamental shaft speed (1x order, 44.4 Hz) and harmonics up to 10x (see Fig. 2b). It leverages the fact that motor vibrations display a strong fundamental frequency and harmonic pattern. It achieved a frequency error of less than 0.30 Hz across 1x-10x orders (see Fig. 2b).

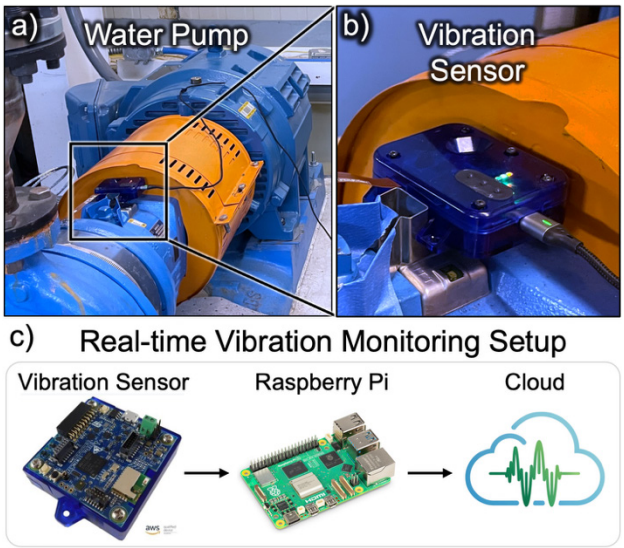


Figure 1: Developmental water pump anomaly detection setup at the Advanced Photon Source. (a) Cooling-water pump with the sensor attached to the pump's coupler end (PCE). (b) Close-up image of the low-cost triaxial MEMS accelerometer on the motor housing. (c) End-to-end data path where the sensor streams vibration data to the Raspberry Pi edge node, which then forwards the data to the PC/cloud for real-time inference.

Content from this work may be used under the terms of the CC BY 4.0 licence (© 2022). Any distribution of this work must maintain attribution to the author(s), title of the work, publisher, and DOI.

ISBN: 978-3-95450-261-5 ISSN: 2673-7000 doi: 10.18429/JACoW-NAPAC2025-WEP007

A SIMULATION OF THE FERMILAB MAIN INJECTOR DUAL POWER AMPLIFIER CAVITIES*

S. M. Stevenson†
Fermi National Accelerator Laboratory, Batavia, IL, USA

Content from this work may be used under the terms of the CC BY 4.0 licence (© 2022). Any distribution of this work must maintain attribution to the author(s), title of the work, publisher, and DOI.

Abstract

The Fermilab Main Injector accelerating cavities have sparking issues when they are run at voltages higher than those required by the PIP-II project. This is a problem Fermilab is working on as planning begins for the next upgrade to the accelerator complex. One of the methods being used to address the issue is the development of a CST Microwave Studio simulation to accurately model the PIP-II dual power amplifier cavities and identify which part(s) of the cavity is causing sparking to develop. The model will also be used to determine if changes to the cavity geometry may allow the cavity to be used at higher voltages before sparking occurs.

INTRODUCTION

The Main Injector at Fermilab is the last stage of the accelerator, accelerating the beam of protons up to 120GeV before it is sent off to the experiments. In order to achieve higher beam power levels in the future, the radio frequency accelerating cavities need to be able to generate more voltage to give the beam. Currently the maximum achievable cavity voltage is limited by arcing in the cavity. It would be beneficial for future accelerator operations to investigate how to mitigate the arcing limit. This paper will discuss the general cavity function, the planned cavity upgrades, and the development of a simulation to model the current behavior of the cavities with the goal of increasing their maximum voltage output.

CURRENT CAVITY COMPONENTS

The cavity has three main parts: the body, the two power amplifiers, and the two ferrite tuners.

The body of the cavity acts like two back-to-back folded quarter wave coaxial resonators. A side view of the cavity is shown in Fig. 1 and a cross-section of the cavity is shown in Fig. 2. The folded aspect of the cavity results in three main elements of the cavity geometry: the inner conductor, the intermediate cylinder, and the outer conductor. The region of the cavity inside the intermediate cylinder is kept under a vacuum level of roughly 5e-8 Torr, while the part of the cavity outside the intermediate cylinder is not under vacuum. The outer conductor is shaped like an octagon instead of a cylinder, which both helps maintain structural integrity as well as make it easier to mount external components on the cavity. The intermediate cylinder and inner conductors are both cylindrical. The main feature of the intermediate cylinder is the ceramic regions on either end to allow fields to travel uninhibited through the cavity while the vacuum is preserved. The inner conductor's main feature is the two accelerating gaps in the center of the cavity. Beam passing through the cavity will be insulated from fields by the beam pipe until it passes across the two gaps before exiting the cavity.

The power amplifiers use tetrode style vacuum tubes to control the final power input into the cavity. There are two power amplifiers on each cavity that operate in a push-pull configuration. Each power amplifier is currently configured to operate with a maximum output of 150 kW. The power amplifiers are physically mounted on the top of the cavity and use a coupling loop to transfer power to the cavity with a 1:12.1 anode gap to accelerating gap voltage ratio, nominally generating a voltage of 210 kV across the gaps.

The two ferrite tuners are magnetically coupled to the cavity on the two lower 45 degree faces of the outer conductor. The ferrite tuners are used to tune the cavity from 52.808 to 53.104 MHz during the 1.2 seconds each batch of beam is in the Main Injector. Physically, they function as coaxial structures filled with alternating copper and ferrite disks. Each tuner is wound with 10 bus bar turns that act as an inductive structure to generate a magnetic field when a bias current is applied (note the bus bar turns are not shown in the model). This bias changes the ferrite disk permeability, causing the resonant frequency of the cavity to change, or tune.

CURRENT VS. PLANNED CAVITY UPGRADES

Fermilab is currently executing an accelerator complex upgrade referred to as "PIP-II". Part of the PIP-II project is the addition of a second power amplifier to the existing Main Injector cavities in order to increase the power delivered to the beam. With the PIP-II project about half-way completed, Fermilab is now planning what the next goals of the accelerator should be, with a continuing emphasis on increasing the power of the proton beam. The method chosen to increase the power of the beam is to accelerate the same number of protons faster, with a goal of halving the time each batch of protons spends in the Main Injector. This necessitates a higher cumulative accelerating voltage from the cavities.

To achieve the greater voltage requirements, either the number of Main Injector accelerating cavities needs to be doubled or the amount of voltage each cavity can produce needs to be substantially increased. Building and installing that many more cavities is challenging due to cost, the civil construction required, and a lack of available space in the tunnel. This leaves generating more voltage from the current cavities, designing new ones that can produce the extra

* This manuscript has been authored by FermiForward Discovery Group, LLC under Contract No. 89243024CSC000002 with the U.S. Department of Energy, Office of Science, Office of High Energy Physics.
† susanna@fnal.gov

ISBN: 978-3-95450-261-5 ISSN: 2673-7000 doi: 10.18429/JACoW-NAPAC2025-WEP008

A W-BAND CORRUGATED WAVEGUIDE FOR HIGH-EFFICIENCY HIGH-GRADIENT WAKEFIELD ACCELERATION

B. Leung[1], A. Ody[2], C. Phillips[1], C. Whiteford[2], D. Mihalcea[1], E. Wisniewski[2], G. Chen[2], G. Ha[1], O. Ramachandran[1], J. Power[2], P. Piot[2], S. Doran[2], W. Liu[2], X. Lu[1,2]
[1]Department of Physics, Northern Illinois University, DeKalb, IL, USA
[2]Argonne National Laboratory, Lemont, IL, USA

Abstract

Radiofrequency (RF) structures in the sub-terahertz regime are promising for structure wakefield acceleration due to their ability in achieving high gradients in a reduced footprint. We report on the design, fabrication, and testing of a metallic corrugated waveguide operating at 110 GHz, tailored to the 45 MeV electron beam parameters at the Argonne Wakefield Accelerator (AWA). The experiment utilized the emittance exchange (EEX) beamline at AWA for longitudinal bunch shaping in two configurations: (1) a single short drive bunch to demonstrate high decelerating gradients, and (2) a two-bunch scheme featuring a triangularly shaped drive bunch followed by a long witness bunch to probe the wakefield and achieve a high transformer ratio. We present the experimental design and results, which show good agreement with simulation predictions.

INTRODUCTION

Collinear wakefield acceleration (CWA) is one of the two schemes in structure wakefield acceleration (SWFA). In this approach, a high-charge drive bunch and a trailing, lower-charge witness bunch are sent through the same structure. The wakefield generated by the drive bunch is used to accelerate the witness bunch. The transformer ratio (TR)—defined as the accelerating gradient experienced by the witness bunch divided by the decelerating gradient experienced by the drive bunch—quantifies how efficiently energy is transferred from the drive to the witness. Longitudinally symmetric bunches (e.g., Gaussian) have a theoretical upper limit of 2 for the TR. This limitation can be exceeded using longitudinal bunch shaping techniques [1–3].

Various longitudinal distributions, such as the triangular and doorstep profiles, have been shown to yield TRs greater than 2 [4]. Sending such shaped drive bunches through dielectric structures has demonstrated high-gradient, high-efficiency acceleration [5], and the feasibility of achieving similar performance in metallic structures has also been demonstrated [6].

CWA is particularly attractive in the sub-terahertz (THz) regime due to the high shunt impedance resulting from frequency scaling, which enables high gradients at lower drive bunch charges, especially with shaped bunches. Moreover, RF pulses in this regime are confined to short durations, allowing efficient acceleration. The combination of short pulse length and high frequency can also reduce the RF breakdown probability of the structure [7, 8].

Our objective in this work was to design, fabricate, and test a metallic *W*-band corrugated waveguide operating at 110 GHz at the Argonne Wakefield Accelerator (AWA), using the 45 MeV electron beam under various bunch shaping configurations. The electron beam is generated by an *L*-band photocathode RF gun and accelerated in a linac. It then passes through an optional transverse mask before entering the emittance exchange (EEX) beamline for bunch shaping [9]. The EEX beamline consists of two dipole magnet pairs sandwiching a transverse deflecting cavity, enabling exchange between the beam's horizontal and longitudinal phase spaces.

We utilized the EEX for two primary purposes: (1) to generate short drive bunches for demonstrating high-gradient wakefield excitation, and (2) to generate two-bunch trains—comprising a longitudinally shaped drive bunch and a delayed witness bunch—to demonstrate wakefield acceleration with a high transformer ratio (TR). In the single-bunch case, the EEX was used without a mask to produce a high-charge, short electron bunch with a high peak current. In the two-bunch case, a triangular-shaped mask was inserted to produce a longitudinally triangular drive bunch followed by a long witness bunch, allowing the demonstration of a high TR.

In both configurations, the beam was sent through the *W*-band corrugated structure. Wakefield measurements were performed using a single-shot longitudinal phase space (LPS) diagnostic system at the end of the beamline, comprising a transverse deflecting cavity and a spectrometer. A schematic layout of the EEX beamline at AWA is shown in Fig. 1.

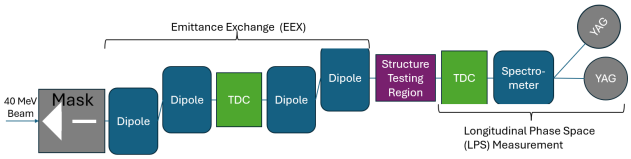


Figure 1: The beamline layout of the emittance exchange (EEX) beamline at the AWA facility. When a transverse mask is placed in the beam path, the EEX beamline can be utilized to create a longitudinally shaped drive bunch. A longitudinal phase space (LPS) measurement system, which includes a transverse deflecting cavity and a dipole magnet, is at the end of the beamline.

Content from this work may be used under the terms of the CC BY 4.0 licence (© 2022). Any distribution of this work must maintain attribution to the author(s), title of the work, publisher, and DOI.

ISBN: 978-3-95450-261-5 ISSN: 2673-7000 doi: 10.18429/JACoW-NAPAC2025-WEP011

ANALYSIS OF VAPOR DIFFUSION Nb_3Sn COATING AT FERMILAB: MINIMIZING IMPURITIES USING TOF-SIMS

N. Tagdulang*, B. Tennis, D. Bafia, J. Lee, S. Posen, G. Eremeev
Fermi National Accelerator Laboratory, Batavia, IL, USA
T. Peterson, M. Kelly, Argonne National Laboratory, Argonne, IL, USA

Abstract

Nb_3Sn demonstrates steady advancements offering reduced power cost in superconducting radio-frequency cavities due to its high critical temperature, quality factor, and achieved accelerating gradient. However, theoretical estimates of its radio-frequency parameters have not been achieved due to several potentially limiting mechanisms: tin spots, patchy regions, defects, thermal impedance, and impurities. While some of these limitations have been intensively studied, impurity analysis in Nb_3Sn coatings has received less attention. We report an investigation of impurities in several vapor-diffused Nb_3Sn coated samples using time-of-flight secondary ion mass spectroscopy (TOF-SIMS) and show allowable impurity levels in view of superconducting cavity performance. Challenges and lessons learned in maintaining clean Nb_3Sn coatings are also discussed.

INTRODUCTION

Nb_3Sn superconducting radio frequency (SRF) cavities have been extensively studied due to their promising superconducting properties, theoretically, they far surpasses the current state-of-the-art Nb cavities. The Nb_3Sn cavities could reach superconducting transition (T_c) and superheating field (H_{sh}) both twice as high as that of Nb, while having an unloaded quality factor (Q_0) at 4 K comparable or higher to that of Nb at 2 K. Such cavities, therefore, theoretically, can reach accelerating gradient (E_{acc}) to roughly 100 MV/m in standard 1.3 GHz Tesla cavity [1]. These predicted properties not only provide an avenue for frontier research of linear accelerators, but also reduce cryogenic and capital costs. Hence, this is currently being pursued in many research groups around the world, both for basic research studies and industrial applications [2–6].

The vapor diffusion method is presently the leading technique to deposit Nb_3Sn on SRF cavities. Primarily, it involves two steps of heating: at 500 °C where $SnCl_2$ evaporates and is allowed to nucleate on the substrate, and at 1100 °C where the Sn coating and annealing are enabled. However, the best Nb_3Sn-coated cavity to date has achieved an accelerating gradient of $E_{acc,max} = 24$ MV/m ($B_{pk,max} = 95$ mT), less than that of the well-performed Nb cavities. Moreover, the reproducibility of this coating remains a challenge. These can be attributed to any or a combination of the following reasons: unreacted Sn spots, patchy regions, thermal impedance, surface roughness, cracking of the Nb_3Sn coating, substrate dependence, and impurities [1, 2, 4, 7, 8].

* ntagdula@fnal.gov

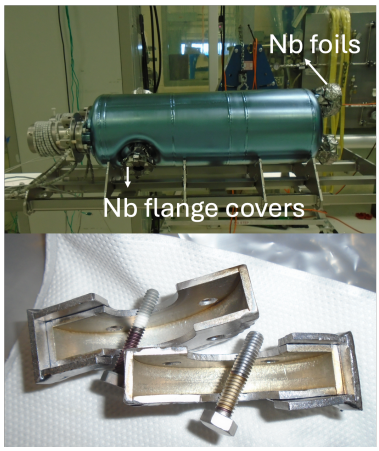


Figure 1: Top: QWR 145 prepared for Nb_3Sn coating. Bottom: A photograph of a flange cover after the coating process.

There are continued studies aimed at understanding each of these effects. However, although the effect of Ti as impurity was assumed to be the cause of some degraded coatings performance at JLAB [9], there are only a few studies performed on the effect of impurities on cavity RF performance.

Figure 1, at the top, shows QWR 145 cavity, sitting on the Nb frame. As seen in the figure, the NbTi flanges were covered with flange covers made of Nb to minimize the diffusion of Ti during coating. In addition, they were covered with Nb foils for further security. The bottom of the figure depicts a Nb flange cover after a Nb_3Sn coating; one can see an obvious discoloration. These coatings provide us with the opportunity to explore the effect of Ti on Nb_3Sn-coated cavities. This contribution, therefore, is our first attempt to rationalize the effect of Ti on cavity performance in the same coating chamber. Moreover, we show what other impurities are found on the Nb_3Sn coated samples and how we minimized them using TOF-SIMS.

THE Nb_3Sn SAMPLES AND CAVITY RF PERFORMANCE

The cavities used in this study are B9AS-AES-002, QWR 218, and QWR 145 as listed in Table 1. The corresponding frequencies are also listed. We specify B9AS-AES-002 as the baseline, since many cavities coated in Fermilab showed common performance. It can be seen that QWR 145 achieved the highest maximum peak magnetic field of $B_{pk,max} = 100$ mT with the lowest surface resistance. To our knowledge, this is the best achieved so far in Nb_3Sn. This is followed by QWR 218, with $B_{pk,max} = 74$ mT, higher than

Content from this work may be used under the terms of the CC BY 4.0 licence (© 2022). Any distribution of this work must maintain attribution to the author(s), title of the work, publisher, and DOI.

ISBN: 978-3-95450-261-5 ISSN: 2673-7000 doi: 10.18429/JACoW-NAPAC2025-WEP013

COMPACT ELECTRON BUNCHER WITH TUNABLE PERMANENT MAGNET FOCUSING*

K. A. Shipman†, R. L. Hemphill, Q. R. Marksteiner, M. A. Mealy,
D. E. Patrick, W. P. Romero, M. Sanchez Barrueta, S. R. Syed, H. Xu
Los Alamos National Laboratory, Los Alamos, NM, USA

Abstract

We present a compact electron buncher that uses a permanent magnet setup for beam focusing. The buncher modulates the input direct-current beam into 5.7-GHz bunch train. The buncher consists of two radiofrequency (RF) cavities. Immediately downstream of each RF cavity, there is an electrostatic potential depression (EPD) section. An EPD section in an electrically insulated beam pipe biased with a negative high voltage. The EPD method remarkably shortens the buncher structure by rapidly forming the bunch train. Each of the RF cavities and the EPD sections uses an individual set of rectangular permanent magnets, arranged in a circular array, which provide a solenoid-like focusing field. The polarity of the magnets is configured to form an alternating on-axis magnetic field orientation for minimizing the total weight. Coarse adjustment of the magnetic field is achieved by adding or removing permanent magnet rectangles. For fine adjustments, the rectangles are moved evenly in the radial direction. We show simulation results of the buncher performance and the tunable magnetic focusing. Initial experimental results are also reported.

INTRODUCTION

Accelerators deployed in space are used to advance space science and support a range of operational missions. For example, injecting electron beams into the Earth ionosphere and magnetosphere enables active probing and mapping of the space plasma, deepening our understanding of auroral phenomena [1]. Electron beams can also generate very-low-frequency (VLF) plasma waves in the Van Allen belts, which interact with and remediate high-energy electrons which pose a threat to low-Earth-orbit (LEO) satellites [2]. Large fluxes of such electrons arise after extreme space-weather events or high-altitude nuclear explosions (HANEs); once trapped in the Earth magnetic field, they can reduce the longevity of satellites. One mitigation strategy is to scatter these electrons with VLF waves, forcing them to precipitate into the Earth atmosphere. A promising driver for these waves is beam–plasma interaction from space-based electron accelerators, yet this approach still faces significant hurdles: minimizing beam loss, limiting energy spread, and designing compact, space-qualified accelerator systems for in-situ operation.

In this paper we present design and simulation results for a compact, power-efficient C-band (5.712 GHz) electron beam buncher, extending the work we reported at the 2024 International Particle Accelerator Conference (IPAC) [3]. The buncher converts an input, direct-current (DC) beam into a train of bunches at a repetition rate matched to the RF frequency of the accelerator in the downstream. The buncher adopts a klystron-inspired layout: a driven, input RF cavity is followed by an idler cavity, while the overall length is minimized with the electrostatic potential-depression (EPD) technology [4].

Moreover, we have introduced a continuously tunable permanent-magnet focusing scheme for the electron beam buncher. Rectangular bar magnets are mounted azimuthally and concentrically around each cavity and EPD section. Low-carbon steel pole pieces between the sections guide the magnetic flux to the paraxial region to provide a solenoid-like magnetic field distribution for beam focusing. For compact accelerator applications, such as space missions, permanent magnets are intrinsically advantageous, because they do not consume power, and thus no power supplies are required. In our permanent magnet assembly, the continuous tuning is achieved through a combination of coarse and fine tuning mechanisms.

ELECTRON BUNCHER DESIGN

Figure 1 shows the longitudinal cross section of the electron beam buncher system. The system incorporates an electron gun (model EGG-3103, Kimball Physics) that produces a 10-keV, 50-mA DC electron beam. Solenoid 1 provides magnetic field (400–500 Gauss) for the cathode for the purpose of reducing the beam scalloping when the bunches are developed. The second solenoid provides the initial focusing for the beam to be injected into the buncher structure.

The buncher has four sections, and it is a hybrid circuit involving both the RF and the high voltage (HV) components. The circuit is assembled using a clamping method, onto the 304 stainless steel mounting plate. Surrounding each section are the rectangular permanent magnet segments whose position is tunable, which are addressed in the next section. Figure 2 shows an external view of the complete buncher assembly. The buncher measures 121.84-mm in length.

The input RF cavity receives a fraction of 1 W of 5.712-GHz RF power from the source, and provides the initial bunching of the input, DC electron beam. The RF power is coupled into the cavity through a dedicated port using a small magnetic loop coupler.

* Work supported by U.S. Department of Energy through the Laboratory Directed Research and Development program of Los Alamos National Laboratory, under project number 20240136ER.

† kshipman@lanl.gov

Content from this work may be used under the terms of the CC BY 4.0 licence (© 2022). Any distribution of this work must maintain attribution to the author(s), title of the work, publisher, and DOI.

ISBN: 978-3-95450-261-5 ISSN: 2673-7000 doi: 10.18429/JACoW-NAPAC2025-WEP014

CONSIDERATION OF HTS RAPID-CYCLING MAGNET FOR STAGED MUON ACCELERATION

H. Piekarz†, Fermi National Accelerator Laboratory, Batavia, IL, USA

Content from this work may be used under the terms of the CC BY 4.0 licence (© 2022). Any distribution of this work must maintain attribution to the author(s), title of the work, publisher, and DOI.

Abstract

A possible application of the HTS (*Re*BCO) rapid-cycling dipole magnet in the first stages of muon acceleration consisting of Recirculating Linear Accelerator (RLA) and followed-up first Rapid Cycling Synchrotron (RCS-1) is presented. The projected *Re*BCO magnet hysteresis loss is discussed in terms of the liquid helium coolant choice and the option with the striated *Re*BCO conductor for the further significant reduction of the hysteresis power loss.

INTRODUCTION

The *Re*BCO magnet is described in Ref. [1]. The short muon lifetime requires rapid acceleration to minimize the decay losses on the way to the muon collider injection energy. As the muon lifetime is the shortest at low energies the muon acceleration is arranged in stages [2] consisting of the Recirculating Linear Accelerator (RLA) for the fastest initial acceleration followed with the sequence of multiple Rapid Cycling Synchrotrons (RCSs) to reach the beam injection energy of the Muon Collider. The RLA consists of the linear accelerator (LA) where the muons gain energy, and the Returning Synchrotrons (RSs) at both ends of the LA to facilitate subsequent multiple accelerations.

The RCSs accelerator magnetic field determines the ring length for the muon exit energy, and the field ramping speed sets the acceleration period which should be as close as possible to the muon total circulation time. For this reason, the RCS's must use the dipole magnets of a very high ramping speed. The RSs dipole magnet can operate in the DC mode, but the AC mode allows for a very significant power saving, especially for the Muon Collider proposed operation only at 5 Hz and the muon circulation times in the range of small fraction of a millisecond. Consequently, the RS synchrotrons should also be based on the rapid-cycling magnets.

ARRANGEMENT OF RLA AND RCS-1

The proposed arrangement of the RLA is shown in Fig. 1. The RLA comprises of the dual polarity 0.4 GeV muon source, the 8 GeV LA and four RS synchrotrons at each end of LA. The 0.4 GeV μ^+ and μ^- muons enter the 8 GeV LA in its centre and while traveling in opposite directions are accelerated to 4 GeV. Both muon species with help of the RSs 1-2-3-4-5-6-7 pass seven times through the LA to be accelerated to the total of 60 GeV. Each muon species uses its own RS1 and RS7 while sharing the RSs 2-3-4-5-6. Based on the 8 GeV Linac [3] currently under construction at Fermilab (SRF 1300 MHz, 33.7 MV/m, 20 cryomodules @ 12.5 m), the 8 GeV LA beam path is about 260 m. With the RSs 2 T top B-field the approximated muon paths and the flight times are given in Table 1. The estimated muon path in the RLA is ~ 6000 m and the flight time is ~ 20 μs.

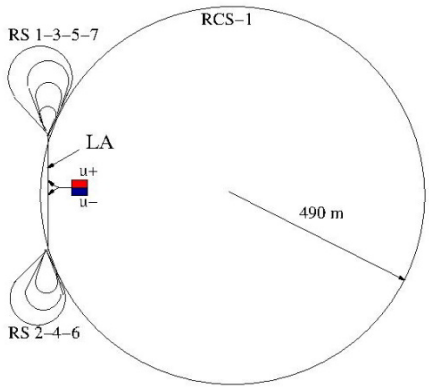


Figure 1: Arrangement of RLA and RCS-1 with 8 GeV LA. For clarity only RS 1 and RS 7 paths for μ^+ muons are shown.

Table 1: Approximated Muon Paths and Flight Times

RLA components	**Beam path**	**Flight time**
	[GeV]	[m]	[μs]
RS1	4	192	0.64
RS2	12	426	1.42
RS3	20	509	1.70
RS4	28	593	1.98
RS5	36	677	2.26
RS6	44	760	2.53
RS7	52	844	2.81
RS 1-7	4 - 52	4001	13.14
LA	0.4 - 60	1875	5.50
RLA	0.4 - 60	5876	18.64

The fast-ramping dipole magnet is constructed with the Fe3%Si laminations for which the B-field-to-current linear response is up to 1.7 T with the full saturation at 2 T limiting the range of muon exit energy for a given accelerator circumference. The energy range of the RCS accelerator can be expanded, however, by increasing the accelerator average magnetic field. This can be achieved by combining the rapid-cycling low-field ac magnets with the high-field dc magnets [4]. For the average accelerator B-field of 3 T

* This manuscript has been authored by FermiForward Discovery Group under Contract No. 8924024CS000002 with the U.S. Department of Energy, Office of Science, Office of High Energy Physics, USA. Views and opinions are those of the author and do not necessarily reflect those of the DOE.

† hpiekarz@fnal.gov

ISBN: 978-3-95450-261-5 ISSN: 2673-7000 doi: 10.18429/JACoW-NAPAC2025-WEP015

CO-SPUTTER DEPOSITION OF Nb_3Sn LAYER INTO SRF CAVITY USING Nb-Sn COMPOSITE TARGET*

M. S. Shakel[1,†], H. E. Elsayed-Ali[1], G. Eremeev[2], U. Pudasaini[3], A. Valente-Feliciano[3]
[1]Old Dominion University, Norfolk, VA, USA
[2]Fermi National Accelerator Laboratory, Batavia, IL, USA
[3]Thomas Jefferson National Accelerator Facility, Newport News, VA, USA

Abstract

Nb_3Sn, with its superior superconducting critical temperature (T_c ~18.3 K) and superheating magnetic field (H_{sh} ~400 mT), is considered a promising material for superconducting radiofrequency (SRF) cavities, offering enhanced cryogenic performance compared to bulk Nb cavities. A Nb_3Sn coating technique has been developed for SRF cavities using co-sputtering of Nb-Sn composite target in a DC cylindrical magnetron sputtering system. The composite target configuration and discharge conditions for co-sputtering were optimized to deposit Nb-Sn films on flat Nb substrates, followed by annealing to form Nb_3Sn. Several methods have been explored to improve the surface homogeneity of the Nb_3Sn coating, including optimizing a two-step annealing process and a light Sn recoating process. A 1.5 µm Nb-Sn co-sputtered film was deposited on the interior of a 2.6 GHz Nb SRF cavity and annealed at 600 ^{0}C for 6 h, followed by 950 ^{0}C for 1 h. Cryogenic RF testing of the annealed cavity demonstrated a T_c of 17.8 K, confirming the formation of Nb_3Sn. Then, the annealed cavity underwent a light Sn recoating treatment and attained a quality factor (Q_0) of 8.5E+08 at 2.0 K.

INTRODUCTION

SRF cavities made from high-purity Nb have played a central role in modern particle accelerators due to their excellent superconducting properties and ease of fabrication into complex structures [1-5]. Significant progress in cavity performance has been achieved through advancing surface preparation techniques such as electropolishing, doping, and heat treatments to improve the Nb cavity surface quality [6-9]. However, bulk Nb cavities are now approaching their fundamental performance limits in terms of accelerating gradient and surface resistance [10, 11]. Nb_3Sn, an A15 compound, offers several advantages over Nb, including a higher T_c and H_{sh}, nearly double those of Nb, can improve SRF cavity efficiency and enable operation at elevated temperatures, thereby reducing cryogenic load and operating costs [12-14]. The most widely used method for coating Nb_3Sn onto Nb cavities is Sn vapor diffusion [15-17]. Recently, a cryomodule based on vapor diffused Nb_3Sn coated Nb cavities has demonstrated an accelerating gradient of about 10 MV/m with low cryogenic loss at 4.4 K [18]. While effective, this process presents challenges such as the need for stringent control on Sn evaporation sources, non-uniform patchy regions, Sn-deficient areas on the coating layer, and the requirement for high processing temperatures [16, 19]. Magnetron sputtering is an alternative method offering improved control over film stoichiometry, deposition rate, and lower substrate temperatures [20-22]. We discuss the deposition of Nb_3Sn onto a 2.6 GHz Nb SRF cavity using a composite Nb-Sn target inside a custom-designed DC cylindrical magnetron sputtering system [23]. The process development includes optimization of the co-sputtering target configuration and plasma discharge conditions to achieve suitable stoichiometry, followed by optimizing post-deposition annealing methods, including using a light Sn recoating. Lastly, cryogenic RF test results of the co-sputtered Nb_3Sn coated cavity are presented.

CO-SPUTTERING DEPOSITION OF NB-SN ON FLAT SUBSTRATES

To identify the optimum composite Nb-Sn target configuration and discharge condition, several combinations of Nb and Sn ring targets (OD 0.9", ID 0.8") were tested using the bottom magnetron of the cylindrical sputter coater. The lengths of the Nb and Sn targets in the composite configuration were adjusted to achieve the desired Nb-Sn stoichiometry in the sputtered film. The target configuration shown in Fig. 1(a) was identified as optimal. Fig. 1(b) shows the corresponding plasma discharge at 11 mTorr Ar pressure for 53 mA discharge current. One strong plasma glow ring appears around the central Nb target, while three weaker glow rings are observed around the Sn targets. These glow rings correspond to the magnetic field distribution across the magnetron surface [23]. Using this target configuration, Nb-Sn films were deposited on flat Nb substrates ($10 \times 10 \times 3$ mm^3) mounted at three representative locations of a mock 2.6 GHz SRF cavity: at top beam tube, equator, and bottom beam tube. Before deposition, the chamber's base pressure reached 2×10^{-7} Torr. The magnetron speed was adjusted to ensure uniform coating thickness, and ~0.5 µm thick Nb-Sn films were deposited on Nb samples at the beam tubes and equator.

* This work is supported by DOE, Office of Accelerator R&D and Production, Contract No. DE-SC0022284. With partial support by DOE, Office of Nuclear Physics DE-AC05-06OR23177 to JLab and Contract No. DE-AC02-07CH11359, and Early Career Award to G. Eremeev. This manuscript has been authored by FermiForward Discovery Group, LLC under Contract No. 89243024CSC000002 with the DOE, Office of Science, Office of High Energy Physics.
† Email: mshak001@odu.edu

Content from this work may be used under the terms of the CC BY 4.0 licence (© 2022). Any distribution of this work must maintain attribution to the author(s), title of the work, publisher, and DOI.

ISBN: 978-3-95450-261-5 ISSN: 2673-7000 doi: 10.18429/JACoW-NAPAC2025-WEP016

DEMONSTRATION OF A SHEET ELECTRON BEAM PRODUCTION FROM A UNCD FIELD EMITTER ARRAY*

W. Choi†, D. Kim, H. Andrews, C.-C. Chang, M. Zuboraj, E. I. Simakov
Los Alamos National Laboratory, Los Alamos, NM, USA

Abstract

We used nitrogen-doped ultra-nanocrystalline diamonds to fabricate field emitter arrays and demonstrate production of a sheet electron beam. Diamond cathodes in the form of arrays of 1 by 81 pyramids were fabricated and tested at 20 kV. Beam images were recorded at several distances from a grid anode and used to estimate beam sizes. We found that the beam divergence angles are 0.23° in x direction, and 1.2° in y direction. There were a few obstacles during the experiments such as nonuniform emission and grid patterns in the beam images. They will be addressed in the future.

INTRODUCTION

Ultra-nanocrystalline diamond (UNCD) is a promising material for field emitters because of its mechanical and chemical stability, high thermal conductivity, and low electrical resistivity [1, 2]. UNCD deposited on flat surfaces can serve as a field emitter with its very small grain size. However, making a field emitter array (FEA) with a pyramid shape offers advantages, as it facilitates the characterization of beam emission area and emission properties. In addition, the pyramid shape reduces turn-on voltage for field emission from the arrays. A diamond field emitter array (DFEA) can be fabricated using conventional thin-film techniques, including Si-mold transfer, nanodiamond deposition via chemical vapor deposition (CVD), and brazing [3].

FEAs are widely used to realize cold cathodes which have several advantages over traditional thermionic and photo cathodes. The cold cathodes utilize field emission; therefore they don't require heating and laser systems. DFEAs are capable of operating under poor vacuum condition ($> 10^{-5}$ Torr) due to their high resistance to contamination and inherently low outgassing features [4]. Electron sources employing a cold cathode are compact, which can be essential for realizing table-top accelerators, dielectric laser accelerators, terahertz vacuum tubes, and more [5, 6].

We attempt to make sheet electron beams (SEBs) using DFEAs. SEBs are typically shaped like ellipses or rectangles that can be easily fabricated with DFEAs. Because of its shape, an SEB is capable of carrying more beam current than a conventional pencil beam. Also, an SEB with high aspect ratio can efficiently interact with planar structures.

We proposed to demonstrate fabrication of a special shaped field emitter array to produce an SEB for high frequency vacuum tubes. At Los Alamos, we established a field emitter array test stand where we can apply voltages up to a negative 40 kV to test field emitter arrays in a vacuum level of 10^{-7} Torr or lower. At this test stand, we can take beam images, measure beam current and study beam divergence. We fabricated diamond cathodes in the form of arrays of 1 by 81 pyramids and used them to demonstrate production of an SEB.

FABRICATION OF A DFEA

Fabrication process of a DFEA is illustrated in Fig. 1. Starting with dry oxidation of a Si wafer, the desired array of emitters is written using electron beam lithography with multi-pass method to draw precise patterns. A layer of SiO_2 is developed and subsequently removed using inductively coupled plasma etching. The exposed Si layer is further etched using tetramethylammonium hydroxide, an anisotropic etchant, resulting in the formation of inverted pyramidal structures. Then, a layer of UNCD is deposited on top of the Si layer using a CVD machine. The diamond layer is brazed onto a molybdenum substrate, and the Si and SiO_2 layers are etched away. The fabricated DFEA cathode is thoroughly cleaned and characterized using scanning electron microscopy (SEM). More details in fabrication and deposition of UNCD can be found in [3].

To demonstrate the generation of an SEB from a DFEA, we fabricated a DFEA with an array of 1 by 81 pyramids. The base of the pyramids is 25 µm and the pitch of the array is 50 µm. SEM analysis revealed a few blunt and double tips;

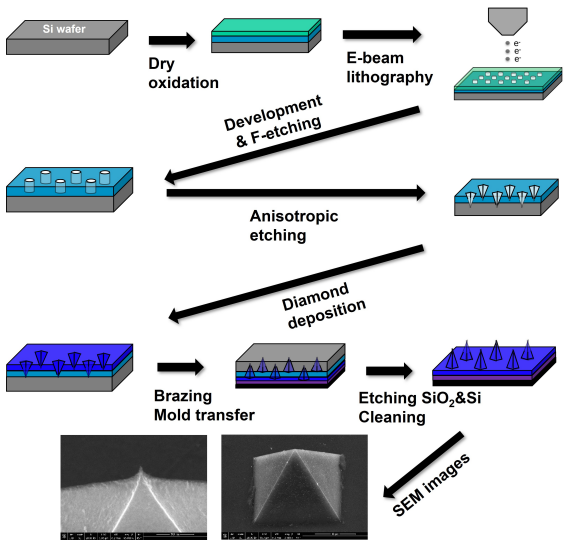


Figure 1: Overview of the fabrication process for DFEA.

* This work was supported by Los Alamos National Laboratory's Laboratory Directed Research and Development (LDRD) Program (20230110ER) and was performed, in part, at the Center for Integrated Nanotechnologies, an Office of Science User Facility operated for the U.S. Department of Energy (DOE) Office of Science.

† wonjin@lanl.gov

Content from this work may be used under the terms of the CC BY 4.0 licence (© 2022). Any distribution of this work must maintain attribution to the author(s), title of the work, publisher, and DOI.

ISBN: 978-3-95450-261-5 ISSN: 2673-7000 doi: 10.18429/JACoW-NAPAC2025-WEP017

DESIGN AND COLD TEST OF A NOVEL WAVEGUIDE POWER SPLITTER FOR DISTRIBUTED POWER COUPLING IN SHORT-PULSE ACCELERATION

S. Colmekci*, M. Shapiro, X. Lu[1†]
Northern Illinois University, DeKalb, IL, USA
[1]also at Argonne National Laboratory, Lemont, IL, USA

Abstract

Radiofrequency (RF) breakdown is the major limitation to achieving higher accelerating gradients. Recent experimental evidence shows that this limitation can be mitigated by reducing the RF pulse length to a few nanoseconds at X-band frequencies. One key challenge in designing an accelerator operating in the short-pulse regime is achieving the required short filling time. In this work, we designed a novel waveguide power splitter that can be used to independently feed an array of accelerating cells. A prototype X-band waveguide array for a one-to-four power splitter has been designed, fabricated, and tested, where the input power is equally split into four output waveguides with the desired phase advance per cell. A 3D-printed prototype has been used for low-power microwave measurements. The results, including measurements in the frequency and time domains, agree well with the simulations. Ongoing work includes designing a multi-cell accelerator based on this concept for two-beam acceleration with short RF pulses.

INTRODUCTION

A primary goal in designing radiofrequency (RF) accelerator structures is to enhance the accelerating gradient for a given input power while reducing the probability of RF breakdown. The likelihood of RF breakdown has been found to depend on both the accelerating gradient and the length of the RF pulse [1]. At a given breakdown rate, higher gradients can be achieved with shorter RF pulses. Recent studies have shown that short RF pulses on the order of a few nanoseconds can enable accelerating gradients approaching 300 MV/m [2, 3].

One challenge in designing an accelerating structure that operates with short RF pulses is achieving the required short filling time, particularly in a multi-cell structure. Distributed RF power coupling or individual power coupling [4–10] are promising concepts that could enable significantly shorter filling times. To operate cavities in this regime, an RF power distribution network is needed. This work presents a novel waveguide power splitter designed for distributed RF coupling in accelerator structures at *X*-band. Power splitting is achieved using specially designed septa on the shared waveguide walls.

A prototype of the power splitter has been designed, fabricated, and tested. In this one-to-four power splitter prototype, the input RF power is equally divided among four parallel output waveguides at a center frequency of approximately 11.7 GHz, with a desired phase advance between adjacent output ports. The four output waveguides can be connected to individual accelerating cavities to drive them simultaneously and independently for short-pulse acceleration. This design can be adapted to waveguide systems at other frequencies.

DESIGN AND SIMULATION OF THE WAVEGUIDE POWER SPLITTER

The *X*-band power splitter, operating with short RF pulses at 11.7 GHz, was designed using the computer simulation technology (CST) Microwave Studio. The frequency was selected based on the available wakefield power extractor at AWA, which provides short, high-peak-power RF pulses [2].

Figure 1 shows the vacuum model of the waveguide power splitter. It is designed to evenly distribute RF power among four output ports near the center frequency of 11.7 GHz and to provide a 90-degree phase advance between adjacent output ports. The design consists of one input port (Port 1 in Fig. 1), three identical septa, and four output ports (Ports 2–5 in Fig. 1). Each septum features a triangular-shaped cut on the shared broad waveguide wall to facilitate power splitting. The dimensions of the septa and waveguides can be tuned to adjust the phase and power distribution at the output ports. CST simulation results in both the frequency and time domains are presented in the next section and are benchmarked against the low-power measurement results.

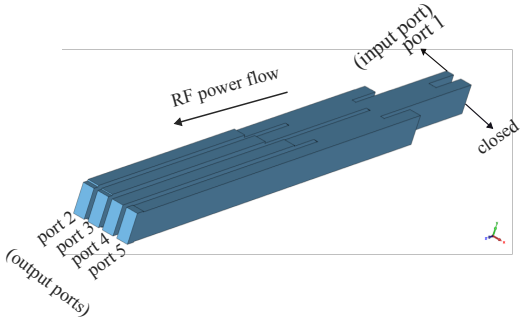


Figure 1: Vacuum part of the waveguide array power splitter, where power splitting is achieved by the septa design (not shown).

* scolmekci1@niu.edu
† xylu@niu.edu

Content from this work may be used under the terms of the CC BY 4.0 licence (© 2022). Any distribution of this work must maintain attribution to the author(s), title of the work, publisher, and DOI.

ISBN: 978-3-95450-261-5 ISSN: 2673-7000 doi: 10.18429/JACoW-NAPAC2025-WEP020

DESIGN OF A LOW-POWER PROOF-OF-CONCEPT MULTI-STAGE AMPLIFIER TEST STAND TO MODEL AND IMPLEMENT OUTPHASING CONTROL FOR THE LANSCE 805 MHZ SOLID-STATE HIGH-POWER RF AMPLIFIER*

M. C. Brown†, J. T. Bradley III, L. J. Castellano, K. Griego, S. Kwon, J. T. M. Lyles, S. J. Russell, M. Sanchez Barrueta, P. Torrez, J. A. Valladares, P. J. Van Rooy
Los Alamos National Laboratory, Los Alamos, NM, USA

Abstract

Los Alamos Neutron Science Center (LANSCE) has a project to investigate the feasibility for a replacement radio-frequency (RF) amplifier that is not reliant on vacuum electron tubes, has a similar footprint, and equivalent RF functionality. Gallium Nitride (GaN) on Silicon Carbide (SiC) high electron mobility transistors (HEMT) will be used in combined configuration. To maintain existing operational capabilities with these GaN amplifiers, the low-level control system needs to be modified for maximum transistor lifetime. The HEMT operates in a saturated condition, with a constant amplitude drive signal to avoid the high-power dissipation of linear operation with reduced drive. This leaves the phase of the RF inputs as a control mechanism, utilizing outphasing for amplitude modulation of the multistage amplifier. The GaN amplifiers also require a bias sequencing/protection board that is being designed and tested separately. To test and verify the control system, a low power test rack using commercial wideband RF components was built. This model system includes drive control, four 10 W amplifier stages, a final combination chassis, and accelerator timing system. The information from this test rack will be used to learn how to efficiently control a multistage high-power GaN amplifier to fit the requirements of the LANSCE linear accelerator.

INTRODUCTION

The LANSCE linear accelerator (linac) currently uses klystrons at the core of its high-power radio-frequency (HPRF) system. These tube amplifiers can provide over a megawatt of RF power to it's coupled-cavity linac (CCL), which is able to accelerate a 100 MeV H– proton beam up to 800 MeV. This beam is crucial for supporting four of LANSCE's user facilities. LANSCE aims to run 24/7 during the annual run cycle, which demands high service hours out of the klystrons. When one fails, a replacement from a new batch is installed in its place while troubleshooting to maximize beam uptime. The newer klystrons have been failing at a faster rate and experiencing higher infant mortality [1]. This places a significant strain on the replacement inventory and spares have struggled to be satisfactorily replenished.

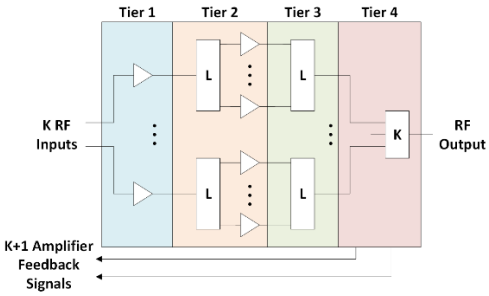


Figure 1: Multistage GaN Power Amplifier Architecture.

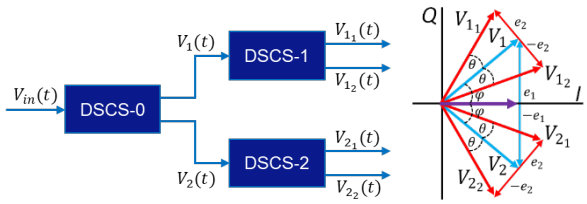


Figure 2: 4-way DSCS Expansion and Vector Diagram.

To address the mortality issues facing the LANSCE HPRF systems, alternative amplifier technology is being investigated. Solid-state power amplifiers (SSPA) show the most promise and are widely used across accelerator facilities [2, 3]. The technology that has emerged as having high power density, operating frequency, and long lifetimes necessary for LANSCE operations is newly developed Gallium Nitride (GaN) high electron mobility transistors (HEMT) on Silicon Carbide (SiC) that are capable of output 5 kW of RF power on a single chip [4]. This power density allows for a manageable multistage amplifier (Fig. 1) that can output the necessary 1.25 MW power to match the current capabilities of the LANSCE klystrons. To drive these HEMTs efficiently and get the longest lifetime out of them, constant RF drive power and bias voltage are needed. This leaves few options for the necessary RF amplitude control that LANSCE demands. Outphasing power amplifiers have demonstrated a viable approach for introducing amplitude and phase control [5, 6]. A four-way outphasing control system that uses multiple digital signal component separators (DSCS), shown in Fig. 2, is the leading solution to match the low amplitude and phase errors as well as the required control

* Work supported by the U.S Department of Energy through the Los Alamos National Laboratory, operated by Triad National Security, LLC, for the National Nuclear Security Administration of U.S. Department of Energy (Contract No. 89233218CNA000001). Research presented in this article was supported by the Laboratory Directed Research and Development program of Los Alamos National Laboratory under project number 20240723DI. Approved for unlimited release, LA-UR-25-28091.
† mikebrown@lanl.gov

Content from this work may be used under the terms of the CC BY 4.0 licence (© 2022). Any distribution of this work must maintain attribution to the author(s), title of the work, publisher, and DOI.

ISBN: 978-3-95450-261-5 ISSN: 2673-7000 doi: 10.18429/JACoW-NAPAC2025-WEP021

DESIGN OF AN OPTICAL AMPLIFIER FOR AMPLIFIED OSC IN IOTA FACILITY AT Fermilab*

A. Mondal†, J. Ruan, J. Jarvis
Fermi National Accelerator Laboratory, Batavia, IL, USA

Abstract

Optical stochastic cooling (OSC) is a cutting-edge beam cooling technology that enables high-bandwidth cooling and control of the phase space of particle beams. It has recently been successfully, experimentally, demonstrated in Fermilab's IOTA storage ring, marking a major step forward in beam cooling. One promising way to boost OSC performance is by adding a high-gain optical amplifier. However, this amplifier must be carefully designed to meet the specific constraints of the OSC system. A major challenge lies in the limited optical delay, which is just 6 mm for the case of IOTA and restricts us to use a short-length gain medium. Additionally, IOTA's high repetition rate and the relatively long bunch length, limits the peak power available for the pump laser without damaging the crystal, which is crucial for achieving strong nonlinear gain. Furthermore, it's essential to preserve the phase coherence of the OSC radiation during amplification, which further complicates the amplifier design. This report details a specialized amplifier setup that addresses these challenges, includes simulations of the integrated system, and summarizes the latest experimental progress and results.

INTRODUCTION

Since the proposal of optical stochastic cooling (OSC) in early ninties it is regarded as a superior beam cooling technology to control the phase-space density of particle beams due to its much wider optical bandwidth comparing to the conventional stochastic method [1, 2]. OSC has recently been experimentally demonstrated, establishing it as a powerful beam manipulation technique capable of cooling, heating, and controlling both ensembles and single particles [3]. With the core physics validated, current efforts at the Integrable Optics Test Accelerator (IOTA) are focused on advancing OSC performance through the implementation of an optical amplifier to enhance radiation from the pick-up undulator [4]. We explore the use of an optical parametric amplifier (OPA) for this purpose, leveraging its high gain and broad tunability across the visible to mid-infrared (MIR) spectrum [5]. A typical OPA consists of a high-power pump laser and a nonlinear crystal, which is transparent to both pump and signal frequencies, ensuring minimal absorption and thermal load. The amplification is parametric, involving virtual transitions and no net energy exchange with the crystal, enabling efficient power scaling without heat accumulation. To achieve amplification, both energy and momentum (phase-matching) conservation must be satisfied. The process generates an idler wave at frequency $\omega_i = \omega_p - \omega_s$ as required by $\hbar(\omega_p - \omega_s - \omega_i) = 0$ [5, 6]. The gain scales hyperbolically with the product of crystal length and pump amplitude [5]. The pump intensity we can use for the process is limited by the thermal damage threshold occurring due to the small linear absorption of the pump in the crystal. In our experiment, the length of the crystal is limited by the delay budget created by sending the electron beam via a bypass between the pick-up and kicker undulators [3]. In the current IOTA configuration, we estimated a delay budget around 6 mm within which all optical components including dichroic coupling mirrors, delay-adjustment plates, and a relay telescope must be accommodated. A critical requirement for OSC is the preservation of the undulator radiation's phase throughout amplification and transport. The relay optics should ensure a $\pm I$ transfer matrix while suppressing depth-of-field effects. In this work, we demonstrate a design achieving up to 40 dB amplification under these constraints, maintaining the phase integrity essential for OSC functionality.

THEORY

Initial design studies for the amplified OSC system were performed in Synchrotron Radiation Workshop (SRW) [3]. Based on available nonlinear crystals and commercially viable pump lasers, we selected undulator parameters that yield broadband radiation centered at 2.1 μm with a FWHM of 1.6 μm. For amplification, we used a periodically poled lithium niobate (PPLN) crystal for its high nonlinear coefficient and large acceptance bandwidth [7]. Pumped by a high-energy, narrowband laser at 1.064 μm. The amplification process was modeled using coupled-wave equations for difference-frequency generation (DFG), assuming low pump depletion and slowly varying envelopes. The signal (A_s) and idler (A_i) field amplitudes evolve as

$$\frac{dA_s}{dz} = \frac{2j\omega_s^2 d_{\text{eff}}}{k_s c^2} A_p A_i^* e^{j\Delta k z}, \quad \frac{dA_i}{dz} = \frac{2j\omega_i^2 d_{\text{eff}}}{k_i c^2} A_p A_s^* e^{j\Delta k z}, \tag{1}$$

where A_n and ω_n ($n = p, s, i$) are the complex amplitudes and angular frequencies of the pump, signal, and idler, respectively. The phase mismatch is $\Delta k = k_p - k_s - k_i$, d_{eff} is the effective nonlinear coefficient, and c is the speed of light in vacuum. In quasi-phase-matching, the spontaneous polarization of PPLN is periodically inverted to achieve first-order, type zero phase-matching. This modifies the mismatch as $\Delta k = k_p - k_s - k_i - 2\pi/\Lambda$, where Λ is the poling period.

* Work supported by Fermi Forward Discovery Group, LLC under Contract No.89243024CSC000002 with the U.S. Department of Energy, Office of Science, Office of High Energy Physics.

† amondal@fnal.gov

Content from this work may be used under the terms of the CC BY 4.0 licence (© 2022). Any distribution of this work must maintain attribution to the author(s), title of the work, publisher, and DOI.

ISBN: 978-3-95450-261-5 ISSN: 2673-7000 doi: 10.18429/JACoW-NAPAC2025-WEP022

DESIGN OF A SHIPPING FIXTURE FOR A COMPACT CRYOMODULE HERMETIC ASSEMBLY

J. Lewis[1,†], G. Ciovati[1,2,3], N. Huque[2], J. Armstrong[2], K. Harding[2]
[1]Mechanical and Aerospace Engineering, Old Dominion University, Norfolk, VA, USA
[2]Jefferson Lab, Newport News, VA, USA
[3]Center for Accelerator Science, Old Dominion University, Norfolk, VA, USA

Abstract

Two conduction-cooled 915 MHz superconducting radio frequency hermetic assemblies must be safely transported from the Jefferson Lab in Newport News, VA to General Atomics in San Diego, CA for performance testing in a custom horizontal test cryostat. One hermetic assembly consists of a 2-cell 915 MHz cavity, a coaxial fundamental power coupler, and the warm-to-cold transition beam tubes. The second hermetic assembly consists of a 2-cell 915 MHz cavity only. The assemblies will be transported on a flatbed air-ride trailer over the approximate 4000 km distance. Design requirements included adequate attenuation of 4g vertical axis, 5g beamline axis, and 1.5g lateral axis shock events. The isolation system was designed using helical wire-rope isolators with modal and transient finite element analysis performed in Ansys. Results show shock attenuation of a 10 ms half-sine pulse input to < 1g in the vertical axis, < 1.5g in the beamline axis, and < 0.5g in the lateral axis for both assemblies at the specified design loads and all structural stresses are kept below the material yield limits. Additionally, the natural frequencies of both isolation systems adequately attenuate the fundamental modes of the critical structures.

INTRODUCTION

In support of the development of a conduction-cooled 915 MHz superconducting radio frequency (SRF) cryomodule, this study highlights the development of a shipping fixture for transporting two separate hermetic assemblies, shown in Fig. 1, approximately 4000 km from Jefferson Lab in Newport News, VA to General Atomics in San Diego, CA via a flatbed air-ride trailer. Transportation exposes the assemblies to vibrational and shock environments which pose significant risk of damage if not properly isolated [1]. The design requirements set by Jefferson Lab include adequate attenuation of 5g shock loads in the beamline direction, 4g vertical, and 1.5g such that shock-induced stresses are kept sufficiently below material yield limits. Additionally, the fundamental mode of the isolation system must account for the natural frequencies of the ground transportation vehicle and all critical structures in the hermetic assemblies to prevent vibrational-induced damage. Critical components include the Nb cavities, the Cu antenna of the fundamental power coupler (FPC), and the FPC Al ceramic window. The inner surfaces of both cavities will be coated in Nb_3Sn at 1200 °C for 6 h, reducing the yield of the Nb to ~31 MPa. The Nb_3Sn layer has shown to be easily damaged when the Nb substrate undergoes any plastic deformation. To ensure this does not occur, the stress limit for both cavities was set at ≤15.5 MPa, half of the estimated yield strength [2]. The high purity Cu antenna of the FPC has a yield of ~33 MPa and the Al ceramic window has a flexural strength of ~296 MPa [3].

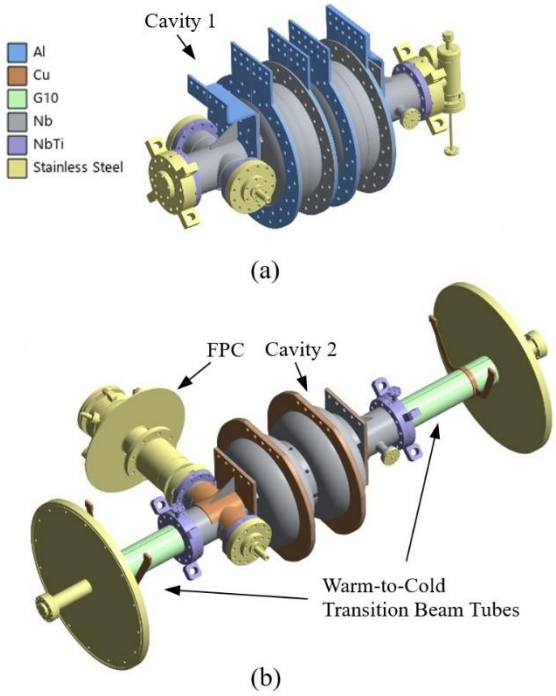


Figure 1: (a) The hermetic assembly consisting of an SRF cavity only. (b) The hermetic assembly consisting of an SRF cavity, coaxial FPC, and warm-to-cold transition beam tubes. The Cu antenna and Al ceramic window are housed within the FPC.

SHIPPING FIXTURE DESIGN

The shipping fixture consists of two primary structures, an outer and inner frame. The hermetic assembly is mounted to the inner frame while the outer frame is mounted to the trailer of the transporting truck. The two frames are then connected through helical wire-rope isolators. The non-linear stiffness characteristics of these isolators provides unique vibrational, K_v, and shock, K_s, spring-rates for six different loading orientations, making them a cost-effective and versatile isolation device. The wound stainless-steel cables provide energy dissipation resulting

* Work supported by the U.S. DOE Office of Accelerator R&D and Production and the Office of Nuclear Physics through Jefferson Science Associates, LLC under U.S. DOE Contract No. DE-AC05-06OR23177.
† jacobl@jlab.org

Content from this work may be used under the terms of the CC BY 4.0 licence (© 2022). Any distribution of this work must maintain attribution to the author(s), title of the work, publisher, and DOI.

ISBN: 978-3-95450-261-5 ISSN: 2673-7000 doi: 10.18429/JACoW-NAPAC2025-WEP023

DESIGN STUDY OF AN RF-KICKER MODULE FOR BUNCH CLEANING AT THE ATLAS POSITIVE-ION INJECTOR

D. Sinha*, G. Ha[1], Northern Illinois University, Dekalb, IL, USA
M.P. Kelly, B. Mustapha, C. Dickerson, Argonne National Laboratory, Lemont, IL, USA
[1]also at Argonne National Laboratory, Lemont, IL, USA

Abstract

Positive-Ion Injector (PII) at ATLAS accelerator facility can accelerate heavy ions and has three key subsystems: an Electron Cyclotron Resonance (ECR) ion source, a 12-MHz multi-stage beam bunching system, and a 12-MV superconducting linac accelerator. The first stage of the bunching system is the multi-harmonic buncher that operates at 12.125 MHz and creates a bunch train with period of 82.5 ns at a 70% bunching efficiency. The remaining un-bunched beam must be removed to avoid the production of undesirable 'satellite' bunches, which can quench the superconducting solenoids downstream during operation. In this paper, We present our progress on the study of a low frequency kicker for the ATLAS Low Energy Beam Transport (LEBT) and intended, ultimately, to improve the transmission efficiency for high-intensity beams through ATLAS.

INTRODUCTION

The Argonne Tandem Linac Accelerator System (ATLAS) at Argonne National Laboratory is a superconducting linear accelerator designed for the acceleration of both stable and neutron-rich heavy-ion beams spanning a broad mass range [1]. It provides high-quality beams for high-precision investigations in nuclear structure, reaction dynamics near the Coulomb barrier, and tests of fundamental symmetries. High-charge heavy ion beams are central to these efforts because their high charge states improve acceleration efficiency, allowing delivery of intense, high-energy beams for diverse applications. These include not only nuclear structure and reaction dynamics studies, but also fusion–evaporation and transfer reactions, strong-field QED experiments, radiation effects in materials, and advanced research in ion beam therapy and radiobiology [2]. However, the use of high-charge beams introduces significant operational challenges in superconducting accelerator environments. Their high ionization power leads to substantial localized energy deposition with minor beam losses and trigger quenches in superconducting cavities and magnets as observed in the Positive ion injector Linac in ATLAS.

* z1836207@students.niu.edu

In this work, we present the design study of a normal-conducting RF kicker intended to remove the primary sources of quenching——highly charged satellite bunches—— that originate from the temporal tails of the main bunches during acceleration in the Radio-Frequency Quadrupole (RFQ).

NEED FOR A KICKER DEVICE

To understand aforementioned satellite bunch forming mechanism in ATLAS, the Low Energy Beam Transport(LEBT) section of the ATLAS facility (Fig. 1) was simulated in TRACK3d [3].

The LEBT section extracts ion beams from a Electron Cyclotron Resonance (ECR) ion source and conditions them for injection into the Positive-Ion Injector (PII) linac. It includes a multiharmonic buncher [4] that imposes a time-dependent energy modulation to bunch the beam longitudinally, followed by magnetic elements for transverse focusing. The beam is then directed into a RFQ, which provides initial acceleration, transverse focusing, and additional bunching.

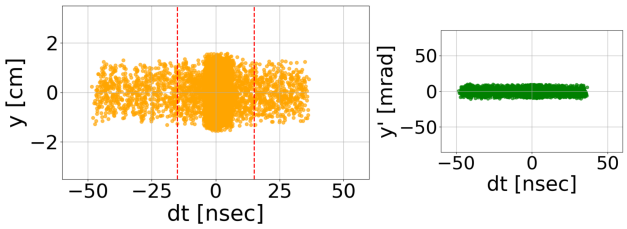


Figure 2: Transverse longitudinal correlations plotted at the entrance of quadrupole triplet magnet.

The transverse and longitudinal correlation of a Xe_{136} bunch (Fig. 2), with charge state of 20^+, was obtained at the entrance of the quadrupole triplet in Fig. 1. It reveals a well-defined temporal core with lower-density tails. Its transverse phase space also exhibits well-defined core, supporting efficient downstream transport and high-quality injection into subsequent accelerating structures.

The longitudinal phase space of the Xe_{136}^{20+} beam (Fig. 3) shows densely populated particles near the temporal center

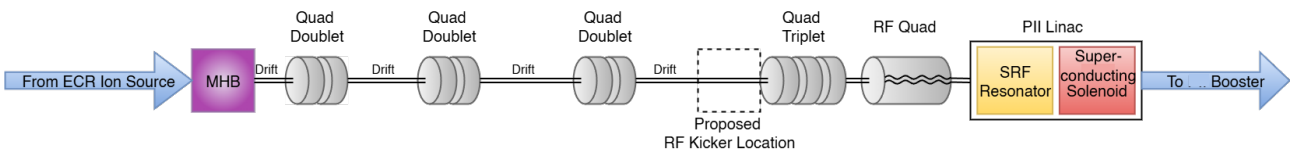


Figure 1: The Low Energy Beam Transport (LEBT) section of the ATLAS facility.

Content from this work may be used under the terms of the CC BY 4.0 licence (© 2022). Any distribution of this work must maintain attribution to the author(s), title of the work, publisher, and DOI.

ISBN: 978-3-95450-261-5 ISSN: 2673-7000 doi: 10.18429/JACoW-NAPAC2025-WEP024

DESIGN STUDY OF NOVEL DEUTERON CYCLOTRON AUTO-RESONANCE ACCELERATOR

Y. Jiang[1,†], X. Chang[1], J. H. Hirshfield[1], S. Shchelkunov[2], M. A. Palmer[2], M. Gai[3]
[1]Omega-P R&D, Inc., New Haven, CT, USA
[2]Brookhaven National Laboratory, Upton, NY, USA
[3]University of Connecticut, Groton, CT, USA

Abstract

A novel deuteron cyclotron auto-resonance accelerator (dCARA) is described here. It is predicted to produce a 40-MeV, 125 mA CW deuteron beam, with notable features including continuous acceleration without bunching for good beam stability, high efficiency, wide beam aperture, and an exceptionally short length of 1.6 meters. Such an accelerated beam can be used to produce the intense neutron flux via breakup of deuterons on a low-Z target. It is estimated that 5-10 small dCARA-based modules could provide the same level of transmutation as one acceleration driven system (ADS) employing a GeV-level 25-MW linac. Other applications of dCARA include medical isotope production system, or fusion prototypic neutron source for testing inner-wall materials for a future fusion power reactor.

INTRODUCTION

The scientific concept that underlies a deuteron Cyclotron Auto-Resonance Accelerator (dCARA) has its origins in the phenomenon of Cyclotron Auto-Resonance Accelerator (CARA), which was introduced decades ago [1]: there exists a regime of motion of a charged particle in a static uniform magnetic field, in which the particle interacts and preserves an initial condition of cyclotron resonance with a transverse electromagnetic wave, even when the Lorentz factor increases. The CARA mechanism has been demonstrated in the 1990's via its electron accelerator manifestation [2].

The dCARA can continuously accelerate deuterons at arbitrary injection phases, and the final beam energy is independent of the injection phase. Yet the direction of the exit beam depends on the injection phase, as the charged beam goes along a gyrating trajectory along a longitudinal magnetic field, where the initial transverse kick depends on the polarization angle of the transverse electromagnetic field. With continuous injection of a beam during a full RF cycle, the output beam follows a circular path. The sweeping beam intersection on a planar target perpendicular to the cavity axis constitutes self-scanning. Here the "self" is to emphasize the differences to the scanning method used in the conventional industrial linacs where alternative current electromagnets deflect the charged particles off-axis to create a zigzag path on a beam window. CARA self-scanning completes a full scanning path at a time scale of tens of nano-seconds (as RF period) instead of a few milliseconds, without using additional alternative current electromagnets.

Hence, the CARA differs fundamentally from conventional accelerators, such as linear accelerators (linacs), conventional cyclotrons, or multiple-pass machines (microtrons, Rhodotrons), all of which involve bunched beams. Particularly, the readers shall not confuse CARA with conventional cyclotrons. In cyclotrons, charged particles are accelerated outwards from the center of a flat cylindrical vacuum chamber along a spiral path in a plane; while in CARA, the particles are propagating with a significant longitudinal velocity along a conical spiral path.

The novel breakthrough of dCARA is to utilize a single compact TEM mode cavity as its accelerating structure [3], because the TEM cavity diameter can be significantly smaller than for other resonant modes otherwise it would be impractical due to the excessively large diameter waveguides and magnet bore radii required for ion acceleration.

BEAM DYNAMIC STUDY OF dCARA

The conceptual beam dynamics design was carried out using CST Studio Particle Tracking solver and preliminarily tested using Particle-In-Cell (PIC) simulation. The deuterons move on helical orbits around a strong magnetic field, acquiring energy continuously and without bunching during many revolutions within the cavity, in synchronism with the rotating radio-frequency fields. The main magnet for dCARA is a superconducting solenoid with a bore diameter < 1m and magnetic field strength < 7 T. The dimension of the main magnet is considered conventional since it is similar to those for commercial magnets now used in nuclear magnetic resonance (NMR) medical diagnostic systems.

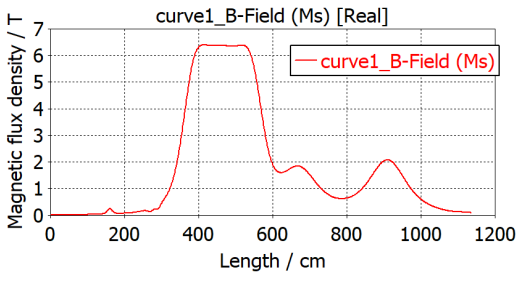


Figure 1: Magnetic field along the z-axis of the dCARA.

The beam transport system is composed of a low energy beam transport (LEBT) and a high energy beam transport (HEBT) section to guide the deuteron beam (CW or

† yong.jiang@aya.yale.edu

Content from this work may be used under the terms of the CC BY 4.0 licence (© 2022). Any distribution of this work must maintain attribution to the author(s), title of the work, publisher, and DOI.

ISBN: 978-3-95450-261-5 ISSN: 2673-7000 doi: 10.18429/JACoW-NAPAC2025-WEP027

DEVELOPMENT OF COMBINED FUNCTION DIPOLE-QUADRUPOLE PMQ MAGNETS FOR NSLS-II UPGRADE*

P. N'Gotta†, A. Banerjee, M. Breitfeller, T. Brookbank, S. Brooks, O. Chubar, F. DePaola, L. Doom, R. Faussete, R. Gambella, B. Holland, R. Hubbard, P. Joshi, A. Khan, B. Kosciuk, F. Lincoln, M. Musardo, D. Padrazo, R. Palcek, B. Parker, M. Seegitz, T. Shaftan, S. Sharma, V. Smaluk, C. Spataro, C. Stelmach, T. Tanabe, V. Teotia, R. Todd, G. Wang
Brookhaven National Laboratory, Upton, NY, USA
C. Doose, A. Jain, M. Jaski, Argonne National Laboratory, Lemont, IL, USA
J. DiMarco, Fermilab, Batavia, IL,USA

Content from this work may be used under the terms of the CC BY 4.0 licence (© 2022). Any distribution of this work must maintain attribution to the author(s), title of the work, publisher, and DOI.

Abstract

This paper focuses on the R&D performed for the development of permanent magnets-based dipoles-quadrupoles combined function magnets (PMQs) for the future NSLSII upgrade based on "complex bend" lattice. This new lattice uses PMQs that provide both bending (dipole) and strong focusing (quadrupole) magnetic field on the electron beam. The permanent magnet technology is suitable for the high magnetic field strengths (0.5 T, 130 T/m) required for such combine function magnets. PM technology leads to a compact magnet design that is essential in realizing the complex bend lattice concept, as well as a passive magnet solution which does not require electrical power supply, reducing power consumption by ~ 80% (from 1.7 MW to 0.3 MW for NSLS-II). Two PMQs magnets designs are under consideration: A hybrid design that uses both PM and soft iron poles, and Halbach type that is a pure PM design. Both PMQ designs present challenges in achieving the specified magnetic field quality due to their higher sensitivity to errors (mechanical tolerances and PM properties). This paper presents cost-effective designs and prototypes results for hybrid and Halbach PMQs, addressing various technical challenges while meeting the magnetic field requirements of the magnets for the NSLS-II upgrade.

INTRODUCTION

A new lattice concept, known as the "complex bend (CB)," has been adopted for the upgrade of the NSLS-II storage ring [1-3]. This lattice uses a large number of bending magnets pushing the Multi-Bend Achromat lattice (MBA) concept. Each magnet includes both bending and strong focusing fields, keeping the beta functions and dispersion oscillating at low values resulting in low emittance beam. This compact lattice design provides more space for insertion devices and other components. The requirement of compact, high-strength combined-function magnets can only be achieved with PMQs with small bore aperture of 16 mm [4].

This R&D aims to demonstrate the feasibility of such PMQs with either Halbach [5] or Hybrid [6] design. The Halbach PMQ provides the most compact design and presents almost a unique design to generate all the field specification. This magnet design has not been used in storage ring because of technical challenges related to field quality and radiation damage concern with the PM material close to the electron and X-ray beam. The Hybrid design, which is less sensitive to PMs errors with the use of iron poles, is a robust solution adopted by several other upgrade project [7]. This paper presents the magnetic design of both Halbach and hybrid PMQs, with their prototypes and magnetic measurement results. Various field harmonic correction solutions for the Halbach PMQ are presented with a correction capability of more than 100 units of the Root Square Sum (RSS) of field harmonics.

MAGNETIC DESIGN

The PMQ design parameters are presented in Table 1. The CB element use 15 CF PMQs with various field and gradient specification. The field and gradient presented in the table is the most challenging case. A vertical gap of 8 mm in the horizontal plane for the X-ray beam is specified on the outboard side. The selected PM material grade is Sm_2Co_{17} with a 1.15 T remanence for better temperature stability and radiation resistance. Ideally the magnet design should provide a gradient tuning of ~2% for flexibility. Including higher-order multipoles (e.g., sextupole) in the field is envisaged.

Table 1: Magnet Design Parameters

Parameter	Specification	Unit
Field-Gradient	0.5-130	T-T/m
Bore radius	8	mm
GFR	±3	mm
Harmonics RSS	≤10	units
Length	100	mm

Halbach PMQ Designs

The Halbach PMQ designs are presented in Fig. 1. The 3D magnetic models are built with Radia [8]. The designs use 16 PMs wedges with a magnetization angle modulation to generate the CF field and gradient with a low harmonic content (~10 units). The first design, based on CBETA magnet design [9], use a combination of magnetization

** This information is controlled by the U.S. Department of Commerce Export Administration Regulations 15 CFR Parts 730-774 as EAR99 Technology.*

† pngotta1@bnl.gov

ISBN: 978-3-95450-261-5 ISSN: 2673-7000 doi: 10.18429/JACoW-NAPAC2025-WEP029

DEVELOPMENTS IN LUME-ACE3P INCLUDING S-PARAMETER OPTIMIZATION FOR S3P

L. Fowler, D. Bizzozero, SLAC National Accelerator Laboratory, Menlo Park, CA, USA

Content from this work may be used under the terms of the CC BY 4.0 licence (© 2022). Any distribution of this work must maintain attribution to the author(s), title of the work, publisher, and DOI.

Abstract

We present here the introduction of optimization to LUME-ACE3P (LUME: Lightsource Unified Modeling Environment; ACE3P: Advanced Computational Electromagnetics 3D Parallel). LUME-ACE3P is a Python wrapper that streamlines workflows for ACE3P, a suite of finite element solvers for electromagnetic fields in complex geometries. LUME-ACE3P offers parameter sweep capabilities, which was previously the only means to perform optimization with this code. In the integration of LUME-ACE3P with the optimization package Xopt, we facilitate efficient and easy to use optimization for accelerator component design. We present the LUME-ACE3P-Xopt workflow with an example problem.

COMPONENT CODES

ACE3P

ACE3P (Advanced Computational Electromagnetics 3D Parallel) is a suite of codes for solving for electromagnetic fields in complex geometries [1]. It is based on high-order curved finite elements, and implemented in C++ using MPI routines for parallel processing. ACE3P is structured as a toolkit with different modules, listed in Fig. 1. ACE3P workflow consists of generating a geometry in Cubit [2], converting the Cubit output file into NetCDF form using the processing tool acdtool, running ACE3P, and post processing in a software like Paraview [3], as shown in Fig. 2.

ACE3P (Advanced Computational Electromagnetics 3P)

Frequency Domain:	Omega3P	– Eigensolver (damping)
	S3P	– S-Parameter
Time Domain:	T3P	– Wakefields and Transients
Particle Tracking:	Track3P	– Multipacting and Dark Current
EM Particle-in-cell:	Pic3P	– RF guns & space charge effects
Multi-physics:	TEM3P	– EM, Thermal & Mechanical analysis
Static Particle-in-cell:	Gun3P	– DC guns & space charge effects

Figure 1: ACE3P modules.

For this paper, we will focus on the S3P module. S3P calculates the scattering parameters of RF components by solving Maxwell's equations in the frequency domain. S3P supports dielectric and ferric materials and offers absorbing and PML boundary conditions.

LUME-ACE3P

LUME-ACE3P (LUME: Lightsource Unified Modeling Environment) is a set of Python code interfaces for running ACE3P workflows (including Cubit and postprocessing routines) with the intent of running parameter sweeps or optimization problems [4]. The base structure of LUME-ACE3P is built on LUME [5]. LUME-ACE3P supports the S3P and Omega3P modules in ACE3P. To perform a parameter sweep or optimization run, a user needs to provide the following:

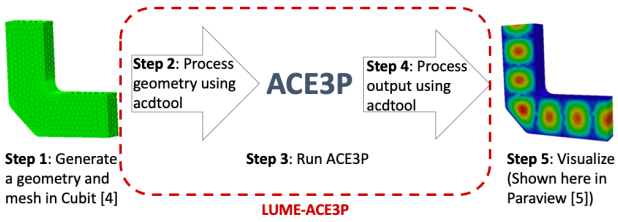


Figure 2: ACE3P workflow with LUME-ACE3P workflow overlaid.

- a LUME-ACE3P configuration file (.yaml) containing the workflow settings, input/output parameters, and ACE3P settings (this may also go in the optional ACE3P input file)
- a Cubit journal (.jou) file for editing (required for remeshing)
- a batch script (.batch) for submitting a job to the appropriate HPC resources
- (OPTIONAL) an acdtool postprocess file (e.g. .rfpost) with desired postprocessing settings (only needed for Omega3P)
- (OPTIONAL) an ACE3P file (.s3p or .omega3p) for setting ACE3P parameters like boundary conditions (if not included, this information must be specified in the LUME-ACE3P configuration file)

Before this result, running optimization with LUME-ACE3P would have required trial and error. While running a parameter sweep with LUME-ACE3P requires little time in set up from the user, it is a computationally expensive way to solve a problem like optimization that can be done in much fewer steps.

Xopt

Xopt is a Python package for optimization [6]. It supports twelve different optimization algorithms of genetic, Bayesian and deterministic types. To run an optimization problem, a user needs to specify a VOCS (variables, objectives, constraints) dictionary object and a sim function. The sim function takes input parameters and returns the quantity

ISBN: 978-3-95450-261-5 ISSN: 2673-7000 doi: 10.18429/JACoW-NAPAC2025-WEP030

EFFICIENT CONTINUOUS-WAVE NORMAL CONDUCTING ACCELERATOR FOR INDUSTRIAL APPLICATIONS*

R. A. Rimmer[1,†], J. Armstrong[1], M. Dion[1], E. Gomez[2], F. Hannon[3], R. J. Hwu[4], Y. J. Hwu[4], C. Jing[2], K. Jordan[1], R. Kostin[2], M. Marchlik[1], L. Sadwick[4], H. Wang[1], S. Wang[1]
[1]JLab, Newport News, VA, USA
[2]Euclid Techlabs, Bolingbrook, IL, USA
[3]Phase Space Tech, Lund, Sweden
[4]InnoSys Inc, Salt Lake City, UT, USA

Abstract

A normal conducting, high power, high efficiency copper linear accelerator prototype is being developed for industrial applications. The system will be powered by low-cost high-efficiency magnetron RF sources and will use a gridded thermionic cathode electron gun. Leveraging the significant accelerator expertise at JLab and industry partners, these technologies will be combined to deliver high-power (>100 kW) electron beams with energies of 1 MeV or higher that are cost-effective to produce and operate. The design is modular such that energy and power can be increased by adding additional sections as required. The status of the design, prototype fabrication and plans for a beam demonstration at JLab are described.

INTRODUCTION

There is a growing need for compact, reliable, powerful and affordable continuous wave (CW) electron beam sources for various industrial applications including replacements of isotope-based radiation sources. A compact, efficient and powerful CW electron linear accelerator (LINAC) beam source suitable for static or mobile applications is being developed [1]. The proposed design is readily scalable to ≥5 MeV and ≥100 kW power.

This project is developing a prototype section of such a LINAC, starting with a 30 kV electron source, operating up to 1 MeV, 20 kW CW, scalable to a 100 kW demonstration and ultimately higher power industrial systems, see Table 1. The LINAC will operate at 915 MHz to take advantage of commercial magnetron sources that are available for ≤ $2/W [2]. The system will use a gridded thermionic electron gun to pre-bunch the beam and solenoid focusing to guide it through the LINAC. RF to beam efficiency is expected to exceed 75% at high power.

LINAC DESIGN

Since the electron gun will operate at 30 kV the LINAC must accept particles traveling at less than the speed of light, and accelerate them rapidly. To accommodate the electron's varying velocity the cell lengths are adjusted according to the beta along the acceleration path, see Fig. 1. The cavity operates in standing wave in the pi mode. The gradients in each cell are made to be equal so the energy gain is roughly linear with distance. Figure 2 shows the field amplitude and Fig. 3 the energy gain along the LINAC. After the first LINAC cavity additional beta one modules may be used for further acceleration.

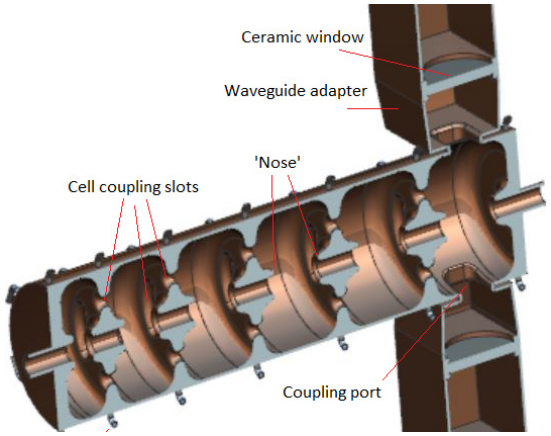


Figure 1: Graded-beta pi mode standing wave LINAC.

Table 1: Key Performance Parameters for the Developmental Stages of the Systems

	Prototype System	Demo System	Industrial System
Energy	1 MeV	1-5 MeV	1-5 MeV
Current	20 mA	1-100 mA	≤500 mA
Power	20 kW	≤100 kW	≤500 kW
Cost	N.A.	<$10/W	<$10/W
Efficiency	~35%	>50%	>75%

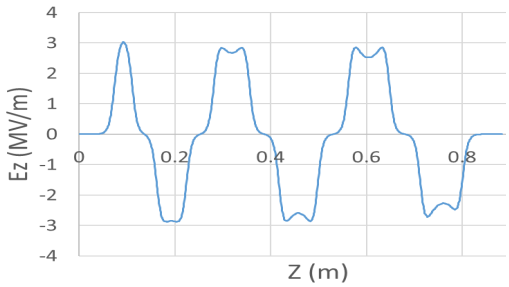


Figure 2: Field profile in the LINAC cavity.

*This research was supported by the U.S. Department of Energy, National Nuclear Security Administration, Office of Defense Nuclear Nonproliferation Research and Development (DNN R&D) and by the U.S. Department of Energy, Office of Science, Office of Nuclear Physics under contract DE-AC05-06OR23177
† rarimmer@jlab.org

Content from this work may be used under the terms of the CC BY 4.0 licence (© 2022). Any distribution of this work must maintain attribution to the author(s), title of the work, publisher, and DOI.

ISBN: 978-3-95450-261-5 ISSN: 2673-7000 doi: 10.18429/JACoW-NAPAC2025-WEP032

HIGH POWER 805 MHz SOLID STATE AMPLIFIERS USING GaN ON SiC HEMT FOR LANSCE CCL*

J. T. M. Lyles†, M. S. Barrueta, J. T. Bradley III, M. C. Brown, T. W. Hall,
S. I. Kwon, S. J. Russell, J. A. Valladares, P. J. Van Rooy, J. A. Vega
Los Alamos National Laboratory, Los Alamos, NM, USA

Abstract

The Los Alamos Neutron Science Center uses a coupled-cavity linac (CCL) to accelerate H- ions from 100 to 800 MeV. It is powered by forty-four 1.25 MW 805 MHz klystrons of older design. Continued supplies of identical klystrons for the linac operation beyond 2050 are uncertain. We have embarked on a feasibility study for a replacement RF amplifier without vacuum electron tubes, that fits in the space of one klystron. Commercial silicon LDMOS transistors have reduced power above 600 MHz and are limited by the maximum drain to source breakdown voltage. We selected high voltage Gallium Nitride (GaN) on Silicon Carbide (SiC) high electron mobility transistors (HEMT) to reduce the number of active devices and the complexity of power combining smaller amplifiers. They are able to operate at higher channel temperature and voltage ratings compared to silicon transistors. We have tested devices with 3.6 kW of saturated power at 100 volts, and are planning for 5 kW HEMTs for the final design. Outphasing modulation allows higher efficiency and lower thermal dissipation than class AB linear amplifiers. Power supplies and combining technology are also under study for this system.

INTRODUCTION

LANSCE uses an 800 MeV combined proton/H- linac. Protons of 100 MeV from the drift tube linac are used for isotope production while a subsequent CCL accelerates H- beam from 100 to 800 MeV. This normal conducting structure is powered by forty-four 1.25 MW 805 MHz klystrons, which all together provide approximately 44 MW of peak RF power and 5.3 MW of average power. These klystrons have been manufactured essentially unchanged since their introduction in 1968. Mean time to failure (MTTF) for more recent klystrons is shorter than it was for the original production tubes [1]. The linac must provide beams beyond 2050. There are concerns about relying solely on this vacuum electron tube technology for over 25 more years.

The LANSCE klystrons require 86 kV beam voltage from conventional mains power supplies and capacitor banks, which present their own set of difficulties. The HV transformer/rectifier units are no longer available from the original source, and rebuilding them has had mixed success. Transformer companies are principally committed to supporting utility infrastructure for increasing demands for electrical power. Scientific customers for one-off orders represent a small portion of their market. The 60 Hz AC regulators at LANSCE are similarly difficult to obtain or repair. Seven capacitor banks, each feeding 6-7 klystrons, rely on a large number of oil-paper insulated series/parallel capacitor strings. It is common for component failures to result in collateral damage in the bank due to the 230 kJ of stored energy. As engineering courses have phased out teaching vacuum tube technology and are now concentrating on solid-state devices, a longer period of on-the-job training is required for new personnel working with this equipment. These HV equipment challenges are exacerbated by having a younger engineering team less familiar with HV engineering than the designers who built the systems 53 years ago.

A new initiative is underway to develop a replacement RF power amplifier that can fit in the space of one klystron and its modulator tank [2]. This will use many solid-state amplifier (SSA) pallets combined to produce equivalent or better performance than that of a klystron. This eliminates most obsolescence concerns of the 50+ year-old technology at LANSCE, replacing them with low voltage technology. Interestingly, this work attracts new hires with skills in modern radar, scientific and broadcast high power RF.

SSA DESIGN CONSIDERATIONS

Transistor Technologies

Peak power capability has been a hallmark for vacuum tubes, where the thermal mass is large and the peak to average power ratio can be as high as ten. For a SSA, the most reliable approach is operating in continuous mode, and this has enabled them to replace klystrons or inductive output tubes at dozens of synchrotrons and storage rings worldwide [3]. Pulsed operation, such as for the LANSCE CCL, requires considering the intrinsic peak capability of the individual junctions or channels inside the devices, the packaging for thermal design, and having energy storage with capacitors, not unlike klystrons except at one thousandth of the voltage. Lessons learned from published SSA developments at other accelerators using silicon laterally-diffused metal-oxide semiconductor (LDMOS) have been reviewed for this project. The largest and most challenging pulsed RF SSA is a 1.6 MW long pulse amplifier at CERN for the SPS, where ground breaking performance first required a number of modifications to solve initial problems [4].

*Work supported by the U.S. Department of Energy through the Los Alamos National Laboratory, operated by Triad National Security, LLC, for the National Nuclear Security Administration of U.S. Department of Energy (Contract No. 89233218CNA000001). Research presented in this article was supported by the Laboratory Directed Research and Development program of Los Alamos National Laboratory under project number 20240723DI.

†jtml@lanl.gov

Content from this work may be used under the terms of the CC BY 4.0 licence (© 2022). Any distribution of this work must maintain attribution to the author(s), title of the work, publisher, and DOI.

ISBN: 978-3-95450-261-5 ISSN: 2673-7000 doi: 10.18429/JACoW-NAPAC2025-WEP037

FINAL DESIGN AND FIRST USE OF IN-SITU MEASURING APPARATUS FOR MEASUREMENT OF PERMANENT MAGNET RESILIENCY IN CEBAF'S RADIATION ENVIRONMENT*

E. A. Nissen†, R. M. Bodenstein, K. E. Deitrick, B. R. Gamage,
J. F. Gubeli, I. Neththikumara
Thomas Jefferson National Accelerator Facility, Newport News, VA, USA

Abstract

In this work we outline the final design and initial measurement lessons for the holders and measuring apparatus of the permanent magnet resiliency experiment which is a part of the FFA@CEBAF proposed upgrade. The experiment will expose permanent magnets to the radiation environment of CEBAF. Due to safety regulations we need to measure the magnets in the tunnel without bringing them out, so we designed a mobile measuring system as well as a series of protocols to allow us to speedily measure these samples even under adverse conditions. We also designed our system to be capable of taking measurements even with component failures.

INTRODUCTION

A proposed upgrade for the CEBAF accelerator would use permanent magnets in a Fixed Field Alternating gradient lattice [1]. In order to determine how the permanent magnets will react to a radiation environment, we have created an experiment to leave magnetic material samples in various parts of the CEBAF tunnel while the beam is in operation [2].

Radiation control rules mean that bringing the magnet samples out of the tunnel to measure them would involve sweeping them for potential contamination. Since we are only able to access the tunnel every other week during the experimental run, bringing them out then waiting to put them back in would lose half of the potential radiation exposure time. Therefore, we decided to create an experimental setup that would measure the magnets in-situ [3].

EXPERIMENTAL SETUP

The measurements are made with a Senis AG 3MH6-E Teslameter [4] and a Magnetic Instrumentation, Inc. Helmholtz coil with model 2130 fluxmeter [5]. We capture the data using computer software specifically written for this project. The computer communicates with the Helmholtz fluxmeter and the Teslameter using RS-232 serial connections.

The experimental setup uses exposure plates to hold the samples at particular points in the accelerator. These plates also hold dosimetry, both area dosimeters and small tubes, each of which hold optichromic rods. There are two types of exposure plate, single sample and assembly. Images of the two types of plate are shown in Fig. 1. The single samples are held in holders that contain slots for the Teslameter's probe to fit into. The use of these slots makes sure that we are measuring the same point on each sample as consistently as possible. These sample holders also have notches that make sure they are always put into the correct positions on their plate. We cycled the four different types of samples throughout the different slots to prevent a systematic error that might occur from a sample always being in the same place.



Figure 1: These are the exposure plates for the single samples (top) and assembly holders (bottom).

The assemblies consist of two smaller magnet samples contained in enclosures. These enclosures are then paired up in a holder in one of four different configurations.

- Alpha ⇒ ⇒
- Beta ⇒⇐
- Gamma ⇒⇑
- Delta ⇒

The arrow denotes the direction of the north pole. Both in the single samples and in the assemblies we have kept the poles parallel with the plane of the plate. This makes sure that any stray fields perpendicular to the plate will decay faster so that we can place these magnets near the beamline without interfering with beam operations. Much like the single sample plates, we switched which configuration was in each slot to again reduce systematic errors.

Both types of samples use barcodes to aid in data collection. Each sample gets a specific code. Barcode readers work by sending keystrokes to the computer as if they came from a keyboard. The data acquisition software determines what it's reading based on the first character. An R is a tube with optichromic rods, X is an area dosimeter,

* This material is based upon work supported by the U.S. Department of Energy, Office of Science, Office of Nuclear Physics under contract DE-AC05-06OR23177. Some of the work described in this paper was conducted under the Laboratory Directed Research and Development Program at Thomas Jefferson National Accelerator Facility for the U.S. Department of Energy.
† nissen@jlab.org

Content from this work may be used under the terms of the CC BY 4.0 licence (© 2022). Any distribution of this work must maintain attribution to the author(s), title of the work, publisher, and DOI.

ISBN: 978-3-95450-261-5 ISSN: 2673-7000 doi: 10.18429/JACoW-NAPAC2025-WEP038

FIRST RESULTS FROM A Nb_3Sn-COATED 1.5-CELL 650 MHz SRF CAVITY FOR CRYOGEN-FREE INDUSTRIAL ACCELERATORS*

N. Tagdulang†, K. McGee, I. Gonin, T. Khabiboulline, A. Sukhanov, C. Edwards, M. Henry, B. Tennis, M. K. Ng, G. Eremeev, V. Yakovlev, J. Thangaraj
Fermi National Accelerator Laboratory, Batavia, IL, USA

Content from this work may be used under the terms of the CC BY 4.0 licence (© 2022). Any distribution of this work must maintain attribution to the author(s), title of the work, publisher, and DOI.

Abstract

Fermilab is advancing the development of a compact, high-power electron beam accelerator using superconducting radio frequency (SRF) technology as a non-radioactive alternative to traditional radiological sources. The current design targets continuous-wave (CW) operation at 1.6 MeV and 20 kW. To ensure suitability for industrial environments, the system is being designed for cryogen-free operation, driving the adoption of a novel Nb_3Sn-coated 1.5-cell SRF cavity operating at 650 MHz. This contribution reports on the fabrication, surface preparation, and Nb_3Sn coating process of the cavity, as well as first results from vertical test stand (VTS) measurements performed in a liquid helium bath. These initial tests mark a key milestone toward demonstrating the viability of conduction-cooled Nb_3Sn SRF cavities for industrial-scale deployment.

INTRODUCTION

A meter-long compact linear accelerator (linac) are nowadays being considered to replace traditional radiological sources in many industrial applications driven by growing concerns about security and availability. To compete with alternative methods, the linear accelerator must accelerate electron beams with 1-10 MeV energy, average beam power of hundreds of kW, and in continuous wave (CW) mode. Moreover, it must be robust, cost-effective, and adaptable in harsh industrial settings [1]. Such requirements can be made possible thanks to the recent advancements in the area of, but not limited to, superconducting radio-frequency cavities and conduction cooling technologies [2].

The Illinois Accelerator Research Center (IARC) of Fermilab has currently started the design, construction, and validation of a prototype linac employing a 1.5 cell 650 MHz cavity capable of delivering 12.5 mA of beam current with a beam power of 20 kW, 1.6 MeV beam energy, and in CW mode [3]. Figure 1 shows the schematic of the compact 20 kW linac. The cryostat housing the SRF cavity is about a meter long and a meter in diameter. A small thermionic cathode and low-loss RF coupler are integrated into the cavity, thoroughly designed to minimize the amount of heat generated into the system. Two commercial cryo-coolers are connected to the cavity through 5N aluminum thermal links to provide the necessary cooling capacity via conduction. A key enabler to the usage of this conduction cooling technology and therefore allowing cryogen-free operation is the Nb_3Sn superconductor coating on the inner surface of the cavity. The successful demonstration recently of a single cell Nb_3Sn coated 650 MHz cavity showed that a Q_0 above 1×10^{10} and $E_{acc} = 7$ MV/m is feasible for the 1.5 cell 650 MHz cavity geometry [4]. The cavity would induce heat loss to only about 1.5 W, which is less than the 2 W capability of commercial cryo-coolers to remove heat at 4 K [2]. In this contribution, we report the cavity preparation, Nb_3Sn coating, and the first-ever RF result of a Nb_3Sn-coated 1.5 cell 650 MHz cavity under a helium bath. This progress marks a major step towards the first demonstration of a compact superconducting linac for industrial purposes.

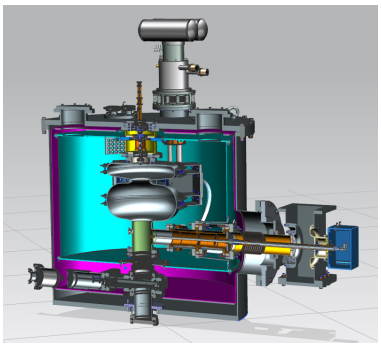


Figure 1: Schematic of 20 kW, 1.6 MeV linac employing 1.5 cell 650 MHz cavity.

CAVITY BASELINE PREPARATION

The SRF cavity used in this work has a length, $L = 0.30$ m, surface geometric factor, $G_s = 197\ \Omega$, peak magnetic field, $B_{pk} = 4.41 * E_{acc}$, and normalized shunt impedance, $r/Q = 178\ \Omega$. For conduction cooling, Nb rings (SRF grade, RRR = 300) were e-beam welded on each cell.

To prepare the inner surface of the cavity for Nb_3Sn coating, we followed the standard procedure for the treatment of the cavities for the International Linear Collider (ILC) with a modified hydrogen degassing step [5]. The Nb cavity received 120 µm bulk EP, 350 °C/12 h baking and 600 °C/10 h for hydrogen degassing, field flatness tuning, and 20 µm light EP with last 10 µm cold EP. Figure 2 illustrates the normalized electric field amplitude along the axis of the cavity between simulated and measured values, the latter obtained using the 'bead-pull' method for field flatness tuning. To reach the desired frequency and the field level between the full cell and the half cell, the full cell was compressed and tuned by 730 kHz.

* Work supported by the Office of Defense Nuclear Nonproliferation Research and Development within the U.S. Department of Energy's National Nuclear Security Administration (DOE/NNSA)

† ntagdula@fnal.gov

ISBN: 978-3-95450-261-5 ISSN: 2673-7000 doi: 10.18429/JACoW-NAPAC2025-WEP040

GRID DISTURBANCE REJECTION VIA IMPROVED DC-LINK VOLTAGE FEEDFORWARD CONTROL FOR L-BEND POWER SUPPLIES IN THE APS UPGRADE*

Y. Ruan† and F. Rafael
Argonne National Laboratory, Lemont, IL, USA

Abstract

As part of the Advanced Photon Source Upgrade, two high-power DC supplies for the L-Bend M1 and M2 magnets were installed. During the APS-U commissioning, a 1-Hz ripple was detected in the output currents of the M1/M2 and slow corrector supplies, leading to 1-Hz beam motion. This low-frequency harmonic originated from the booster ramping supply operating at 1 Hz, causing periodic grid voltage sags. This paper proposes an improved DC-Link voltage feedforward control for the M1/M2 supplies to reject grid disturbances, significantly attenuating the 1-Hz and other low-frequency ripples in the output currents. Combined with regulation circuit modification of the slow corrector power supplies, the 1-Hz harmonic was successfully eliminated from the beam motion.

INTRODUCTION

There are over 1,000 new bipolar power supplies for corrector magnets, along with two high-power DC supplies for the L-Bend M1 and M2 magnets, installed as part of the Advanced Photon Source Upgrade (APS-U). During the APS-U commissioning in early 2024, a 1-Hz beam motion was observed, and the booster ramping supply was identified as the source of the harmonic disturbance. Operating at 1 Hz, the ramping supply draws a significant amount of power from the 480-VAC grid, causing periodic voltage sags, as illustrated in Fig. 1. This grid disturbance introduces harmonics into the DC-Link voltage, affecting the output currents of both the M1/M2 and corrector supplies.

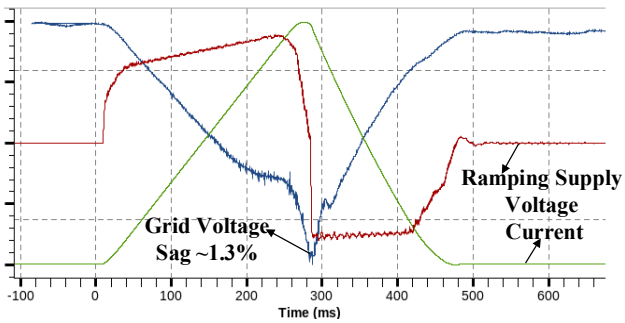


Figure 1: The voltage sag in the AC grid caused by booster ramping supply.

The corrector supplies were designed at Argonne [1-2], and the 1-Hz ripple was successfully attenuated by adjusting the regulation loop through a simple jumper reconfiguration. However, the high-power M1/M2 supplies were designed and fabricated by a vendor, making it more challenging for Argonne to devise a solution. With limited information available, a simulation model was developed in MATLAB/Simulink to explore methods for mitigating the 1-Hz ripple. Simulation results confirmed that employing DC-Link voltage feedforward to automatically adjust the PWM duty ratio was highly effective in rejecting grid disturbances.

It was later discovered that the existing DC-Link voltage sensing circuit excluded low-frequency components, which explains why the previous feedforward control had little effect on rejecting disturbances—this finding was also confirmed by the simulation results. As a result, the DC-Link voltage sensing circuit was modified to incorporate low-frequency signals. Additionally, the controller firmware was updated to accommodate this hardware change. With the modified feedforward control in place, the low-frequency ripples, including the 1-Hz disturbance, were significantly attenuated, resulting in the successful elimination of the 1-Hz beam motion.

GRID DISTURBANCE REJECTION FOR M1/M2 SUPPLIES

Power Circuit and Control Scheme

The L-Bend M1/M2 supplies share a similar power circuit and control scheme, as shown in Fig. 2, with differences in power capacity. The M1 supply is rated at 475 A/1500 V DC, while the M2 supply is rated at 220 A/1000 V DC. Both supplies use an internal step-up transformer that feeds two 6-pulse rectifiers, followed by an IGBT-based bridge. The output current is regulated to track the setpoint provided by the Experimental Physics and Industrial Control System (EPICS).

For both M1 and M2 supplies, there is an outer current control loop and an inner voltage control loop, both implemented digitally in the firmware. The output of the current loop serves as the reference signal u_r for the voltage loop, and the duty ratio e is generated to regulate the output voltage u_{out}, ensuring that the output current tracks the setpoint.

Duty Ratio Correction With DC-Link Voltage Feedforward

The DC-Link voltage feedforward (FF) is already applied in the firmware, which corrects the duty cycle e to compensate for voltage fluctuations and maintain stable output:

$$e\frac{\overline{u_{dc}}}{u_{dc}},$$

* Work supported by the U.S. Department of Energy, Office of Science, Office of Basic Energy Sciences, under Contract No. DE-AC02-06CH11357.
† yruan@anl.gov

Content from this work may be used under the terms of the CC BY 4.0 licence (© 2022). Any distribution of this work must maintain attribution to the author(s), title of the work, publisher, and DOI.

ISBN: 978-3-95450-261-5 ISSN: 2673-7000 doi: 10.18429/JACoW-NAPAC2025-WEP042

HEAVY ION IMPLANTATION ANALYSIS IN GRAPHITE FOR THE FRIB CHARGE SELECTOR*

X. Wang †, T. Kanemura, A.S. Plastun, Facility for Rare Isotope Beams, East Lansing, MI, USA

Abstract

An advanced charge selector is currently under development at the Facility for Rare Isotope Beams (FRIB) to intercept unwanted charge states of stripped heavy ion beams. Rotating graphite wheels are employed to absorb beams with a power up to 5 kW and rms size as small as 0.7 mm × 1.25 mm.

Ion implantation and radiation damage can degrade material properties and lead to structural failure, making foreign ion accumulation a key factor in predicting graphite wheel lifetime. In this study, SRIM simulations and Monte Carlo analysis were used to model implantation with wheel geometry and rotation, followed by diffusion modeling. Results show that optimizing beam position and accounting for diffusion significantly reduce peak ion concentrations, providing essential data for graphite wheel lifetime assessment.

INTRODUCTION

The Facility for Rare Isotope Beams (FRIB), supported by the U.S. Department of Energy's Office of Science, is a state-of-the-art user facility dedicated to advancing nuclear science. Since commencing operations in 2022, FRIB has progressively increased its primary beam power from 1 kW to 20 kW [1]. The facility is now being upgraded for 50 kW operation, with the charge selector among the key devices under development [2].

The charge selector, located in the first folding segment of the accelerator, intercepts unwanted charge states produced after the beam stripper. An advanced design employing a rotating graphite wheel, shown in Fig. 1, is under development [3,4] to replace the existing unit . The upgraded system is designed to intercept beam spots with powers up to 5 kW, beam energies from 17 to 20 MeV/u, and rms sizes as small as 0.7 mm × 1.25 mm.

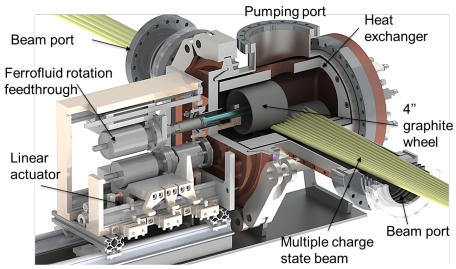


Figure 1: Model the charge selector.

* This material is based upon work supported by the U.S. Department of Energy, Office of Science, Office of Nuclear Physics and used resources of the Facility for Rare Isotope Beams (FRIB) Operations, which is a DOE Office of Science User Facility under Award Number DE-SC0023633.

† wangxiu@frib.msu.edu

As ion beams are continuously implanted into graphite, foreign ions, lattice displacement, and radiation damage accumulate in the material, potentially leading to structural failure [5, 6]. Therefore, determining the foreign ion accumulation behavior is one critical aspect for predicting the operational lifetime of graphite wheels.

After penetrating the graphite, the particles first come to rest through interactions with the target lattice [6]. Under the elevated operating temperatures of the graphite, these implanted particles then diffuse through the material, driven by concentration gradients [7, 8]. Once they diffuse to the surface, the foreign atoms evaporate into the surrounding vacuum environment [7, 9]. This study modeled the implantation and diffusion processes to support lifetime estimation.

METHODOLOGY

Ion Implantation and Rotation

As ions penetrate graphite, they lose energy through scattering events involving Coulomb interactions with the target's atoms and electrons, eventually coming to rest within the material. In this study, SRIM was used to simulate the scattering and stopping locations of ions in graphite. The resulting projected range distribution is described by Eq. (1).

$$\delta_{\text{depth}} = \frac{1}{\sqrt{2\pi}\,\sigma_{\text{depth}}} \exp\left(-\frac{(y-\mu_{\text{depth}})^2}{\sigma_{\text{depth}}^2}\right) \qquad (1)$$

where δ_{depth} is the projected range distribution, μ_{depth} and σ_{depth} are the mean stopping range and the projected straggling range, respectively.

To calculate the ion distribution in the graphite, a Monte Carlo–based model was developed to account for wheel geometry and rotational dynamics. Figure 2 shows the coordinates and calculation schematic: the beam strikes the wheel with the beam center at $(R - y_{\text{offset}}, z_0)$, where R is the wheel radius. The schematic shows a side view of the graphite wheel and illustrates the three main calculation steps.

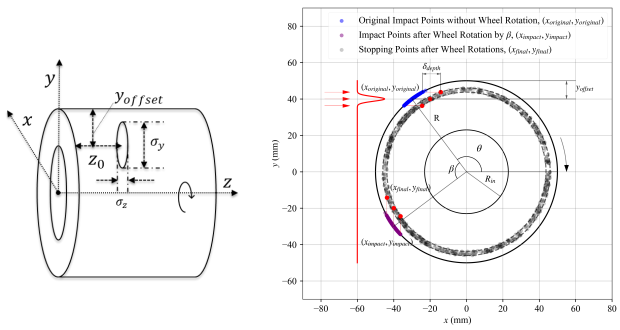


Figure 2: Coordinates (left); calculation schematic (right).

Content from this work may be used under the terms of the CC BY 4.0 licence (© 2022). Any distribution of this work must maintain attribution to the author(s), title of the work, publisher, and DOI.

ISBN: 978-3-95450-261-5 ISSN: 2673-7000 doi: 10.18429/JACoW-NAPAC2025-WEP047

INVESTIGATING DIRAC SEMIMETAL CADMIUM ARSENIDE AS A POTENTIAL LOW-MTE PHOTOCATHODE

T. W. Idso*, A. Ullattuparambil, M. M. Rizi, S. Karkare, Arizona State University, Tempe, AZ, USA
A. Rice, K. Alberi, National Renewable Energy Laboratory, Golden, CO, USA

Abstract

We report on the quantum efficiency (QE) and mean transverse energy (MTE) of photoemitted electrons from cadmium arsenide (Cd_3As_2), a three-dimensional Dirac semimetal (3D DSM) of interest for photocathode applications due to its unique electronic band structure, characterized by a 3D linear dispersion relation at the Fermi energy. Samples were synthesized at the National Renewable Energy Laboratory (NREL) and transferred under ultra-high vacuum to Arizona State University (ASU) for measurement using a photoemission electron microscope (PEEM). The maximum QE was measured to be $3.37 \cdot 10^{-4}$ at 230 nm, and the minimum MTE was 55.8 meV at 250 nm. These findings represent the first reported QE and MTE measurements of Cd_3As_2 and are an important step in evaluating the viability of 3D DSMs as low-MTE photocathodes. Such photocathodes, constrained to lower MTEs by the electronic band structure, may prove effective in advancing beam brightness in next-generation instruments and techniques.

INTRODUCTION

Minimizing the mean transverse energy (MTE) of photoemitted electrons and maximizing the quantum efficiency (QE) are both essential for the generation of bright electron beams. Existing x-ray free electron lasers (XFELs) and emerging concepts for compact XFELs will directly benefit from higher beam brightness which enables stronger lasing gain, shorter pulse durations, and improved temporal coherence [1–3]. Brighter beams can also alleviate the need for larger accelerator footprints, reducing both operational costs and the complexity of beamline components [4]. Additionally, methods like ultrafast electron diffraction and microscopy (UED/UEM) will benefit from enhanced brightness in terms of higher-contrast imaging and improved temporal resolution [5–8]. Achieving low MTEs and high QEs in photocathodes can thus drive significant advances in the design of next-generation instruments and methods where both performance and scalability are critical considerations. However, finding robust photocathodes that meet these criteria is ongoing.

Three-dimensional Dirac semimetals (3D DSMs) are a novel class of materials which are bulk electronic analogues to graphene (a 2D DSM). 3D DSMs exhibit a distinct electronic structure at the Fermi energy in which the dispersion relation is linear in all three momentum directions around the Dirac point thus resulting in several unique phenomena including massless fermions [9].

* tidso@asu.edu

It has been shown previously that emission from bands with low effective mass can theoretically constrain the transverse momentum of emitted electrons [10, 11]. Likewise, electrons that are photoemitted from near the Dirac point can have exceptionally small transverse energies resulting in MTEs potentially below 5 meV, even at room temperature [2]. Consequently, a robust 3D DSM photocathode is of significant interest for the development of brighter electron beams. Cadmium arsenide (Cd_3As_2), which has attracted significant attention following the experimental observation of its 3D DSM phase via angle-resolved photoemission spectroscopy (ARPES) in 2014, is one candidate for such a photocathode [9, 12, 13]. In this proceeding, we present experimental measurements of QE and MTE from Cd_3As_2, address the experimental dispersion relation at room temperature, and investigate the merits of the interstate transport process used for in-vacuum transfer of the Cd_3As_2 photocathode.

EXPERIMENTAL METHODS

Samples were grown on n-type Si:GaAs[001] substrates with a 4 degree miscut toward (111)A. Following desorption of the surface oxide, a 500 nm Si:GaAs buffer was grown, after which samples were capped and moved to a separate II-VI chamber. A thin ZnTe nucleation layer was then grown after decapping, followed by lattice-matched $Zn_xCd_{1-x}Te$ (approximately 20 and 100 nm thick, respectively). Cd_3As_2 was then grown from a Cd effusion source and an As valved cracker cell as described elsewhere [14]. The growth was performed under As-rich conditions and at a temperature of approximately 115 °C. This layer was grown to a thickness of ∼200 nm before the samples were transferred into an ultra-high vacuum (UHV) "suitcase" with a baseline pressure of 10^{-10} Torr.

The UHV suitcase included an ion pump and power supply which provided continual active pumping throughout the duration of the ∼12-hour interstate transfer process from NREL to ASU. Upon arrival, the suitcase was connected to the UHV transfer line in the Photoemission and Bright Beams Lab (PBBL) [15]. The junction was flushed with an inert gas during the connection procedure to minimize air contamination. A bakeout was then performed overnight to bring the vacuum level in the connecting junction down to the high 10^{-10} Torr range before the vacuum suitcase was opened and the samples were transported into PBBL's UHV transfer line via the magnetically coupled transfer arm installed on the suitcase.

After completing the in-vacuum transfer process, the QE and MTE measurements were performed using a photoemission electron microscope (PEEM) [16]. The pressure in the

Content from this work may be used under the terms of the CC BY 4.0 licence (© 2022). Any distribution of this work must maintain attribution to the author(s), title of the work, publisher, and DOI.

ISBN: 978-3-95450-261-5 ISSN: 2673-7000 doi: 10.18429/JACoW-NAPAC2025-WEP049

PROGRESS REPORT ON TWO-BUNCH EXCITATION OF WAKEFIELD IN DIELECTRIC STRUCTURES*

C. Phillips†[1], B. Leung[1], X. Lu[1,2], P. Piot[2], E. Wisniewski[2], J. Power[2], S. Doran[2], E. Gomez[3], L. Stan[2]
[1] Northern Illinois University, DeKalb, IL, USA
[2] Argonne National Laboratory, Lemont, IL, USA
[3] Euclid Techlabs, Bolingbrook, IL, USA

Abstract

Wakefield accelerators have the potential to achieve accelerating fields in the GV/m range, offering a promising path to more compact and cost-effective acceleration compared to conventional methods. Structure-based wakefield accelerator (SWFA) technology provides a viable approach to implementing beam-driven wakefield acceleration. An experiment at the Argonne Wakefield Accelerator (AWA) will utilize dielectric-lined structures to explore multi-beam excitation of wakefields for wakefield-pulse shortening and mapping of the transverse wakefield topology. These structures were commercially sourced and require a thin metallic film deposited on their outer surface. The first part of this paper summarizes the preparation of these structures. In parallel, a two-bunch beam configuration is required to support the experimental investigation, where one bunch excites the wakefield and the second serves as a loading or probe bunch. The experimental generation and testing of this two-bunch scheme at AWA are presented in this work.

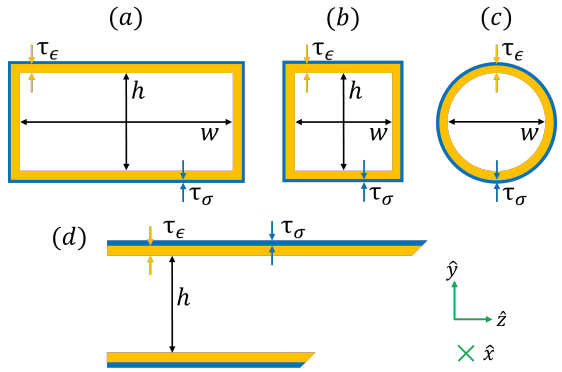


Figure 1: Cross-sectional views [in (x, y) plane] of the rectangular (a), square (b), and circular (c) structures along with longitudinal (y, z) slice of the angled cut circular structure for 35°. The structures have an inner height h, width w, dielectric thickness τ_ϵ, and conductor coating thickness of τ_σ, and all have the same length along the z direction. The shaded areas and dark lines represent the dielectric material and the metallic layer on its outer surface, respectively.

INTRODUCTION

Wakefields are produced by charged particles traveling between two or more dielectric surfaces. By carefully tailoring how they are produced, we are able to create localized regions of high energy gradients that can be used to accelerate a following bunch. This process, referred to as dielectric wakefield acceleration (DWFAs), has significantly higher gradients than standard RF cavities and has been studied using circular [1, 2] and slab structures [3, 4]. DWFA is a sub class for structure wakefield acceleration (SWFA) being explored for next-generation energy-frontier collider [5] or compact future light source [6, 7]. This process employs a high-charge "drive" bunch that creates the wake and a lower-charged "witness" bunch that experiences acceleration. An appealing development is to recycle the wake from a drive bunch.

The planned experiment will especially test whether a properly delayed "loading" bunch can suppress the wake generated by the drive bunch, enabling accurate characterization of the field for potential energy recovery. At the Argonne Wakefield Accelerator (AWA) facility, this will be implemented using same-charge dual-bunch excitation of dielectric-wakefield accelerators (DWFAs). The approach has two main components: (1) a properly delayed loading bunch, and (2) a dielectric structure with a non-90° cut at the exit (Fig. 1(d)), allowing the particles to continue straight while the radiation travels at an angle to be studied.

To investigate the influence of geometry and ,e.g., possibly control of transverse wakefield [8], three dielectric structures with different cross-sectional geometries - circle, square, and rectangle - have been prepared (Fig. 1(a-c)). These geometries are expected to affect the wakefield behavior, especially to suppress unwanted fields and identify loci of zero transverse force [9]. This paper describes the experimental setup, configuration, and preliminary results from the two-bunch tests.

Additionally, this paper describes the metallic coating applied to the outer surfaces of the dielectric structures. To prevent electromagnetic fields from propagating through the structures' side walls, the metallic layer must be 2–3 times the skin depth δ_s. For frequencies within [70, 140] GHz,

* The work performed at the Center for Nanoscale Materials was supported by the U.S. Department of Energy (DOE), Office of Basic Energy Sciences, under Contract No. DE-AC02-06CH11357. The Argonne Wakefield Accelerator (AWA) is supported by the DOE Office of Science, High Energy Physics, under Contract No. DE-AC02-06CH11357. CP, BL, and in part XL, are supported by DOE Contract No. DE-SC0022010 awarded to Northern Illinois University.
† z1907262@students.niu.edu

Content from this work may be used under the terms of the CC BY 4.0 licence (© 2022). Any distribution of this work must maintain attribution to the author(s), title of the work, publisher, and DOI.

ISBN: 978-3-95450-261-5 ISSN: 2673-7000 doi: 10.18429/JACoW-NAPAC2025-WEP050

PRELIMINARY INTRODUCTION OF THE IOTA BAKE SYSTEM

T. K. Thompson, D. R. Maclean
Fermi National Accelerator Laboratory, Batavia, IL, USA

Abstract

The Integrable Optics Test Accelerator (IOTA) ring is vital to the advancement of accelerator sciences, and a large part of its attractiveness to accelerator physicists is its modularity and the versatility that this function provides. Up until this point, the FAST accelerator has provided electron beam for the studies in IOTA. With the soon to be commissioned IOTA Proton Injector in lieu, the requirement for better vacuum to support future proton studies in the ring have arrived. Our solution is the IOTA Bake System which has the goal of facilitating this requirement.

THE BAKE SYSTEM

IOTA is a modular storage ring designed to be manipulated frequently for the purposes of supporting a variety of scientific studies. The addition of the IOTA Proton Injector (IPI), which will be commissioned in Fall 2025, creates an increased need for operational vacuum levels after inserting or removing elements from the ring. There's also significant value gained from improving the vacuum in regard to the lifetime of particles as they orbit the ring.

According to Associate Scientist, Nilanjan Banerjee [1], if the baking of IOTA can reduce the partial pressure of water by a factor of 10, we predict the lifetime of 2.5 MeV proton beam will increase by a factor of 2. For comparison, residual gas scattering present in 1e-9 Torr vacuum limits proton beam to a lifetime of 7 minutes. Considering the current mean vacuum levels in IOTA is roughly ~6e-10 Torr, it is possible the ring will pump down into 1e-11 Torr range after baking the system.

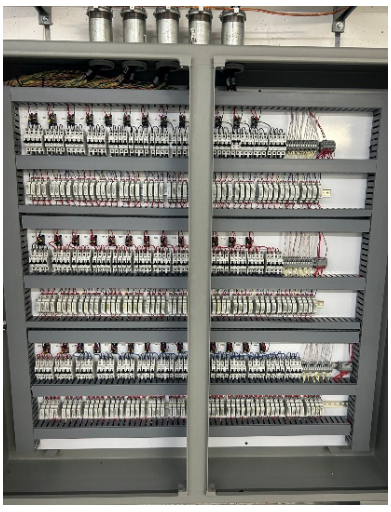


Figure 1: Breaker-Relay buildout.

The IOTA Bake System in its current state consists of 160 thermocouple channels, as well as a corresponding 160 powered channels to energize the conically wrapped heat tape, and a PLC used for control and operation of the system. A core safety feature of the bake system is the breaker configuration (Fig. 1). 5 A circuit breakers are connected to 10 A solid state breakers that are grouped into fours and are wired in series to a 25 A safety relay that removes power from the four channels if one of the channels trips. Each of the safety relays are wired into a corresponding GFIC breaker.



Figure 2: PLC buildout.

The PLC and its associated software is Productivity Suite v4.2.1.8. The buildout consists of twenty P2-08THM thermocouple analog input modules that supports 8 thermocouple channels each, six P2-32TD1P DC output modules that provide thirty-two 12-24VDC sinking outputs for powering the heat tape, as well as a power supply and control module (Fig. 2). The current PLC code was done by Mark Obrycki and has built in soak times to gradually increase the heat safely and also trip limits that open the previously stated breaker and relay chains (Fig. 3).

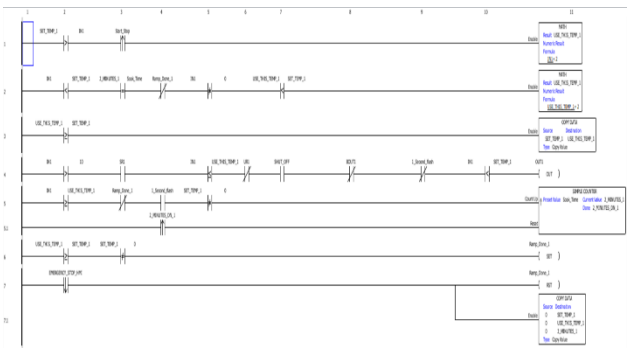


Figure 3: PLC operation code.

The design of the system has the wiring of both the thermocouple and the heat tape power source being wired from

Content from this work may be used under the terms of the CC BY 4.0 licence (© 2022). Any distribution of this work must maintain attribution to the author(s), title of the work, publisher, and DOI.

ISBN: 978-3-95450-261-5 ISSN: 2673-7000 doi: 10.18429/JACoW-NAPAC2025-WEP052

IMPROVEMENTS TO THE LANSCE CCL KLYSTRON EVALUATION*

A. S. Waghmare†, W. B. Haynes‡, C. Richman
Los Alamos National Laboratory, Los Alamos, NM, USA

Abstract

This paper describes the existing procedure for LANSCE 805 MHz klystrons testing and evaluation and realized avenues for improvement. Each of the 1.25 MW klystrons used for driving LANSCE CCL (side Coupled Cavity Linac) are tested during first installation or following a fault in operations. The executed testing process includes high potting, pulsing, and full power RF testing. Generated testing data is used for evaluation and certification of spare units for the linac. In this paper, we hope to breakdown this expert-dependent, lengthy 1–2 month process and examine improvements which can accelerate time to evaluation. The goal of this paper is to fully capture the current procedures and investigate improvements to modernize our legacy systems and processes.

INTRODUCTION

LANSCE uses 44 modulated-anode style klystrons for driving the CCL cavities. To verify proper operation during first on-site testing and for evaluating suspicious behavior these klystrons need to be tested as per the process shown in Fig. 1. Currently there are only two test stands dedicated to testing klystrons and evaluating their performance. These test stands are equipped with the diagnostics and controls required to perform all the necessary steps and gather sufficient testing data for evaluation purposes. The goal of the evaluation process is to certify klystron -modulator spares required to keep beam production running.

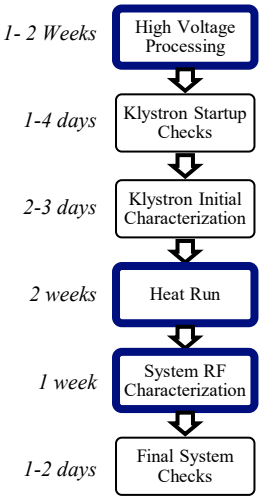


Figure 1: Current LANSCE 805MHz klystron-modulator testing and evaluation process.

*Work supported by US DOE and Laboratory Directed Research and Development (LDRD)
†aditya@lanl.gov
‡wbhaynes@lanl.gov

As LANSCE struggles to keep up production level beam due to equipment obsolescence and legacy equipment reaching end of life [1], the testing and evaluation process needs to be re-evaluated and accelerated. This will ensure faster evaluation of spare units increasing the beam uptime for the accelerator and upholding mission-critical 800MeV energy levels. This paper describes the different steps part of the CCL production klystron testing process, data generated during klystron testing, and metrics used for klystron evaluation. Improvements that are currently being investigated to advance evaluation metrics and increase overall system reliability and performance are also presented.

TESTING PROCESS

The typical testing process undertaken to test each klystron is shown in Fig. 1. This process is highly dependent and inherently slow because it depends on the feedback from the klystron itself. Some units perform better than others and some need to be further investigated to make a complete evaluation. The typical timeline for a full evaluation is typically 1-2 months with the steps highlighted in blue from Fig. 1 taking the longest.

High Voltage Processing

In the first step, klystrons are high-potted to check the hold-off voltage between the two different ceramics insulators: mod-anode to the cathode (lower ceramic) and mod-anode to the body (upper ceramic). If the operator can reasonably achieve 110kV on the lower ceramic and 120kV on the upper ceramic with little to no arcing for approximately 1 hour, then this check is said to be complete. If sufficiently high hold-off voltages cannot be established or if the tube demonstrates excessive arcing the tube must be processed to meet these hold-off voltage requirements as per Fig. 2.

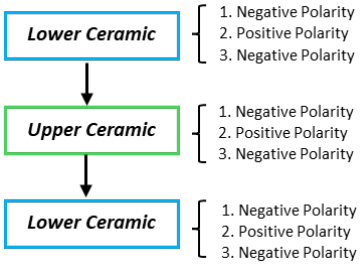


Figure 2: Typical high voltage processing procedure to reduce arcing and improve hold-off voltage.

HV processing allows the operator to condition out breakdown issues within the electron gun of the vacuum tube [2] which allows the klystron to run for longer with a reduction in arcing and related issues leading to eventual failure. Improvements are typically characterized by a

Content from this work may be used under the terms of the CC BY 4.0 licence (© 2022). Any distribution of this work must maintain attribution to the author(s), title of the work, publisher, and DOI.

ISBN: 978-3-95450-261-5 ISSN: 2673-7000 doi: 10.18429/JACoW-NAPAC2025-WEP055

LIGHT-INDUCED ENHANCEMENT OF QUANTUM EFFICIENCY IN III-NITRIDE PHOTOCATHODES

M. Moeini Rizi*, A. Ullattuparambil, S. Karkare, Arizona State University, Tempe, AZ, USA
A. Lanjani, F. S. Shahedipour-Sandvik, State University of New York-Albany, Albany, NY, USA
L. Lathpandura, P. Saha and L. Cultrera, Brookhaven National Lab, Upton, NY, USA

Content from this work may be used under the terms of the CC BY 4.0 licence (© 2022). Any distribution of this work must maintain attribution to the author(s), title of the work, publisher, and DOI.

Abstract

High quantum efficiency (QE) semiconductor photocathodes are essential for generating high average beam current and brightness. One class of semiconductor photocathodes considered for use in photoinjectors for unpolarized and polarized electron beams are III-nitride heterostructures. These materials can exhibit negative electron affinity at the surface by utilizing intrinsic polarization fields to engineer the band structure without the need for additional surface treatments. In this study, using photoemission electron microscopy (PEEM) for characterization, we investigate the effects of light exposure on the surface of III-nitride photocathodes show that the QE changes significantly when exposed to UV light. Although III-nitride photocathodes are known for their robustness, our findings indicate that laser exposure can significantly alter their QE. Our observations reveal the need for a detailed investigation of photo-induced effects on QE in III-Nitride photocathodes.

INTRODUCTION

The development of bright and high-current electron sources is critical for the advancement of accelerator-based applications such as free-electron lasers, ultrafast electron diffraction, and next-generation colliders [1–3]. Semiconductor photocathodes have emerged as key enablers due to their potential to deliver high QE, customized band structure, and tunable emission properties [4,5]. Among different semiconductors, III-nitride materials such as GaN have been the focus of considerable research due to their ability to attain negative electron affinity(NEA) using Cs overlayers [6–8]. While they are more robust than traditionally used NEA GaAs(Cs/O) cathodes, the Cs-based activation layer is still very sensitive to vacuum conditions resulting in QE degradation in poor vacuum conditions. It was recently shown that intense internal fields due to self-polarization and piezoelectric effects in the wurtzite phase of GaN can be leveraged to engineer photocathode structures that do not require cesium to achieve effective NEA [9]. Previous studies have shown high QE of over 1% and a low mean transverse energy of under 100 meV from such Cs-free NEA GaN surfaces [9,10]. Such GaN-based photocathodes have an extremely robust surface that is stable in atmospheric conditions. Because of the chemical inertness of such surfaces, it has been assumed that the QE from these surfaces will be extremely stable. In this work we show that this assumption in not entirely accurate. Despite the robust surface we show that ultraviolet laser exposure can significantly alter the surface condition and lead to significant changes in quantum efficiency. These results suggest that light exposure modifies the surface electronic structure of GaN, making it essential to perform a more systematic study of the QE when exposed to light.

EXPERIMENTAL METHODS

N-polar GaN photocathodes reported here were grown by metal organic chemical vapor deposition (MOCVD). Nominally, on-axis 2–sapphire wafers with mis-cut toward the m-plane were used as substrates. An N-polar unintentionally doped (UID) GaN template layer was grown on the sapphire substrate using growth conditions reported elsewhere [11]. The N-polar photocathode structure was then overgrown on the template layer consisting of nominally 450 nm p-GaN with 10 nm UID GaN cap layer [12]. The samples were

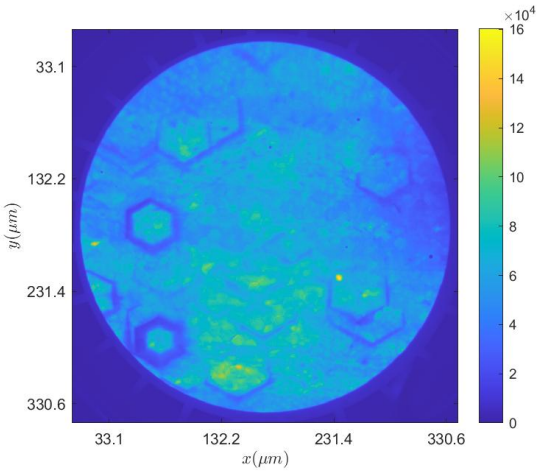


Figure 1: PEEM image of the GaN N-polar surface using the 240 nm Hg lamp source showing hexagonal structures.

grown at SUNY Albany and shipped to ASU. At ASU, they were cleaned in 30% HCl for 1 minutes and then rinsed with DI water to remove any oxide layer and surface contaminants. After the HCl cleaning, the samples were inserted in the load lock of a PhotoEmission Electron Microscope (PEEM) ultra-high-vacuum (UHV) chamber in less than 15 minutes. The samples were transferred into the chamber after a 12 hour bakeout of the load lock at 120 °C at a pressure less than 10^{-7} torr before transferring into the PEEM-UHV chamber with a pressure of 10^{-10} torr.

The PEEM was used to obtain a photoemission map of the surface and measure the QE. High resolution images of

* mmoeinir@asu.edu

ISBN: 978-3-95450-261-5 ISSN: 2673-7000 doi: 10.18429/JACoW-NAPAC2025-WEP056

LLRF COMMISSIONING OF THE CEBAF C75 UPGRADES SAM 2024/25 *

J. K. Tiskumara†, R. Bachimanchi, M. Geesaman, K. Hesse, S. Higgins, K. Jyamfi, J. Latshaw, C. Mounts, T. Plawski, J. Settle
Thomas Jefferson National Accelerator Facility, Newport News, VA, USA

Abstract

During Jefferson Lab's Scheduled Accelerator Maintenance (SAM) in 2024, two C75 cryomodules were installed in CEBAF with JLab's Low Level RF (LLRF) 3.0 digital control system. Three key processes of JLab's LLRF commissioning include completing Interlock verification, klystron characterization, and cavity characterization. This paper summarizes the preparation, automation and commissioning efforts for the new cryomodule installation and controls checkout.

INTRODUCTION

C75 Cryomodules, SRF Commissioning/ Installation

During the SAM 2024, two cryomodules with C20 type cavities in CEBAF, which were installed in the early 1990s, were replaced by new C75 style refurbished cryomodules. The C75 cavities are 5-cell cavities manufactured by Research Instruments (RI), GmbH in Germany with an operational accelerating gradient (Eacc) of 19.1 MV/m and a quality factor (Qo) of at least 8×10^9 at a temperature of 2.07 K (helium pressure of 29 ±0.1 Torr) [1].

Each of the cavities was combined and tested as pairs in the Vertical Test Area (VTA) prior to the cryomodule assembly. These cryomodules were then tested in the Cryomodule Test Facility (CMTF) for operational conditions (maximum gradient, Field emission) before being installed in the LINAC [1]. One of the cryomodules was plasma processed for high field emission detected during these tests [1]. These cryomodules were installed in the North LINAC (1L09) and South LINAC (2L05).

High Power Installation - CPS and HPA

The existing instrumentation and connections were removed from the selected zones so that new components could be installed. The Cathode Power Supply (CPS) and Main Distribution Panel (MDP) breakers were replaced with higher rated current breakers. The transformer, diode stack, HV wiring, and HV capacitor were also replaced. A Silicon Controlled Rectifier (SCR) was installed to allow the high voltage in the zone to be adjusted electronically.

LLRF COMMISSIONING

The C75 cavities are controlled by JLab's LLRF 3.0 systems, which were developed to replace the legacy LLRF systems in CEBAF [2,3]. These systems utilize the Self-Excited Loop Amplitude and Phase (SELAP) algorithm for cavity control. This algorithm is a fully functional phase and amplitude locked Self Excited Loop [2, 3].

LLRF Installation

As a part of the controls upgrade, the Field Control Chassis (FCC) were installed along with the heater/High Power Amplifier (HPA)/interlock/resonance chassis, and their associated power supplies. The heater, IR, probe, and stepper motor cables are connected to the cryomodule. The external calibrations (ECAL) and internal calibrations of the FCC receivers were measured in-situ. These calibrations are critical for determining cavity quality factor and gradient.

ECAL values primarily address cable losses, waveguide coupling factors, and additional attenuation in the FCCs, while also including the cavity's external quality factor and beam-based calibration factor [4]. This additional attenuation is added to the FCC inputs to adjust the input signal, ensuring that the maximum input power to the chassis remains slightly below the ADC saturation point. This approach maximizes the ADC counts for the applied input power. Single-point calibrations are performed to determine and verify these values. The mean waveguide coupling factor is approximately 40 dB, while the mean cable loss between the service buildings (which house the FCCs) and the LINAC tunnel is approximately 3 dB [4].

Pre-Commissioning - Part 1: Testing into Shorts

As a standard test practice to verify the functionality of CPS and HPA, shorting plates were installed on the waveguide. With the shorting plates installed, HPA can be tested without applying any power into the cavities. As a part of the testing RF was applied to generate less than 100 watts of power. During the test, the Klystron Reflected Power (KRRP) readback was monitored to verify the corresponding KRRP interlock, which removes the RF drive to the Klystron to prevent damage. All of the klystrons/FCCs were checked to ensure the forward power (CRFP) and reflected power (CRRP) measurements were similar and were also verified by measuring with an independent power meter.

Klystron characterization was performed next to measure the performance of the klystron. It involves ramping the drive power from minimum to maximum for a very short time interval with a single fixed frequency (tone) while the cavity forward power magnitude and phase are measured. The klystron characterization is a critical step of commissioning because it enables a mapping between the FCC drive signal (GASK) and the power measured by the coupler downstream of the isolator. It also establishes the

*Authored by JSA, LLC under U.S. DOE Contract DE-AC05-06OR23177 and DE-SC0005264. The U.S. Govt. retains a non-exclusive, paid-up, irrevocable, worldwide license to publish or reproduce this for U.S. Govt. purposes.
† jkt@jlab.org

Content from this work may be used under the terms of the CC BY 4.0 licence (© 2022). Any distribution of this work must maintain attribution to the author(s), title of the work, publisher, and DOI.

ISBN: 978-3-95450-261-5 ISSN: 2673-7000 doi: 10.18429/JACoW-NAPAC2025-WEP057

LOW FREQUENCY RIPPLE CURRENT ATTENUATION FOR SLOW CORRECTOR POWER SUPPLIES IN THE APS UPGRADE*

Y. Ruan† and F. Rafael
Argonne National Laboratory, Lemont, IL, USA

Content from this work may be used under the terms of the CC BY 4.0 licence (© 2022). Any distribution of this work must maintain attribution to the author(s), title of the work, publisher, and DOI.

Abstract

As part of the Advanced Photon Source Upgrade (APS-U), approximately one thousand bipolar power supplies were installed to power the slow corrector magnets. During the APS-U commissioning, a 1-Hz harmonic was detected in the beam motion. This harmonic originated from the 480V AC grid, caused by the booster ramping power supply operating at 1 Hz. The resulting grid disturbance introduced low-frequency ripples into both the corrector magnet power supplies and the L-Bend M1/M2 supplies, leading to the observed 1-Hz beam motion. This paper proposes two methods to mitigate these ripples in the corrector supplies: setpoint compensation using repetitive control, and regulation circuit adjustments through a simple jumper reconfiguration. The second approach was adopted and applied to all slow corrector magnet power supplies. Operational data showed that the low-frequency ripples were significantly attenuated in the corrector supplies, and in combination with fine-tuning of the L-Bend M1/M2 supplies, the 1-Hz beam motion was successfully eliminated.

INTRODUCTION

During the APS-U commissioning in early 2024, a 1-Hz beam motion was observed, and the booster ramping supply was identified as the source of the issue. The ramping supply operates at 1 Hz, causing the 480 VAC grid to sag every second, which in turn produces low-frequency ripples in the 80 raw power supplies that energize approximately 1,000 bipolar power supplies for the slow corrector magnets around the storage ring. These AC/DC raw supplies use uncontrolled rectifiers, meaning that grip ripples are directly transferred to the DC output. Similarly, the 1 Hz with other low frequency transients also affects the DC-Link voltage of the L-Bend M1 and M2 supplies, which also rely on uncontrolled rectifiers. The grid voltage sag, captured in Fig. 1, shows a drop of approximately 1.3%, followed by a recovery as the booster ramping supply current rises and falls.

One potential solution to address the 1-Hz ripple in the corrector supplies would involve replacing the high-power AC/DC raw supplies with PWM-controlled DC supplies. However, with over 1,000 units involved, this approach would be both costly and time-consuming.

In this paper, we propose and analyze two practical methods that require minimal hardware changes to address the issue: (1) setpoint compensation using repetitive control, which can be implemented through controller firmware; and (2) analog regulation loop adjustment via a simple jumper reconfiguration. Simulation models were developed using MATLAB/Simulink, and results confirmed the effectiveness of both methods. Due to its simplicity and ease of implementation, the jumper reconfiguration was approved and applied to all slow corrector supplies during the August 2024 shutdown. Operational data confirmed that low-frequency ripples were significantly attenuated, with reductions of 19.8× for the 1-Hz ripple, 13.9× for the 2-Hz ripple, and 9.1× for the 3-Hz ripple.

Further tuning of the L-Bend M1/M2 supplies was conducted in September 2024 to mitigate grid disturbances. With the fine-tuning of the slow correctors and M1/M2 supplies, the 1-Hz harmonic was successfully eliminated from the beam motion.

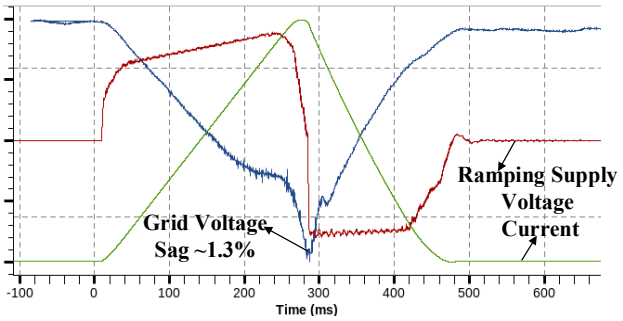


Figure 1: The voltage sag in the AC grid caused by the booster ramping supply.

RIPPLE ATTENUATION OF BIPOLAR SUPPLIES

Power Circuit of the Bipolar Supply

Figure 2 illustrates the power circuit and control scheme of the bipolar power supply, which was designed in-house at Argonne [1, 2]. This is a DC/DC supply, with its input voltage provided by a raw AC/DC supply. The raw supply consists of a multi-winding stepdown transformer and two 6-pulse rectifiers that convert the 480-VAC grid voltage to approximately 40 VDC. Across the storage ring mezzanine, there are 80 such raw supplies, powering more than 1,000 bipolar supplies.

An FPGA-based controller, designed in -house, serves as the interface between the power supply and the Experimental Physics and Industrial Control System (EPICS). The controller receives the current setpoint from EPICS and converts it into a reference signal, which is then fed to the analog proportional-integral (PI) regulation circuit in the bipolar power supply. Each controller can manage up to eight bipolar supplies.

* Work supported by the U.S. Department of Energy, Office of Science, Office of Basic Energy Sciences, under Contract No. DE-AC02-06CH11357.
† yruan@anl.gov

ISBN: 978-3-95450-261-5 ISSN: 2673-7000 doi: 10.18429/JACoW-NAPAC2025-WEP058

MAGNETIC FIELD AND FORCE CALCULATION OF THE NEW SCU PROTOTYPES*

Y. Shiroyanagi†, E. Anliker, M. Kasa, I. Kesgin, Y. Ivanyushenkov
Argonne National Laboratory, Lemont, IL, USA

Abstract

New 0.5-m-long superconducting undulator (SCU) magnet prototypes were designed based on lessons learned from the previous full-length (1.5-m) magnet experiences. The original monolithic magnets have all-steel poles. The new cores have plastic-back poles to avoid electrical shorts of superconducting wires to cores. A magnetostatic calculation was made for a one-period model for each of two designs under consideration. Then magnetostatic and mechanical analyses were also conducted for the prototype SCUs with period lengths of 29.5 mm and 23.5 mm. The software used for this simulation is ANSYS Maxwell and Mechanical. Both the magnetostatic and the mechanical analyses confirm the validity of the new design.

INTRODUCTION

New prototypes of superconducting undulators (SCUs), measuring 0.5 meters in length, have been developed by incorporating lessons learned from earlier designs of full-length (1.5-meter) magnets. These prototypes utilize a 0.6-mm-diameter Nb-Ti wire as the conductor. Unlike the original monolithic magnets, which featured all-steel poles, the updated designs integrate plastic-back poles to prevent electrical shorts between the superconducting wires and the cores. The detailed design of these prototypes, including the use of plastic poles, has been finalized [1]. This paper compares the magnetostatic calculations and mechanical analyses of the original and new prototypes, which feature 29.5 and 23.5 periods, respectively. Electromagnetic simulations were performed using ANSYS Maxwell, while structural analyses were conducted using ANSYS Mechanical [2]. A summary of the SCU parameters is presented in Table 1. Additionally, the end correction scheme has been implemented and is explained in a later section [3].

Table 1: SCU Parameters

	Unit	Value
Period Length	mm	16.5
Periods	N	23.5 or 29.5
Magnetic Gap	mm	8
Pole Width	mm	3
Groove Width	mm	5.25
Groove Depth	mm	4.15
Full Coil Turns	N	53
Conductor Dia.	mm	0.6
Main Current	A	450

* Work supported by the U.S. DOE Office of Science-Basic Energy Sciences, under Contract No. DE-AC02-06CH11357.
† email address: yshiroyanagi@anl.gov

ONE-PERIOD MODEL

Magnetic fields and forces were calculated using a one-period model with periodic boundary conditions for three different configurations: an air core (without steel), a full-steel pole design, and a new design incorporating both plastic and steel poles.

Air Core

The magnetic field was calculated for the coils-only case (air core) using periodic boundary condition in the z-direction, $\mathbf{B}(z + z_0) = \mathbf{B}(z)$, $z_0 = 16.5$ mm. Figure 1(a) illustrates the geometry of the four coils and the direction of the currents. The maximum field on the axis B_{peak} is 0.669 T at 450 A as shown in Fig. 1(b). The magnetic field within the conductor is depicted in the cross section in Fig. 1(c), while the overall field distribution is shown in Fig. 1(d). The maximum field, B_{max} = 2.20 T, occurs at the edge of the conductor. Figure 1(e) shows the forces acting on one coil (F_x, F_y) at six coil segments. The force at each section of the conductor is directed outward, as indicated.

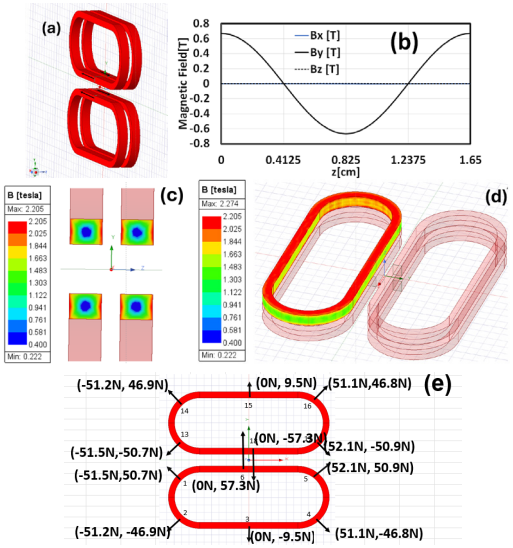


Figure 1: (a) Geometry, (b) on-axis magnetic field, (c) magnetic field at y-z cross-section of the coils, (d) magnetic field in one of the coils, (e) magnetic forces on a top coil and a bottom coil in six segments.

The total force on the top coils is $F_y = -111.5$ N, while the total force on the bottom coils is $F_y = 111.3$ N, indicating that the forces are attractive.

Content from this work may be used under the terms of the CC BY 4.0 licence (© 2022). Any distribution of this work must maintain attribution to the author(s), title of the work, publisher, and DOI.

ISBN: 978-3-95450-261-5 ISSN: 2673-7000 doi: 10.18429/JACoW-NAPAC2025-WEP060

NEW DEVELOPMENT AND TESTING FACILITY FOR HPRF SSA SYSTEM AT LANSCE CCL

J. Vega†, J. T. M. Lyles, T. W. Hall, M. Sanchez Barrueta,
J. A. Valladares, M. C. Brown, S. J. Russell
Los Alamos National Laboratory, Los Alamos, NM, USA

Abstract

A high-power RF test facility developed at the Los Alamos Neutron Science Center (LANSCE) to evaluate components of a RF Solid-State Amplifier (SSA) system operating at 805 MHz and targeted for a final output power of 1.25 MW. The system is powered by a 100 V DC supply and stabilized with a 0.1 F capacitor bank to support transient power demands, capable of storing up to 1.125 kJ of energy. The SSA utilizes Gallium Nitride (GaN) on Silicon Carbide (SiC) high electron mobility transistors (HEMTs) and employs water cooling to manage thermal loads and ensure stable operation under high duty-factor pulsed conditions. Multiple HEMT amplifier modules will be power combined to achieve the full 1.25 MW output, with the aim of enhancing reliability, modularity, and maintainability in accelerator RF infrastructure. Integrated protection procedures allow for secure shutdown of RF drive and DC power in the event of overvoltage, overcurrent, or thermal excursions. This test configuration supports ongoing evaluation of solid-state amplifier performance, thermal handling, and integration with RF passive components under realistic operational conditions.

INTRODUCTION

A new test facility has been developed at the Los Alamos Neutron Science Center (LANSCE) to evaluate solid-state amplifier (SSA) systems operating at 805 MHz, targeting 1.25 MW output for accelerator applications, see Fig. 1. This effort addresses the growing need for RF sources that are modular, scalable, and maintainable—critical for supporting high-duty-factor pulsed operation in modern accelerator infrastructures. The SSA design employs Gallium Nitride (GaN) on Silicon Carbide (SiC) high electron mobility transistors (HEMTs), offering several advantages over legacy vacuum tube-based systems, including improved fault tolerance, lower voltage operation, and reduced maintenance. The modular nature of the system allows individual amplifier units to operate independently, simplifying upgrades, diagnostics, and staged power scaling. A key focus of the project is to demonstrate a path forward for replacing aging RF infrastructure, such as klystron-based sources, which are increasingly difficult to maintain and no longer manufactured. By validating the SSA architecture in a realistic environment, this work supports the transition to modern, solid-state-based RF solutions that align with current safety, reliability, and operational standards. This paper outlines the facility's design, including DC power delivery, amplifier module integration, thermal management, protection mechanisms, and performance characterization under accelerator-relevant conditions.

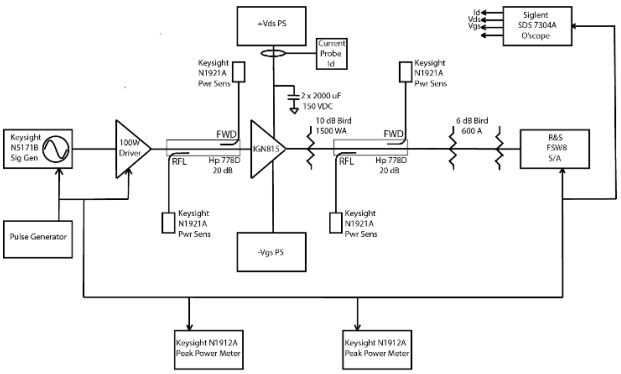


Figure 1: Block diagram of SSA Test System.

POWER ARCHITECTURE

The current generation SSA system replaces legacy klystron-based RF sources that operated at approximately 90 kV DC, representing a significant improvement in lab safety and power handling [1]. Lowering the operating voltage by nearly three orders of magnitude reduces the complexity of insulation, arcing risk, and personnel hazard during maintenance or fault scenarios. The transition to low-voltage, high-current solid-state devices therefore supports not only improved modularity and reliability but also aligns with modern safety standards in accelerator environments.

The DC power for the SSA modules is provided by a TDK-Lambda GEN100-50 programmable supply, operating at 100 V and up to 50 A. The unit is powered from a standard 208 V AC line, simplifying infrastructure requirements and reducing installation constraints compared to traditional high-voltage systems. The power supply features protections for overvoltage. Its compact form factor allows it to be integrated directly into the test stand rack alongside RF and control systems.

Each SSA module also includes onboard 1000 µF capacitors positioned on the drain side of the GaN device. These capacitors are critical for managing fast power transients during pulsed operation, locally stabilizing the supply voltage during high-current draw events. By providing immediate energy buffering at the device level, they mitigate the impact of voltage sag due to cable inductance or distributed impedance on the main DC rail. This localized energy storage enhances pulse fidelity, improves RF output stability,

* Work was performed under the auspices of the US Department of Energy by Triad National Security, LLC, under contract 89233218CNA000001.

† javierv@lanl.gov

Content from this work may be used under the terms of the CC BY 4.0 licence (© 2022). Any distribution of this work must maintain attribution to the author(s), title of the work, publisher, and DOI.

ISBN: 978-3-95450-261-5 ISSN: 2673-7000 doi: 10.18429/JACoW-NAPAC2025-WEP061

NSLSII RF-SHIELDED BELLOWS OFFSET TESTING

R. Todd, A. Khan, P. Palecek, M. Seegitz, T. Shaftan, V. Smaluk, G. Wang
Brookhaven National Laboratory, Upton, NY, USA

Content from this work may be used under the terms of the CC BY 4.0 licence (© 2022). Any distribution of this work must maintain attribution to the author(s), title of the work, publisher, and DOI.

Abstract

The NSLSII storage ring contains over 180 RF shielded bellows over its 792 m circumference. Three of these bellows are instrumented with RTD temperature sensors on the internal components to monitor and validate expected performance. The temperature data showed an increasing internal temperature trend during successive 500 mA beam operation on one of these bellows. This bellows and many other installed bellows throughout the ring, are near to or over the vertical and horizontal offset tolerance. Offsets can create an RF path between the sleeve and fingers, which raised concern there was degradation of performance resulting from the offset condition. The bellows was removed and inspected with some visual signs of discoloration and loose RTD anchor points were also observed. With the prospects of moving from 400 mA to more permanent 500 mA operation, a test was conducted to confirm internal temperatures were safe. Two fully instrumented bellows were remotely offset under steady beam operation while observing the internal temperatures. The bellows with offset geometry was also studied with GdfdL code. The experimental results will be presented and compared to the wake-potential calculations.

INTRODUCTION

The design of the RF-shielded bellows used in NSLSII underwent careful impedance evaluation during the design stage [1]. Furthermore, the bellows design was tested in the APS storage ring [2]. Both the analysis and testing showed acceptable performance.

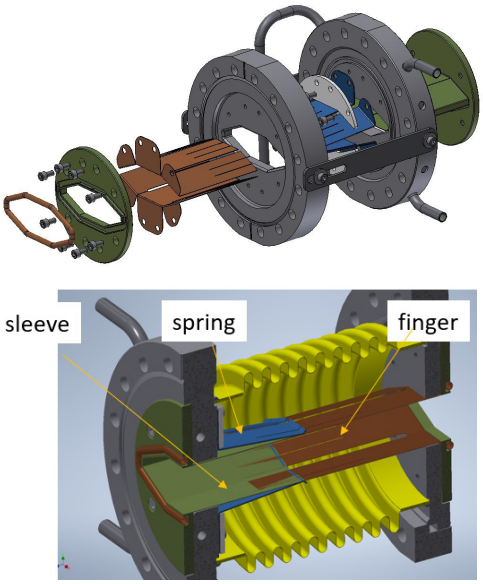


Figure 1: Exploded and section view of RF-shielded bellows.

NSLSII machine commissioning involved careful evaluation of the vacuum system performance including both the monitoring of dynamic pressure as well as vacuum component temperature. The later included the installation of temperature sensors on all vacuum flanges and potential locations of high temperature. The storage ring includes over 180 RF shielded bellows. The bellows includes fingers that are pinched between a sleeve and spring assembly as shown in Fig. 1.

Only three bellows were instrumented with temperature sensors to monitor the internal RF components during commissioning and installed in straight sections where higher temperatures typically occur. A total of six thermocouple sensors are located on the sleeve, spring and finger. Three on the top and three on the bottom. These special bellows are shown in Fig. 2.

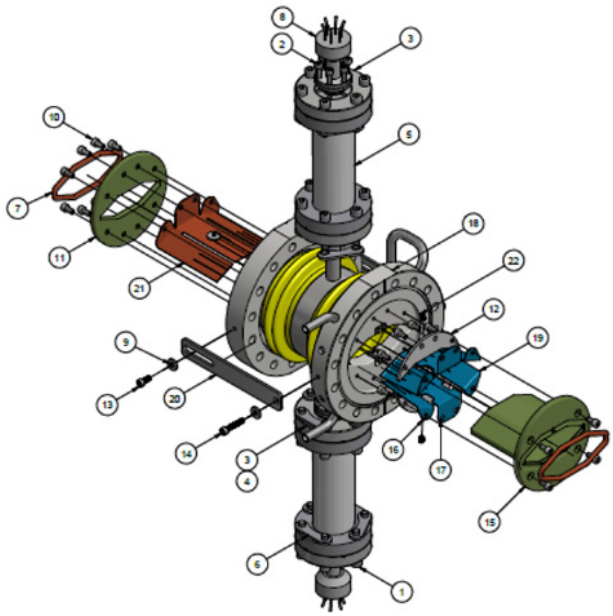


Figure 2: Instrumented bellows with internal thermocouples.

Temperatures were stable and acceptable during commission up to and including 400 mA operation. However, during periodic study periods of 500 mA, temperatures on two of the three bellows increased (Fig. 3). All external sensor connections and modules were confirmed good.

The offsets of the bellows were measure and C18 was found to have the greatest misalignment and near the design limits of ±2 mm vertical and ±1 mm horizontal. The measured value was 1.45 mm (V) and 0.83 mm (H). The trend showed successive worsening during each 500 mA study. A FLIR camera did not substantiate high internal temperatures due to unknown emissivity and thermal shielding, but did show higher heating on the top leading to some concern the sensor readings were accurate (Fig. 4).

ISBN: 978-3-95450-261-5 ISSN: 2673-7000 doi: 10.18429/JACoW-NAPAC2025-WEP062

ONE-TO-ONE MAPPING BETWEEN THE ELECTROMAGNETIC MODES OF CYLINDRICAL AND COAXIAL HALF-WAVE CAVITIES*

F. Ahmed[1,2,†], J. R. Delayen[1,2], S. De Silva[1,2]
[1]Old Dominion University, Norfolk, VA, USA
[2]Thomas Jefferson National Accelerator Facility, Newport News, VA, USA

Abstract

Design of radio frequency (RF) couplers and diagnostics require a good understanding of the electromagnetic mode patterns of RF cavities. This study investigates the adiabatic transformation of transverse magnetic (TM) modes of a cylindrical cavity into transverse electromagnetic (TEM) modes of a coaxial cavity by gradually introducing an inner conductor. Using CST Studio Suite, we simulate the eigenmode evolution as the geometry transforms from a pure cylindrical to a coaxial configuration. We track the behavior of TM_{010} through TM_{014} modes to observe the continuous evolution into the corresponding TEM_0 through TEM_4 modes of the coaxial cavity. The process is governed by the evolution of the electric field orientation as the geometry shifts, enabling the axial TM fields to reorient into the radial electric field configuration of TEM modes. Field patterns, eigen-frequencies, and mode identities are analyzed throughout the transition. The results provide simulation-based evidence that TM to TEM conversion occurs without generation of newer eigenmodes, offering a valuable insight into the design of transition regions in superconducting RF (SRF) systems and provides a foundation for experimental validation.

INTRODUCTION

Transitions between different RF cavity geometries are common in superconducting radio frequency (SRF) systems, particularly at interfaces involving input couplers, pickup probes, and diagnostic ports. Cylindrical cavities typically support transverse magnetic (TM) modes, while coaxial structures support transverse electromagnetic (TEM) modes [1]. Ensuring a smooth transition between these structures without introducing additional resonant modes is essential for maintaining mode purity and minimizing power reflection.

A common example occurs is SRF input couplers, where RF power is delivered through a coaxial line into a cavity resonating in a TM mode, such as TM_{010}. To avoid unwanted coupling or mode conversion losses, the coaxial-to-cavity interface must be carefully designed to ensure that the field structures match. Similar transitions are found in pickup probes used to monitor cavity fields, where coaxial lines extract signals from TM modes. In these applications, the introduction of an inner conductor near the cavity wall must not excite higher-order or spurious modes.

* Work supported by U.S. Department of Energy Award DE-SC0025560.
† fahme005@odu.edu

In this work, we use CST Studio Suite to take a closer look at how the TM modes of a cylindrical cavity transform into TEM modes as we gradually introduce an inner conductor. We simulate how TM_{010} through TM_{014} modes evolve into their corresponding TEM_0 through TEM_4 modes in a coaxial structure. Our main goal is to show that this transition happens without the generation of any new modes. The electric field reorients smoothly from being primarily axial in the TM modes to radial in the TEM modes, indicating an adiabatic transformation. This one-to-one mapping gives us confidence that such transitions can be used reliably in SRF systems without introducing unwanted resonances.

CAVITY GEOMETRY

The model geometry consists of a cylindrical RF half-wave cavity with a fixed length that is dimensioned to ensure that its resonant frequencies fall within the operational range of modern accelerator systems.The outer radius is chosen to shift the cutoff frequencies of transverse electric (TE) modes away from the operating range of the TEM modes.A central coaxial gap is introduced symmetrically from both ends by inserting an inner conductor. The dimensions of the geometry is given in Table 1.

Table 1: Cavity Dimensions

Parameters	Value [mm]
Cavity length (L)	460
Outer conductor radius	101
Inner conductor radius	50

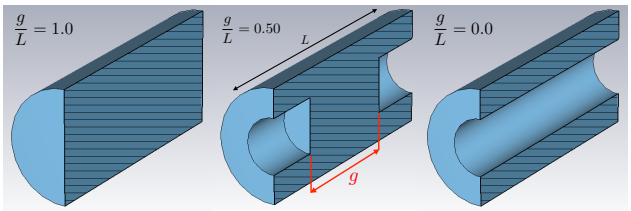


Figure 1: Geometry transformation from cylindrical cavity (left) to coaxial cavity (right) structure.

The gap parameter g represents the remaining central length after subtracting the equal-length coaxial recesses introduced from each end of the cavity, such that g = L – 2d, where L is the total cavity length and d is the depth of each cut from both ends. By varying the value of g,

Content from this work may be used under the terms of the CC BY 4.0 licence (© 2022). Any distribution of this work must maintain attribution to the author(s), title of the work, publisher, and DOI.

ISBN: 978-3-95450-261-5 ISSN: 2673-7000 doi: 10.18429/JACoW-NAPAC2025-WEP064

PASSIVE PLASMA LENS EXPERIMENTS AT FACET-II

S. Meng*, C. Hansel, V. Lee, M. Litos, E. Ros, University of Colorado Boulder, Boulder, CO, USA
E. Adli, G. J. Cao, University of Oslo, Oslo, Norway
R. Ariniello, C. Emma, S. Gessner, M. J. Hogan, A. Knetsch, N. Majernik, B. O'Shea, D. Storey
SLAC National Accelerator Laboratory, Menlo Park, CA, USA
S. Corde, LOA, ENSTA Paris, CNRS, Ecole Polytechnique,
Institut Polytechnique de Paris, Palaiseau, France
C. E. Doss, Lawrence Berkeley National Laboratory, Berkeley, CA, USA
T. N. Dalichaouch, C. Joshi, K. A. Marsh, C. Zhang
University of California Los Angeles, Los Angeles, CA, USA

Content from this work may be used under the terms of the CC BY 4.0 licence (© 2022). Any distribution of this work must maintain attribution to the author(s), title of the work, publisher, and DOI.

Abstract

The beam-driven, passive plasma lens can provide axisymmetric focusing with strengths orders of magnitude greater than conventional quadrupole magnets, while remaining ultra-compact. These characteristics make it attractive for beam matching into a plasma wakefield accelerator and for controlling beam divergence downstream of plasma stages. Optimal performance can be achieved in the underdense regime, resulting in a linear focusing force and emittance preservation of the focused beam. We report progress on experimental results from SLAC's FACET-II facility, where we utilized a fs Ti:Sapphire laser pulse to ionize hydrogen gas from a supersonic gas jet to focus several hundred pCs of charge of a 10 GeV electron beam.

INTRODUCTION

A plasma wakefield accelerator (PWFA) can produce accelerating gradients orders of magnitude stronger than those of conventional radio-frequency structures, which allows development of compact accelerators that can benefit future colliders and light sources. Several milestones have been achieved to demonstrate high energy gain, high efficiency acceleration, and low energy spread beam [1–3]. Moving toward future accelerators, preserving emittance in a PWFA stage is crucial for achieving high luminosity in colliders and high brightness in light sources.

In a PWFA, a leading electron drive bunch generates a strong longitudinal wakefield that can accelerate a trailing witness bunch. To prevent emittance growth caused by chromatic phase mixing of the witness bunch, its Twiss parameter β must be matched according to the condition $\beta = \sqrt{2\gamma_b}/k_p$, where γ_b is the Lorentz factor of the electron bunch and k_p is the plasma wave number. For a 10 GeV electron bunch and a 1×10^{16} cm^{-3} plasma density, a typical parameter at the FACET-II facility at SLAC National Accelerator Laboratory, the required β the entrance of the PWFA stage is about 1 cm. Achieving such a small value is challenging with conventional electromagnetic quadrupole magnets. Several approaches have been proposed to provide such strong focusing, with one prevalent method being the use of a plasma density ramp [4, 5]. However, this approach typically requires a long plasma matching section and precise control of the plasma density profile. Hence, the use of plasma lens has been discussed [6], providing focusing gradients on the order of MT/m, which can significantly shorten the plasma ramp section and thus allows efficient phase-space matching.

The proposed plasma lens experiment at FACET-II aims to realize a specific type of plasma lens [6, 7]. Its strong focusing arises from the transverse wakefield generated by the drive bunch. The lens is thin so that the witness bunch experiences minimal energy gain. Ideally, the lens operates in the underdense regime, where the drive bunch density $n_b > n_p$, allowing it to generate an electron-depleted ion column in which the emittance of the witness bunch can be preserved. In this paper, we report preliminary results of a submillimeter, beam-driven, passive plasma lens using a preformed, laser-ionized plasma. The peak focusing gradient is approximately 0.4 MT/m, which is orders of magnitude stronger than conventional quadrupoles (1 T/m), permanent magnet quadrupoles (500 T/m [8]), and active plasma lenses (3.5 kT/m [9, 10]).

EXPERIMENTAL SETUP

The experimental setup, shown in Fig. 1, uses a two-bunch electron beam generated by a notch collimator, with the drive bunch carrying a charge of 780 pC and the witness bunch 650 pC. The plasma lens is pre-formed by ionizing neutral hydrogen gas from a supersonic jet using a 3 mJ, [insert pulse duration] fs Ti:sapphire laser. The laser propagates transversely to the beamline, so the electron beam traverses the plasma width, resulting in a thin lens configuration. A simulated initial plasma density profile using the experimental laser parameter is shown in Fig. 2 where the initial plasma width is only 132 µm. The delay between the laser pulse and the arrival of the electron beam can be adjusted to allow plasma expansion, thereby increasing the plasma length for stronger lensing and reducing the plasma density to reach the underdense regime easier.

The gas jet (see Fig. 1 (b)) is a canonical de Laval nozzle, operating at 50 psi and placed 1.5 cm below the electron beam. Detailed specifications of the nozzle are provided in the paper [11]. The neutral hydrogen gas profile is calibrated through simulations using ANSYS Fluent, with the resulting

* shutang.meng@colorado.edu

ISBN: 978-3-95450-261-5 ISSN: 2673-7000 doi: 10.18429/JACoW-NAPAC2025-WEP065

PERFORMANCE ENHANCEMENT OF MEDIUM TEMPERATURE BAKED NIOBIUM SRF CAVITY BY SURFACE CONTAMINATION REMOVAL*

V. Chouhan†, D. Bice, A. Cravatta, A. Murthy, A. Netepenko, T. Ring, D. Smith, G. Wu
Fermi National Accelerator Laboratory, Batavia, Illinois, USA

Content from this work may be used under the terms of the CC BY 4.0 licence (© 2022). Any distribution of this work must maintain attribution to the author(s), title of the work, publisher, and DOI.

Abstract

Medium-temperature (mid-T) baking, typically conducted at 300–350°C, enhances the quality factor of niobium (Nb) superconducting radio frequency cavities. High vacuum furnace baking is commonly preferred for its practicality in large-scale processing. However, surface contamination, such as niobium carbide formed during vacuum furnace baking, can limit the quench field and degrade the quality factor of the cavity. To investigate this effect, a 1.3 GHz single-cell Nb cavity underwent mid-T baking, followed by a chemical treatment to remove the surface contaminants. Post-treatment measurements revealed a significant improvement in both the quality factor and the quench field.

INTRODUCTION

Superconducting radio frequency (SRF) cavities made of high RRR niobium are key components in modern particle accelerators, enabling efficient acceleration of charged particles through their high gradients (E_{acc}) and quality factors (Q_0). To further reduce RF losses and improve operational efficiency, various surface treatment techniques have been developed, including nitrogen doping [1] and thermal baking. Medium-temperature (mid-T) baking in the range of 300–350°C has emerged as a promising method to enhance the Q_0 of niobium cavities, particularly at medium RF fields [2, 3]. This technique alters the near-surface composition by oxygen diffusion, suppressing BCS surface resistance and RF losses [2]. Mid-T baking at 350°C has been selected for the PIP-II low-beta 650 MHz cavities [4]. Mid-T baking can be performed either in situ, with the cavity actively pumped during the baking, or by placing the cavity in a high-vacuum furnace. The latter method is generally preferred for mass production of cavities.

Despite the observed Q_0 enhancement, mid-T baked cavities often quench at relatively low accelerating gradients of below 25 MV/m. The origin of this reduced quench field remains under investigation. One hypothesis is that niobium carbides, potentially formed during mid-T baking in the furnace, contribute to degraded cavity performance.

To investigate this possibility, a post-bake surface treatment that removes only the topmost RF-active layer without significantly altering the oxygen concentration is desirable. In this work, we explore the application of an ultralight chemical removal process, removing the top RF layer, to a mid-T baked cavity. The goal is to evaluate the effect of surface contaminants on cavity performance and determine whether this minimal surface treatment can improve the performance of mid-T baked cavities.

* Fermi Forward Discovery Group, LLC under Contract No. 89243024CSC000002 with the U.S. Department of Energy, Office of Science, Office of High Energy Physics.
† vchouhan@fnal.gov

CAVITY SURFACE PROCESSING

A 1.3 GHz Nb single-cell cavity (TE1RI010) was selected for the mid-T baking study. The cavity was initially processed with bulk EP, degassed at 900°C for 3 h, and baked at 120°C for 48 h to establish its baseline performance. The cavity was then treated with 5 µm EP to eliminate 120 °C bake effect before adding mid-T baking at 350°C for 3 hours. Following this, ultralight EP, designed to remove approximately 100 nm of the top RF layer, was applied to evaluate the impact of any surface contaminants formed during the mid-T bake. The cavity was tested in a vertical cryostat after each major processing step. Figure 1 shows the sequence of processing and testing steps applied to the cavity.

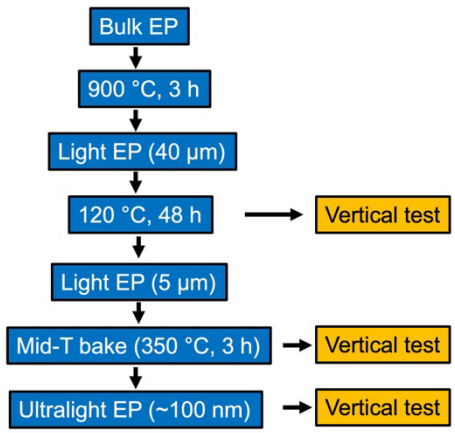


Figure 1: Processing steps applied to the 1.3 GHz single-cell cavity.

Mid-T Baking

Mid-T baking of this cavity was performed in a vacuum furnace, usually used for degassing of the cavity. The cavity flanges were covered with Nb caps to protect the cavity's inner surface from direct line-of-sight exposure to the furnace heaters. The temperature was ramped up at a rate of 3 °C/min until it reached 350°C, where it was held constant for 3 h to complete the bake, followed by furnace cooling. Figure 2 presents the temperature and pressure profiles recorded during the mid-T baking process.

Ultralight EP

An ultralight EP was applied to the mid-T baked surface with the aim of removing the top 100 nm surface. This was intended to eliminate any contaminants formed within the

ISBN: 978-3-95450-261-5 ISSN: 2673-7000 doi: 10.18429/JACoW-NAPAC2025-WEP066

PLASMA PROCESSING OF SRF CAVITIES AT JEFFERSON LAB: EXPERIMENT RESULTS AND SIMULATION INSIGHT*

I. H. Senevirathne†, T. Powers, N. Raut
Thomas Jefferson National Accelerator Facility, Newport News, USA

Content from this work may be used under the terms of the CC BY 4.0 licence (© 2022). Any distribution of this work must maintain attribution to the author(s), title of the work, publisher, and DOI.

Abstract

Plasma processing of superconducting radio frequency (SRF) cavities has been an active research effort at Jefferson Lab (JLab) since 2019, aimed at enhancing cavity performance by removing hydrocarbon contaminants and reducing field emission. In this experiment, processing using argon-oxygen and helium-oxygen gas mixtures to find minimum ignition power at different cavity pressure was investigated. Ongoing simulations are contributing to a better understanding of the plasma surface interactions and the fundamental physics behind the process. These simulations, combined with experimental studies, guide the optimization of key parameters such as gas type, RF power, and pressure to ignite plasma using selected higher-order mode (HOM) frequencies. This paper presents experimental data from argon-oxygen and helium-oxygen gas mixture C75 and C100 cavity plasma ignition studies, as well as simulation results for the C100-type cavity based on the COMSOL model previously applied to the C75 cavity.

INTRODUCTION

Plasma cleaning using noble gases like argon (Ar) or helium (He) in combination with oxygen (O_2) is a common surface treatment technique to remove organic contaminants [1]. When RF power is applied to an SRF cavity filled with the gas mixture, the oscillating electric field accelerates free electrons. These energetic electrons ionize the gas mixture, producing reactive species such as Ar^+ or He^+, along with highly reactive oxygen radicals (O) and ions (O_2^+, O^+ and O^-). Although Ar and He are inert gases and they do not directly participate in chemical reactions with the contaminants, they help sustain the plasma. Meanwhile, the reactive oxygen species chemically react with organic contaminants (hydrocarbons, for example), breaking C–H and C–C bonds to form volatile products like CO, CO_2, and H_2O. This phenomenon can be represented in a simple form: $\mathbf{C_xH_\gamma + O^- \rightarrow CO_2 + H_2O}$, where reactive oxygen atoms oxidize hydrocarbons. This chemical oxidation effectively cleans the surface at the molecular level.

At Jefferson lab, plasma processing efforts includes plasma treatment of multi-cell cavities, cavity pairs, and in-situ processing of cryomodules. A robust and repeatable plasma processing procedure has been developed for the C100 style cavities, resulting in significant energy gain, averaging around 2.7 MV/m per cavity [2]. Plasma processing has also been successfully optimized for the C75-type cavities, establishing reliable ignition.

* Work supported by the funding announcement DE-FOA-0003261
† iresha@jlab.org

PLASMA IGNITION EXPERIMENT

We conducted a plasma ignition experiment using argon (Ar) helium (He) and oxygen (O_2) mixtures to determine the minimum RF power required to ignite a room temperature plasma in different cells of the C75 and C100 superconducting radio-frequency (SRF) cavities.

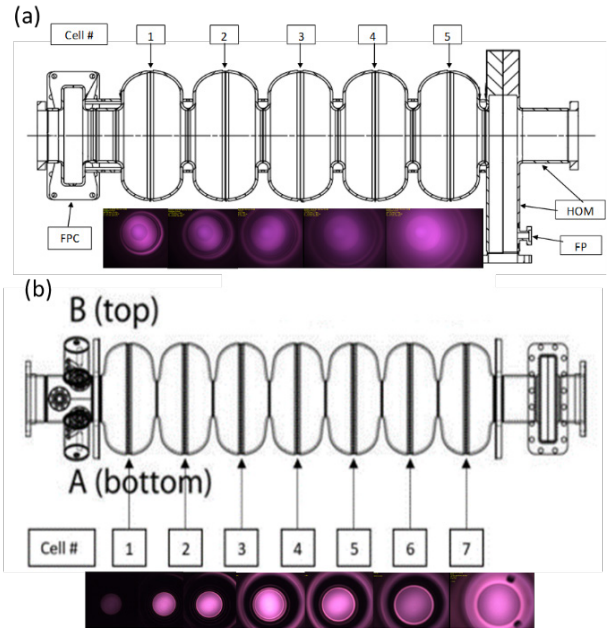


Figure 1: Cell numbering on (a) C75 cavity and (b) C100 cavity along with camera view of argon-oxygen plasma inside each cell.

S-parameters, particularly S11 and S21, are used to characterize the coupling and transmission behavior of electromagnetic modes in SRF cavities. S11 represents the reflection coefficient at the input port and provides insight into how efficiently a mode couples into the cavity, larger negative values indicate stronger coupling. S21, on the other hand, measures transmission through the cavity, helping identify whether specific modes, such as higher-order modes (HOMs), are propagating or suppressed. In plasma ignition experiments, HOMs, often dipole modes are commonly excited because they typically exhibit better coupling than the fundamental accelerating mode. Furthermore, the fundamental power coupler (FPC) setup for cryogenic operations of beam loaded cavity, therefore couples only minimal power into fundamental modes in room temperature. For plasma processing of C100-type cavities, TE111 HOMs in the 1850–2050 MHz range are used due to strong coupling via ILC-style HOM couplers, with 20 – 95% of applied power entering the cavity [3]. During

ISBN: 978-3-95450-261-5 ISSN: 2673-7000 doi: 10.18429/JACoW-NAPAC2025-WEP067

STUDY OF UNCORRELATED RESONANCE CROSSING IN A CONTROLLED ENVIRONMENT

Jack Kelley*,[1,2], Oleksii Beznosov,[1], Joseph Devlin,[3], D. P. Barber,[4]
[1]Los Alamos National Laboratory, Los Alamos, NM, USA
[2]Virginia Tech, Blacksburg, VA, USA [3]Cornell University, Ithaca, IL, USA
[4]University of New Mexico, Albuquerque, NM, USA

Content from this work may be used under the terms of the CC BY 4.0 licence (© 2022). Any distribution of this work must maintain attribution to the author(s), title of the work, publisher, and DOI.

Abstract

This paper deals with estimating spin depolarization in planned very high energy electron-positron storage rings like the FCC-ee. The paper covers three aspects of the work: 1) the putative so-called uncorrelated resonance crossing due to noise in the spin-rotation phase advance caused by photon emission in synchrotron radiation. This is expected to suppress the depolarization caused by synchrotron sideband resonances, 2) a study of the performance of our code on multiple high performance systems, and 3) the novel exploitation of a high order Magnus expansion applied to spin transport. The study uses Monte-Carlo spin-orbit tracking for a simple model of spin motion, the so-called single resonance model, augmented by the effects of radiation. The results presented here represent the first steps of a planned detailed large-scale exploration.

INTRODUCTION

We make use of a simple one-degree of freedom model (hereafter referred to as SM1) for an electron storage ring, first discussed in Ref. [1]. SM1 is adapted from the so-called single resonance model (SRM) [2] by adding a noise term and damping to model depolarization of electrons due to spin diffusion in the trivial setting of the SRM. In SM1, a particle with normalized phase-space coordinates is modeled as a 2D random process $Y(\theta) = (Y_1(\theta), Y_2(\theta))$ governed by the stochastic differential equation (SDE)

$$\mathrm{d}Y = (-bJY - \varepsilon Y)\mathrm{d}\theta + \sqrt{\varepsilon}\mathrm{d}W_\theta,\ J = \begin{bmatrix} 0 & 1 \\ -1 & 0 \end{bmatrix}, \quad (1)$$

with the initial values of Y belonging to the distribution $Y(0) \sim \mathcal{N}_2(0, \frac{1}{2}I_2)$ where I_2 is the 2×2 identity matrix. Here W_θ denotes the two-dimensional Wiener process, and b and ε are constant parameters that model the betatron oscillation frequency and the synchrotron radiation strength, respectively.

Note that if $\varepsilon = 0$, that is, noise and damping are not present, the model reduces to a simple harmonic oscillator with frequency b. Further note that if noise is ignored, we get a deterministic, damped harmonic oscillator with random initial condition with a known solution for every random sample. This makes this problem amenable to the exponential Euler method, where each step is a result of evaluating

$$Y(\theta_{n+1}) = e^{-\Delta\theta(bJ+\varepsilon I)}Y(\theta_n) + \sqrt{\varepsilon}\Delta W_n, \quad (2)$$

where the components of the two-vector ΔW_n are sampled from the normal distribution $\mathcal{N}(0, \sqrt{h})$ independently at each step for a step size $h = \Delta\theta$. Note that, since the Stern-Gerlach effect can be neglected at high energy, the orbital equations can be solved independently of the spin equation, but the spin equation requires intermediate samples at azimuths θ_n.

THOMAS-BMT EQUATION FOR SM1

The matrix version of the spin equation for SM1 is

$$\frac{\mathrm{d}S}{\mathrm{d}\theta} = \Omega(Y(\theta))S,\ \ \Omega(Y) = \nu_0 J_0 + \sigma_0 \sum_{j=1}^{2} J_j Y_j, \quad (3)$$

where $\vec{S}$ is the unit-norm spin vector with initial condition $\vec{S}(0) = \vec{S}_0$ and $J_0^{1,2} = J_1^{3,2} = J_2^{1,3} = 1$.

Here ν_0, the spin tune on the closed design orbit, models spin precession frequency around the vertical, and σ_0 is the so-called resonance strength. In the absence of damping and diffusion, the invariant spin field (ISF) in our model is given by

$$\hat{n}(y) = \frac{1}{\sigma(y)}\begin{pmatrix} y_1 \\ y_2 \\ \zeta \end{pmatrix},\ \ \sigma(y) := \sqrt{y^{\mathrm{T}}y + \zeta^2},\ \ \zeta := \frac{\nu_0 - b}{\sigma_0}. \quad (4)$$

Then, as a first step to going beyond SM1 and modeling noise in the spin phase advance, we add a modulation at the synchrotron tune and add noise to that tune. Then ν_0 is replaced by

$$\nu = \nu_0(1 + \delta\sin((\nu_s + \xi)\theta + \phi)) \quad (5)$$

where ν_s in the synchrotron tune. We choose a typical fractional energy spread $\delta = 0.005$ and a typical ν_s of 0.03 while $\xi \sim \mathcal{N}(0, 0.001)$. δ is proportional to $\frac{\Delta E}{E}$.

NUMERICAL METHOD

While in the previous section we have described our spin with a 3-vector, in our numerical method we compute the spin update via an accumulated quaternion q before transforming q back to a matrix in $\mathbb{R}^{3\times3}$ to take measurements. To compute the procession of each particle's spin through the ring we keep track of q, which represents the rotation of the spin vector S from its initial position S_0 to the current position $S(\theta)$. We start the simulation with q_0 corresponding to the quaternion $\langle 1, 0, 0, 0\rangle$ and update this rotation quaternion

* jackkelley@vt.edu

ISBN: 978-3-95450-261-5 ISSN: 2673-7000 doi: 10.18429/JACoW-NAPAC2025-WEP069

PRELIMINARY COMPUTATIONAL STUDY ON MINIMIZING LONGITUDINAL EMITTANCE IN PHOTOINJECTOR

M. K. Seo*, S. H. Park, Korea University, Sejong, Korea
G. Ha†, Northern Illinois University, DeKalb, USA

Content from this work may be used under the terms of the CC BY 4.0 licence (© 2022). Any distribution of this work must maintain attribution to the author(s), title of the work, publisher, and DOI.

Abstract

Recently, we proposed a novel photoinjector that incorporates an emittance exchange (EEX) beamline. Previous studies demonstrated promising 4D emittance performance of an EEX-based injector, but the beam's longitudinal emittance at the linac exit still limits the final transverse emittance downstream of the EEX stage. We performed a comprehensive scan of injector parameters—including gun phase, laser spot size and pulse length, and solenoid strengths to (1) estimate the minimum achievable longitudinal emittance, (2) identify sources of emittance growth, and (3) explore mitigation strategies. Here, we present the status of this study. Simulations were carried out using General Particle Tracer (GPT) including space-charge effects.

INTRODUCTION

The brightness of most modern accelerators has been tremendously improved over the last several decades. While we achieve sub-micron scale transverse emittance [1] and kilo-Ampere level peak currents [1], longitudinal emittances are often much higher than the transverse emittances. It is obvious that improving the longitudinal emittance will provide significant advantages on a variety of scientific accelerator facilities. Therefore, R&D is required to understand the minimum achievable longitudinal emittance and the mechanism of emittance growth, similar to Ref. [2].

Currently, from the simulations for Argonne Wakefield Accelerator facility [3], we believe the major sources of longitudinal emittance growth are (i) nonlinear correlation from RF curvatures and nonlinear space charge forces and (ii) a large energy spread at the periphery of the beam, which must be originated from space charge effects entangled with RF fields in the cavity. Radial dependency of accelerating fields can also introduce an increase of uncorrelated energy spread.

To explore the opportunity of generating a low longitudinal emittance, resulting in significant boost for 4D emittance, we previously ran simulation with an emittance exchange (EEX) beamline [1]. In this study, we have exchanged the transverse and longitudinal phase spaces via the EEX beamline. Then, the nonlinear correlation now in the transverse phase space was corrected using recently proposed transverse wiggler-based linearization [4]. A large spread at the periphery of the beam was simply blocked using a wide slit. With such treatment, the simulation for 100 pC beam showed promising and exciting results of the final transverse emittance of 0.63 μm and the final longitudinal emittance of 0.4 μm [1].

While the previous study demonstrated the feasibility of achieving low longitudinal emittance, the emission mechanism suggests that the minimum achievable longitudinal emittance seems not inherently larger than that of transverse planes. We conducted injector parameter scan to explore minimum achievable longitudinal emittance using the beamline at the AWA facility. This paper discusses observations from the parameter scan.

PARAMETER SCAN SETUP AND RESULT

For the injector parameter scan, we modeled AWA facility's drive beamline [3] using General Particle Tracer (GPT) code [5]. Scan variables and their scan ranges are summarized in Table 1. The charge of the beam was set to 100 pC, and the beam was accelerated up to 44 MeV to account future experiment using the EEX beamline [1]. The parameter scan results are shown in Fig. 1.

Table 1: Parameters used for the scan. Gun phase scan includes 41°, 42°, 43°, and 44°.

Parameters	Value	Step
Gun phase [deg]	20–50	5°
Matching solenoid ampere [A]	150–270	5 A
Number of α-BBO crystals	0–5	1
Laser radius on cathode [mm]	0.2–0.3	0.01 mm

We also note another important point regarding the linearization. Harmonic cavities are a usual choice to compensate RF curvature from accelerating cavities [6]. However, such compensation mechanism is insufficient to fully linearize the phase space. Among the sources of nonlinear correlations, the second (or at most third order) polynomial components, such as RF curvature, will only be removed. As shown in Fig. 2, longitudinal phase space can easily have remaining nonlinear correlations, which increases the emittance. To address this issue, we assume to use transverse wiggler with EEX beamline [1]. For this process, we apply 20th-order polynomial fit to the phase space and subtract it from the phase space as shown in Fig. 2 (b). Table 2 also shows a significant difference between these two cases. We also apply the periphery cut to further reduce the longitudinal emittance. 20% of outermost particles are removed.

* tjalsrb1@korea.ac.kr
† gha@niu.edu

ISBN: 978-3-95450-261-5 ISSN: 2673-7000 doi: 10.18429/JACoW-NAPAC2025-WEP070

PROGRESS OF POLARIZED ION SOURCES AT BNL*

D. Raparia[1,†], E. Beebe[1], A. Cannavo[1], C. Ianzano[3], J. Maxwell[2] , R. Millner[3] , A. Poblahguev[1], J. Ritter[1], A. Sukhanov[1], N. Wuerfel[3]
[1]Brookhaven National Laboratory, Upton, NY, USA
[2]Thomas Jefferson National Accelerator Facility, Newport News, VA, USA
[3]Laboratory for Nuclear Science, Massachusetts Institute of Technology, Cambridge, MA, USA

Abstract

The OPPIS has undergone multiple upgrades since 2000, with the most recent completed in 2022. Improvements to the Rb and Na cells have reduced vapor dispersion in the beamline, significantly lowering consumption and improving source stability. Plasmatron modifications extended component lifetimes. These upgrades enabled reliable Run-24 operation, with a mean current of 350 µA, 300 µs pulse width, and ~80% polarization delivered at the 200 MeV linac exit.

Development is also underway for a high-intensity (2×10^{11} ions/pulse) polarized $^3He^{++}$ source for the future EIC. The approach uses metastability-exchange optical pumping of high-purity ^{3}He gas in a strong magnetic field, followed by ionization in EBIS. In tests with an "open" cell, 80–85% polarization has been achieved. The final gas cell configuration is now being tested with a 5 T EBIS solenoid magnet.

INTRODUCTION

The Relativistic Heavy Ion Collider (RHIC) is currently the only operational collider capable of accelerating and colliding polarized proton beams, achieving ~60% polarization [1]. The upcoming Electron-Ion Collider (EIC) will extend this capability to polarized electron–ion collisions, including $^3He^{++}$ beams [2]. Polarized protons for RHIC are produced using the Optically Pumped Polarized H^- Ion Source (OPPIS) [3], which provides 0.5–1.0 mA (up to 1.6 mA) in 400 µs pulses with 80–85% polarization. The polarized H^- beam is accelerated to 200 MeV in the Linac, then injected into the Booster, where it is adiabatically captured in a single bunch of $\sim4\times10^{11}$ protons. The bunch is accelerated to 2.5 GeV, transferred to the Alternating Gradient Synchrotron (AGS), and further accelerated to 24.3 GeV, delivering ~70% polarization to RHIC. The use of Siberian Snakes in AGS and RHIC effectively suppresses depolarizing resonances, preserving 60–65% polarization through the full acceleration cycle.

Preserving polarization during acceleration will again rely on Siberian Snakes. To meet EIC requirements, the ion source must deliver $\sim2\times10^{11}$ $^3He^{++}$ ions in a 20 µs pulse, implying a peak current of ~2000 µA—about 1,000× higher than past $^3He^{++}$ sources. The proposed source is based on the Electron Beam Ion Source (EBIS) at Brookhaven National Laboratory (BNL) [4]. Polarized ^{3}He gas will be produced via Metastability Exchange Optical Pumping (MEOP) in a 5 T solenoidal field, then injected into EBIS where it will be ionized by a 10 A electron beam. The goal is to achieve 2.5×10^{11} $^3He^{++}$/pulse at ~70% polarization, followed by acceleration to 2 MeV/u using a Radio Frequency Quadrupole (RFQ) and IH linac for injection into the Booster.

OPPIS

The proton polarization techniques employed in the Optically Pumped Polarized H^- Ion Source (OPPIS), as detailed in [5, 6], are structured into five core functional components: the Fast Atomic Beam Source (FABS), helium cell (He-cell), rubidium cell (Rb-cell), Sona transition region, and the sodium (Na) jet ionizer and extraction system. Both the He-cells and the Rb-cell operate within the 3 T magnetic field provided by a superconducting solenoid (Fig. 1).

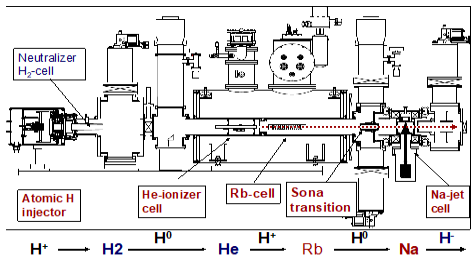


Figure 1: Layout of the OPPIS.

The FABS cathode underwent a redesign that included the addition of a small nozzle and an increase in the outer rim thickness to 3.2 mm. This new nozzle geometry enhances gas flow shaping into the discharge channel and promotes a more uniform wear pattern on the cathode. These changes significantly extended cathode lifetime—eliminating typical blistering and clustering effects seen previously. While the older cathodes averaged two months of operation, the current plasmatron design has now run for 29 weeks without failure.

For Run-24, a new Rb-cell design was implemented. In contrast to the earlier configuration (Fig. 2a, left), where the Rb reservoir was directly exposed to the beam channel, vessel that holds the liquid Rb, which then diffuses evenly through four lateral slits into an inner copper cylinder (Fig. 2c). To improve thermal regulation, a cooling groove was added to the stainless vessel (Fig. 2a), and a copper shield was mounted above it to ensure uniform temperature distribution (Fig. 2b).

* Work supported by U.S. Department of Energy
† raparia@bnl.gov

Content from this work may be used under the terms of the CC BY 4.0 licence (© 2022). Any distribution of this work must maintain attribution to the author(s), title of the work, publisher, and DOI.

ISBN: 978-3-95450-261-5 ISSN: 2673-7000 doi: 10.18429/JACoW-NAPAC2025-WEP073

PROGRESS UPDATE ON COMPRESSED ULTRASHORT PULSE INJECTOR DEMONSTRATOR

W. H. Tan*, A. Dhar, J. Hernandez, E. A. Nanni
SLAC National Accelerator Laboratory, Menlo Park, CA, USA

Content from this work may be used under the terms of the CC BY 4.0 licence (© 2022). Any distribution of this work must maintain attribution to the author(s), title of the work, publisher, and DOI.

Abstract

Stable high gradient operation of a photoinjector is important for generating high brightness electron beams. The Argonne Wakefield Accelerator (AWA) facility recently commissioned an X-band photoinjector at 400 MV/m cathode field without significant breakdown rates using nanosecond RF pulses generated from a wakefield accelerator. We propose to develop an X-band photoinjector at 500 MV/m cathode field fed by ultrashort RF pulses generated by RF pulse compression technology developed at SLAC National Accelerator Laboratory, named as Compressed Ultrashort Pulse Injector Demonstrator (CUPID). The klystron based pulse compression is more stable and allows higher repetition rate. Here we provides the progress update of CUPID project, in particular on the mechanical design of the electron gun, solenoid's requirement and design constraints.

INTRODUCTION

The invention of photoinjector enabled the generation of high brightness electron beams, where photoemitted electrons are accelerated to high energies by a radiofrequency electron gun to suppress the degradation of beams' brightness due to charge repulsion [1, 2]. High brightness electron beams are important for accelerator-based applications, where the two most notable ones are being the free-electron-lasers (FELs) and electron microscopy [3].

The quality of an electron beam is given by its six-dimensional brightness, $\mathcal{B}_{6D} = 2I/\varepsilon_n^2\sigma_\gamma$, where I, ε_n and σ_γ are the beam current, transverse emittance and normalized rms energy spread respectively [4]. High accelerating gradient at the cathode can achieve bright electron beams since the brightness is proportional to the square of the applied field at the cathode, but comes with RF breakdowns $\mathcal{B}_{6D} \propto E^2$ [4–11]. One possible way to achieve high gradient is to reduce the time duration of the feeding in RF pulses since phenomenological studies showed that the breakdown rate is proportional to the applied field gradient but inversely proportional to the RF pulse duration [12]. The Argonne Wakefield Accelerator (AWA) achieved high gradient at ~400 MV/m without significant breakdowns on an X-band 11.7 GHz gun [13]. AWA achieved this by using a wakefield accelerator that accelerates 400 nC electron bunches to high energies and generates ~10 ns high power RF pulses from a power-extraction-and-transfer structure (PETS) [14].

We propose to develop Compressed Ultrashort Pulse Injector Demonstrator (CUPID), a 1.6 cell electron gun that can achieve high gradient with ultrashort high power RF pulses generated by a RF pulse compressor at 11.424 GHz to utilize the available X-band klystrons of the same frequency and a RF pulse compressor at SLAC [15]. In this paper, we discuss the design of the CUPID electron gun, the solenoid's requirement, design constraints and preliminary beam dynamics studies.

* whtan@slac.stanford.edu

CUPID GUN DESIGN

The CUPID electron gun is designed to operate at 500 MV/m at the cathode fed by a 300 MW, 10 ns RF pulse. This is achieved by designing the electron gun to operate in the transient regime where RF pulses fill the gun quickly and reflect back. The exit of the CUPID gun is modeled as a 11.43 mm waveguide to connect to an available TM_{01} X-band mode launcher [16, 17]. This allows us to have flexibility in reusing the existing mode launcher. Figure 1(a) shows the mechanical design of the CUPID gun with the attached TM_{01} mode launcher and superimposed electric field map, all enclosed inside a solenoid. This mockup solenoid is designed to evaluate the physical dimensions needed for the full solenoid design. Figure 1(b) shows the zoomed-in view of CUPID gun and the mode launcher. Based on the current design, the solenoid needs to have a bore diameter larger than 70 mm diameter of the flange and a length shorter than 75 mm.

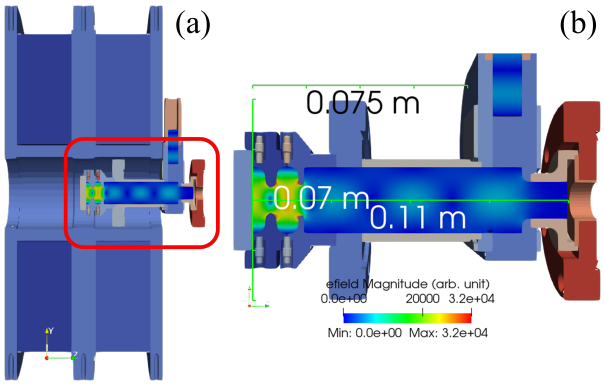


Figure 1: (a) The design of CUPID gun with an attached TM_{01} mode launcher, its fieldmap and a mockup solenoid. (b) Zoomed-in view. The gun assembly has 70 mm diameter, 75 mm (110 mm) long before (after) the attached mode launcher.

Figure 2 shows the evolution of the beam energy at the on-crest phase. The beam energy out of the gun exit is 4.7 MeV. Since the CUPID gun is designed to operate in a transient regime, there are traveling waves present in the waveguide

ISBN: 978-3-95450-261-5 ISSN: 2673-7000 doi: 10.18429/JACoW-NAPAC2025-WEP075

RADIO-FREQUENCY HARDWARE CONSIDERATIONS FOR A HIGH-POWER SOLID-STATE AMPLIFIER*

T. W. Hall†, M. Brown, J. Lyles, S. Russell, M. Sanchez Barrueta, J. Vega
Los Alamos National Laboratory, Los Alamos, NM, USA

Content from this work may be used under the terms of the CC BY 4.0 licence (© 2022). Any distribution of this work must maintain attribution to the author(s), title of the work, publisher, and DOI.

Abstract

A feasibility study is developing a prototype solid state power amplifier to supplant or replace 805 MHz klystrons powering the coupled-cavity linac at the Los Alamos Neutron Science Center (LANSCE). We are considering the RF passive hardware used for such an amplifier. The power from individual transistor pallets that provide 5 kW each must be power-combined to the requisite 1.25 MW needed to replace a klystron. Various approaches are being considered for combining Additionally, the protection of the various components from reflected power is essential to avoiding damage to the pallets and all of the passive RF components such as combiners and connectors. The use of magic tees as both combiners and isolators is discussed, and circulators are another critical component for this design. Finally, as power is combined, another concern is the power handling of connectors, and the balance between performance and the practicality of the large number of connectors becomes crucial.

INTRODUCTION

LANSCE provides an 800 MeV beam of H^- to four user facilities, and klystrons have been used as the RF power sources to the coupled-cavity linac (CCL). Recently, there has been a high mortality rate for these klystrons [1,2]. Solid state power amplifiers (SSPA) could potentially supplement these diminishing RF sources due to the new development of Gallium-Nitride (GaN) transistors that are capable of outputting up to 5 kW on a single chip [2, 3]. This high power density reduces the footprint of a 1.25 MW SSPA to a size that can be matched to our present RF galleries. The use of SSPA would also eliminate the high voltage power supplies and the oil tanks that house the present modulators.

This paper will address some of the challenges with the RF that are present with building such an amplifier. First, the possible combining methods will be discussed to address their how they could be used either on their own or together with other techniques to achieve 1.25 MW from individual 5 kW transistors. Next, circulators will be discussed as a method of protection for the transistors from reflections internal and external to the SSPA. Finally, the power handling of RF connectors internal to the SSPA is discussed.

* Work supported by the U.S. Department of Energy through the Los Alamos National Laboratory, operated by Triad National Security, LLC, for the National Nuclear Security Administration of U.S. Department of Energy (Contract No. 89233218CNA000001). Research presented in this article was supported by the Laboratory Directed Research and Development program of Los Alamos National Laboratory under project number 20240723DI.

† twh@lanl.gov

POWER COMBINATION

A significant obstacle to the design of the SSPA is the power combining of the 5 kW transistors. Any combination scheme will have to combine power from hundreds transistors to reach 1.25 MW, and the total SSPA footprint should be small enough to fit within the present footprint of the klystrons. The SSPA will be driven by multiple inputs of differing phase (out-phasing) as the means of amplitude and phase control [4, 5], so those variations must avoid deleterious effects like reflected power in the combination scheme. Other unintentional variations such as transistor gain should also be well managed in the combination scheme.

Impedance Matched Combiners

A large class of combiners matches sections of impedances to combine two or more inputs. A simple case of such a combiner is the Wilkinson topology [6], which isolates the inputs from each other and minimizes reflections via quarter wave transformers between input and output and resistors between inputs. Gysel proposed a solution to the common problem of the overheating of isolated resistors by instead dedicating a grounded load to each input to better dissipate that heat [7]. Another combiner of this type is the hybrid combiner, whose two inputs must be offset by 90° to get a single combined power.

Any of these could be used in a corporate combining structure where two transistors are combined, then the output of those is combined with two others and so on. This method would require too much space in the form of combiners and also has greater additive losses than other combination schemes so this is not a viable option. Practically, the number of 5 kW transistors that can be combined with these options is four or less due to the limitations on the voltage hold-off of connectors and the thermal management of the matching loads.

Radial combiners are an interesting case of impedance matched combiners. The physical structure of this results in N inputs evenly spaced at some distance along a circular layout with the output perpendicular to their plane. The S-matrix for an N-way combiner is

$$S = \begin{bmatrix} 0 & \frac{1}{\sqrt{N}} & \frac{1}{\sqrt{N}} & & \frac{1}{\sqrt{N}} \\ \frac{1}{\sqrt{N}} & -\frac{N-1}{N} & \frac{1}{N} & \cdots & \frac{1}{N} \\ \frac{1}{\sqrt{N}} & \frac{1}{N} & -\frac{N-1}{N} & & \frac{1}{N} \\ & \vdots & & \ddots & \\ \frac{1}{\sqrt{N}} & \frac{1}{N} & \frac{1}{N} & \cdots & -\frac{N-1}{N} \end{bmatrix} \quad (1)$$

where port 1 is the output port and ports 2 through $N + 1$ are the input ports. This does not have the isolation of other

ISBN: 978-3-95450-261-5 ISSN: 2673-7000 doi: 10.18429/JACoW-NAPAC2025-WEP076

R&D PROGRESS OF ELECTRON CYCLOTRON RESONANCE ACCELERATOR*

Y. Jiang[1,†], X. Chang[1], J.L. Hirshfield[1], S. Shchelkunov[2], M.A. Palmer[2]
[1]Omega-P R&D, Inc., New Haven, CT, USA
[2]Brookhaven National Laboratory, Upton, NY, USA

Content from this work may be used under the terms of the CC BY 4.0 licence (© 2022). Any distribution of this work must maintain attribution to the author(s), title of the work, publisher, and DOI.

Abstract

Several attractive features of a novel electron Cyclotron Resonance Accelerator (eCRA) include: a compact robust room-temperature single-cell RF cavity as the accelerator structure; continuous ampere-level high current output without bunching; and a self-scanning accelerated energetic e-beam, obviating need for a separate beam scanner. Hence an eCRA can be highly compact and efficient to produce high power electron beams and x-ray beams. The applications of the eCRA includes the replacement of Cs-137 based dosimeter calibration systems, and the replacement of Co-60 based sterilization systems. The R&D progress of eCRA is reported here. A 2-MeV eCRA Demonstrator is under construction at BNL to validate the eCRA acceleration mechanism experimentally. A 5-MeV eCRA Upgrade with high beam power is in the design phase.

INTRODUCTION

Radioactive sources have been used in a variety of beneficial applications including sterilization of medical devices, irradiation to reduce the food-borne illnesses transmission, instrument calibration, National Security, et al [1]. However, radioactive sources pose both safety and security risks, if these sources are mishandled. Replacement technologies for radionuclide sources, using accelerator-based X-ray generators, are available or possible for most irradiation applications. To produce x-rays, high-energy accelerated electrons strike a heavy metal target and are rapidly decelerated, generating bremsstrahlung photons with a broad and continuous energy spectrum with all energies below the maximum energy (that of the electrons) and an average energy of about one-third of the maximum energy.

But to substitute Cobalt-60 irradiation directly, a high power accelerator capable of delivering a high power electron beam with energy not less than 5 MeV and with high RF-to-beam efficiency is desired. Our novel design of an eCRA-driven e-beam/X-ray generator system can provide a novel system to fulfil the needs of irradiation applications with compact size and high efficiency.

DESCRIPTION OF eCRA

The physical principle underlying eCRA [2] differs fundamentally from the principles underlying all other types of particle accelerators such as linacs or cyclotrons.

The eCRA concept uses a compact robust room temperature single-cell microwave cavity as the accelerator structure to produce a continuous, high current, un-bunched, self-scanning e-beam, with a projected RF-to-beam efficiency about 80%; and obviating the need for an active e-beam scanner [2, 3]. The theoretical and numerical analysis of eCRA can be found in Ref. [2]. Simulations have demonstrated that for electrons injected into a TE_{111} rotating-mode cylindrical cavity immersed in a strong axial magnetic field, high current beams with accompanying heavy beam loading experience acceleration to multi-MeV levels. The eCRA can continuously accelerate charged particles at arbitrary injection phases. With continuous injection of a beam during a full RF cycle, the output beam follows a circular (elliptical) path for circular (elliptical or linearly) polarized RF field. The sweeping beam intersection on a planar target perpendicular to the cavity axis constitutes self-scanning, which completes a full scanning path at a time scale of nanoseconds instead of milliseconds without using alternative current electromagnets.

EXPERIMENTAL EFFORTS OF eCRA DEMO

An eCRA-based e-beam accelerator, the BNL eCRA demonstrator (DEMO) [3], is under construction at BNL to validate the eCRA acceleration mechanism and beam manipulation and serve as a test bed for the x-ray generator design and its x-ray characteristics study. It is designed around some existing components including the S-band microwave waveguides and hybrids, solenoid magnets, iron flux cages and support frame, to significantly reduce the hardware costs. Yet the magnetic field strength is only about 0.25 T at the cavity region, limited by the specification of existing solenoids, hence it is expected to produce electron beams with beam energy about 2.0 MeV.

As shown in Fig. 1, the CST Particle Studio simulation of the eCRA validates that an 18 keV input electron beam with a radius of 5 mm and energy spread of 10% is accelerated to 2.0 MeV inside the eCRA. A thin titanium foil (25~100 micron in thickness) attached to a slotted copper plate is used as the cavity end wall and a beam window to allow the accelerated electron beam to transmit without much energy loss while blocking the microwave from leaking into the downstream beam pipe. However, the CST results can't reflect the reduction of beam energy due to the beam interception with the titanium foil and copper frame. Hence a GEANT4 based program G4beamline is used to simulate the beam-matter interaction approximately. As shown in the histogram of the

* Work supported by a LDRD 23-060 at Brookhaven National Laboratory
† yong.jiang@aya.yale.edu

ISBN: 978-3-95450-261-5 ISSN: 2673-7000 doi: 10.18429/JACoW-NAPAC2025-WEP078

RF AMPLIFIER SYSTEM RECONFIGURATION PLANS FOR NEW DTL AND RFQ*

M. S. Barrueta †, R. Bratton, T.W. Hall, J. Lyles, H. Xu
Los Alamos National Laboratory, Los Alamos, NM, USA.

Abstract

The first 100 MeV of acceleration for protons and H- ions at the Los Alamos Neutron Science Center (LANSCE) is presently accomplished with a Cockroft-Walton generator (750 keV), followed by four Alvarez drift tube linac (DTL) cavities commissioned in 1970. The RF duty factor is 12 %, leading to significant thermal loading in the room temperature copper structures. Increasing obsolescence and structural reliability problems have created the need for replacements to these systems. The LANSCE Modernization Project (LAMP) developed a conceptual design for the Medium Energy Beam Transport (MEBT) and the Drift Tube Linac (DTL) using new accelerator components. This approach utilizes a Radio Frequency Quadrupole (RFQ) and six replacement DTL cavities. The current 201.25 MHz radio-frequency power amplifier system was replaced 10 years ago and has demonstrated high reliability with Diacrode tube lifetimes over 60,000 hours. We propose an RF amplifier topology that leverages this RF system to provide the required power for the LAMP conceptual design through innovative reconfiguration of the amplifiers.

INTRODUCTION

The LANSCE accelerating structures have been largely unmodified since their installation in 1972. In recent years, the initial Cockcroft–Walton accelerating structures and DTL cavities [1] have suffered significant downtime affecting the beam production. The LAMP efforts are dedicated to developing a conceptual upgrade to the front-end portion of the linac that ensures the continuing operation of the accelerator into 2050. This paper describes the proposed upgrade for the high-power RF amplifiers providing the accelerating voltages for the new structures.

CURRENT SYSTEM

LANSCE's current front-end is composed of Cockcroft–Walton direct-current accelerators (for H+ and H-) that allow injection at 750 keV into the DTL. This is one of the last operating structures of this topology world-wide.

The current DTL consists of four cavities for which the exit energy and required peak RF power (data from 2024 production) is captured in Table 1. The cavities were originally constructed with their maximum length determined by the in-house accelerator design facilities, which were eventually repurposed for testing different accelerator components. From 2014 to 2021, the high-power triode-based RF amplifiers that had been operating for 45 years were progressively upgraded. Module 1 (feeding the first linac cavity) is powered by a 20 kWpk solid-state device driven tetrode amplifier [2] (Fig. 1). Because of the cavity's power requirements are close to the amplifier ratings, a circulator was added for the protection of the amplifier against reflected power spikes caused by arcs in the accelerating structure or transmission line. The amplifier produces its RF output by drawing direct current (DC) from a 480 VAC-15 kVDC power supply feeding a capacitor room that stores the energy consumed during the RF pulse without producing excessive droop (Fig. 2).

Table 1: DTL Cavities' Current Exit Energy [3]

Cavity	Exit Energy (MeV)	RF excitation power [MWpk]
1	5.39	0.28
2	41.33	2.3
3	72.72	2.1
4	100	2.4

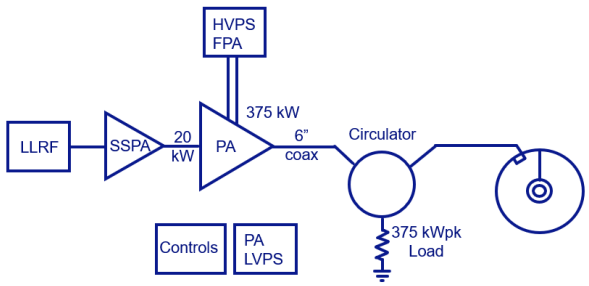


Figure 1: Block diagram of the current amplifier chain feeding the first DTL cavity (Module 1).

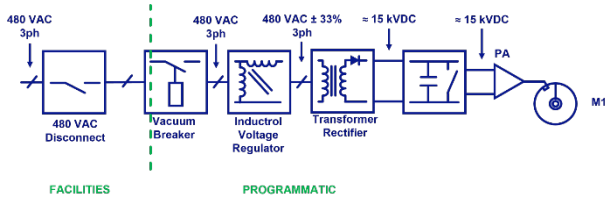


Figure 2: Block diagram of the power supply for Module 1.

Modules 2-4 consist of a 5 kWpk solid-state amplifier feeding a 200 kWpk capable intermediate power amplifier (IPA). The output of the IPA is divided through a hybrid splitter and power provided to two-Diacrode® final power amplifiers (FPAs). Their outputs are recombined to produce the required cavity power (Fig. 3)[4].

Each module has its own capacitor bank and is fed by its own transformer/rectifier (TR), inductrol voltage regulator

* Work supported by the United States Department of Energy, National Nuclear Security Agency, under contract 89233218CNA000001.
† msb@lanl.gov

Content from this work may be used under the terms of the CC BY 4.0 licence (© 2022). Any distribution of this work must maintain attribution to the author(s), title of the work, publisher, and DOI.

ISBN: 978-3-95450-261-5 ISSN: 2673-7000 doi: 10.18429/JACoW-NAPAC2025-WEP079

RF BREAKDOWN AND DARK CURRENT STUDIES IN SHORT-PULSE ACCELERATION

Gaurab Rijal, Michael Shapiro, Xueying Lu[1], Northern Illinois University, DeKalb, IL, USA
Scott Doran, John Power, Argonne National Laboratory, Lemont, IL, USA
[1]also at Argonne National Laboratory, Lemont, IL, USA

Abstract

Recent experimental studies at the Argonne Wakefield Accelerator (AWA) have shown that operating RF cavities with short pulses of only a few nanoseconds in duration can raise the accelerating gradient to nearly 400 MV/m in a series of X-band structure tests. These results motivate further investigation into the breakdown physics underlying the short-pulse acceleration regime. In this work, we present analytical models and numerical simulations of dark current dynamics in X-band cavities driven by short RF pulses. These studies explore key phenomena associated with RF breakdown across various time scales. Building on these insights, we describe the design and experimental plan for a single-cell X-band RF cavity for high-power breakdown tests with short pulses. The cavity is designed to operate at 11.7 GHz and optimized for high-gradient operation with 6 ns long RF pulses and integrated with RF breakdown diagnostics. This work aims to deepen the understanding of RF breakdown physics in the short-pulse regime and to support the development of compact linear accelerators for future applications.

INTRODUCTION

The pursuit of a higher accelerating gradient is central to the development of compact linear accelerators for applications in medical therapy, industrial systems, and future high-energy physics experiments. In recent years short-pulse acceleration has emerged as a promising technique to mitigate RF breakdown and achieve gradients well beyond conventional limits. Specifically, operating RF cavities with nanosecond-scale pulse has demonstrated a significant reduction in breakdown probability while enabling a peak surface field exceeding 400 MV/m in X-band structures. Experimental work at Argonne Wakefield Accelerator (AWA) has shown that X-band cavities driven by a 6ns long RF pulse can sustain a much higher gradient [1–4]. These observations call for a deeper theoretical and experimental understanding of breakdown and dark-current dynamics in this short-pulse regime.

To investigate these effects, this paper first summarizes a study of dark current dynamics [5] in an existing X-band photocathode cavity [1]. Building on these insights, the second part of this paper introduces the design and experimental plan for a dedicated single-cell X-band cavity at 11.7 GHz, optimized for short-pulse operation and equipped with advanced RF diagnostics. Together, these efforts aim to understand the scaling laws and mechanisms that govern breakdown onset in short-pulse regime.

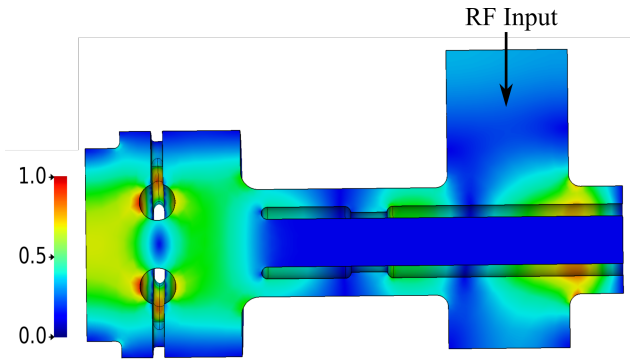


Figure 1: Normalized electric field distribution along the midplane of the X-band photogun cavity at 11.7 GHz, with peak field enhancement near the iris region.

DARK CURRENT STUDY IN AN X-BAND PHOTOCATHODE CAVITY

In this section, we present both electron trajectory analysis and particle-in-cell (PIC) simulations to study dark current dynamics in an X-band photocathode cavity. The cavity is a $1 + \frac{1}{2}$-cell standing-wave structure, overcoupled to achieve a low loaded quality factor (Q_L) and a short RF filling time compatible with nanosecond-scale input pulses. The electric field distribution in the photocathode cavity is shown in Fig. 1. A comprehensive description of the design and high-power testing of the photocathode cavity is provided in [1]. To identify regions susceptible to dark current growth and multipacting, we begin by simulating the trajectories of field-emitted electrons launched from the iris under steady-state RF fields. Sample electron trajectories emitted from iris surface at electric field of 40 MV/m field is shown in Fig. 2(a). The resulting trajectories show that a majority of the emitted electrons impact the cavity sidewall.

To study multipacting behavior under the transient short-pulse operation, we performed CST PIC simulations using RF signals of different temporal profile. Secondary electron emission (SEE) was enabled on the sidewall surface of region I in the half-cell as shown in Fig. 2(b). Two RF input pulses were considered, as illustrated in Fig. 2(c): one with a 3 ns rise, 3 ns flat-top, and 3 ns fall, and another with a 30 ns rise. Seeding electrons were emitted from iris and simulation setup is consistent with method described in [6]. The simulation results are presented in Fig. 3, showing the on axis electric field (left axis) and the total number of multipacting electrons (right axis) over time. In the case of the 3–3–3 ns pulse [Fig. 3(a)], The observed multipacting peaks during both the rising and falling edges of the 3–3–3 ns pulse correspond to resonance orders $N = 1$ through 4.

Content from this work may be used under the terms of the CC BY 4.0 licence (© 2022). Any distribution of this work must maintain attribution to the author(s), title of the work, publisher, and DOI.

ISBN: 978-3-95450-261-5 ISSN: 2673-7000 doi: 10.18429/JACoW-NAPAC2025-WEP082

SPUTTER COATING OF Nb_3Sn INTO SRF CAVITY USING STOICHIOMETRIC TARGET*

M. S. Shakel[1,†], U. Pudasaini[2], G. Eremeev[3], A. Valente-Feliciano[2], H. E. Elsayed-Ali[1]
[1]Old Dominion University, Norfolk, VA, USA
[2]Thomas Jefferson National Accelerator Facility, Newport News, VA, USA
[3]Fermi National Accelerator Laboratory, Batavia, IL, USA

Abstract

Nb_3Sn has emerged as a leading alternative material due to its higher superconducting critical temperature (T_c ~18.3 K) and superheating field (H_{sh} ~400 mT), promising a viable solution to the intrinsic performance limit currently faced by Nb superconducting radiofrequency (SRF) cavities. We sputter-coated Nb_3Sn inside Nb SRF cavity using a stoichiometric Nb_3Sn tube target in a DC cylindrical magnetron sputter coater. The target was fabricated by growing an estimated >20 µm thick Nb_3Sn layer on a Nb tube via Sn vapor diffusion using Jefferson Lab's coating system. Nb-Sn films of thickness about 150 nm were sputter-deposited onto flat Nb samples at positions representing the beam tubes and equator of a 2.6 GHz Nb cavity. Post-deposition annealing at 950 °C for 3 h resulted in the formation of Nb_3Sn. Microstructural analysis of the annealed films was carried out to investigate the morphology and structure of the Nb_3Sn films. Later, a 2.6 GHz Nb SRF cavity was coated with a ~1.2 µm thick sputtered Nb-Sn film using a stoichiometric Nb_3Sn target, followed by annealing. Cryogenic RF testing of the annealed cavity demonstrated a T_c of 17.8 K, indicating the formation of Nb_3Sn. After a light recoating treatment, the cavity achieved a quality factor (Q_0) of 6.7E+08 at lower field at 2.0 K.

INTRODUCTION

Nb_3Sn is a promising candidate for next-generation SRF cavities due to its favourable superconducting properties, enabling efficient operation at higher temperatures compared to bulk Nb cavities, which is approaching its theoretical performance limit [1-3]. Nb_3Sn coated cavities can operate efficiently at 4.2 K while maintaining high quality factors, potentially replacing Nb cavities operated at 2 K and significantly reducing cryogenic operating costs [4-6]. The most widely used method for coating Nb_3Sn onto Nb SRF cavities is the Sn vapor diffusion process [7-9]. However, magnetron sputtering has the potential to provide a viable alternative to deposit Nb_3Sn at lower temperatures on different substrates, offering improved control over film composition, uniformity, and deposition rate. [10, 11]. Previous works have demonstrated Nb_3Sn coating into SRF cavities using a DC cylindrical magnetron sputtering system via multilayer sequential and co-sputtering methods [12, 13]. In this work, we extend the sputtering approach by coating a 2.6 GHz Nb cavity using a stoichiometric Nb_3Sn tube target, custom-fabricated for use in a cylindrical magnetron sputter coater. The sputtering parameters were optimized, and Nb_3Sn coating was first deposited on flat Nb substrates inside a mock cavity, and later into a 2.6 GHz Nb cavity. This method enables direct deposition of Nb-Sn films from the stoichiometric Nb_3Sn target surface, hence offering more precise control over the coating composition onto the inner surface of the Nb SRF cavity.

STOICHIOMETRIC TARGET PREPARATION AND PLASMA DISCHARGE

A stoichiometric Nb_3Sn tube target was prepared by growing a thick Nb_3Sn layer on a high-purity Nb tube (99.95% purity). First, the Nb tube (OD 0.9'' × ID 0.8'' × length 4.5'', purchased from Matsurf Inc.) underwent buffered chemical polishing (BCP) using a 1:1:1 mixture of HF (49%), HNO_3 (70%), and H_3PO4 (85%), removing approximately ~25 µm from the surface.

Later, Nb_3Sn layer was grown on the surface of the Nb tube by Sn vapor diffusion method using the Nb_3Sn coating system at Jefferson Lab [14]. The Nb tube was suspended vertically inside a Nb chamber using a Nb wire during the coating. High-purity Sn (99.9999%, Alpha Aesar), loaded into a crucible, and SnCl2 (99.99%, Sigma Aldrich) powder, packaged into Nb foil pieces, were placed on a Nb cover plate at the chamber's base. The chamber was closed at both ends using Nb covers with molybdenum fasteners inside an ISO4 cleanroom and later transferred to the Nb_3Sn coating furnace. The temperature profile for Nb_3Sn growth included a nucleation step at (540 ± 10) ^{0}C for 90 min, preceded by a ramp at 6 ^{0}C/min from room temperature. This was followed by a ramp at 12 ^{0}C/min to the coating temperature of (1195 ± 10) ^{0}C. The coating temperature was cumulatively kept constant for 148 h to grow a Nb_3Sn coating of a thickness of about 20 µm on the Nb tube target surface. The temperature runs were interrupted after ~60 hours to prevent Sn exhaustion and to allow refilling of the Sn source.

As shown in Fig. 1(a), the stoichiometric Nb_3Sn target was installed on the bottom magnetron of the cylindrical sputter coater, which has two magnetrons that can move axially in the vertical direction. The cylindrical magnetrons

* This work is supported by DOE, Office of Accelerator R&D and Production, Contact No. DE-SC0022284. With partial support by DOE, Office of Nuclear Physics DE-AC05-06OR23177 to JLab, and Contract No. DE-AC02-07CH11359, and Early Career Award to G. Eremeev. This manuscript has been authored by FermiForward Discovery Group, LLC under Contract No. 89243024CSC000002 with the DOE, Office of Science, Office of High Energy Physics.
† Email: mshak001@odu.edu

Content from this work may be used under the terms of the CC BY 4.0 licence (© 2022). Any distribution of this work must maintain attribution to the author(s), title of the work, publisher, and DOI.

ISBN: 978-3-95450-261-5 ISSN: 2673-7000 doi: 10.18429/JACoW-NAPAC2025-WEP083

STATUS OF THE EXPERIMENTAL DEMONSTRATION OF GW POWER GENERATION FROM THz-TBA

G. Ha*, Northern Illinois University, DeKalb, IL, USA
S. H. Park, K. Kim, J. Ko, B. Oh, M. Seo, Korea University, Sejong, Korea
H.-S. Kong, J. H. Kim, J. Kim, H. J. Kwak, S.-H. Kim
Pohang Accelerator Laboratory, Pohang, Korea
G. Chen, S. Doran, W. Liu, J. Power, B. Popovic, E. Wisniewski
Argonne National Laboratory, Lemont, IL, USA
C. Jing, Euclid Techlabs, Bolingbrook, IL, USA

Abstract

We present the current status of preparation for the experimental demonstration of GW power generation from THz-TBA. This paper covers the status of structure fabrication, RF power extraction and absolute power measurement plan, and THz drive beam preparation. Currently, 0.4 THz structures are being fabricated using two improved methods over previous fabrication techniques. RF power extraction will be achieved using an on-axis horn antenna and off-axis parabolic mirrors. The RF power will be detected with a bolometer and calibrated based on the total beam energy loss measured by a spectrometer. In recent machine studies, we successfully generated a high-charge bunch train (1 nC/bunch) compatible with 0.4 THz structure.

INTRODUCTION

A multi-institutional collaboration is underway to develop the physics and technology for terahertz two-beam acceleration (THz-TBA). This collaboration has developed a fabrication method for corrugated wakefield structures in the sub-THz regime [1]. The fabrication quality of the structure was confirmed at Argonne Wakefield Accelerator facility by benchmarking simulated wakefields against measured wakefields using a 40-MeV electron beam [1, 2].

Following this initial successful demonstration, efforts have been made to pursue the next major milestone of the collaboration: generating >1 GW of power from a corrugated structure. In preparation for a subsequent high-gradient demonstration, we selected 0.4 THz as the structure's fundamental frequency. While retaining the disk-stacking method and high-temperature, high-pressure bonding, the disks forming the corrugation were produced using the LIGA process at Pohang Accelerator Laboratory storage ring [3]; see Fig. 1. This structure was fabricated in the summer of 2024.

After the structure fabrication, two major challenges have been explored over the past year including machine study. An experiment to demonstrate high-power generation is now planned for early 2026. This paper mainly discusses the two aforementioned challenges: (i) drive bunch train generation, and (ii) power extraction and its measurement.

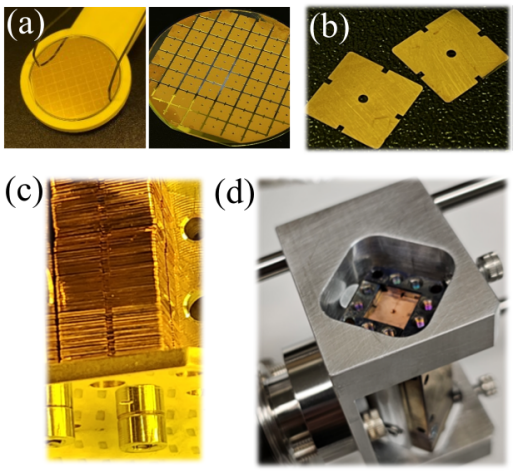


Figure 1: Corrugated structure fabrication. (a) Fabrication of plates with a hole. (b) Fabricated plates with different inner hole diameters. The design specifications are: (1) a hole diameter of 1.00 mm with a plate thickness of 40 µm, and (2) a hole diameter of 1.08 mm with a thickness of 230 µm. (c) Stacked plates prior to bonding. (d) Fabricated structure mounted on a motorized actuator.

DRIVE BUNCH TRAIN GENERATION

Laser Pulse Train

We considered two different methods for generating sub-THz compatible bunch trains [4, 5]. While the deflecting cavity-based method can produce high-quality bunch trains, it requires significant space and multiple cavities. In contrast, the laser-based method showed surprisingly reasonable quality with a much simpler setup compared to the cavity-based approach. The laser-based method was implemented, and a laser splitter system was constructed as shown in Fig. 2 (a).

During the initial experimental verification, we encountered an intensity unbalance issue. Each beam splitter divides the laser pulse into two. However, the intensity ratio can easily deviate from the ideal 50:50, typically ranging from 45:55 to 50:50. The intensities of the first four laser pulses can be easily balanced using attenuators or even irises, thanks to the MLA [6]. However, the next splitter stages uses both the transmitted and reflected pulses from the previous stage. As a result, any imbalance introduced at this

* gha@niu.edu

Content from this work may be used under the terms of the CC BY 4.0 licence (© 2022). Any distribution of this work must maintain attribution to the author(s), title of the work, publisher, and DOI.

ISBN: 978-3-95450-261-5 ISSN: 2673-7000 doi: 10.18429/JACoW-NAPAC2025-WEP084

LANSCE CCL KLYSTRON HIGH-POTTING INVESTIGATION AND IMPROVEMENTS*

A. S. Waghmare†, W. B. Haynes, C. Richman, J. A. Valladares
Los Alamos National Laboratory, Los Alamos, NM, USA

Abstract

LANSCE uses 44 805 MHz klystrons to power the Coupled Cavity Linac (CCL). Modulated anode tubes such as the 1.25 MW LANSCE klystrons need high voltage testing and processing prior to full operation. This not only verifies the klystron can hold-off HV but also allows the klystron to process out some internal imperfections prior to being pulsed by the modulator for the accelerator. The LANSCE accelerator is a relatively long pulse machine, and improper processing can lead to premature degradation in the performance of the tube. This paper describes recent improvements to the 1.25 MW 805 MHz klystron HV check and conditioning process through the development of a new high-potting test stand. High-potting setup and techniques that were historically used are contrasted with the new implementation. Our goal is to improve LANSCE operations by accelerating the high-potting process and reducing expert time and dependence. The new test stand will optimize legacy processes by improving diagnostics, automating control and reducing inconsistencies and process invariability due to human factors. Analysis and automation efforts for this critical process are discussed along with current benefits and future work.

CURRENT PROCESS

Goal

The goal of the high-potting process is to test the voltage hold-off strength of the klystron and carefully recondition the tube if it cannot hold-off required HV. The main indicators used for evaluation of this step are the hold-off voltage (V_{HO}), leakage current (I_{Leak}), and the vacuum ion pump current (I_{IP}).

High Voltage Testing

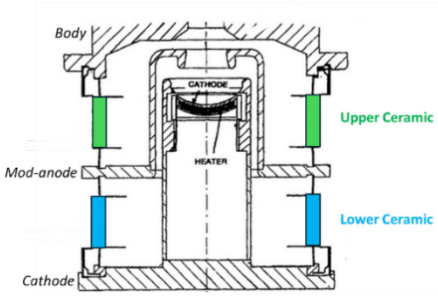


Figure 1: Internal klystron gun structure showing the different sections for high-potting (derived from R. Kowalczyk SLAC "RF Source Vacuum Tube Cost," May 2017).

Klystrons are high potted to check the hold-off voltage between the (see Fig. 1) two different ceramic insulators: mod-anode to the cathode and mod-anode to the body. For high-potting the lower ceramic, HV is connected to the cathode, and the mod-anode is grounded. For the upper ceramic, the cathode is connected to the mod-anode, and the body of the klystron is held at ground potential. The benchmark is for the klystron to reasonably hold-off 110 kV on the lower ceramic and up to 120 kV on the upper ceramic with little to no arcing for approximately 1 hour. Once this is achieved the klystron is high-potted with the modulator tank as a final check. These three test conditions allow us to isolate different parts of the electron gun and test them individually for their ability to withstand high voltage.

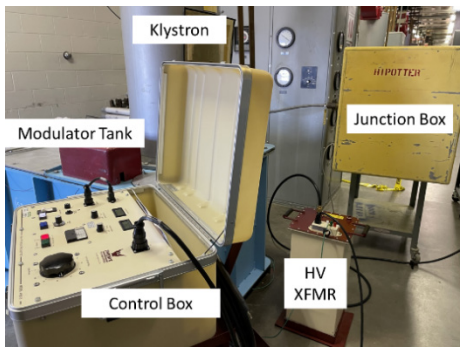


Figure 2: Existing HV testing and processing setup.

If the klystron fails to meet these hold-off voltage benchmarks or has excessive arcing, the tube is slowly processed with HV attempting to improve the electron gun voltage stress points on high field surfaces.

High Voltage Processing

HV processing allows the operator to condition out breakdown issues within the vacuum tube which allows the klystron to run for longer with a reduction in arcing and related issues leading to eventual failure. Improvements are typically characterized by an increase in hold-off voltage and reduction in leakage current and ion pump current.

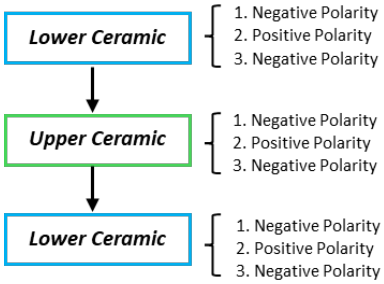


Figure 3: Typical high voltage processing procedure to reduce arcing and improve hold-off voltage.

* - Work supported by US DOE and Laboratory Directed Research and Development (LDRD)
† - aditya@lanl.gov, wbhaynes@lanl.gov

Content from this work may be used under the terms of the CC BY 4.0 licence (© 2022). Any distribution of this work must maintain attribution to the author(s), title of the work, publisher, and DOI.

ISBN: 978-3-95450-261-5 ISSN: 2673-7000 doi: 10.18429/JACoW-NAPAC2025-WEP085

START-TO-END SIMULATIONS OF A COMPACT, LINAC-BASED POSITRON SOURCE

S. Crisp*, R. Goldman[1], A. Ismail[2], S. Gessner[2]
SLAC National Accelerator Laboratory, Menlo Park, USA
[1]also at University of California, Los Angeles, USA
[2]also at Stanford University, USA

Content from this work may be used under the terms of the CC BY 4.0 licence (© 2022). Any distribution of this work must maintain attribution to the author(s), title of the work, publisher, and DOI.

Abstract

Slow positrons are increasingly important to the study of material surfaces. For these kinds of studies, the positrons must have low emittance and relatively high brightness. Unfortunately, fast positron sources like radioactive capsules or linac driven sources have broad energy and angular spread, which make them difficult to capture and use. Moderators are materials that produce slow, mono-energetic positrons from a fast positron beam. Since their efficiencies are typically less than 10^{-3} slow e^+ per fast e^+, research into how to maximize efficiency is of great interest. Previous work has shown that using a linac, one can decelerate the fast positron beam in order to greatly increase moderation efficiency. We present here start-to-end simulations using G4beamline to model a 100 MeV electron beam incident upon a Tungsten target, focused by an adiabatic matching device, and decelerated by a 1.3 GHz, 5-cell pillbox cavity. We show that by decelerating the positrons after their creation we can increase the number of positrons under 500 keV by 15 times, translating to a 16.3 times improvement in moderation efficiency, and therefore leading to a brighter positron source.

INTRODUCTION

Slow positron facilities around the world enable basic science through the use of properties unique to positrons. At the NEPOMUC positron facility, an intense positron source has been employed to drive positron annihilation lifetime spectroscopy to measure vacancy-like defects through the use of positron lifetime studies [1], as well as a multitude of other instruments for surface and volume characterization. At KEK, Total Reflection High-Energy Positron Diffraction (TRHEPD) takes advantage of the unique ability of positrons to totally reflect from surfaces to measure only a few atomic layers deep [2]. Doing this quickly and with high resolution requires an intense (>10^9 e^+/s) slow positron beam, where slow is generally defined as less than $30 - 40$ keV [3]. At SLAC National Accelerator Laboratory, we are developing a Compact Positron Source [4] and are interested in producing beams which are both high intensity and ultrashort to complement the existing MeV-UED facility [5]. This would add yet another tool to the positron physics toolkit – Ultrafast Positron Diffraction, which would enable an entirely new area of surface sensitive pump-probe experiments. This kind of experiment requires maximizing the efficiency of the positron source, since without large numbers of particles these measurements would be too time-intensive to take.

Fast positrons are initially generated either by use of β^+ emitters like ^{22}Na or through pair production, which can provide a much higher intensity source. In either case, these fast positrons have high divergence and energy spread, so while one could simply capture a particular energy slice, this excludes the use of the vast majority of the initial positrons. Slow positron facilities instead use a process called moderation, which cools the positron distribution into a nearly mono-energetic beam, with the energy distribution essentially being a thermal spectrum [6].

These slow positrons have significantly reduced energy spread and emittance such that despite moderators having efficiencies of $\epsilon \approx 10^{-3}$ slow positrons per incident positron, the beams which exit a positron moderator are several orders of magnitude brighter. Although rare gas solid moderators like neon have been demonstrated to have $\epsilon \approx 10^{-2}$, these degrade quickly in high flux environments, such as in linac based positron sources. In the simplest case, a moderator is a thin metal foil for which positrons have a negative work function. This means that a positron which scatters throughout the fields and thermalizes before annihilation has some probability of diffusing to the surface and being reemitted with energy equal to ϕ ($\phi_W = -3$ eV), and energy spread equal to the thermal energy, on the order of meV [7]. Some facilities follow this initial moderator by a remoderation stage [8], or by the use of a buffer gas trap which can both accumulate and further cool positron beams [9], both of which further increase beam brightness. For this paper, we will limit ourselves to the use of a single 50 µm Tungsten foil as a moderator, while acknowledging that further work is necessary to fully optimize the moderator geometry.

Whilst other slow positron facilities utilize various complexities of target-moderator assemblies, none so far has experimentally demonstrated an increase moderation efficiency by preemptively slowing the positron bunch before the initial moderation stage. At CLIC, the positron bunch is slowed in the cell of the linac, but this is used only to capture more charge in a bucket before accelerating to higher energy for collider applications [10]. In this paper, we follow on the work of Long et al. [11], who found via simulation that using a 108 MHz cavity tuned to a decelerating phase between the target and moderator could increase the moderator efficiency by 20 times. In this paper, we present a design based on a 100 MeV electron accelerator source combined

* scrisp11@slac.stanford.edu

ISBN: 978-3-95450-261-5 ISSN: 2673-7000 doi: 10.18429/JACoW-NAPAC2025-WEP086

THE PULSED ION REFLEX KLYSTRON: A NEW ACCELERATOR FOR HIGH EFFICIENCY VOLTAGE CONVERSION

D.J. Mengel, G.P. Jackson
Beam Alpha Incorporated, West Chicago, IL, USA

Content from this work may be used under the terms of the CC BY 4.0 licence (© 2022). Any distribution of this work must maintain attribution to the author(s), title of the work, publisher, and DOI.

Abstract

Beam Alpha has developed a kilowatt-scale fusion microreactor that directly converts nuclear energy to electrical energy with an output of 1.6 MV DC. The "Pulsed Ion Reflex Klystron" has been developed to transform this to useful electrical power. This tube aims to achieve high efficiencies by directing negative ions through a re-entrant resonant cavity hundreds of times to gradually transfer energy from the moving particles to said cavity. Ideal axial and radial fields for achieving this particle motion have been derived and simulated for two different modes of operation, one involving isochronous bunches and one involving repeated harmonic switching.

INTRODUCTION

In this paper, two different tube topologies for efficiently implementing the conversion from 1.6 MV DC to a transformable RF wave [1] will be presented and compared. This RF wave can then be rectified into an intermediate ~400V DC bus, allowing for easy conversion to other useful power levels. The first topology is an isochronous design, where particle bunches oscillate back and forth inside the tube [2] with equal frequency regardless of how much energy has already been coupled out of them. The second design utilizes harmonic switching, so that a bunch's period of oscillation through the tube decreases by one cavity oscillation period per pass through the cavity.

IDEAL ISOCHRONOUS POTENTIAL

A parabolic axial potential causes nonrelativistic particles to take the same amount of time to accelerate to z=0 regardless of initial rest position. Axial voltage is:

$$V(z) = -\frac{2\pi^2 m_i f^2}{q} z^2 \quad (1)$$

Where m_i is the ion mass, f is the frequency of axial particle oscillation and q is the elementary charge. A resonant cavity is then placed at z = 0 to couple energy out of ion bunches.

This potential is problematic because of its inherent defocusing nature in a cylindrical geometry, where radial electric field at a small distance from the axis is:

$$E_r = -\frac{r}{2}\frac{dE_z}{dz} \quad (2)$$

Where E_r is radial electric field, E_z is axial electric field, and r is radial position. [3] Thus, a parabolic potential as described above will produce a defocusing force on negative ions resulting in exponential outward motion.

To combat this, a perturbation must be applied to the potential to produce strong focusing. The perturbation must be quasi-periodic over voltage increments of double the average cavity deceleration voltage, so particle bunches experience a specially-tuned temporary inward force each time they slow down to a halt. The basic waveform and amplitude of this perturbation can be fully derived simply from the desire to maximize stable initial ion pulse length and the fact that axial and radial bunching must occur in order to keep ions inside of the tube. Once a desired cavity oscillation frequency and voltage are decided on, there are no other significant free parameters. The perturbation is removed at voltages below a threshold value, under which ions will be ejected from the tube.

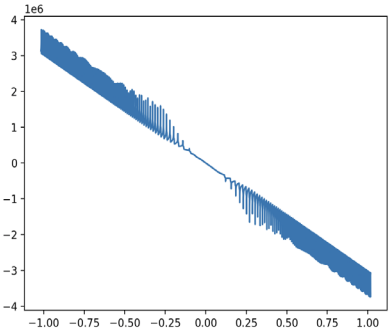


Figure 1: Ideal E_z over z for a 1.6 MV, 2.778 MHz Isochronous Pulsed H- Ion Reflex Klystron with 8.101 kV peak cavity voltage, perturbation threshold 108 kV.

For a 1.6 MV, 2.78 MHz hydrogen ion tube with resonant cavity voltage of 8.101 kV, the amplitude of this perturbation ranges from about 300-900 volts, resulting in a 2 M long tube with electric field p-p perturbation of about 600 kV/M throughout (Fig. 1). Lowering operation frequency results in the same voltage curve, just stretched, and thus electric field is directly proportional to frequency.

HARMONIC SWITCHING POTENTIAL

When the axial potential is changed to be proportional to $z^{\frac{2}{3}}$, the time necessary for a bunch to accelerate from rest to the center of the tube is now linearly proportional to initial potential energy. In the non-relativistic case:

$$V(z) = -\frac{(3\pi\sqrt{2})^{\frac{2}{3}}}{4}\left(\frac{m_i}{q}\right)^{\frac{1}{3}}\left(\frac{V_0}{t_0}\right)^{\frac{2}{3}}|z|^{\frac{2}{3}} \quad (3)$$

Where t_0 is the time necessary to accelerate to z=0 from $V(z) = V_0$. This curve has a positive second derivative, meaning that with the exception at z=0, the potential will be radially focusing instead of defocusing. As such, no significant perturbation is needed for radial focusing (Fig. 2).

A potential like this decelerates ion bunches by utilizing harmonic switching each time the bunch goes back and forth through the tube. The last time the beam passes through the cavity it will have been 5/2 periods of cavity oscillation since the second-to last pass. The third-to-last pass will also be 5/2 periods before the second, but ion motion will occur on the other side of the tube. The next two

ISBN: 978-3-95450-261-5 ISSN: 2673-7000 doi: 10.18429/JACoW-NAPAC2025-WEP087

THERMAL ANALYSIS AND PRELIMINARY COOLDOWN PERFORMANCE OF THE CANTED SCU CRYOSTAT*

Y. Shiroyanagi†, E. Anliker, M. Kasa, I. Kesgin, Y. Ivanyushenkov
Argonne National Laboratory, Lemont, IL, USA

Abstract

The SCU cryostat, featuring two 1.5-meter-long Nb-Ti superconducting undulators (SCUs), is currently being built for the Advanced Photon Source Upgrade. The final design, along with the thermal and mechanical models of this cryocooler-cooled, liquid helium-based cryostat, has been completed. The cryostat has been fabricated, and preliminary cool-down tests were conducted both with and without the two 1.5-meter-long Nb-Ti SCUs. This paper presents a comparison between the measured and calculated thermal performance of the cryostat.

INTRODUCTION

Currently, new 1.5-meter-long SCU (superconducting undulator) magnets are being constructed with a robust insulation scheme [1]. Cryogenically, these new magnets are almost identical to the previous ones, except for the use of plastic on the back side. Therefore, it is valuable to report the results of the cooldown test and analysis using the original 1.5-meter-long SCU magnets within the 4.8-meter-long cryostat. Figure 1 shows a photograph of the cryostat. Figure 2(a) shows the 3D model of the cryocoolers and a cold mass consisting of the liquid helium (LHe) tank, magnets, and the beam chamber. This cryostat comprises three cooling circuits: the thermal shield cooling circuit, the beam chamber cooling circuit, and the magnet and LHe tank cooling circuit. Cooling is provided by six cryocoolers, five 4-K cryocoolers (Sumitomo RDE-418D4) and one 10-K cryocooler (Sumitomo RDK-408S).

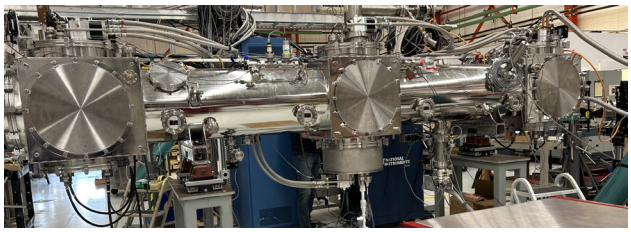


Figure 1: A photograph of the cryostat.

The first stages of all six cryocoolers cool the magnet leads and the thermal shield. The beam chamber is cooled independently from the magnet and the LHe tank. The magnets and LHe tank are cooled by the 2nd stages of five 4-K cryocoolers. The beam chamber is cooled via the busbar by the 2nd stage of one 10-K cryocooler. The magnets are cooled by LHe circulating through the helium channel in the magnet cores, allowing the system to operate in a zero-boiloff mode [2, 3]. Figure 2(b) illustrates the cross section of the LHe tank. The LHe tank is constructed with a stainless-steel wall that is 5.94 mm thick, a copper cladding of the same thickness, and a stainless-steel bottom plate that is 19.05 mm thick, as shown in Fig. 2(b). Cooling power from the 4-K cryocoolers is transferred through the copper thermal links and copper cladding. Temperature sensors are located on the side of the bottom stainless-steel plate and the surface of the copper cladding.

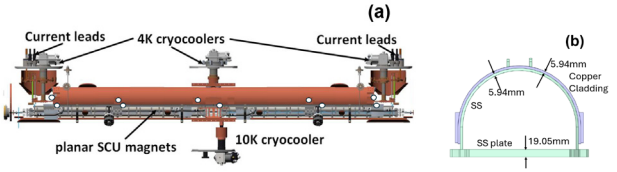


Figure 2:(a) 3D model of the cryostat coldmass and six cryocoolers, (b) cross section of LHe tank.

COOLDOWN WITH LHe TANK ONLY

Initially, a preliminary cooldown is performed without the magnets and beam chamber. Figure 3 displays the temperatures of the five 2nd-stage cold heads during the cooldown of the liquid helium tank alone. It took approximately 70 hours for all the 2nd stages of the 4-K cryocoolers to reach around 6 K. The LHe tank itself reached approximately 6 K within the first 80 hours. Figure 4 illustrates the measured temperatures of the copper cladding and the stainless-steel bottom plate before and after the transfer of liquid helium. After the transfer, the copper cladding reached a temperature of 4.2 K, while the stainless-steel bottom plate remained between 4.6 and 4.7 K. This results in a temperature difference of approximately 0.5 K between the copper cladding and the stainless-steel bottom plate. Despite the transfer of LHe, the temperature difference between the copper cladding and the stainless-steel bottom plate remained around 0.5 K.

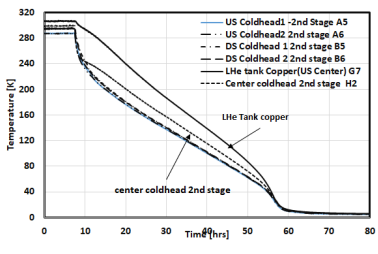


Figure 3: Cooldown curve of the 2nd stages of cryocoolers and LHe tank.

The excess cooling power is defined as the difference between the total available cooling power and the heat load

* Work supported by the U.S. DOE Office of Science-Basic Energy Sciences, under Contract No. DE-AC02-06CH11357.
† email address: yshiroyanagi@anl.gov

Content from this work may be used under the terms of the CC BY 4.0 licence (© 2022). Any distribution of this work must maintain attribution to the author(s), title of the work, publisher, and DOI.

ISBN: 978-3-95450-261-5 ISSN: 2673-7000 doi: 10.18429/JACoW-NAPAC2025-WEP091

TRANSVERSE DEFLECTING CAVITY OPTIMIZATION FOR ACTIVE CONTROL OF ELECTRON BEAM ENERGY CHIRP*

H. Xu†, Q. Marksteiner, N. Yampolsky
Los Alamos National Laboratory, Los Alamos, USA
G. Chen, A. DeSimone[1], S. Doran, G. Ha[1], W. Liu, R. Margraf-O'Neal, J. Power, E. Wisniewski[1]
Argonne National Laboratory, Lemont, USA
[1]also at Northern Illinois University, DeKalb, USA

Abstract

The Transverse Deflecting Cavity Based Chirper (TCBC) is a novel concept of imposing and removing a significant energy chirp of an ultrarelativistic electron beam. The TCBC method requires much less footprint, compared to the conventional chirping and dechirping method involving operating a linear accelerator off-crest. When the compressed bunch is very short, the dechirping has to rely on the wakefields. We present our updated design of the L-band (1.3 GHz) transverse deflecting cavity (TDC) for demonstrating the TCBC concept at the Argonne Wakefield Accelerator (AWA) Facility. Our TDC design update is based on the original design provided by Tsinghua University. The TDC design update focused on ensuring improved performance under more intense electromagnetic fields, reducing the peak pulsed temperature rise. The tuners of the TDC were meanwhile reworked to allow greater adjustability of the resonant frequency and of the electromagnetic field balance among the cells. We also report the tolerance study of the TDC. Two copies of the TDC with the updated design are currently under fabrication with Dymenso, LLC.

INTRODUCTION

At Los Alamos National Laboratory (LANL), a novel approach of creating and removing the energy chirp in an ultrarelativistic electron beam is under investigation, namely the Transverse Deflecting Cavity Based Chirper (TCBC) method [1]. The conventional method of imposing and eliminating the energy chirp involves accelerating the electron beam off the RF phase crest, leading to inefficient utilization of the available space and longer linear accelerator (linac) sections. In comparison, the TCBC brings about a better optimized tradeoff of beamline arrangement: a dedicated TCBC beamline is inserted for imposing and eliminating the energy chirp, but the benefit is that all linac modules can operate at an RF phase optimized solely for the purpose of beam acceleration, leading to a net reduction of beamline length and thus cost.

The key element of the TCBC beamline is the radiofrequency (RF) transverse deflecting cavities (TDC). A typical TCBC beamline involves three TDCs. The first TDC creates a linear transverse momentum kick long the beam; the head and tail of the beam are kicked in opposite directions, with the center of the beam unperturbed. The second TDC imprints a linear energy difference according to the transverse position of the beam particles, creating or eliminating the energy chirp. The third TDC resets the transverse momentum distribution initially created by the first TDC. Quadrupoles are involved between neighboring TDCs for precise control of the transverse phase spaces of the beam.

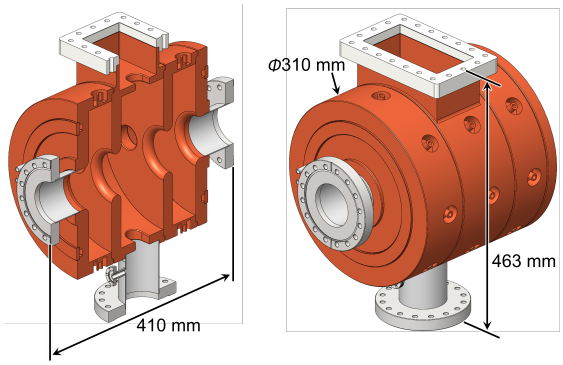


Figure 1: Half section view and external view of the 1.3-GHz TDC model in SolidWorks.

A LANL-AWA collaboration has been established for experimentally demonstrating the TCBC concept at AWA with a 40-MeV electron bunch [2]. The preliminary beamline configuration has been determined, and refined beamline modeling is ongoing.

In this paper, we report the design upgrade of the 1.3-GHz TDCs currently in operation at Argonne Wakefield Accelerator (AWA) Facility. The TDCs at AWA were initially designed and fabricated at Tsinghua University [3]. For the TCBC experimental study, LANL and AWA put an effort together to refine the TDC design, before the fabrication of two new copies of the TDC. The TDC, with refined features added, is shown in Fig. 1.

RF DESIGN REFINEMENT

The RF design refinement of the TDC included three revisions. First, we increased the fillet size of the RF coupling apertures between the coupling cells and the central cell, and of the input RF power coupling slot. Second, we adjusted the inner diameters of the three cells to ensure that when the TDC operates at the designed temperature, the resonant frequency shall be 1300.00 MHz. Third, we performed tol-

* Work supported by U.S. Department of Energy through the Laboratory Directed Research and Development program of Los Alamos National Laboratory, under project number 20240231ER.
† haoranxu@lanl.gov

Content from this work may be used under the terms of the CC BY 4.0 licence (© 2022). Any distribution of this work must maintain attribution to the author(s), title of the work, publisher, and DOI.

ISBN: 978-3-95450-261-5 ISSN: 2673-7000 doi: 10.18429/JACoW-NAPAC2025-WEP092

ULTRA-VIOLET LASER TRANSVERSE SHAPING WITH PHASE PLATES

T. Jogand-Coulomb*, N. Majernik, C. Emma, B. O'Shea, G. Just, A. Osman, T. Xu, Y. Liu, K. Li, S. Marchesini[1], A. Sakdinawat, N. Burdet, G. Yocky, M. Hogan, D. Magana, A. Marinelli[1], Z. Huang[1], A. Halavanau†
SLAC National Accelerator Laboratory, Menlo Park, CA, USA
[1]also at Stanford University, Stanford, CA, USA

Abstract

Shaping ultraviolet (UV) laser beams is critical for optimizing photoinjector performance for applications in free-electron lasers (FELs) and beyond. It has been shown that a 50% truncated Gaussian beam can achieve the lowest emittance via space charge compensation at LCLS-I. However, conventional shaping techniques to prepare this beam are limited by significant power losses or are not adapted for UV light. Here we report a high-precision transverse-shaping technique based on custom fused-silica phase plates with >99% transmission at 253 nm. This approach enables spatial beam profile tailoring and significantly enhances beam stability at the photocathode. Using IMPACT-T simulations, we predict a 33% (from 0.67 µm to 0.45 µm) reduction in normalized emittance for a 250 pC bunch at LCLS-I. Experimental implementation at FACET-II demonstrated a 37% emittance reduction (from 5.4 µm to 3.4 µm) at 1.6 nC. These results establish phase-plate beam shaping as a high-fidelity, low-loss approach for high-brightness photoinjectors. Implementation at LCLS-II which will enable stable operation at megahertz repetition rates is underway.

INTRODUCTION

The performance and cost of x-ray free-electron lasers depend critically on transverse emittance of the electron beam [1–6]. It has been shown that for the Linac Coherent Light Source (LCLS-I) the optimal transverse ultraviolet profile at the photocathode to reduce emittance is a Gaussian truncated at 50% [7, 8]. The cost and performance of the FEL depends on stable and reliable beam delivery. There are three major areas of improvement for this at LCLS: (i) refining the transverse profile, (ii) reducing transverse jitter, (iii) reducing charge jitter. Solving these problems would reduce tune-up time significantly and allow for more beam delivery and user experiments.

Despite advances in existing shaping techniques such as spatial light modulators [9, 10] and digital mirror devices [11], these techniques still incur significant power losses or lack compatibility with UV drive wavelengths. Here, we present a high-precision transverse shaping method based on custom fused-silica phase plates designed via an optical Iterative Fourier Transform Algorithm (IFTA) [12]. Our phase plates exhibit greater than 99% transmission at 253 nm, enabling tailored spatial profiles without sacrificing laser energy at the cathode. This method also stabilizes the transverse jitter of the beam at the cathode. We characterize the effectiveness of this technique through Impact-T simulations [13] at LCLS-I and experimental results at FACET-II.

* tcoulomb@slac.stanford.edu
† aliaksei@slac.stanford.edu

SIMULATIONS & THEORY

We implement a custom Fresnel-propagation code to model the transport of a $\lambda = 253$ nm field through our photoinjector optics. We initialize a two-dimensional Gaussian field via the complex q-parameter [14]:

$$\hat{E}(\omega, x, y, 0) = \frac{1}{q(0)} \exp\left[-i\frac{k}{2}\frac{x^2+y^2}{q(0)}\right], \tag{1}$$

where $q = z + iz_R$, $z_R = \frac{\pi\omega_0^2 n}{\lambda}$, $k = \frac{2\pi}{\lambda}$ is the wavenumber and ω_0 is the waist radius. Then we can apply the transfer functions for a lens and propagation through air to propagate the field in space. The lens transfer function [15] is as follows,

$$h_L = \exp\left[-i\frac{k}{2}\frac{x^2+y^2}{f}\right], \tag{2}$$

where f is the focal length of the lens determined by the lens maker equation for a given material with a given radius of curvature. We can apply this transfer function in real space using,

$$\hat{E}(\omega, x, y, 0) \cdot h_L. \tag{3}$$

To propagate through space, we apply the Fresnel propagation transfer function in k-space [16].

$$H_f = \exp\left[iz\sqrt{k^2 - (k_x^2 + k_y^2)}\right] \tag{4}$$

$$\mathscr{F}^{-1}\left[\mathscr{F}\left[\hat{E}(\omega, x, y, 0)\right] \cdot H_f(k_x, k_y, z)\right] \tag{5}$$

To tailor the transverse profile at the photocathode, we design a phase mask using an optical IFTA (Fig.1) which performs the Fourier transforms using an optical propagator to the Fourier plane. This is a variation of the HIOA [12, 17, 18] but keeps the Fourier plane in real space to perform accurate shaping. Starting from a fully randomized phase $\phi_0(x, y)$, each iteration follows in a four step process,

$$E_k = \mathscr{P}\left[|E_{meas}| \exp[i\phi_k]\right], \tag{6}$$

$$\hat{E_k} = |E_{target}| \exp[i\Phi_k], \tag{7}$$

$$E'_k = \mathscr{P}^{-1}\left[|E_{target}| \exp[i\Phi_k]\right] \tag{8}$$

$$E_{k+1} = |E_{meas}| \exp[i\phi_{k+1}]. \tag{9}$$

Here, $\mathscr{P}$ denotes forward Fresnel propagation (lens $+f$ then free-space $+f$) and $\mathscr{P}^{-1}$ its inverse (free-space $-f$ then lens

Content from this work may be used under the terms of the CC BY 4.0 licence (© 2022). Any distribution of this work must maintain attribution to the author(s), title of the work, publisher, and DOI.

ISBN: 978-3-95450-261-5 ISSN: 2673-7000 doi: 10.18429/JACoW-NAPAC2025-WEP095

UNDERSTANDING THE RHIC TRIPLET MAGNET VIBRATIONS IN PREPARATION FOR EIC

F. Micolon, J. Greene, Brookhaven National Laboratory, Upton, NY, USA

Content from this work may be used under the terms of the CC BY 4.0 licence (© 2022). Any distribution of this work must maintain attribution to the author(s), title of the work, publisher, and DOI.

Abstract

Throughout its operation, the RHIC triplet magnets have been subject to a mechanical vibration around 10 Hz. These mechanical vibrations were found to produce a beam orbit jitter that was detrimental to the collider luminosity. During RHIC operation, this has been effectively mitigated by the implementation of a fast feedback orbit control system. For the Electron Ion Collider (EIC) Hadron Storage Ring (HSR), the RHIC triplet package will be modified, magnets will be removed, and the cryogenic lines will be rearranged inside the cryostat. A comprehensive analysis of the RHIC triplet vibration has been undertaken to ensure that the planned triplet piping modifications would not increase the current triplet magnet vibrations and overwhelm the existing fast feedback control system. This paper aims to describe the current understanding of the root cause and kinematic of the RHIC triplet vibrations and offer mitigation options for EIC.

INTRODUCTION

During commissioning and early operation, RHIC has been plagued by a horizontal beam orbit jitter leading to luminosity degradation. The beam jitter, and the luminosity loss had a frequency around 10 Hz [1] and they were found to come from the triplet quadrupole magnets roll vibrations. A fast orbit feedback system was implemented and used until the end of RHIC operation. For EIC, the RHIC triplet cryostat will be modified to rearrange the cryogenic distribution piping and remove the D0 superconducting dipoles. This study was undertaken to ensure the expected roll vibration would stay under control and to find ways to improve the triplet stability.

MOTIVATION

The so-called triplets are the string of final-focusing quadrupole magnets located on each side of the six interaction region (IR) of RHIC, which are long drift straight section (grey areas in Fig. 1).

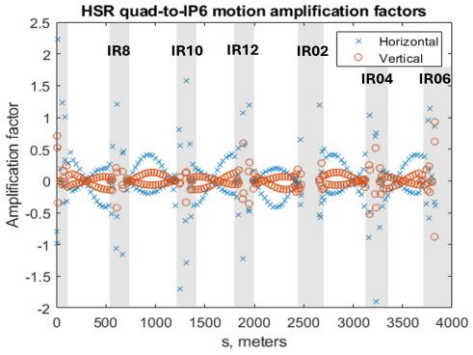


Figure 1: Transfer function from HSR quad motion to collision IP beam motion for a 275 GeV proton lattice [2].

While these triplet magnets have a moderate quadrupole field gradient compared to the arc quadrupole (48 T/m vs. 71 T/m), they are longer and their location at a much larger beam beta function makes them particularly susceptible to beam orbit alteration. Figure 1 depicts the transfer function between each quadrupole motion and the associated beam orbit motion at the collision IP for the EIC HSR. The triplet quadrupoles consistently have higher amplification factors compared to the arcs quadrupoles (Fig.1). And a stable beam orbit is particularly critical for EIC given its reduced IP beam size compared to RHIC [2] and high susceptibility to beam emittance blowup from beam-beam interaction.

PREVIOUS INVESTIGATIONS

From early on, the RHIC beam orbit jitter has been attributed to a triplet cold mass vibrations and linked to a helium pressure oscillation [3]. Direct investigations of the triplet vibrations with geophones and laser doppler have been made at the triplet sector 5 and 6 [4] and show that the beam orbit oscillation matches well with the Q2 sector 5 measured vibration (Ref. [4], Fig. 5). Pressure transducers were mounted on the cryogenic system at IR6 valve box and show a clear oscillation of the pressure in the magnet helium line at ~10.7 Hz with a peak-to-peak amplitude of 6.8 kPa [5]. Recent physics simulations show that the beam emittance growth from the beam-beam interaction at the IP explained the fast luminosity degradation seen before the implementation of the 10 Hz fast orbit feedback system [6].

VIBRATION MEASUREMENTS

Vibration measurements have been made in the RHIC tunnel during the maintenance days of RHIC run 2025 and were reported in [2]. The same setup has been used to measure the vertical vibration on the triplet magnet cryostat supports. The triplet vacuum vessel supports have an overhang which translates a magnet roll into a vertical distortion of the vacuum vessel supports that can be measured by a geophone (Fig. 2). Table 1 reports the vertical motion resonance as well as the integrated rms displacement measured on the vacuum vessel.

From these measurements, it appears that the odd sectors are more affected than the even sectors. Helium flows counterclockwise in the ring, so the helium leaves the valve box at each IR (cryogenic valves, heat exchanger, current leads) before going to the odd sector triplets, it flows through the arc magnets before reaching the even sector triplet and is finally routed to the valve box of the next IR. This suggests that pressure oscillations are generated in the valve boxes and are damped through the next arc before they reach the even sector triplets. It is also clear all cold masses of a given triplet show the same peak frequency. This can be explained by the stiff torsional coupling of the interconnect bellows between cold masses.

ISBN: 978-3-95450-261-5 ISSN: 2673-7000 doi: 10.18429/JACoW-NAPAC2025-WEP097

GROUND VIBRATION STUDIES IN THE RHIC TUNNEL IN VIEW OF EIC

F. Micolon, B. Podobedov, Brookhaven National Laboratory, Upton, NY, USA

Content from this work may be used under the terms of the CC BY 4.0 licence (© 2022). Any distribution of this work must maintain attribution to the author(s), title of the work, publisher, and DOI.

Abstract

As beam sizes get smaller at the collision point, the ground vibrations and their amplification through the accelerators supporting structures need more careful considerations. These mechanical disturbances can produce a beam orbit jitter that is detrimental to a collider, through loss of luminosity, beam-emittance blowup or collimator loss. In preparation for the Electron-Ion Collider (EIC), measurements of the ground vibrations in the RHIC tunnel were carried out. This paper will summarize the measurement methodology and present its main results. The expected effect on the hadron and electron beam jitter will be briefly reviewed and we will discuss some design consideration on the new electron ring magnet supports to mitigate this effect.

INTRODUCTION

Ground vibrations have long been a point of attention for collider design. And this has become increasingly important as new collider projects aim at smaller beam size at the interaction point (IP). Vibration of accelerator components lead to beam orbit jitter at the IP. This can affect luminosity but also lead to beam emittance blow-up from beam-beam interaction. Beam orbit jitter can also lead to unwanted beam losses at the collimators.

During its early operation, RHIC was subject to a large horizontal beam orbit jitter from the high-focussing quadrupole magnets motion which impacted its luminosity [1]. The HL-LHC project has also seen a renewed interest for the subject with a smaller collision beam size [2], Super KEK-B sees luminosity variations correlated with vibrations of the final focussing magnet [3] and requires a fast orbit feedback system. And similarly, the FCC-ee project is also planned to include a fast orbit feedback system [4].

MOTIVATION AND BEAM EFFECTS

EIC will collide flat beams with reduced vertical rms IP beam size (σ_{IP}) compared to RHIC in a ~1:10 vertical/horizontal ratio (see Table 1 from Ref. [5, 6]).

Table 1: RHIC and EIC RMS Beam Sizes Compared

Beam size at IP	Vertical	Horizontal
RHIC [5]	77 μm	77 μm
EIC [6]	8.5 μm	95 μm

EIC will also operate at the limits of beam-beam tune-shift in both colliding rings (HSR and ESR), as well as with record-large crossing angle at the IP. It was shown in Ref. [7, 8] that to limit the hadron beam emittance growth to <10%/hr, the beam jitter needs to be ≤2.5% σ_{IP}. For EIC, 2.5% σ_{IP} equates to 213 nm rms of tolerable vertical beam jitter and 2.4 μm rms horizontal.

In previous studies, the RHIC tunnel was reported as having a poor vibration stability [9] compared to other accelerator sites, with up to 118 nm rms integrated displacement @1Hz. This study aims to improve our understanding of the RHIC vibration environment and inform the design of vibration-sensitive accelerator equipment for EIC.

SETUP AND METHODOLOGY

Vibration data were collected in the RHIC tunnel during the run 25 maintenance days to be representative of a physics run conditions (pumps, fans, cryogenic plant). All measurements were done during daytime when human activities are generating the most cultural noise [9].

A SM-24 geophone was used to probe the vertical ground velocity. The signal acquisition was done through a ADS1256 24-bits ADC with a 32x PGA owing to the relatively low sensitivity of this geophone. The SM-24 geophone has its natural resonance frequency at 10 Hz, its sensitivity has been extrapolated from 10 Hz to 4 Hz. The results were processed to get the displacement PSD and the integrated displacements RMS from 100 Hz to 4 Hz following the methodology described in [10].

A data acquisition rate 500 Hz is found to be a good trade-off between frequency resolution and ADC noise. Blank acquisitions of the complete acquisition system (without geophone) give a voltage noise of σ~0.5 μV. Using the SM-24 sensitivity, the corresponding integrated RMS displacement is always <0.2nm which shows that the signal-to-noise ratio is appropriate for this analysis.

Note: while the integrated RMS displacement is commonly given between 100-1 Hz, we will report values from 100-4 Hz for the tunnel due to the limitations of our setup. At selected locations, two L4-C geophones were used for coherence measurements down to 1 Hz.

GROUND VIBRATION RESULTS

EIC Machine Detector Interface – Sector 5

In sector 5, vibration data were collected with the L4-C geophone setup down to 1 Hz at I-05Q10 (~154 m from the IP) and at I-05Q2 (~28 m from the IP) (see Figs. 1 and 2).

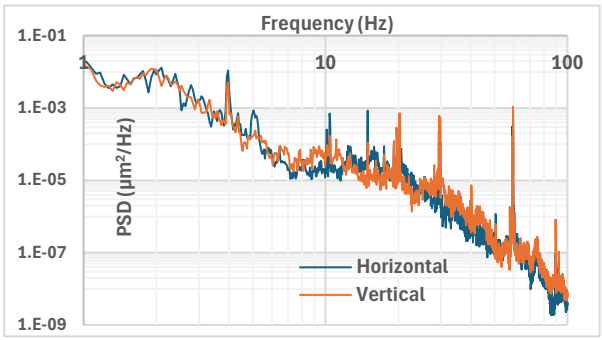


Figure 1: Displacement PSD for I-05Q2.

ISBN: 978-3-95450-261-5 ISSN: 2673-7000 doi: 10.18429/JACoW-NAPAC2025-WEP100

UPGRADED PHOTOINJECTOR LASER PULSE TRAIN GENERATOR AT THE ARGONNE WAKEFIELD ACCELERATOR*

R. Margraf-O'Neal,[1†], J. Xu[1,2], J. Power[1], S. Doran[1], J. Hlavenka[1], A. Ody[1], P. Piot[1], T. Zhou[3]
[1]Argonne National Laboratory, Lemont, IL, USA
[2]University of Wisconsin-Madison, Madison, WI, USA
[3]Lawrence Berkeley National Laboratory, Berkeley, CA, USA

Content from this work may be used under the terms of the CC BY 4.0 licence (© 2022). Any distribution of this work must maintain attribution to the author(s), title of the work, publisher, and DOI.

Abstract

The Argonne Wakefield Accelerator (AWA) facility operates a high-charge (100s of nC) electron beam in a bunch train, with eight electron bunches at a 769 ps spacing matching the linac operating frequency of 1.3 GHz. AWA's electron beam is optimized for producing large wakefields in resonant structures to study structure wakefield acceleration. This is achieved by maximizing total beam charge, and by correct bunch train timing to enhance the wakefield via inter-bunch coherence. The properties of the bunch train are determined by a "multisplitter" in the photoinjector laser system, in which a series of beamsplitters splits one laser source into eight - ideally equal - pulses. However, AWA's previous system did not split pulses evenly, with up to a 2:1 ratio between pulse energies within a train. Damaging electrical breakdown events within the electron gun, driven by high single bunch charge, occurred at lower total charge in this non-uniform set-up, limiting maximum charge. Thus, a new multisplitter using polarizing beamsplitters and half-wave plates (HWPs) was implemented. Unlike the previous fixed-ratio beam-splitter design, the new system enables tuning the splitting ratio for each beamsplitter, resulting in a more uniform pulse train. Large 2" optics and uncoated HWPs are also used to increase the laser intensity damage threshold (LIDT). This paper presents the design, characterization and lessons learned in early commissioning of AWA's upgraded laser pulse train generator.

INTRODUCTION

Pulse train generators have been implemented in photocathode laser systems across many accelerator facilities [1,2], and are well suited for creating pulses separated by 10s of ps to several ns. Figure 1A shows the existing AWA multisplitter (Excitech EX-PE-4OO), installed around 2015. Four non-polarizing beamsplitters are arranged in 3 delay lines to create 16 pulses, 8 of which are sent to the photocathode. The pulses are separated by 769 ps, and can be finely tuned using motorized delay stages in each delay line.

The beam splitters in the existing AWA multisplitter are not perfect 50-50 splitters, leading to different losses in each straight-ahead versus delay line. As a result, the bunches within the bunch train produced by this laser system were not uniform, and differed in charge by up to a factor of two. During high-charge operations, we observed that the higher the single electron bunch charge within our train was, the higher the chance of dielectric breakdown within the electron gun. Thus, to maximize the overall charge in the bunch train, having an equal charge in each bunch is important.

To create a more uniform train, we designed an upgraded multisplitter using polarized beamsplitters, shown in Fig. 1B. In this design, as illustrated in Fig. 2, s-polarized light is passed into the delay line of each stage, while p-polarized light continues straight. These beam splitters are optimized for 56° reflections, thus the trapezoidal shape of the first delay stage. For the second and third delay stages, a bow-tie configuration was used instead for compactness.

MATERIALS AND METHODS

Placement within the AWA Laser System

The AWA laser system consists a 785 nm laser which is frequency-tripled to produce 262 nm UV light. Light from a Coherent Vitara-T oscillator is amplified by a Ti:Sapphire regenerative amplifier driven by a Spectra Physics Ascend laser system. A subsequent multipass amplifier powered by a Powerlite DLS Laser system further increases the pulse power. The pulse is compressed to 300 fs, and then undergoes frequency tripling to 262 nm. The pulse train generator, or "multisplitter," then splits the pulse into up to 8 pulses separated at 769 ps. The beam is subsequently sent through a series of α-BBO crystals to stretch the pulse length to 6 ps, and a multi-lens-array homogenizer system [3] to create a smooth flat-top profile, before delivery to a Cs_2Te photocathode.

Multisplitter Construction and Alignment

We assembled the new multisplitter (Fig. 3) using polarizing beamsplitters (Eksma Optics: $R_s > 99.5\%$, $T_p = 95\%$@262nm), half-wave-plates and dielectric mirrors (Lattice Electro Optics: CWO-262-02-20-NoAR, RX-262-45-UF-2038). Large optics were used to provide 2 in aperture across the pulse train generator. Due to the dielectric mirrors having high reflectivity from 45° to normal incidence, but lower reflectivity at high angles, dielectric mirrors were used in the 2L and 4L delay lines, while additional polarizers were used in the 1L delay. We aligned and tested this set-up at ≈25% pulse energy (0.245 mJ). After angular adjustment of each optic, the HWPs were rotated to achieve the most uniform pulse train. Flags were used to block the beam to measure pulses sequentially on a downstream photodetector. Total transmission was 50.2%.

* This work is supported by the U.S. Department of Energy, under contract No. DE-AC02-06CH11357.

† rmargrafoneal@anl.gov

ISBN: 978-3-95450-261-5 ISSN: 2673-7000 doi: 10.18429/JACoW-NAPAC2025-WEP101

BOOSTER CAVITY DAMPER REDESIGN FOR PIP-II

D. Pieper†, B. Vaughn, R. Madrak
Fermilab, Batavia, IL, USA

Abstract

A new Higher Order Mode (HOM) damper was designed and tested for the Booster accelerator cavity at Fermilab. In anticipation of the PIP-II upgrade, it was discovered that the higher beam intensity of PIP-II may cause beam instability due to an excited mode at 105 MHz. This unfortunately corresponds with the cavity's 2nd order harmonic mode, which will sweep from 86-105.7 MHz.

The new damper is a modification of an existing damper that was designed to reduce an existing static HOM at 83 MHz, with the new design intending to cover the 2nd order HOM as well. The existing damper uses an inductive coupling loop to extract RF energy from the cavity which then goes through a filter in order to reflect the fundamental frequency back into the cavity while passing HOMs to a dump load. The new damper intends to replace the filter portion of the system with a wider band variant while also changing the topology from a coaxial cable loop filter to a componentized PCB-based design.

Primary design challenges include bandwidth coverage, impedance matching of the various modes, long term thermal and mechanical stability, radiation hardness, and high voltage handling. Initial designs achieved the desired damping but were found to quickly succumb to destructive arcing due to the voltages present. More finalized designs intend to address this problem through circuit redesigns and the use of hardier components.

EXISTING DAMPER SYSTEM

In the Fermilab Booster accelerating cavity, in addition to the fundamental mode used to accelerate protons, there exist a number of unwanted higher order modes (HOMs). These HOMs occur as a result of the cavity's geometry and can be excited by the beam [1]. HOMs are undesirable as they create unwanted acceleration of the beam in ways that create beam instability. To mitigate these HOMs, passive damper structures are added to the cavity to remove energy from the HOMs and dissipate it outside of the cavity.

Dampers are composed of three features, (1) an inductive or capacitive coupler inside the cavity that extracts energy from the cavity at various frequencies, which are then sent through (2) a filter that reflects the fundamental mode back into the cavity (to prevent wasting desired RF accelerating energy) while passing the unwanted HOMs through to (3) a resistive load. Currently there exist three passive dampers for handling HOMs at 83MHz, 167 MHz, and 220 MHz [2]. The 167 MHz and 220 MHz HOMs represent third and fourth order harmonics of the fundamental mode at 53 MHz. For clarification, since the Booster's fundamental mode actually tunes from 38 MHz to 53 MHz over the course of a cycle, with the HOMs also moving by a similar amount as well, the modes are defined here according to their frequency at the top of the cycle. This is also because these modes are at their highest power level at the top of the cycle, meaning damping is most critical at those frequencies. Meanwhile, the 83 MHz mode is a static mode related to features in the cavity unaffected by the tuners and thus doesn't move in frequency over the cycle. A diagram of the 83 MHz damper, as well as pictures of its installed parts is shown below in Fig. 1.

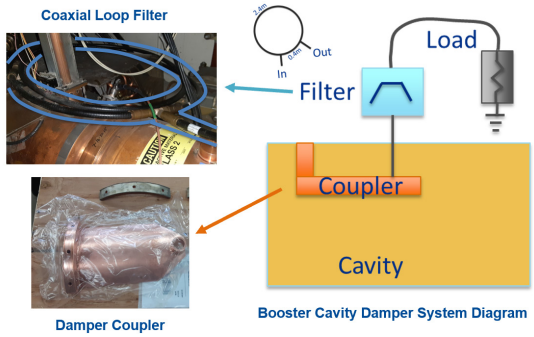


Figure 1: Diagram of 83 MHz damper and pictures of physical parts.

Note that for the 83 MHz mode, there are actually two dampers on either side of the cavity, each with their own filter. The coupler for the 83 MHz damper is an inductive loop made from a plate formed to the curvature of the cavity and shorted at one end (which also serves as its physical support in the cavity) while also connected to an external N-type port connector on the other end, from which coupled energy is extracted out of the cavity. A split-path filter is connected to this port in order to only pass the 83 MHz mode. This filter is realized through the use of two lengths of looped coaxial cable that create a path split at a T-junction at the connector port before being re-combined at an output T-junction, which subsequently leads to a high-power load located upstairs in the Booster gallery. The two coaxial path lengths, which are 0.4 m and 2.4 m, respectively, are chosen such that the recombined fundamental signal cancels at the output, forming a standing wave node at that location. This prevents the fundamental mode from being sent to the load while still passing the 83 MHz mode, damping the HOM.

105 MHz MODE DAMPING

After the completion of the PIP-II upgrade of the Fermilab facility, the beam intensity going to Booster will be increased. At this new intensity, there is concern that the 2nd order mode which peaks at 105 MHz will start to be a source of beam instability. Although this mode exists in the cavity at current intensity levels, it is not strong enough to be considered a source of concern but will be after PIP-II.

* This manuscript has been authored by FermiForward Discovery Group, LLC under Contract No. 89243024CSC000002 with the U.S. Department of Energy, Office of Science, Office of High Energy Physics

Content from this work may be used under the terms of the CC BY 4.0 licence (© 2022). Any distribution of this work must maintain attribution to the author(s), title of the work, publisher, and DOI.

ISBN: 978-3-95450-261-5 ISSN: 2673-7000 doi: 10.18429/JACoW-NAPAC2025-THXN01

ADVANCED ML METHODS FOR BEAM TUNING AT FRIB*

K. Hwang†, Jinyu Wan, Tong Zhang, Tomofumi Maruta, Qiang Zhao, Alexander Plastun, Kei Fukushima, Peter Ostroumov, Facility for Rare Isotope Beams, East Lansing, MI, USA

Content from this work may be used under the terms of the CC BY 4.0 licence (© 2022). Any distribution of this work must maintain attribution to the author(s), title of the work, publisher, and DOI.

Abstract

Experiments with rare isotope beams at FRIB are highly time-constrained, making rapid setup and delivery of high-quality ion beams critical to maximizing scientific output. The Bayesian framework is particularly well-suited for this challenge, offering sample-efficient optimization, principled incorporation of prior knowledge, and uncertainty-aware inference. In particular, Bayesian Optimization (BO) has proven to be an efficient and general approach for the non-sequential, static nature of beam-tuning tasks. To further accelerate convergence, Prior-Mean-Assisted Bayesian Optimization (pmBO) was developed, enabling rapid adaptation from prior belief to real-time machine conditions with minimal computational overhead. In parallel, a virtual diagnostic for the beam's transverse quadrupolar moment (BPM-Q) has been developed to provide non-invasive, fast measurements of beam envelope information. To optimize the reconstruction of Courant-Snyder parameters from BPM-Q data, Bayesian Active Learning (BAL), employing a differentiable beam envelope simulator as a surrogate model, has been implemented. Together, these developments illustrate the power of Bayesian methods in achieving faster, more accurate beam-tuning.

INTRODUCTION

Experiments at Facility for Rare Isotope Beams (FRIB) require frequent switching of diverse primary ion beams, imposing strict time constraints that necessitate rapid setup and delivery of high-quality beams to maximize scientific productivity. Beam tuning within a limited time is a complex task. The high dimensionality, coupled with nonlinear and noisy system responses, renders traditional tuning methods inefficient, particularly under tight time constraints. Advanced machine learning (ML) techniques offer a powerful solution.

This paper presents several advanced ML methods developed or adapted for beam tuning at FRIB. We begin by explaining why the Bayesian Framework, including Bayesian Optimization (BO), is particularly well-suited for this task. We then discuss enhancements to BO. To address high-dimensional parameter spaces, we introduce the Surrogate-gradient Assisted optimizer. Additionally, we present a virtual diagnostic (VD) for the beam's transverse quadrupolar moment (BPM-Q) and demonstrate how Bayesian Active Learning (BAL) optimizes the reconstruction of Courant-Snyder parameters despite the VD inaccuracy.

* Work supported by the U.S. Department of Energy, Office of Science, Office of Nuclear Physics, under Award Number DE-SC0024707 and used resources of the FRIB Operations, which is a DOE Office of Science User Facility under Award Number DE-SC0023633

† hwang@frib.msu.edu

BO FOR BEAM TUNING

Why BO is Well-Suited

BO leverages a probabilistic model, such as the Gaussian Process (GP), to explicitly assess uncertainty quantification (UQ) and related metrics. This approach offers several advantages for beam tuning.

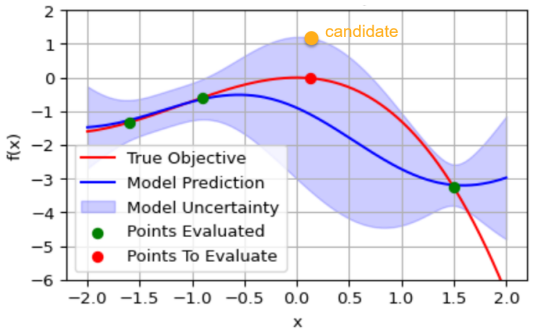


Figure 1: Illustration of sample-efficient optimal search for an objective $f(x)$, over x control parameters considering model uncertainty towards the optimum [1]. Green dots: training data, Yellow dot: the candidate queried BO.

Sample Efficiency Probabilistic modeling enables a principled balance between exploration and exploitation for active learning of the objective toward optimal control (Fig. 1). This allows BO to efficiently converge using as few data samples as possible. Such sample efficiency is especially beneficial in beam tuning tasks, where each evaluation involves adjusting magnet strengths—requiring power supply ramping over a few seconds—followed by measurement averaging over a few seconds to reduce noise. These time-consuming steps limit the number of feasible evaluations, making efficient data use critical. Furthermore, the surrogate model training in BO typically takes a few seconds allowing it to run in parallel with the objective evaluation process.

Noise Robustness Beam parameter measurements are inherently noisy. While temporal averaging reduces variance, residual noise persists. Probabilistic modeling in BO naturally incorporates this noise, typically by adding a learnable noise term to the GP kernel function, which corresponds to a Gaussian likelihood with additive noise.

Comparison with RL Unlike Reinforcement Learning (RL), which is designed for sequential, dynamic tasks (e.g., robotics) where a Markov Decision Process is assumed, BO is designed for static optimization problems that are common in beam development tuning. BO can also naturally incorporate prior models trained on offline data, such as those learned from simulation data, similar to approaches in

ISBN: 978-3-95450-261-5 ISSN: 2673-7000 doi: 10.18429/JACoW-NAPAC2025-THAN01

AI-DRIVEN NEUTRINO DIAGNOSTICS AND RADIATION-HARD BEAM INSTRUMENTATION FOR NEXT-GENERATION NEUTRINO EXPERIMENTS*

S. Ganguly†, Fermi National Accelerator Laboratory, Batavia, IL, USA

Content from this work may be used under the terms of the CC BY 4.0 licence (© 2022). Any distribution of this work must maintain attribution to the author(s), title of the work, publisher, and DOI.

Abstract

The Long Baseline Neutrino Facility (LBNF) at Fermilab will deliver a high-intensity, multi-megawatt neutrino beam to the Deep Underground Neutrino Experiment (DUNE), enabling precision tests of the three-neutrino paradigm, CP violation searches, neutrino mass ordering determination, and supernova neutrino studies. In order to accelerate DUNE's physics reach and ensure robust beam operations, we propose an integrated AI-driven framework with real-time diagnostics and radiation-hardened instrumentation. A physics-informed digital twin is at the heart of this Real-Time Beam Integrity Monitor. By reconstructing pion phase space from muon profiles and exploiting magnetic horn optic linearity, it enables spill-by-spill beam correction and flux stabilization. By using this approach, flux-related systematics could be reduced from 5% to 1%, potentially accelerating the discovery of CP violations by four to six years. Complementing this, a US–Japan R&D effort will deploy a LGAD-based muon monitor in the NuMI beamline. Time of Flight (ToF) measurements can be acquired with picosecond precision using this radiation-hard system, enhancing sensitivity to horn chromatic effects. Simulations confirm strong responses to these effects. Machine learning models can predict beam quality and horn current with sub-percent accuracy. This scalable, AI-enabled strategy improves beam fidelity and reduces systematics, transforming high-power accelerator operations.

INTRODUCTION

The Long Baseline Neutrino Facility (LBNF) [1] at Fermilab will deliver a multi-megawatt, high-intensity neutrino beam to the massive detectors of the Deep Underground Neutrino Experiment (DUNE) [2], enabling precise tests of the three-neutrino flavor paradigm, direct searches for CP violation, determination of neutrino mass ordering, and detailed studies of supernova neutrino interactions. Although DUNE is baselined to achieve its physics goals independently, recent advancements in AI-driven diagnostics and real-time accelerator control provide a unique opportunity to surpass baseline performance at a significantly lower cost.

A major driver of sensitivity in DUNE is the precision of the neutrino flux prediction. Achieving percent-level accuracy in flux normalization can reduce the overall systematics to below 3%, potentially shortening the runtime needed for key measurements by several years. Current beam flux uncertainties at the source are approximately 2-3%, and new approaches are required to suppress this contribution further.

Muon monitors, placed downstream of the decay pipe, offer a unique window into the phase space of parent pions. Since muons and neutrinos are produced together in pion decays, measurements from the muon monitors provide indirect but valuable information about the resulting neutrino flux. The current implementations, however, are limited in time resolution and cannot capture correlations between events. A machine-learning-based diagnostic framework aims to improve flux prediction and enable adaptive beam control in this work. The approach uses correlations between real-time signals from muon monitors and upstream instrumentation to infer the pion phase space and chromatic beamline effects [3], such as those arising from horn current fluctuations. These models are trained using a physics-informed digital twin, allowing us to bridge simulation and real-world conditions. Figure 1 demonstrates the impact of horn current uncertainty on neutrino flux prediction. A typical uncertainty of ± 3 kA (1%) leads to flux variations exceeding 5% in the peak energy region, while reducing the uncertainty to ± 0.15 kA suppresses this effect to below 1%. This motivates the need for precision monitoring and inference frameworks that can resolve such variations on a spill-by-spill basis. The machine learning strategy developed in this work aims to achieve this resolution using only muon monitor signals, enabling both tighter flux constraints and future feedback-based beam optimization.

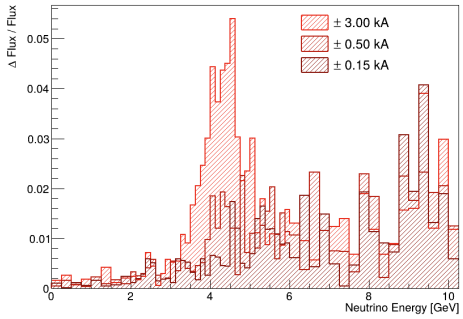


Figure 1: Relative change in neutrino flux as a function of energy for horn current variations of ± 3, ± 0.5, and ± 0.15 kA. Smaller uncertainty in horn current reduces the fractional flux variation by up to a factor of five.

MUON MONITORING AND BEAM CORRELATION

As part of the Neutrino Beam Instrumentation system for LBNF, dedicated detectors monitor secondary and tertiary particles. This provides essential information for beam alignment, anomaly detection, and long-term diagnostics. Its two

*

† sganguly@fnal.gov

ISBN: 978-3-95450-261-5 ISSN: 2673-7000 doi: 10.18429/JACoW-NAPAC2025-THAN02

FERMILAB BOOSTER BEAM LOSS MODELLING AND REBALANCING USING BAYESIAN METHODS*

N. Kuklev†, J. Eldred, M. Balcewicz
Fermi National National Laboratory, Batavia, IL, USA

Content from this work may be used under the terms of the CC BY 4.0 licence (© 2022). Any distribution of this work must maintain attribution to the author(s), title of the work, publisher, and DOI.

Abstract

To meet PIP-II upgrade requirements, Fermilab Booster losses need to be reduced by 50% compared to present levels. So far, simulations are not good enough to predict loss patterns. Thus, an extensive Booster tune up will be necessary to achieve required performance. In this paper we present an effort to build a data-driven loss model using Bayesian techniques, and subsequently to rebalance losses for higher trip margins. We first created several sets of spatially and temporally isolated orbit and optics knobs, and trained Gaussian process models for each beam loss monitor as well as beam current. Novel techniques of uncertainty constraints and approximate GP fitting were introduced to handle safety and timing requirements. We then performed single and multi-objective tuning using scalarized objectives comprised of critical beam loss locations. We achieved significant rebalancing of losses, increasing margins by 25%, as well as an overall improvement in transmission efficiency of 0.4%. Automated data collection is being developed so that more accurate surrogate models can be trained over time.

INTRODUCTION

Fermilab Booster is a key component of the Fermilab accelerator complex. It provides 8 GeV protons to various users directly, as well as sending beam to the Recycler/Main Injector. For the upcoming LBNF/DUNE experiments, PIP-II upgrade will increase the power on target to 1.2 MW. It includes a new superconducting linac, a new BTL transfer line, and various improvements to the complex including the Booster. Key changes for Booster are the increase of injection energy to 800 MeV, higher beam intensity (from $4.8\text{x}10^{12}$ to $6.7\text{x}10^{12}$), a new painting scheme, new collimation and RF systems, and a faster ramp rate of 20 Hz. Given that the Booster is a 50-year old machine with aging hardware, areas of concern have been identified in terms of machine reliability and capability to operate at PIP-II parameters. In terms of beam dynamics, significant challenges are expected due to extreme levels of space charge at injection, as well as new instabilities at transition crossing.

Maximum Booster power is determined primarily by administrative beam loss limits, with PIP-II requiring a two-fold reduction in relative losses as compared to the current levels. An extensive simulation campaign is ongoing to better understand and control beam dynamics, but so far it has proven difficult to obtain quantitative agreement with experimental data, especially for local loss distribution. Thus, it is expected that an extensive experimental tune-up campaign will be necessary to commission the Booster for PIP-II.

Driven by PIP-II requirements as well as challenges in the DOE GARD roadmap [1, 2], several AI/ML projects were recently started at Fermilab, focusing on development of advanced optimization algorithms, fast differentiable simulations, and integrated facility-scale virtual accelerators (digital twins) ([3]. Using virtual accelerators for algorithm and application testing has proven effective in ensuring smooth commissioning [4, 5]. To create a virtual accelerator for loss optimization, we started developing a data-driven surrogate model (in place of a standard simulation). A key concern was training data availability. Recently, an electrical substation fire has taken down Main Injector and freed up majority of cycles for parasitic beam studies - a unique opportunity we took advantage of. In this paper, we describe our results in applying Bayesian methods to experimentally explore, learn, and manipulate the beam loss distribution in the Booster.

BOOSTER DETAILS

Fermilab Booster is a rapid cycling synchrotron with 24 sectors (short (S) and long (L) subsections). Main combined function magnets are connected to a shared resonant power supply. In addition, there are 48 independently powered correction elements with dipole, quadrupole, skew quadrupole, sextupole, and skew sextupole components [6]. Booster diagram is shown in Fig. 1.

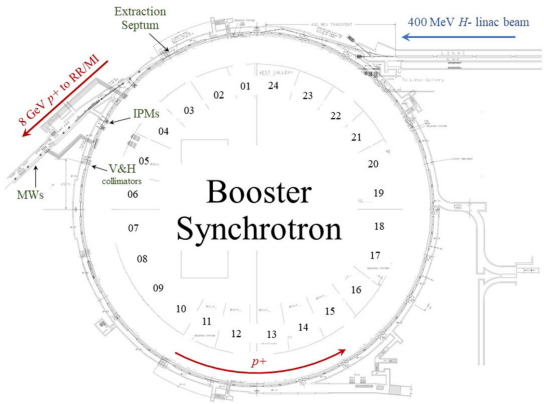


Figure 1: Booster synchrotron with sectors marked.

Time-dependent current ramps with up to 64 points can be set, forming thousands of potential knobs. Such high dimensionality is infeasible for Bayesian methods. Based on physics considerations and typical operator tasks, we defined two subsets of interest. First set contained 4D (x/y/px/py) injection closed orbit bumps. Adjusting injection trajectory

* This manuscript has been authored by FermiForward Discovery Group, LLC under Contract No. 89243024CSC000002 with the U.S. Department of Energy, Office of Science, Office of High Energy Physics.
† nkuklev@fnal.gov

ISBN: 978-3-95450-261-5 ISSN: 2673-7000 doi: 10.18429/JACoW-NAPAC2025-THAN03

ULTRAFAST THz DETECTION AND ENHANCED ELECTRO-OPTICAL TIMING FOR LONGITUDINAL BEAM DIAGNOSTICS AT FREE ELECTRON LASERS*

Andreas Penirschke†,[1], Bernhard Scheible[1], Rahul Yadav[1], Michael Kuntzsch[2], Marie Kristin Czwalinna[3], Holger Schlarb[3]
[1] Technische Hochschule Mittelhessen, Friedberg, Germany
[2] Helmholtz-Zentrum Dresden Rossendorf HZDR, Dresden, Germany
[3] Deutsches Elektronen-Synchrotron DESY, Hamburg, Germany

Content from this work may be used under the terms of the CC BY 4.0 licence (© 2022). Any distribution of this work must maintain attribution to the author(s), title of the work, publisher, and DOI.

Abstract

This work presents recent advancements in precision longitudinal beam diagnostics for Free Electron Lasers (FELs), focusing on the integration of ultra-fast, zero-bias Schottky diode-based terahertz (THz) detectors and enhanced electro-optical bunch arrival-time monitors (EO-BAMs). These innovations are vital for both currently operating and forthcoming FEL facilities, where achieving sub-picosecond timing accuracy and reliable low-charge diagnostics is critical for optimal machine performance and experimental success.

The THz detectors enable broadband, single-shot detection with picosecond time resolution, which is crucial for diagnostics such as real-time bunch compression monitoring at high repetition rates. Concurrently, the upgraded EO-BAM systems incorporate novel printed circuit board (PCB) pickup architectures optimized for ultra-low charge operation down to the sub-picocoulomb range, achieving femtosecond-level timing precision.

Together, these complementary technologies address the growing demands in FEL facilities for non-invasive, high-speed, and high-accuracy beam characterization, enabling improved synchronization, diagnostics, and accelerator performance optimization.

ULTRAFAST THz DETECTORS

Recent advances in semiconductor terahertz (THz) detection technology have innovated beam diagnostics across the accelerator community, establishing THz detectors asversatile, multi-purpose diagnostic tools deployed at numerous accelerators for diverse longitudinal and transverse beam characterization applications. The widespread adoption of THz diagnostic systems spans numerous accelerator facilities worldwide, including European XFEL and FLASH @ DESY (Germany), LCLS @ SLAC (USA), SwissFEL @ PSI, (Switzerland), TELBE and ELBE @ HZDR (Germany), ALICE @ Daresbury Laboratory (UK), KARA and FLUTE @ KIT (Germany), the Advanced Photon Source (USA), and KAERI THz FEL (South Korea). The developed THz technology covers diverse detector architectures including zero-bias Schottky diodes [1], GaAs field-effect transistors with ultra-broadband coverage (0.2 - 29.8 THz) [2], antenna-coupled detector arrays [3], electro-optical sampling systems [4], and specialized cavity-type beam position monitors [5]. These systems operate across frequency ranges from sub-THz to far-infrared (> 50 THz), enabling comprehensive spectroscopic analysis of accelerator-generated coherent radiation.

In this work, we focus on zero-bias Schottky diodes (ZBSDs) that provide compact, cryogen-free, real-time monitoring of bunch profiles at facilities such as TELBE and FLASH. Operable across a frequency range from approximately ~ 0.05 to over 5 THz, these room-temperature devices suppress shot noise by eliminating the need for external bias and achieve an impulse response on the order of ~ 100 ps, a noise-equivalent power (NEP) close to 10 pW $\sqrt{\text{Hz}}^{-1}$ and voltage responsivities approaching 500 kV W^{-1} (see Fig. 1). The detector was tested using both a table-top setup for frequencies up to 1.2 THz and a Free Electron Laser (FEL) facility for extended characterization up to 5.56 THz [1]. Saturation characteristics at selected frequencies as well as the voltage responsivity compared on picosecond and millisecond timescales were investigated.

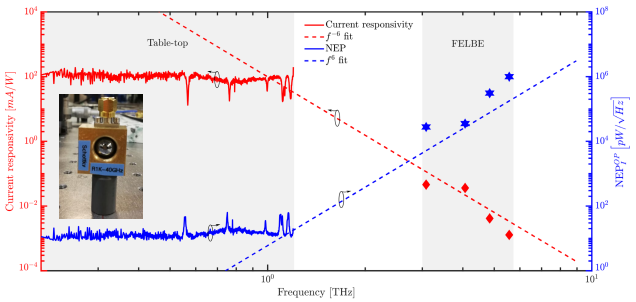


Figure 1: Responsivity and noise equivalent power of the log-spiral antenna-coupled broadband zero-bias Schottky detector [1].

Selected THz Application within a BCM Monitor

A study of a high-speed detector system for longitudinal bunch diagnostics in the terahertz domain at TELBE was presented, in which fast, room-temperature operable zero-bias Schottky diodes were used to measure electron bunch lengths via coherent transition radiation (CTR) [6].

* This work is supported by the German Federal Ministry of Research, Technology and Space (BMFTR) under contract no. 05K22RO1 and 05K22RO2.
† andreas.penirschke@iem.thm.de

ISBN: 978-3-95450-261-5 ISSN: 2673-7000 doi: 10.18429/JACoW-NAPAC2025-THYD01

COLLECTIVE EFFECTS: CHALLENGES AND SOLUTIONS FOR THE EIC PROJECT*

A. Blednykh†
Brookhaven National Laboratory, Upton, NY, USA

Content from this work may be used under the terms of the CC BY 4.0 licence (© 2022). Any distribution of this work must maintain attribution to the author(s), title of the work, publisher, and DOI.

Abstract

The Electron-Ion Collider (EIC) project at Brookhaven National Laboratory aims to deliver groundbreaking insights into the fundamental structure of matter through high-energy collisions involving electrons, ions, protons, or helium-3 nuclei. Achieving the desired luminosity and maintaining stability in this complex accelerator environment pose significant challenges, particularly concerning impedance and collective effects. One such challenge is ensuring beam stability during electron cooling at the injection energy in the Hadron Storage Ring (HSR) to effectively mitigate proton emittance growth. Potential solutions include advanced simulation techniques using the ELEGANT code and applying the Haissinski solution for the proton beam to determine single-bunch instability thresholds, both with and without a second harmonic cavity.

INTRODUCTION

The Electron-Ion Collider (EIC) is a next-generation accelerator facility under construction at Brookhaven National Laboratory, designed to collide polarized electrons with polarized protons and heavy ions at high luminosity and variable center-of-mass energies [1]. The EIC complex comprises multiple accelerator stages (Fig. 1), including a DC photoelectron gun, a 750 MeV S-band LINAC, the Beam Accumulator Ring (BAR, 750 MeV) – with design led by the NSLS-II team - the Rapid Cycling Synchrotron (RCS, 0.750→18 GeV), and two high-energy storage rings: the Electron Storage Ring (ESR) and the Hadron Storage Ring (HSR). Electrons are accelerated in the RCS from 0.750 GeV to 5, 10, or 18 GeV and subsequently injected into the ESR at the corresponding energy. Hadrons are injected into the HSR at 23.8 GeV and ramped to their final energies - ranging from 41 to 275 GeV - depending on the species, including protons (p), ions, or He^3.

The goal of the EIC is to deliver a design luminosity of up to 10^{33}-10^{34} $cm^{-2}s^{-1}$, enabled by advanced features such as beam cooling systems, a 25 mrad crab crossing angle, high beam currents - up to I_{av}=2.5 A with M=1160 bunches of σ_s~7 mm length in the ESR, and up to 0.7 A / 1 A with M=290 and M=1160 bunches of σ_s~60 mm in the HSR during storage. At injection energy, the bunch length in the HSR is expected to be significantly longer, around σ_s~1.5 m. Since the collective effects topic in the EIC project covers multiple ring accelerators, this paper focuses on single-bunch stability at injection energy and the associated contributions from coupling impedance and space charge impedance in the HSR.

* Work supported by Brookhaven Science Associates, LLC under Contract No. DE-SC0012704 and DE-AC02-06CH11357 with the U.S. Department of Energy.
† blednykh@bnl.gov

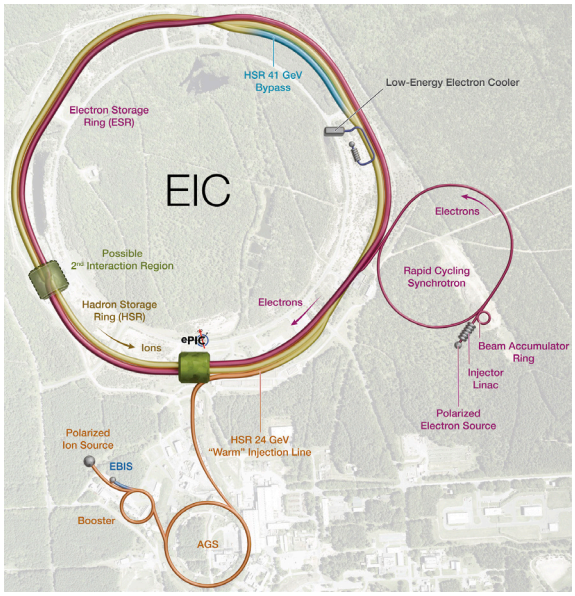


Figure 1: Top view schematic of the Electron-Ion Collider (EIC) accelerator complex, including the electron and hadron injector chains, the Beam Accumulator Ring (BAR), the Rapid Cycling Synchrotron (RCS), and the Electron and Hadron Storage Rings (ESR and HSR).

HSR

Table 1 presents the HSR beam intensity parameters at different energies, based on species acceleration. In this paper, single-bunch (SB) stability in the HSR is studied at the injection energy of 23.8 GeV, where the combination of long bunches ($\sigma_\tau \approx 5\,ns$), achieved using second harmonic RF cavity (49.2 MHz), and high peak current (~3.5 A), presents significant collective effects challenges for maintaining low horizontal and vertical emittances achieved by electron cooling [2]. The HSR beam screen, shown in Fig. 2, consists of an amorphous carbon–coated, copper-clad stainless-steel pipe inserted into the existing RHIC stainless steel vacuum chambers, primarily within the arc sections. The beam screen is actively cooled and is expected to operate at cryogenic temperatures, ~4 K.

The profile of the HSR vacuum chamber varies along straight sections depending on the requirements of the associated subsystems. In IR2, the vacuum chamber is designed to accommodate the low-energy electron cooler [2]. In IR4, the normal-conducting RF cavities and injection stripline kickers are installed. IR6 houses the ePIC detector chamber, where the hadron and electron beam pipes merge into a common section. This region requires careful

ISBN: 978-3-95450-261-5 ISSN: 2673-7000 doi: 10.18429/JACoW-NAPAC2025-THYD02

COMPARISON OF PREDICTED AND MEASURED COLLECTIVE EFFECTS IN A FOURTH GENERATION STORAGE RING*

Ryan Lindberg, Argonne National Laboratory, Lemont, IL, USA

Content from this work may be used under the terms of the CC BY 4.0 licence (© 2022). Any distribution of this work must maintain attribution to the author(s), title of the work, publisher, and DOI.

Abstract

Predicting, measuring, and mitigating collective instabilities in storage rings is important to maximize their performance. We will describe our efforts to theoretically compute and characterize collective effects during the design process, and how these continue during early operations. We then show how these predictions compare to measured collective effects at the APS-U, both with and without the harmonic cavity to lengthen the bunch.

INTRODUCTION

The Advanced Photon Source (APS) at Argonne National Laboratory recently underwent a major upgrade in which the third generation, double bend achromat lattice was replaced by a seven bend achromat with reverse bends [1]. This resulted in a reduction of the natural emittance by nearly two orders of magnitude, down to $\varepsilon_{x,0} = 42$ pm. In addition, the average operating current was doubled to 200 mA, so that the brightness for X-rays above 1 keV was increased by more than two orders of magnitude. Several other improvements were made to ensure that the brightness increase can be fully used, including upgrades to X-ray beam lines and the addition of a passive fourth harmonic cavity to lengthen the bunch [2, 3], thereby increasing the lifetime while mitigating other deleterious effects associated with a high peak current, including rf heating, intrabeam scattering, and other collective effects.

As part of our efforts to optimize performance, we spent considerable time during the design phase trying to compute and minimize collective effects. For example, all storage ring components were analyzed with electromagnetic solvers [4, 5], and the resulting impedances were then summed to form the ring impedance, as described in [6, 7]. For example, the longitudinal impedance was formed as

$$Z_{\parallel}(\omega) = \sum_{\text{elements } j} Z_{\parallel,j}(\omega), \tag{1}$$

where j labels the impedance element; for an element located at s_j where the beta function is $\beta_x(s_j)$, the β_x-weighted horizontal dipole impedance for the ring is

$$\left\langle \beta_x Z_x^D(\omega) \right\rangle = \sum_{\text{elements } j} \beta_x(s_j) Z_{x,j}^D(\omega), \tag{2}$$

with similar expressions used along the vertical y and for the quadrupolar impedance.

Early tracking simulations using the ring impedance in `elegant` [8, 9] were used to set a target chromaticity of $\xi_{x,y} \gtrsim 5$ to insure transverse stability, and to identify components that would benefit from a redesign to reduce the associated impedance. For example, extensive study of the flange gaps helped set tolerances on the inner diameter for the rf gaskets. Later tracking simulations showed a large margin for both transverse and longitudinal stability in the "high brightness" mode using 324 bunches, such that fills with 200 mA total current divided amongst $\gtrsim 108$ bunches should be completely stable. The "timing" mode of 48 bunches, on the other hand, had a transverse stability margin of just over a factor of two in current, while simulations indicated that the microwave instability would be mildly operative and inflate the energy spread from 0.135% to approximately 0.15%.

CALCULATIONS AND MEASUREMENTS BEFORE AND DURING COMMISSIONING

In addition to the early simulation efforts described above, there was significant work done before and during commissioning to predict and mitigate collective instabilities. First, the impedance model continued to evolve as the vacuum design [10, 11] matured. This effort often involved a few iterations with the engineers as they tried to simplify manufacture and installation considerations while keeping within cost constraints, all while insuring that the impedance was acceptable. While designs for the BPMs, absorbers, flanges, and most kickers and transitions were completed prior to the final design report (FDR) [12], there remained a number of unique components that had not been completed. In addition, the location of many components in the rf sectors was not yet fixed, and the transitions to small apertures that were needed to absorb synchrotron radiation were unknown.

The full design and layout of all components was not complete until just prior to the installation phase. Hence, the impedance model continued to evolve after the FDR until the dark time. We give a sense for how significant the resulting additions and changes are in Fig. 1. Panel (a) shows that the longitudinal impedance mostly changed in the low- and high-frequency range; the low-frequency changes reflect a mature understanding of the various apertures and components, while the difference observed at high frequency results largely from our decision to NEG-coat (but not activate) certain aluminum chambers to reduce the photon stimulated desorption. Panel (b) gives a sense of how the transverse impedance evolved by plotting the real part of the β-weighted horizontal dipole impedance: in addition to the low- and high-frequency contributions noted before, the additional increase of the transverse impedance is mostly due to several small aperture absorbers needed to protect sensitive components from synchrotron radiation. While these updates are significant, we emphasize that important

* Work supported by the U.S. Department of Energy, Office of Science, Office of Basic Energy Sciences, under Contract No. DE-AC02-06CH11357.

ISBN: 978-3-95450-261-5 ISSN: 2673-7000 doi: 10.18429/JACoW-NAPAC2025-THYD03

HALO FORMATION IN HIGH-INTENSITY LINACS: MODELING AND ADVANCED PHASE SPACE DIAGNOSTICS*

T. E. Thompson†, A. Aleksandrov, K. Ruisard, A. Zhukov, ORNL, Oak Ridge, TN, USA

Content from this work may be used under the terms of the CC BY 4.0 licence (© 2022). Any distribution of this work must maintain attribution to the author(s), title of the work, publisher, and DOI.

Abstract

Work at the Spallation Neutron Source (SNS) Beam Test Facility (BTF) aims to characterize halo formation in the early stages of a high-power linac and to reproduce halo measurements using well-benchmarked particle-in-cell simulations. The BTF is equipped with advanced phase space diagnostics that enable detailed characterization of beam distributions at the beginning and end of a 2.5 MeV, 10-meter test beamline. Diagnostic capabilities include direct measurement of the 6D phase space distribution, as well as imaging of 2D phase space projections with 6 orders of magnitude in dynamic range. This talk compares predictions from the PyORBIT code to measured distributions and discusses the parameters and limitations of the simulation model.

INTRODUCTION

The Beam Test Facility (BTF) is a Front-End replica of the Spallation Neutron Source (SNS), using an identical ion source and radio frequency quadrupole (RFQ) to produce a medium energy (2.5 Mev) H- beam. Downstream of the RFQ is a diagnostic heavy ~10-meter beam line with the capability to perform 6D measurements [1] and 2D high dynamic range (HDR) measurements [2, 3]. In addition to these diagnostics, the BTF contains a 9.5 cell permanent magnet quadrupole FODO line, allowing for beam transport studies [4] and the transport of matched and mismatched beams.

During initial conditioning, the SNS's optics settings were configured for the designed matched case but had higher-than-acceptable loss levels [5]. To get to its current loss level, the optics are continually empirically adjusted driving the SNS from a matched condition to a mismatched one. One source of losses in the SNS is the formation of halo, potentially driven by mismatch. Understanding the relationship between halo and mismatch provides insight into the SNS loss mechanisms and the reasons behind the SNS operating in a mismatched optics condition. The novel HDR measurements at the BTF allow for scans that measure the beam distribution from the beam's high-density core to regions at 10^{-6} of peak particle density (approximate loss tolerance to meet <1 W/m losses for a 1 GeV H- beam).

This research aims to explore the effect of mismatch on the expansion of emittance and formation of halo in a medium energy beam. It aims to expand the groundwork laid by the Low Energy Demonstration Accelerator (LEDA) at Los Alamos National Lab (LANL) [6] by increasing the dynamic range of phase space measurements to 10^6 with novel HDR measurement capabilities significantly improving upon previous phase space diagnostics [3].

DEFINING MATCH, MISMATCH, AND HALO

This research uses the following definitions for match, mismatch and halo:

Match:

- The phase space that produces the lowest maximal RMS amplitude in the FODO line.

Mismatch:

- All phase spaces other than the matched phase space.
- Degree of mismatch determined with the Mismatch Factor (M) defined by:

$$M = \left[1 + \frac{\Delta + \sqrt{\Delta(\Delta+4)}}{2}\right]^{1/2} - 1 \quad (1)$$

$$\Delta = (\Delta\alpha)^2 - \Delta\beta\Delta\gamma \quad (2)$$

$$\Delta\beta = \beta - \beta_m, \quad \Delta\alpha = \alpha - \alpha_m, \quad \Delta\gamma = \gamma - \gamma_m, \quad (3)$$

- Where the subscript m denotes the Twiss Parameters of the matched phase space.

Halo:

- All beam occupying regions of particle density below 10^{-4} of peak particle density.

DETERMINING MISMATCHED OPTICS CASES

All optics cases are defined by their Twiss Parameters a quarter-cell before the first FODO quad. There is only one matched case but a large region of possible mismatched cases. To narrow this region, this research considers only symmetric cases of mismatch where $\alpha_y = -\alpha_x$ and $\beta_y = \beta_x$.

* This material is based upon work supported by the U.S. Department of Energy, Office of Science, Office of High Energy Physics. This work has been authored by UT-Battelle, LLC under Contract No. DE-AC05-00OR22725 with the U.S. Department of Energy. This research used resources at the Spallation Neutron Source, a DOE Office of Science User Facility operated by the Oak Ridge National Laboratory. The US government retains and the publisher, by accepting the article for publication, acknowledges that the US government retains a nonexclusive, paid-up, irrevocable, worldwide license to publish or reproduce the published form of this manuscript, or allow others to do so, for US government purposes. DOE will provide public access to these results of federally sponsored research in accordance with the DOE Public Access Plan (https://www.energy.gov/doe-public-access-plan)

† thompsonte@ornl.gov

ISBN: 978-3-95450-261-5 ISSN: 2673-7000 doi: 10.18429/JACoW-NAPAC2025-THYN01

HOW NITROGEN AND OXYGEN SHAPE SRF CAVITY PERFORMANCE*

H. Hu†[1], Y.-K. Kim[1,2], D. Bafia[2]
[1]University of Chicago, Chicago, IL, USA
[2]Fermi National Accelerator Laboratory, Batavia, IL, USA

Content from this work may be used under the terms of the CC BY 4.0 licence (© 2022). Any distribution of this work must maintain attribution to the author(s), title of the work, publisher, and DOI.

Abstract

Nitrogen and oxygen-based surface treatments have enabled superconducting radiofrequency (SRF) cavities to reach higher gradients and lower losses. However, the exact mechanisms by which these treatments improve cavity performance remain largely unknown. This work provides new insights into the role of nitrogen and oxygen in SRF cavity performance by using time-of-flight secondary ion mass spectrometry (ToF-SIMS) to quantify the concentrations and depth profiles of nitrogen and oxygen impurities within niobium cutouts. This work correlates these impurity profiles with cavity performance measurements, including surface resistance and quality factor. The results demonstrate that while both nitrogen and oxygen enhance performance, ten times more oxygen is required to achieve the same reduction in BCS resistance as nitrogen.

INTRODUCTION

Improving the performance of superconducting radiofrequency (SRF) cavities is the key to enabling the next generation of particle accelerators such as the International Linear Collider (ILC) or the 8 GeV Booster Replacement Linac at Fermilab [1,2]. Two key performance metrics are quality factor (Q_0) and accelerating gradient (E_{acc}). Higher Q_0 cavities will lower operating costs and helium expenses [3]. High E_{acc} cavities make accelerators more efficient per unit length and enable future accelerators to reach higher energies.

The performance of the SRF cavity depends primarily on the composition of the first 100 nm of the surface, defined by the penetration length of superconducting currents [4]. The presence of free hydrogen in the surface has long been a limiting factor for high performance SRF cavities [5, 6]. At superconducting temperatures, free hydrogen dissolved within the Nb lattice will precipitate and form highly lossy niobium hydrides [7]. Many studies have been conducted on the development of surface treatments to minimize these prohibitive effects through the introduction and diffusion of impurities such as oxygen and nitrogen [8–11].

The state-of-the-art high Q_0 treatment of nitrogen doping introduces uniform and dilute concentrations of nitrogen into the surface [8]. A key performance feature of a N doped cavity is the anti Q-slope, an increase in Q_0 with increasing E_{acc}, which typically occurs at E_{acc} below 20 MV/m [8]. While there are some theories which propose the cause of anti-Q slope, there is no general consensus on which underlying mechanisms are responsible for it [12–15]. One theory is that nitrogen impurities act as a trap for interstitial hydrogen, reducing the concentration of free hydrogen and the losses from niobium hydrides [16].

The presence of interstitial oxygen in the Nb lattice has also been shown to have a similar effect as nitrogen [16]. Recent work has highlighted the role of diffused oxygen in improved SRF cavity performance [17–19]. A new surface treatment termed oxygen doping (200°C × 20 hours of *in-situ* baking) displays high Q_0 performance by introducing an approximately uniform concentration of oxygen in the surface without completely removing the oxide [17]. O doped cavities exhibit anti-Q slope, a feature previously considered to be unique to N doped cavities [20, 21]. Given the similarities in performance, it has been proposed that impurities in the surface layer of N and O doped cavities perform similar functions in mitigating sources of loss [16, 22]. First principle calculations suggest that it is energetically favorable H to bond with O and N interstitials instead of with Nb [16]. In this work, we correlate material studies with cavity studies to quantify the effect of interstitial O and N on SRF cavity performance and better understand the underlying mechanisms that drive .

EXPERIMENTAL METHOD

We prepared an array of single-cell TESLA shaped 1.3 GHz Nb cavities and Nb cavity cutouts from cavity TE1AES008 with a standardized EP baseline treatment of 120 µm electropolishing (EP) removal, 800°C degassing for 3 hours in an ultra high vacuum (UHV) furnace, and 40 µm EP removal. We then applied the treatments described in Table 1 to each corresponding cavity and cutout sample. One set of treatments consisted of *in-situ* baking at 120°C and 200°C at various durations. *In-situ* baked cavities were assembled prior to baking, and vacuum was maintained throughout the baking and testing. EP and N doped cavities were assembled post-treatment. The specific procedures for N doping treatments are described in Ref. [8]. To ensure a one-to-one comparison of the cutout surface to the inner surface of a cavity, we baked cutouts *in-situ* and maintained vacuum to avoid the regrowth of the native niobium oxide and minimize chances of contamination.

We analyzed cutouts with time-of-flight secondary ion mass spectrometry (ToF-SIMS) to obtain depth profiles of the impurities present in the Nb lattice. Each reported impurity depth profile is taken as the average of three 200 µm × 200 µm spots on each sample. The sputter crater

* This manuscript has been authored by the FermiForward Discovery Group, LLC under contract No. 89243024CSC000002 with the U.S. Department of Energy, Office of Science, Office of High Energy Physics. This work was supported by the University of Chicago.

† hannahhu@uchicago.edu

ISBN: 978-3-95450-261-5 ISSN: 2673-7000 doi: 10.18429/JACoW-NAPAC2025-THP003

A COMPACT 2D CARBON BEAM SCANNER WITH INTERLEAVED SADDLE COILS*

B. Mustapha†, A. Ravichandran, J. Nolen, Argonne National Laboratory, Lemont, IL, USA
R. Meinke, E. Soiman, 3D Magnetics, LLC, Concord, MA, USA

Content from this work may be used under the terms of the CC BY 4.0 licence (© 2022). Any distribution of this work must maintain attribution to the author(s), title of the work, publisher, and DOI.

Abstract

Scanning magnets are used in proton and ion beam therapy to produce a radiation dose conforming to the cancerous tumor. In most existing beam delivery systems, two separate magnets are used to scan the beam in the transverse planes. To enable more compact beam delivery systems and gantries, a combined function 2D scanner magnet with a short working distance to place at the end of the system is highly desirable. Earlier designs suffer from field non-uniformity in at least one plane. A compact 2D scanner magnet has been designed to produce high-field uniformity in both planes. The scanner was designed for carbon ions and could be easily scaled down for protons and other light ions. The design is based on saddle coils where the coils of the two magnets are interleaved to balance both field properties and power losses when scanning in both planes. The simulated field performance shows better than 0.5% field uniformity in both planes within the useful aperture of the magnet. This represents a significant improvement over the prior art of the elephant-ear scanner design. The proposed implementation using a ceramic support bobbin and a novel cooling approach is presented.

INTRODUCTION

In existing carbon ion and most proton beam gantries, the scanning magnets are placed prior to the last bend of the beam delivery system [1]. This requires the last gantry magnets to have a large aperture diameter of ~ 20 cm which greatly increases their mass and cost. Placing the scanning magnets in the final drift, as is presently implemented in the ProNova superconducting (SC) proton gantry [2], a next-generation carbon beam gantry can be much more cost effective. By demonstrating this technology with a working distance of ~ 3 m, it becomes feasible to implement SC carbon ion beam gantries with a footprint comparable to present-day proton beam gantries [3]. For protons, this same scanner can double the field size or allow SC proton gantries and fixed beam delivery systems to be even more compact with a ~ 1 m working distance.

The scanners must have as short as possible working distance so that they can be placed after the last gantry bending magnet to enable the use of small aperture magnets. The concept of a 3D scan, in x-y, and energy is shown in Fig. 1 [4]. For compactness, the x-y scanners can be combined into a single combined function 2D scanner magnet. Combined with programmed intensity variation during the 3D scan, this method is known as Intensity Modulated Particle Therapy (IMPT).

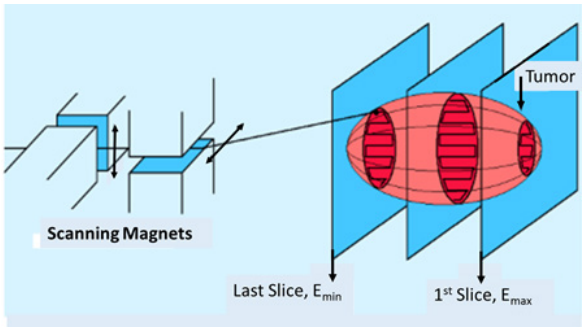


Figure 1: Concept of a 3D, x-y and depth scan of a tumor.

SPECIFICATIONS AND DESIGN OPTIONS

The general specifications for a carbon beam scanner magnet satisfying the requirements are shown schematically in Fig. 2 with more details listed in Table 1. While in most cases a 40 cm scanning field is not needed, some spine tumors require a wide field at least in one dimension.

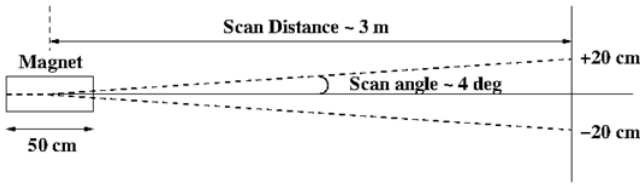


Figure 2: Schematic layout of 1D beam scanning using a 0.5 m long magnet with a working distance of ~ 3 m covering a +/- 20 cm field.

Table 1: Design specifications for a 2D carbon beam scanner magnet with ~ 3 m working distance and 40 cm scanning field.

Parameter	Value
Beam rigidity, T.m	6.6 (430 MeV/u C^{6+})
x-y deflection angle, deg	4.2 (40x40 cm at 3 m)
Bend radius, m	6.6
Peak field, T	1
Effective length, m	0.5
Good field area, cm	6
Scanning frequency, Hz	100

Based on these specifications, we have developed different design options for a compact 2D carbon beam scanner. In addition to the already known elephant-ear design [5], we developed a novel 2D interleaved saddle coil design,

*This work was supported by the U.S. Department of Energy, under Contract No. DE-AC02-06CH11357. This research was supported through the Accelerator Stewardship program under the DOE/ARDAP office.
† brahim@anl.gov

ISBN: 978-3-95450-261-5 ISSN: 2673-7000 doi: 10.18429/JACoW-NAPAC2025-THP004

ADVANCED GROWTH AND CHARACTERIZATION OF ALKALI ANTIMONIDE PHOTOCATHODES FOR BRIGHT BEAM APPLICATIONS

T. Hasan,* O. Chubenko, Northern Illinois University, DeKalb, IL, USA
J. Power, S. Doran, E. Wisniewski, G. Chen, P. Piot
Argonne National Laboratory, Lemont, IL, USA

Abstract

The properties of photoemitting electron sources are key determinants of performance in advanced electron accelerator applications, such as particle colliders, X-ray free electron lasers, ultra-fast electron diffraction and microscopy experiments. Therefore, low mean transverse energy (MTE), high quantum efficiency (QE) along with long operational lifetime and robustness under high electric fields and laser fluences must be demonstrated by the photocathode for these bright beam applications. Recent investigations have revealed that the epitaxial growth of single crystal cesium antimonides can be achieved by photocathode growth on lattice matched substrates. In this work, the experimental setup for highly promising alkali antimonide photocathode growth by molecular beam epitaxy on lattice matched substrates and *in-situ* characterization with reflection high-energy electron diffraction (RHEED) has been considered. To adapt the L-band RF gun of Argonne Cathode Test-stand (ACT) for extensive testing of alkali antimonides in real accelerator conditions, compatible cathode plug design and smooth transportation process have been developed and also described in this paper.

INTRODUCTION

Due to their low positive electron affinity, alkali antimonide photocathodes (e.g., Cs_3Sb, K_2CsSb, Na_2KSb, etc.) are great candidates for electron sources with high quantum efficiency (QE) in the visible light range. Moreover, these materials demonstrate reduced physical roughness and crystalline structure if grown on lattice-matched singe-crystal substrates [1–3]; thus, low mean transverse energy (MTE) can be achieved by these photocathodes. Therefore, these electron sources are highly promising for bright beam applications such as particle colliders, x-ray free electron lasers (XFELs), ultrafast electron diffraction (UED) and microscopy (UEM). One of the key challenges for bright electron sources is achieving long lifetimes and robustness under high electric field gradients and intense laser fluences. Although cesium antimonide (Cs_3Sb) photocathodes are sensitive to vacuum conditions and require more sophisticated experimental setup as compared to metal cathodes, they still can be robust enough to be used in photoinjectors with high gradients. These photocathodes have been studied in DC guns previously; however, no experiment has been carried away to test their performance in the RF or SRF environment.

The goal of this work is to grow high quality alkali antimonide photocathodes at Northern Illinois University (NIU) with advanced *in-situ* characterization techniques and test them at Argonne Cathode Test-stand (ACT) of Argonne Wakefield Accelerator (AWA) Facility.

ALKALI ANTIMONIDE PRODUCTION

The NIU alkali antimonide growth system is based on the growth chamber received from Fermi National Accelerator Laboratory (FermiLab), which was previously used to grow cesium telluride photocathodes. It is built around a 10″-diameter vacuum chamber (Fig. 1) and uses an INFN-style plug (Fig. 2). One turbo pump, one sublimation pump, and two ion pumps are used to achieve UHV conditions.

The system is operated by 5 different manipulators. Manipulator A exerts its action by means of permanent magnet and can move a storing carriage along the chamber. The carriage, shown in the inset of Fig. 1, can hold up to 5 cathode plugs. Manipulator B is also operated by a permanent magnet that can grab one plug at a time to move it along the beamline. Manipulators C, D and E are operated via bellows. A rigid pincer in the top of manipulator D can grab the cathode from the carriage and place it to the growth position and vice versa. Manipulator C rides inside manipulator D where a halogen bulb is inserted inside the hollow and can be moved up to the bottom surface of the cathode surface to heat it up. The temperature of the cathode can be measured by a thermocouple inserted through a hole in the cathode plug. Manipulator E moves a thickness monitor in and out to the growth path for calibration of the deposition rates. A mask attached to the SAES source control makes sure that the particles are only deposited on desired surface of the plug. The transfer cross (or "vacuum suitcase" shown in Fig. 1) separated by a gate valve ensures the photocathode transportation from a growth facility to the testing facility in UHV environment.

Some system upgrades are underway to improve alkali antimonide photocathode growth and *in situ* characterization. More efficient and long-lasting effusion cells in combination with gate valves will be used for the film deposition instead of SAES dispensers. This will allow us to avoid frequent source replacements and vacuum interruptions. The epitaxial growth of Cs_3Sb films can be achieved through the codeposition of Cs and Sb on a lattice-matched substrate such as STO (100), 3C-SiC (100), Al2O3 (1010) and TiO2 (001) [2]. To ensure *in situ* monitoring of the epitaxial growth of Cs_3Sb throughout film deposition, the Reflective High Energy Electron Diffraction (RHEED) system has arrived

* thasan@niu.edu

Content from this work may be used under the terms of the CC BY 4.0 licence (© 2022). Any distribution of this work must maintain attribution to the author(s), title of the work, publisher, and DOI.

ISBN: 978-3-95450-261-5 ISSN: 2673-7000 doi: 10.18429/JACoW-NAPAC2025-THP005

ADVANCING CONDUCTION-COOLED 650 MHz SRF TECHNOLOGY FOR INDUSTRIAL ACCELERATORS AT FERMILAB'S IARC

Y. Ji*, C. Edwards, A. Sukhanov, N. Solyak, J. Thangaraj, S. Kazakov, I. Gonin,
V. Yakovlev, M. Henry, J. Helsper, Fermi National Accelerator Laboratory, Batavia, USA
D. McGinnis, BL Monitor & Control AB, Brantevik, Sweden

Content from this work may be used under the terms of the CC BY 4.0 licence (© 2022). Any distribution of this work must maintain attribution to the author(s), title of the work, publisher, and DOI.

Abstract

The National Nuclear Security Administration (NNSA) funds the Illinois Accelerator Research Center (IARC) at Fermilab in developing a high-power, conduction-cooled Superconducting Radio Frequency (SRF) accelerator tailored for industrial applications requiring robust and efficient operation. A 650 MHz, 1.6 MeV, 20 kW SRF accelerator is currently under development, employing a conduction cooling approach to simplify cryogenic requirements and enhance accessibility for industrial use. The accelerator's control system is implemented on the Blinky Lite platform, selected for its open-source architecture, secure remote access capabilities, and operational flexibility—attributes advantageous for industrial deployment and sustained operation. A dedicated beamline is designed to measure essential beam parameters and test the integrated performance of the accelerator and control systems, thereby validating their operational readiness for intended applications.

MOTIVATION FOR THE COMPACT SRF ACCELERATORS

Cobalt-60 (Co-60) has long been the primary technology for sterilizing medical devices. However, growing safety, security, and environmental concerns are driving a global transition away from isotope-based sterilization. At the same time, existing X-ray and electron beam (e-beam) systems often fail to provide the beam power, reliability, or cost efficiency required for high-throughput industrial use.

The demand for deployable, U.S.-manufactured alternatives has intensified, with strong support from the Office of Radiological Security (ORS) for solutions that enhance both resilience and security. In response, Fermilab, in partnership with the National Nuclear Security Administration (NA-22), is developing a next-generation 20 kW, 1.6 MeV continuous e-beam system operating at 650 MHz (Fig. 1) [1].

This platform employs an Nb_3Sn superconducting cavity [2] cooled by commercial cryocoolers [3, 4], eliminating the need for complex cryogenic infrastructure and enabling push-button operation without specialized staff. Its compact and rugged design, with an integrated RF gun and efficient RF system, makes it suitable for large-scale industrial deployment. While optimized for medical device sterilization, the system also holds promise for environmental applications such as PFAS remediation and waste treatment [5]. This paper will focus on the control system architecture and beamline design that enable reliable, high-throughput performance.

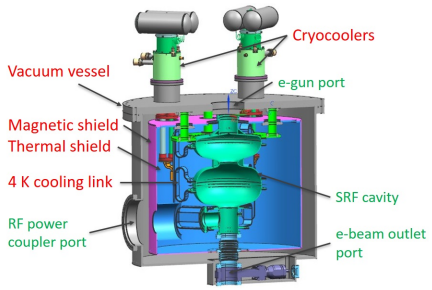


Figure 1: Section view of the 1.6 MeV 20 kW 650 MHz conduction-cooled SRF e-beam accelerator.

BLINKY LITE CONTROL SYSTEM

A reliable and fully integrated control system is essential for deploying compact accelerators in industrial environments. To meet this need, the project adopts the Blinky Lite control system, a lightweight, full-stack solution that includes all necessary features for efficient and secure operation. The system integrates device interfaces, communication protocols, configuration databases, alarm and notification systems, device viewers, plotting tools, as well as access and setting history, ensuring seamless operation and comprehensive oversight. The control system architecture is demonstrated in Fig. 2.

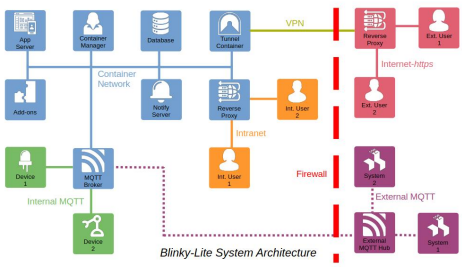


Figure 2: Blinky Lite Architecture.

Because industrial facilities often operate continuously, unexpected issues can arise at any time, including during overnight shifts when experts may be off-site. The Blinky Lite [6] system addresses this challenge by providing secure remote access, allowing engineers to monitor and intervene in real time from the field. This capability enhances both reliability and responsiveness, which are critical for high-throughput applications. Ultimately, the control system supports the project's goal of delivering a compact, rugged accelerator that can be reliably operated in industrial settings without the constant presence of specialized personnel.

* yji210@fnal.gov

ISBN: 978-3-95450-261-5 ISSN: 2673-7000 doi: 10.18429/JACoW-NAPAC2025-THP007

ANALYTICAL MODEL FOR THE TRANSITION TO SUPERRADIANCE IN SEEDED FREE-ELECTRON LASERS

R. R. Robles*, E. Hemsing, A. Marinelli, G. Stupakov[1]
SLAC National Accelerator Laboratory, Menlo Park, CA, USA
[1]also at xLight, Inc., Stanford, CA, USA

Content from this work may be used under the terms of the CC BY 4.0 licence (© 2022). Any distribution of this work must maintain attribution to the author(s), title of the work, publisher, and DOI.

Abstract

Free-electron lasers (FEL) seeded by short radiation pulses can exhibit superradiant behavior. In the superradiant regime, the pulse simultaneously compresses and amplifies as it propagates through the FEL, making superradiance very promising for pushing the performance limits of attosecond x-ray FELs. To date, this regime has been studied in asymptotic limits, but there is no model for how the initially linear dynamics of the seeded FEL transition into the nonlinear superradiant behavior. We derive an analytical model for the 1D FEL seeded by a short pulse which accurately captures the linear dynamics, the nonlinear superradiant evolution, and the smooth transition between them. Our model fills a critical gap in our understanding of FEL superradiance and nonlinear time-dependent FEL physics more broadly, and may provide a bridge to the corresponding problem in three-dimensions, and analogous problems in other fields exhibiting soliton behavior.

INTRODUCTION

The dynamics of the one-dimensional (1D) FEL are accurately described by a set of equations of motion for the particles and a wave equation for the electric field [1–3]. The particles are described by a ponderomotive phase $\theta_j = (k_r + k_u)\bar{z}_j(t) - \omega_r t$ and a scaled relative energy deviation $\hat{\eta}_j = (\gamma_j - \bar{\gamma})/\rho\bar{\gamma}$, where k_r and k_u are the radiation and undulator wavenumbers, respectively, $\bar{\gamma}$ is the average Lorentz factor of the bunch, and ρ is the Pierce parameter. These coordinates satisfy the equations of motion

$$\frac{d\theta_j}{d\hat{z}} = \hat{\eta}_j, \tag{1}$$

$$\frac{d\hat{\eta}_j}{d\hat{z}} = -(ae^{-i\theta_j} + \text{c.c.}), \tag{2}$$

where $\hat{z} = 2\rho k_u z$, with z the distance along the undulator, and a is the scaled electric field strength, which satisfies

$$\frac{\partial a}{\partial \hat{z}} + \frac{\partial a}{\partial \zeta} = \langle e^{i\theta_j} \rangle, \tag{3}$$

where $\zeta = 2\rho\theta$ describes the scaled position within the electron bunch, and the average $\langle e^{i\theta_j} \rangle$ is taken over a thin slice centered at ζ. Figure 1 shows the typical behavior of the numerical solution of these equations seeded by a short Gaussian field, in this case with amplitude 10^{-4} and width $\sigma_\zeta = 0.5$. Panel (a) shows the evolution of the temporal power profile along the undulator length. The short Gaussian seed initially undergoes exponential amplification and lengthens as a result of its slippage across the electron bunch. This is called the linear regime, as the electron dynamics in this region are only a small perturbation to their initial conditions. Once the field amplitude reaches the order unity, the electron dynamics become non-perturbative, leading to saturation of the field amplitude (reflected in panel (b)). After that saturation point, the pulse enters the solitonlike superradiant regime, in which the highly nonlinear dynamics lead to rapid pulse shortening and quadratic amplification of the peak power [4–7].

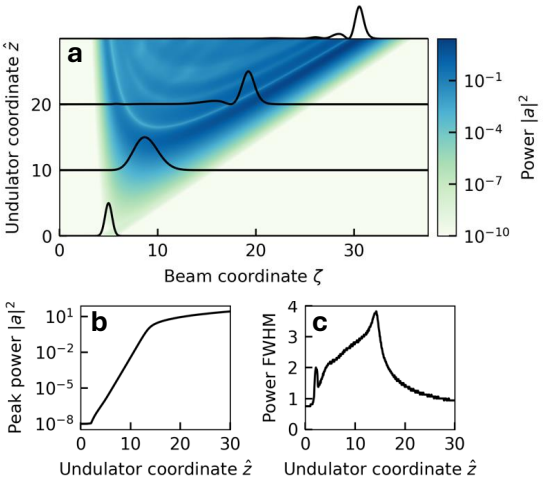


Figure 1: Typical dynamics of an FEL seeded by a short, low-power pulse. (a) The evolution of the field power versus beam coordinate and undulator position. (b) The peak power of the pulse versus undulator length. (c) The full-width at half-maximum (FWHM) of the power profile versus undulator length.

The dynamics in the linear ($\hat{z} \lesssim 10$ in Fig. 1) and nonlinear ($\hat{z} \gtrsim 15$) regimes have been studied extensively analytically. The linear regime has an exact Green's function solution [8–10]. The nonlinear solitonlike regime has been studied in isolation using scaled coordinates, yielding, among other results, an approximate hyperbolic secant form for the pulse shape [11, 12]. However, studies of the nonlinear regime to date have ignored the initial value problem, providing asymptotic scaling laws but failing to connect the nonlinear evolution to the particular initial conditions seeding the FEL instability.

In the remainder of this paper we develop an analytical solution of the full initial value problem of the solitonlike superradiant FEL in one dimension. We focus on the case

* riverr@stanford.edu

ISBN: 978-3-95450-261-5 ISSN: 2673-7000 doi: 10.18429/JACoW-NAPAC2025-THP008

AN ELECTROSTATIC FUSION COLLIDER FOR INTERSTELLAR PROPULSION

G.P. Jackson[2,†], G.E. Bittlingmaier[1], A.S. Lee[1]
[1]Beam Alpha Incorporated, West Chicago, IL, USA
[2]Hbar Technologies, LLC, West Chicago, IL, USA

Content from this work may be used under the terms of the CC BY 4.0 licence (© 2022). Any distribution of this work must maintain attribution to the author(s), title of the work, publisher, and DOI.

Abstract

In order to reach the nearest star Proxima Centauri within a century, a distance of 4.224 ly from our solar system, the average spacecraft velocity needs to be 4.2% of the speed of light. Therefore, according to the rocket equation, the weighted average exhaust velocity needs to be over 1% of the speed of light for reasonable ratios of dry mass to fuel mass. The fusion reactor architecture presented herein consists of an electrostatic charged particle trap that brings two ion beams into collision with equal and opposite momentum. The two fusion channels under consideration for interstellar missions are p/Li7 and He3/He3, utilizing an array of low mass electrodes that minimize interactions with fusion daughters escaping from the collision point and focused to generate thrust. A terrestrial prototype colliding beam accelerator has been built to determine the viability of achieving collider luminosities commensurate with the requirements of this application. A novel architecture overcomes past Coulomb scattering limitations. Reactor and propulsion system design parameters are presented in this paper along with fabrication and testing status.

PROPULSION

The fusion reactor architecture used in the proposed propulsion system [1] consists of an electrostatic charged particle trap [2-4] that brings two ion beams into collision with equal and opposite momentum. For the purposes of this paper only deceleration at Proxima Centauri is addressed.

Assume a fuel mass of M_{fuel} before deceleration. After expending all of the fuel the spacecraft mass is represented as M_{dry}. Let N be the number of mass stream species, each with a fraction of the total exhaust mass α_i and exhaust velocity with respect to the spacecraft v_i. The change in spacecraft velocity ΔV is

$$\Delta V = \sum_{i=1}^{N} \alpha_i v_i \ \mathrm{Ln}\left(1 + M_{fuel}/M_{dry}\right) \quad , \quad (1)$$

where

$$1 = \sum_{i=1}^{N} \alpha_i \quad . \quad (2)$$

Figure 1 shows the relationship of Eq. (1) as a function of the mass-weighted average exhaust velocity. Observe the diminishing returns upon fuel-to-dry mass ratio approaching 20:1, as the ratio between spacecraft and exhaust velocity levels out. In order to decelerate a spacecraft from at least one percent of the speed of light, the fusion daughter particle velocities escaping the propulsion system must also be at least one percent of lightspeed. Hence direct fusion daughter emission from the collider is required.

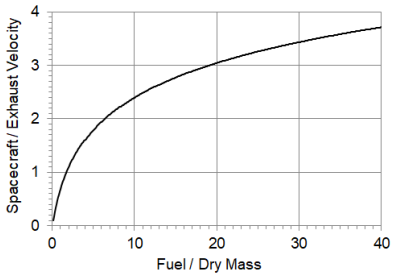


Figure 1: Rocket equation prediction of change in spacecraft velocity relative to the weighted average exhaust velocity as a function of ratio of fuel to dry mass.

The proposed architecture to accomplish this task is illustrated in Fig. 2. Assuming a 100-year transit time, a constant 10-year acceleration, and a 10-year deceleration burn, the peak spacecraft velocity during the 80-year coast period is 0.042c. The peak acceleration of the spacecraft is 0.029 m/s^2. This is approximately 0.3% of gravity at the Earth surface, allowing the use of fragile spacecraft components such as electrodes composed of thin wires similar to the vacuum ion gauge pictured to the right.

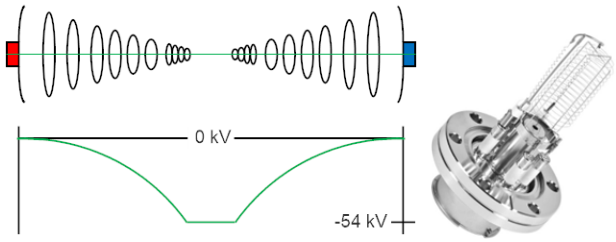


Figure 2: On the left side, illustration of the electrostatic electrode array of the fusion collider (top) and the axial potential (bottom). The right side is a picture of a standard vacuum ion gauge.

This collider architecture enables direct fusion daughter escape. Utilizing an electrostatic nozzle[1], the escaping particles are focused into a coherent exhaust stream while maintaining their initial kinetic energy.

FUSION CROSS SECTIONS

One nuclear fusion fuel combination under consideration is helium-3 on helium-3. As graphed in Fig. 3, this reaction has a peak cross section of 0.115 barns. In a symmetric collider this peak corresponds to a beam kinetic energy of 4 MeV. For axial confinement the depth of the axial potential must therefore be at least 2 MV. Operating the electrostatic collider at a axial potential depth of 1 MV is possible with only a 20% reduction in cross section. A 40% drop in cross section allows operation at 500 kV.

ISBN: 978-3-95450-261-5 ISSN: 2673-7000 doi: 10.18429/JACoW-NAPAC2025-THP009

AUTOMATIC MEASUREMENT OF THE STRAY MAGNETIC FIELD IN THE RCS LOCATIONS OF RHIC BY USING THE SPOT ROBOT

P. Xu, Y. Cui, O. Dim, K. Drees, H. Huang, Y. Luo, W. Stern, A. Sukhanov, D. Toner, Q. Wu
Brookhaven National Laboratory, Upton, NY, USA
H. Witte, MIT Bates Research and Engineering Center, Middleton, MA, USA

Abstract

The Electron Ion Collider (EIC) will collide high energy and highly polarized hadron and electron beams with luminosities up to $10^{34}/cm^2/s$. In the Conceptual Design Report baseline scope, the electron beams, accelerated in the Rapid Cycling Synchrotron (RCS), are vulnerable to the outside magnetic field due to its low injection energy at 400 MeV. In addition, when the Hadron Storage Ring (HSR) and Electron Storage Ring (ESR) are in operation, the leaking field from the HSR might also affect the operation of RCS, because they are close to each other. Mapping the stray magnetic field throughout the Relativistic Heavy Ion Collider (RHIC) tunnel (will be used for EIC) is essential to assess its impact on potential low-energy electron beam injection. A robot dog (SPOT) is used to automate the measurement of this stray magnetic field during the RHIC (or future EIC) operation at any location continuously. This quadrupedal robotic technology can also be applied to other future applications, including radiation, temperature, pressure, and other properties measurement during EIC operation.

INTRODUCTION

In the conceptual design report (CDR) baseline scope of the electron ion collider [1, 2], the electron beams, accelerated in the Rapid Cycling Synchrotron (RCS) [3], are designed at the injection energy at 400 MeV. At this low energy, the dipole field in the ring is as low as 57 Gauss, the electron beams thus are very sensitive to the ambient magnetic field (1-2.5 Gauss could kick beam out of the pipe). In addition, the magnetic fields due to the Hadron Storage Ring (HSR) and the Electron Storage Ring (ESR) being at full energy could also affect the RCS operation. The magnetic field at the RCS locations of the Relativistic Heavy Ion Collider (RHIC) tunnel have been mapped entirely without operation [4]. Measuring the stray magnetic field during RHIC operation is important to study the effect of the HSR to RCS design, however, access is limited during the operation. Therefore, a robot is used to automatically measure the magnetic field without people access. The robot used is the "SPOT" from Boston Dynamics [5, 6]. Layout of the EIC at the conceptual design phase is shown in Fig. 1, where the dark blue is the RCS ring, the light blue is the ESR, and red is the HSR.

EXPERIMENTAL METHOD

The RCS location is shown at Fig. 2 by the representative design at interaction point (IP) 12, where the center is located about 40 cm from the tunnel wall and about 35 cm from the ground. For the rest section in the tunnel, the RCS locations are similar.

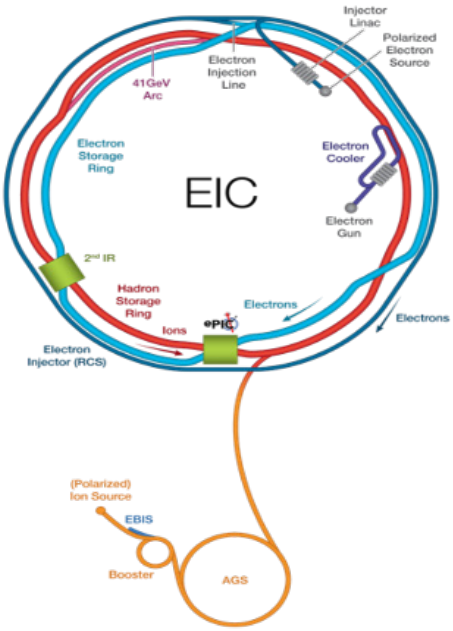


Figure 1: Layout of the EIC at the conceptual design phase. The dark blue is the RCS ring, the light blue is the ESR, and red is the HSR.

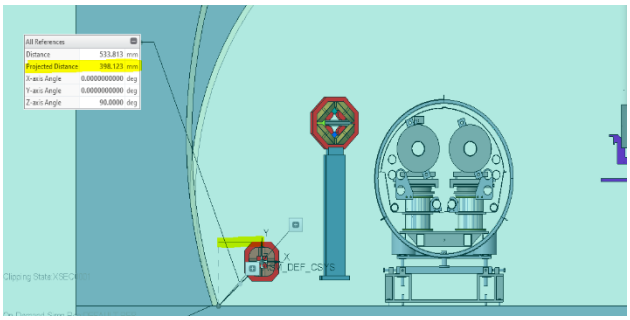


Figure 2: RHIC interaction point (IP) 12 layouts, where the lower left is the location of the RCS, the center is about 40 cm from the wall and 35 cm from the ground.

To automatically measure the magnetic field, the SPOT needs to map the route before RHIC operation. First, it reads the Fiducial as the initial position, shown in Fig. 3. Then, the SPOT moves back and forth (Fig. 4 and Fig. 5) using the remote controller based on the planned locations. The route is mapped and stored in the SPOT with the LiDAR technology [7]. After mapping the route, the superconducting magnets of RHIC are turned on after sweeping (no staff inside, but the SPOT is there).

Content from this work may be used under the terms of the CC BY 4.0 licence (© 2022). Any distribution of this work must maintain attribution to the author(s), title of the work, publisher, and DOI.

ISBN: 978-3-95450-261-5 ISSN: 2673-7000 doi: 10.18429/JACoW-NAPAC2025-THP011

BEAM BUNCHERS FOR LANSCE MODIFICATION PROJECT*

S. S. Kurennoy, Los Alamos National Laboratory, Los Alamos, NM, USA

Abstract

The Los Alamos Neutron Science Center (LANSCE) accelerator complex delivers both protons and negative hydrogen ions with various beam time patterns simultaneously to multiple users. The LANSCE linac front end is still based on Cockcroft-Walton voltage generators. An upgrade of the front end to a modern, RFQ-based version – a part of the LANSCE Modernization Project (LAMP) – is now in the conceptual design stage. The LAMP will need beam bunchers both in the low-energy transport (LEBT, 100 keV) before RFQ, and in the medium-energy transport (MEBT, 3 MeV) after RFQ. We use CST modeling to develop buncher cavities for LAMP. A few RF cavity types for MEBT: re-entrant, quarter-wave, and half-wave – are considered and compared. The LEBT low frequency buncher is different: it is a two-gap structure driven by an LC-circuit and used for beam velocity bunching.

INTRODUCTION

We consider design options for beam bunchers in the LAMP LEBT and MEBT. The low frequency buncher (LFB) is used in LEBT to form special high-charge bunches for time-of-flight experiments. The LFB imposes an energy tilt on a continuous 100-keV H^- beam chopped to about 25 ns, which is equivalent to 5 RF periods of the LAMP drift-tube linac (DTL) operating at RF frequency of 201.25 MHz, for beam velocity bunching at the RFQ entrance [1]. Such high-charge bunches are separated by 1.8 μs. A similar scheme with LFB is used in the LANSCE linac front end at 750 keV [2]. The LANSCE LFB is an RF device driven by an external LC circuit at 16.77 MHz (1/12 sub-harmonic of 201.25 MHz).

The MEBT transfers the beams from the RFQ, where they are bunched and accelerated to the energy of 3 MeV, to the DTL. The preliminary LAMP MEBT design [1] anticipates four bunchers at RF frequency of 201.25 MHz with the beam aperture radius a = 1.8 cm and effective voltage V_{eff} = 90 kV [1]. Clearly, minimizing the buncher cavity footprint along the beamline is highly desirable. We use these parameters to evaluate and compare three different buncher designs: re-entrant TM_{010}-mode resonator, quarter-wave and half-wave RF cavities – using EM modeling in CST Studio [3].

LEBT BUNCHERS

The low frequency buncher (LFB) looks like a coaxial structure, see a simplified model in Fig. 1. Its inner beam pipe has two narrow transverse gaps, with the central piece supported by an isolated radial rod (not shown). The LC circuit voltage is fed via rod to this central piece, while the end pieces and cylindrical enclosure are grounded. The LFB enclosure length is 22 cm, the beampipe inner radius is 1.5875 cm, and the gap widths are 0.4 cm. The gap edges are rounded. The gap centers are separated by the distance $\beta\lambda/2$ = 13 cm, where β = 0.0146 for 100-keV protons or H^- ions, and λ = 17.877 m is the wavelength at 16.77 MHz. The LFB electric field is calculated either in electrostatics or by an eigensolver as a quasi-static mode. The calculated field is the same; the on-axis field is plotted for the applied potential of 5 kV/gap in the inset of Fig. 1.

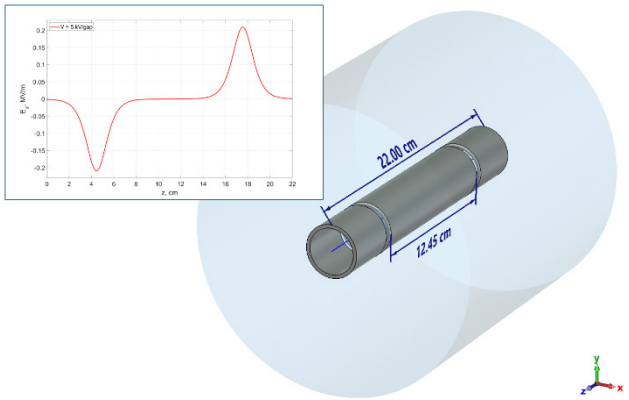


Figure 1: Vacuum volume in CST model of LFB (outer enclosure walls not shown).

More details and PIC simulations of longitudinal beam dynamics with LFB can be found in [2, 4].

MEBT BUNCHERS

We consider three design options for the 201.25-MHz beam bunchers at 3 MeV (β = 0.08) in the LAMP MEBT – reentrant single-gap, quarter-wave (QW), and half-wave (HW) resonators The cavity CST models are shown in Fig. 2, keeping their relative sizes in approximately correct ratios.

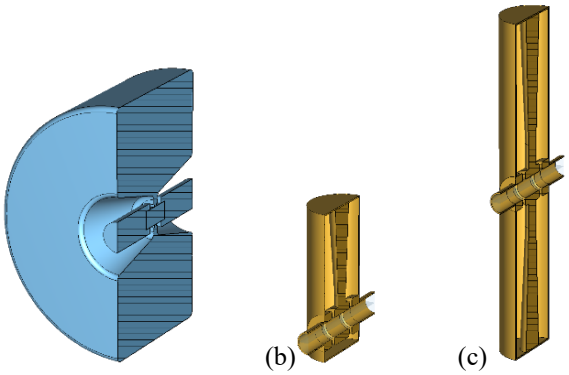


Figure 2: MEBT buncher cavities, cut view: (a) re-entrant (vacuum volume only), (b) QW, and (c) HW resonators.

For all these RF cavities we assume the beam aperture radius 1.8 cm and total effective voltage V_{eff} = 90 kV. For QW and HW resonators it means 45 kV/gap. The re-entrant

*This work was performed under the auspices of the US Department of Energy by Triad National Security under contract 89233218CNA000001.

Content from this work may be used under the terms of the CC BY 4.0 licence (© 2022). Any distribution of this work must maintain attribution to the author(s), title of the work, publisher, and DOI.

Content from this work may be used under the terms of the CC BY 4.0 licence (© 2022). Any distribution of this work must maintain attribution to the author(s), title of the work, publisher, and DOI.

BEAM DYNAMICS IN LANSCE ACCELERATOR FACILITY WITH LOWER ENERGY*

Y. K. Batygin†, E. Henestroza, S. S. Kurennoy, LANL, Los Alamos, NM, USA

Abstract

In operation of the LANSCE accelerator facility, occasionally it is required to provide beam at a lower beam energy than the nominal energy of 800 MeV. In this paper we examine the regime when the last sector of the LANSCE linear accelerator is off, so that the beam energy becomes 700 MeV. The purpose of our study is to evaluate beam quality and required changes in the accelerator setup. Lower beam dynamics affects Coupled-Cavity Linac, Switchyard, high-energy beamlines, and beam accumulation in Proton Storage Ring (PSR). The original design of the injection beamline to the PSR at a nominal energy of 800 MeV assumes elimination of cross-terms in the beam 6D sigma-matrix at the point of injection. However, these terms are amplified when a 700-MeV beam is injected. Comparison of beam dynamics with nominal and lower energy operation is presented.

INTRODUCTION

Los Alamos Neutron Science Center (LANSCE) accelerator facility has been in operation for more than 50 years delivering important information for national security and fundamental nuclear physics. Currently it works in multi-beam operation regime, delivering beams to five experimental areas [1]. The layout of the accelerator facility is shown schematically in Figure 1.

The accelerator is equipped with two independent injectors for H^+ and H^- beams. Each injector has a Cockcroft-Walton type generator and an ion source to produce either positively charged protons (H^+) or negatively charged hydrogen ions (H^-) with a final energy of 750 keV. Two independent beamlines deliver H^+ and H^- beams, merging at the entrance of a 201.25 MHz Drift Tube Linac (DTL). The DTL performs acceleration up to the energy of 100 MeV. After the DTL, the Transition Region beamline directs the 100 MeV proton beam to the Isotope Production Facility (IPF), while H^- beam is accelerated up to the final energy of 800 MeV in an 805 MHz Coupled Cavity Linac (CCL). The H^- beams, created with different time structures imparted by a low-energy chopper, are distributed in the Switch Yard to Lujan Neutron Science Center, Weapons Neutron Research Facility (WNR), Proton Radiography Facility (pRad), and Ultra-Cold Neutron Facility (UCN). The accelerator operates at a 120 Hz repetition rate with 625 μs pulse length. Parameters of all beams are presented in Table 1.

Within operation, sporadically it is necessary to deliver beams to experimental targets with lower energy. In this paper, we provide initial results of beam dynamics study in accelerator facility with reduced energy.

*Work supported by US DOE under contract 89233218CNA000001
† batygin@lanl.gov

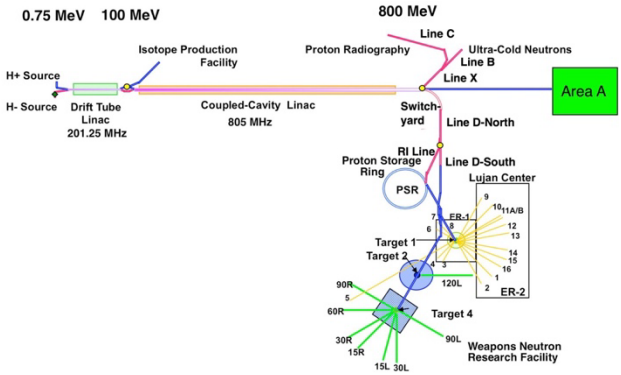


Figure 1: Overview of the LANSCE accelerator and user facility complex.

Table 1: Beam Parameters of LANSCE Accelerator

Area	Rep. Rate (Hz)	Current/ Bunch (mA)	Average Current (μA)	Average Power (kW)
Lujan	20	10	100	80
IPF	100	4	230	23
WNR	100	25	4.5	3.6
pRad	1	10	<1	<1
UCN	20	10	10	8

BEAM DYNAMICS IN COUPLED CAVITY LINEAR ACCELERATOR

LANSCE 805 MHz Side-Coupled Linac (CCL), accelerates particles from 100 MeV to 800 MeV. The CCL consists of 104 tanks, which are grouped into 44 accelerating modules (modules 5-48). Modules 5-12 contain 4 accelerating tanks each, while modules 13-48 contain 2 tanks each. Every tank contains multiple (34 - 61) accelerating cells with constant geometrical velocity within the interval of β_g = 0.4311 – 0.84056. Each CCL module is fed by RF power from a klystron, having a maximum design output power of 1.25 MW with a pulse width of 1000 μs. The beam focusing is provided by quadrupole doublets placed between accelerating tanks.

Energy gain per module in CCL is changing from 13 MeV at the beginning of the linac to 16 MeV at the end of linac. The CCL linac has a length ~ 700 m with an average real estate gradient of dW/dz = 1 MeV/m, and average accelerating field E = 1.15 MV/m, providing acceleration with the synchronous phase $\varphi_s = -30°$. The transverse CCL normalized acceptance is changing from ε_{ch} (100 MeV) = 1.75 π cm mrad at the beginning to ε_{ch} (800 MeV) =

ISBN: 978-3-95450-261-5 ISSN: 2673-7000 doi: 10.18429/JACoW-NAPAC2025-THP013

BEAMLINE OPTICS DESIGN OF A NEW TWO-ROOM TREATMENT SUITE AT THE MCLAREN PROTON THERAPY CENTER*

G. H. Gillespie[1,†], J. Gordon[2], J. Konzer[3]
[1]G. H. Gillespie Associates, Inc., Del Mar, CA, USA
[2]Pyramid Technical Consultants, Henfield, UK
[3]McLaren Regional Medical Center, Flint, MI, USA

Content from this work may be used under the terms of the CC BY 4.0 licence (© 2022). Any distribution of this work must maintain attribution to the author(s), title of the work, publisher, and DOI.

Abstract

A fixed-beam, two room suite with upright chairs for patient positioning, is being installed at the McLaren Proton Therapy Center (MPTC). The MPTC is an operational multi-room cancer treatment center. The new suite adds a third (A) and fourth (B) room by branching upstream of the two clinically active treatment rooms. It was required to fit into a pre-existing single treatment room vault. This imposed a number of constraints on the beamlines of the new suite. The new beamline uses a Y-shaped selection dipole to switch between the suite's room A and room B. The design was further constrained by the need to replicate the clinically active rooms' beam characteristics at the new patient locations. This paper provides an overview of the methodology of the design studies for the new beamlines together with selected results. The work helped to establish the feasibility of installing a two-room treatment suite into a space originally designed for a gantry-based single treatment room.

INTRODUCTION

The new treatment rooms [1] at the MPTC center around the use of two upright patient chairs of the LEO design [2]. This treatment modality offers a cost-effective alternative to conventional gantry-based treatment [3]. The two rooms are located in an existing room area designated TR3 at MPTC. The location of the TR3 room, together with rooms TR1 and TR2 at MPTC, was shown in Fig. 1 of reference [4]. The layout of the beamlines required them to fit within existing shield walls, while also allowing space for the patient treatment chair, monitoring and positioning equipment. The task was to design beamlines that could deliver existing synchrotron beams [4] to the TR3 isocenters for A and B with beam characteristics that match of those at the isocenters of the existing rooms TR1 and TR2. Figure 1 shows the final beamline layout discussed in this paper.

DESIGN CONSTRAINTS

The constraints imposed upon the design derived from two primary requirements. The new 2-room treatment suite needed (1) to fit within an existing room and (2) deliver a beam at new isocenter locations as good as those delivered to the current treatment isocenters. The requirement (2), on the beam parameters at the new isocenter locations, is critical for the optics design, and derives directly from the need to minimize the impact on the existing treatment planning system. The existing room was originally designed for a gantry type treatment room, essentially identical to the existing TR1 and TR2 rooms. However, the LEO chair and new nozzle system have a longer air gap to isocenter distance, an increase of 290 mm compared to the existing treatment rooms. The result is a longer distance between the last magnetic optics component and the new treatment isocenters. The installation and commissioning of the new beamlines could not impact existing operations nor result in any facility down time. The existing TR3 room selection magnet CBM1 was to be used. The quadrupoles needed to be air-cooled so no new water lines would be added. The locations of all magnets, diagnostics, and vacuum system components were further restricted to be consistent with existing shielding and vault walls.

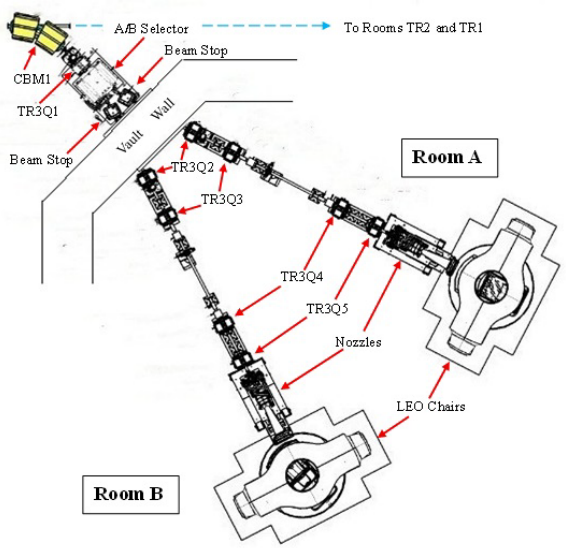


Figure 1: Room TR3 final beamline layout.

A primary consequence of the requirement to fit within the existing TR3 room was that the angle between the two beamlines A and B was constrained to be within a narrow range near 30°. The maximum distance, from the exit of the existing CBM1 magnet which directs the beam into the TR3 area, to the locations of the A and B isocenters is just over 11.6 meters. The resulting total effective (reference trajectory) lengths of the beamlines to the patient isocenters were thus constrained to be about 12 m. A 1.3-meter section of each beamline was unavailable for magnetic elements due to the vault wall. The last 3-meter section was reserved for the nozzle and air gap sections. The magnets and associated beam diagnostics were confined to be

* Work supported by McLaren Proton Therapy Center
† email address: accelsoft@ghga.com

ISBN: 978-3-95450-261-5 ISSN: 2673-7000 doi: 10.18429/JACoW-NAPAC2025-THP014

BEAM LOSS MODELING AND MITIGATION DUE TO INTRA-BEAM STRIPPING *

S. Kakkar† [1], V. Morozov[2], L. Lee[1], N. Evans[2], A. Zhukov[2], A. Hoover[2]
[1]University of Tennessee, Knoxville, TN, USA
[2]Oak Ridge National Laboratory, Oak Ridge, TN, USA

Abstract

Intra-Beam Stripping (IBS) is a critical beam loss mechanism in high-intensity H- linacs and presents a significant limitation to increasing beam power. This work presents a computational framework to evaluate and mitigate IBS-induced beam losses along the Spallation Neutron Source (SNS) LINAC. The calculation is based on an analytic theory and involves evaluation against simplified analytically solvable cases. We then applied our algorithm to Gaussian bunches with a known probablity density functions(PDFs). We next extended our algorithm to arbitrary bunch distributions using Neural Spline flow (NSF) models trained on PyORBIT tracking data. In the future, we plan to validate our algorithm experimentally and apply it to design effective mitigation strategies.

INTRODUCTION

High-intensity H- linear accelerators are crucial components of modern accelerator facilities, enabling high beam power for a range of scientific and practical applications. The SNS at Oak Ridge National Laboratory (ORNL) relies on these machines to deliver high-power beams for ambitious experimental programs. However, a persistent challenge for those accelerators is the control and mitigation of beam loss. Even small, uncontrolled losses can lead to radiation activation, increased maintenance, and ultimately limit facility upgrades and operations [1].

IBS is one of the primary mechanisms causing beam loss in these accelerators. It is due to the close electromagnetic interactions within dense H- bunches that lead to the loss of the electrons, and its effect increases with higher beam intensity (Fig. 1). Lebedev and Nagaitsev [2] developed foundational analytical models widely used for IBS predictions, but those often assume ideal Gaussian beam distributions and overlook complex, realistic beam shapes [3].

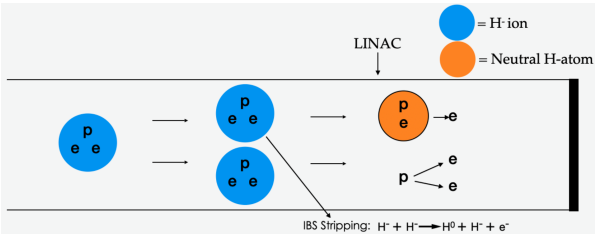


Figure 1: Electron stripping from H^- ions due to IBS.

This work aims to bridge the gap by expanding established analytic models with simulation-based and machine learning techniques. We combine Lebedev's foundational theory with neural network methods trained on detailed tracking data to model even the most complex, non-Gaussian bunch profiles and include collective effects like space charge. By carefully benchmarking this approach and applying to practical scenarios at SNS, we aim to provide more accurate IBS loss rate predictions and contribute to developing effective mitigation strategies for current and future high-intensity H- linacs.

LOSS RATE CALCULATION

The particle loss rate due to intra-beam stripping (IBS) is modeled using analytical expression developed by Lebedev and Solyak [2]. The general form of this loss rate is given by:

$$\frac{dN}{dt} = \frac{N^2}{2}\int |\mathbf{u}|\, \sigma_H(|\mathbf{u}|) f(\mathbf{v}_1, \mathbf{r}_1) f(\mathbf{v}_2, \mathbf{r}_2)\, \delta(\mathbf{r}_1 - \mathbf{r}_2)\, d\Gamma_1\, d\Gamma_2$$

Here:

- $\frac{dN}{dt}$ is the total particle loss rate due to intra-beam stripping.
- N is the number of particles in the bunch.
- $\mathbf{u} = \mathbf{v}_1 - \mathbf{v}_2$ is the relative velocity between two interacting particles.
- $\sigma_H(|\mathbf{u}|)$ is the H^- stripping cross-section, which depends on the relative velocity.
- $f(\mathbf{v}_1, \mathbf{r}_1)$,$f(\mathbf{v}_2, \mathbf{r}_2)$ are the 6D phase space density functions of two particles.
- $\delta(\mathbf{r}_1 - \mathbf{r}_2)$ ensures that only particles at the same position interact.
- $d\Gamma_1$, $d\Gamma_2$ are the phase space volume elements for each particle.

Monte Carlo Integration Approach

The loss rate integral is high-dimensional and cannot be solved analytically for realistic beam distributions. We evaluate it numerically using a Monte Carlo method, where random pairs are sampled from a specified distribution and the integrand is computed for each sample.

All calculations are performed in the rest frame of bunch, where the reference particle is at rest. This makes it easier to describe particle motion using transverse angles and momentum spread along the beam direction. In this frame, it is simpler to calculate both the relative velocity between

* This manuscript has been authored in part by UT Battelle, LLC under Contract No. DE-AC05-00OR22725 with the U.S. Department of Energy. This research used resources at the Spallation Neutron Source, a DOE Office of Science User Facility operated by the Oak Ridge National Laboratory.
† nlns1@ornl.gov

Content from this work may be used under the terms of the CC BY 4.0 licence (© 2022). Any distribution of this work must maintain attribution to the author(s), title of the work, publisher, and DOI.

ISBN: 978-3-95450-261-5 ISSN: 2673-7000 doi: 10.18429/JACoW-NAPAC2025-THP015

BEAMNETUS AT BROOKHAVEN NATIONAL LABORATORY*

W. H. Li†, A. Lueangaramwong, M. Babzien, D. Choge, M. Fedurin, M. J. Ilardi, I. V. Pogorelsky, M. N. Polyanskiy, N. Ramistella, Y. Sakai, S. Shchelkunov, N. Vafaei-Najafabadi[1], M. A. Palmer
Accelerator Facilities Division, Brookhaven National Laboratory, Upton, NY, USA
[1]also at Stony Brook University, Stony Brook, NY, USA

Abstract

BeamNetUS is a national network of accelerator facilities that aims to provide broader access to the unique capabilities of accelerated particle beams. Two facilities at Brookhaven National Laboratory are part of the inaugural year of BeamNetUS, the Accelerator Test Facility (ATF) and the Low Energy Accelerator Development (LEAD) facility, and are scheduled to each host one BeamNetUS user experiment.

The ATF features an RF photocathode electron LINAC, a femtosecond Ti:Sa laser, and a high-peak-power long-wave infrared (LWIR) laser. These tools can be synchronized for joint use or operated individually, facilitating the development of advanced beam manipulation and measurement techniques, accelerator and laser technologies, and the exploration of low-plasma-density regimes.

The LEAD facility provides an ultrafast electron diffraction (UED) apparatus, utilizing an RF electron gun and Ti:Sa laser to enable dynamic studies of material structures, as well as investigations involving low-energy electron beams.

In addition to these two accelerator facilities, Brookhaven National Laboratory provides administrative support for the network. Further expansion is planned for 2026, including both increased user hours at ATF and LEAD as well as the potential inclusion of several other facilities at the lab.

INTRODUCTION

BeamNetUS is a United States Department of Energy (DOE)-sponsored network of accelerator facilities designed to facilitate the broader use and development of accelerator technology [1]. One of the primary missions of BeamNetUS is to raise awareness and improve access to accelerator R&D facilities that are often not normally available for external users. This past fiscal year was the pilot year for the program, with eight proposals awarded beamtime at the nine participating facilities. Two of the BeamNetUS facilities are located at Brookhaven National Laboratory (BNL), the Accelerator Test Facility (ATF) and the Low Energy Accelerator Development (LEAD) facility. In addition to hosting experiments at these two facilities, BNL provides administrative support for the network as whole.

* BeamNetUS is an initiative within the DOE Office of Science to provide expanded access to its suite of accelerator research facilities. This work has been supported by Brookhaven Science Associates under Contract No. DE-SC0012704 with the U.S. Department of Energy, Office of Science.

† wli4@bnl.gov

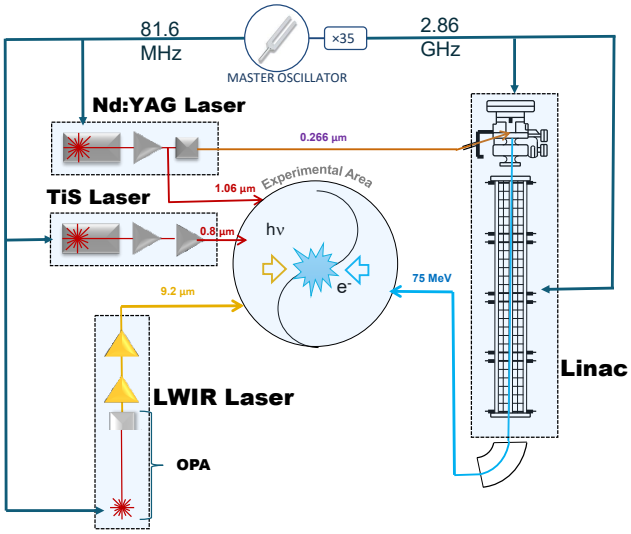


Figure 1: A diagram of the three primary ATF capabilities, consisting of the electron LINAC, the LWIR laser, and the NIR lasers. All three capabilities are synchronized and can be used simultaneously for a single experiment.

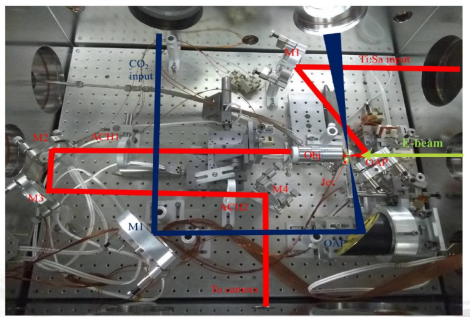


Figure 2: An example of an experimental setup utilizing all three ATF capabilities simultaneously.

ACCELERATOR TEST FACILITY

The Accelerator Test Facility (ATF) has supported user experiments for over 30 years, and, since 2015, has been designated as a DOE Office of Science national user facility [2]. The facility offers three primary capabilities: the electron LINAC, the long-wave infrared (LWIR) laser, and the near-infrared (NIR) lasers, summarized in Fig. 1. A unique feature of the facility is that any combination of the three capabilities can be utilized simultaneously for a single experiment. In fact, around 40 % of user experiments over the past year required the use of all three capabilities, with an example setup shown in Fig. 2.

Content from this work may be used under the terms of the CC BY 4.0 licence (© 2022). Any distribution of this work must maintain attribution to the author(s), title of the work, publisher, and DOI.

ISBN: 978-3-95450-261-5 ISSN: 2673-7000 doi: 10.18429/JACoW-NAPAC2025-THP017

CALCULATIONS OF EMITTANCE MEASUREMENTS VIA INVERSE COMPTON SCATTERING*

M. Kaemingk†, P. M. Anisimov, E. I. Simakov
Los Alamos National Laboratory, Los Alamos, NM, USA
J. B. Rosenzweig
University of California, Los Angeles, CA, USA

Abstract

Recent simulation work has indicated that next generation photoinjectors will be capable of delivering beams with emittances below 100 nm for bunch charges of a few hundred pico-Coulombs. Experimentally validating these results by measuring such emittances is challenging due to the high resolution required. Additionally, in some cases it is desirable for these characterization measurements to be non-destructive, and to have the capability of selecting subsets of the beam. One technique that has been considered is the use of inverse Compton scattering (ICS) spectra to measure the emittance. Here we present simulation results on the use of ICS to measure 50 nm – 500 nm emittances for a 250 pC bunch charge electron beam.

INTRODUCTION

High brightness electron beams have become an important tool in a wide variety of applications. Thus producing and characterizing high brightness electron beams is an important area of research in accelerator physics. High gradient cold copper C-band photoinjectors provide a promising pathway for producing high brightness electron beams [1, 2]. Researching this technology and demonstrating its use in producing high brightness electron beams are some of the aims of the cathodes and radio-frequency interactions in extremes (CARIE) project at Los Alamos National Laboratory (LANL) [3–5].

In previous work we have performed multi-objective optimizations studying the brightness limits of electron beams produced by the photoinjector designed for the CARIE project [6, 7]. In the work reported in Ref. [6], we obtained 2D transverse normalized RMS emittances (hereafter called simply emittances) below 150 nm for beams with 250 pC per bunch. Similar work with 100 pC bunch charge beams, we find emittances below 100 nm. Additionally, in Ref. [7] we explored the use of sacrificial charge to enhance brightness following the work in Ref. [8]. In this mechanism, the initial charge is greater than the final desired charge. During non-laminar focusing of the beam, the space charge forces apply an impulse which linearizes the phase space of a subset of the beam, resulting in a bright core surrounded by diffuse tails, as shown in Fig. 1. In this way, we obtained normalized RMS emittances well below 100 nm for a final bunch charge of 250 pC.

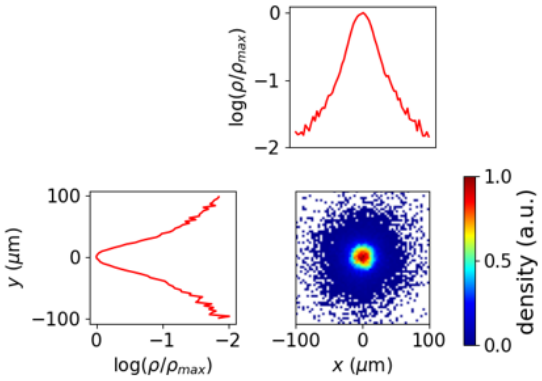


Figure 1: Example beam profile from optimizations using sacrificial charge. The top figure and bottom left figure show the log of the normalized beam profiles. There it is clear the tails do not follow a Gaussian-like distribution, but rather the existence of a halo surrounding the beam core.

Validating these simulation results requires a way to measure emittances on the 100 nm scale. In the case of the simulations with sacrificial charge, it is necessary to measure the emittance of a subset of the beam with dimensions on the scale of 10 m. The resolution required and the need for discriminating between the beam core and the surrounding tails poses a challenge for commonly used emittance measurement techniques. In this work we perform calculations exploring inverse Compton scattering (ICS) as a possible emittance measurement technique.

CALCULATION DESCRIPTION

We compute the ICS spectra in the following way. Using the Distgen package [9], we generate a particle group with properties similar to the beam properties we observed in the optimizations previously mentioned. We vary the emittance of this particle group by setting its transverse momentum spread to $mc\epsilon_n/\sigma_\perp$, where m is the electron mass, c is the speed of light, ϵ_n is the emittance, and $\sigma_\perp$ is the transverse RMS size. For each particle we then carry out the following steps:

- Generate a list of vector corresponding to incident and scattering photon directions.
- Transform the incident and scattered vectors to the particle reference frame.

* Work supported by the Laboratory Directed Research and Development program of Los Alamos National Laboratory under project number 20230011DR.

† kaemingk@lanl.gov

Content from this work may be used under the terms of the CC BY 4.0 licence (© 2022). Any distribution of this work must maintain attribution to the author(s), title of the work, publisher, and DOI.

ISBN: 978-3-95450-261-5 ISSN: 2673-7000 doi: 10.18429/JACoW-NAPAC2025-THP019

COMPLEX BEND PROTOTYPE COMMISSIONING RESULT*

G.M. Wang†, B. Bacha, A. Caracappa, J. Choi, F. DePaola, L. Doom, R. Gambella, Y. Hidaka, Y. Hu, B. Kosciuk, F. Lincoln, D. Padrazo, T. Shaftan, S. Sharma, M. Song, V. Smaluk, R. Todd, X. Yang
Brookhaven National Laboratory, Upton, NY, USA

Abstract

For the NSLS-II upgrade, a novel Complex Bend (CB) optics solution has been proposed to achieve near-diffraction-limited emittance. A key challenge in this design is the requirement for high-gradient quadrupoles (150 T/m) in a compact space. To demonstrate feasibility, a CB prototype was developed and tested using the NSLS-II linac beamline, scaling the beam energy to 100–200 MeV while maintaining strong focusing. The prototype utilized a 16-wedge symmetric Halbach permanent magnet design, achieving a gradient of 140 T/m within ultra-compact quadrupoles. The CB beamline was installed and commissioned in two phases, first as a strong periodic focusing element and later as a combined bending and focusing system. The beam commissioning results showed good agreement with theoretical models, confirming that the Complex Bend functions effectively as both a strong focusing and bending element by offsetting CB poles. This validates the strong focusing design of the Complex Bend for future synchrotron light source upgrades.

INTRODUCTION

The National Synchrotron Light Source II (NSLS-II) is a 3 GeV, third-generation light source at Brookhaven National Laboratory with an emittance at 1 nm-rad in the horizontal plane and 8 pm-rad vertically, providing high brightness. It has been in operation since 2015 and has steadily increased both the beam current and the number of beamlines while maintaining high operational reliability. Currently, there are 29 beamlines in routine operation at a beam current of 500 mA.

To further increase photon brightness and coherence, low emittance is highly desired to enhance experiments' imaging resolution, coherence, scan time, etc. For NSLS-II future upgrade, we explored one optics solution to approach diffraction-limited emittance, using a novel concept, 'complex bend' element [1-3]. Complex Bend (CB) is a sequence of dipole poles with strong alternate focusing to maintain the beta-function and dispersion oscillation at low values. Using Complex Bends instead of regular dipoles in the ring lattice will minimize the $\mathcal{H}$-function and reduce horizontal emittance, while localizing bending to a small portion of the storage ring circumference, thereby freeing more space for insertion devices.

In the complex bend lattice design, a major challenge is achieving the high-gradient focusing quadrupoles of 150 T/m within a compact space. To prove the the feasibility of the full-scale CB for a 3 GeV machine, we designed a prototype of CB by scaling beam energy down to 100-200 MeV while preserving high-gradient focusing for experiments using NSLS-II linac beam. We scaled the Complex Bend parameters from 3 GeV down to 100 MeV, which corresponds to a reduction in magnetic rigidity (BR) by a factor of $C_E = 0.033$. We also reduced the quadrupole pole length by a factor of $C_L = 6$ while keeping the values of bend angle and $\sqrt{K_1}L_Q$ the same as for the 3 GeV CB cell. The drift between the poles is reduced by a factor of 2, considering the space limitations. The CB prototype pole is 46 mm long and consists of four cells, with the field gradient at 150 T/m. The dipole component is realized by offsetting quads in ~mm. Table 1 compares the bend magnet parameters for NSLS-II lattice, upgraded CB lattice scaled prototype.

Table 1: Bending Magnets Parameters

	NSLS-II Dipole	3 GeV CB	100-200 MeV Prototype
Length (m)	2.6	3.1	0.50
Cell Length (cm)	-	62	12.3
Bending Angle per Cell (°)	6	1.2	1.2
Gradient (T/m)	0	250/-250	150/-150
β_{Xmax} / β_{Xmin} (m)	3.7/0.7	0.94/0.22	0.22/0.09
η_{max} / η_{min} (mm)	137/0	4.41/8.52	0.5/0.3

PROTOTYPE OF COMPLEX BEND

To achieve the required high gradient, we adopted a standard 16-wedge symmetric Halbach permanent magnet quadrupole (PMQ) design [4]. As shown in Fig. 1, the overall dimensions of each pole is 46.7 mm (L) × 43.75 mm (W) × 40 mm (H), with a 12.7 mm quad aperture and 8 mm vacuum aperture.

We built a total of nine poles, eight of which were used for the 4-cell CB prototype beamline test. Figure 2 shows the magnetic measurement results. The integrated field ranges from 6.45 to 6.50 T, compared to the specification of 7.05 T. The measured gradient ranges from 137 to 139 T/m, against the specified 149.6 T/m. However, the field variation among the 9 quads is small, <1% difference, with an average gradient of 139.1 +/- 0.6 T/m. Therefore,

* Work supported by DOE under contract No. DE-SC0012704.
† gwang@bnl.gov

Content from this work may be used under the terms of the CC BY 4.0 licence (© 2022). Any distribution of this work must maintain attribution to the author(s), title of the work, publisher, and DOI.

CRITICAL DESIGN ISSUES OF THE NOVEL MULTI-BEAM LANSCE FRONT END

Y. K. Batygin†, Los Alamos National Laboratory, Los Alamos, NM, USA

Abstract

The proposed novel 100 MeV injector for the modernization of the LANSCE Accelerator Facility aims to replace the existing injector based on 750-keV Cockcroft-Walton columns. The specific feature of the LANSCE accelerator is the simultaneous delivery of beams with multiple beam flavors to several targets. The acceleration of various beams in a single RFQ provides less flexibility for optimizing acceleration and focusing parameters compared to the existing LANSCE setup, due to differences in beam current, charge per bunch, and beam emittances. An important issue in the low-energy beam transport of the injector is the different degrees of space charge neutralization of the multi-component beam. Coupling between degrees of freedom in the presence of strong space charge forces of the beams results in unavoidable beam mismatch in the Front End and requires careful six-dimensional matching of beams with accelerator structures. The paper discusses key issues in the proposed Front End and proposes ways to mitigate them.

INTRODUCTION

LANSCE linear accelerator [1] consists of a 201.25 MHz Drift Tube Linac (DTL) accelerating particles from 0.75 MeV to 100 MeV and an 805 MHz Coupled-Coupled Linac (CCL), accelerating particles from 100 MeV to 800 MeV [2]. This accelerator facility simultaneously delivers various beams to multiple targets. A 100 MeV proton beam is delivered to the Isotope Production Facility (IPF), while 800 MeV H- beams are distributed to four experimental areas: the Lujan Neutron Scattering Center, the Weapons Neutron Research facility (WNR), the Proton Radiography facility (pRad), and the Ultra-Cold Neutron facility (UCN). To reduce long-term operational risks and to realize future beam performance goals in support of the laboratory missions, we developed a novel Front End including a high-brightness Radio-Frequency Quadrupole (RFQ) based injector [1, 3, 4].

LOW ENERGY BEAM TRANSPORT

The conceptual layout for the new RFQ-based system contains a 100-keV injector with a 3-MeV RFQ (see Fig. 1). Planned low-energy injector includes two independent transports merging H^+ and H^- beams at the entrance of the RFQ. Beamlines are aimed at performing beam matching with subsequent simultaneous acceleration of H^+/ H^- beams with multiple beam flavors in a single RFQ. Multi-beam structure is achieved with beam chopping and bunching in LEBT.

Because H^- beam leg accommodates 2 different types of beams (LBEG/UCN/pRad and WNR), the transverse matching assumes adjustment of eight Twiss parameters to the RFQ. From the operation experience of exiting the LANSCE facility, it follows that matching of multiple beams requires empirical adjustment of Low Energy Beam Transport (LEBT) elements, since different H^- beams have different emittances and charge per bunch. It is required to have a sufficiently large number of independently controlled focusing elements in LEBT. Figure 1 illustrates the LEBT design with 2 solenoids and 5 quadrupoles per leg, with an additional solenoid in the common LEBT beamline. The 3-MeV Medium Energy Beam Transport contains several choppers and rebunchers to match beams to the novel DTL. After RFQ and MEBT, beams are accelerated in the Drift Tube Linac from 3 MeV up to 100 MeV.

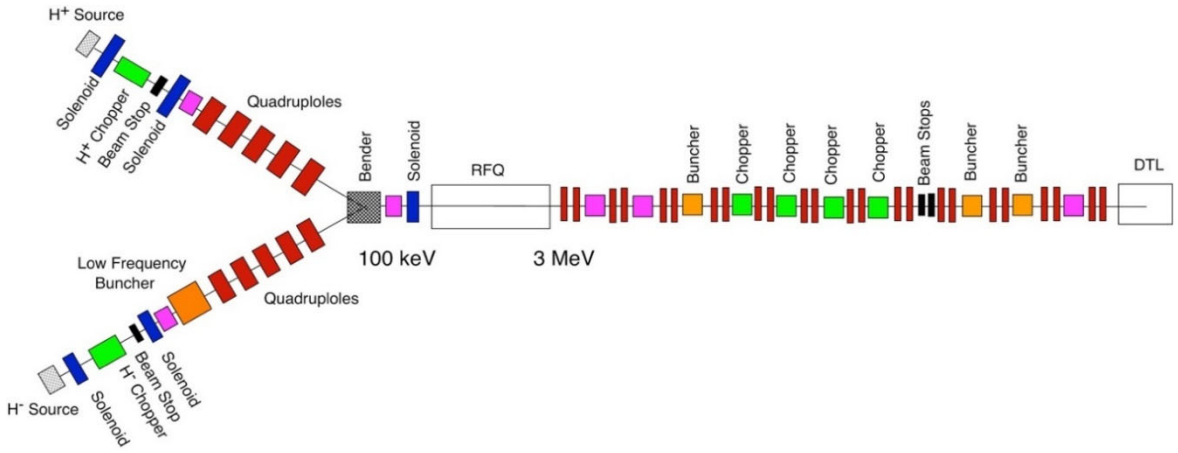


Figure 1: Layout of the proposed LANSCE Front End with distributed beam chopping.

† batygin@lanl.gov

Content from this work may be used under the terms of the CC BY 4.0 licence (© 2022). Any distribution of this work must maintain attribution to the author(s), title of the work, publisher, and DOI.

ISBN: 978-3-95450-261-5 ISSN: 2673-7000 doi: 10.18429/JACoW-NAPAC2025-THP021

IOTA EXPERIMENT FOR PROTON PULSE COMPRESSION AT EXTREME SPACE-CHARGE

J. Eldred, D. Neuffer, J.-F. Ostiguy*, Fermi National Accelerator Laboratory, Batavia, IL, USA

Abstract

A γ_T scheme may be required for the PIP-II era performance or ACE-MIRT era performance of the Booster. PIP-II era operations of the Fermilab proton complex will require the Fermilab Booster to increase beam intensity from 4.5e12 to 6.7e12 protons, while also increasing its ramp from 15 Hz to 20 Hz. These changes pose particular challenges for transition-crossing in the Booster, where longitudinal beam quality must be controlled in order to facilitate slip-stacking in the Recycler Ring later in the Main Injector cycle. Two novel γ_T-jump schemes are proposed, termed "Double γ_T jump" and "Partial γ_T-jump", which optimize the magnitude of the γ_T-jump within optics and power supply constraints.

INTRODUCTION

The Fermilab proton complex is currently constructing the PIP-II Linac [1], the LBNF beamline, and DUNE detectors which constitute an ambitious upgrade of the Fermilab long-baseline neutrino science program and mesonic beamline capabilities. These upgrades will include an increase in Booster beam intensity from 4.5e12 to 6.7e12 and increase in the Booster ramp rate 15 Hz to 20 Hz, requiring a nearly factor of two increase in delivered 8 GeV beam power for neutrino cycles. To reduce beam loss activation under this increased power, successful operations of the PIP-II era Booster requires improved performance at every stage, including transition-crossing.

The recent P5 recommendations [2] illustrate further how the performance of the Fermilab Booster is critical for the advancement of the neutrino science. Area Recommendation 13 specifically states to "assess the booster synchrotron and related systems for reliability risks through the first decade of DUNE operation, and take measures to preemptively address these risks." In addition, P5 Recommendation 2 also calls for the implementation of "ACE-MIRT" [3], which will require the Main Injector to occur nearly twice as frequently, the Fermilab Booster neutrino duty cycle to increase, and the beam quality from the Booster to be improved above current conditions.

In this paper we develop and propose a γ_T-jump system to improve transition-crossing performance of the Booster in the PIP-II era. Although much of the analysis presented here is hardware-agnostic, we further consider the possibility of a γ_T-jump system that could be implemented with existing Booster correctors [4] requiring only a beampipe and power-supply upgrade.

* jseldred@fnal.gov

Table 1: (top) Longitudinal emittance benchmark for present operation and PIP-II era operation. (bottom) Longitudinal emittance from PyORBIT simulations, where the $\epsilon_{95\%}$ has been scaled to match $\epsilon_{97\%}$ in gaussian beams.

Requirements	$\epsilon_{97\%}$	Notes
Present Operation	0.11 eV·s	Elog Apr 2024
Present RF Bucket Limit	0.14 eV·s	[5]
PIP-II requirements	0.10 eV·s	[1]
PIP-II RF Bucket Limit	0.22 eV·s	[5]
Simulations	$1.22\epsilon_{95\%}$	**Notes**
6.7e12 with quad damper	0.15 eV·s	[9] (no jump)
and with $\Delta\gamma_T$ = ~0.24	0.115 eV·s	[9] (30A)
and with $\Delta\gamma_T$ = ~0.82	0.093 eV·s	[9] (55A)

TRANSITION-CROSSING PERFORMANCE REQUIREMENTS

The PIP-II CDR [1] sets an objective for longitudinal beam emittance $\epsilon_{97\%}$ = 0.10 eV·s extracted from the Fermilab Booster to ensure low-loss slip-stacking performance in the Fermilab Recycler. The primary justification for this performance target in the PIP-II CDR is the longitudinal acceptance of the slip-stacking RF bucket, however a more careful analysis by Eldred and Zwaska [5] reveals a substantially looser requirement. In reality, the requirement is more complex: a full consideration should account for the momentum spread after bunch rotation, beam-loading effects in slip-stacking RF cavities, and deliberate misphasing to mitigate Recycler instabilities. Consequently, it is prudent to optimize longitudinal beam quality from the Booster regardless and conservatively it should not deviate too much beyond present performance. A γ_T-jump system may also help with mode-coupling instabilities observed at transition [6, 7].

Recent PyORBIT simulations by Ostiguy [8, 9] have studied the longitudinal beam quality delivered by the Booster, driven by the space-charge inducted mismatch while crossing transition.

Table 1 shows a range of longitudinal emittance benchmarks compared to a range of simulated performances with transition-crossing. The 30-A γ_T-jump may be sufficient for PIP-II era running to achieve performance not far from present operation of the Booster (at lower intensities).

DESIGN CONSIDERATION

Although previously the Booster had a resonant γ_T-jump system [10], it was never used operationally because the Booster had insufficient orbit control. Based on the Teng [11] design, we can estimate the sign and the magnitude of the

Content from this work may be used under the terms of the CC BY 4.0 licence (© 2022). Any distribution of this work must maintain attribution to the author(s), title of the work, publisher, and DOI.

ISBN: 978-3-95450-261-5 ISSN: 2673-7000 doi: 10.18429/JACoW-NAPAC2025-THP022

DESIGN OF A MICROBUNCHED ELECTRON COOLER ENERGY RECOVERY LINAC

K. Deitrick*, S. Benson, B.R. Gamage, J. Guo, I. Neththikumara, R. Rimmer, T. Satogata, N. Sereno, S. Setiniyaz, Thomas Jefferson National Accelerator Facility, Newport News, VA, USA
J. Conway, B. Dunham, R. Eichhorn, C. Gulliford, V. Kostroun, C. Mayes, K. Smolenski, N. Taylor, Xelera Research LLC, Ithaca, NY, USA
W. Bergan, D. Kayran, E. Wang, D. Xu, Brookhaven National Lab, Upton, NY, USA
N. Wang, Cornell University, Ithaca, NY, USA

Abstract

Microbunched electron Cooling (MBEC), a type of Coherent electron Cooling (CeC), is a possible way to cool high energy protons; such an electron cooler can be driven by an energy recovery linac (ERL). The beam parameters of this design are based on cooling 275 and 100 GeV protons at the Electron-Ion Collider (EIC), requiring 150 and 55 MeV electrons, respectively. If implemented, a high energy cooler would serve to increase the average luminosity of the collider by mitigating the emittance growth caused by various processes. This ERL is designed to deliver a bunch charge of 1 nC, an average current of 100 mA, and strict requirements on the transverse emittance, slice energy spread, and longitudinal distribution profile. This paper covers the current state of the design.

INTRODUCTION

The Electron-Ion Collider (EIC) is a partnership project between Brookhaven National Lab (BNL) and Thomas Jefferson National Accelerator Facility (TJNAF) to be constructed at BNL, using much of the existing infrastructure of the Relativistic Heavy Ion Collider (RHIC). Collisions occur between the hadrons in the Hadron Storage Ring (HSR) and the electrons supplied by the Electron Storage Ring (ESR); in order to maintain a high average polarization of the ESR, bunches are frequently replaced using the Rapid Cycling Synchrotron (RCS). While most of the magnets for the HSR are repurposed RHIC magnets, already installed in the existing tunnel, both the ESR and RCS will have to be installed. In the current scope of the EIC, only one interaction region (IR) is supported, sited at the current IR6 of RHIC; however, it is highly desired that a second IR may be supported at IR8 in the future, and design efforts support that eventuality [1].

The present EIC baseline only includes cooling of the injected hadron beam prior to ramping. However, it is possible that a future upgrade to improve the luminosity will be desired, requiring the hadron bunches to be cooled during collision in order to maintain the beam emittance [2].

ERL DRIVEN COOLER

The ERL design presented here is intended to cool a high energy hadron beam with microbunched electron cooling; the lattice is presented with the optics suitable for the EIC 275 and 100 GeV protons, which requires 150 and 55 MeV electrons, respectively. The necessary beam parameters for both energies are given in Table 1; for an explanation of the development of these parameters, please see [3]. Given the significant beam power necessary, it is clear that an energy recovery linac (ERL) is required - the operational power to produce the same beam parameters with a linac is prohibitive; additionally, using an ERL reduces the radiation considerations at the beam dump. Closed optics exist for both operational modes, shown in Fig. 1.

Table 1: The electron beam parameters for the two proton beam energies. The electron beam longitudinal distribution is assumed to be a supergaussian of order ~4.

Proton Energy	**100 GeV**	**275 GeV**
Gamma	107.6	294
Energy (MeV)	55	150
Bunch charge (nC)	1	
Rep. rate (MHz)	98.5	
Avg. current (mA)	98.5	
rms bunch length (mm)	9	7
Peak current (A)	10	13
Slice energy spread $dp/p(10^{-4})$	0.6–1.5	0.4–0.8
Norm. trans. emit. (mm−mrad)	2.8	

LAYOUT

A representative layout of the ERL is shown in Fig. 2. In beamline order during energy recovery, the sections are the injector, the merger, the booster, the bunch compressor and high energy bypass lines (PX), the main linac, the beam dump, the laser heater, transport to the cooling section, the cooling section (modulator, amplifier, and kicker), the first turnaround, the return line, and the second turnaround – after which, the beam begins energy recovery. Alternatively, the beam can be steered through the merger into the diagnostic line.

The injector consists of a photocathode DC gun and a cryomodule containing three superconducting radio frequency (SRF) cavities – two 197 MHz quarter-wave resonators (QWRs) and a 591 MHz single-cell cavity. The beam is

* kirstend@jlab.org

Content from this work may be used under the terms of the CC BY 4.0 licence (© 2022). Any distribution of this work must maintain attribution to the author(s), title of the work, publisher, and DOI.

ISBN: 978-3-95450-261-5 ISSN: 2673-7000 doi: 10.18429/JACoW-NAPAC2025-THP025

DEVELOPMENT OF SODIUM POTASSIUM ANTIMONIDE PHOTOCATHODES FOR USE OF COHERENT ELECTRON COOLING*

K. P. Mondal[1,†], R. Begay[1], L. Cultrera[1], M. Gaowei[1], J. Walsh[1], Y. Yang [2]
[1]Brookhaven National Laboratory, Upton, NY, USA
[2]State University of New York at Stony Brook, Stony Brook, NY, USA

Abstract

Alkali antimonide photocathodes are promising candidates for high-brightness electron sources due to their high quantum efficiency (QE), fast response time, and compatibility with ultra-high vacuum systems. In this work, we report the growth and characterization of Na-K-Sb photocathodes using a custom-built UHV deposition system developed for Coherent Electron Cooling (CeC) applications. Photocathodes were fabricated via sequential deposition of Sb, K, and Na on Mo substrates, followed by optimization of deposition parameters to maximize QE and ensure spatial uniformity. QE maps revealed uniform photocathode response with values reaching ~3.5%, while additional Sb-K "yo-yo" layers further enhanced QE to ~7% with moderate trade-off in uniformity. The films exhibit good thermal and vacuum stability, highlighting their suitability for long-duration accelerator operations. These results demonstrate both the reproducibility and performance potential of Na-K-Sb photocathodes for advanced photoinjector systems.

INTRODUCTION

The Coherent Electron Cooling (CeC) scheme marks a significant advancement in accelerator technology by enabling rapid phase-space cooling of ion beams [1-4]. This method is especially vital for future high-luminosity facilities such as the Electron-Ion Collider (EIC), where maintaining high beam brightness and low emittance is essential for achieving design performance targets [5].

CeC is the photoinjector, which relies on robust photocathodes capable of generating high-current, low-emittance electron beams with minimal dark current and long operational lifetimes. Alkali antimonide photocathodes have emerged as strong candidates due to their combination of high quantum efficiency (QE), fast temporal response, and improved stability in vacuum [6-7].

In particular, Na-K-Sb photocathodes offer better thermal and vacuum stability than more conventional alkali antimonide variants like Cs_3Sb and K_2CsSb. These qualities make them especially attractive for long-duration accelerator operations [8-9].

Beyond QE, the spatial uniformity of the photocathode's QE plays a critical role in determining beam quality. Non-uniform QE distribution can lead to the increase of mean transverse emittance (MTE), current density modulation, and overall degradation of beam performance. Thus, optimizing both QE and its uniformity is crucial for high-brightness beam sources [10-11].

In this work, we report on the growth and characterization of Na-K-Sb photocathodes using a custom UHV photocathode growth system. We emphasize spatial QE uniformity, demonstrate reproducibility across multiple samples, and investigate techniques—such as Sb-K "yo-yo" method—to enhance QE without compromising stability or uniformity.

EXPERIMENTAL

Photocathodes were grown on polished molybdenum (Mo) pucks, which serve as stable and inert substrates for alkali antimonide films. Prior to deposition, the pucks were annealed at 400 °C for 7 hours under ultra-high vacuum (base pressure ~10^{-11} Torr) to remove surface contaminants and improve film adhesion.

Na-K-Sb photocathodes were synthesized using sequential deposition of antimony (Sb), potassium (K), and sodium (Na) in a UHV system (Fig. 1) equipped with in-situ QE monitoring and post-growth QE mapping capabilities. Sb was deposited using a thermal evaporator at a thickness of ~15 nm and a rate of ~2 nm/min under a base pressure of 1.5×10^{-11} Torr. Potassium and sodium were deposited using SAES getter sources, with typical K deposition rates of ~0.8 nm/min.

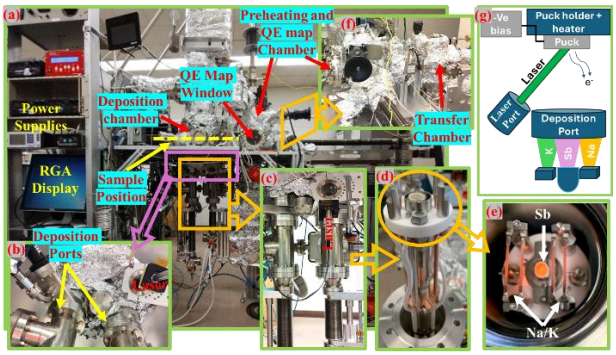


Figure 1: (a) The BNL UHV CeC photocathode growth system at IO, BNL, with in situ QE and QE map measurements, (c) magnified view of attached tube having source cluster inside, (d) both source clusters with electrical connection and crucible, (e) top view of source cluster having alkali material getter source and Sb crucible are indicated, (f) magnified perpendicular view the system where transfer chamber is indicated, (g) schematic of sequential/co-evaporation [12].

The film thickness and deposition rates were monitored using a quartz crystal microbalance (QCM). The substrate temperature was maintained at 90 °C during Sb deposition

* Work is supported by Brookhaven Science Associates, LLC under Contract No. DE-SC0012704 with the U.S. Department of Energy
† kmondal@bnl.gov

Content from this work may be used under the terms of the CC BY 4.0 licence (© 2022). Any distribution of this work must maintain attribution to the author(s), title of the work, publisher, and DOI.

ISBN: 978-3-95450-261-5 ISSN: 2673-7000 doi: 10.18429/JACoW-NAPAC2025-THP026

DEVELOPMENT OF SUPERCONDUCTING ADAPTIVE GAP UNDULATOR (SC-AGU)*

T. Tanabe, M. Musardo, D. Hidas, T. Brookbank, J. Rank, P. N'Gotta
Brookhaven National Laboratory, National Synchrotron Light Source-II, Upton, NY, USA

Content from this work may be used under the terms of the CC BY 4.0 licence (© 2022). Any distribution of this work must maintain attribution to the author(s), title of the work, publisher, and DOI.

Abstract

The concept of the Adaptive Gap Undulator has been proposed for some time. However, utilizing a permanent magnet-based device complicates the design due to the necessity of independent gap control for each segment and, in the case of an in-vacuum undulator, the requirement for a flexible continuity sheet to mitigate image current heating. The adoption of SC magnets eliminates these concerns. The SC-AGU prototype will comprise three sections of magnetic arrays with a total length of 60 cm, with the central section featuring a smaller gap than the end units. To achieve this, a UHV chamber will be designed for eventual fabrication, incorporating a non-uniform aperture that conforms to the beam envelope. Furthermore, to maintain a constant fundamental photon energy and maximize on-axis spontaneous emission, each SC section will be engineered with distinct period lengths, with the central section possessing a shorter period than the end units.

This paper presents the methodology for end-field analysis, encompassing detailed simulations to characterize the magnetic field distribution at the extremities of each magnetic array. Particular emphasis is placed on the impact of field quality at junctions and its influence on radiation properties, ensuring the optimization of on-axis spontaneous emission while preserving the electron beam's 'stay-clear' area and mitigating impedance constraints imposed by the undulator magnet structure. Other practical information such as power supplies, quench detection and vacuum chamber design is also included.

INTRODUCTION

For storage-ring insertion devices (IDs), an increase in ID length necessitates a commensurately wider gap to satisfy the stay-clear aperture constraint. To mitigate this limitation, the constant-resonant-energy undulator (CREU) was proposed [1]. Although the CREU is conceptually ideal, fabricating an undulator with a continuously varying period length along the axial direction is pragmatically challenging. The adaptive-gap undulator (AGU) simplifies the magnetic architecture relative to the CREU [2], particularly when implemented in a superconducting-undulator (SCU) configuration, as it incorporates no moving components.

Our R&D prototype aims to surpass the performance of conventional NbTi-wire-based devices. Nb_3Sn conductors have been demonstrated to generate superior magnetic fields [3]. However, the standard wind-and-react (W&R) process demands reaction at exceedingly high temperatures and protracted annealing intervals. The National Institute for Materials Science (NIMS) is developing ultra-thin A15 composite wires, 0.03–0.05 mm in diameter, to facilitate highly flexible Rutherford cables [4]. Such cables can follow a react-and-wind (R&W) regimen, thereby simplifying yoke fabrication and obviating high-temperature baking.

The principal issues yet to be resolved are: 1) devising a phasing strategy for each segment that preserves an acceptably low phase error; 2) ensuring that R&W Nb_3Sn conductors are deployed with a minimum bending radius exceeding 20 mm to prevent degradation of current-carrying capacity, thereby necessitating the conception of a yoke geometry capable of accommodating this requirement; and 3) developing a novel vacuum chamber featuring a variable aperture.

MAGNET DESIGN

For R&D purpose, an AGU with three short sections (~20 cm each) is proposed. Table 1 shows the essential parameters of magnetic array in each segment. Segments are tuned to the same resonant energy.

Table 1: AGU Array Parameters

	Segment 1 [Center]	**Segment 2 & 3 [Sides]**
Period Length λ_u, [mm]	14.0	15.5
Deflection Parameter K	2.2	2.05
Pole Gap [mm]	5.0	6/5

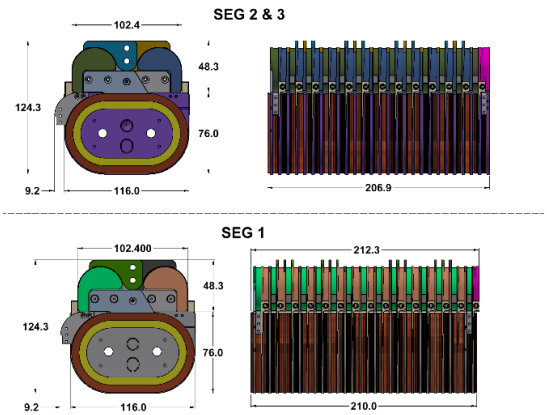


Figure 1: Yoke design for three segments.

The R&W NbSn3 wire requires the minimum bending radius of 20 mm to avoid degradation of performance. Therefore, a novel yoke design with spools for each half period was developed. Figure 1 shows the yoke design for segment 2 and 3 in the upper position, and segment 1

ISBN: 978-3-95450-261-5 ISSN: 2673-7000 doi: 10.18429/JACoW-NAPAC2025-THP027

DEVELOPMENT OF THE ROCKING CURVE IMAGING SETUP AT BL17-2 AT SSRL

Y. Hong *, M.D. Balcazar, R. Robles, R. Arthur, C. Takacs, T. Sato, D. Zhu, A. Halavanau
SLAC National Accelerator Laboratory, Menlo Park, CA, USA

Content from this work may be used under the terms of the CC BY 4.0 licence (© 2022). Any distribution of this work must maintain attribution to the author(s), title of the work, publisher, and DOI.

Abstract

We report the implementation of a silicon (111) channel cut crystal as an x-ray beam expander for the rocking curve imaging (RCI) at Stanford Synchrotron Radiation Light Source (SSRL). Recently, we utilized an undulator source located at beamline 17-2 with the new beam expander to the perform rocking curve imaging of diamond (400) and (220) reflections. The beam expander is installed as part of an existing RCI optics setup, previously commissioned at beamline 10-2. We achieved horizontal beam magnifications of up to $M = 1.38$ at 6.951 keV and $M = 2.25$ at 9.831 keV. This work presents the updated RCI setup, and the experimental results validating its performance. Future improvements to the setup are also mentioned.

INTRODUCTION

Rocking curve imaging (RCI) is a common technique for characterizing diffraction Bragg crystals. The essence of the technique is to prepare a very well collimated beam and rock the crystal in the diffraction plane along the Darwin window. This measurement is typically done in the non-dispersive geometry. Synchrotron light sources, such as bend magnet or wigglers are perfect for RCI as they provide high average photon flux and a spatially large beam size. However, recently more and more synchrotrons employ undulator insertion devices, and with the 4-th generation upgrades, the beam sizes are now much smaller. This fact requires beam expansion, in addition to angular collimation, to perform RCI measurements. In this paper, we report on recent RCI experiments at the SSRL beamline 17-2, using an undulator insertion device.

We previously reported on the RCI program developed at the SSRL beamline 10-2. In brief, the RCI setup supported Bragg and Laue geometry measurements for 5 different photon energies. We refer the reader to the [1] for more information.

At beamline 17-2, asymmetric Bragg reflections are employed for double beam expansion. The experimental setup is schematically shown in Fig. 1(a). The horizontal expander consists of an symmetric-asymmetric channel-cut Si(111) crystal fabricated according to relation described in [2, 3], with dimensions designed for a theoretical magnification of $M = 2.5$ at 9.831 keV (Fig. 1(b)). This value represents a practical compromise between beam size expansion and combined reflectivity in a channel-cut. Figure 2 presents the calculated reflectivity curves (red) for different magnifications, where the observed angular shifts between reflections originate from x-ray refraction at the asymmetric surface (blue). As M increases, the angular overlap between the two reflections reduces, leading to a noticeable reduction in peak reflectivity and integrated diffracted intensity. These findings guide the practical design limits of Si(111) channel-cut beam expander.

The calculated overall diffraction efficiency is summarized in Fig. 3, showing that as M increases from 1 to 7, and a higher-resolution calculation for the practical range $M = 2$ to 4, where a nearly linear reduction in total output intensity and a gradual decrease in peak reflectivity is observed. We also note that for practical reasons, the Bragg angle in the channel-cut expander must be away from 45°, since the x-rays are $\sigma-$polarized. In our setup, the Bragg angle is 11.6° for 9.831 keV, and 16.5° for 6.951 keV.

Also note that, the Si(111) expander is mounted on a precision expander mount designed so that the center of the rotation axis coincides exactly with the center of the symmetric reflection surface. This geometry ensures that the Bragg angle can be adjusted easily when switching between different photon energies, without introducing additional alignment errors other than a horizontal shift. This horizontal shift of the expanded beam when switch between photon energies is less than the width of the analyzer crystal and well within the horizontal travel range of subsequent analyzer crystal and sample mount. The theoretical center-to-center beam offset between incoming beam and expanded beam is 1.7 cm and 2.14 cm for 6.951 keV and 9.831 keV, respectively. As a result, during experiments, the photon energy can be switched without moving either the analyzer or the sample stage.

After the beam has been horizontally expanded, it is propagated into the previously built and commissioned RCI setup with the asymmetric Si (531) crystal [4]. The vertical expansion ratio in the setup is about 30 [1]. The final rectangular, highly collimated beam then illuminates the sample, which is rocked around its Bragg reflection.

EXPERIMENT

Setup

The proof-of-principle experiment was carried out on beamline 17-2 at SSRL. The incoming 9.831 keV x-ray beam of 4 × 0.2 mm was expanded horizontally first to 9 × 0.2 mm with the channel cut expander (Fig. 1(a)), resulting in the magnification value $M = 2.25$. A final beam size of 9 × 8 mm was attained at the sample position (Fig. 1(b)). We also tested the magnification of the channel cut expander at 6.951 keV, with the measured magnification value is $M = 1.38$. We measured the total x-ray transmission (beamline output to the sample) of about 3% at 9.831 keV

* hong274@slac.stanford.edu

ISBN: 978-3-95450-261-5 ISSN: 2673-7000 doi: 10.18429/JACoW-NAPAC2025-THP028

DIGITAL TWIN FRAMEWORK FOR PIP-II LINAC: AI-DRIVEN MULTI-SCALE MODELING FROM ION SOURCE TO 800 MeV

A. Pathak*, P. Hanlet, T. Miceli
Fermi National Accelerator Laboratory, Batavia, IL, USA

Abstract

The PIP-II linac will enable more than 1.2 MW beam power for DUNE, requiring unprecedented operational reliability across its warm front end (RFQ, MEBT) and five distinct SRF sections operating at 162.5/325/650 MHz. We present a comprehensive digital-twin framework that combines a fully differentiable fast beam-transport core with neural-network surrogates trained on high-fidelity PIC simulations, capturing space charge and nonlinear dynamics beyond traditional envelope codes while achieving $10^4\times$ speedup at $< 1\%$ accuracy. End-to-end differentiability enables gradient-based optimization across 500+ parameters simultaneously (impractical with previous tools), while the model incorporates static/dynamic errors and serves as a virtual-commissioning platform for diverse hardware integration. The framework facilitates reinforcement learning for pulsed/CW mode transitions, predictive maintenance through anomaly detection, and autonomous tuning algorithm development with real-time execution capability. Validation against physics simulations shows excellent agreement for the front end, with initial results indicating potential for 30% commissioning-time reduction and proactive fault mitigation, providing a scalable blueprint for operating next-generation high-intensity accelerators.

INTRODUCTION

The PIP-II SRF linac will deliver more than 1.2 MW beam power for DUNE, with a chopped front end (RFQ, MEBT) feeding five SRF sections at 162.5/325/650 MHz. High-current operation imposes tight uncontrolled-loss limits (order 1 W/m in low-energy sections) and frequent retuning under microphonics, detuning, thermal drifts, and hardware constraints [1–3].

Conventional online toolchains—fast linear/second-moment transport with occasional PIC checks—are mismatched to these requirements: envelope models miss nonlinear space-charge and field-map effects that drive halo and loss, while PIC is generally too slow for shot-to-shot supervisory use or many-parameter optimization. Recent advances in differentiable beam-physics [4], controls-integrated virtual accelerators [5, 6], and data-driven optimization/anomaly detection [7–9] enable a different approach.

We present a controls-integrated, *end-to-end differentiable* digital twin for the PIP-II front end. A symplectic transport core M is augmented by a learned surrogate K_θ trained on high-fidelity PIC to capture nonlinear space charge and RF effects, with measured disturbances injected via $E(\xi)$. The mapping, objectives, and gradients are used for state estimation, virtual diagnostics, and (when enabled) tuning under EPICS with policy safeguards. **Scope:** this paper reports read-only (shadow/replay) validation on RFQ→MEBT and HWR lattices, demonstrating task-level accuracy within target tolerances at $\sim 10^4\times$ runtime speedup; closed-loop operation is summarized briefly.

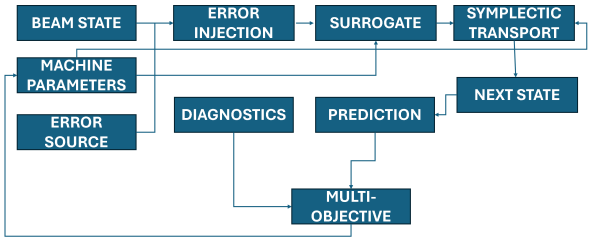


Figure 1: Overview of the differentiable mapping $x_{k+1} = M(p_k) \circ K_\theta(x_k, p_k) \circ E(\xi_k)$ and the objective $J(\mathbf{p})$ that compares predictions $\hat{\mathbf{y}}(s;\mathbf{p})$ to measurements $\mathbf{y}_{\text{obs}}(s)$.

DIGITAL TWIN FRAMEWORK

Problem Formulation

Let $\mathbf{p} \in \mathbb{R}^{N_P}$ denote machine parameters (RF amplitudes/phases, magnet gradients, correctors, chopper timing) and $\mathbf{x}$ the beam state. The differentiable state update is

$$\mathbf{x}_{k+1} = \Phi_\theta(\mathbf{x}_k, \mathbf{p}_k, \xi_k) = M(\mathbf{p}_k) \circ K_\theta(\mathbf{x}_k, \mathbf{p}_k) \circ E(\xi_k), \quad (1)$$

where M is a symplectic transport core, K_θ a learned surrogate trained on PIC data, and E injects error processes ξ_k (misalignments, phase/voltage jitter, microphonics, ripple).

For tuning, we minimize a loss comparing predictions to measurements and penalizing longitudinal mismatch and loss proxies:

$$\min_{\mathbf{p}} J(\mathbf{p}) = \sum_{s\in\mathcal{S}} \Big[w_{\text{orb}} \|\mathbf{y}_{\text{obs}}(s) - \hat{\mathbf{y}}(s;\mathbf{p})\|_2^2 + w_{\text{long}}\, \mathcal{L}_{\text{long}}(s) + w_{\text{loss}}\, \mathcal{R}_{\text{loss}}(s) \Big], \quad (2)$$

where $\mathcal{S}$ indexes BPM/TOF/toroid locations, $\hat{\mathbf{y}}$ are virtual diagnostics from the twin, $\mathbf{y}_{\text{obs}}$ are measurements, $\mathcal{L}_{\text{long}}$ penalizes phase/energy errors, and $\mathcal{R}_{\text{loss}}$ penalizes loss proxies (e.g., halo mass beyond $n\sigma$). Robust variants evaluate J under sampled ξ (expectation or CVaR_α) without optimizing over ξ. Figure 1 summarizes the mapping in Eqs. (1)–(2) and the associated objective.

* abhishek@fnal.gov. This manuscript has been authored by Fermi Forward Discovery Group under Contract No. 89243024CSC000002 with the U.S. Department of Energy, Office of Science, Office of High Energy Physics.

Content from this work may be used under the terms of the CC BY 4.0 licence (© 2022). Any distribution of this work must maintain attribution to the author(s), title of the work, publisher, and DOI.

ISBN: 978-3-95450-261-5 ISSN: 2673-7000 doi: 10.18429/JACoW-NAPAC2025-THP030

EMULATION OF TWO-PASS GAIN IN A CAVITY-BASED XFEL VIA SELF-SEEDING AT LCLS

M. D. Balcazar*, A. Lutman, T. Sato, F. J. Decker, Z. Huang, A. Halavanau, D. Zhu
SLAC National Accelerator Laboratory, Menlo Park, CA, USA

Abstract

This work presents an experimental study emulating a two-pass gain scenario in a cavity-based X-ray free-electron laser (CBXFEL) using a self-seeding configuration at LCLS. In this "7+7" arrangement, radiation generated by the first seven hard X-ray undulators (HXUs) is spectrally filtered by a high-resolution self-seeding crystal monochromator and used to seed a second set of seven undulators downstream. This setup mimics the regenerative amplification process expected in the CBXFEL cavity, where the seed pulse is recirculated and overlapped with a second trailing electron bunch. By systematically reducing the number of post-crystal undulators (from 9 to 5), we quantified the spectral amplification ratio by comparing the self-seeded peak signal to the SASE background. These results confirm the feasibility of seeding with the initial seven HXUs and provide a valuable benchmark for extrapolating gain in future two-bunch CBXFEL demonstration experiments.

INTRODUCTION

The cavity-based X-ray free electron laser (CBXFEL) project [1–6] is an ongoing effort at SLAC to develop the next generation of radiation light sources. In contrast to a conventional FEL where the X-ray pulse is generated through a single pass through the undulators, CBXFEL utilizes four Bragg crystal optics to form a *resonant* cavity. Through this process, the cavity output X-rays promise to deliver a fully coherent beam – both transversely and longitudinally – while simultaneously amplifying the pulse via FEL gain.

The CBXFEL project will make use of the first seven hard X-ray undulators (HXUs) at LCLS in combination with the two-bunch operation mode of the electron accelerator to demonstrate two-pass gain. In this scheme, the first electron bunch generates a seed X-ray pulse that is recirculated through the cavity to overlap both temporally and spatially with the second, fresh electron bunch. Seeding is an active area of R&D in the field of FELs, and self-seeding [1] has become a widely adopted technique at facilities worldwide. As this experiment shows, self-seeding techniques can also serve as a stepping stone toward next-generation light sources. In this study, the two-pass gain envisioned by CBXFEL is emulated using a self-seeding approach. Specifically, the seven designated HXUs [7] are used before the self-seeding crystal and another seven after it, a configuration we refer to as "seven plus seven". This emulation aims to demonstrate that the first seven undulators can effectively serve as a seed, and that the subsequent seven can achieve XFEL gain, as promised by the CBXFEL concept.

* mdbm@slac.stanford.edu

EXPERIMENT

Setup

The experiment was conducted using the hard X-ray beamline at LCLS. The output X-ray spectra were measured using the spectrometer located downstream of the XPP hutch in the LCLS X-ray Transport (XRT) tunnel. To emulate the two-pass gain scheme proposed by the CBXFEL project, a hard X-ray self-seeding (HXRSS) setup was utilized. The first seven CBXFEL-designated HXUs were used to generate the initial pulse, followed by additional undulators positioned after the HXRSS crystal as shown in Fig. 1.

The photon energy selected for this study was 7.625 keV and the primary configuration used the (220) reflection in Laue configuration of the HXRSS diamond crystal. At a wavelength of 7.625 keV the crystal Bragg angle is 40.14°, close to the 45° design angle for CBXFEL at 9.831 keV and (400) reflection. The self-seeding setup was then tuned and optimized to achieve its purpose of spectrum filtering and seed creation.

Afterwards, spectral measurements were performed for a sequence of undulator configurations. Starting with 7+13 HXUs and progressively reducing the number of post-crystal undulators to 7+9, 7+8, 7+7, 7+6, 7+5, and finally 7+0 taken as a reference baseline. For each configuration, the resulting X-ray spectrum was recorded using the XRT spectrometer to characterize the evolution of FEL gain.

Experimental Results

The first step in the analysis included a filter on electron beam parameters. The filter was applied to the raw dataset so that only shots within a narrow ~ 2 MeV e-beam energy window were considered [8]. Similarly, shots were filtered based on the beam peak current, keeping those within a 50 A window band centered at the peak of the distribution. This filtering step was crucial for reducing noise and isolating shots with stable beam parameters for meaningful analysis. Following the filter on electron beam parameters, the filtered shots were further screened based on signal strength (maximum intensity) in the detector for each event. Only the top 10% of shots, ranked by peak signal, were kept for the final analysis. This additional filtering step ensured that only the controlled events with strong, well-defined signals contributed to the results.

After filtering, the data was next processed to obtain an average spectrum from the detector. To suppress noise and emphasize spectral features, a Savitzky–Golay filter (window size of 20 and polynomial order 3) was applied to each dataset. This produced a smoothed signal from the detector.

Content from this work may be used under the terms of the CC BY 4.0 licence (© 2022). Any distribution of this work must maintain attribution to the author(s), title of the work, publisher, and DOI.

ISBN: 978-3-95450-261-5 ISSN: 2673-7000 doi: 10.18429/JACoW-NAPAC2025-THP031

EVALUATING A TRANSITION-JUMP SYSTEM FOR THE FERMILAB MAIN INJECTOR USING XSUITE

A. P. Schreckenberger*, R. Ainsworth, M. Xiao, Fermilab, Batavia, IL, USA

Abstract

We describe an Xsuite simulation framework for the Fermilab Main Injector (MI) along with an evaluation of transition-crossing behaviors in the accelerator. In particular, we studied the introduction of quadrupole magnets into the lattice as part of a transition-jump system that will be implemented through the 2^{nd} Proton Improvement Plan (PIP-II). Simulated beam losses spurred by transition-induced instabilities were assessed under several systematic effects, including MI quad errors, magnet-to-magnet variability in the jump magnets, power-supply errors, and timing jitter.

OVERVIEW

Accelerating particles through transition has yielded well-documented challenges that necessitated both technological developments and the consideration of instabilities [1–3]. Commonly referenced by its Lorentz factor γ_t, an accelerator's transition is set by the lattice. In the Fermilab Main Injector (MI), $\gamma_t \approx 21.6$ and remains static.

Beam behaviors rapidly change as the ramp nears transition, particularly with regard to the longitudinal dynamics, and circular accelerators must quickly shift configuration conditions in order to maintain particle storage. In the MI, flipping the RF phase from ϕ_s to $\pi - \phi_s$ and adjusting the chromaticity are the primary vehicles for retaining stability.

Despite these controls, measurable detriments manifest near the time of the transition crossing (t_{γ_t}), and simulations demonstrate both distortions of the longitudinal phase space and induced beam losses. Figure 1 (*left*) shows the longitudinal phase-space distribution from Xsuite [4] for the MI lattice at 5.25 ms before transition. Comparing this shape to Fig. 1 (*right*), which depicts the distribution near transition, highlights some of the impacts on beam behavior; the bunch length is spatially compressed, and $\delta = \Delta p/p$ is smeared.

In the MI, instabilities and beam losses driven by nonadiabatic motion and chromatic nonlinearities are the primary concerns [5]. Both of these instabilities emerge in time windows around transition, $t_{\gamma_t} \pm T_c$, where T_c refers to either nonadiabatic (T_{na}) or nonlinear (T_{nl}) considerations. Within $t_{\gamma_t} \pm T_{na}$, particles are unable to keep up with the rapidly changing bucket shape. Meanwhile, chromatic nonlinearities induce the Johnsen effect, which generates a non-constant γ_t for the particle ensemble. From the functional forms of T_{na} and T_{nl}, we expect $T_{na} \approx 1.819$ ms and $T_{nl} \approx 1.113$ ms in the accelerator. Using Eqs. (1) and (2), we reconsider the domain of interest in terms of γ units.

$$\Delta\gamma_{na} = \dot{\gamma} T_{na} \approx 255.6\,\text{Hz} \times 1.819\,\text{ms} = 0.465, \quad (1)$$

$$\Delta\gamma_{nl} = \dot{\gamma} T_{nl} \approx 255.6\,\text{Hz} \times 1.113\,\text{ms} = 0.284, \quad (2)$$

* wingmc@fnal.gov

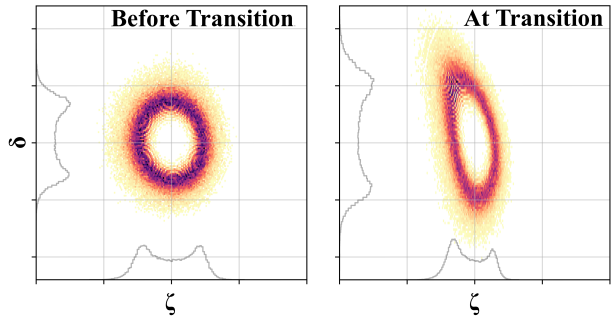


Figure 1: Longitudinal phase-space distributions in arbitrary units for the MI lattice using a predefined particle ensemble. The left distribution is captured 5.25 ms before transition, and the right distribution is captured at transition.

where $\dot{\gamma}$ reflects the ramp rate at the time of transition. This transformation simplifies the process of gauging γ_t mitigation strategies since related beam instabilities can arise at any point during acceleration when $|\Delta\gamma| = |\gamma_t - \gamma| < \dot{\gamma} T_c$.

The assessed γ_t-jump scheme relies on the relationship between γ_t and the lattice. By powering additional quadrupole magnets inserted into the MI, we can alter the value of γ_t and manipulate $|\Delta\gamma|$ to reduce the durations of the instability envelopes and thus energy losses.

XSUITE SIMULATION STUDIES

Using quadrupoles to control γ_t is not a novel concept. The jump scheme selected for this analysis is based on Refs. [6, 7], and both sources predate the MI's construction. While this upgrade method promises improvements in beam efficiency, care must be taken to satisfy constraints with the jump-magnet placements so as not to detrimentally perturb the tunes, dispersions, or betas (β_x, β_y).

Four viable stations, each consisting of two focusing and defocusing quadrupoles, have been identified at locations around the MI ring. The defocusing magnets need to be installed in the straight sections where the dispersion magnitude is minimized, and focusing elements should be placed in the arcs with a π phase advance established between the γ_t-jump elements. In the ideal case, the values of β_x and β_y should be the same across the magnets in a set.

Figure 2 displays the proposed magnet locations for the γ_t-jump system injected into the Xsuite lattice, assuming quadrupole lengths of 21.59 cm. The Courant-Snyder (CS) parameters for these positions are included in Table 1. The four stations are separated into two groups that reflect the MI's symmetry. Across two adjoined stations, the jump magnets are arranged in an F-F-DD-DD-F-F order, where F indicates a focusing magnet, and DD designates two adjacent defocusing quadrupoles. Given space constraints, the

Content from this work may be used under the terms of the CC BY 4.0 licence (© 2022). Any distribution of this work must maintain attribution to the author(s), title of the work, publisher, and DOI.

ISBN: 978-3-95450-261-5 ISSN: 2673-7000 doi: 10.18429/JACoW-NAPAC2025-THP033

FEASIBILITY OF PROTON BUNCH COMPRESSION IN AN OPERATIONAL HIGH-POWER ACCELERATOR*

A. Hoover†, V. Morozov, A. Narayan, M. Piller
Oak Ridge National Laboratory, Oak Ridge, TN, USA

Abstract

A muon collider (MC) would require a high-power proton driver to generate intense muon beams at the start of the accelerator chain. Like other high-power facilities, the driver would accumulate intense proton bunches via charge-exchange injection from a linac into a ring. However, unlike other facilities, the MC would require an extreme longitudinal compression of the bunch. We aim to experimentally study the proposed compression scheme at the Spallation Neutron Source (SNS), which boasts a world-leading proton bunch intensity. In this paper, we describe the operating parameters of the SNS compared to the MC design, the capabilities of the current RF system, and the available beam diagnostics in the SNS accumulator ring. We also present initial simulations and experiments to judge the feasibility of the proposed research.

INTRODUCTION

A muon collider (MC) would require a high-power proton driver (PD) to generate intense muon beams at the start of the accelerator chain [1]. Like other high-power facilities, the PD would accumulate intense proton bunches via charge-exchange injection from an H- ion linac into a ring. However, unlike other facilities, the MC would require an extreme longitudinal compression of the bunch to a few nanoseconds in length. Although the proposed compression scheme is straightforward, the envisioned beam power (2-4 MW), energy (5-10 GeV), repetition rate (10 Hz), and compressed bunch length (2 ns) would lead to an unprecedented charge density that could excite various resonances and instabilities, possibly leading to beam loss.

The Spallation Neutron Source (SNS) at Oak Ridge National Laboratory (ORNL) is a close analogue of the PD and could be used to experimentally test the bunch formation process at high space charge intensities [2]. This paper begins to investigate the feasibility of such experiments. In the following sections, we describe the SNS accelerator layout, operational parameters, and available beam diagnostics. We then discuss a set of initial simulations and experiments performed at the SNS in the past year. Finally, we mention several collective effects that could influence the beam dynamics during compression.

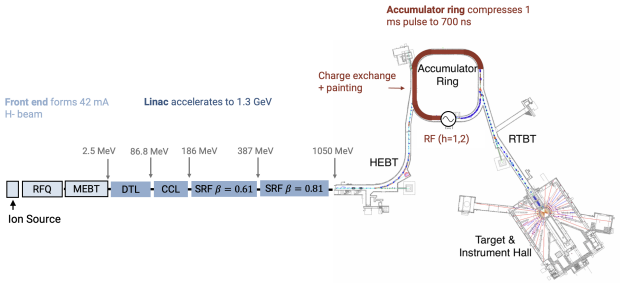


Figure 1: Overview of the SNS accelerator.

SNS FACILITY AND DIAGNOSTICS

A diagram of the SNS accelerator is shown in Fig. 1. The SNS generates neutrons by colliding intense proton pulses with a liquid mercury target. Each so-called *macropulse* on the target is the superposition of over 1000 *minipulses* injected from a 400-meter linear accelerator (linac) into a 250-meter accumulator ring (AR) at 1.3 GeV energy. The accumulated beam is extracted and transported from the ring to the target in a 150-meter Ring-Target Beam Transport (RTBT). The SNS operates at a world-leading 1.8 MW beam power at 60 Hz repetition rate, with plans ramp the power from 1.8 to 2.8 MW over the next few years [3].

Figure 2 shows the space charge perveance $Q \propto \lambda / \beta^2 \gamma^3$ (where λ is the longitudinal charge density and β, γ are the relativistic factors) as a function of the beam energy at 2.8 MW beam power. The dashed line on the far right shows the nominal bunch length in the ring, while the line on the left shows an estimated minimum bunch length after compression. At the nominal beam energy of 1.3 GeV, strong compression would begin to probe the MC space charge regime. The SNS can also lower the beam energy to 0.8 GeV by shutting off cavities at the end of the linac. At this lower energy, moderate to strong compression could probe the full range of possible space charge intensities in the MC.

A suite of diagnostics is available to measure the beam in the SNS accumulator ring (AR). In addition to beam position monitors (BPMs) and beam loss monitors (BLMs), an electron scanner [4] provides instant turn-by-turn beam profiles along the x and y axes. The AR also hosts a beam instability monitor (BIM) [5] to measure fast-rising beam instabilities and a beam current monitor (BCM) to measure the longitudinal charge distribution on each turn. After the ring, four wire scanners (WS) provide slow but stable measure-

* This manuscript has been authored by UT-Battelle, LLC, under Contract No. DE-AC05-00OR22725 with the U.S. Department of Energy. The United States Government retains, and the publisher, by accepting the article for publication, acknowledges that the United States Government retains a non-exclusive, paid-up, irrevocable, world-wide license to publish or reproduce the published form of this manuscript, or allow others to do so, for United States Government purposes. The Department of Energy will provide public access to these results of federally sponsored research in accordance with the DOE Public Access Plan (http://energy.gov/downloads/doe-public-access-plan)

† hooveram@ornl.gov

Content from this work may be used under the terms of the CC BY 4.0 licence (© 2022). Any distribution of this work must maintain attribution to the author(s), title of the work, publisher, and DOI.

ISBN: 978-3-95450-261-5 ISSN: 2673-7000 doi: 10.18429/JACoW-NAPAC2025-THP034

FEASIBILITY STUDIES OF THE STOCHASTIC COOLING SYSTEM IN THE PROTON STORAGE RING EDM EXPERIMENT*

B. Dhital†, H. Huang, W. Morse, and Y. Semertzidis, Brookhaven National Laboratory, NY, USA

Abstract

This study explores the feasibility of implementing stochastic cooling in the proposed proton electric dipole moment (pEDM) storage ring to be constructed at Brookhaven National Laboratory. Investigating fundamental physics phenomena, such as the electric dipole moment (EDM) of protons, demands highly precise experimental setups. In such precision experiments, intra-beam scattering (IBS) causes emittance growth, which degrades beam quality and limits the spin coherence time (SCT), a key parameter for sensitive EDM detection. The integration of a stochastic cooling system for stored polarized proton beams offers a potential solution by mitigating the effects of IBS, suppressing emittance growth, stabilizing beam dynamics, and enhancing the overall efficiency of the storage ring. This paper examines the feasibility of incorporating such a system into the proton EDM storage ring and evaluates its potential to preserve beam polarization and quality, both essential for advancing EDM experiment.

INTRODUCTION

The proton Electric Dipole Moment (pEDM) experiment is the first direct search for proton EDM, aiming to probe Standard Model predictions of any particle EDM [1]. Using a storage ring with "frozen-spin" methodology to detect minute vertical polarization rotations [2], it builds on successful Muon g-2 techniques from Fermilab, Brookhaven, and CERN for long-term charged particle storage with precise spin tracking [3–5]. This paper discusses recent development on pEDM experiment, beam optics design, intra-beam scattering effects, and beam cooling requirements for preserving beam quality and spin coherence time.

The detection of a proton electric dipole moment through storage ring experiments has captivated particle physicists for several decades [6–9]. Recent advances have introduced a novel hybrid storage ring configuration designed to eliminate primary systematic uncertainties under the frozen spin approach. This innovative design employs electric bending plates to guide the polarized proton beam while implementing magnetic focusing in place of electric focusing. The magnetic focusing configuration enables simultaneous clockwise and counterclockwise beam storage, effectively canceling systematic errors associated with out-of-plane dipole electric fields. Systematic uncertainties from quadrupole electric fields can be mitigated through sequential runs employing magnetic focusing of varying intensities [9].

* Work was supported by Brookhaven Science Associates, LLC, under Contract No. DE-AC02-98CH10886 with the U.S. Department of Energy.

† bdhital@bnl.gov

Experimental Technique

The spin $\vec{S}$ precession rate for a particle at rest in the presence of magnetic $\vec{B}$ and electric $\vec{E}$ fields is given by

$$\frac{d\vec{S}}{dt} = \vec{\mu} \times \vec{B} + \vec{d} \times \vec{E}, \tag{1}$$

where magnetic and electric dipole moments are defined as $\vec{\mu} = (gq/2m)\ \vec{S}$ and $\vec{d} = (\eta q/2mc)\ \vec{S}$, respectively. Hence, the above Eq. (1) can be written as

$$\frac{d\vec{S}}{dt} = \vec{\Omega} \times \vec{S}, \tag{2}$$

where $\vec{\Omega} = \vec{\omega}_a + \vec{\omega}_\eta$, ω_a and ω_η stand for precession due to magnetic and electric dipole moments, respectively. For $\vec{\beta} \cdot \vec{E} = 0$ and $\vec{\beta} \cdot \vec{B} = 0$, the motion of the spin vector based on T-BMT [10] simplifies,

$$\vec{\omega}_a = -\frac{q}{m}\left[G\vec{B} - \left(G - \frac{1}{\gamma^2 - 1}\right)\frac{\vec{\beta} \times \vec{E}}{c} + \frac{\vec{B}_\parallel}{\gamma} - \frac{(\vec{\beta} \times \vec{E})_\parallel}{c\beta^2}\right], \tag{3}$$

$$\vec{\omega}_\eta = -\frac{\eta q}{2m}\left[\frac{\vec{E}}{c} + \vec{\beta} \times \vec{B}\right], \tag{4}$$

$$\vec{\Omega} = \vec{\omega}_a + \vec{\omega}_\eta, \tag{5}$$

$$\frac{d\vec{S}}{dt} = \vec{\Omega} \times \vec{S}. \tag{6}$$

Here $\parallel$ represents horizontal (in-plane) projection of a vector and G stands for the proton magnetic anomaly.

Setting $\vec{B} = 0$ and selecting the "magic momentum" $\gamma = \sqrt{1 + 1/G}$ yields the optimal conditions to run this experiment. For protons, the "magic" parameters are given in Table 2. With these parameters, Eq. (3) becomes

$$\vec{\omega}_a = \frac{q}{m\gamma c\beta^2}(\vec{\beta} \times \vec{E})_\parallel. \tag{7}$$

It is now clear that a vertical electric field would generates a nonzero radial component for $\vec{\omega}_a$, which would look like the EDM signal with one beam direction. With horizontal $\vec{E}$ field and $\vec{\beta}(\vec{E} = \vec{E}_\parallel, \vec{\beta} = \vec{\beta}_\parallel)$, the above condition simplifies further into $\vec{\omega}_a = 0$, which is also known as the *frozen spin* condition. In this arrangement, the spin precesses into the vertical direction only due to the EDM contribution,

$$\Omega \propto \eta E, \tag{8}$$

linearly in the timescale of the injection $\Omega \propto dS_y/dt$. And hence $dS_y/dt \propto \eta E$ is the fundamental principle of measuring the proton EDM.The magic momentum parameters for the proton is given in the following Table 1.

Content from this work may be used under the terms of the CC BY 4.0 licence (© 2022). Any distribution of this work must maintain attribution to the author(s), title of the work, publisher, and DOI.

ISBN: 978-3-95450-261-5 ISSN: 2673-7000 doi: 10.18429/JACoW-NAPAC2025-THP035

FINAL DESIGN OF CARIE PHOTOINJECTOR CAVITY WITH PLUG INSERT *

H. Xu†, A. Alexander, P. M. Anisimov, G. Bustos, W. Choi, T. Grumstrup, S. Rocha, E. I. Simakov, T. Tajima, Los Alamos National Laboratory, Los Alamos, USA
G. Lawler, J. Rosenzweig, University of California, Los Angeles, Los Angeles, USA

Abstract

At Los Alamos National Laboratory (LANL), we finalized the design of a 1.6-cell C-band RF photoinjector cavity for the Cathodes And Radiofrequency Interactions in Extremes (CARIE) project. The photoinjector cavity is intended to operate at 5.712 GHz, with an intense electric field on the photocathode up to 240 MV/m, producing 250-pC electron bunches at room temperature. The photoinjector cavity design focused on minimizing the peak electric and magnetic fields. The distributed RF coupling waveguide network design was optimized for achieving minimized vacuum pressure at the photocathode plug emitting surface. Mechanical design considerations included photocathode plug alignment and symmetric ports for incident and reflected laser. The photoinjector was fabricated and was received at LANL in July 2025. In this paper, we report the design, fabrication, and preliminary low-power test results for the photoinjector.

INTRODUCTION

At Los Alamos National Laboratory (LANL), a C-band (5.712 GHz) radiofrequency (RF) photoinjector cavity was developed for testing advanced photocathodes under high accelerating gradients at room temperature. The testing will be performed at the Cathodes And Radiofrequency Interactions in Extremes (CARIE) test stand [1, 2]. We expect to achieve electric field magnitude of 100–240 MV/m at the center of the cathode. The RF photoinjector cavity was fabricated by Dymenso, LLC, located in San Francisco, USA, and received at LANL in July 2025. The cavity is currently under low-power characterization and tuning. A photograph of the photoinjector cavity is shown in Fig. 1.

The 5.712-GHz standing-wave RF photoinjector cavity uses a 1.6-cell, π-mode geometry, which was originally proposed at University of California, Los Angeles (UCLA) [3]. The cell profile optimization for peak electric field mitigation and shunt impedance maximization was provided by SLAC National Accelerator Laboratory. The distributed RF coupling design, photocathode plug insertion geometry in the cavity, and the mechanical engineering and design were completed at LANL. The photocathode plug design was originally invented at INFN, later modified at SLAC. We further revised the plug tip geometry for the CARIE test stand at LANL.

* Work supported by U.S. Department of Energy through the Laboratory Directed Research and Development program of Los Alamos National Laboratory, under project number 20230011DR.

† haoranxu@lanl.gov

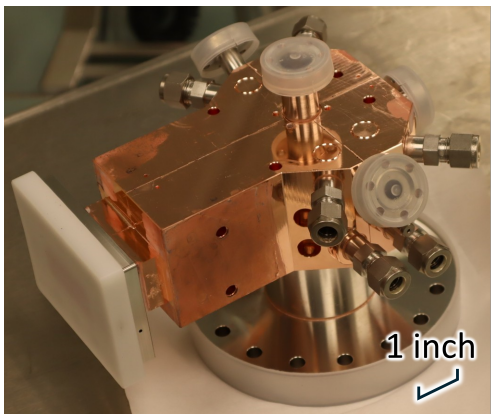


Figure 1: Photograph of the CARIE C-band (5.712 GHz) photoinjector cavity received at LANL.

CAVITY DESIGN

The C-band photoinjector cavity design is illustrated in the three-quarter cross section view in Fig. 2. The cavity was modeled in SolidWorks. The cavity was designed to be fabricated as a brazed assembly of four copper quadrants. The four-quadrant brazing method was applied to fabricate all the features of this new design. In each cell of the cavity, three symmetry stubs were designed to eliminate the dipole mode content of the RF fields; electron beam numerical simulations showed that this geometry significantly reduced the output electron beam emittance [4, 5]. Meanwhile, compared to the previous design [4], the RF coupling waveguide network has been modified to maximize the vacuum conductance for the cathode cell. The vacuum flange on the

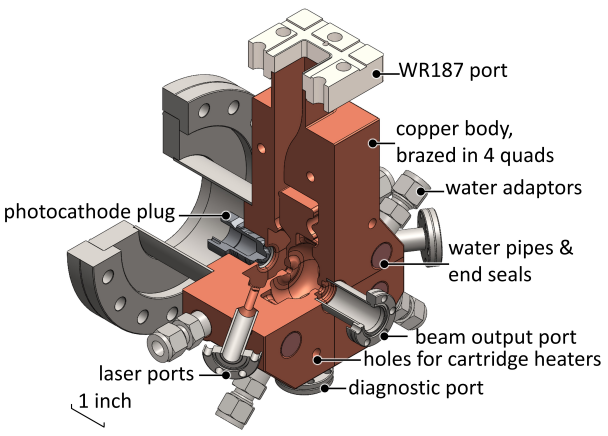


Figure 2: Three-quarter cross section view of the CARIE C-band standing-wave photoinjector design in SolidWorks.

Content from this work may be used under the terms of the CC BY 4.0 licence (© 2022). Any distribution of this work must maintain attribution to the author(s), title of the work, publisher, and DOI.

ISBN: 978-3-95450-261-5 ISSN: 2673-7000 doi: 10.18429/JACoW-NAPAC2025-THP040

GROWTH AND CHARACTERIZATION OF GAAS-BASED SPIN-POLARIZED PHOTOCATHODES*

P. Saha†, L. Cultrera, M. Boukhicha, T. Tsang, L. Lathpandura, R. Bagy, J. Walsh
Brookhaven National Laboratory, Upton, NY, USA
A. Muhowski, S. Hawkins, V. Patel
Sandia National Laboratories, Albuquerque, NM, USA

Content from this work may be used under the terms of the CC BY 4.0 licence (© 2022). Any distribution of this work must maintain attribution to the author(s), title of the work, publisher, and DOI.

Abstract

Spin-polarized electron sources find application in both high-energy and nuclear physics experiments. We describe in detail the design and characterization of different photocathodes based on GaAs/GaAsP superlattice structures. These structures are fabricated with a Distributed Bragg Reflector (DBR) aimed at achieving a high quantum efficiency (QE) ~20% in addition to a high electron spin polarization (ESP) ~85% at the desired wavelength of 780 nm. We present the QE and ESP measurements of photoemitted electrons as a function of wavelength of incident light, along with morphological and photoluminescence measurements.

INTRODUCTION

Spin-polarized electron sources play a critical role in various fields of fundamental physics research, be it nuclear physics or high-energy physics. Examples include the study of nuclear structure, understanding the dynamics of strong interactions, and electro-weak nuclear physics [1].

Historically, bulk GaAs with high quantum efficiency (QE) and moderately high electron spin polarization (ESP) of the order of 35-40% (theoretically the maximum possible ESP 50%), was used as a source of spin-polarized electrons [2]. Strained GaAs-based photocathodes were developed to lift the degeneracy of the heavy-hole (hh) and light-hole (lh) valence bands, which was limiting the ESP to a maximum of 50% in bulk GaAs. The strained photocathodes yielded a higher ESP, but the QE was low due to the low thickness of the samples used to prevent any strain relaxation [3]. To circumvent the problem of low QE and strain relaxation, strain-compensated superlattice (SL) structures based on AlGaAs/GaAs, GaAs/GaAsP, AlInGaAs/GaAsP, InGaAs/AlGaAs, GaAsSb/AlGaAs were designed which were fabricated with a Distributed Bragg Reflector (DBR) [4, 5]. The SL structures leverage the use of quantum wells (QWs) and quantum barriers (QBs) to further increase the hh-lh band splitting while the use of DBR enhances QE by increasing optical absorption through multiple photon passes within the resonant cavity.

* The work is supported by Brookhaven Science Associates, LLC under Contract DE-SC0012704 with the U.S. DOE. Sandia National Laboratories is a multimission laboratory managed and operated by National Technology & Engineering Solutions of Sandia, LLC, a wholly owned subsidiary of Honeywell International Inc., for the U.S. Department of Energy's National Nuclear Security Administration under contract DE-NA0003525.

† psaha3@bnl.gov

To meet the requirements of the different applications of spin-polarized electron sources for example, the Electron-ion collider, International Linear Collider etc, it is critical to push the performance limits of the sources than the existing cathodes in terms of QE and ESP. In this paper, we discuss our effort to design, grow and characterize GaAs/GaAsP based spin-polarized photocathodes to generate electron beam with a high QE and a high ESP simultaneously.

DESIGN AND GROWTH OF PHOTOCATHODE STRUCTURES

The strain-compensated superlattice (SL) photocathodes were grown via the Molecular Beam Epitaxy (MBE) technique at Sandia National Laboratories. These structures were designed to accommodate a large number of GaAs QWs and GaAsP QBs, which enables the production of electrons with both high ESP and QE [6].

The photocathode structure is similar to that reported in the previous works [7], except in the choice of the Fabry–Pérot spacer layer. In the present structure, a nominally 290 nm thick tuning layer $Al_{0.15}Ga_{0.85}As_{0.81}P_{0.19}$ was grown as the Fabry–Pérot spacer instead of $GaAs_{0.81}P_{0.19}$. AlGaAsP was selected for its higher band gap energy, which suppresses electron excitation from this layer within the target wavelength range, thereby preventing dilution of the ESP from unwanted electron contributions.

Material	Thickness (nm)	Doping level (cm^{-3})	
GaAs	4	$p = 3 \times 10^{19}$	
$GaAs_{0.62}P_{0.38}$	3.85	$p = 5 \times 10^{17}$	30 pairs
GaAs	3.85	$p = 5 \times 10^{17}$	
$Al_{0.15}Ga_{0.85}As_{0.81}P_{0.19}$	290	$p = 1 \times 10^{18}$	
$AlAs_{0.78}P_{0.22}$	58	$p = 1 \times 10^{18}$	10 pairs
$GaAs_{0.81}P_{0.19}$	65	$p = 1 \times 10^{18}$	
$GaAs_{0.81}P_{0.19}$	2000	$p = 1 \times 10^{18}$	
GaAs -> $GaAs_{0.81}P_{0.19}$	2750	$p = 1 \times 10^{18}$	
GaAs buffer	200	$p = 1 \times 10^{18}$	
GaAs substrate		$p > 1 \times 10^{18}$	

Figure 1: Schematic of the SL-DBR GaAs/GaAsP photocathode. The GaAs surface layer was capped with amorphous As at the end of the epitaxial growth to prevent any surface contamination.

Figure 1 shows the schematic representation of the complete photocathode structure, consisting of the substrate, DBR, and superlattice layer with a heavily doped final layer

ISBN: 978-3-95450-261-5 ISSN: 2673-7000 doi: 10.18429/JACoW-NAPAC2025-THP041

HIGH ENERGY HEAVY ION SINGLE EVENT EFFECTS (HE HISEE): PLANNING FOR THE FUTURE OF MICROELECTRONICS

K. LaBel[1,†], K. Avery[1], S. Biedron[1], J. DeFilippi[1], D. Marrujo[1], J. Miller[1], G. Van Dyk[1], M. Bedel[2], E. Everts[3], R. Leonard[3], A. Lowe[3], J. Millspaugh[3], M. Stapleton[4], T. Turflinger[5]
[1]Trusted Strategic Solutions (TSS), Roseville, CA, USA
[2]Naval Surface Warfare Center Crane Division, Crane, IN, USA
[3]JRC Integrated Solutions (JRC), Washington, DC, USA
[4]Scientific Research Corporation, Contractor support to the Test Resource Management Center (TRMC) Nuclear Modernization, Atlanta, GA, USA
[5]The Aerospace Corporation, Chantilly, VA, USA

Content from this work may be used under the terms of the CC BY 4.0 licence (© 2022). Any distribution of this work must maintain attribution to the author(s), title of the work, publisher, and DOI.

Abstract

One unique accelerator application is the testing of microelectronics for utilization in space. In particular, space provides two environmental challenges that provide exposure to energetic heavy ions: galactic cosmic rays (GCRs) and solar particle events (SPEs). These particles cause risk by depositing charge in microelectronics, potentially causing operational errors or even destructive failure.

Testing electronics with a variety of ground-based accelerators is not new. What is new is the increasing need for high energy (> 100 MeV/n) heavy ions with ~40% of all testing predicted to require this high energy by 2030. This is primarily for two reasons:

- Mission-enabling advanced stacked microelectronics technologies such as 3D packaged devices that will require higher energy to penetrate to the sensitive locations within these devices.
- Increased demand to perform system-level testing using "large irradiation area" kinematics. This large area also allows for large sample sizes to be irradiated simultaneously for efficiency.

Presently, there is only one domestic accelerator that can achieve high energy heavy ions—Brookhaven National Laboratory's NASA Space Radiation Laboratory. Here, we discuss the requirements needed by the test community and the domestic effort to close the gap in the number of test hours. A current government-funded study is underway to analyze options for the future.

INTRODUCTION

Why are we concerned with GCRs and SPEs? They can cause single event effects (SEEs), see, for example, Refs. [1, 2]. The take home point—an SEE may not cause immediate failures, but they can still have latent damage that causes a failure later-in-time or reduced lifetime. Let's examine.

GCRs (aka heavy ions) are atomic nuclei from which all surrounding electrons have been stripped away during their high-speed passage through the galaxy. Supernova remnants are widely believed to be a major source of cosmic rays, particularly those within our galaxy thought to be accelerated by the powerful shock waves generated during supernova explosions. SPEs are similar particles to GCRs, but they only happen during some solar events. Figure 1 below illustrates what we don't want to see in space: a destructive event. Testing on the ground allows us to determine the sensitivities and find alternatives or safe operational conditions.

There are basically two variants of radiation effects for electronics: long-term/cumulative effects and transient or single-particle effects.

Long-Term/Cumulative Effects

Total ionizing dose (TID) or displacement damage:

- Parametric shifts (e.g., power consumption, operating frequency,…), and /or functional failures;
- Units: krads (material) or displacement damage dose (DDD).

Transient or Single-Particle Effects

Single-event effects (SEEs)

- Soft errors (e.g., bit flip in a memory).
- Hard errors (e.g., device failure or faults that are uncorrectable).
- Single-event latchup (SEL) is a common concern.
- Units: linear energy transfer (LET) in MeV*cm^2/mg (heavy ions); energy in MeV (protons).

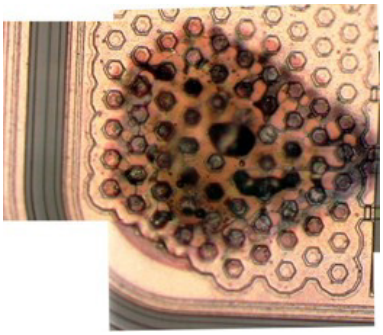


Figure 1: Destructive event in a power device during ground-based SEE testing. Photograph courtesy of NASA.

As seen in Fig. 2, much of what is desired for SEE testing is standard for many facilities that perform science research. However, there are some unique requirements and constraints for SEE testing, see, for example, Ref. [3]. Figure 3 below demonstrates a typical SEE test configuration at a real test. Events are measured on operational

† klabel@tss.llc

ISBN: 978-3-95450-261-5 ISSN: 2673-7000 doi: 10.18429/JACoW-NAPAC2025-THP042

HOLLOW-CORE ANTI-RESONANT FIBER OPTICS AS A PATH TOWARDS PRACTICAL LASER-UNDULATOR BASED X-RAY SOURCES*

G. Bruhaug[1,†], N. Kabadi[2], J.W. Lewellen[1], E.I. Simakov[1], M.S. Freeman[1], J.L. Schmidt[1], B.E. Carlsten[1], N. Yampolsky[1], D.A. Chin[2], G.W. Collins[2], L.P. Neukirch[1]
[1]Los Alamos National Laboratory, Los Alamos, USA
[2]Laboratory for Laser Energetics, Rochester, USA

Abstract

A new technique for laser-electron beam production of monochromatic x-ray sources using hollow-core, anti-resonant fiber optics is explored. This is predicted to produce vastly brighter, more monochromatic (<<1 % BW) x-ray sources than traditional inverse Compton sources and may provide a path towards a practical laser-undulator x-ray source.

INTRODUCTION

Tunable, monochromatic x-ray sources, in the form of x-ray free electron lasers (XFEL) have proven to be revolutionary radiation sources for materials science, biology, and even plasma physics [1]. The utility of such x-ray sources cannot be overstated and there is considerable interest in the construction of more XFELs to serve a broader suite of applications [2]. However, the large size, driven by the need for electrons in the ~10 GeV range, and thus, high cost, of such machines limits the number that can reasonably be built, even for national security applications such as were proposed for the MaRIE XFEL [3]. Significant effort has been focused on improving conventional XFEL technology so as to shrink the machines to a size conceivable for a top-tier research university to construct, although the costs and size would remain large and these techniques rely on nearly order of magnitude leaps in accelerator gradients [2]. Other projects seek to utilize laser-plasma accelerator technology to dramatically shrink the needed accelerator, although challenges remain with achieving the needed beam parameters and achieving the required repetition rate for typical XFEL applications [4].

In addition to the typical technical challenges, there are also materials science applications that require higher x-ray energies [3] than are typical for current XFELs, as well as significant interest in high-brightness pulses for the study of high-energy-density physics (HEDP) conditions [5]. These emerging requirements add further constraints to the challenge of lowering the size, and thus costs, for XFELs or XFEL-like x-ray sources. Typical HEDP applications require $>10^{10}$ monoenergetic photons on target in <100 ps flashes [5], while materials science with high-Z mate-rials demands photon energies approaching 100 keV [2, 3].

A promising solution has been seen in the development of bright inverse Compton Sources (ICS) which can instead utilize 10's of MeV electrons and thus accelerators that are orders of magnitude smaller and cheaper. ICS x-ray sources also have no challenge with 100 keV photon production [6], which is benefi-cial for high-Z material science and nuclear physics. The challenge lies in the typical low brightness of ICS x-ray sources, where photon production scales as Ne instead of Ne2 in XFELs [1, 5, 6]. Thus, large amounts of circulating beam current and scattering lower power are needed to generate useful ICS x-ray sources. Previous work has shown that modern accel-erators and lasers can create ICS x-ray sources that fit some of the needs of HEDP [5] and high-Z material science [6], but there remains many unmet x-ray source requirements for those applications. This paper outlines a proposal to massively enhance ICS x-ray production using Anti-Resonant Hollow-Core Fiber (HC-ARF) optics to increase the interaction length and thus increase the x-ray production efficiency as well as potentially create a true laser-undulator.

INVERSE COMPTON SCATTERING

Inverse Compton Scattering (ICS) can be thought of as the optical analog to a traditional magnetic wiggler and as such is an incoherent photon production pro-cess. The number of x-rays generated, and the central energy can be described by Eq. (1) and (2) [5]:

$$E_x \approx \frac{E_L}{4\gamma^2}\left[1 + a_0^2 + \gamma^2\theta^2 + {\phi^2}/{4}\right] \quad (1)$$

$$N_x = \sigma_T \frac{N_e N_L}{2\pi(\sigma_e^2+\sigma_L^2)}. \quad (2)$$

In Eq. (1) E_x and E_L are the x-ray and laser photon energies respectively, γ is the Lorentzian gamma of the electron beam, a_0 is the normalized laser electric field, θ is the observation angle, and ϕ is the interaction angle (typically 0). For Eq. (2) N_x, N_e, and N_L are the number of x-rays, electrons, and laser photons respectively. The Thompson scatter cross section is σ_T, while the laser and electron beam sizes at interaction are σ_e and σ_L respectively. The inversely quadratic relationship with the beam sizes should be immediately noted and that N_L is very dependent on the interaction geometry. If the length of the scattering volume can be decoupled from the laser spot size via external laser confinement or advanced laser shaping techniques, then N_x scales linearly with interaction region length for a given laser intensity [5].

LASER UNDULATOR

The description of ICS as an optical analogue to magnetic wigglers then naturally lead to the concept of a laser undulator (LU) and true x-ray lasing using only 10's of

* Work supported by the DOE NNS, BeamNetUSA, and NSF OPAL
† gbruhaug@lanl.gov

Content from this work may be used under the terms of the CC BY 4.0 licence (© 2022). Any distribution of this work must maintain attribution to the author(s), title of the work, publisher, and DOI.

ISBN: 978-3-95450-261-5 ISSN: 2673-7000 doi: 10.18429/JACoW-NAPAC2025-THP045

IMPLEMENTATION OF ELECTRON–X-RAY BEAM OVERLAP DIAGNOSTIC INSTRUMENT AT LCLS

M. D. Balcazar*, A. Lutman, F. J. Decker, A. Montironi, D. Cesar, G. Franzen, H. Wang, X. Permanyer, D. Zhu, T. Sato, A. Halavanau, Z. Huang
SLAC National Accelerator Laboratory, Menlo Park, CA, USA

Content from this work may be used under the terms of the CC BY 4.0 licence (© 2022). Any distribution of this work must maintain attribution to the author(s), title of the work, publisher, and DOI.

Abstract

We report on the commissioning results of the newly implemented Beam Overlap Diagnostic (BOD) instrument at the hard X-ray line of the Linac Coherent Light Source (LCLS). As part of the CBXFEL project at SLAC, the instrument is designed to facilitate alignment between the relativistic electron beam entering the undulator line and the X-rays returning from the CBXFEL cavity via the return line. The station features two interchangeable targets: (1) a boron doped CVD diamond screen for direct imaging of the electron beam; and (2) a YAP:Ce scintillator for detecting returning X-rays in the cavity. Emission from either target, whether generated by electron-induced cathodoluminescence or X-ray-induced scintillation, is captured using a nanosecond-resolution fast-gated optical/UV camera. We present results from recent commissioning runs, including direct electron beam imaging, beam size and position characterization in both single- and two-bunch modes, and observations of coherent radiation linked to early microbunching, with implications for the laser heater configuration.

INTRODUCTION

For the next generation of X-ray free electron lasers (XFEL), the cavity-based XFEL is a promising approach to achieve fully coherent X-ray pulses and orders-of-magnitude increased brightness. At the Linac Coherent Light Source (LCLS) at SLAC, the Cavity-based X-ray Free Electron Laser (CBXFEL) project [1–6] aims to utilize four Bragg diamond crystals to circulate X-rays in a rectangular cavity scheme to seed a second electron bunch and achieve two-pass gain. One of the key requirements for the successful operation of the cavity is the ability to overlap the recirculating X-rays with the second fresh electron bunch. This overlap must be achieved both spatially and temporally in order to obtain lasing in the undulator. To achieve the spatial overlap between X-rays and electron beams, a specially designed instrument – known as Station F – was developed.

The paper presents the first commissioning results of Station F, including the direct observation of the LCLS relativistic electron beam in both single- and two-bunch modes. The size and position of the electron beam are directly measured using the beam overlap diagnostic (BOD) instrument across multiple shots. In addition, the effect of background radiation emission from optical microbunching instability along the electron accelerator is investigated, and its relationship to the laser heater energy is characterized.

EXPERIMENT

Setup

The experimental setup utilizes the hard X-ray beamline at LCLS. The BOD instrument, Station F, is located at the entrance of the undulator hall, right after the first CBXFEL chicane and before the first hard X-ray undulator (HXU). The electron bunch energy for this test was 10.7 GeV with a charge of 175.34 pC. Station F consists of two targets mounted on a paddle with a linear stage in the vertical direction. Each target can be individually selected by different encoder positions. The first target is a YAP:Ce with UV fluorescence, which is intended to capture returning X-rays in the cavity [6]. More relevant for this study is the second target, a 5 × 5 mm diamond screen which is suitable to directly image the electron beam through optical cathodoluminescence [7–10]. While the design for Station F consists of a gated Andor iStar camera with wide spectral acceptance, this initial experiment focused on exclusively imaging the electron beam, thus a simple GigE camera along with an optical lens were used. The exposure time was adjusted accordingly to capture the luminescence of the target after the interaction.

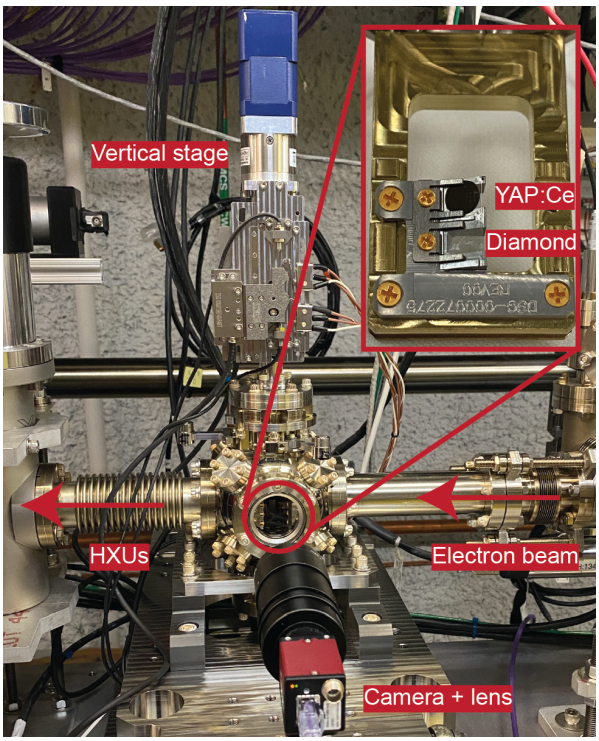


Figure 1: BOD instrument and its interchangeable targets.

* mdbm@slac.stanford.edu

ISBN: 978-3-95450-261-5 ISSN: 2673-7000 doi: 10.18429/JACoW-NAPAC2025-THP047

ISOCHRONOUS INDUCTION CELL STORAGE RING*

M. P. Ehrlichman†, M. Bai, D. Ratner
SLAC National Accelerator Laboratory, Menlo Park, CA, USA
R. G. Boyes, University of Wisconsin, Madison, WI, USA

Content from this work may be used under the terms of the CC BY 4.0 licence (© 2022). Any distribution of this work must maintain attribution to the author(s), title of the work, publisher, and DOI.

Abstract

A challenge in realizing a steady-state microbunching (SSMB) light source is achieving a high average current from a stored beam with a peak current low enough to avoid collective effects that spoil the longitudinal phase space. We are investigating a potential solution to this challenge that combines recent advances in isochronous transport and induction cells. We adapt anti-bend unit cells to yield an arc whose R_{56} can be adjusted near-zero on a per-arc basis. This fine control of momentum compaction allows for better mitigation of effects that spoil the longitudinal phase space. A consequence of RF technology is that high average current can only be achieved in a storage ring by pushing peak current, as only 1-2% of the circumference actually stores current. High peak current drives other design considerations which result in a fast churning of the longitudinal phase space. A ring with low peak current to avoid this churning has an average current too low to be a useful light source. Induction cells with a reset time of 10 ns have recently been developed for cinematographic radiography. An induction cell could allow over 95% of the ring to store current, yielding a high average current and low peak current. Here we outline an investigation to explore the beam dynamics and technology of such an isochronous induction cell storage ring.

INTRODUCTION

As a potential path to a steady-state microbunching (SSMB) light source [1], we are investigating an isochronous storage ring with a continuous beam. A ring that is isochronous to high order on a per-arc basis is obtained by adapting the anti-bend cell design proven in the recently commissioned SLS upgrade [2]. A continuous beam is obtained by replacing the RF system with active-active reset induction cells, a technology that has advanced significantly in recent years [3].

Depicted in Fig. 1, the beam in a conventional light source storage ring is bunched so that only a few percent of the ring circumference contains charge. This is a consequence of the RF system, which is used to restore energy to the beam that is lost in the bend magnets and insertion devices. Without the RF system, the beam energy would decay, and the beam would quickly be lost.

The fraction of the RF cycle where charge can be stored is called an RF bucket, whose height is given by the RF voltage. A high RF voltage is necessary for a long beam lifetime but the sharp slope focuses the beam into a short bunch. In the commonly used 500 MHz RF system, the wavelength is 60 cm long, but the bunch is only about 1 cm long. Thus only about 1.7% of the ring contains charge. Third-harmonic cavities are often used to flatten the potential well and lengthen the bunch, but this yields only a factor of 2 or 3 in lengthening.

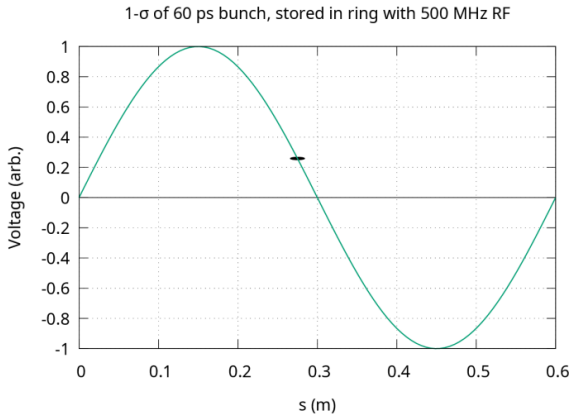


Figure 1: Voltage waveform in a 500 MHz RF cavity. The abscissa is drawn to scale with 1-σ of a 60 ps bunch. Particles can only be stored slightly off the zero-crossing of the RF, leaving most of the waveform devoid of charge.

Recent advances in active-reset induction cell technology raise the possibility of using induction cells in place of RF cavities. An induction cell is essentially a transformer, where one loop of the core is attached to a ramping power supply and the other loop is the beam itself. The power supply is ramped during the beam passage, which generates a dB/dt and delivers an accelerating E-field to the beam. The ramp profile can be shaped to provide barriers at the ends of the ramp. Once per revolution the induction cell must be reset, necessitating a gap in the beam on the order of 10 nanoseconds. In a 100 m storage ring, all but 10 nanoseconds of the ring could contain charge, a greater than 90% fill. More sophisticated ramp profiles, perhaps spanning multiple cells and turns, may be considered to yield a truly continuous beam with 100% of the storage ring containing charge. Thus induction cells raise the possibility of unbunched, continuous-beam electron-storage rings. Assuming a Gaussian profile, each bunch in a 500 mA beam in a 100 m ring has a peak current of 10 A, or about 25×10^7 e$^-$/mm. A continuous beam would have a peak current of about 1×10^7 e$^-$/mm.

Continuous electron beams in induction storage rings have not yet been extensively studied. Induction cells have been tested successfully in proton rings [4, 5]. Recent consideration of induction cell rings is available at [6]. The University

* Work supported by GARD ABP
† mpe@slac.stanford.edu

ISBN: 978-3-95450-261-5 ISSN: 2673-7000 doi: 10.18429/JACoW-NAPAC2025-THP048

LAMP FRONT-END RFQ OPTIMIZATION FOR MICROPULSE PRODUCTION*

H. Xu†, S. Sosa Guitron, D. Gorelov, J. Upadhyay, K. Bishofberger, D. Dimitrov, S. Kurennoy, L. Rybarcyk[1], Los Alamos National Laboratory, Los Alamos, USA
[1]also at COMPA Industries Inc., Los Alamos, USA

Abstract

The LANSCE Accelerator Modernization Project (LAMP) aims at upgrading the front end of the LANSCE accelerator, involving one single radio-frequency quadrupole (RFQ) at 201.25 MHz for simultaneously accelerating both proton (H+) and negative hydrogen ion (H-) beams from 100 keV to 3 MeV. To meet the diverse set of beam requirements at various user stations, the RFQ must be capable of accelerating a continuous-wave-like beam as well as a pulsed input beam. We introduce the design optimization of the LAMP conceptual design RFQ, ensuring that all LAMP key performance parameters are satisfied. The optimization of the overall configuration of the low energy beam transport (LEBT) beamline for shaping the phase spaces of the WNR beam pulse at the entrance to the RFQ is also addressed.

INTRODUCTION

At Los Alamos National Laboratory (LANL), the Los Alamos Neutron Science Center (LANSCE) accelerator system has been in operation for over fifty years, and modernization is now essential to ensure continued support for future experiments. The LANSCE Accelerator Modernization Project (LAMP) aims to upgrade the front end of the LANSCE accelerator system, highlighting an injector system based on a 201.25-MHz radio-frequency quadrupole (RFQ) [1]. The scope of LAMP upgrade is from the ion sources to the exit of the Drift-Tube Linac (DTL). The LAMP project will lead to enhanced reliability and improved beam quality at LANSCE.

At LANSCE, both proton (H+) beams and negative hydrogen ion (H-) beams are produced. The proton (H+) beam is provided for the Isotope Production Facility (IPF) at 100 MeV. For the negative hydrogen ion (H-) beam, several distinct timing structures are established. Short beam pulses with a period of 1.8 µs are provided to the Weapons Neutron Research (WNR) facility; each short pulse (also referred to as a "micropulse") is formed by H- particles captured within one 201.25-MHz RF period (5 ns) by the end of the DTL at 100 MeV, which is further accelerated by the Coupled-Cavity Linac (CCL) to 800 MeV. The H- beam for most other experimental facilities are continuous-wave-like (CW-like) [2].

* This work benefited from the use of the LANSCE accelerator facility. Work was performed under the auspices of the US Department of Energy by Triad National Security under contract 89233218CNA000001.

† haoranxu@lanl.gov

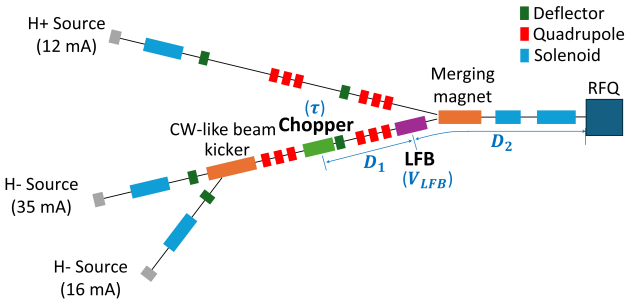


Figure 1: Schematic of the LAMP front end beamline, from the ion sources to the RFQ. The medium-energy beam transport beamline and the DTL sections of the LAMP beamline are not shown.

The LAMP front end must produce identical beam species and timing structures as those currently available at LANSCE. A schematic of the LAMP conceptual design beamline from the ion sources to the RFQ is provided in Fig. 1. One H+ ion source and two H- ion sources are involved. The 16-mA H- source provides the input beam for the CW-like time pattern, and the 35-mA H- source provides the input beam to be shaped into the WNR timing structure. To form the WNR beam pulse for input into the RFQ, the low-energy beam transport (LEBT) uses a chopper to produce a 20–30 ns H- pulse, which is then modulated by a subharmonic (low-frequency) buncher (LFB) to velocity-bunch the beam, providing an increased instantaneous current at the center of the pulse. The merging magnet deflects the H+ and H- beams to be merged before they enter the RFQ. In particular, the H+ beam and the WNR H- beam are accelerated simultaneously by the RFQ.

During the conceptual design stage of LAMP, the most significant challenge was to ensure that the WNR beam (micropulse) should contain sufficient beam charge within a single bunch. Now, the LAMP conceptual design has been developed and all requirements imposed by the key performance parameters (KPPs) have been met. An overview of the conceptual design parameters of the LAMP RFQ is provided in Table 1.

RFQ PARAMETRIC STUDY

As mentioned above, the LAMP RFQ is used for bunching and accelerating both the H+ and H- beams, and for all timing patterns. Therefore, when designing the RFQ, the parametric optimization was multifaceted. Three major factors were considered: CW-like H- beam transmission, its emittance at

Content from this work may be used under the terms of the CC BY 4.0 licence (© 2022). Any distribution of this work must maintain attribution to the author(s), title of the work, publisher, and DOI.

ISBN: 978-3-95450-261-5 ISSN: 2673-7000 doi: 10.18429/JACoW-NAPAC2025-THP051

LOW ENERGY ACCELERATOR DEVELOPMENT FACILITY UPGRADES*

S. V. Shchelkunov†,1, J. Alzamora[1], M. Babzien[1], M. Fedurin[1], T. Ilardi[1], V. Janucik[2], K. Kusche[1], A. Lueangaramwong[1], W. Li[1], R. Muskopf[3], M. Palmer[1], M. Peniera[1], K. Roy[1], Y. Sakai[1], A. Simmonds[1], G. Stenby III[1], L. Wallace[4]
[1]Brookhaven National Laboratory, Upton, USA
[2]St. John's University, Jamaica, New York, USA
[3]SUNY New Paltz, Paltz, USA
[4]Stony Brook University, Stony Brook, USA

Abstract

The Low Energy Accelerator Development (LEAD) Facility is a part of the Accelerators Facilities (AF) Division of the Brookhaven National Laboratory (BNL). The facility has three capabilities and runs a program specifically targeting new collaborations for user-driven research. The first and oldest of capabilities is the Ultrafast Electron Diffraction (UED) capability. The other two are radiation-shielded bunkers.

At the UED, the deployment of a new stable solid-state modulator and klystron is in progress. The beamline updates are now being introduced into place for a National Aeronautics and Space Administration Jet Propulsion Laboratory (NASA JPL) electron irradiator for Single Event Effects (SEE) testing; and the capability for UED testing is being expanded.

In both bunkers (153 and 77 sq. m) a range of cooling, air, electrical, fire protection, and RF (radio frequency) capabilities are presently being introduced. The first bunker will accommodate the Electron Cyclotron Resonance (eCRA) Demonstrator (a project together with Omega- P R&D). The deployment is expected to start in the last quarter of 2025.The second bunker will accommodate the superconducting radiofrequency (SRF) photo-gun (a project by Euclid Techlabs, LLC) to be the electron beam source for an envisioned Ultrafast Electron Microscopy (UEM) capability.

LEAD FACILITY

The LEAD Facility is in building 912 at BNL (Fig.1). It is a part of the Accelerators Facilities (AF) Division [1] together with the Accelerator Test Facility (ATF). Unlike the ATF, however, the LEAD is a non-dedicated user facility.

RADIATION-SHIELDED BUNKERS

The two shielded bunkers are available with shielding being two layers of concrete blocks to eliminate seams. The roof's total thickness is 1.35 m; the wall's total thickness is 1.83 m.

As of now, both bunkers (Fig. 2) have distributed piping for the compressed air serviced by a central compressor located outside the bunkers at about 100 psi. The cooling pipes are connected to the two Carrier Aqua Snap chillers located outside the building (Fig. 3, left). There are cable trays in a configuration that separate power, signal and magnet power cables.120 V, 208 V, and 480 V electric services are installed with house and experimental power separated.

A new storage cage was erected with work areas for the user technical support (Fig. 3, right).

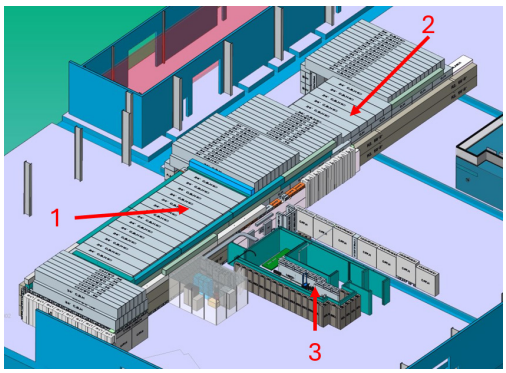


Figure 1: LEAD Facility capabilities – bunker #1 (1), bunker #2 (2), and the UED (3).



Figure 2: Bunker utilities – compressed air (left, 1), cooling (left, 2), cable trays (left, 3), and electrical (right).



Figure 3: Carrier Aqua Chillers (left), and the storage cage with work areas outside the bunkers (right).

* Described upgrades are supported by the Office of High Energy Physics, US Department of Energy (DoE)
† sshchelku@bnl.gov

Content from this work may be used under the terms of the CC BY 4.0 licence (© 2022). Any distribution of this work must maintain attribution to the author(s), title of the work, publisher, and DOI.

ISBN: 978-3-95450-261-5 ISSN: 2673-7000 doi: 10.18429/JACoW-NAPAC2025-THP052

MEASUREMENTS OF SINGLE-SHOT ATTOSECOND X-RAY PULSES AT HIGH REPETITION RATE*

V. Guo†, P. Franz, E. Isele, R. Robles, E. Thierstein, J. Wang
Stanford University, Stanford, CA, USA
K. Borne, M. Britton, D. Cesar, X. Li, M.F. Lin, R. Obaid, N. Sudar, J. Cryan, T. Driver, A. Marinelli
SLAC National Accelerator Laboratory, Menlo Park, CA, USA

Abstract

Electron dynamics in molecules occur on attosecond timescales and drive fundamental processes such as photosynthesis, catalysis, and chemical bond transformations. Understanding these phenomena requires tools with both high temporal resolution and the capability to probe molecular dynamics at high repetition rates. Here, we present the first single-shot measurements of attosecond soft X-ray pulses at the superconducting LCLS-II accelerator. Using an angle-resolving electron time-of-flight spectrometer, we perform angular streaking measurements with high energy and angular resolution, enabling a complete reconstruction of the spatial and temporal profiles of the pulses. These measurements showcase the attosecond science capabilities of LCLS-II at unprecedented repetition rates and provide the foundation for controlling and shaping X-ray pulses to study ultrafast dynamics in complex systems with precision.

INTRODUCTION

Electronic motions in molecular systems occur on sub-femtosecond time-scales. In order to resolve these dynamics, sub-femtosecond sources are needed. Previous experiments at LCLS have demonstrated attosecond capabilities at 120 Hz. This operation mode, named X-ray laser-enhanced attosecond pulse generation (XLEAP), can provide isolated attosecond pulses with tens of microjoules of energy, which is more than six orders of magnitude greater compared to common table-top high harmonic generation (HHG) sources [1, 2]. Here, we report the development of attosecond pulse generation to kHz repetition rates and a pulse reconstruction technique for full spectrotemporal characterizations.

METHODS

Data Collection

The X-ray pulse characterization is done via angular streaking measurements taken with a Multi-Resolution 'Cookiebox' (MRCO) detector, which consists of 16 time-of-flight (ToF) spectrometers forming a circular array in the plane perpendicular to the direction of X-ray propagation [3]. It is designed to be compatible with the ultimate 1 MHz repetition rate of LCLS-II, replacing the coaxial velocity mapping imaging spectrometer from previous LCLS pulse measurements, which can only operate at low repetition rates [4]. During data collection, x-rays ionize a sample gas, generating photoelectrons that are then streaked with an overlapped circularly polarized infrared laser. The spectrometer records hits from photoelectrons as digitized times of flight from the interaction point to the detectors.

Pulse Reconstruction

The X-ray pulse reconstruction is done using gradient descent optimization based on a basis representation of isolated attosecond pulses (IAPs) [5]. Since the spectral profiles of IAPs approximately have compact support, based on the Nyquist-Shannon sampling theorem, the electric field of an X-ray pulse can be completely determined by the reconstruction of points sampled above twice its bandwidth. The Whittaker-Shannon interpolation formula then allows the field to be represented by a decomposition onto a basis of orthogonal sinc functions,

$$E(t) = \sum_k E(t_k)\,\mathrm{sinc}(p(t - t_k)), \tag{1}$$

where p is the sampling frequency [6, 7].

The effect of streaking can be simulated for each basis function from analytically solving the time-dependent Schrodinger equation for the laser-atom interaction in the Strong-Field Approximation (SFA). Then, the probability distribution of photoelectrons associated with an IAP can be decomposed into

$$b(\vec{p}) = \sum_n c_n f_n(\vec{p}), \tag{2}$$

where $f_n(\vec{p})$ is the simulated streaking pattern of each basis function. The measured streaking pattern in experiment can then be described by

$$B(\vec{p}) = \sum_n \sum_m c_n^* c_m f_n^*(\vec{p}) f_m(\vec{p}), \tag{3}$$

and the basis coefficients c_n can be optimized to reconstruct the original X-ray electric field [5].

PRELIMINARY RESULTS

Simulation

To demonstrate the possibility of pulse reconstruction under experimental conditions and estimate the error in reconstructions, we first perform reconstructions on simulated attosecond pulses. Streaking traces are calculated from SFA simulations, and Poisson sampling noise is added to the sim-

* This work was supported by US Department of Energy contract nos. DE-AC02-76SF00515, the DOE-BES Accelerator and detector research program, and DOE-BES, Chemical Sciences, Geosciences, and Biosciences.

† vguo@slac.stanford.edu

Content from this work may be used under the terms of the CC BY 4.0 licence (© 2022). Any distribution of this work must maintain attribution to the author(s), title of the work, publisher, and DOI.

ISBN: 978-3-95450-261-5 ISSN: 2673-7000 doi: 10.18429/JACoW-NAPAC2025-THP053

MEASURING ORBIT RESPONSES WITH OSCILLATING TRAJECTORIES IN THE FERMILAB LINAC*

A. Shemyakin†, A. Pathak, R. Sharankova, Fermilab, Batavia, IL, USA

Abstract

Recording changes in beam transverse positions reported by Beam Position Monitors (BPMs) in response to a beam deflection by an upstream dipole corrector (orbit response) is a powerful tool for analysis of accelerator optics and assisting with machine tuning. In the Fermilab Linac, orbit responses are recorded by oscillating the currents of up to 19 correctors, providing faster, drift-resistant measurements through frequency-domain analysis. This report describes the technique, including error estimations and consistency checks and shows an example of the measurements.

INTRODUCTION

The linear properties of transverse accelerator optics can be characterized using Orbit Response Matrix (ORM) that contains responses of BPMs to changes in currents of dipole correctors [1, 2]. Initially started in the circular accelerators, similar techniques are being applied now to linear [3] accelerators as well. A powerful way to record the ORM is to use sinusoidal excitation of the correctors. It is used in the rings (for example, [4,5]) but commonly not in the linacs. Here we are describing the method (mostly following Ref. [6]) and details of its implementation at Fermilab 400 MeV Linac and show a corresponding example.

METHOD

In a beam line or linear accelerator with uncoupled linear optics, the change of the beam position Δx_j recorded by a BPM #j at the longitudinal location z_j is proportional to deflection by the dipole corrector $\Delta\theta$

$$\Delta x_j\left(z_j,t\right)=\Delta\theta\sqrt{\beta_x\left(z_j\right)\beta_{x1}}\sin\varphi_j, \tag{1}$$

where β_{x1} and $\beta_x\left(z_j\right)$ are Twiss beta-functions in the location of the corrector and BPM, correspondingly, and φ_j is the betatron phase advance between the corrector and the BPM.

Let the corrector current change with time in sinusoidal manner with frequency $fc=\frac{\omega}{2\pi}$ producing the deflection amplitude θ, while recording N_p BPM readings with frequency fb at moments $t_k=\frac{k}{fb}$. The set of readings is

$$x_{jk}\equiv\Delta x_j\left(z_j,t_k\right)=$$

$$=aO_j\sin\omega t_k=\theta\sqrt{\beta_x\left(z_j\right)\beta_{x1}}\sin\varphi_j\sin 2\pi k\frac{fc}{fb}. \tag{2}$$

Application of the Discrete Fourier Transform (DFT) to the data set $\left\{x_{jk}\right\}$ delivers the frequency components c_{jm}:

$$c_{jm}=\frac{1}{\sqrt{N_p}}\sum_{k=0}^{N_p-1}x_{jk}e^{i\frac{2\pi m}{N_p}k}. \tag{3}$$

Since x_{jk} are real numbers, the spectrum is mirror-symmetrical with respect to its center, and below only frequency components $0\le m\le\frac{N_p}{2}$ are considered.

The oscillation frequency and the total number of sampling points can be chosen so that

$$N_p\frac{fc}{fb}=P, \tag{4}$$

where P is an integer indicating the number of full oscillations periods during the measurement. In this case, direct substitution of Eq. (2) and Eq. (4) into Eq. (3) yields only the line at the driving frequency:

$$c_{jm}=\begin{cases}\frac{\sqrt{N_p}}{2}aO_j, m=P\\ 0, m\ne P\end{cases} \tag{5}$$

The set of the measured oscillation amplitudes $\left\{aO_j\right\}$ for the given deflection defines the orbit response (or "differential trajectory"). Note that DTF returns amplitudes and phases. The phase follows the phase of the exiting signal or, if the positive change of the corrector current results in a negative BPM response, it is shifted by π. Correspondingly, the differential trajectory component is equal to the amplitude or its negated value.

As soon as the condition of Eq. (4) is fulfilled, the BPM response is a single line in the frequency domain. It allows oscillating simultaneously multiple correctors at different frequencies, extracting the differential trajectory for each corrector from the same BPM signal at the corresponding frequencies [4]. The spectrum will show a peak for each k-th corrector at harmonic P_k.

The error of measuring the oscillation amplitude is determined by the strength of the noise component at the driving frequency $\sigma_j L$. In approximation of low-amplitude white noise around the oscillation frequency, it can be estimated [6] as

$$\sigma_{jP}=\frac{\sigma_{noise}}{\sqrt{2}}, \tag{6}$$

where σ_{noise} is the rms value of the recorded frequency components with exclusion of all oscillation frequencies and specific components (e.g. low-frequency drifts or power supply noise) observable without excitation. The signal-to-noise ratio $\left(S/N=\frac{aO_j}{\sigma_{jP}}\right)$ improves with the number of recorded points as $1/\sqrt{N_P}$, and the differential trajectory can

* This work was produced by FermiForward Discovery Group, LLC under Contract No. 89243024CSC000002 with the U.S. Department of Energy, Office of Science, Office of High Energy Physics.

† shemyakin@fnal.gov

Content from this work may be used under the terms of the CC BY 4.0 licence (© 2022). Any distribution of this work must maintain attribution to the author(s), title of the work, publisher, and DOI.

ISBN: 978-3-95450-261-5 ISSN: 2673-7000 doi: 10.18429/JACoW-NAPAC2025-THP054

MITIGATING TRANSITION IN THE FERMILAB BOOSTER USING A TRIPLE PHASE JUMP *

J.-F. Ostiguy†, C. M. Bhat
Fermilab, Batavia, IL, USA

Abstract

The PIP-II project will significantly enhance neutrino production for DUNE, Fermilab's flagship long-baseline neutrino oscillation experiment, by doubling the beam power delivered by the accelerator complex. To achieve this, the total charge injected from the new PIP-II linac into the Booster rapid cycling synchrotron (RCS) will increase from 4.5×10^{12} to 6.5×10^{12} protons per pulse. Simultaneously, the Booster's ramp rate will rise from 15 to 20 Hz, while the injection energy will go from 400 MeV to 800 MeV.

The Booster accelerates the beam to 8 GeV and crosses transition at $\gamma_t = 5.45$. In current operations, no dedicated γ_t jump system is employed; instead, longitudinal emittance growth is controlled via an active quadrupole-mode feedback system. Downstream, the Recycler Ring uses slip-stacking to accumulate beam and increase bunch intensity. However, this process imposes a constraint on the longitudinal emittance at Booster extraction, limiting it to 0.1 eV·s (95%) to avoid excessive particle loss.

Because collective effects scale with intensity, additional measures to mitigate transition crossing may be required to stay below this limit. One potential approach is the so-called triple phase-jump technique. While the method has known limitations, it offers some advantages: it can be implemented using the existing digital low-level RF (LLRF) system, requires no additional magnets or pulsed power supplies, and remains compatible with quadrupole-mode feedback.

INTRODUCTION

The PIP-II project currently under construction at Fermilab will replace the existing 400 MeV warm linac with a new 800 MeV superconducting machine. The total charge injected from the new PIP-II linac into the Booster rapid cycling synchrotron (RCS) will represent an increase from 4.5×10^{12} to 6.5×10^{12} protons per pulse. Simultaneously, the Booster resonant power supply system will be modified to increase the ramp rate from 15 to 20 Hz.

The Booster accelerates the beam to 8 GeV and crosses transition at $\gamma_t = 5.45$. In current operations, no dedicated γ_t jump system is employed; instead, longitudinal emittance growth is controlled via an active quadrupole-mode feedback system. To further increase intensity, the extracted beam is slip-stacked at fixed energy in the downstream Recycler ring. It is subsequently transferred to the main Injector synchrotron and accelerated to 120 GeV. The slip-stacking process imposes a constraint on the longitudinal emittance at Booster extraction. To prevent excessive particle loss, this limit is set 0.1 eV-s (95%).

A distinctive feature of the Fermilab Booster is that the bending magnets entire aperture is under vacuum and the beam is directly exposed to the magnet laminated poles. This arrangement side steps issues with eddy currents induced in a metallic beam chamber by the rapidly changing bending field. A downside of the design is that both the resistive and the reactive parts of the longitudinal impedance are substantial and exhibit a complicated frequency dependence [1].

TRANSITION

In general, deviations in both synchronous orbit size L_s and particle velocity v_s are proportional to momentum deviation. The force experienced by a particle depends on the rf phase when it arrives at a cavity; particles which deviates from the synchronous momentum experience phase slippage due to slightly different revolution frequencies. The phase slip factor η is defined as the relative change in frequency per unit of change in relative momentum deviation:

$$\eta = \frac{\Delta\omega/\omega_s}{\Delta p/p_s} = \left[\frac{\Delta v}{v_s} - \frac{\Delta L}{L_s}\right] . \quad (1)$$

Transition takes place when η changes sign. To preserve stability, the rf restoring force must also change sign. For a single particle crossing transition is accomplished in a transparent way, by simply jumping the rf phase from ϕ_s to $\pi - \phi_s$ at the precise instant where the energy reaches $\gamma = \gamma_t$.

In the presence of collective effects, while the rf force changes sign, the collective forces do not. The net focusing mismatch across transition causes phase space filamentation and emittance increase. Other phenomena also contribute and may also be significant; they are not addressed here. The magnitude of the mismatch scales with intensity, making it likely that additional special measures will be needed to limit the emittance blowup in the PIP-II era. By far the most effective is the so-called gamma-t jump which involves very rapidly changing the slip factor by pulsing a set of dedicated quadrupoles at transition. While it is not excluded, cost considerations aside, a gamma-t jump system presents special technical difficulties in a machine like the Fermilab Booster where combined function magnets are used to achieve a high packing fraction and available space is at a premium.

In this context, we have been exploring less effective mitigation techniques that may nevertheless be useful, more economical and possibly usable in combination with oth-

* Fermi National Accelerator Laboratory (Fermilab) is operated by Fermi Forward Discovery Group, LLC for the U.S. Department of Energy under contract 89243024CSC000002

† ostiguy@fnal.gov

Content from this work may be used under the terms of the CC BY 4.0 licence (© 2022). Any distribution of this work must maintain attribution to the author(s), title of the work, publisher, and DOI.

ISBN: 978-3-95450-261-5 ISSN: 2673-7000 doi: 10.18429/JACoW-NAPAC2025-THP055

MULTI-GeV FFA BEAM TRANSPORT TEST AT CEBAF *

S. Ogur†, A. Bogacz, D. Khan, E. Nissen
Thomas Jefferson National Accelerator Facility, Newport News, VA, USA
S. Brooks, D. Trbojevic, Brookhaven National Laboratory, Upton, NY, USA

Content from this work may be used under the terms of the CC BY 4.0 licence (© 2022). Any distribution of this work must maintain attribution to the author(s), title of the work, publisher, and DOI.

Abstract

Jefferson National Lab (JLab) is planning an upgrade project to increase the beam energy in the Continuous Electron Beam Accelerator Facility (CEBAF) to 22 GeV with high polarization electron beams by using Fixed Field Alternating-gradient (FFA) magnets. The utilization of the FFA magnets for the 10-22 GeV beam energy range is unprecedented; therefore, their efficacy will need validation. For this reason, JLab is considering the design of an FFA magnet test bench, i.e., a half or full FFA cell, that would be deployed in the current CEBAF machine in the 5-11 GeV range. This test bench would evaluate the FFA magnet's field uniformity, permanent magnet resiliency, and beam optics. In this report, we present the preliminary design and status of this planned beamline for the FFA beam transport test at CEBAF.

INTRODUCTION

The 22 GeV CEBAF upgrade plans on replacing the highest-energy arcs with advanced beamline sections composed of periodic cells employing Fixed Field Alternating-gradient (FFA) magnets [1]. Each FFA cell comprises a pair of combined-function permanent magnets. The magnet design is inherently complex due to the high field strength, oval aperture, and open mid-plane configuration, which helps suppress synchrotron radiation. The resulting lattice is uniquely designed to meet the stringent beam dynamics requirements of six co-propagating electron beams. This configuration is critical for achieving precise beam focusing and orbit control. The proposed FFA cell layout features alternating focusing and defocusing combined function magnets that simultaneously provide strong field gradients and bending components.

FFA beamlines are typically categorized as scaling or non-scaling, depending on whether the magnetic field profile scales with particle momentum (i.e., the betatron tune varies with momentum). In this case, the proposed design is classified as a non-scaling FFA magnet. Moreover, particles across a broad momentum range remain confined within the magnet aperture, each following a distinct but stable orbit.

The racetrack FFA design requires precise configuration of beam optics to ensure stable beam transport warranted by well-understood beam dynamics across a wide range of energies. For this reason, JLab is planning to have an FFA test insert in the current CEBAF, either at Beam Switchyard (BSY) dump line or Hall C beam line; the overview of the CEBAF complex is presented in Fig. 1.

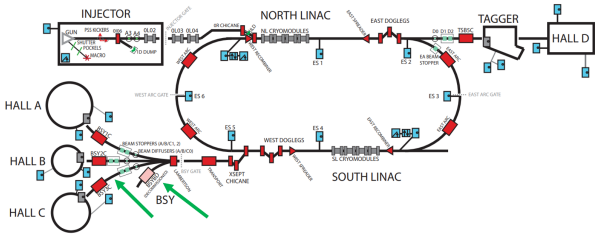


Figure 1: CEBAF complex, and proposed FFA testbed possible locations shown with green arrows.

An instrumented test site in the BSY dump line or Hall C line would enable systematic evaluation of magnet performance, including field uniformity and alignment, both essential for maintaining beam stability and minimizing losses in the 5-11 GeV energy range. Such a test site would need to provide flexibility to simulate different operational scenarios, allowing for optimization of beam optics and early identification of potential design issues. To facilitate that, we have proposed exploratory studies, as a lab-directed R&D project, to design a "testbed" capable of probing the beam transport through the FFA magnets. Its role extends beyond field quality validation currently being carried out at JLab [2]; it is also essential for refining design parameters and ensuring that the final accelerator beamline satisfies the requirements for reliable and stable operation. Investing in a comprehensive test bench will contribute significantly to the success of the CEBAF energy upgrade project and allow us to quantify the reliability and performance of FFA-based accelerator technology overall.

POSSIBLE TEST-SITES

The initial goal of this study is to identify and optimize potential test sites compatible with CEBAF's current operational energy range. We will first investigate the feasibility of implementing an experimental insert in the BSY dump line and Hall C, serving as a testbed for FFA beam transport within this energy range, approximately matching the energy ratio (~ 2.2) envisioned for the full 22 GeV CEBAF upgrade.

Although the BSY dump line is not currently in operation, it could be refurbished and repurposed as a high-energy test facility for proof-of-principle FFA validation [3]. Notably, Cornell BNL ERL Test Accelerator (CBETA) also conducted a fractional arc test prior to its full installation [4]. Specifically, we aim to measure beam orbits through a single or a full FFA magnet, i.e. "half-cell" or "full-cell" configuration, over the 5-11 GeV range at the BSY dump line. This

* This material is based upon work supported by the U.S. DOE, Office of Science, Office of Nuclear Physics contract DE-AC05-06OR23177.
† ogur@jlab.org

ISBN: 978-3-95450-261-5 ISSN: 2673-7000 doi: 10.18429/JACoW-NAPAC2025-THP056

TRANSPORT OF 12 GeV POSITRON BEAMS AT Ce$^+$BAF *

S. Ogur†,[1], J. Benesch[1], A. Bogacz [1], J. Grames[1], V. Lizárraga-Rubio[1,2], Y. Roblin[1], A. Seryi[1], A. Sy[1], D. Turner[1], A. Ushakov[1] , E. Voutier[3]
[1]Thomas Jefferson National Accelerator Facility, Newport News, VA, USA
[2]Universidad de Guanajuato, León, Guanajuato, México
[3]Université Paris-Saclay, CNRS/IN2P3, IJCLab, Orsay, France

Abstract

Jefferson Lab (JLab) is developing a concept to upgrade the Continuous Electron Beam Accelerator Facility (CEBAF) to additionally deliver spin-polarized continuous-wave positron beams for its nuclear physics program users (Ce$^+$BAF 12 GeV). The concept involves repurposing the Low Energy Recirculator Facility (LERF) at JLab as a dual injector, first producing 100-300 MeV spin-polarized electron beams which are subsequently used for the generation and formation of 123 MeV continuous-wave positron beams. The positron beams are transported to CEBAF and injected for acceleration up to 12 GeV, tailored to the requirements of its four experimental halls. Given the higher emittance of the secondary positron beams, the CEBAF optics are optimized for low dispersion and low beta functions to enhance transmission within the Ce$^+$BAF acceptance limits and with an R_{56} to manage the positron beams bunch length and energy spread. Potential bottlenecks are being investigated through both optical modeling and measurements using an electron beam, as well as degraded electron beams, to map the 6d acceptance of CEBAF as it is today. This presentation shares preliminary results from multi-particle tracking simulations of the positron beam up to 11 GeV, including spatial, momentum, and spin characteristics, and explores the feasibility of delivering beams simultaneously to multiple experimental halls via extraction optics.

INTRODUCTION

Polarized positron beams are of growing interest in nuclear physics for studies of nucleon structure and two-photon exchange effects. Jefferson Lab (JLab) has demonstrated, through the PEPPo (Polarized Electrons for Polarized Positrons) concept [1], that such beams can be produced, and is now evaluating their acceleration in CEBAF. The proposed Ce$^+$BAF 12 GeV upgrade aims to deliver either low-current, highly polarized positrons (I > 50 nA, P ≈ 60%) or high-current, unpolarized positrons exceeding 1 µA [2]. This trade-off arises from limitations in positron generation and capture efficiency [3]. While CEBAF currently provides a continuous-wave (cw) electron beam, the upgrade would enable cw positron delivery as well. A comparison of current and proposed CEBAF capabilities is shown in Table 1.

Table 1: CEBAF Operational Electron Machine Parameters and Positron Upgrade Plan Comparison

Parameter	Electrons	Positrons
Hall Multiplicity	4	1 or 2
Energy (ABC/D)	11/12 GeV	11/12 GeV
Beam Rep. [MHz]	249.5/499	249.5/499
Duty Factor	100% cw	100% cw
Unpolarized Int.	170 µA	> 1 µA
Polarized Int.	170 µA	> 50 nA
Beam Polarization	> 85%	> 60%
Fast/Slow Helicity Reversal	1920 Hz / Yes	1920 Hz / Yes

CEBAF supports four nuclear physics experiments across Halls A, B, C, and D, delivering electron beams simultaneously to all halls. In contrast, positron beam delivery may be limited by the current extraction system, specifically the septum blade. To address this, beam dynamics studies are ongoing to accommodate the larger positron beam size, and a septum replacement is under consideration. Accordingly, the hall multiplicity listed in Table 1 may change.

The new injector at LERF and its transport line are designed to support both the CEBAF positron upgrade and the planned CEBAF 22 GeV Fixed Field Alternating Gradient (FFA) upgrade [4].

LERF TO NORTH LINAC OPTICS

The positron upgrade plan is being carried out in accordance with not interfering with the current CEBAF electron beam delivery. To illustrate, the positron transport line makes uses of existing facilities and would have a separate electron injector to impinge on the high Z-material, then it would be accelerated up to 123 MeV [3]. Those positrons then would be injected into the CEBAF north linac for further acceleration up to 12 GeV. The layout, generated from the beam optics survey is given in Fig. 1.

The beam optics design positions the transport beamline suspended from the CEBAF tunnel ceiling along the inner wall, opposite the accelerator on the outer wall. The positron injector merges at north linac, mirroring the last two dipoles of the operational CEBAF electron injector. The transport line maintains a clearance ensuring tunnel access during cart operations. The line descends and joins the junction at the last injector chicane dipole, *MBLR04*. Figure 2 shows a 3D optics plot of this merging section generated with ELEGANT [5].

* This material is based upon work supported by the U.S. DOE, Office of Science, Office of Nuclear Physics contract DE-AC05-06OR23177
† ogur@jlab.org

Content from this work may be used under the terms of the CC BY 4.0 licence (© 2022). Any distribution of this work must maintain attribution to the author(s), title of the work, publisher, and DOI.

ISBN: 978-3-95450-261-5 ISSN: 2673-7000 doi: 10.18429/JACoW-NAPAC2025-THP058

OPTIMIZATION OF KICKER LOCATION FOR PSEUDO SINGLE BUNCH OPERATION IN SPEAR3*

P. Liu†, K. Tian, T. Rabedeau, J. Safranek
SLAC National Accelerator Laboratory, Menlo Park, CA, USA

Abstract

The Pseudo Single Bunch (PSB) operation mode is being developed at Stanford Synchrotron Radiation Lightsource (SSRL) to address growing interests from time-resolved experiments. To accommodate both regular user and timing user experiments simultaneously, a fast electron kicker will be installed in one of the long straight sections at SPEAR3. This kicker will provide a large spatial separation between the main bunch trains and the camshaft bunch. The resulting x-ray spatial separation from undulator beamlines will be highly dependent on the location of the PSB kicker to be installed. We present here considerations of the PSB kicker location with beamline simulations in both low and high repetition rate modes.

INTRODUCTION

The third-generation electron storage ring SPEAR3 [1] at SSRL serves a large user community with high-intensity photon beams from VUV to hard x-ray regime. The machine is optimized to produce a high average photon flux for most user experiments. To simultaneously accommodate timing users, SPEAR3 is typically filled in a hybrid pattern with 500 mA total beam current distributed in four bunch trains and a camshaft bunch, as shown in Fig. 1. The camshaft bunch, with up to 20 mA current, sits in the middle of a 120-ns gap. The bunch spacing within the train is ~2.1 ns.

A Pseudo Single Bunch (PSB) operation mode is being developed at SPEAR3 [2] for timing experiments to further suppress the sample irradiation from the multi-bunch trains. For this PSB operation, a fast stripline kicker will be installed in one of the long straight sections [2] (see Fig. 1) to kick the camshaft bunch. This vertically separates the camshaft from the main bunch trains (or main beam). The kicker can be run in both Low Repetition Rate (LRR) mode and High Repetition Rate (HRR) modes [2]. In LRR mode, the camshaft completes a motion cycle in three revolutions in the ring, with turn 0, 1, and 2 respectively having 0, Δy_1, and Δy_2 separation from the main bunch train for a particular beamline [2, 3]. In HRR mode, the camshaft has approximately a constant separation from the main bunch train for a particular beamline. For example, Figure 2 shows the camshaft separation from the main beam for both LRR and HRR modes at the BL17 undulator center, with the PSB kicker centered at different locations in the straight section.

As can be seen, the location of the PSB kicker has a significant impact on the vertical separation between the camshaft and the main beam. For beamlines with a simple focusing element such as compound refractive lens or curved mirrors, the electron position separation Δy is directly proportional to the x-ray beam separation Δy_x (from the camshaft and the main beam) at the focal plane by $\Delta y \sim M\Delta y_x$, with M the magnification of the focusing element. The electron angle separation $\Delta y'$ determines the number of photons that will pass through beamline components and arrive at the final focal plane. In principle, Δy and $\Delta y'$ with the same sign have the best overall effect with large x-ray spacing and large rejection of the main beam. Here, we study the impact of the PSB kicker location on the rejection of x-rays from the

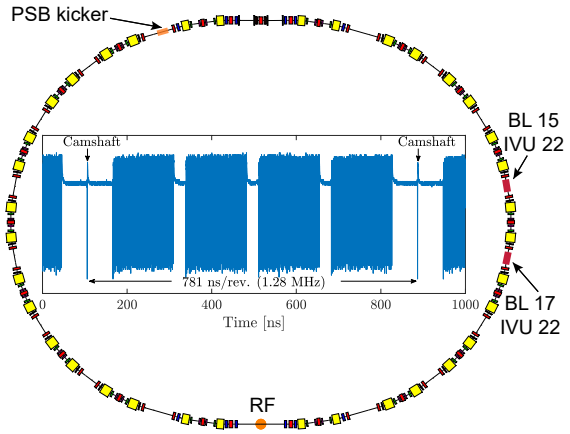


Figure 1: Layout of SPEAR3 lattice. PSB kicker and undulators for two beamlines (BL15 and BL17) used in this work are highlighted. Inset shows the typical fill pattern in SPEAR3 with a camshaft bunch sitting in the middle of two bunch trains with a ~120-ns gap.

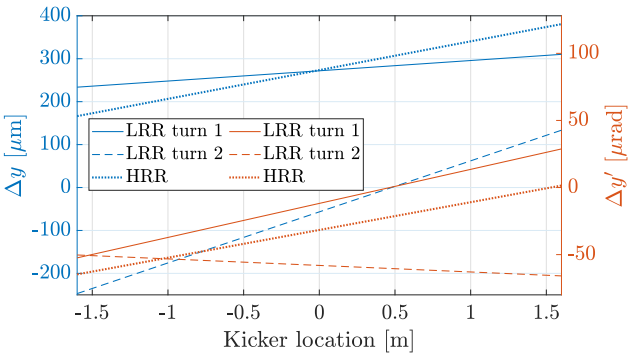


Figure 2: Vertical separation in position and angle between camshaft and main beam at the center of the BL17 undulator with a PSB kick angle of 85 μrad. Kicker location $z = 0$ refers to the midpoint of the long straight section.

* Work supported by U.S. Department of Energy under Contract No. DE-AC02-76SF00515.

† Email: peifan@slac.stanford.edu

Content from this work may be used under the terms of the CC BY 4.0 licence (© 2022). Any distribution of this work must maintain attribution to the author(s), title of the work, publisher, and DOI.

ISBN: 978-3-95450-261-5 ISSN: 2673-7000 doi: 10.18429/JACoW-NAPAC2025-THP059

ORTHOGONAL DIRECTIONS CONSTRAINED GRADIENT METHOD FOR BEAM OPTICS CORRECTION*

T. Gorlov†, S. Cousineau, N. Evans, A. Aleksandrov
Oak Ridge National Laboratory, Oak Ridge, TN, USA

Abstract

An Orthogonal Directions Constrained Gradient Method (ODCGM) has been developed and experimentally used for optimization and correction of H^- optical beam parameters for laser assisted charge exchange injection (LACE) experiments. LACE experiment requires precise tune up of H^- beam parameters for high efficiency stripping. High precision tuning of beam parameters cannot be done in one step due to miscellaneous errors of power supplies and other factors. Then, subsequent application of the optic correction method considered here can do fine tune up of the beam. A simple experimental demonstration of ODCGM is presented.

INTRODUCTION

In this paper we consider an Orthogonal Directions Constrained Gradient Method (ODCGM) method for precise tune-up of H^- beam parameters for Laser Assisted Charge Exchange injection (LACE) experiments [1,2]. This method has been studied [3] in math and computation sciences for general optimization problems. Here we adopted this method for the practical problem of ion beam optics optimization.

The LACE project considers interaction of H^-/H^0 bunch with a powerful laser for excitation and stripping of hydrogen beam (see Fig. 1). High efficiency excitation and stripping of a hydrogen beam requires extremely precise adjustment of beam parameters at the interaction point. The ion beam must be strongly focused at the interaction point. Also, other parameters such as dispersion must be adjusted precisely for crab-crossing scheme of laser-bunch interaction [4].

During normal SNS operation, we are not required to tune up the beam with high precision in order to provide beam transport. Unfortunately, this approach will not work for high-accuracy beam tune up required by LACE due to the errors of magnet fields and input H^- beam parameters. Also, the model of beam propagation used for beam tune-up has its own error. H^- beam parameters at the focal point of interaction are very sensitive to all listed errors. Standard tune-up methods can be used for preliminary optics setup for LACE at the interaction point. Then, we can apply the ODCGM method for beam optics correction and precise tune-up of the desired parameters at the focal point. The ODCGM algorithm calculates the quadrupole magnet corrections based on correction of one selected beam parameter to the desired accuracy while keeping other selected optical beam parameters unchanged. The method is very similar to the beam orbit correction technique [5] used at the SNS. The orbit correction method uses corrector magnets and a linear accelerator model to correct the orbit position. The beam optics correction method considered here uses quadrupole magnets to correct beam optics parameters instead of orbit. For this purpose, the ODCGM algorithm adopted and developed here is based on local gradient mechanism of search for optimal beam correction. The algorithm of the method itself can also be applied to other problems in accelerator physics, not only beam optics tune-up.

In this paper, we first describe the LACE optimization problem using the ODCGM algorithm.

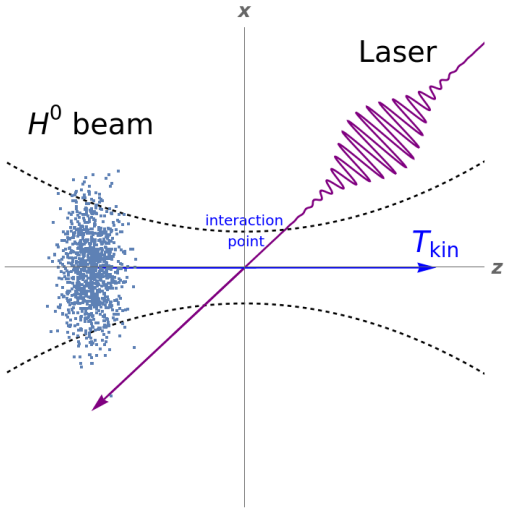


Figure 1: Interaction of H^0 bunch with laser.

BEAM OPTICS CORRECTION ALGORITHM

Beam optics is normally characterized by the Twiss parameters α, β, ϵ for the vertical and horizontal directions. Dispersion parameters $D, \partial D/\partial z$ that play important role in LACE beam tune up are also considered. For simplicity, we will denote all beam parameters as p_i. Figure 2 schematically represents the beam along the z axis with beam parameters $p_1 ... p_n$ that can generally vary with z_i. In our problem, we consider the tune-up parameters only at one location of laser-bunch interaction. Using the input Twiss parameters and

* This manuscript has been authored by UT-Battelle, LLC, under Contract No. DE-AC05-00OR22725 with the U.S. Department of Energy. The United States Government retains, and the publisher, by accepting the article for publication, acknowledges that the United States Government retains a non-exclusive, paid-up, irrevocable, world-wide license to publish or reproduce the published form of this manuscript, or allow others to do so, for United States Government purposes. The Department of Energy will provide public access to these results of federally sponsored research in accordance with the DOE Public Access Plan (http://energy.gov/downloads/doe-public-access-plan).

† tg4@ornl.gov

Content from this work may be used under the terms of the CC BY 4.0 licence (© 2022). Any distribution of this work must maintain attribution to the author(s), title of the work, publisher, and DOI.

ISBN: 978-3-95450-261-5 ISSN: 2673-7000 doi: 10.18429/JACoW-NAPAC2025-THP060

PERFORMANCE REQUIREMENTS FOR THE LANSCE ACCELERATOR MODERNIZATION PROJECT*

J.W. Lewellen†, K. Bishofberger, G.E. Dale, D.A. Dimitrov, H. Gaus, J. Medina, S. Mosby, S. Swickley, S. Spernjak, C.E. Taylor, R.T. Thornton
Los Alamos National Laboratory, Los Alamos, NM, USA

Abstract

The LANSCE accelerator concurrently accelerates two beam species, H^+ and H^-, and delivers beam to five distinct user stations, including slow and fast neutron scattering centers, ultra-cold neutron research, proton radiography, and isotope production. The LANSCE Accelerator Modernization Project (LAMP) will replace the initial sections of LANSCE, from the ion sources through the end of the 100-MeV drift-tube linac. The combination of multiple user stations, and the unique operation of LANSCE, present unique challenges and opportunities.

In this paper, we present the performance requirements for LAMP, an overview of the project status and timeline, an overview of the conceptual design, and outlook.

PERFORMANCE REQUIREMENTS

The LANSCE accelerator, shown in Fig. 1, presently uses Cockcroft-Walton DC injectors, supplying H^+ and H^- beams at 750 keV to a drift-tube linear accelerator (DTL). The H^+ beam is split off at 100 MeV to supply the Isotope Production Facility (IPF); the H^- beam is accelerated to 800 MeV by a cavity-coupled linac, and directed to one of the remaining four user facilities: Proton Radiography (pRad); Ultra-Cold Neutrons (UCN); Weapons Neutron Research (WNR); and the Lujan Neutron Scattering Center (Lujan). Figure 1 shows an overall depiction of the facility.

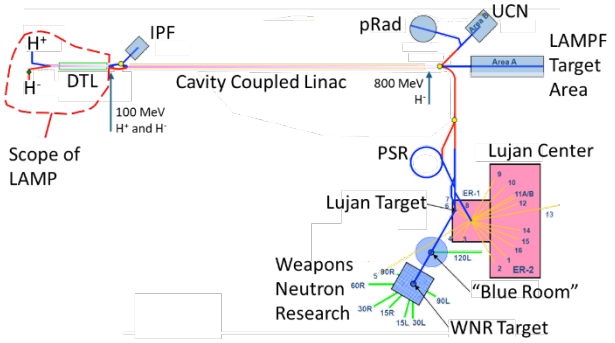


Figure 1: An overview of the LANSCE accelerator and user facilities. See text above for acronym definitions.

LANSCE generates 625-μs beam macropulses at a repetition rate of 120 Hz, with macropulses being interleaved between the various user facilities. During typical operations, Lujan receives beam at 20 Hz; the remaining 100 pulses per second are used to concurrently accelerate H^+ and H^- beams directed to IPF and WNR, respectively.

The LANSCE Accelerator Modernization project (LAMP) will replace the upstream portions of the 50-year-old LANSCE accelerator, from the ion sources through the end of the drift-tube linac. The project has multiple performance requirements in terms of beam delivery to the various user facilities, as well as general goals for availability, uptime, etc., and are specified in the LAMP Program Requirements Document [1].

General Requirements

LAMP must supply H^+ and H^- ion beams at 100 MeV, with the proper timing structure, peak and average beam current for each of the LANSCE user facilities. This requires high flexibility in macropulse bunch pattern generation.

LAMP must be designed to support 5300 beam hours of operation per annual run cycle with greater than 90% availability. (As LAMP scope extends only through the end of the DTL, the distinction between "support" versus "deliver" is important to make.) This requirement has implications for beam loss downstream of LAMP, and thus parameters such as beam emittance, to which the majority of LANSCE user stations are otherwise insensitive.

Finally, as a "soft" condition, LAMP will work towards developing a design that not require modification of the physical infrastructure of the LANSCE site. This includes, for instance, attempting to stay within the cooling and electrical power capacity of the existing facility; modifications to existing buildings – shielding enclosures and outer walls in particular – are also to be avoided. Figure 2 shows a CAD model of the LAMP conceptual design in the existing LANSCE accelerator vault.

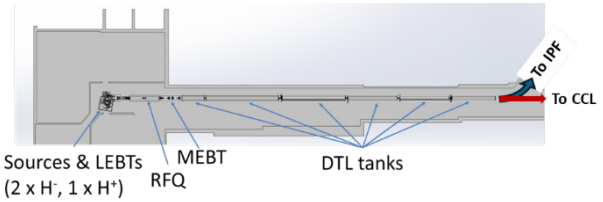


Figure 2: The LAMP conceptual physics design overlaid onto the existing LANSCE vault and building envelope.

Isotope Production Facility

The Isotope Production Facility (IPF) produces isotopes for the US medical isotope program, as well as for various research and characterization efforts.

IPF requires an average beam current of 250 μA, delivered at a rate of 100, 625-μs macropulses per second. H^+ beams for IPF are accelerated concurrently through the

* Work was performed under the auspices of the US Department of Energy by Triad National Security under contract 89233218CNA000001. LA-UR-25-27893
† jwlewellen@lanl.gov

Content from this work may be used under the terms of the CC BY 4.0 licence (© 2022). Any distribution of this work must maintain attribution to the author(s), title of the work, publisher, and DOI.

ISBN: 978-3-95450-261-5 ISSN: 2673-7000 doi: 10.18429/JACoW-NAPAC2025-THP061

PHOTON STIMULATED DESORPTION BEAMLINE AT NSLS- II

R. Todd[1], O. Chubar[1], M. Ferreira[2], C. Hetzel[1], S. Hulbert[1], P. Palecek[1], M. Seegitz[1], T. Shaftan[1]
[1] Brookhaven National Laboratory, Upton, NY, USA
[2]ESS, Lund Sweden

Abstract

Understanding synchrotron induced gas desorption plays an important role in predicting vacuum behaviour of accelerators. Investigations of new materials and coatings require careful study of their desorption yield for potential use in upgrading NSLS-II as well as other accelerator facilities. A beamline at NSLS-II, dedicated to the study of novel and proposed vacuum materials has been constructed and commissioned to advance further research into desorption behaviour. The PSD of stainless steel, OFHC copper and NEG coated copper, some of which for use in the future Electron-Ion Collider at BNL, have been measured and will be presented. These newly established desorption rates will be used as inputs to advanced modelling tools such as MolFlow+ and SynRad+ [1] for accurate predictions of vacuum behaviour and design optimization. The existing layout and future plans for the beamline will be presented.

EXPERIMETNAL

The method used to measure the desorption will be similar in the method used at NSLS and other synchrotrons around the world. A significant body of work exists on desorption studies of various materials, coatings and surface conditions [2-17]. However, new materials, geometry and surface condition, and optimization of cleaning methods should be evaluated and measured to gain confidence in design choices prior to selection.

The beamline is located at port 14-BM at NSLSII and will be supplied with light from a 3-pole wiggler and dipole bending magnet (shown in Figs. 1 and 2).

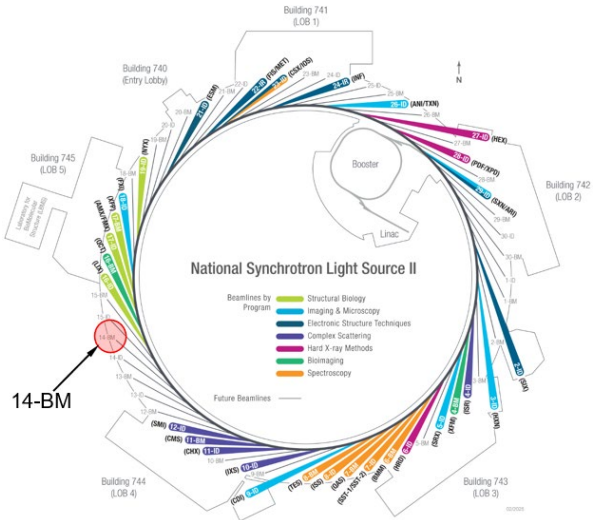
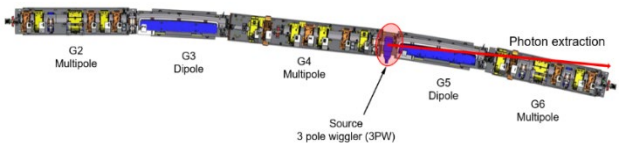
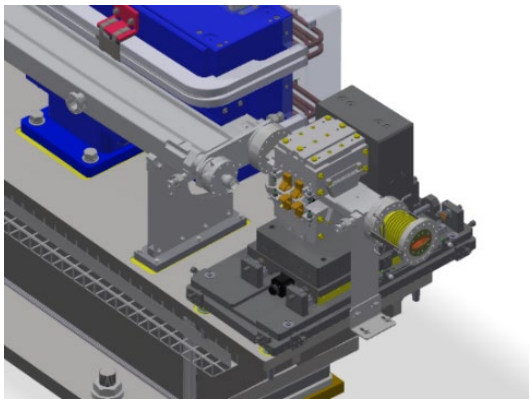


Figure 1: Location of beamline at NSLSII.





(a)



(b)

Figure 2: (a) Three pole wiggler (3PW) upstream of bending magnet dipole (BM), (b) Picture of beamline endstation with NEG coated copper prototype vacuum chamber for the EIC electron storage ring.

Together, the 3PW and BM produce the characteristic light reaching the sample (Fig. 3).

Content from this work may be used under the terms of the CC BY 4.0 licence (© 2022). Any distribution of this work must maintain attribution to the author(s), title of the work, publisher, and DOI.

ISBN: 978-3-95450-261-5 ISSN: 2673-7000 doi: 10.18429/JACoW-NAPAC2025-THP062

PHYSICS MODEL TO STUDY RESONANT COMPTON SCATTERING*

W. Delooze†, Y. K. Wu
FEL Laboratory, TUNL, and Department of Physics, Duke University, Durham, NC, USA

Abstract

Over the past several decades, the elastic interaction between photons and electrons known as Compton scattering, has been the foundational mechanism for generating high-energy photon beams, particularly in the gamma-ray regime. Resonant interactions between photons and atomic systems offer significantly enhanced resonant cross-sections, often several orders of magnitude greater than what is achievable through conventional Compton scattering of electron and photon beams. The Gamma Factory initiative at CERN aims to exploit this enhancement by employing ultra-relativistic, partially stripped ion beams to generate high-intensity gamma-ray beams. In this work, we first examine the energy-matching requirements for resonance. We then present a semi-classical model based on a damped-driven oscillator to describe resonant Compton scattering. This model provides physical insight into the resonant cross-section and the limitations imposed by beam-beam interactions. We also propose a framework for simulating the scattering process.

INTRODUCTION

In 1923, Arthur Compton discovered the elastic scattering of photons by electrons, now known as Compton scattering. In this experiment, energy and momentum were transferred from the photon to the electron, resulting in an increase of x-ray wavelength after scattering from graphite [1]. Following the emergence of charged particle accelerators in the 1960s, interest grew in using relativistic electrons to reverse the direction of the energy exchange, producing a high-energy photon beam. Today, high-intensity light source facilities worldwide utilize Compton scattering to generate real x-ray and gamma-ray beams employed in various fields. For example, the nearly monochromatic and highly polarized gamma beam at the High Intensity Gamma-ray Source (HIGS) facility supports research in particle physics, nuclear physics, and astrophysics [2].

While these machines are capable of producing intense and energetic gamma-ray beams, they remain limited by the very small Thomson cross-section, $\sigma_T \approx 6.65 \times 10^{-29}$ m^2. This limitation can be overcome by using resonant Compton scattering, where photons interact with electrons bound by relativistic atomic systems in which resonance arises from internal transitions. The Gamma Factory (GF) [3, 4] is a proposed future Compton gamma source (CGS) at CERN that aims to exploit this resonant process. The primary goal of the GF is to generate intense, polarized gamma-ray beams with energies ranging from 1–400 MeV and a total flux that is several orders of magnitude greater than what is achievable with conventional CGSs. The GF has the potential to make a significant contribution to many different sub-fields of physics [3, 4].

KINEMATICS OF SCATTERING

We start with the conventional Compton scattering of a photon and an electron, as shown in Fig. 1, [5]. The 4-momentum conservation yields the scattered photon energy:

$$E_\gamma = \frac{\hbar\omega(1-\beta\cos\theta_i)}{1-\beta\cos\theta_f+\frac{\hbar\omega}{\gamma mc^2}(1-\cos\theta_{\rm ph})}, \quad (1)$$

where θ_i is the angle between the incident photon and incident electron, θ_f is the angle between the scattered photon and the incident electron, and $\theta_{\rm ph} = \theta_i - \theta_f$ is the angle between the incident and scattered photons. The scattered photon energy is maximized for the head-on backscattering case:

$$E_\gamma = \gamma^2(1+\beta)^2\hbar\omega, \quad (2)$$

where $\theta_i = \pi$ and $\theta_f = 0$.

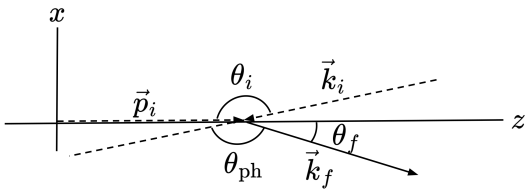


Figure 1: The collision scheme for Compton scattering.

In contrast, resonant Compton scattering differs in a few important ways. For a simple two-state system with a ground state and an excited state, the condition for resonant scattering requires that the energy of the photon in the ion rest frame matches the energy level difference (ΔE) between the two states:

$$\hbar\omega' = \Delta E = E_{\rm excited} - E_{\rm ground}. \quad (3)$$

For head-on collisions, this constrains the laser wavelength:

$$\lambda = 2\pi\gamma(1+\beta)\frac{\hbar c}{\Delta E}, \quad (4)$$

where λ is the wavelength of the laser in the laboratory frame.

Figure 2 shows the required relationship between λ and γ for resonant scattering over a range of maximum scattered gamma-ray energies. A wide range of gamma-ray energies is accessible by selecting different ion species while tuning the

* This research is supported in part by the U.S. Department of Energy under Grant No. DE-FG02-97ER41033.
† william.delooze@duke.edu

Content from this work may be used under the terms of the CC BY 4.0 licence (© 2022). Any distribution of this work must maintain attribution to the author(s), title of the work, publisher, and DOI.

ISBN: 978-3-95450-261-5 ISSN: 2673-7000 doi: 10.18429/JACoW-NAPAC2025-THP064

RADIOISOTOPE PRODUCTION AT SNS (RIPS)*

J. Griswold†, Y. Lee, E. Asano, S. Kim, S. Cousineau,
D. Rotsch, J. Duran, D. Stracener, B. Rasco, F. Pilat
Oak Ridge National Laboratory, Oak Ridge, TN, United States

Abstract

A unique opportunity exists to investigate alternative radionuclide production technologies using the high-energy proton beams available at the Spallation Neutron Source (SNS) at Oak Ridge National Laboratory (ORNL). The Second Target Station (STS) is being built to address emerging science challenges in energy, security, and transportation. STS will complement the capabilities of the First Target Station and High Flux Isotope Reactor by providing capabilities for materials research that requires the combined use of intense, long-wavelength (cold) neutrons, and instruments that are optimized for exploration of complex materials. The construction of the STS beamline to the target also presents an opportunity to capitalize on additional applications, such as producing high-demand radioisotopes for medical applications.

Work began in 2024 to investigate the possibility of Radioisotope Production at SNS (RIPS) through four main goals: (1) identification of isotopes of interest through modeling and simulation of prospective irradiation parameters and target compositions, (2) development of a target design concept that can receive high-energy beam pulses from the SNS accelerator, (3) identification of enhanced isotope separation methods for SNS-produced radionuclides, and (4) development of a design concept for an experimental/demonstration test stand. An overview of the project and progress toward achieving these goals is presented herein.

INTRODUCTION

The original design of the SNS facility was a 1 GeV, 1.4 MW proton accelerator used for neutron production primarily for materials science applications. Recently, the SNS accelerator successfully completed the Proton Power Upgrade project to double the beam power capability to 2.8 MW and beam energy to 1.3 GeV. The accelerator is expected to ramp up to a full beam power of 2.8–3 MW within a few years. Because the First Target Station has a power limit of 2 MW, an additional 0.8–1 MW of beam power will be available until the Second Target Station (STS) becomes operational in the mid- to late 2030s. After STS completion, 100–300 kW will remain accessible, depending on the final power capability of the accelerator, which is expected to be approximately 3 MW. This beam power can be leveraged for alternative applications such as radioisotope production without compromising the DOE Basic Energy Sciences neutron production mission. This ability presents a unique cost leveraging opportunity for producing isotopes without the construction cost of an accelerator. The potential location for a radioisotope production station is shown in Fig. 1.

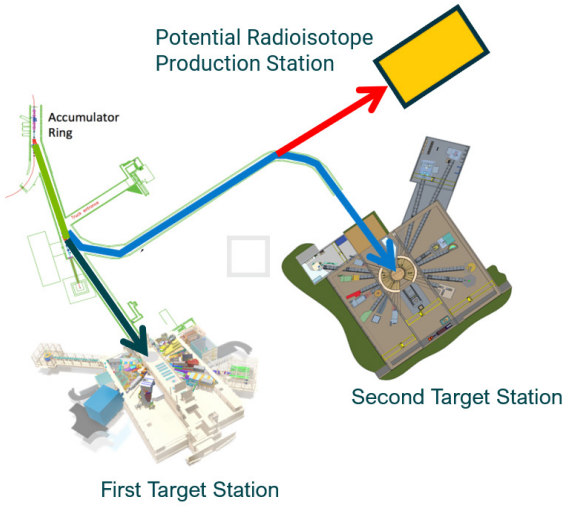


Figure 1: Location of potential RIPS facility at SNS.

Radioisotope production at this high energy range has been performed on a small scale at the European Organization Nuclear Research's (CERN's) MEDICIS facility which uses high-energy proton beams (1.4 GeV), albeit at orders of magnitude lower average beam current in comparison to SNS [1]. Higher beam current irradiations to produce radionuclides have been performed at TRIUMF Laboratories in British Columbia, Canada. TRIUMF operates a 500 MeV proton beam to produce various radioisotopes, including the highly sought-after targeted alpha therapy (TAT) medical radionuclide ^{225}Ac [2]. Radioisotope production with high-energy (>1 GeV) protons at SNS would be the first of its kind in the US DOE laboratory complex.

MODELING AND SIMULATION

The viability of large-scale production of radioisotopes at SNS may be realized by initially identifying radionuclides of interest through modeling and simulation. Four Monte Carlo (MC) particle transport codes—Monte Carlo N-Particle (MCNP) [3], GEometry ANd Tracking (GEANT4) [4], Fluctuierende KAskade (FLUKA) [5], and

* Notice: This manuscript has been authored by UT-Battelle, LLC, under contract DE-AC05-00OR22725 with the US Department of Energy (DOE). The US government retains and the publisher, by accepting the article for publication, acknowledges that the US government retains a nonexclusive, paid-up, irrevocable, worldwide license to publish or reproduce the published form of this manuscript, or allow others to do so, for US government purposes. DOE will provide public access to these results of federally sponsored research in accordance with the DOE Public Access Plan (https://www.energy.gov/doe-public-access-plan).

This work is supported by the Oak Ridge National Laboratory Directed Research and Development Program.

† griswoldjr@ornl.gov

Content from this work may be used under the terms of the CC BY 4.0 licence (© 2022). Any distribution of this work must maintain attribution to the author(s), title of the work, publisher, and DOI.

ISBN: 978-3-95450-261-5 ISSN: 2673-7000 doi: 10.18429/JACoW-NAPAC2025-THP065

RADIOISOTOPE PRODUCTION AT THE SPALLATION NEUTRON SOURCE: DESIGN CONCEPT OF EXPERIMENTAL TARGET STATION *

Y. Lee†, W. D. Willis, I. Popova, S. H. Kim, S. Cousineau and J. Griswold
Oak Ridge National Laboratory, Oak Ridge, TN, USA

Abstract

Completion of the Proton Power Upgrade Project for the Spallation Neutron Source (SNS) accelerator at Oak Ridge National Laboratory opens an opportunity to utilize reserve beam power of more than 100 kW for applications beyond neutron production. One of these applications is the production of critical radionuclides. To demonstrate the feasibility of using the reserve beam power to produce radioisotope at SNS, a design concept of a small-scale experimental target station in the Linac Dump area has been developed. This experimental facility will provide isotope yield benchmarking data using protons in the GeV range. It will also enable additional research and development in isotope handling and radiochemical separation. The target station consists of a target module enclosed in a vessel and concrete shielding. Particle transport calculations and thermo-mechanical simulations are used to determine beam parameters, decay time, isotope yield, shielding dimensions, and target design parameters. Calculations verified that the irradiated capsule can be handled manually using hands-off tools and transported to a hot cell in a shielded container for post-irradiation characterizations.

INTRODUCTION

The Spallation Neutron Source (SNS) accelerator at Oak Ridge National Laboratory will be able to deliver beam power beyond what is required for operating two neutron sources, the first and second target stations. The surplus beam power can be utilized for other applications such as medical isotope production. Computational analyses showed the technical feasibility of a medical isotope production target that receives 250 kW beam power from the SNS accelerator [1]. Particle transport analyses showed that the 1.3 GeV proton beam at SNS has a high potential to produce a large amount of medical isotopes thanks to its long stopping range in target materials. To validate the calculated isotopes yields, there is a need to perform a small scale proof-of-concept experiment using the SNS proton beam. The purpose of the experiment would be to provide benchmarking data to validate concepts and computational results, and to acquire basic demonstration for the isotope production, handling, and separation processes. This will allow early identification in gaps of knowledge or processes that need to be addressed to consider a full-scale concept for radioisotope production. In this paper, we present a design concept of a small-scale experimental target station at SNS. The design focuses on maximizing potential for learning while maintaining a low-cost, "minimal demonstration" philosophy. The design includes particle transport calculations to estimate isotopes yields and shielding, engineering of a target insertion device, and choice of pathways for isotope separation. A critical consideration for the design configuration is that it does not affect the primary neutron production mission in any way.

LOCATION AND BEAM PARAMETERS

The area directly upstream of the SNS linac dump is chosen for the installation of a test target irradiation stand. Figure 1 shows the area where test target is foreseen. There are two 6-way crosses with 6" flanges unoccupied. One of these flanges can be used for the installation of an irradiation port.

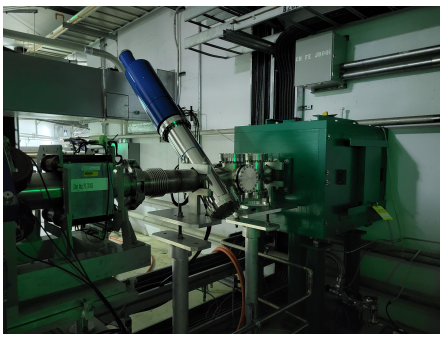


Figure 1: The area where test target is chosen to be stationed.

Protons are routinely transported to the SNS linac dump for beam studies. By deactivating the last quadrupole magnet pairs, the beam profile on the target has a Gaussian shape with σ_x =8 mm and σ_y =3 mm at the potential test target location which is about 14 meters upstream from the SNS linac dump surface. The proton energy can be varied comfortably between 800 MeV and 1.3 GeV. For the beam study, the time averaged beam power is limited below 7 kW with the maximum allowed beam pulse energy of 33 kJ. The beam on the linac dump has a pulsed structure with repetition rates up to 60 Hz, which can vary upon experimental needs. The pulse length is 1 ms. The actual beam conditions on the test target should be determined by the how much beam power the test target assembly can endure and the required shielding to

* Notice: This manuscript has been authored by UT-Battelle, LLC, under contract DE-AC05-00OR22725 with the US Department of Energy (DOE). The US government retains and the publisher, by accepting the article for publication, acknowledges that the US government retains a nonexclusive, paid-up, irrevocable, worldwide license to publish or reproduce the published form of this manuscript, or allow others to do so, for US government purposes. DOE will provide public access to these results of federally sponsored research in accordance with the DOE Public Access Plan (https://www.energy.gov/doe-public-access-plan).

† leey1@ornl.gov

Content from this work may be used under the terms of the CC BY 4.0 licence (© 2022). Any distribution of this work must maintain attribution to the author(s), title of the work, publisher, and DOI.

ISBN: 978-3-95450-261-5 ISSN: 2673-7000 doi: 10.18429/JACoW-NAPAC2025-THP066

RADIOISOTOPE PRODUCTION AT THE SPALLATION NEUTRON SOURCE: DESIGN CONCEPT OF ISOTOPE PRODUCTION TARGET *

Y. Lee†, S. H. Kim, S. Cousineau, J. Griswold
Oak Ridge National Laboratory, Oak Ridge, TN, USA

Abstract

Upon completion of the Second Target Station (STS) Project in the mid 2030s, the Spallation Neutron Source accelerator at Oak Ridge National Laboratory will deliver a 2.7 MW proton beam to the neutron production targets. In the post-STS phase, the accelerator will have a reserve beam power capacity of at least 100 kW beyond what the two neutron production targets will receive, which could potentially be ramped up to 300 kW. In this paper, a design concept for a radioisotope production target that could utilize 250 kW of the reserve beam power capacity is presented. The target consists of thorium discs encapsulated in 316L austenitic steel shells that are cooled by water. The estimated post-irradiation activity of Ac-225 and Ra-225, critical medical radioisotopes used in targeted alpha therapy cancer treatment, is calculated at the end of bombardment after a 14 day long irradiation time. Thermal and structural analyses are performed on the basis of calculated nuclear heating data. The technical feasibility of a high-power target under a 250-kW beam load with an extremely low duty factor of $3.5 \cdot 10^{-6}$ is presented from thermal, structural, and fatigue lifetime perspectives.

INTRODUCTION

With the completion of the Proton Power Upgrade (PPU) Project of the Spallation Neutron Source (SNS) at Oak Ridge National Laboratory (ORNL) [1], the SNS accelerator will be able to send 1.3 GeV proton beam to the first and second target stations at a beam pulse repetition rate of 60 Hz with a pulse energy of up to 50 kJ·pulse^{-1}. As the first and second target stations are designed to operate at 2 MW and 700 kW respectively, the SNS accelerator will have up to 300 kW reserve beam power that can be utilized for other applications than neutron production.

Among many applications, the 1.3 GeV protons can be used to produce radioisotopes of clinical importance. In this paper, we explore the feasibility of medical isotope production using 250 kW of the reserve beam power. As a study case, a thorium target is considered for the production of Ac-225 and Ra-225 which is used as a generator for Ac-225. Ac-225 is a candidate material for targeted alpha therapy (TAT) with increasing future demand with anticipated supply shortage [2, 3].

In the current configuration of the SNS linear accelerator (LINAC), there is no available extraction beamline suitable for long pulse applications. A more feasible solution would be to construct a new beamline extending from the future Ring to Second Target (RTST) beamline as shown in Fig. 1. A radioisotope production target in this area will receive short pulse beams extracted from the accumulator ring. Challenges with the 250 kW radioisotope production target design for this scenario are the high beam pulse energy and short pulse structure of the SNS beam with a pulse length of 700 ns. In this paper, we show the feasibility of a 250 kW radioisotope production target concept that is under a high dynamic beam load with an extremely low duty factor of $3.5 \cdot 10^{-6}$ by performing particle transport, thermal, and mechanical simulations.

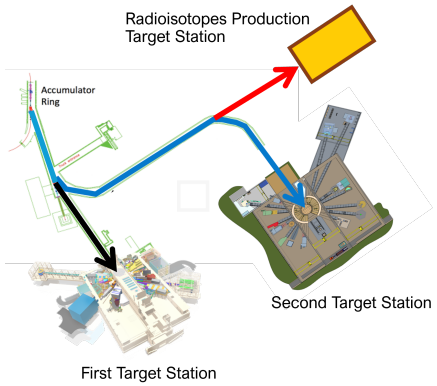


Figure 1: Potential location of the radioisotope production target station at SNS.

TARGET CONCEPT

We consider a target for the Radioisotope Production at the Spallation Neutron Source (RIPS) that receives a 1.3 GeV proton beam at a repetition rate of 5 Hz with a beam pulse energy of 50 kJ. The beam profile on the target is approximated by a super-Gaussian function, where the beam current density on the target is described by

$$i_{\text{proton}} = \frac{I_{\text{proton}}}{2\sqrt{2}\,\Gamma(\frac{1}{4})^2\,\sigma_x\,\sigma_y} \exp\left[-\frac{1}{2}\left(\frac{x^4}{\sigma_x^4} + \frac{y^4}{\sigma_y^4}\right)\right], \quad (1)$$

where I_{proton} is the proton current. The peak current density of the super-Gaussian beam is only a fraction of a Gaussian beam with the same proton current and standard deviations. A super-Gaussian beam on the target can be realized by using

* Notice: This manuscript has been authored by UT-Battelle, LLC, under contract DE-AC05-00OR22725 with the US Department of Energy (DOE). The US government retains and the publisher, by accepting the article for publication, acknowledges that the US government retains a nonexclusive, paid-up, irrevocable, worldwide license to publish or reproduce the published form of this manuscript, or allow others to do so, for US government purposes. DOE will provide public access to these results of federally sponsored research in accordance with the DOE Public Access Plan (https://www.energy.gov/doe-public-access-plan).

† leey1@ornl.gov

Content from this work may be used under the terms of the CC BY 4.0 licence (© 2022). Any distribution of this work must maintain attribution to the author(s), title of the work, publisher, and DOI.

ISBN: 978-3-95450-261-5 ISSN: 2673-7000 doi: 10.18429/JACoW-NAPAC2025-THP070

SIMULATION OF THE THERMOELECTRIC EFFECT IN A MULTI-METALLIC SUPERCONDUCTING CAVITY *

N. K. Raut†, N. Stilin, J. Vennekate, S. Wang, G. Ciovati
Jefferson Lab, Newport News, VA, USA

Abstract

Superconducting radio-frequency accelerating cavities made with different material layers, such as copper, Nb or Nb_3Sn, are susceptible to thermoelectric effects due to differences in Seebeck coefficients between the metals. A temperature gradient across the surfaces can drive thermoelectric currents, which may impact the cavity performance. A layered Cu/Nb/Nb_3Sn single-cell cavity was tested with cryocoolers in 2022. Three heaters were mounted on the cavity surface at different locations and three single-axis cryogenic fluxgate magnetometers were attached close to the cavity equator. A linear increase in the magnetic field was measured while increasing the heaters' power. The cavity setup was analysed with COMSOL and the results showed a trend similar to that observed in the experiment. This contribution details the approach chosen for the simulation and some of the challenges encountered.

INTRODUCTION

Superconducting radio-frequency (SRF) cavities with high quality factor are used in particle accelerators, quantum computing, and the study of fundamental physics [1–4]. Niobium is the primary material of choice for these SRF cavities. Niobium-tin (Nb_3Sn) coated cavities have demonstrated comparable performance at higher cryogenic temperatures [5]. Recently, conduction-cooled SRF cavities have gained attention for industrial applications due to their compact design and cost effectiveness [6].

SRF cavities composed of different material layers, such as copper, Nb, or Nb_3Sn, are prone to thermoelectric effects due to variations in Seebeck coefficients [7]. Temperature gradients across these layers can induce thermoelectric currents that may degrade cavity performance. Figure 1 illustrates the concept of thermoelectric current generation in a multi-layered structure. A temperature gradient across materials with different Seebeck coefficients generates a potential difference, which in turn drives a thermoelectric current [8]. The equivalent circuit model demonstrates how the total current flow depends on both the temperature gradient and the electrical resistance of each layer.

This study presents a COMSOL Multiphysics simulation of thermoelectric behaviour in a layered conduction-cooled SRF cavity. A detailed comparison between the simulation and experimental results is also provided.

* This material is based upon work supported by the U.S. Department of Energy, Office of Science, Office of Accelerator R&D and Production, Accelerator Stewardship and Accelerator Development Program, and the Office of Nuclear Physics under contract DE-AC05-06OR23177.

† raut@jlab.org

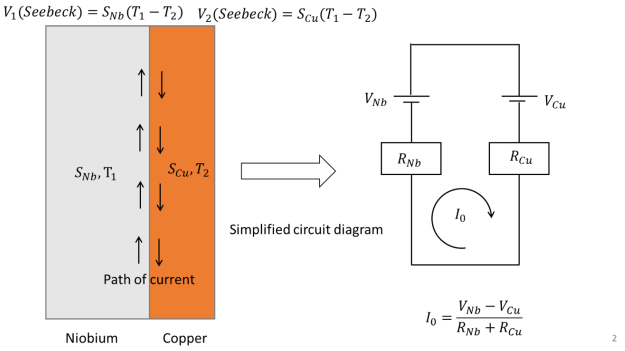


Figure 1: Conceptual illustration of thermoelectric current generation in layered materials with different Seebeck coefficients.

952.6 MHz MULTI-LAYER CAVITY

The experimental and simulated system implement a layered Cu/Nb/Nb_3Sn single-cell 952.6 MHz cavity [6]. Proceeding outward from the cavity interior, the inner surface consists of a ~3 μm thick Nb_3Sn layer, followed by a ~4 mm thick Nb layer and a ~7 mm thick Cu layer.

To enhance thermal conduction, a 19 mm thick OFHC copper ring was formed around the equator and a cooling plate of the same thickness was formed on one of the beam tubes. Commercial closed-cycle refrigerators known as cryocoolers are attached to the cooling plate and at two locations (top and bottom) of the cooling ring, through flexible Cu thermal straps. Figure 2 shows the positions of the heaters and of the three cryogenic single-axis fluxgate magnetometers (FGMs) used in the experiment, which were replicated in the simulation. Two heaters were mounted on the copper ring at the equator, and one on the beam tube section.

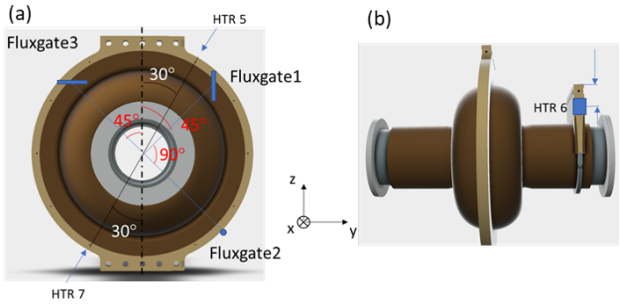


Figure 2: Layout showing the position of the heaters and FGMs used in the experiment (a)-(b).

Content from this work may be used under the terms of the CC BY 4.0 licence (© 2022). Any distribution of this work must maintain attribution to the author(s), title of the work, publisher, and DOI.

ISBN: 978-3-95450-261-5 ISSN: 2673-7000 doi: 10.18429/JACoW-NAPAC2025-THP071

SIMULATIONS OF POSITRON INJECTOR FOR Ce$^+$BAF*

A. Ushakov†,1, J. Benesch[1], J. Grames[1], V. Lizárraga-Rubio[2], S. Ogur[1], R. Rimmer[1], Y. Roblin[1], D. Turner[1], E. Voutier[3], S. Wang[1]
[1]Thomas Jefferson National Accelerator Facility, Newport News, VA, USA
[2]University of Guanajuato, León, Mexico
[3]Paris-Saclay University, CNRS/IN2P3/IJCLab, Orsay, France

Abstract

A baseline concept for a continuous wave (CW) polarized positron injector was developed for the Continuous Electron Beam Accelerator Facility (CEBAF) at Jefferson Lab. This concept is based on the generation of CW longitudinally polarized positrons by a high-current, polarized electron beam (1 mA, 130 – 370 MeV, and 90% longitudinal polarization) that passes through a rotating, water-cooled, tungsten target. The simulation results for the Ce$^+$BAF injector at the Low Energy Recirculator Facility (LERF) are presented, including positron beam generation, capture, energy selection, and acceleration to 123 MeV. The positron yield (or positron current) and longitudinal polarization are calculated considering the longitudinal and transverse CEBAF acceptances (< 1% energy spread, 1.2 mm bunch length and normalized emittance of 100 mm·mrad). The impact of target thickness, drive electron beam energy, and transverse size on positron yield within the required emittance limit is evaluated.

INTRODUCTION

A conceptual design for Ce$^+$BAF 12 GeV beginning with a new e$^+$ injector at the LERF and ending with injection into CEBAF was developed in 2023 [1, 2]. The positron production and polarization transfer from a CW longitudinally polarized electron beam to positrons via bremsstrahlung radiation and e$^+$e$^-$-pair production in a high-Z conversion target, referred as the PEPPo (Polarized Electrons for Polarized Positrons) technique [3], has been adopted to generate positrons. The e$^+$ injector design includes a conversion target, a capture system (based on a focusing solenoid and normal conducting CW capture cavities), an energy selection chicane, an SRF linac, and a bunch compression chicane. This design met the CEBAF physics required positron intensity and polarization requirements (> 50 nA with > 60% polarization, and > 1 µA with low polarization). While the skeleton design was functionally sound, it was built from idealized magnetic and radio-frequency cavity components [2]. To develop the second-generation e$^+$ injector design, start-to-end tracking simulations were performed. The design incorporates detailed absorber and solenoid models at the target [4], as well as a realistic model of an normal-conducting capture cavity [5]. It also uses CEBAF-style beamline magnets and an SRF cryomodule.

The first-generation injector design met CEBAF's requirements for longitudinal acceptance, with an rms momentum spread < 1% and a bunch length < 1.2 mm [2]. However, the normalized emittance of about 1500 mm·mrad at the end of the 123 MeV e$^+$ injector significantly exceeded the CEBAF emittance limit of 100 mm·mrad. The e$^+$ yield (or current) of the updated injector design was calculated within the required emittance limit for a highly polarized mode (> 60% longitudinal polarization) with a drive electron beam energy of 130 MeV. The evolution of main e$^+$ beam parameters along the injector beamline is presented in this paper. The first evaluations aimed at reducing emittance without penalizing the final e$^+$ beam current. These studies explored the e$^+$ yield for different transverse sizes of the electron beam at the target, as well as for different target thicknesses and electron beam energies.

POSITRON INJECTOR MODEL AND SIMULATION RESULTS

The `elegant` code [6] was used to design a e$^+$ injector layout and calculate beam parameters. Figure 1 shows a schematic layout of the e$^+$ injector. The following abbreviations are used for injector components: bucking solenoid (BS), conversion target (T), solenoids of capture system (S1, S2), shielding (SH), normal conducting capture cavity (NC RF), matching sections (MS1, MS2), dipoles (D1–D4), beam collimators (C1–C5), CEBAF superconducting module C75 (SRF Module).

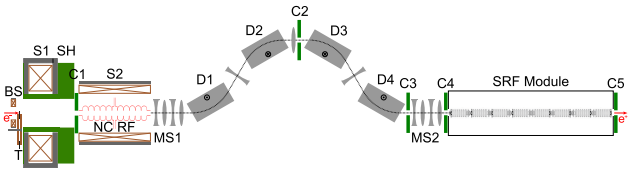


Figure 1: Schematic layout of positron injector.

The electron drive beam used in the simulations below assumes a current of 1 mA at 130 MeV, 90% longitudinal polarization and transverse RMS beam size of 1 mm. The development of an electron source with such a high current and a charge lifetime exceeding 1000 Coulombs is ongoing [7] and it is conducted under a Laboratory Directed Research and Development (LDRD) Program at the JLab. Geant4 [8, 9] has been used to calculate the positron conversion in a 4 mm thick tungsten target. Geant4 data at the

* Work supported by the U.S. Department of Energy, Office of Science, Office of Nuclear Physics under contract DE-AC05-06OR23177. The research described in this paper was conducted under the Laboratory Directed Research and Development Program at Thomas Jefferson National Accelerator Facility for the U.S. Department of Energy.

† ushakov@jlab.org

Content from this work may be used under the terms of the CC BY 4.0 licence (© 2022). Any distribution of this work must maintain attribution to the author(s), title of the work, publisher, and DOI.

ISBN: 978-3-95450-261-5 ISSN: 2673-7000 doi: 10.18429/JACoW-NAPAC2025-THP072

SINGLE-SHOT LONGITUDINAL PHASE-SPACE MEASUREMENT OF THERMIONIC-CATHODE GUN BEAM AT THE APS LINAC*

T. Suzuki†,1, S. Lidia, Michigan State University, East Lansing, MI, USA
K. P. Wootton, Argonne National Laboratory, Lemont, IL, USA
[1]also at Argonne National Laboratory, Lemont, IL, USA

Abstract

Advancements in particle accelerator technology hinge on our ability to precisely measure and understand the behavior of high-brightness beams. Following the installation of the new photo-cathode gun (PCG) laser at the front-end of the Advanced Photon Source (APS) linac, commissioning studies are needed to understand and bring the new PCG beam up to operational standard. In the present work, we present initial measurements characterizing the longitudinal phase-space of the thermionic-cathode gun (TCG) electron beam using a transverse deflecting cavity (TCav) located at the end of the APS linac. Downstream of the TCav, which deflects the beam vertically, lies the B1 horizontal bending magnet and three Chromium Oxide screens placed at three different locations where the beam is intercepted and imaged. Measurements of the TCG beam longitudinal phase-space are discussed and compared to previous measurements of the PCG beam longitudinal phase-space.

INTRODUCTION

Longitudinal phase space studies were initiated to explore the capabilities of the RG2 electron gun in conjunction with the TCav diagnostic system in preparation for PCG comissioning. These studies follow the foundation established by Sun's study in 2021 [1]. The primary goal was to refine the operational parameters (e.g. TCav RF phase, magnet strengths) and assess the beam characteristics under parameter variations.

For these studies, the beam energy selected was 425 MeV. RF conditioning was performed bringing the TCav to approximately 19 MW which correlates to a deflection strength of 3.8 MV [1]. A diagram showing the relevant components of the APS linac is shown in Fig. 1.

INITIAL SETUP

First, the Particle Accumulator Ring (PAR) triple stop is closed to prevent injection into the storage ring. Before making changes, a save compare restore (SCR) file is created. Then, initial measurements establish the image calibration and confirm normal operation of RG2 beam to FL1, FL2, and FL3 (see example in Fig. 2). Before changing B1 current values, the control law feedback for corrector magnets is turned off to avoid railing correctors. Lastly, necessary camera, klystron, and timingResets GUI panels are opened for parameter control.

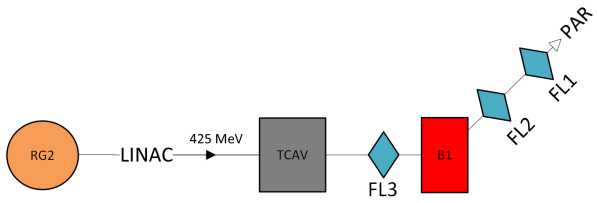


Figure 1: APS linac diagram.

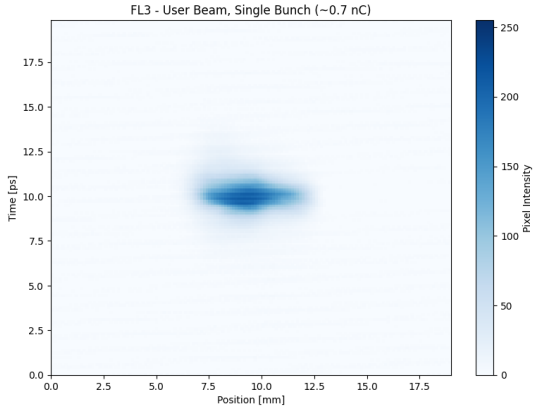


Figure 2: Example of normal TCG beam without TCav deflection showing on FL3.

LATTICE OPTIMIZATION

The APS linac lattice was optimized to minimize the beta functions and maximize the horizontal dispersion at FL1 using elegant [2,3]. The resulting magnet strengths from the simulation in physics units were converted to engineering units (Amps) using a scaling factor derived from the nominal linac lattice parameters. After adjusting the magnets, an image was taken to confirm the beam was minimized and showing on FL1. Note that the lattice optimization was only applied to FL1 measurements.

TCAV TIMING

Under the low level RF GUI panels are RF control and RF measurements panels. Through the RF measurements panel, we can launch the other panels to vary the klystron trigger settings such that the timing of the TCav's deflection

* Work supported by Laboratory Directed Research and Development (LDRD) funding from Argonne National Laboratory, provided by the Director, Office of Science, of the U.S. DOE under Contract No. DE-AC02-06CH11357.

† tsuzuki@anl.gov

Content from this work may be used under the terms of the CC BY 4.0 licence (© 2022). Any distribution of this work must maintain attribution to the author(s), title of the work, publisher, and DOI.

ISBN: 978-3-95450-261-5 ISSN: 2673-7000 doi: 10.18429/JACoW-NAPAC2025-THP074

SLAC MeV ULTRAFAST ELECTRON DIFFRACTION FACILITY UPGRADE PLANS*

R. J. England†, T. Xu, F. Ji, C. J. Duncan, S. P. Weathersby, S. Philip, Y. Liu, X. Cheng, S. Bhattacharyya, T. Wolf, M. F. Lin, C. Hampton, M. Mo, R. Lemons, P. Kramer, M. Othman, E. Nanni, T. Vecchione, A. H. Reid
SLAC National Accelerator Laboratory, Menlo Park, CA, USA

Abstract

Mega-electronvolt ultrafast electron diffraction (MeV-UED) is a complementary tool to X-ray based instruments that has enabled ground-breaking studies in condensed matter physics and chemical science. The SLAC MeV-UED facility uses a state-of-the-art 1.6-cell RF photoinjector to deliver 3 to 4 MeV electrons for a variety of pump-probe studies in solids, liquids, and gases, with over 6600 delivered hours and >87 publications since 2021. To broaden the scientific opportunities, facility expansion and enhanced instrument performance of MeV UED have been heavily requested. We discuss near and long-term plans for upgrade and expansion of MeV-UED, with improvements in user delivery, system performance, data acquisition, and temporal and momentum-space resolution.

INTRODUCTION

The MeV-UED instrument at SLAC began operating in 2014 and has since been developed into a powerful tool for understanding molecular structural dynamics and the coupling of electronic and nuclear motions in a variety of material and chemical systems. In 2019, MeV-UED became a user facility as an instrument of LCLS, and since then MeV-UED has dramatically exceeded performance expectations, both in capability and scientific production. Driven by a broad array of collaborating teams at SLAC and around the world, the MeV-UED instrument has enabled over 71 publications since 2019, the majority in high-impact journals including four publications in *Science* and two in *Nature*, together with four PhDs. With strong DOE support, SLAC's MeV-UED facility has brought about a new paradigm in ultrafast electron diffraction and made significant contributions to the DOE Basic Energy Science mission to understand and ultimately control matter and energy at the electronic, atomic, and molecular levels. However, continuing performance enhancements to the MeV-UED instrument are needed to remain at the scientific and technological forefront [1]. We are developing a phased R&D approach that includes designing a higher brightness electron source for MeV-UED to allow for substantial near-term improvements in time and momentum-space resolution, and setting the stage for future expansion of the facility to include a second user beam line.

* Work supported by U.S. Department of Energy, Office of Science, Office of Basic Energy Sciences under Contract No. DE-AC02-76SF00515 and FWP-10075, 100713, 100940, and 101293

† england@slac.stanford.edu

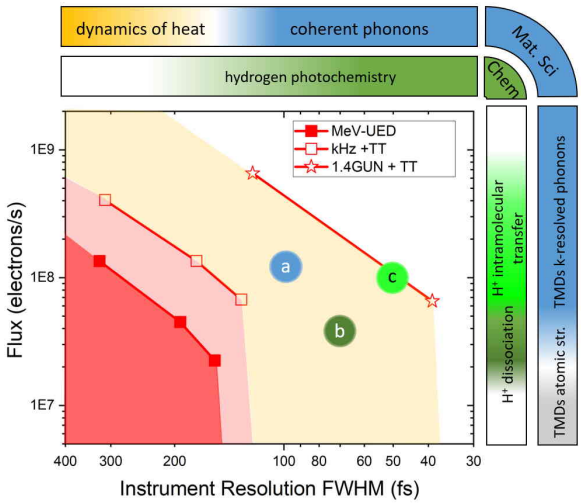


Figure 1: Current and future operational envelopes for the MeV-UED instrument. Solid squares & red region show the current MeV-UED flux/time operation boundary. Open squares & light-red region show the projected performance of MeV-UED with 1 kHz operation and a 1st generation time tool (TT). Open stars & yellow region show the performance of the proposed 1.4 cell gun together with a time tool and pump laser compression. Three specific example science cases are identified: (a) k-resolved transient phonon measurement of mono-layer WSe_2, (b) photodissociation of ammonia, and (c) intramolecular proton transfer in 2-nitrophenol.

SCIENCE DRIVERS AND ENABLERS

The SLAC MeV-UED facility has cultivated a diverse program addressing cutting-edge science across the Basic Energy Sciences portfolio which has capitalized on UED's intrinsic advantages of high cross section, low damage/energy deposition, and its access to both nuclear and electronic atomic distributions. The MeV-UED user workshop held at SLAC in September 2022 and the MeV-UED instrument workshop held in March 2023 identified three key improvements to keep the SLAC MeV-UED at the scientific forefront:

- Improve the instrument sensitivity via increased electron flux and single electron detection.
- Reduce the instrument time resolution below 150 fs towards a goal of 50 fs.
- Lower the transverse beam emittance to enable micro-focused beams and to reach a momentum resolution of $\Delta q = 0.01\ \mathrm{\AA}^{-1}$.

Content from this work may be used under the terms of the CC BY 4.0 licence (© 2022). Any distribution of this work must maintain attribution to the author(s), title of the work, publisher, and DOI.

ISBN: 978-3-95450-261-5 ISSN: 2673-7000 doi: 10.18429/JACoW-NAPAC2025-THP076

SPIN-TRANSPARENT STORAGE RINGS FOR QUANTUM COMPUTING*

R. Suleiman†, Thomas Jefferson National Accelerator Facility, Newport News, VA, USA
M. Grau, Old Dominion University, Norfolk, VA, USA
V. S. Morozov, Oak Ridge National Laboratory, Oak Ridge, TN, USA

Content from this work may be used under the terms of the CC BY 4.0 licence (© 2022). Any distribution of this work must maintain attribution to the author(s), title of the work, publisher, and DOI.

Abstract

Spin-transparent storage rings, in which any spin orientation returns to its original state after a full revolution, offer a promising new platform for quantum computing when combined with ion traps. These rings present several key advantages: they can store large numbers of qubits, enable long quantum coherence times – lasting up to several hours – support long storage lifetimes, and operate at room temperature. Such characteristics make spin-transparent rings an attractive and scalable solution for implementing complex quantum algorithms that require deep circuit depths and high qubit counts. Moreover, the extended coherence time makes this technology well-suited for applications in quantum sensing and quantum memory.

SPIN-TRANSPARENT STORAGE RING

A spin-transparent (ST) storage ring [1] is designed to make the spin dynamics degenerate, that is, the spin transformation in one turn around the ring is an identity transformation. The spin-transparency property of such a ring holds regardless of the precise geometry, provided the ring is flat and the net bending angle over one turn is zero. The most natural ST topology is a figure-8 ring configuration. A conventional magnetic ring has a distinct spin direction $\vec{n}_0$ where the spins of all particles precess around. The rate of this precession is called a spin tune ν. In the conventional magnetic ring, $\vec{n}_0$ is in the vertical direction. All the spins precess about the vertical magnetic fields of the bending dipoles. Since the spins precess about magnetic field $G\gamma$ times faster than momentum, where G is the particle's anomalous gyro-magnetic ratio and γ is the relativistic factor, the spin makes $G\gamma$ revolutions about the vertical direction in one particle turn around a conventional circular ring ($\phi = G\gamma \oint d\theta = 2\pi G\gamma$ and $\nu = G\gamma$).

The spin components perpendicular to $\vec{n}_0$ decohere in the conventional ring. The main cause of this decoherence is the spread in ν due to the spread in the particle energies $\Delta\gamma$, which is always present in a particle beam: $\Delta\nu = G\Delta\gamma$. For practical beam parameters, total polarization decoherence occurs in several thousand turns.

The ST ring configuration offers a universal solution to this decoherence problem. Clearly, since the bending angle $\int d\theta$ in one turn is zero, the spin rotation in one turn is also identically zero, independent of the particle energy ($\phi = G\gamma \oint d\theta = 0$). For a particle of any given energy, the spin rotation in one arc is completely compensated by an equal but opposite rotation in the other arc. This compensation mechanism is analogous to the spin-echo effect observed in NMR, where opposing spin rotations cancel out over a cycle.

In an ideal ST ring, any initial spin orientation remains unchanged after one complete revolution around the ring. This means the spin state is preserved from turn to turn, regardless of its initial direction – effectively "freezing" the spin configuration. However, in real-world rings, several effects lead to deviations from this ideal behavior. The primary source of deviation arises from imperfections in the ring, which distort the actual closed orbit relative to the ideal design orbit. A secondary source of deviation comes from particle betatron and synchrotron oscillations about the closed orbit. These oscillations influence on spin dynamics is of higher order compared to the dominant effect from closed orbit distortions.

In the context of closed-orbit distortion, vertical orbit distortion is of primary concern because it leads to a net spin rotation over one full turn around the ring. This vertical distortion is mainly caused by misalignments of vertical quadrupole magnets and the roll of dipole magnets. The sensitivity of the spin to such errors can be effectively evaluated using the spin response function formalism for ST rings [2]. This effect has been investigated particularly in the context of GeV rings. Both theoretical analysis and simulations have shown that the imperfection spin effect can be measured and mitigated using a local 3D spin corrector, consisting of weak magnetic elements [3]. The implementation of such compensation measures, combined with precise control of alignment errors, is essential for achieving the required spin coherence time.

The strengths of ST ring technology include its exceptionally long coherence times – lasting several hours – and its capacity to store a large number of particles. To scale beyond the current maximum number of stored particles, one possible approach is the use of multiple rings.

QUANTUM COMPUTING

Quantum computers [4] have the potential to make significant impact in the fields of cryptography [5], machine learning [6], and pharmacology [7] owing to their ability to execute critical algorithms with dramatically increased computational efficiency compared to classical systems. A wide range of physical platforms are currently under development for quantum computation, spanning much of modern physics. However, it remains uncertain which technology

* This work is supported by the U.S. Department of Energy, Office of Science, Office of Nuclear Physics under contract DE-AC05-06OR23177 and by UT- Battelle, LLC, under contract DE-AC05-00OR22725.This research described was conducted under the Laboratory Directed Research and Development Program at Thomas Jefferson National Accelerator Facility for the U.S. Department of Energy.

† suleiman@jlab.org

ISBN: 978-3-95450-261-5 ISSN: 2673-7000 doi: 10.18429/JACoW-NAPAC2025-THP077

STATUS OF MICROBEAM LINATRON™ (MBL) PRODUCT LINE DEVELOPMENT AT VAREX IMAGING CORPORATION

A.V. Mishin†,1, A. Anderton[1], R. LaFave[2], S. Proskin[1]
[1]Varex Imaging Corporation, Salt Lake City, UT, USA
[2]Varex Imaging Corporation, Las Vegas, NV, USA

Content from this work may be used under the terms of the CC BY 4.0 licence (© 2022). Any distribution of this work must maintain attribution to the author(s), title of the work, publisher, and DOI.

Abstract

The High Energy Systems (HES) group at Varex Imaging Corporation (Varex) introduced a new concept and design for Accelerator Beam Centerline (ABC) (patent pending), which can be used on compact commercial electron linear accelerators in the 1-20 MeV energy range, delivering substantially reduced focal spot, for example, less than 0.5 mm focal spot on a beam stopping target, thus improving imaging qualities with the produced Bremsstrahlung. The first 6 MeV prototype tests have been completed successfully, and the work continues to build and test a 3 MeV and 9 MeV ABC prototypes. These linac systems will be marketed under the brand name MicroBeam LINATRON™ (MBL) series. The design and experimental data obtained to date are presented.

INTRODUCTION

Varex Imaging Corporation (Varex), based in Salt Lake City, Utah, is a leading innovator, developer, and manufacturer of X-ray imaging component solutions. Varex's Security and Industrial Products (SIP) business manufactures high-energy linear accelerators (LINACs) and has created a design and production line for independently developed ABCs, which are now produced in Salt Lake City. The HES group in Salt Lake City and Las Vegas has been leading the development and has been instrumental in advancing this technology. Varex is now shipping prototypes of most of the models and in the process of moving models to production [1]. Along with replacing the previous linac models, new ABCs and LINACs are under development [2, 3]. As a part of this innovation, we developed a new design and tuning method (patent pending) that can reliably produce small, true Gaussian focal spots with Full Width Half Max (FWHM) of less than 600 μm without any external magnetics. The newly obtained small focal spots have the potential to provide a better image than the focal spots obtained in most standard structures. In addition, the spots are normally measured by FWHM parameter, a true spot size measured at the base of its profile for non-Gaussian profile is much larger than that for a Gaussian spot. We found only a few publications with enough details, where a 950 keV linac with a small spot under 0.6 mm was described, however, it seemed to utilize a magnetic system, perhaps quadrupoles. Some other information we found which would not offer any substantial details when submillimeter (SUBMM) spots were referenced [4, 5].

† andrey.mishin@vareximaging.com

NEW ABC DESIGN

The idea has been nurtured by the presenting author for quite a long time, and it required a different approach to designing and tuning of the RF structure, and to the beam optics design. In previous publications, we enclosed graphs, which present design data for the three linacs at our classic ABC and LINAC parameters – at 3, 6, and 9 MeV, correspondingly [2]. The outside envelope of the 6 MeV submillimeter design is the same as the standard 6 MeV design, either triode (TEG) or diode (DEG) electron gun version, and can replace the standard ABC in any of our systems.

PROTOTYPES AND TEST RESULTS

We selected the first prototype of the submillimeter ABC to operate at 6 MeV, because it is the most popular unit we build, representing over 90% of the standard ABCs at this energy. The first 6 MeV ABC prototype was built and tested at the end of CY2024; it went through extensive testing and demonstrated favourable results. The presenting author mentioned the first results in his monography published in American Journal of Modern Physics in February 2025 year [1].

First MBL Prototype at 6 MeV

It is important to mention, that the standard ABC delivers the best focal spot of 1.0±0.2 mm, while similar third party linacs or their predecessors normally would deliver spots with FWHM of 1.5 mm in diameter. Designing a SUBMM prototype was our next step in spot reduction, following our continuous improvement policy. We have designed, built and high-power tested two 6 MeV submillimeter units for the new MBL product line, both of which delivered less than 600 μm spot size (estimated 350±150 μm in various versions and while operating in a range of parameters). In the first unit, we observed only 12.5% maximum dose rate reduction (700 R/min@1m) sited in a 6 MeV ABC, compared to a standard 6 MeV unit (800 R/min@1m) while operating with 500 μm. The second unit was designed to minimize the spot size, which, in turn reduced the maximum dose to 250 R/min@1m, and for the smallest spot sizes it operated at approximately 50 R/min@1m. This second unit was selected for further testing. During our initial tests, we have completed measurement of the linac key parameters including electron beam energy, the corresponding dose rates, and the spot sizes at these measured parameters. Note the units were equipped with the triode electron guns giving us a couple of options for some parameters adjustments. In addition, the design

ISBN: 978-3-95450-261-5 ISSN: 2673-7000 doi: 10.18429/JACoW-NAPAC2025-THP079

STUDY OF NONLINEAR BEAM DYNAMICS OF AN ASYMMETRIC NSLS-II LATTICE

Minghao Song*, Guimei Wang, Timur Shaftan
Brookhaven National Laboratory, Upton, NY, USA

Abstract

NSLS-II is planning an upgrade to an ultra-low emittance storage ring using a novel lattice concept, the complex bend, composed of combined-function magnets. To evaluate technical challenges and study beam dynamics with complex bend, two bending magnets of existing NSLS-II bare lattice are proposed to be replaced with complex bends, introducing lattice asymmetry. To study the impact of asymmetry on NSLS-II bare lattice, an asymmetric lattice is developed by adjusting quadrupole triplets in the Cell 8 long straight section. This paper presents the modified linear optics, optimization of nonlinear dynamics, and a comparison with the nominal bare lattice. The optimized asymmetric bare lattice is also experimentally measured in the machine, and dynamic aperture measurements are reported.

INTRODUCTION AND MOTIVATION

In recent decades, storage ring light sources have developed rapidly toward achieving lower emittance, allowing for the generation of higher-brightness photon beams. One of the upgrade methods adopted in new-generation storage rings is the use of the complex bend, a novel magnet design first proposed for the NSLS-II upgrade [1]. The complex bend has experienced several stages of development: it started as a series of short dipole magnets interleaved with strong quadrupoles [2], then evolved to a layout where quadrupoles are transversely shifted to create dipole fields [3], and finally reached the current design using permanent magnets with combined magnetic fields, either of the Halbach type or Hybrid type [4, 5]. Using this latest version of the complex bend, low-emittance storage ring designs have been developed for the NSLS-II upgrade at beam energies of 3 GeV [6] and 4 GeV [7].

To assess the potential limitations and technical challenges introduced by the complex bend lattice, we propose a near-term plan to replace the two bending magnets in a single NSLS-II lattice supercell with complex bends. This modification will allow us to study the beam dynamics involving complex bends during regular machine operation. However, the change breaks the symmetry of the current NSLS-II lattice. To minimize this impact on normal operations, it is essential to maintain high injection efficiency and a long beam lifetime in the resulting asymmetric lattice. In this study, an asymmetric NSLS-II lattice was created by adjusting only the quadrupole triplets within the Cell 8 long straight section. This paper presents both simulation and experimental results on the nonlinear beam dynamics of the modified lattice. The results indicate that performance degradation caused by the lattice change can be improved through further optimization. These studies pave the way for the future upgrade of NSLS-II to a complex bend-based lattice.

* msong1@bnl.gov

ASYMMETRIC NSLS-II LATTICE

The NSLS-II storage ring lattice consists of 30 cells, each configured with a double-bend achromat (DBA) lattice structure [8]. The NSLS-II lattice is designed with 15 superperiods, where each superperiod contains one long and one short straight section. In the development of an asymmetric NSLS-II lattice, beta functions were modified within the Cell 8 long straight section by adjusting the strengths of the quadrupole triplets located in that region. The quadrupole strengths before and after the change are presented in Table 1. As a result of this change, the lattice tunes deviated from those of the operational NSLS-II lattice. To restore the desired fractional tunes to $(\nu_x, \nu_y) = (0.22, 0.26)$, slight adjustments were made to the quadrupole triplets in the long straight sections of other cells. Figure 1 shows layout of the developed asymmetric NSLS-II lattice, where the black dashed box indicates the region where the beta functions were modified as a result of changes in the strengths of the quadrupole triplets.

Table 1: Strengths of Quadrupole Triplets Within the Cell 8 Long Straight Section Before and After the Lattice Modification

Quadrupole	K1 [m^{-2}] (before)	K1 [m^{-2}] (after)
QH1G6C07B/ QH1G2C08A	-0.641957315	-1.123111246
QH2G6C07B/ QH2G2C08A	1.436730571	1.632228331
QH3G6C07B/ QH3G2C08A	-1.753550425	-1.721123947

NONLINEAR LATTICE OPTIMIZATION

Due to the modification of the linear optics in the developed asymmetric NSLS-II lattice, the performance of nonlinear beam dynamics has degraded, as illustrated in Fig. 2. Consequently, it is necessary to optimize the asymmetric bare lattice to improve the nonlinear beam dynamics performance, specifically by achieving sufficiently large dynamic aperture (DA) and momentum aperture (MA).

In the DA and MA optimization process, the harmonic sextupoles SH1, SH3, and SH4 located in the long straight section of Cell 8 are optimized independently. The strength of each harmonic sextupole is constrained within the current operational threshold of 40 T/m^2. Optimization is carried

Content from this work may be used under the terms of the CC BY 4.0 licence (© 2022). Any distribution of this work must maintain attribution to the author(s), title of the work, publisher, and DOI.

ISBN: 978-3-95450-261-5 ISSN: 2673-7000 doi: 10.18429/JACoW-NAPAC2025-THP081

THE APS LINAC RF STATION UPGRADE STATUS*

Y. Yang†, N. DiMonte, G. Fystro, D. Meyer, A. Nassiri, T. Smith, Y. Sun, S. G. Wang
Advanced Photon Source, Argonne National Lab, Lemont, IL, USA

Content from this work may be used under the terms of the CC BY 4.0 licence (© 2022). Any distribution of this work must maintain attribution to the author(s), title of the work, publisher, and DOI.

Abstract

The Advanced Photon Source (APS) linac has reliably delivered high-quality electron beams for over 30 years. To support the APS upgrade and ensure continued operation, a major refurbishment is underway. As part of this project, two of the linac's five operating radio frequency (RF) stations have been upgraded with solid-state modulator-powered klystrons and new digital low-level radio frequency (LLRF) systems. This upgrade has notably improved the linac's performance. This paper summarizes these improvements and describes our next plans.

INTRODUCTION

The Advanced Photon Source (APS) upgrade is demonstrating remarkable success, with the newly installed storage ring meeting its design specifications and setting a new record for electron beam emission [1]. These achievements mark a significant milestone in advancing the capabilities of the APS for cutting-edge scientific research.

To support the upgraded APS, the linear accelerator (linac) must deliver higher energy and maintain exceptional reliability [2]. However, many components of the existing APS linac have become outdated or obsolete. To address these challenges, a comprehensive refurbishment project is currently underway. This initiative aims to enhance the linac's performance and ensure greater stability, aligning with the demands of the upgraded APS.

The refurbishment project [3] includes several critical areas.

- **RF System Upgrade** upgrading RF stations to 50 MW capacity using new klystrons , solid-state modulators, and digital low level rf controls, enabling the linac to achieve higher energy and better stability [4].
- **RF guns development and installation** New RF guns were designed, tested and installed to replace the deteriorating Gen-III guns [5].
- **Magnet Power Supply Replacement** Replacing aging power supplies to ensure consistent and precise operation.
- **Timing System** Upgrading the timing system for better synchronization and control accuracy.

RF STATION UPGRADE

As shown in Fig. 1, a new RF station is developed to replace the old ones in the APS linac gallery. This involves replacing PFN-type modulators with Scandinova K400 solid-state modulators. In addition, Cannon E3712 klystrons, which are capable of generating a peak power of 60 MW, are installed to replace the TH2128 klystrons. The obsolete analog LLRF systems are being replaced with state-of-the-art Libera Digital LLRF systems [6].

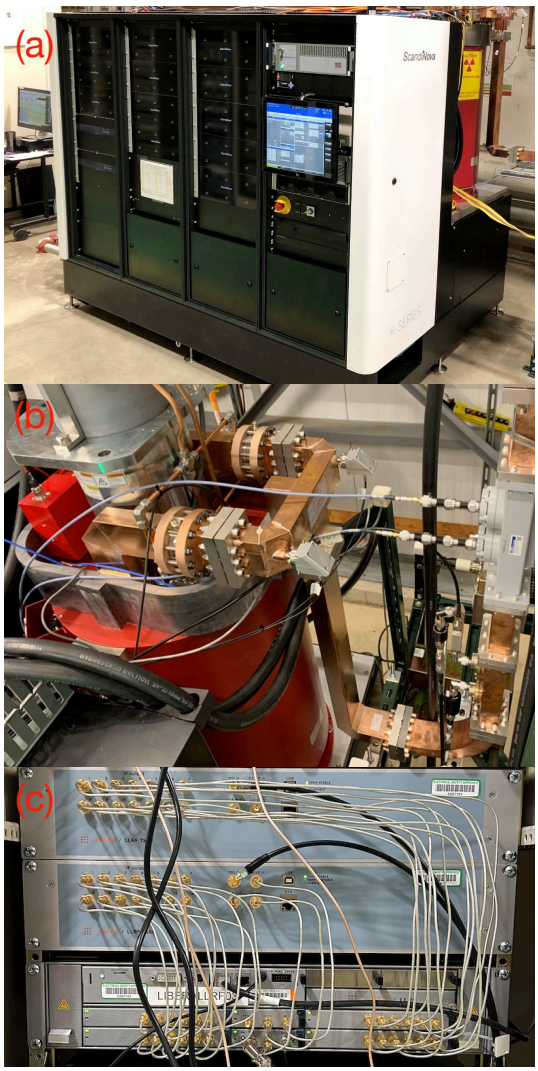


Figure 1: The New RF station consists of (a) Scandinova K400 modulator (b) Cannon E3712 klystron and (c) Libera DLLRF system.

The APS linac setup is illustrated in Fig. 2. The electron beam is generated by one of two thermionic RF guns and is subsequently accelerated through three sectors of S-band accelerators, L2, L4 and L5. Each sector consists of four accelerating structures. The linac is powered by six RF stations, designated K1 through K6, with five stations (K1 through K5) currently in full operational mode. The RF stations K2, K4, and K5 power the linac sectors L2, L4, and L5 through SLED power compressors. K1 powers the

* Work supported by U.S. Department of Energy, Office of Science, Office of Basic Energy Sciences, under Contract No. DE-AC02-06CH11357.
† yaweiyang@anl.gov

ISBN: 978-3-95450-261-5 ISSN: 2673-7000 doi: 10.18429/JACoW-NAPAC2025-THP084

THE POTENTIAL HIGH ORDERS OF VERTICAL ELECTRIC FIELD SYSTEMATIC EFFECT DUE TO HYPERBOLIC/ELLIPTICAL DEFORMED ELECTRODE PLATES IN THE PROTON-EDM RING

J. Lee, Stony Brook University, Stony Brook, NY, USA
B. Dhital, H. Huang, W. Morse, BNL, Upton, NY, USA
Y. Semertzidis, KAIST, Daejeon, Republic of Korea

Abstract

To achieve high precision in a storage ring experiment, it is essential to eliminate field errors up to a certain order to ensure they do not contribute to systematic effect to the experiment. In this study, we modeled electrode plates of electrostatic deflector with hyperbolic/elliptical shape deformation schemes. We analyzed the resulting beam dynamics and spin effects caused by these higher-order electric field errors and explored the potential systematic effects introduced by such deformed electrostatic deflectors within the proton Electric Dipole Moment (pEDM) Symmetric-Hybrid ring design.

INTRODUCTION

The non-magic electric field terms in pEDM physics are described by the following equation:

$$\frac{d\vec{S}}{dt} = \frac{q}{mc\beta^2\gamma}(\vec{\beta} \times \vec{E})_{\parallel} \times \vec{S} \tag{1}$$

where the subscript $\parallel$ denotes the horizontal projection of a vector.

For a pEDM beam in longitudinal polarization mode, these terms can be expanded into two terms as:

$$\left|\frac{dS_y}{dt}\right| = \frac{q}{mc\beta^2\gamma}\beta_y E_z S_z \tag{2a}$$

$$\left|\frac{dS_y}{dt}\right| = \frac{q}{mc\beta^2\gamma}\beta_z E_y S_z \tag{2b}$$

In this study, the first term (Eq. (2a)) is negligible, as we assume the electrostatic deflector deforms only in the transverse plane, resulting in a longitudinal electric field $E_z = 0$.

Numerically, based on Eq. (2b), to achieve a spin precession rate of $|dS_y/dt| < 1$ nrad/s, the vertical electric field must satisfy $E_y < 2$ nV/m.

The systematic effects of the vertical electric field E_y, arising from dipole and quadrupole forms, have been investigated in Refs. [1, 2]. Additionally, Ref. [3] provides a brief analysis of systematic effects due to tilted electrode plates, considering various roll-angle misalignments while assuming perfectly flat electrode plates. This study focuses on modeling the deformation of the electrostatic deflector (bent electrode plates) that induces the vertical electric field E_y systematic effect. The geometric configurations of these deformations are illustrated in Fig. 1.

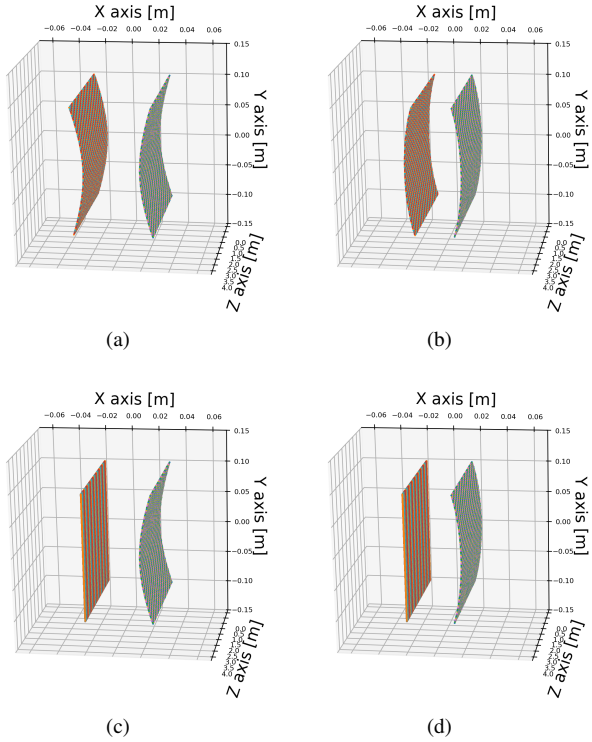


Figure 1: The hyperbolic/elliptical deformed electrode plates of electrostatic deflector in 3D view. (a-b). Double plates deformed; (c-d) Single plate deformed.

HYPERBOLIC CYLINDER SHAPE DEFORMATION

In this study, we model the deformation of an electrostatic deflector, assuming that the two electrode plates deform only in the transverse plane, following a hyperbolic shape, while remaining straight along the longitudinal z-direction, resulting in a hyperbolic cylinder geometry.

The elliptic coordinate (A, α, z) is used for this modeling and defined as

$$x = c\cosh A\cos\alpha \tag{3a}$$

$$y = c\sinh A\sin\alpha \tag{3b}$$

$$z = z \tag{3c}$$

where A is a nonnegative real number, $\alpha \in [0, \pi]$, and c is a constant related to the focal distance of the hyperbolic geometry.

Content from this work may be used under the terms of the CC BY 4.0 licence (© 2022). Any distribution of this work must maintain attribution to the author(s), title of the work, publisher, and DOI.

ISBN: 978-3-95450-261-5 ISSN: 2673-7000 doi: 10.18429/JACoW-NAPAC2025-THP086

TIME-OF-FLIGHT ENERGY MEASUREMENTS WITH BPMS *

A. Shemyakin†, J. Kuharik, R. Sharankova
Fermilab, Batavia, IL, USA

Content from this work may be used under the terms of the CC BY 4.0 licence (© 2022). Any distribution of this work must maintain attribution to the author(s), title of the work, publisher, and DOI.

Abstract

The energy of a bunched non-relativistic ion beam can be deduced from measuring the beam phases in neighbouring Beam Position Monitors (BPMs). This report discusses implementation of such a procedure at the PIP-II H- linac being constructed at Fermilab. The case when the flight time between BPMs is longer than the period of BPM frequency is considered in more detail. When absolute BPM phase calibration is not available, the BPM phase information can be used to track deviations of the beam energy from the desired value. Such "energy deviation" parameter is operationally implemented at the transfer line between 400 MeV Linac and the Booster, and its analog is expected to be used in the transfer line from PIP-II as well.

INTRODUCTION

The PIP-II linac being constructed at Fermilab will accelerate H- ions up to 800 MeV [1]. At this energy, the ions are not highly relativistic, $\gamma = 1.85$, where $\gamma = \left(1 - \frac{v^2}{c^2}\right)^{-\frac{1}{2}}$, v is the ion velocity, and c is the speed of light. In this case, the beam energy can be calculated by measuring the flight time between BPMs in drift space. Such technique, commonly referred to as Time-of-Flight (ToF) measurement, is widely used in ion accelerators (see, for example, Ref. [2]). Typically, the BPMs report the phase offset of the bunch centroids with respect to an RF reference. For absolute energy measurements, the delays in cables and electronics need to be calibrated, as it is planned for PIP-II. If such calibration is not available but the drifts in the delays are low enough, one can use the BPM phase signals to track deviations of the beam energy from a reference. This method is implemented at Fermilab's transfer line between Linac and Booster.

ABSOLUTE ENERGY MEASUREMENTS

The PIP-II linac design includes an instrumentation RF reference line along the linac (similar to [2], [3]) that allows absolute phase calibration of BPMs. For the ToF measurement, one or several RF cavities are turned off creating a drift space in the longitudinal plane, and BPM phase signals are measured. In most cases at PIP-II, the flight time is larger than the BPM RF period:

$$2\pi f \frac{L_1}{v} = \Delta\varphi_1 + N_1 2\pi, \quad (1)$$

where $\Delta\varphi_1$ is the fractional phase difference between the BPM phases, L_1 is the distance between the BPMs, f is the BPM frequency (162.5 MHz for PIP-II), and N_1 is the integer number of periods. A procedure that includes detection of the pulse fronts to eliminate the uncertainty with N_1 is being discussed but has not been implemented.

The uncertainty in N_1 corresponds to a large uncertainty in the kinetic energy. As an example, Table 1 shows the relative energy error $\Delta E_k/E_k$ associated with assumption of N_1 greater by 1 than the N_1 actual value for the first two BPMs in the beginning of each PIP-II linac section. The uncertainty is resolved if the initial energy is known a priori with accuracy better than 10%.

Table 1: Energy Uncertainties and Energy Errors

BPM location (section)	Initial E_k (MeV)	$\Delta E_k/E_k$ (%)	$\delta E_k/E_k$ (%)
MEBT	2.1	22.7	0.08
HWR	2.1	28.2	0.10
SSR1	10.3	32.8	0.12
SSR2	32	32.7	0.12
LB	177.6	29.0	0.11
HB	516	34.2	0.14
Linac energy	800	41.7	0.19

The uncertainty can be resolved without assumptions about the energy if three BPMs are available in the drift space, with some restrictions on the distances L_1 and L_2 between neighboring BPMs. Similar to Eq. (1),

$$2\pi f \frac{L_2}{v} = \Delta\varphi_2 + N_2 2\pi. \quad (2)$$

From Eq. (1) and Eq.(2),

$$N_2 = N_1 \frac{L_2}{L_1} + \frac{1}{2\pi}\left(\Delta\varphi_1 \frac{L_2}{L_1} - \Delta\varphi_2\right) \quad (3)$$

To determine the energy, one can use the requirement that both N_1 and N_2 are integer as follows:

1. Calculate for several integers k

$$M_k = k \frac{L_2}{L_1} + \frac{1}{2\pi}\left(\Delta\varphi_1 \frac{L_2}{L_1} - \Delta\varphi_2\right) \quad (4)$$

2. Calculate the fractional part of M_k

$$R_k = |M_k - integer[M_k]| \quad (5)$$

3. Choose k^* that gives the minimum of R_k since N_2 must be an integer. For the ideal measurement, R_{k^*} is zero, and $N_1 = k^*$.
4. Calculate the velocity from Eq.(1)

$$v = \frac{2\pi f L_1}{\Delta\varphi_1 + 2\pi N_1} \quad (6)$$

and then the kinetic energy $E_k = (\gamma - 1)Mc^2$, where M is the ion mass.

For demonstration purposes, the procedure was simulated at the transition between SSR1-2 and SSR2-1 cryomodules. To create a drift space, the last SSR1-2 cavity and the first two SSR2-1 cavities are turned off, and distances between consecutive BPMs are L_1 = 1.785 m, and L_2 = 2.25 m. The values of fractional phases differences

* This work was produced by FermiForward Discovery Group, LLC under Contract No. 89243024CSC000002 with the U.S. Department of Energy, Office of Science, Office of High Energy Physics.
† Email address: shemyakin@fnal.gov

ISBN: 978-3-95450-261-5 ISSN: 2673-7000 doi: 10.18429/JACoW-NAPAC2025-THP089

TRAVELING-WAVE CHOPPER STRUCTURES FOR LANSCE MODIFICATION PROJECT

S. S. Kurennoy, Los Alamos National Laboratory, Los Alamos, NM, USA

Content from this work may be used under the terms of the CC BY 4.0 licence (© 2022). Any distribution of this work must maintain attribution to the author(s), title of the work, publisher, and DOI.

Abstract

The Los Alamos Neutron Science Center (LANSCE) accelerator complex delivers both protons and negative hydrogen ions with various beam time patterns simultaneously to multiple users. The LANSCE linac front end is still based on Cockcroft-Walton voltage generators. An upgrade of the front end to a modern, RFQ-based version – a part of the LANSCE Modernization Project (LAMP) – is now in the conceptual design stage. The LAMP will need fast beam choppers both in the low-energy transport (LEBT, 100 keV) before RFQ, and in the medium-energy transport (MEBT, 3 MeV) after RFQ. We use CST modeling to develop fast traveling-wave current structures for LAMP MEBT and LEBT beam choppers. A few structure types: plate-coax helix, meander-folded stripline on high-dielectric-constant substrate, and double-helix – are considered and compared. The structures must provide short rise / fall times of the deflecting electric field (1-ns class in MEBT), while still making possible for the chopper pulse generators to deliver the required voltages at high repetition rates.

INTRODUCTION

The Low Energy Beam Transport (LEBT) chopper creates required beam time structures by chopping out (removing by deflecting from the beam path) unwanted parts of a continuous beam transported in LEBT from the ion source to the RFQ. The unchopped parts of the beam propagate through the LEBT, while the deflected parts are deposited on an absorbing target. The chopper system must turn deflection on and off within a short time interval, because the beam parts within the pulse front and end will be only partially deflected and will form unwanted tails of the beam pulse downstream.

The Medium Energy Beam Transport (MEBT) chopper removes unwanted beam bunches by deflecting them to a target from a bunched beam transported through the MEBT from RFQ to the Drift-Tube Linac (DTL) entrance. The unchopped bunches propagate through the MEBT to DTL, while the deflected bunches are deposited on a target downstream of chopper. Ideally, the system should turn deflection on and off in the time interval between the bunches to prevent partially chopped / deflected bunches.

In both cases the chopper system consists of a deflecting structure, where the beam-deflecting fields are created, and a pulse generator (pulser) that feeds the structure with voltage pulses having a needed time pattern. Required fast switching on/off of chopper deflecting fields can be achieved using traveling slow-wave chopper structures – two plates with voltage pulses of equal amplitude but opposite sign – where the deflecting field pulse propagates along the structure with the same velocity as the beam.

If a beam travels at velocity βc along the z-axis, and its deflection is in the y-direction (transverse to the structure plates), the deflecting Lorentz force per unit charge is $F_y / q = E_y + \beta Z_0 H_x$, where $Z_0 = \sqrt{\mu_0 / \varepsilon_0} = 120\pi\ \Omega$. The maximal deflecting electric field is $E_{max} = V/h$, where $\pm V$ are potentials on two plates and $2h$ is the distance between them. Normalizing the above deflection force to E_{max}, we define the chopper deflection efficiency $\eta = \eta_e - \eta_m$, where $\eta_e = E_y/E_{max}$ is the electric efficiency and $\eta_m = -\beta Z_0 H_x/E_{max}$ is the magnetic reduction [1, 2].

The main chopper parameters - length L, aperture $a = 2h$, and required voltage from pulse generator V – are defined by beam dynamics design. The beam deflection angle α is related to these parameters as follows:

$$\alpha \cong \frac{q}{mc^2\beta^2\gamma}\frac{\eta \Delta V L}{a} \cong \frac{q}{2W}\frac{V_{eff} L}{a}, \qquad (1)$$

where q and m are the charge and mass of beam particles (protons or H^-), $\gamma = (1-\beta^2)^{-1/2}$, η is the structure efficiency defined above, $\Delta V = 2V$ is the voltage between two plates, and $V_{eff} = \eta V$.

The chopper system rise and fall times depend on both system elements – structure and voltage pulse generator. If these elements have the rise / fall times t_s and t_p, correspondingly, the chopper rise / fall times can be estimated as $t_c = (t_s^2 + t_p^2)^{1/2}$. One more effect influences the chopper structure rise / fall time. Even if the voltage on chopper plates is turned on instantaneously, in the regions near the plate ends the fields vary from zero to maximal value – the edge effect. If a beam travels at velocity βc through these edge regions in the structure with aperture a, it effectively experiences field change that is equivalent to rise / fall time $t_e \approx a/\beta c$ [2]. This effect can be noticeable in LEBT, where the beam size is large while the velocity is low.

MEBT CHOPPERS

There are a few fast traveling-wave chopper structures developed since 1980s, see in [1, 2] – strip-coax helix at LANSCE [3], meander-line choppers for SNS [4] and CERN [5], and more recently, dual-helix beam deflector at FNAL [6]. These structures were designed for the proton beam energies 2-3 MeV (except LANSCE – 750 keV) and demonstrated rise / fall times t_s in the range 1 – 4 ns. Complementing them with a fast pulse generator providing high voltage amplitude (> 1 kV), especially at high repetition rate (~MHz in bursts), is more challenging.

The main requirements for LAMP MEBT choppers are defined [7, 8] by the RFQ and DTL RF frequency of 201.25 MHz, which corresponds to RF period 4.97 ns, beam dynamics design [8], and by the required beam time patterns.

ISBN: 978-3-95450-261-5 ISSN: 2673-7000 doi: 10.18429/JACoW-NAPAC2025-THP091

TUNING OF A FORCE-NEUTRAL ADJUSTABLE-PHASE UNDULATOR*

M. Qian†, Y. Piao, J. Xu
Argonne National Laboratory, Lemont, IL, USA

Abstract

We present tuning experiences for trajectory and phase error correction in a hybrid permanent magnet-based adjustable-phase undulator (APU). The APU, which we developed, features a period length of 17.2 mm, an effective field of 0.55 T, a gap of 8.5 mm, and a total length of 2.4 m. This planarly polarized undulator adjusts field intensity through the longitudinal movement of magnet arrays, with mechanically linked additional magnet arrays for force compensation. The focus of this report is on the tuning methods, which our engineering experience demonstrates to be highly effective in optimizing the performance of this type of undulator.

INTRODUCTION

Adjustable-phase undulators (APUs) offer several advantages over traditional adjustable-gap undulator (AGU) designs. By enabling phase tuning through small, low-inertia displacements, APUs allow for much faster spectral or polarization switching, which is especially valuable in time-resolved experiments. Their compact mechanical structure—free from large vertical motions—not only simplifies integration but also enhances robustness. In addition, the reduced number of moving components improves mechanical reliability and long-term stability, while lowering maintenance demands [1].

While most previously constructed APUs have been based on pure permanent magnet designs [2], the Advanced Photon Source (APS) has initiated the development of hybrid-type APUs that incorporate ferromagnetic materials to enhance performance and flexibility. The long-term goal is to demonstrate the feasibility of hosting multiple APU arrays within a highly constrained footprint [3].

APU17.2 (Fig. 1) is the second hybrid-type, permanent magnet-based APU developed at APS, which reuses the magnet arrays from a legacy planar undulator. The original device is of the AGU type with a minimum magnetic gap of 11.5 mm. In the current APU17.2 configuration, the device is designed as an out-of-vacuum system with a fixed magnetic gap of 8.5 mm. It features a period length of 17.2 mm, an effective field of 0.55 T, and a total length of 2.4 m.

To mitigate strong vertical and longitudinal magnetic forces, a force-compensation magnet array was incorporated. This reduced the magnetic force per period from approximately 34 N to about 2 N, significantly lowering the mechanical load and improving stability. The APU17.2 is actuated along a single axis using a servo motor with a resolver for commutation. High-precision position control is achieved by directly servoing the motor with feedback from a linear encoder, providing accurate and repeatable motion across the tuning range. This device has been fabricated and tuned. During its development, new insights were gained—particularly regarding electron trajectory correction and phase error tuning—which are presented in this report.



Figure 1: Photo of APU17.2 during magnetic measurement.

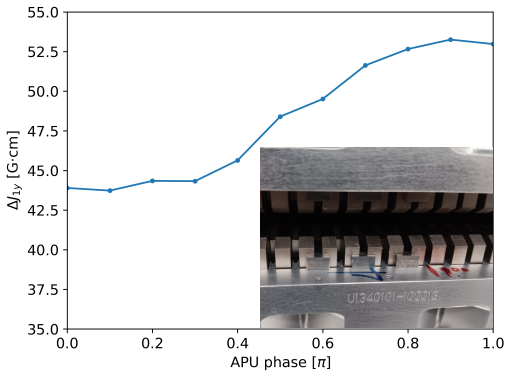


Figure 2: Trajectory signatures of a pair of side shims measured using a long flipping coil. The embedded panel in the bottom right illustrates the side shims attached to the undulator magnet arrays.

TRAJECTORY TUNING

Trajectory straightness is critical for undulator performance, as deviations can degrade the quality of the emitted radiation. In the case of APU17.2, trajectory tuning is accomplished using iron shims, similar to the side shims employed at the APS [4]. We identified a shim geometry that remains stable across all undulator phases without requiring additional measures to secure the shims. The trajectory signatures, defined as the integrated dipole field of the shims, were measured and found to be effective across all APU phases, as shown in Fig. 2. This configuration shows stronger integrated fields at larger APU phases (smaller K), unlike AGUs where shim effects weaken at low K.

* Work supported by the U.S. DOE Office of Science, Office of Basic Energy Sciences, under Contract No. DE-AC02-06CH11357.
† mqian@anl.gov

Content from this work may be used under the terms of the CC BY 4.0 licence (© 2022). Any distribution of this work must maintain attribution to the author(s), title of the work, publisher, and DOI.

ISBN: 978-3-95450-261-5 ISSN: 2673-7000 doi: 10.18429/JACoW-NAPAC2025-THP093

UPDATE ON SEPTUM MAGNET REDESIGN AT LANSCE PROTON STORAGE RING*

H. Xu†, C. Buechler, A. Garcia, E.-H., Huang, G. Johnson, J. W. Lewellen, C. Taylor
Los Alamos National Laboratory, Los Alamos, NM, USA

Abstract

We report the progress of redesigning the septum magnet at the LANSCE Proton Storage Ring (PSR). The septum magnet at the PSR is used for extracting the accumulated 800-MeV proton beams for transport to the target stations. The existing septum magnet uses parallel, planar coils creating a uniform deflecting magnetic field. However, one coil plate co-locates with the septum; the placement results in the coil, witnessing intense radiation dose rates, receiving accumulated damage to the epoxy potting during the PSR operation. The redesigned septum magnet uses a low carbon steel septum, and the coils are positioned farther away from the beam pipes. This placement is expected to reduce the radiation dose rate on the coil pack, and, combined with adoption of a more radiation-resistant potting epoxy, increases the operating lifetimes. The magnet pole tips are refined with shim features to provide a sufficiently wide flat-field region. The mechanical engineering of the yoke components and the supporting structures is underway. Particle tracking simulations of the proton beam deflection in the septum magnet were performed, and the comparison of performance between the existing and the redesigned septum magnets is reported.

INTRODUCTION

At Los Alamos National Laboratory (LANL), the Los Alamos Neutron Science Center (LANSCE) Proton Storage Ring (PSR) accumulates 800-MeV proton bunches to increase the peak current delivered to the experimental target stations. To extract the accumulated proton beam, a set of electrostatic kickers generate a horizontal offset, and then the septum magnet deflects the beam into the extraction beamline.

The septum magnet is also referred to as the RODM01 septum magnet, where RODM represents "Ring Outlet Dipole Magnet." A photo of the RODM01 magnet is shown in Fig. 1 [1]. The beam pipes of the circulating proton beam and of the deflected beam are separated by a 7-mm septum. In Fig. 1, the rectangular beam pipe is for the deflected beam, sandwiched between two planar coils that provide a 0.6-T uniform vertical magnetic field; the beam pipe with a greater vertical dimension is for the circulating beam.

The PSR beam extraction process imposes two major requirements on the septum magnet. First, the deflected beam must witness a uniform magnetic field. Second, the circulating beam, when traveling through the RODM01 magnet, must witness minimal magnetic field. Therefore, the coil geometry shown in Fig. 2 was adopted. The advantages of this coil geometry are that the deflecting magnetic field is very uniform, and that the magnetic field division is very sharp, leading to minimal field leakage into the region of the circulating beam. Meanwhile, there are two major disadvantages. First, the coils are directly adjacent to the beam pipes, where the beam loss, and thus radiation dose rates are at local maxima; second, the coil on one side has to co-locate within the septum, causing the current density to be very high (over 90 A/mm^2). A photo of the coil pair of the RODM01 magnet is provided in Fig. 3.

At LANSCE PSR, the RODM01 coils must be replaced every five to seven years. The damages have been observed on the epoxy potting of the coils, in the form of cracking

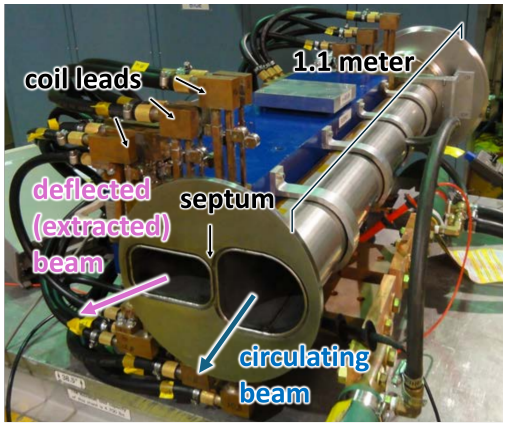


Figure 1: The RODM01 septum magnet used at LANSCE PSR, under magnetic field mapping.

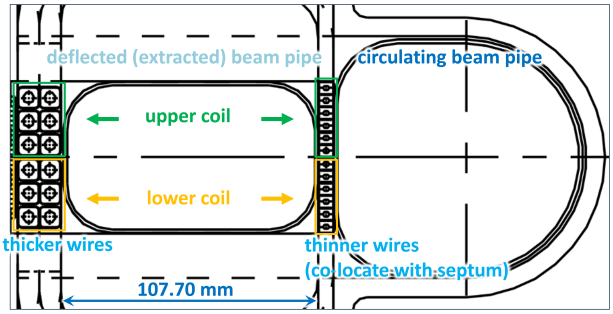


Figure 2: RODM01 coil geometry. Two parallel, planar coils build up a uniform, vertical magnetic field in the beam pipe region for the deflected beam. The upper and the lower sections of the coils on both sides are assembled separately, forming a coil pair.

* This work benefited from the use of the LANSCE accelerator facility. Work was performed under the auspices of the US Department of Energy by Triad National Security under contract 89233218CNA000001.

† haoranxu@lanl.gov

Content from this work may be used under the terms of the CC BY 4.0 licence (© 2022). Any distribution of this work must maintain attribution to the author(s), title of the work, publisher, and DOI.

ISBN: 978-3-95450-261-5 ISSN: 2673-7000 doi: 10.18429/JACoW-NAPAC2025-THP094

UPDATES ON SCIENTIFIC AND R&D HIGHLIGHTS AT SLAC MeV-UED FACILITY *

F. Ji[1†], J. England[1], C. Duncan[1], T. Heinz[2], P. Kramer[1], R. Lemons[1], F. Liu[2], Y. Liu[1], M. Mo[1], S. Philip[1], A. Raja[3], A. Reid[1], X. Shen[1], S. Weathersby[1], J. Xie[4], T. Xu[1], A. Zimmerman[2], Y Zhu[5]
[1]SLAC National Accelerator Laboratory, Menlo Park, CA, USA
[2]Stanford University, Stanford, CA, USA
[3]Lawrence Berkeley National Laboratory, Berkeley, CA, USA
[4]University of California, Berkeley, CA, USA
[5]Brookhaven National Laboratory, Upton, New York, USA

Content from this work may be used under the terms of the CC BY 4.0 licence (© 2022). Any distribution of this work must maintain attribution to the author(s), title of the work, publisher, and DOI.

Abstract

Ultrafast electron diffraction using MeV energy beams (MeV-UED) has enabled unprecedented scientific opportunities in the study of ultrafast structural dynamics in a variety of gas, liquid and solid-state systems. The SLAC MeV-UED program began in 2014 and became an LCLS user facility in 2019. This work will review recent R&D efforts for enhancing the resolution, flux and electron detection of the MeV-UED instrument. Additionally, the integration of Al/ML techniques is being explored to optimize facility operations and accelerate scientific discovery. In all, these will open new avenues for explorations in key areas of ultrafast science.

INTRODUCTION

Ultrafast electron diffraction using MeV energy beams (MeV-UED) has led to a new paradigm in ultrafast electron scattering [1]. MeV electron probes lead to atomic spatial resolution together with sub-picosecond temporal resolution [2]. Furthermore, MeV electrons can provide pure kinetic scattering signals for samples with a given thickness, which makes it possible to achieve quantitative understanding of observables via physics-based modeling. The SLAC MeV-UED program starts in 2014 and became an LCLS-II user facility since 2019. MeV-UED has enabled unprecedented scientific opportunities in ultrafast structural dynamics, including observations of bond dissociation, coherent ground state wavepacket motion after electrocyclic ring-opening, simultaneous observation of electronic and nuclear structure changes in a molecule undergoing non-adiabatic dynamics, hydrogen bond strengthening in liquid water, and phase switches of materials with exotic functional properties. MeV-UED will continue to complement LCLS-II X-ray science and remain the promise of enabling scientific opportunities in key areas. To maximize the science impact of UED, improvements in temporal/spatial resolutions, electron flux and electron detection are required. Figure 1(c) illustrates the current and future performance envelope for the MeV-UED instrument. The solid squares show points on the current MeV-UED flux/temporal resolution boundary where higher electron flux can be achieved at the expense of temporal resolution. The open squares show the expected performance of MeV-UED following undergoing R&D efforts (upgrade to 1 kHz operation, 1st generation time-tool and laser pump dispersion compensation). Open stars show the performance of a proposed high brightness gun [3] together with an arrival time monitor and hollow-fiber pump laser compression. By pushing the flux/temporal resolution boundary, novel science cases will be enabled. These include resolving structural and electronic dynamics during photo-dissociation events, the study of intramolecular Proton transfer & migration dynamics, investigating momentum-resolved transient phonon populations in thin mono-layer materials, as well as exploring energy pathways and structure-function relationships in hetero-structure based low dimensional systems [4].

In this work, we review recent R&D efforts at the SLAC MeV-UED facility, including the kHz repetition rate upgrade, the adoption of the LCLS ePix10k as a single-electron detector, as well as the integration of AI/ML techniques to optimize operations and accelerate discovery. Collectively, these developments will enhance instrument resolution, increase electron flux, and improve detection efficiency, paving the way for explorations in key areas of ultrafast science.

kHz REPETITION RATE UPGRADE

UED experiment requires high signal-to-noise ratio (SNR) for extraction of weak signals and resolving fs structural dynamics in different systems. Increasing the repetition-rate is the most straightforward way to improve SNR within the same integration time. Practically, choice of repetition rate requires considerations in multiple limiting factors including RF electron source, available laser energy and sample relaxation times. Since 2019, the SLAC MeV-UED facility has routinely operated at 360 Hz for user experiments. Upgrade to 1080 Hz pump-probe data acquisition rate is one of the major effort that has been conducted to further improve the SNR. To this end, both laser and RF systems were improved: an upgrade of the infrared laser system (Ti:Sapphire Coherent Legend Elite Duo + SPA) was completed in April 2021 to accommodate kHz pump&probe experiments. A ScandiNova RF Klystron (Figure 1(d)) has been installed and conditioned

* Work supported by U.S. Department of Energy Office of Science, Basic Energy Sciences under Contract No. DE-AC02-76SF00515, and FWP-10075, 100713, 100940, and 101293
† Corresponding author: fuhaoji@slac.stanford.edu

ISBN: 978-3-95450-261-5 ISSN: 2673-7000 doi: 10.18429/JACoW-NAPAC2025-THP095

USER RESEARCH AT BNL'S ACCELERATOR TEST FACILITY*

I. Pogorelsky[1,†], M. Babzien[1], M. Polyanskiy[1], D. Choge[1], M. Fedurin[1], W. Li[1], Y. Sakai[1], N. Vafaei-Najafabadi[1,2], S. Biedron[3,4], M. A. Palmer[1]
[1]Brookhaven National Laboratory, Upton, USA
[2]Stony Brook University, Stony Brook, USA
[3]Element Aero, Chicago, USA
[4]Center for Bright Beams, Ithaca, USA

Content from this work may be used under the terms of the CC BY 4.0 licence (© 2022). Any distribution of this work must maintain attribution to the author(s), title of the work, publisher, and DOI.

Abstract

The Accelerator Test Facility (ATF) at Brookhaven National Laboratory (BNL) is a U.S. Department of Energy (DOE) Office of Science user facility, equipped with a high-brightness RF electron LINAC, a femtosecond Ti:sapphire laser, and a multi-terawatt long-wave infrared (LWIR) laser. This unique suite of tools, capable of both synchronized and independent operation, enables transformative research across a wide range of disciplines. This paper outlines the advanced capabilities available at ATF and highlights present and emerging opportunities for user collaboration.

INTRODUCTION

The ATF [1] has supported user experiments for over 30 years and has been formally recognized as one of the DOE Office of Science's proposal-driven, peer-reviewed user facilities since 2015 [2]. It serves as a flagship facility under the Accelerator Stewardship program and, as of 2024, is also a member of the BeamNetUS network [3].

ATF delivers 20–75 MeV electron beams from a linear accelerator (LINAC) initiated by a high-brightness RF photocathode gun. Typical beam parameters include a normalized emittance of 1 μm, energy spread of 0.1%, charge around 1 nC, and bunch durations ranging from 200 fs to 10 ps, including multi-bunch operation.

The ATF's 5-TW, 9.2-μm LWIR laser is a one-of-a-kind system that has pioneered several technological breakthroughs, such as the first use of chirped-pulse amplification in a gas laser, multi-isotope CO_2 laser amplification, and a solid-state laser front end. Together with the co-located electron LINAC and lower-power NIR lasers, these resources provide a powerful platform for frontier research in laser-plasma acceleration, high-brightness X-ray sources via inverse Compton scattering (ICS), and other advanced studies. Some of these opportunities are illustrated in this paper.

LWIR LASER DEVELOPMENT

LWIR radiation is advantageous for both fundamental and applied science due to its strong ponderomotive interaction with electrons, low critical plasma density, and other favourable wavelength-dependent scaling laws. ATF is extending current laser capabilities from a 5 TW, 2 ps toward the multi-terawatt, sub-picosecond regime. By 2028, the goal is to achieve 15 TW in 500 fs using a 10 mJ OPCPA seed; by 2029, the facility aims for 25 TW in 100 fs using a post-compression stage [4]. These upgrade steps are illustrated by Fig. 1.

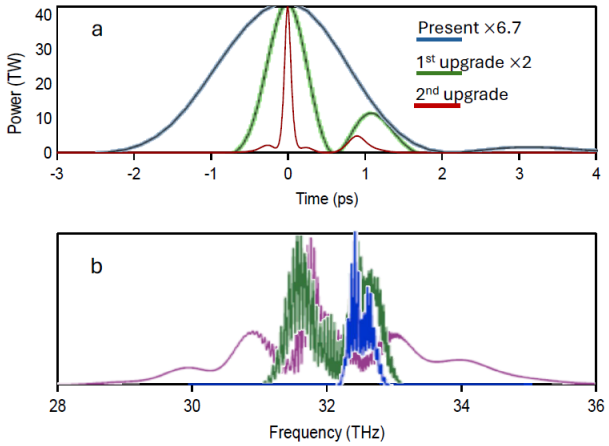


Figure 1: (a) Simulated laser output pulse profiles normalized to the 2nd upgrade's peak power; (b) corresponding normalized output pulse spectra.

USER RESEARCH PROGRAM

A broad range of user experiments are conducted using ATF's laser and electron beams, supported by additional diagnostic and computational tools as detailed on the ATF website [1]. These activities are also summarized in the annual ATF user meetings [5], with the latest held April 29–May 1, 2025 [6].

Combined Laser and Electron Beam Studies

LWIR lasers are particularly suited to particle acceleration due to favourable scaling of electron quiver energy ($\sim\lambda^2$) and critical plasma density ($\sim 1/\lambda^2$) with laser wavelength. In laser wakefield acceleration (LWFA) at low plasma densities ($n_e \approx 10^{16}$ cm^{-3}), the increased trapping volume ($\sim n_e^{-3/2}$) facilitates LWFA regimes where beam qualities approach conventional RF accelerators [7, 8].

Precise *collinear* injection of relativistic electron bunches into plasma wakes is critical: spatial tolerances are on the order of tens of microns. Simulations in Fig. 2 [9] illustrate how misalignment affects energy spread. With co-located LWIR laser and high-brightness electron LINAC, the ATF is uniquely positioned for this kind of

* Work supported by the U.S. Department of Energy under contract DE-SC0012704. Additional support comes from BNL Laboratory Directed Research and Development grants #20-010 and #21-001 and DOE Program grant B&R #KA2601020. Additional funding provided by the US Department of Energy Accelerator Stewardship Program Grants.
† igor@bnl.gov

ISBN: 978-3-95450-261-5 ISSN: 2673-7000 doi: 10.18429/JACoW-NAPAC2025-THP096

VISUALIZATION TOOLS FOR EGUN SIMULATIONS

K. Casey*, M. Shumail†
SLAC National Accelerator Laboratory, Menlo Park, CA, USA

Abstract

DC electron guns are essential sources of moderate-energy electron beams for both particle accelerators and klystrons. EGUN is one of the simulation software tools employed to design such DC guns. EGUN produces detailed data of electron ray trajectories for a given gun geometry, cathode temperature, bias-voltage, and beam current — whether space-charge limited or not. We use Mathematica and Python for advanced mathematical processing and visualization of the EGUN data. For example, we generate phase-space plots at various longitudinal cross-sections and show the evolution of phase-space parameters along the beam axis. The visualization we generate is much richer than the simple trajectory plots generated by EPLOT software that accompanies EGUN. In this work, we present an example of a practical klystron gun and the results of our post-processing software.

SLAC ELECTRON TRAJECTORY PROGRAM

The SLAC Electron Trajectory Program, also known as EGUN, was last updated in 1979 [1]. Although the software is old, it is reliable. For those reasons, instead of rewriting new software in a more modern language, we wrote code that will run EGUN without requiring the user to program in FORTRAN.

EGUN has a plotting tool, EPLOT, which mirrors the electron gun geometry along the z-axis, showing the electric field lines and the electron trajectories. All of this information is stored in one of six files, each containing unlabeled sections of data. To simplify data access, we create code that automatically extracts and organizes relevant information.

ELECTRON GUN

To validate the accuracy of our code, we used the geometry of a gun currently used for an experiment involving a small linear accelerator [2]. Without access to the original drawings of the Hermosa Electronics Gun (Fig. 1), we had it profiled using a precision metrology tool. With the dimensions, we could begin to use this gun geometry for simulations.

EGUN accepts only circles and straight lines for geometry calculations, so we converted the metrology data into a series of lines and arcs using Mathematica. This processed geometry was then used in the EGUN input.

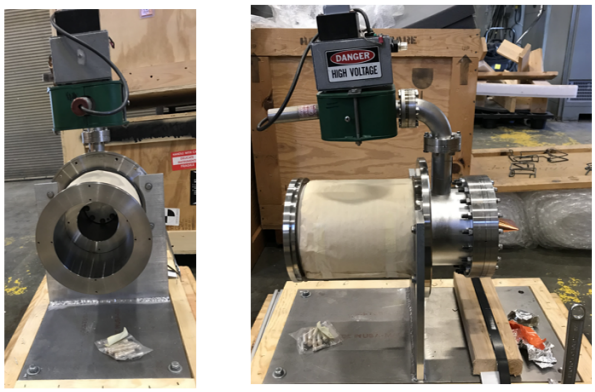


Figure 1: Hermosa Electronics Gun Big, version 7, 3 cm^2 planar cathode.

EGUN vs MATHEMATICA VISUALIZATION

EPLOT outputs the gun geometry, electric field lines, and electron trajectories, with minimal control over display parameters beyond zooming. In contrast, Mathematica allows for fine control of the plotted content, easy export of graphics and data, and automatic labeling of extracted quantities (Fig. 2).

We write functions to extract specific data, enabling quick determination of results such as current saturation without manually combing through files. EGUN also produces data for phase-space parameters at various longitudinal positions, beam size and divergence, and emittance values.

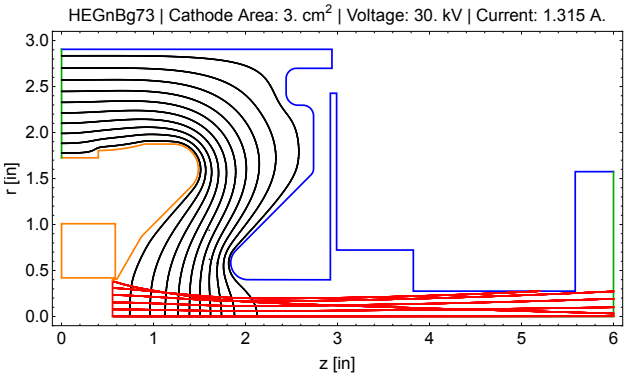


Figure 2: EGUN data of the Hermosa Electronics Gun plotted in Mathematica. The black lines are the electric field, the red lines are the electron trajectory.

* kncasey@usc.edu
† shumail@slac.stanford.edu

Content from this work may be used under the terms of the CC BY 4.0 licence (© 2022). Any distribution of this work must maintain attribution to the author(s), title of the work, publisher, and DOI.

ISBN: 978-3-95450-261-5 ISSN: 2673-7000 doi: 10.18429/JACoW-NAPAC2025-FRAD02

DESIGN OF RING ELECTRON COOLER *

S. Seletskiy†,1, J. Kewisch [1], A. Fedotov [1], Y. Jing [1], D. Kayran[1], J. Unger[2], G. Hoffstaetter[2]
[1]Brookhaven National Laboratory, Upton NY, USA
[2]Cornell University, Ithaca NY, USA

Abstract

Electron cooling at high energy requires large average current in the cooling section (CS), which can be achieved by reusing the same electron beam on many passes through the CS. One of the options to realize this cooling scheme is to use an electron storage ring. In this paper we describe a conceptual design of the Ring Electron Cooler (REC), as a potential future application for the Electron Ion Collider. The REC uses 150MeV electrons to cool protons in hadron ring while electrons themselves are being cooled by radiation damping wigglers installed in electron storage ring. Design of the REC considers electrons' space charge, an effect of proton-electron focusing, a beam-beam scattering in the CS and electrons' intra-beam scattering in the storage ring, as well as other collective effects. In this paper we discuss the status of the REC design and describe multiparametric optimization involved in the design efforts.

INTRODUCTION

Cooling of protons in the Electron Ion Collider (EIC) [1] at top energy ($\gamma = 273$) to counteract the IBS-driven emittance growth will be beneficial to the EIC performance. Electron Cooling [2] can provide such a capability.

Expanding electron cooling to the high energies requires substantial electron current in the cooling section. To relax requirements to an injector, one can reuse the same electron beam on multiple turns. In this paper we consider a multi-turn electron cooling based on the Ring Electron Cooler.

Electron bunches, used in the REC, are stored in a dedicated storage ring, and the same e-bunches are reused for the cooling on multiple turns. The electrons' emittances are preserved during the storage cycle by counteracting heating caused by various scattering mechanisms with radiation damping facilitated by dedicated damping wigglers.

The REC utilizes a non-magnetized RF-based electron cooling, which was successfully applied at LEReC [3-6] during RHIC operation in 2019-2021 runs.

RING ELECTRON COOLER

The Ring Electron Cooler is located in the IR2 region of the EIC Hadron Storage Ring sharing the cooling section with the EIC Low Energy Cooler (LEC) [7].

While the LEC "precools" the protons at the injection energy to the design emittances (Table 1), the REC's preserves the emittances at the collision energy by providing horizontal and longitudinal cooling times of 2 and 3 hours respectively.

* Work supported by Brookhaven Science Associates, LLC under Contract No. DE-SC0012704 with the U.S. Department of Energy
† seletskiy@bnl.gov

REC Layout and Lattice

The REC layout is shown in Fig. 1. The REC lattice is shown in Fig. 2.

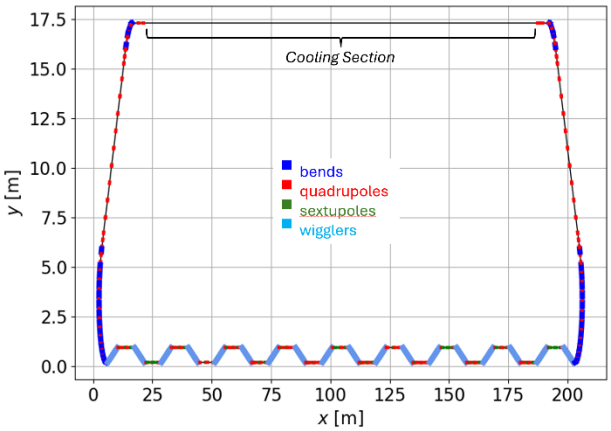


Figure 1: The Ring Electron Cooler layout.

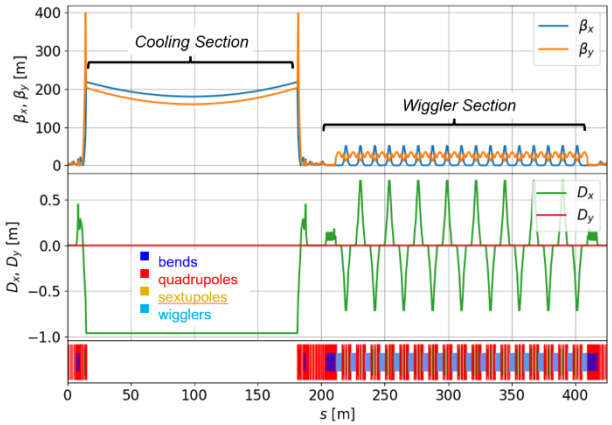


Figure 2: The Ring Electron Cooler lattice.

The REC includes a 170 m long cooling section shielded by several layers of μ-metal. The BPMs and correctors are located every 12 m in the CS.

Opposite to the cooling section there is a wiggler section containing 18 damping wigglers. The wigglers must provide enough radiation cooling of the electron bunches to counteract the effects of the IBS and beam-beam scattering (BBS) of electrons on protons in the CS.

The arcs connecting the wiggler section and the CS contain 10 m long straight sections with adjustable optics suitable for placement of the REC injection and RF systems.

REC Parameters

The REC parameters are listed in Tables 1 and 2.

Content from this work may be used under the terms of the CC BY 4.0 licence (© 2022). Any distribution of this work must maintain attribution to the author(s), title of the work, publisher, and DOI.

ISBN: 978-3-95450-261-5 ISSN: 2673-7000 doi: 10.18429/JACoW-NAPAC2025-FRAD03

CRABBING SCHEMES FOR THE ELECTRON-ION COLLIDER*

Y. Luo†, J. S. Berg, M. Blaskiewicz, C. Montag, S. Nagaitsev, V. Ptitsyn, F. Willeke, D. Xu,
Brookhaven National Laboratory, Upton, NY, USA
Y. Hao, Facility for Rare Isotope Beams, Michigan State University, East Lansing, MI, USA
J. Qiang, Lawrence Berkeley National Laboratory, Berkeley, CA, USA
V. Morozov, Oak Ridge National Laboratory, Oak Ridge, TN, USA

Abstract

The Electron-Ion Collider (EIC), to be constructed at Brookhaven National Laboratory, will collide polarized high-energy electron beams with polarized proton and ion beams, achieving peak luminosities of up to $1 \times 10^{34}\text{cm}^{-2}\text{s}^{-1}$ in the center-of-mass energy range of 20–140 GeV. Crab cavities will be used in both EIC rings to compensate for geometric luminosity loss due to the large crossing angle of 25 mrad at the interaction region. In the baseline design, a local crabbing scheme is adopted for both EIC storage rings, in which crab cavities are installed on both sides of the interaction region, with an ideal horizontal phase advance of 90 degrees between the interaction point and the crab cavities. In this article, we study the feasibility of using a global crabbing scheme and the crab waist scheme for the EIC. In particular, we examine the case in which the crab cavities in the Electron Storage Ring (ESR) are unavailable during early EIC commissioning. In this scenario, the electron beam's beam-beam parameter must be reduced to avoid electron losses during injection.

LOCAL CRABBING SCHEME

For the EIC design [1, 2], the full crossing angle in the interaction region (IR) is 25 mrad. To recover the geometric luminosity loss due to the large crossing angle, we adopt local crabbing scheme with crab cavities on both sides of interaction point (IP) in both HSR and ESR. Figure 1 shows the schematic plot of crabbing scheme for the EIC.

For the local crabbing scheme, the ideal horizontal phase advance between the crab cavities and the interaction point (IP) should be 90 degrees. The crab cavity applies a longitudinal-position-dependent horizontal kick to the particles based on their arrival time at the cavity or, equivalently, their longitudinal displacement from the bunch center. This generates a longitudinally dependent horizontal orbit offset, or crab dispersion, denoted as dx/dz, in the ring. In the local crabbing scheme, two sets of crab cavities placed symmetrically on both sides of the interaction region (IR) create a 180-degree local crab dispersion bump. The required crab dispersion at the IP should equal half the crossing angle, i.e., $dx/dz|_{IP} = -12.5$ mrad. After applying a Lorentz boost transformation into the head-on collision frame, the two bunches effectively collide as if there were no crossing angle.

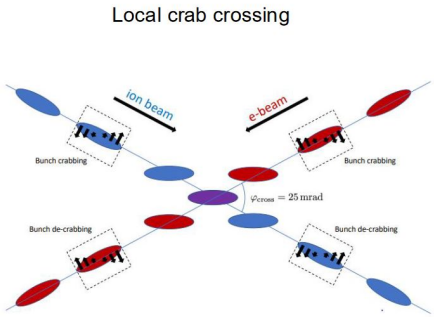


Figure 1: Schematic plot of crossing angle collision with crab cavities in the EIC.

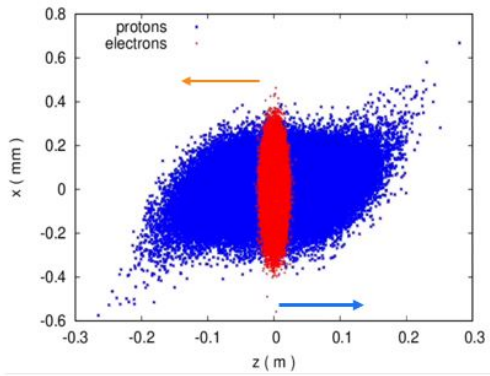


Figure 2: Particle distributions with only 197 MHz crab cavities in the HSR. Here 394 MHz crab cavities are applied in the ESR.

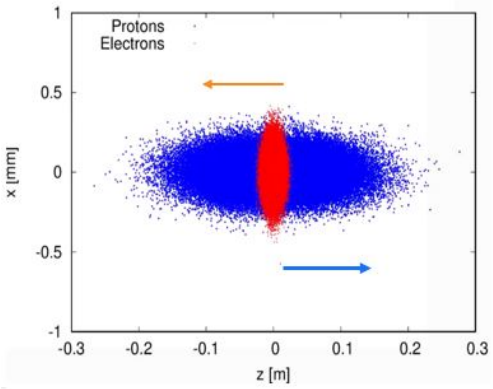


Figure 3: Particle distributions with both 197 MHz and 394 MHz crab cavities in the HSR. Here 394 MHz crab cavities are applied in the ESR.

* Work supported by the U.S. Department of Energy, Office of Science under contracts DE-SC0012704 and DE-AC05-06OR23177

† yluo@bnl.gov

Content from this work may be used under the terms of the CC BY 4.0 licence (© 2022). Any distribution of this work must maintain attribution to the author(s), title of the work, publisher, and DOI.